ISSN 1983-4195

IBRACON

IBRACON Structures and Materials Journal

Revista IBRACON de Estruturas e Materiais

Volume 14, Number 4
August 2021

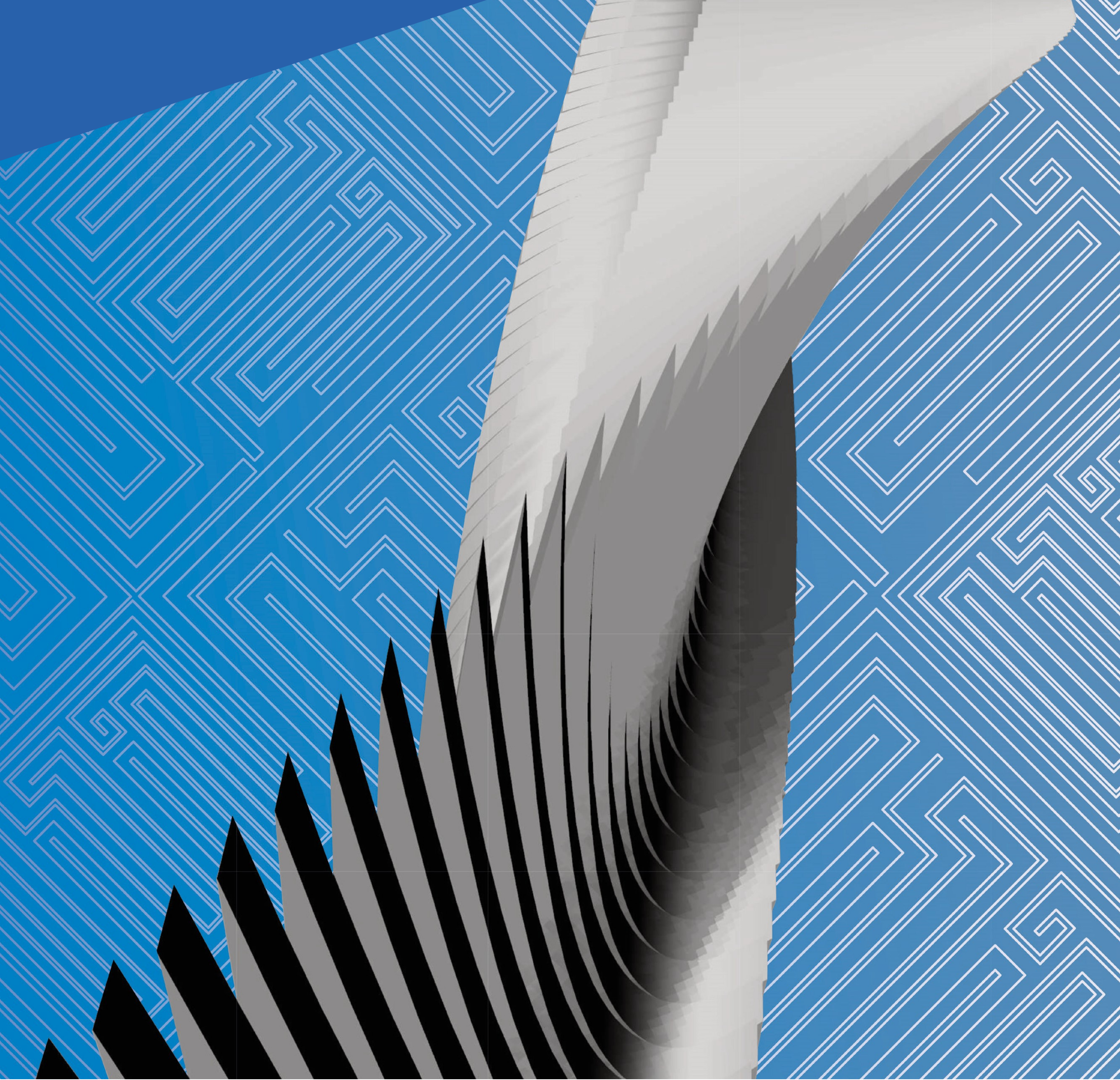

ISSN 1983-4195
Volume 14, Number 4
August 2021

IBRACON Structures and Materials Journal
Revista IBRACON de Estruturas e Materiais

Contents

Cover: Parametric Tower

Courtesy: Marcela Noronha P. de O. e Sousa

IBRACON

Ibracon Structures and Materials Journal is published bimonthly (February, April, June, August, October, and December) by IBRACON.

IBRACON
Instituto Brasileiro do Concreto Founded in 1972

Av. Queiroz Filho, nº 1700 — sala 407/408
Torre D — Villa Lobos Office Park
CEP 05319-000 — São Paulo, SP — Brazil
Phone: +55 11 3735-0202
Fax: +55 11 3733-2190
E-mail: riem@ibracon.org.br
Website: http://www.ibracon.org.br

Cover design & Layout: Editora Cubo
www.editoracubo.com.br

Aims and Scope

Aims and Scope

The IBRACON Structures and Materials Journal (in Portuguese: Revista IBRACON de Estruturas e Materiais) is a technical and scientific divulgation vehicle of IBRACON (Brazilian Concrete Institute), published every two months. Each issue has 12 to 15 articles and, possibly, a technical note and/or a technical discussion regarding a previously published paper. All contributions are reviewed and approved by professionals with recognized scientific competence in the area. The IBRACON Structures and Materials Journal is an open access Journal, free of charges for authors and readers.

Objectives

The IBRACON Structures and Materials Journal´s main objectives are:

- Present current developments and advances in concrete structures and materials.
- Make possible the better understanding of structural concrete behavior, supplying subsidies for a continuous interaction among researchers, producers, and users.
- Stimulate the development of scientific and technological research in the areas of concrete structures and materials, through papers peer-reviewed by a qualified Editorial Board.
- Promote the interaction among researchers, constructors and users of concrete structures and materials and the development of Civil Construction.
- Provide a vehicle of communication of high technical level for researchers and designers in the areas of concrete structures and materials.

Submission Procedure

The procedure to submit and revise the contributions, as well as the formats, are detailed in the Journal Website (ismj.org).

The papers and the technical notes are revised by at least two reviewers indicated by the editors. Discussions and replies are accepted for publication after a review by the editors and at least one member of the Editorial Board. In case of disagreement between the reviewer and the authors, the contribution will be sent to a specialist in the area, not necessarily linked to the Editorial Board. Conflict of interests is carefully handled by the Editors.

Contribution Types

The Journal will publish original papers, short technical notes, and paper discussions. Original papers will be accepted if they are in accordance with the objectives of the Journal and present quality of information and presentation. A technical note is a brief manuscript. It may present a new feature of research, development, or technological application in the areas of Concrete Structures and Materials, and Civil Construction. This is an opportunity to be used by industries, companies, universities, institutions of research, researchers, and professionals willing to promote their works and products under development.

A discussion is received no later than 3 months after the publication of the paper or technical note. The discussion must be limited to the topic addressed in the published paper and must not be offensive. The right of reply is granted to the Authors. The discussions and the replies are published in the subsequent issues of the Journal.

The submission file should be in accordance with the paper template available at the Journal Website. It is recommended that the length of the papers does not exceed 25 pages. Where available, URLs for the references should be provided.

The IBRACON Structures and Materials Journal will conduct the review process for manuscripts submitted in English. Titles, abstracts, and keywords are presented in English, and in Portuguese or Spanish. Articles and technical notes are peer-reviewed and only published after approval of the reviewers and the Editorial Board.

Once accepted, an article is typeset according to the journal layout. The author will be required to review and approve the galleys before publishing. At this stage only typesetting errors will be considered.

Internet Access

The IBRACON Structures and Materials Journal Webpage is available at http://ismj.org.

Sponsors

The funds for the maintenance of the Journal are currently obtained from the IBRACON. The Journal is not supposed to be maintained with funds from private sponsorship, which could diminish the credit of the publications.

Photocopying

Photocopying in Brazil. Brazilian Copyright Law is applicable to users in Brazil. IBRACON holds the copyright of contributions in the journal unless stated otherwise at the bottom of the first page of any contribution. Where IBRACON holds the copyright, authorization to photocopy items for internal or personal use, or the internal or personal use of specific clients, is granted for libraries and other users registered at IBRACON.

Copyright

IBRACON

Av. Queiroz Filho, 1700 – sala 407/408 – Torre D
Villa Lobos Office Park
05319-000 – Vila Hamburguesa
São Paulo – SP
Phone: +55 (11) 3735-0202
E-mail: riem@ibracon.org.br

Disclaimer

Papers and other contributions and the statements made, or opinions expressed therein are published on the understanding that the authors of the contribution are the only responsible for the opinions expressed in them and that their publication does not necessarily reflect the views of IBRACON or of the Journal Editorial Board.

Editorial Board

IBRACON Structures and Materials Journal
Revista IBRACON de Estruturas e Materiais
ISSN 1983-4195 ismj.org

ORIGINAL ARTICLE

Effect of nano-silica on Portland cement matrices containing supplementary cementitious materials

Efeito da nanossílica em matrizes de cimento Portland contento materiais cimentícios suplementares

Thiago Melanda Mendes[a]
Wellington Longuini Repette[b]

[a]Universidade Tecnológica Federal do Paraná – UTFPR, Departamento de Engenharia Ambiental, Londrina, PR, Brasil
[b]Universidade Federal de Santa Catarina – UFSC, Centro Tecnológico – CTC, Departamento de Engenharia Civil, Florianópolis, SC, Brasil

Received 09 June 2020
Accepted 31 December 2020

Abstract: For a controlled granulometry, this study evaluates the effect of nano-silica on mechanical and rheological properties, as well in the microstructure of Portland cement matrices containing a fixed amount of supplementary cementitious materials and three different types of cements. The rheological behavior of cement pastes was evaluated by rotational rheometry and mechanical performance was measured throught the compressive strength. The microstructure was analyzed by intrusion mercury porosimetry and scanning electron microscopy. There was an increasing on the viscosity of the cementitious matrices, as a consequence of the reduction in the inter particle separation of these suspensions. The optimum content of nano-silica varied according to Ca/Si ratio of Portland cement matrices containing supplementary cementitious materials. The use of nano-silica allowed to modify the pore size distribution of cementitious matrices. And the structure of nano-silica in cementitious matrices has occurred in layers or agglomerates of nano-particles covered by hydration products.

Keywords: rheology, compressive strength, microstructure, porosity.

Resumo: Para uma granulometria controlada, este estudo avalia o efeito da nanossílica nas propriedades mecânicas e reológicas, bem como na microestrutura de matrizes de cimento Portland contendo uma quantidade fixa de materiais cimentícios suplementares e três diferentes tipos de cimentos. O comportamento reológico das pastas cimentícias foi avaliado por reometria rotacional e o desempenho mecânico foi medido através da resistência à compressão. A microestrutura foi analisada por porosimetria de intrusão de mercúrio e microscopia eletrônica de varredura. Houve um aumento da viscosidade das matrizes cimentícias, como consequência da redução na distância de separação das partículas dessas suspensões. O teor ótimo de nano-sílica variou de acordo com a relação Ca/Si das matrizes de cimento Portland contendo materiais cimentícios suplementares. O uso da nanossílica permitiu modificar a distribuição do tamanho dos poros das matrizes cimentícias. E a estrutura da nanossílica nas matrizes cimentícias ocorreu em camadas ou aglomerados de nanopartículas recobertas por produtos de hidratação.

Palavras-chave: reologia, resistência à compressão, microestrutura, porosimetria de intrusão de mercúrio.

How to cite: T. M. Mendes and W. L. Repette, "Effect of nano-silica on Portland cement matrices containing supplementary cementitious materials," *Rev. IBRACON Estrut. Mater.*, vol. 14, no. 4, e14401, 2021, https://doi.org/10.1590/S1983-41952021000400001

1 INTRODUCTION

The use of supplementary cementitious materials (SCM) is a currently trend, which can contribute to reducing the environmental impact of the Portland cement industry [1]. Much research has been carried out to obtain new alternative additions, such as basalt [2], marble [3], and granite fillers [4], or red ceramic waste [5]. Mendes et al. [6] showed a gain in compressive strength for mixtures containing 2.5 *wt.*% of basaltic fillers, but for quantities greater than 5 *wt.*%,

Corresponding author: Thiago Melanda Mendes. E-mail: thiagomendes@utfpr.edu.br
Financial support: Araucaria Foundation 668/2014, CNPq – 152200/2019-3.
Conflict of interest: Nothing to declare.

the mechanical properties become smaller than to the reference mixture. The use of nano-materials is another way, which can contribute to improve the mechanical performance of cement-based materials. The efficiency of nano-silica in the mechanical properties of cement-based materials, can be calculated by the ratio between the relative mechanical gain and the nano-silica content. Mendes et al. [7] showed that better efficiency was achieved for mixtures containing low amount of nano-silica.

Thus, the mixture of these alternative additions with nano-silica, nano-cement and carbon nanotubes, can avoid this loss in the mechanical performance of the cement-based materials. Comparing mixtures with 5 and 10 *wt*.% of fly ash, or silica fume or nano-silica, Biricik and Sarier [8] revealed that formulations with nano-silica have the highest compressive strength, followed by the mixtures containing silica fume and fly ash. For mixtures formulated with 5 and 10 *wt*.% of silica-fume and nano-silica, Tóbon et al. [9] demonstrated that the mixture formulated with nano-silica has a better mechanical performance than mixture formulated with silica fume. For concretes containing 1 *wt*.% of nano-silica or 10 *wt*.% of silica-fume and 1 *wt*.% of nano-silica, Jacob et al. [10] showed that the combined effect of silica fume and nano-silica leads to better mechanical performance. Zanon et al. [11] also showed better mechanical performance for mixtures formulated with 0.5 *wt*.% of nano-silica and 10 *wt*.% of silica-fume, when compared to the mixture containing only 0.5 *wt*.% of nano-silica.

When nano-silica is the only supplementary cementitious material (SCM) used, for large quantities of this reactive amorphous silica, the improvement in the mechanical performance is mainly related to the pozzolanic reaction [7]. When combined with other supplementary cementitious material (SCM), the packing effect becomes important for small amounts of nano-silica, reaching a solubility limit of less than 1 *wt.*% [12]. For mixtures containing supplementary cementitious material (SCM), there are no references about the combined effect of nano-silica and cement type on the rheological and mechanical properties, as well on the microstructure of Portland cement matrices. Thus, for a controlled granulometry, the present study aims to evaluate the effect of nano-silica on mechanical and rheological properties, as well on the microstructure of Portland cement matrices containing a fixed amount of supplementary cementitious materials and three different types of cement.

2 MATERIALS AND EXPERIMENTAL PROGRAM

A pure clinker (CP) powder was obtained by ball milling of clinker received from Votorantim Cimentos, for 90 minutes and sieved in a 200 mesh (75 µm). The setting time of pure clinker was controlled by the retarding effect of superplasticizer due to the complexation of Ca^{2+} ions by the superplasticizer [12]. Portland cements CPV-ARI Votorantim (CPV-V) and CPV-ARI InterCement (CPV-I) were also used as binders. These two Portland cements CPV-ARI were selected because they have different chemical compositions, mainly in the Ca/Si ratios 2.22 and 3.01 for CPV-V and CPV-I, respectively. In a previous study [6], it was found that the fine (FF) and the coarse fractions (CF) of basaltic filler, showed similar performance when 15 *wt*.% was added to a Portland CPV-ARI. Silica fume ELKEM 920U (SF), and nano-silicas Akzo Nobel Cembinder 8 (nS_1), Cembinder 30 (nS_2) and Cembinder 50 (nS_3) were used as supplementary cementitious materials (SCM).

The chemical composition of raw materials was measured in molten samples, using the P'ANalytical Axios Advanced fluorescence spectrometer. The specific Surface Area (S.S.A.) was measured by gas adsorption (B.E.T.) with BELSORP MAX equipment. For these measurements the samples were dried at 105ºC, and kept under vacuum of 68.9 Pa at 60ºC for 24 hours. The density was determinate by picnometry of liquids (Table 1). The densities of nano-silicas nS_1, nS_2 and nS_3 were calculated from density and mass concentration of suspensions: 1.4 g/cm^3 and 50%, 1.10 g/cm^3 and 30%, 1.05 g/cm^3 and 15%, respectively. BASF's ADVA 505 poly-carboxylic acid (PC) was used as a dispersant additive.

The mineralogical composition of pure clinker and Portland cements was obtained by X-ray diffraction of pressed samples, using the Philips MPD1880 X-ray diffractometer (Cu 40 kV 30 mA Kα 2θ = 5-70° - 0.2°/s). Transmission Electron Microscopy (TEM) of nano-silica suspensions was performed with Fei Tecnai G2 equipment, operating at 80 and 120 kV. The nano-silica samples were diluted to 1 mg/ml and sonicated for 30 minutes. Five milliliters (5µl) of these diluted suspensions, were dropped into a copper-carbon grid (300 mesh), and covered with Formvar.

Table 1. Physical properties and chemical composition (wt.%) of raw-materials

Description	*SiO_2*	*Al_2O3*	*Fe_2O_3*	*CaO*	*SSA (m^2/g)*	*Density (g/cm^3)*
Pure Clinker (CP)	20.0	4.92	3.34	59.9	0.91	3.15
P. Cement Votorantim (CPV-V)	23.6	6.60	3.09	52.6	1.25	3.05
P. Cement InterCement (CPV-I)	19.5	5.12	2.50	58.8	1.10	3.10
Basaltic Coarse Fraction (CF)	51.8	16.3	11.3	8.80	1.14	2.85
Basaltic Fine Fraction (FF)	51.0	15.1	13.0	9.26	3.20	2.85
Silica Fume (SF)	95.0	n.d.	n.d.	n.d.	14.4	2.20
Cembinder 8 (nS_1)	n.d.	n.d.	n.d.	n.d.	47.3	2.33
Cembinder 30 (nS_2)	n.d.	n.d.	n.d.	n.d.	88.9	2.25
Cembinder 50 (nS_3)	n.d.	n.d.	n.d.	n.d.	44.6	2.54

The granulometric distribution of pure clinker, Portland cements, basaltic fillers and silica-fume was determined with Malvern 2200 laser granulometer. The granulometric distribution of nano-silicas was measured by Dynamic Laser Scattering (DLS), using Microtac Nano-Flex equipment. Part of Portland cements or pure clinker was replaced by silica fume and basaltic filler, an equal amount of these supplementary cementitious materials was used. Thus, these compositions of pure clinker or Portland cement, silica fume and basaltic fillers were combined with nano-silicas. The granulometric distribution of cementitious matrices was adjusted by Equation 1 [13], [14] with D_L = 100 μm; D_S = 0.001 μm (1nm); and distribution coefficients q = 0.37, 0.50, 0.55 and 0.61.

$$CPFT = \left[\left(D_P{}^q - D_S{}^q\right)/\left(D_L{}^q - D_S{}^q\right)\right] \quad (1)$$

where: CPFT = cent percent finer than (%); D_P = Particle diameter (μm); D_S = smallest particle diameter (μm); D_L = Largest Particle diameter (μm); q = coefficient of distribution.

In previous studies [13], [14]; for cementitious matrices containing nano-silica, without supplementary cementitious materials (SCM), the water demand and the consumption of dispersant was adjusted to obtain a self-compacting rheological behavior for these suspensions. In this study, considering that the amount of SCM reaches 33% of the composition, the content of the dispersant was fixed at 2 *wt.*%.

The volumetric concentration of solids (V_S) of the suspensions was calculated from water/solids ratio (w/s) and densities; the volumetric surface area (VSA) was calculated from product of the specific surface area (SSA) and the density of the compositions, following Funk and Dinger [15]. The initial porosity (P_0) was estimated using the linear packing model developed by Yu and Standish [16]. The inter particle separation (IPS) of mixtures was calculated from these results, following Funk and Dinger [15]. The nano-silica suspensions and the dispersant were previously diluted with deionized water. The mixing was performed in a laboratory mixer using a 6 cm diameter axial flow rod, cawles model. Applying the following process: (i) the dry powder was mixed at 586 rpm for 60s; (ii) 2/3 of the suspension (water + dispersant + nano-silicas) were added and mixed at 586 rpm for 120s; (iii) 1/3 of the suspension (water + dispersant + nano-silica) was mixed at 586 rpm for 120s.

A temperature-controlled rheometer with concentric cylinders geometry was used to measure rheological properties of cement pastes. The rheograms were obtained with the control of the shear rate, varying from 10 to 100 s^{-1}, in intervals of 10 s^{-1}. The shear rate was increased from 10 to 100 s^{-1} (upper curve) and reduced from 100 to 10 s^{-1} (downs curve). The rheological behavior of cement pastes was measured 30 seconds after mixing. The tests were performed for 10 g of paste, maintained 30 seconds at each shear rate; the values were recorded in the last 3 seconds. All tests were performed at 23°C. Bingham's model was applied to calculate the yield stress (τ_0) and the viscosity (η) of the suspensions, considering the downs curve. Eight cylindrical specimens (2:5 cm) were molded and compacted manually to avoid molding defects.

The Brazilian Standard ABNT NBR 8045 [17] establishes the accelerated compressive strength for concretes applying the boiling water method. According to this reference, after an initial curing period of 24 hours, the specimens shall be immersed in boiling water (>100ºC) for 2 hours. The specimens were kept at room temperature (22ºC) for 24 hours, and for 18 hours immersed in water at 85ºC. This curing method was employed in order to achieve this accelerated compressive strength of Portland cement matrices. For six specimens, the upper face of was sliced, resulting in a final height of 4 cm. The compressive strength was measured by applying a loading rate of 2.5 MPa/s. Two specimens was lathed, until they reached a diameter of 1 cm and a height of 2 cm, these internal parts of the sample was broken and a small piece was used to perform the mercury intrusion porosimetry (MIP) and the scanning electron microscopy (SEM). The pore size distribution of mixtures was measured using a Micrometrics Pore Size equipment (contact angle = 140°). Microstructure of samples was analyzed by scanning electron microscope (SEM) coupled to an energy dispersive spectrometer (EDS) using Quanta 600 FEI-Philips equipment, operating at 25 kV. The gold coating was applied to the sample surface for this analysis.

4 RESULTS AND DISCUSSIONS

Figure 1 shows the diffractograms of pure clinker and Portland cements CPV-V and CPV-I. The characteristic peak of gypsum (2θ = 11.6°) was identified only for the Portland cement CPV-V. A similar intensity for the tetra calcium ferro-aluminate phase (C_4AF) was identified for all samples (2θ = 12.2° and 60.1°). Tricalcium aluminate (C_3A) was identified for the three binders (2θ = 33.2°). Portland cement CPV-I has the largest amount of di and tricalcium silicates (C_3S/C_2S), followed by Portland cement CPV-V and pure clinker (2θ = 29.5° and 32.2°).

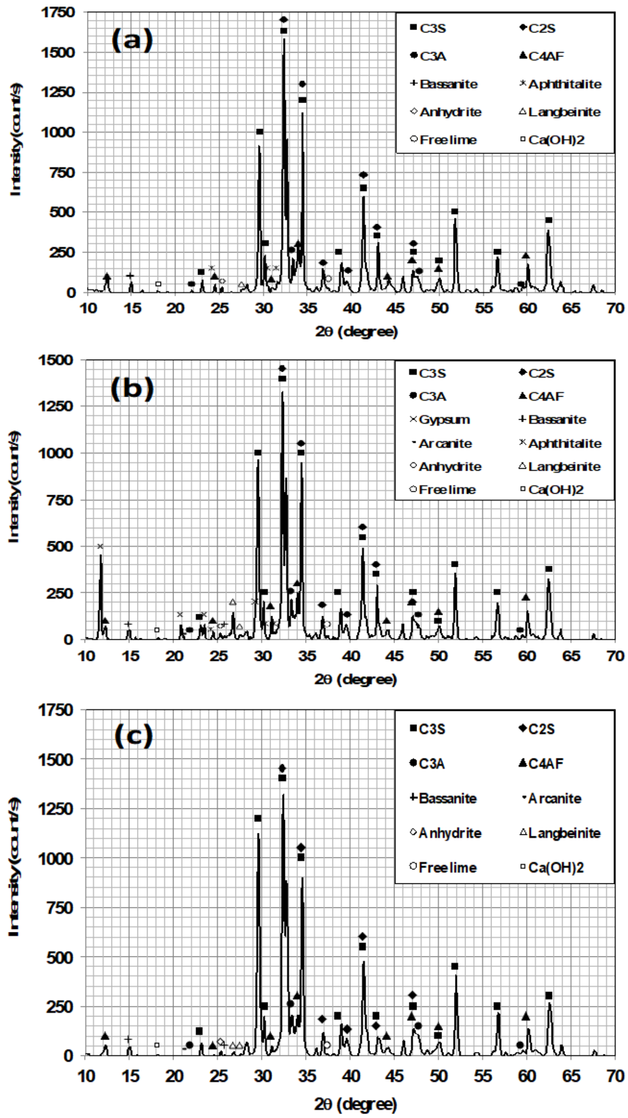

Figure 1. Diffractograms (a) Pure Clinker (b) Portland cement CPV-V (c) Portland cement CPV-I. (C_3S) - $3CaOSiO_2$, (C_2S) - $2CaOSiO_2$, (C_3A) - $3CaOAl_2O_3$, (C_4AF) $4CaOAl_2O_3Fe_2O_3$, Gypsum - $CaSO_42H_2O$, Bassanite - $CaSO_41/2H_2O$, Arcanite - K_2SO_4, Anhydrite - $CaSO_4$, Langbeinite - $K_2Mg_2(SO_4)_3$, Aphthitalite - $(K, Na)_3Na(SO_4)_2$, Free lime – CaO - Portlandite - $Ca(OH)_2$. ASTM C1365 [18]

Figure 2 shows the TEM micrographies of the nano-silicas Cembinder 8 (nS_1), Cembinder 30 (nS_2) and Cembinder 50 (nS_3). The nano-silica Cembinder 8 showed particles ranging from 10 to 60 nm, Figure 2a. While, for the nano-silica Cembinder 30 the particle size ranges from 15 to 24 nm, but some agglomerates larger than 76 nm can be found, Figure 2b. Figure 2c shows the TEM micrography of the nano-silica Cembinder 50, with a large agglomerate of particles, and some particles with a diameter ranging from 7 to 14 nm. Figure 3a shows the particle size distribution of nano-silicas. The particle size distribution of nano-silica Cembinder 8 (nS_1) presents a considerable number of particles coarser than 100 nm (0.1 μm), and a smaller number of nanoparticles (<100 nm), demonstrating the agglomerated condition observed by the TEM image of Figure 2a. The nano-silica Cembinder 30 (nS_2) presented three populations of particles, composed by a small quantity of particles coarser than 100 nm (0.1 μm), probably agglomerates of small particles; a population of particles between 10 and 100 nm (0.01 - 0.1 μm), which are clear observable in the TEM image of Figure 2b; and a considerable population of particles smaller than 5 nm (0.005 μm). Finally, the nano-silica Cembinder 50 (nS_3) present a continuous granulometry of particles ranging from 10 and 1000 nm (0.01 - 1 μm), and a secondary population of particle between 2 and 10 nm (0.002 – 0.01 μm). Figure 2c reveals the presence of particles in this interval, as well agglomerates of nano-particles greater than 100 nanometers (0.1μm). Thus, considering the specific surface area (Table 1) and the particle size distribution of nano-silicas, the presence of this number of particles smaller than 5 nm (0.005 μm) resulted in the highest specific surface area (88.9 m^2/g) for the nano-silica Cembinder 30 (nS_2). While, the similar values of specific surface area of nano-silicas Cembinder 8 (nS1) and Cembinder 50 (nS_3), 47.3 and 44.6 m^2/g, respectively, suggest the agglomerated condition for these both raw-materials.

Figure 3b present the granulometry of pure clinker, and Portland cements CPV-V and CPV-I, they showed a very similar particle size distribution, clearly finer than pure clinker. Figure 3c shows the granulometric distribution of the supplementary cementitious materials. Considering the specific surface area and the particle size distribution, the highest value observed for silica fume, despite of the granulometry observed, suggests its agglomerated condition.

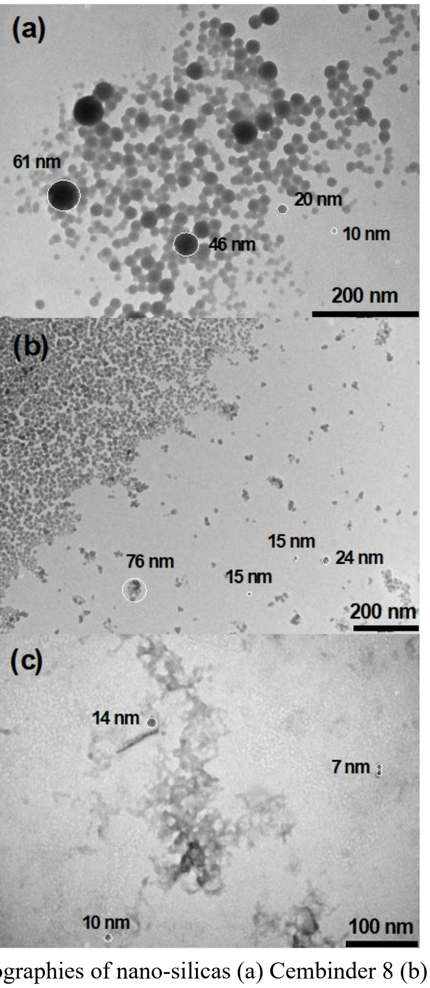

Figure 2. Transmission electron micrographies of nano-silicas (a) Cembinder 8 (b) Cembinder 30 and (c) Cembinder 50

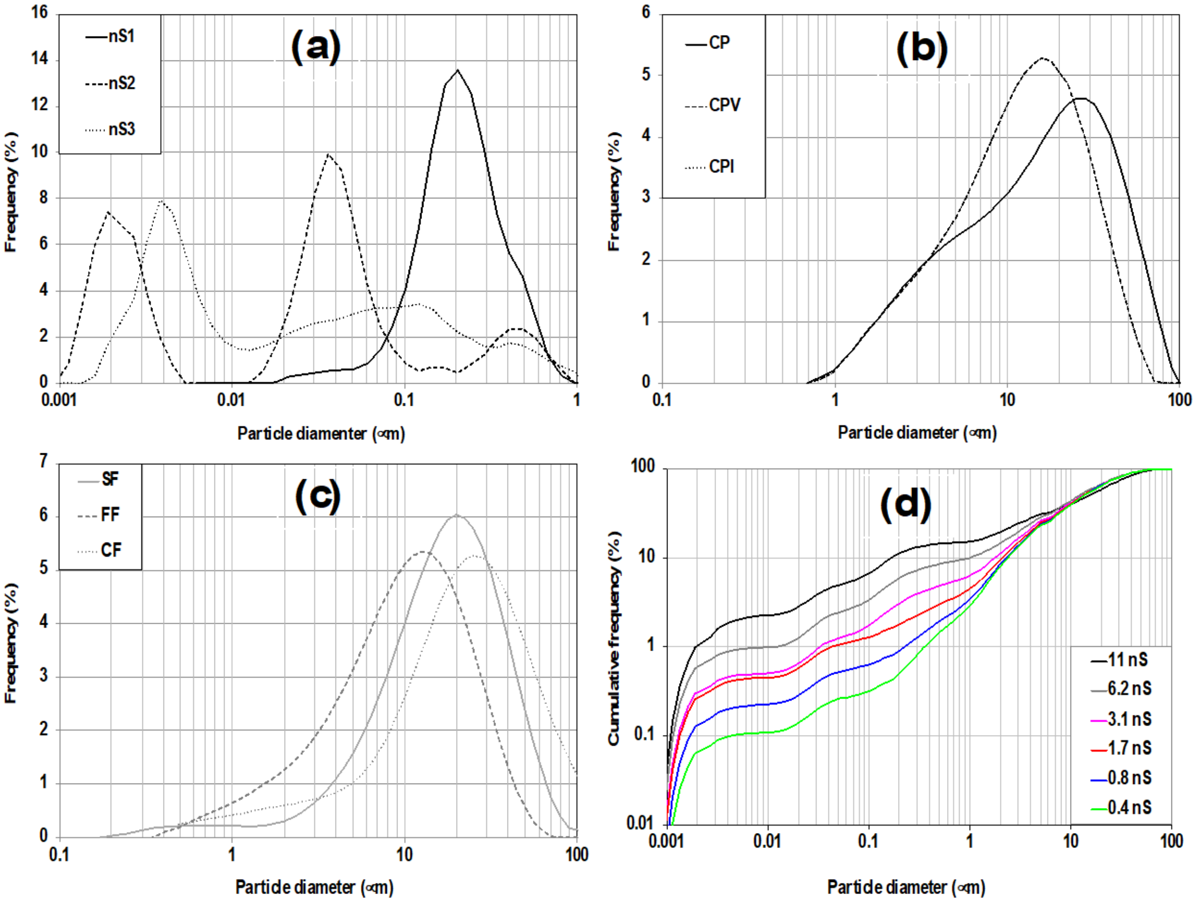

Figure 3. Particle size distribution (a) Nano-silicas (b) Cements and Clinker (c) Supplementary Cementitious materials (d) Mixtures

Table 2 shows the compositions of these formulations, which contain 11, 6.2, 3.16 and 1.70 *wt*.% of nano-silicas, respectively. For mixtures containing 0.85 and 0.42 *wt*.% of nano-silicas, rates were obtained by dividing each amount nano-silica from the previous formulation by 2.

Table 2. Composition of mixtures (wt.%)

Mixture	11 nS	6.2 nS	3.1 nS	1.7 nS	0.85 nS	0.42 nS
Cement or Clinker	59.34	62.54	64.56	65.53	66.10	66.38
Basaltic Filler	14.84	15.64	16.14	16.38	16.53	16.60
Silica Fume	14.84	15.64	16.14	16.38	16.53	16.60
Cembinder 8 (nS_1)	6.26	4.49	1.95	0.64	0.32	0.16
Cembinder 30 (nS_2)	2.73	1.32	0.94	0.80	0.40	0.20
Cembinder 50 (nS_3)	1.99	0.38	0.26	0.27	0.13	0.06

Table 3 lists the results of water/solids (w/s), the volumetric concentration of solids (V_S), the volumetric surface area (VSA), the estimated porosity (P_0), the calculated inter-particle separation (IPS) and the rheological properties: apparent yield stress (τ_0) and viscosity (η). The results of some mixtures and their rheological properties were not presented, because they could not be measured or molded. As the content of nano-silica increases the water demand also increase, as a consequence of the high volumetric surface area (VSA) of the mixtures. The values of inter-particle separation (IPS) are lower than those of mixtures without supplementary cementitious materials (SCM), for mixtures containing only nano-silicas and Portland cements or pure clinker [13], [14]. This difference is mainly related to the greater specific surface area of silica-fume and basaltic fillers. Thus, the type of cement did not affect the rheological behavior of cementitious matrices. In most of the studied mixtures, the dispersant content used was able to keep the yield stress below 1 Pa. However, for mixtures containing 11 *wt.*% of nano-silica, the yield stress reached values around 4 Pa. The same trend was observed for mixtures containing 11 *wt.*% of nano-silica, without SCM [13], [14]. But as the particles become closer the energy needed to keep them moving also increases. Figure 4 shows the effect of inter-particle separation (IPS) on the viscosity of cement pastes formulated with Portland cements, pure clinker, nano-silica and SCM.

Table 3. Composition and physical characteristics of suspensions

Mixture	*PC*	*w/s (%)*	*Vs (%)*	*VSA (m^2/cm^3)*	*P_0 (%)*	*IPS (nm)*	*τ_0 (Pa)*	*η (Pa.s)*
CP + 11 nS	*2.0*	*53.68*	*39.24*	*26.55*	*39.44*	*34.05*	*n.d.*	*n.d.*
CP + 1.7 nS	*2.0*	*25.73*	*56.81*	*12.65*	*33.23*	*20.76*	*n.d.*	*n.d.*
CP + 0.85 nS	*2.0*	*22.35*	*60.17*	*11.08*	*32.66*	*15.98*	*n.d.*	*n.d.*
CP + 0.42 nS	*2.0*	*20.56*	*62.12*	*10.30*	*32.38*	*12.71*	*4.33*	*0.07*
CPV-V + 11 nS	*2.0*	*52.66*	*40.12*	*27.32*	*39.60*	*30.63*	*n.d.*	*n.d.*
CPV-V + 6.2 nS	*2.0*	*30.07*	*53.72*	*20.08*	*36.40*	*14.39*	*n.d.*	*n.d.*
CPV-V + 3.1 nS	*2.0*	*25.80*	*57.32*	*15.96*	*34.42*	*13.78*	*n.d.*	*n.d.*
CPV-V + 1.7 nS	*2.0*	*24.86*	*58.13*	*13.86*	*33.40*	*15.78*	*0.57*	*0.03*
CPV-V + 0.85 nS	*2.0*	*22.57*	*60.42*	*12.49*	*32.92*	*13.17*	*0.01*	*0.02*
CPV-V + 0.42 nS	*2.0*	*20.48*	*62.69*	*11.74*	*32.64*	*9.42*	*0.01*	*0.14*
CPV-I + 11 nS	*2.0*	*52.55*	*39.96*	*26.87*	*38.86*	*32.27*	*4.08*	*0.01*
CPV-I + 6.2 nS	*2.0*	*30.30*	*53.36*	*19.66*	*35.54*	*16.41*	*0.98*	*0.06*
CPV-I + 3.1 nS	*2.0*	*26.04*	*56.67*	*15.47*	*33.46*	*16.92*	*0.54*	*0.03*
CPV-I + 1.7 nS	*2.0*	*23.12*	*59.54*	*13.50*	*32.48*	*14.70*	*0.01*	*0.10*
CPV-I + 0.85 nS	*2.0*	*20.38*	*59.48*	*11.93*	*31.90*	*17.82*	*0.40*	*0.06*
CPV-I + 0.42 nS	*2.0*	*19.64*	*62.67*	*11.15*	*31.61*	*11.73*	*0.01*	*0.16*

* Mixtures CPV-V was formulated with the fine fraction of basaltic filler

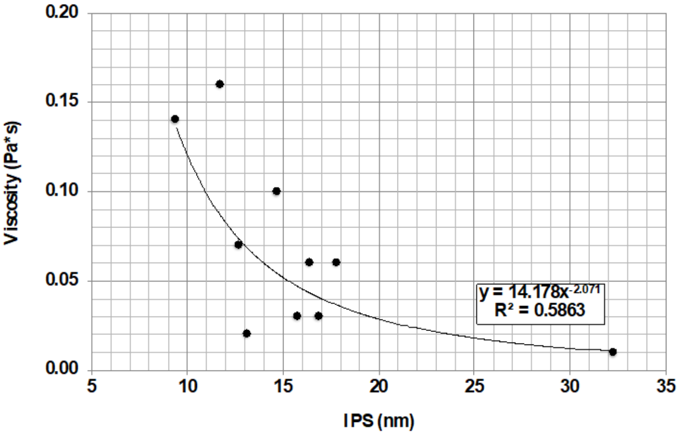

Figure 4. Effect of IPS on viscosity of cement pastes

The Figure 5a shows the effect of water/solids ratio on the compressive strength of cementitious matrices containing nano-silica and SCM. When large amounts of nano-silica were added, an increase in the water demand was necessary, as seen in Table 3, leading to a reduction in compressive strength. The continuous line represents the adjusted exponential equation for all mixtures. The dashed and dotted lines represent 1.25 and 0.75 of the continuous line. Figure 5b shows that the mixtures formulated with pure clinker and nano-silicas, follow the same exponential trend expected for cementitious materials. However, an atypical value (red dot), demonstrated the occurrence of the optimum content of nano-silica, that is, the maximum packing for the composition containing 0.85 *wt*.% of nano-silica. The same situation was observed in Figure 5c, where the mixture containing 0.85 *wt*.% of nano-silica represents the optimum content or maximum packing for the Portland cement CPV-I. Figure 5d shows that the mixture containing 0.42 *wt*.% of nano-silica represents the optimum content for the Portland cement CPV-V. This difference between the limit of solubility of nano-silica in the Portland cement matrices containing supplementary cementitious materials, can be explained by the Ca/Si-Al-Fe ratios of these formulations. For the compositions containing pure clinker and Portland cement CPV-I the Ca/Si-Al-Fe ratios vary from 0.68 to 0.85. In matrices formulated with the Portland cement CPV-V this value ranges from 0.57 to 0.70. These values were calculated considering the chemical composition of Pure clinker and Portland cements, as well the silica fume and the coarse and fine fractions of basaltic fillers. Since these supplementary cementitious materials shall exhibit considerable reactivity due to their nucleation and pozzolanic effects, even for the siliceous fillers by the use of heated curing.

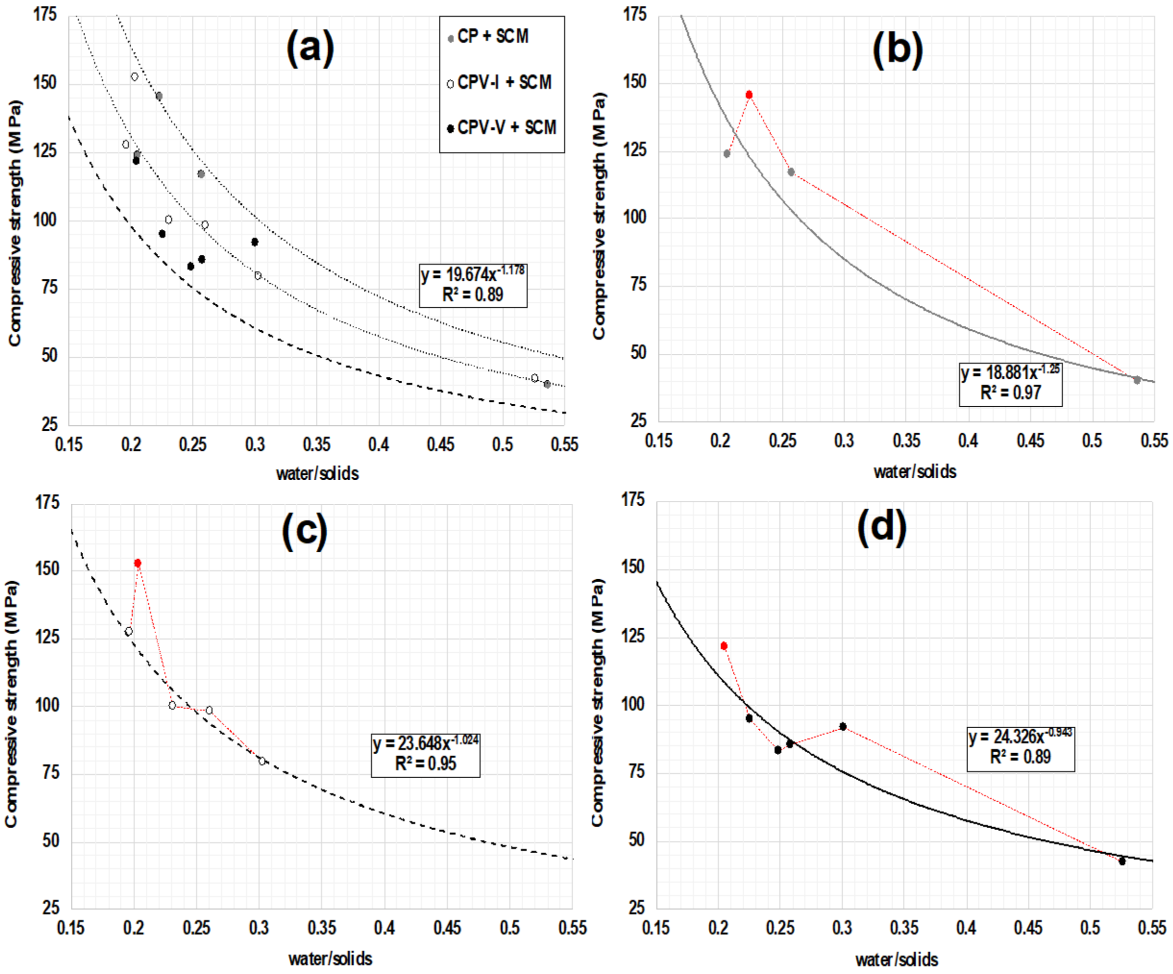

Figure 5. Effect of water/solids on the compressive strength (a) all mixtures (b) Pure clinker (c) Portland cement CPV-I (d) Portland cement CPV-V

Figure 6 shows the pore size distribution and the effect of porosity (P_0) on the mechanical performance of cementitious matrices containing nano-silica, with and without SCM. Porosity is closely related with water/solids ratio of these mixtures, capillary pores (0.01-1 µm) and the pores of air-entrapped bubbles (10-1000 µm) were observed in these three formulations studied. For the nanometric pores (< 100 nm or 0.1 µm), part of this porosity resulted from the capillary pores, and varied due to the different water/solids in the mixtures. Comparing the mixtures containing CPV-V or CP + SCM + 11 nS, Figure 6a and 6b, a change in the pores smaller than 10 nm or a bimodal pore size distribution, was observed for the mixture formulated with pure clinker. This same difference in the pore size distribution was observed for mixtures containing pure clinker and nano-silica, with and without SCM, Figure 6b and 6c. As these mixtures studied used the same amount of nano-silica, the CPV-V cement and pure clinker did not show a considerable difference in chemical or mineralogical composition. The different specific surface areas of these binders led to a change in the pore size distribution. Mendes and Repette [13], [14] showed that this change in nanometric porosity varies according to the nano-silica content and the inter-particle separation. The arrangement of nano-silica in the microstructure of the cementitious matrix, has changed from a layered adsorbed structure, to a porous structure, or to an agglomerated structure of nanoparticles. If nano-silica adsorbs on the surface of coarser grains, this change in microstructure varies according to the specific surface area of the adsorbent material. Despite these differences observed in the nanometric porosity, Figure 6d shows that the mechanical properties of cement matrices containing nano-silica with or without SCM, are closely related to the total porosity.

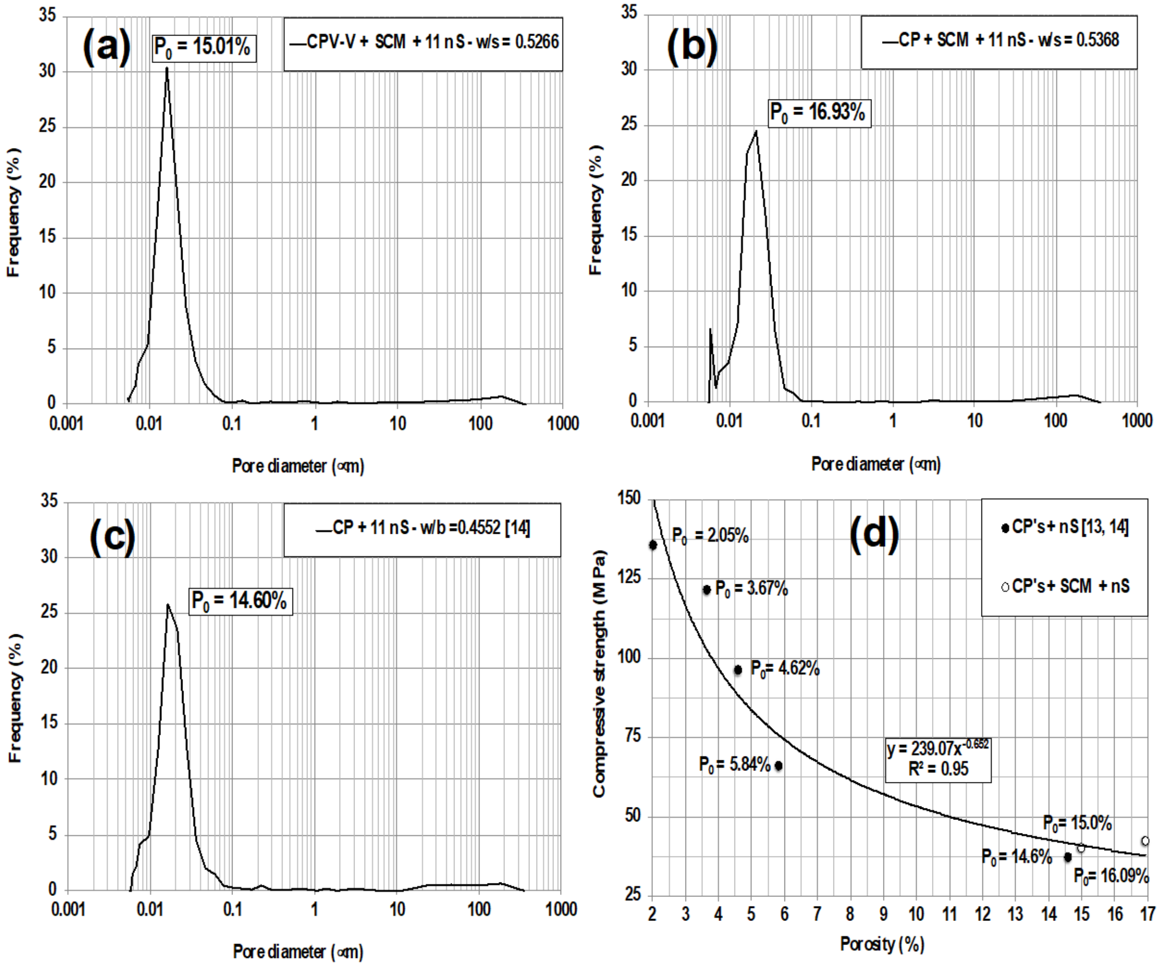

Figure 6. Mercury intrusion porosimetry (a) CPV-V + SCM + 11 nS (b) CP + SCM + 11 nS (c) CP + 11 nS and [14] (d) Compressive strength vs Porosity of Portland cement matrices containing nano-silica with and without SCM [13], [14]

Figure 7 shows the scanning electron micrographs of the mixtures CPV-I + SCM + 0.85 nS and CP + SCM + 0.85 nS, which achieved the highest compressive strengths, 152.5 and 145.5 MPa, respectively. Figures 7a and 7b show the microstructure of nano-silica in the cementitious matrices. As seen, nanoparticles are arranged in a layered structure and some agglomerates of nano-silica, have also been observed. Figure 7c and 7d also shows these agglomerates of nano-silica. Figure 8a presents the chemical composition obtained by the electron dispersive scattering probe (EDS) of the region delimited in Figure 7c. The presence of calcium and silicon ions indicates that these agglomerates can be composed of: nano-silica coated with hydration products such as C-S-H and calcium hydroxide; hydration products like C-S-H/C-A-H, or even both together. Figures 7e and 7f show some agglomerates of nanoparticles, and the structure arranged in layers. Figure 8b shows the chemical composition of the region of Figure 7e, obtained by the EDS probe. A similar content of calcium and silicon, indicates the same condition for the agglomerates of nano-particles seen in Figure 7d. This layered nanoparticles structure can probably be composed by nano-silica coated by hydration products, or the hydration products containing nanoinclusions of nano-silica.

4 CONCLUSIONS

The high specific surface area of nano-silica and supplementary cementitious materials increases the water demand and, consequently, the viscosity of cement pastes.

The optimum content of nano-silica varies according to Ca/Si ratio of Portland cement matrices containing supplementary cementitious materials.

Nano-silica showed a layered or agglomerated structure, modifying the pore size distribution of cementitious matrices containing supplementary cementitious materials.

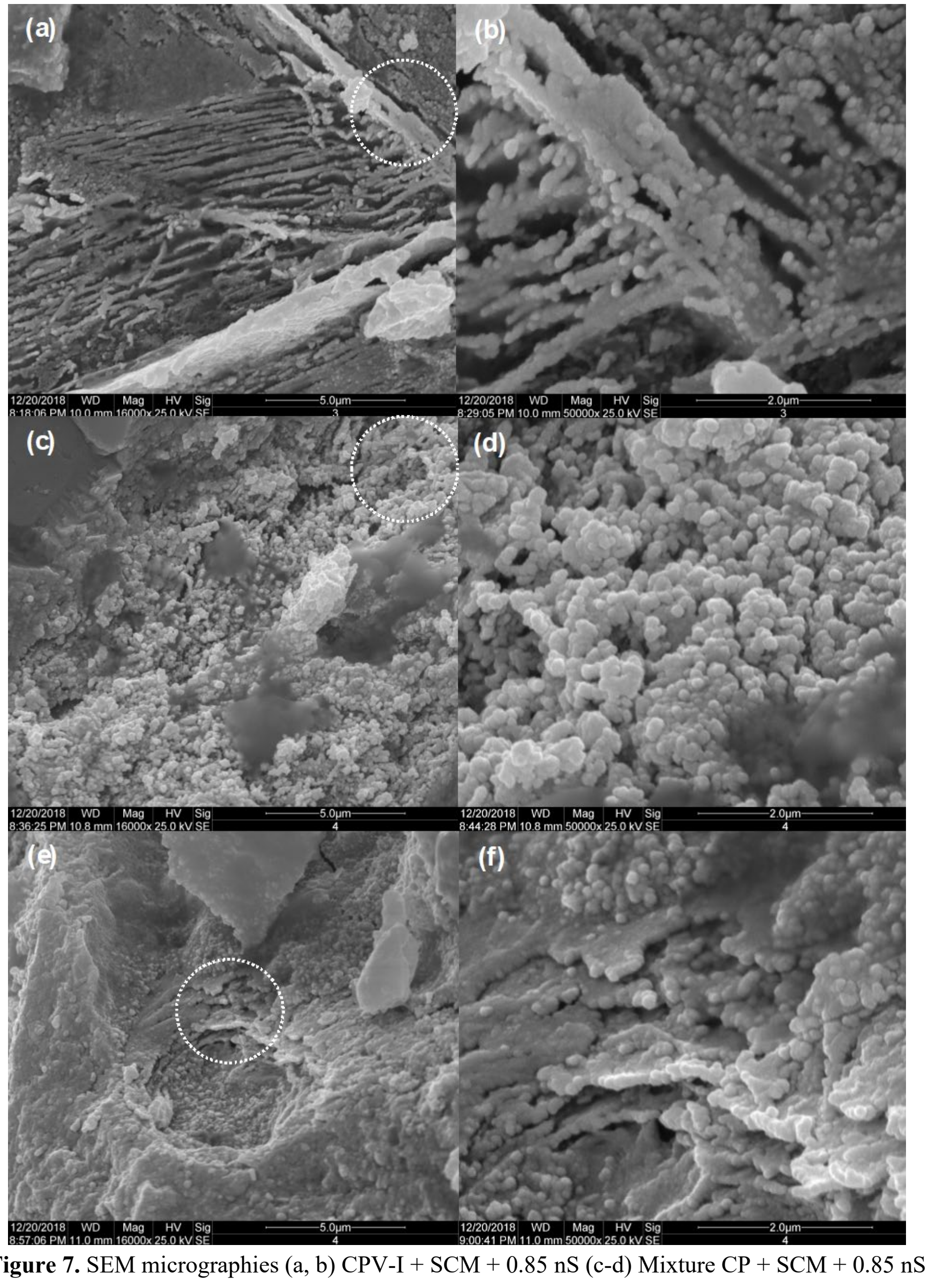

Figure 7. SEM micrographies (a, b) CPV-I + SCM + 0.85 nS (c-d) Mixture CP + SCM + 0.85 nS

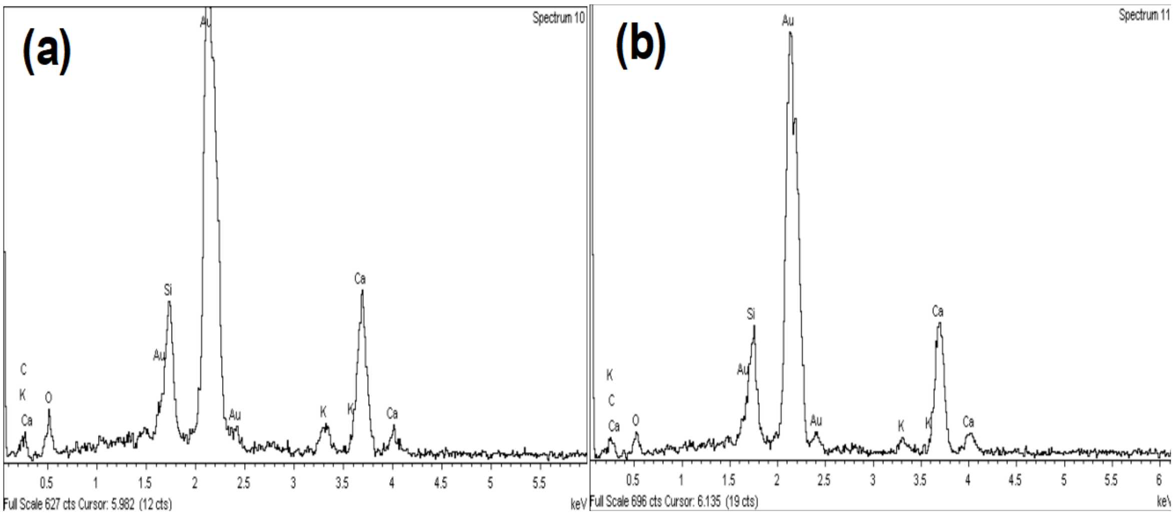

Figure 8. Chemical composition obtained by EDS (a) **Figure 7d** and (b) **Figure 7e**

ACKNOWLEDGEMENTS

The authors acknowledge the Araucaria Foundation, Coordination for the Improvement of Higher Education Personnel (CAPES) and National Council of Scientific and Technological Development (CNPq).

REFERENCES

[1] European Cement Association, *Activity Report 2018.* Brussels: CEMBUREAU, 2018. Accessed: June 9, 2019. [Online]. Available: https://cembureau.eu/media/1818/actvity-report-2018.pdf

[2] L. Laibao, Z. Yunsheng, Z. Wenhua, L. Zhiyong, and Z. Lihua, "Investigation the influence of basalt as mineral admixture on hydration and microstructure formation mechanism of cement," *Constr. Build. Mater.*, vol. 48, pp. 434–440, 2013, http://dx.doi.org/10.1016/j.conbuildmat.2013.07.021.

[3] H. Y. Aruntas, M. Guru, M. Dayi, and I. Tekin, "Utilization of waste marble dust as an additive in cement production," *Mater. Des.*, vol. 31, no. 8, pp. 4039–4042, 2010, http://dx.doi.org/10.1016/j.matdes.2010.03.036.

[4] M. Vijayalakshimi, A. S. S. Sekar, and G. Ganeshm, "Strength and durability properties of concrete made with granite industry waste," *Constr. Build. Mater.*, vol. 46, pp. 1–7, 2013, http://dx.doi.org/10.1016/j.conbuildmat.2013.04.018.

[5] A. L. Castro, R. F. C. Santos, K. M. Gonçalves, and V. A. Quarcioni, "Characterization of blended cements with red ceramic industry waste," *Ceramica*, vol. 63, pp. 65–76, 2017, http://dx.doi.org/10.1590/0366-69132017633652036.

[6] T. M. Mendes, L. Guerra, and G. Morales, "Basalt waste added to Portland cement," *Acta Sci. Technol.*, vol. 38, no. 4, pp. 431–436, 2016, http://dx.doi.org/10.4025/actascitechnol.v38i4.27290.

[7] T. M. Mendes, D. Hotza, and W. L. Repette, "Nanoparticles in cement based materials: a review," *J. Adv. Mater. Rev.*, vol. 40, no. 1, pp. 89–96, 2015.

[8] H. Biricik and N. Sarier, "Comparative study of the characteristics of nano-silica-, silica-fume – fly ash- incorporated cement mortars," *Mater. Res.*, vol. 17, no. 3, pp. 570–582, 2014, http://dx.doi.org/10.1590/S1516-14392014005000054.

[9] J. I. Tóbon, O. J. Restrepo, and J. Payá, "Comparative analysis of performance of portland cement blended with nanosilica and silica fume," *Dyna*, vol. 77, no. 163, pp. 37–46, 2010. Accessed: June 9, 2019. [Online]. Available: http://www.scielo.org.co/scielo.php?pid=S0012-73532010000300004&script=sci_arttext&tlng=en

[10] J. S. Jacob, A. G. Mascelani, R. L. R. Steinmetz, F. A. Dalla Costa, and O. A. Dalla Costa, "Use of silica fume and nano-silica in mortars attacked by acids present in pig mature," *Procedia Struct. Integr.*, vol. 11, pp. 44–51, 2018, http://dx.doi.org/10.1016/j.prostr.2018.11.007.

[11] T. Zanon, R. Schmalz, and F. G. S. Ferreira, "Evaluation of nano-silica effects on concrete submitted to chloride ions attack," *Rev. ALCONPAT*, vol. 8, no. 2, pp. 138–149, 2018, http://dx.doi.org/10.21041/ra.v8i2.274.

[12] T. M. Mendes, W. L. Repette, and P. J. Reis, "Effects of nano-silica in mechanical properties and microstructure of ultra-high-performance concrete," *Ceramica*, vol. 63, no. 365, pp. 387–394, 2017, http://dx.doi.org/10.1590/0366-69132017633672037.

[13] T. M. Mendes and W. L. Repette, "Effect of nano-silica on Portland cement matrix," *Rev. IBRACON Estrut. Mater.*, vol. 12, no. 6, pp. 1383–1389, 2019, http://dx.doi.org/10.1590/s1983-41952019000600009.

[14] T. M. Mendes and W. L. Repette, "Nano-silica added to Portland cement," *Acta Sci. Technol.*, 2021. (in press).

[15] J. E. Funk and D. Dinger, *Predictive Process Control of Crowed Particulate Suspension*, 1st ed. London: Kluwer Publishers, 1994.

[16] A. B. Yu and N. Standish, "Estimation of the porosity of particle mixtures by a linear-mixture packing model," *Ind. Eng. Chem. Res.*, vol. 30, no. 6, pp. 1372–1385, 1991, http://dx.doi.org/10.1021/ie00054a045.

[17] Associação Brasileira de Normas Técnicas, *Concreto – Determinação da Resistência Acelerada à Compressão – Método da Água em Ebulição*, ABNT NBR 8045, 1993.

[18] American Society for Testing Materials, *Standard Method for Determination of the Proportion on Phases of Portland Cement and Portland Cement Clinker Using Powder Diffraction Analysis*, ASTM C1365, 2011.

Author contributions: TMM: conceptualization, data curation, formal analysis, methodology, writing; WLR: funding acquisition, supervision.

Editors: Fernando S. Fonseca, Guilherme Aris Parsekian.

IBRACON Structures and Materials Journal
Revista IBRACON de Estruturas e Materiais
ISSN 1983-4195 ismj.org

ORIGINAL ARTICLE

Reliability analysis of truss structures considering complete failure paths and using the FLHB model

Análise de confiabilidade de treliças considerando caminhos de falha e utilizando o modelo FLHB

Túlio Raunyr Cândido Felipe[a]
Edson Denner Leonel[b]
Vladimir Guilherme Haach[b]
André Teófilo Beck[b]

[a]Marinha do Brasil, Diretoria de Obras Civis da Marinha, Rio de Janeiro, RJ, Brasil
[b]Universidade de São Paulo – USP, Escola de Engenharia de São Carlos, Departamento de Engenharia de Estruturas, São Carlos, SP, Brasil

Received 10 August 2020
Accepted 05 December 2020

Abstract: The study of progressive collapse of structures using numerical models requires accurate modeling of geometrical nonlinearity and material failure behavior. Numerical models must demonstrate stability, such that localized member failures do not trigger numerical instabilities. Also, algorithms should be efficient, to limit the computational burden of analyzing multiple responses when considering the effects of uncertain loads, geometric and material variables. In this scientific domain, a comprehensive non-linear ductile-damage truss-element model has been recently presented by the authors. The model accounts for the geometrical and material nonlinearities observed during progressive collapse of structural systems. In this paper, the Felipe-Leonel-Haach-Beck (FLHB) model is calibrated to describe the response of Ultra-High-Performance Fiber Reinforced Concrete (UHPFRC). Based on a limited number of UHPFRC experimental curves, statistics of FLHB model parameters are obtained. These are employed in the probabilistic analysis of failure paths of truss structures under progressive collapse. Monte Carlo Simulation and the First Order Reliability Method are employed in the probabilistic failure path analyses. Six application examples demonstrate the accuracy, robustness, and efficiency of the FLHB model in evaluation of failure paths of realistic structural systems.

Keywords: progressive collapse, failure paths, truss structures, continuum damage mechanics, reliability analysis.

Resumo: O estudo do colapso progressivo de estruturas, utilizando análise numérica, requer modelos precisos das não-linearidades geométrica e material. Modelos numéricos também precisam se mostrar estáveis, de forma que a falha localizada de um elemento não provoque instabilidades numéricas. Algoritmos precisam ser eficientes, de forma a possibilitar as análises repetitivas, necessárias para avaliar os efeitos das incertezas nas ações, na geometria e nos parâmetros de resistência dos materiais. Neste contexto, um modelo não-linear abrangente foi apresentado recentemente pelos autores, combinando análise plástica com um modelo de dano, para análise de treliças. O modelo leva em conta as não-linearidades material e geométrica observadas durante o colapso progressivo de estruturas hiperestáticas. Neste artigo, o modelo de Felipe-Leonel-Haach-Beck (FLHB) é calibrado para descrever a resposta do concreto de ultra-alto desempenho reforçado com fibras ou *Ultra-High-Performance Fiber Reinforced Concrete* (UHPFRC). Com base em um número limitado de curvas experimentais para o UHPFRC, estatísticas dos parâmetros do modelo FLHB são obtidas. Estas são utilizadas em uma análise probabilística dos caminhos de falha de treliças sob colapso progressivo. Simulação de Monte Carlo e o Método de Confiabilidade de Primeira Ordem são empregados nas análises. A aplicação a seis estruturas-exemplo demonstram a precisão, robustez e eficiência do modelo FLHB em avaliar os caminhos de falha de treliças realísticas.

Palavras-chave: colapso progressivo, caminhos de falha, treliças, mecânica do dano continuo; confiabilidade estrutural.

Corresponding author: André Teófilo Beck. E-mail: atbeck@sc.usp.br
Financial support: The authors acknowledge funding of this research project by Brazilian agencies CAPES (Brazilian Higher Education Council – Finance Code 001), CNPq (Brazilian National Council for Research, grant n. 309107/2020-2) and FAPESP (São Paulo State Research Foundation, grant n. 2017/01243-5).
Conflict of interest: Nothing to declare.

How to cite: T. R. C. Felipe, E. D. Leonel, V. G. Haach, and A. T. Beck, "Reliability analysis of truss structures considering complete failure paths and using the FLHB model" *Rev. IBRACON Estrut. Mater.*, vol. 14, no. 4, e14402, 2021, https://doi.org/10.1590/S1983-41952021000400002

1 INTRODUCTION

Partial collapses such as Ronan Point Tower and Skyline Plaza, and terrorist attacks like those at Oklahoma City and World Trade Center have raised awareness about the importance of robust design, with objective consideration of progressive collapse following local damage by abnormal loads. The new paradigm of robust design requires that structural systems withstand localized damage due to the abnormal loads, without disproportionate extension of the initial damage to the rest of the structural system. Abnormal loads include gas explosions, fire, vehicular collisions, human errors, deterioration processes, and terrorist attacks. Because these loads are characterized by very low probabilities of occurrence and very large impact, structural elements are not always designed to withstand them. Instead, the structural system is designed to withstand the loss of individual elements, which may occur due to such actions. In other words, structural systems should be made robust concerning the loss of individual elements due to abnormal loading.

As well documented in the literature review by Adam et al. [1], numerical modeling is often employed in progressive collapse analysis, as a cheaper complement or substitute for experimental testing. Numerical analysis for progressive collapse can be made using the Finite Element Method (FEM), the Discrete Element Method (DEM), the Applied Element Method (AEM) or Cohesive Element Modeling (CEM). An overview of these methods and discussions about the advantages and disadvantages are presented in Adam et al. [1]. The following elements have been required for proper analysis of progressive collapse using numerical models:

a) non-linear geometrical analysis: due to the large displacements triggered by element failures;
b) non-linear material modeling: to represent material failure, including plasticity and damage;
c) non-linear contact mechanics: to allow for debris pile-up;
d) dynamic analysis: because load re-distributions occur dynamically, or with dynamic load amplification;
e) stability of numerical algorithms: because localized element failures should not trigger numerical instability due to zero tangent stiffness;
f) efficiency: to allow (repetitive) non-linear analysis of real-world structures.

Different methods offer different trade-offs among the requirements above. The DEM and AEM methods are excellent at describing very large displacements and debris pile-up, but the computational cost of solutions is very high. AEM and CEM have the disadvantage that fracture zones need to be identified previously by the user when constructing the model. This paper presents a development in FEM, which is computationally efficient for truss collapse analysis, but which does not aim to compete with other special capabilities of DEM, AEM or CEM.

Complementing points a) to f) above, probabilistic or reliability analysis of progressive collapse is widely desired [2]–[8] because of the large uncertainties involved in material and element failures [9] and due to a large number of hazard loading events with low probability of occurrence. In probabilistic analyses, points e) and f) above increase in importance, as progressive analyses need to be repeated hundreds to thousands of times, considering different realizations of the problem's random variables.

Felipe et al. [10] have introduced a Finite Element (FE) model which is well suited for progressive collapse analysis of truss structures. The model combines the positional FE method, which can handle large displacements, with a ductile-damage model for material failure modeling. The material model considers continuum damage accumulation due to porosity variation. Material damage is related to the hydrostatic component of plastic strains. One unique feature of this model is that critical damage converges to the theoretical limit hypothesized by Lemaitre [11]; hence avoiding the tangent matrix to become ill-conditioned. Hence, individual elements fail, and loads are smoothly re-distributed to other undamaged or less-damaged members. The formulation has been used to describe the exact equilibrium path of different truss structures. Herein, the formulation in Felipe et al. [10] is referred to using the initials of the four authors: the Felipe-Leonel-Haach-Beck (FLHB) model.

This paper extends the results in Felipe et al. [10] in three ways: by calibrating FLHB model parameters to describe the behavior of Ultra-High-Performance Fiber Reinforced Concrete (UHPFRC); by performing a statistical analysis of FLHB model parameters for UHPFRC; and by employing the model in reliability analysis of failure paths of truss structures. The extended model can be utilized in the progressive collapse analysis of truss structures such as bridges and domes.

Progressive collapse of truss structure domes has been studied recently by Yan et al. [12] and Tian et al. [13], using bi-linear elastic-plastic material models. As will be shown herein, consideration of material failure (damage) produces significant changes in the equilibrium path of truss structures.

An extensive literature review reveals few papers addressing progressive failure paths with a probabilistic perspective. Miao and Ghosn [14], [15] studied the reliability-based progressive collapse of highway bridges; the authors used simple analytical models and derived recommended minimal reliability indexes for intact and damaged structures. Ding et al. [16] addressed reliability of steel frames subject to blast loads; the post-blast stage is evaluated by non-linear 3D finite element analysis. A similar analysis of steel-concrete slabs was performed by the same authors in Ding et al. [17] and Feng et al. [18] studied reliability and robustness of reinforced concrete frames against progressive collapse, considering damage and plasticity. As observed, few papers in the literature address reliability analysis of progressive failure paths. The above references are from the last three years, showing that this is also a recent topic.

Due to highly non-linear material behavior at failure, probabilistic analysis of failure paths is usually done using Monte Carlo simulation, using subset simulation [14]–[16] or Latin Hypercube sampling [17]. One exception is Feng et al. [18], where the probability density evolution method is employed. Because the proposed FLHB numerical formulation is fast/efficient for truss structures, brute force Monte Carlo simulation is adopted herein. However, for limit states involving critical displacements in the equilibrium path, it is shown that the First Order Reliability Method (FORM) also provides very accurate results.

Three application examples demonstrate the accuracy, robustness, and performance of the proposed numerical scheme. Real structures have been analyzed and the performance of the proposed formulation contributes to the state of the art of this scientific domain.

2 A TOTAL-LAGRANGIAN FORMULATION FOR MATERIAL AND GEOMETRICAL NONLINEAR ANALYSIS OF FAILURE PATHS

Progressive collapse occurs when structures cannot totally dissipate the kinetic energy, after the occurrence of abnormal loads [19]–[22]. Among the complex energy dissipation mechanisms, there is the plastic work in element deformation and the energy dissipation associated with structural damping [23]. The response of structures during or at the brink of progressive collapse is highly nonlinear [24], [25]. Therefore, material and geometric nonlinearities need to be considered in the analysis of progressive collapse.

In this paper, the FLHB model in Felipe et al. [10] is employed in the reliability analysis of failure paths of concrete truss structures. The model is briefly summarized in this section. Theoretical and implementation details are given in Felipe et al. [10].

The model employs a log-strain measure (ε_{ln}), which is decomposed in elastic and plastic terms. The model assumes: decoupling between elasticity-damage and plastic hardening [26]; von Mises yield criterion and isotropic hardening behavior; variation in porosity at the mesoscale equal to the hydrostatic component of the plastic strain (Gurson model [27]). Porosity variation is the result of growth and coalescence of microcavities. The total mechanical energy is written in terms of nodal positions (instead of displacements) [9], [28], [29].

In the softening regime, stress in the truss element is given by:

$$\tau = \left(1 - D\right)\aleph\varepsilon_{ln}^{e} = \left(1 - D\right)\aleph(\varepsilon_{ln} - \varepsilon_{ln}^{p}) \tag{1}$$

where D is the damage variable, $\aleph$ is the elastic modulus of the undamaged material, superscript $()^{e}$ refers to “elastic”, and superscript $()^{p}$ refers to “plastic”.

The damage evolution law is given in terms of three material parameters: α_1^p, α_2^p and α_3^p [10].

$$D\left(\varphi\right) = \alpha_1^p(\varphi - \varepsilon_{ln,d}^{p})^2 + \alpha_2^p(\varphi - \varepsilon_{ln,d}^{p}) + \alpha_3^p \tag{2}$$

where φ is the plastic extension measure and $\varepsilon_{ln,d}^{p}$ is the initial damage threshold (the fourth parameter to be determined). Thus, the stress-strain response of a structural material is described by two usual parameters: the elastic modulus ($\aleph$) and the yield stress (τ_y), and four new parameters to be determined: $\alpha_1^p, \alpha_2^p, \alpha_3^p$ and $\varepsilon_{ln,d}^p$. In Felipe et al. [10], this model was shown to accurately represent complete stress-strain curves of mild iron, high strength low-alloy steel, copper, aluminum, ASTM A36 steel, gray cast iron, and conventional concrete. In this paper, the model is extended to cover Ultra-High-Performance Fiber Reinforced Concrete (UHPFRC).

One important feature of the FLHB model is that the damage variable in Equation 2 converges to the theoretical critical damage (D_{crit}) hypothesized by Lemaitre [11], and given by:

$$D_{crit} = 1 - \frac{\tau_r}{\tau_u} \tag{3}$$

where τ_r is the rupture stress and τ_u is the ultimate stress. This is particularly relevant for progressive collapse analysis, as it avoids instability of the Hessian matrix, when an isolated truss element fails. Hence, computations can progress in a stable manner, with the load in the failed element being distributed to adjacent elements, until the complete structural collapse.

The solution scheme for the non-linear system of FE equations is based on the Newton-Raphson algorithm with displacement control.

3. MODEL CALIBRATION FOR UHPFRC

In Felipe et al. [10], the FLHB model just reviewed was employed in mechanical analysis of the fully nonlinear stress-strain response of mild iron, high strength low-alloy steel, copper, aluminum, ASTM A36 steel, gray cast iron, and conventional concrete. Herein, the FLHB model is employed in representing the nonlinear response of UHPFRC. UHPFRC is a modern building material and its application in complex engineering structures has increased in the last few years. One practical example is the Oveja Ravine truss footbridge constructed with UHPFRC in Alicante, Spain. Therefore, the analyses below are relevant to the state of the art of nonlinear problems.

The validations refer to uniaxial tests, in which cylindrical specimens have been subject to tensile/compression tests. The specimen dimensions are presented in Table 1. Six specimens are considered in compression, and six in tension (all with identical dimensions). Fiber content of UHPFRC is 2%. Numerical simulations utilize a single finite element and four hundred load steps. The boundary conditions are as follows: uniform axial displacement imposed in one end; fixed (zero) axial displacements at the opposite end. The convergence tolerance of 10^{-6} has been assumed, based on the norm of position changes (see Felipe et al. [10]).

For each experimental curve (to be presented), FLHB model parameters were found by simple least squares. The interested reader can refer to Felipe et al. [10] for details. Results are summarized in Table 2: results for UHPFRC are the mean values (from six curves).

Table 1. Material and geometric data of specimens.

Specimen	Figure	Material	Test	l_0 (*mm*)	A_0 (*mm*^{2})
UHPFRC	1	brittle	tensile	80.0	900.0
UHPFRC	2		compression	100.0	1962.5

Table 2. Material data for the mean FLHB model of UHPFRC.

Specimen	$\aleph$ (MPa)	τ_y (MPa)	$\varepsilon_{ln,d}^p$	α_1^p	α_2^p	α_3^p	D_{crit}
UHPFRC in tension	43854	6.47	$4.34\cdot10^{-4}$	-2730.50	102.86	0.0	0.938
UHPFRC in compression	43854	140.72	$1.86\cdot10^{-4}$	-46130	349.24	0.0	0.660

Figures 1 and 2 show the stress-strain curves and tangent modulus for six UHPFRC specimens with 2% of fibers in tensile and compression tests, respectively. The test results are taken from [30] In comparison to unreinforced concretes, the introduction of fibers reduces the growth of microcavities and the crack coalescence. Thus, it improves material ductility. As a result, UHPFRC presents peak strength higher than cracking strength. Then, when the material reaches the stress τ_y, it starts yielding with constant stress, until the initial damage threshold ($\varepsilon^{p}_{ln,d}$). From this strain level, softening behavior governs the mechanical behavior of UHPFRC. In order not to overdraw Figures 1 and 2 with too many curves, results for the proposed model are shown only for the mean values of model parameters (Table 2). The proposed FLHB model leads to very good fit for each experimental curve, and also describes mean behavior, as shown. The accurate fit applies to stress-strain responses (Figures 1a and 2a), to predicted damage (Figures 1b and 2b), and to tangent modulus (Figures 1c and 2c).

Figures 1b and 2b compare damage evolution in UHPFRC during tensile and compression tests. For the monotonic tests of UHPFRC, critical damage values (Equation 3) are as follows:

$$D_{crit}^{tensile} = 1 - \frac{0.264}{8.336} = 0.968 \text{ and } D_{crit}^{compression} = 1 - \frac{37.98}{148.2} = 0.744 \tag{4}$$

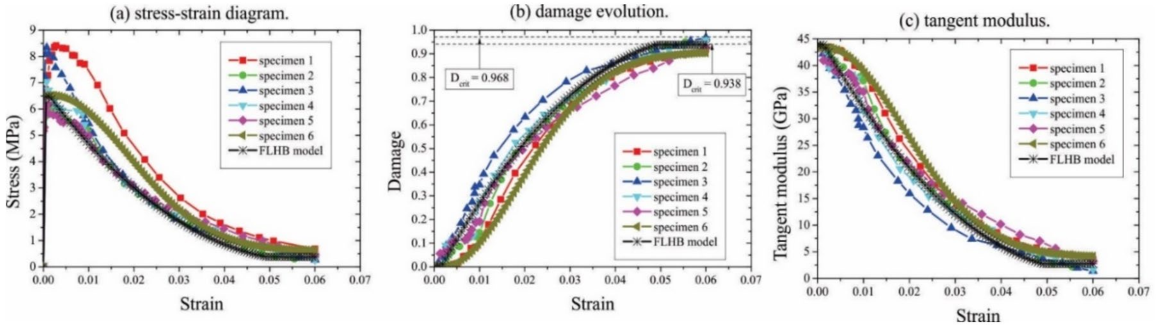

Figure 1. Tensile test at room temperature of UHPFRC with 2% of fibers [30]: (a) stress-strain diagram; (b) damage evolution and (c) tangent modulus.

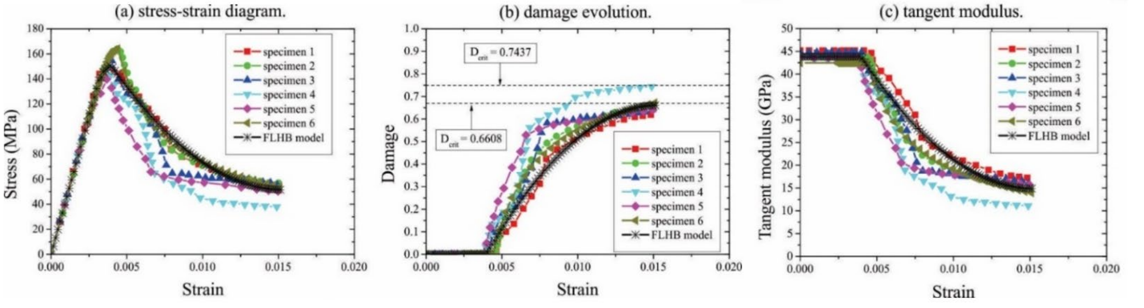

Figure 2. Axial compression at room temperature of UHPFRC with 2% of fibers [30]: (a) stress-strain diagram; (b) damage evolution and (c) tangent modulus.

As observed in Figures 1b and 2b, the proposed model represents properly the damage evolution for UHPFRC. Note that damage evolution in the FLHB model converged to values slightly smaller than the critical damage. This leads to a tangent modulus value approximately equal to the value obtained in experimental curves. Consequently, the FLHB model does not experience instability in the Hessian matrix during computations. This behavior has major importance in the context of progressive collapse analysis because it enables the accurate failure modeling of an isolated truss member, without affecting the positive definiteness properties of the Hessian matrix.

Tables 3 and 4 present the results of a statistical analysis of the FLHB model parameters for UHPFRC, which is based on the twelve experimental responses illustrated in Figures 1 and 2. In this analysis, the model parameters are determined from a simple least square fit to each of the twelve experimental curves in Figures 1 and 2. This gives one value of each model parameter for each experimental curve. Then, the EasyFit® software is employed to find a statistical distribution which describes the six data points, as well as the respective mean and standard deviation. Tables 3 and 4 show the resulting distributions, which passed the chi-square and KS goodness-of-fit tests with 95% confidence. The large coefficient of variation (COV) of the initial damage threshold ($\varepsilon^p_{ln,d}$) draws our attention, which is a consequence of the inherent material variability. We acknowledge that the available database was quite limited (only six samples); hence, the values in Tables 3 and 4 should not be taken as definite. This data is employed in Section 6 in the reliability analysis of the progressive collapse of a 3D truss structure.

Table 3. Statistics for FLHB model: UHPFRC in tension.

Variable	mean	cov	Distribution
$\aleph$ **(MPa)**	43854	0.023	Uniform
τ_y **(MPa)**	6.47	0.115	Normal
$\varepsilon^p_{ln,d}$	$4.34 \cdot 10^{-4}$	0.551	Lognormal
α^p_1	-2730.50	-0.153	Normal
α^p_2	102.86	0.088	Gumbel Min
D_{crit}	0.938	0.027	Uniform

Table 4. Statistics for FLHB model: UHPFRC in compression.

Variable	mean	cov	distribution
$\aleph$ **(MPa)**	43854	0.023	Uniform
τ_y **(MPa)**	140.72	0.078	Normal
$\varepsilon^p_{ln,d}$	$1.86 \cdot 10^{-4}$	0.417	Lognormal
α^p_1	-46130.0	-0.206	Gumbel Min
α^p_2	349.24	0.140	Gumbel Min
D_{crit}	0.660	0.064	Gumbel Max

4. 3D TRUSS FROM THE LITERATURE: COMPARISON OF CONVENTIONAL CONCRETE VERSUS UHPFRC

The twelve-member 3D truss structure illustrated in Figure 3 is a reference example in several papers dealing with nonlinear analysis, e.g [31]–[33]. The proposed formulation is employed in the progressive collapse analysis of this 3D truss structure. The main purpose of this analysis is to compare the behavior of conventional and UHPFRC concrete. The example demonstrates the performance of UHPFRC in arresting progressive collapse, in comparison with conventional concrete.

This truss is composed of 9 nodes and 12 elements. The input data for UHPFRC elements is given in Table 2. The cross-section area for conventional concrete elements is $A_{concrete} = 4A_{UHPFRC} = 7850$ mm^2, which is four times larger than the cross-section area of UHPFRC elements (because the later has higher strength). Material parameters for conventional concrete are: $\aleph$ = 32 GPa; τ_y = 12.7 MPa; $\alpha^p_1 = 14696$; $\alpha^p_2 = 295.19$; $\alpha^p_3 = -0.0216$; $\varepsilon^p_{ln,d} = 3.72 \times 10^{-4}$ and $D_{crit} = 0.441$, according to Felipe et al. [10]. Results are first obtained for geometrical non-linearity only, then for plasticity and damage.

Figure 4 presents the geometric non-linear responses obtained with the proposed formulation and by ANSYS® software. Constitutive law in ANSYS was modelled using the linear elastic model. Notice the good agreement among the responses. It is worth mentioning the accurate representation of the snap-through phenomenon for the displacement value of 49.5 cm, which corresponds to forces of 28480 kN and 83140 kN for UHPFRC and conventional concrete, respectively. Moreover, for such force level, the Hessian matrix determinant is nil, which leads to neutral equilibrium. Consequently, the forces 28480 kN (UHPFRC) and 83140 kN (conventional concrete) represent the limit force values for this truss structure in a stable regime of static equilibrium, accounting for linear elastic material behavior. Notice that conventional concrete has higher stiffness than UHPFRC along the equilibrium trajectory, because $A_{concrete} = 4A_{UHPFRC}$. Then, the cross-section area value of the elements contributes directly to the Hessian matrix. For displacements in the range 49.5 cm to 240 cm, convergence criterion in force cannot be applied because the Hessian matrix determinant is negative (unstable regime). Therefore, the load-displacement curves shown in Figure 4 have been achieved through a convergence criterion based on positions. Remark that the snap-through phenomenon shown in Figure 4 only appears when linear elastic behavior is assumed. When material nonlinearity is considered, these materials fail before snap-through, as discussed below.

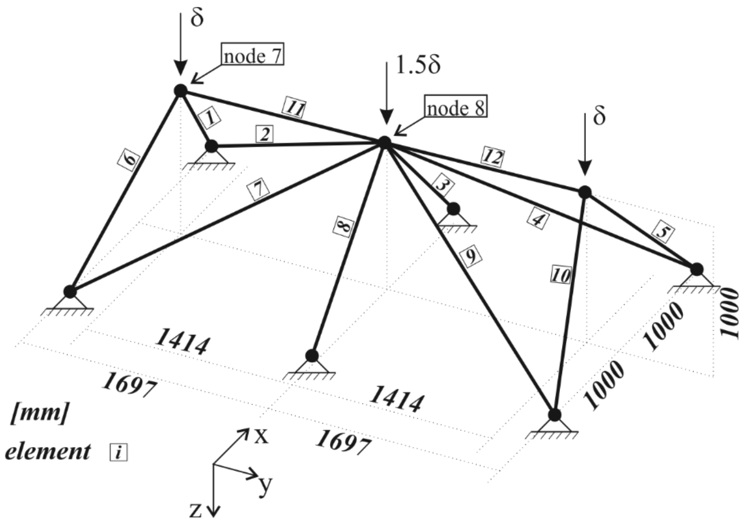

Figure 3. Geometric input data for twelve-member 3D truss.

Figure 5 shows the force vs. displacement curves for nodes 7 and 8 of the truss structure, accounting for geometric and material nonlinearities. It is worth noticing the different behaviors achieved when different modeling assumptions are made (linear elastic, plastic, and plastic with damage). Moreover, the responses presented in Figures 4 and 5 demonstrate clearly that the mechanical description based solely on geometric nonlinearities is not sufficient for the proper representation of the real mechanical structural behavior.

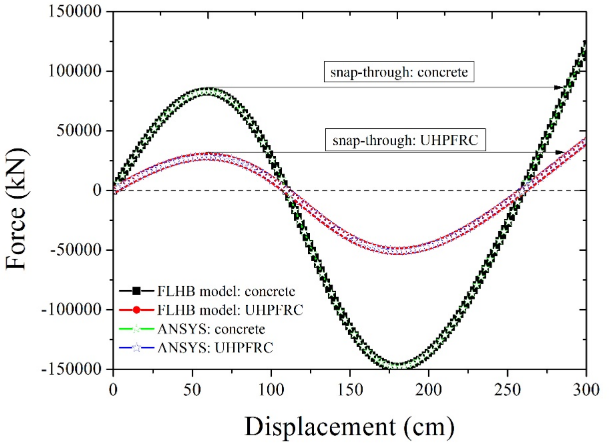

Figure 4. Vertical displacement *vs.* force for node 8, linear material behavior.

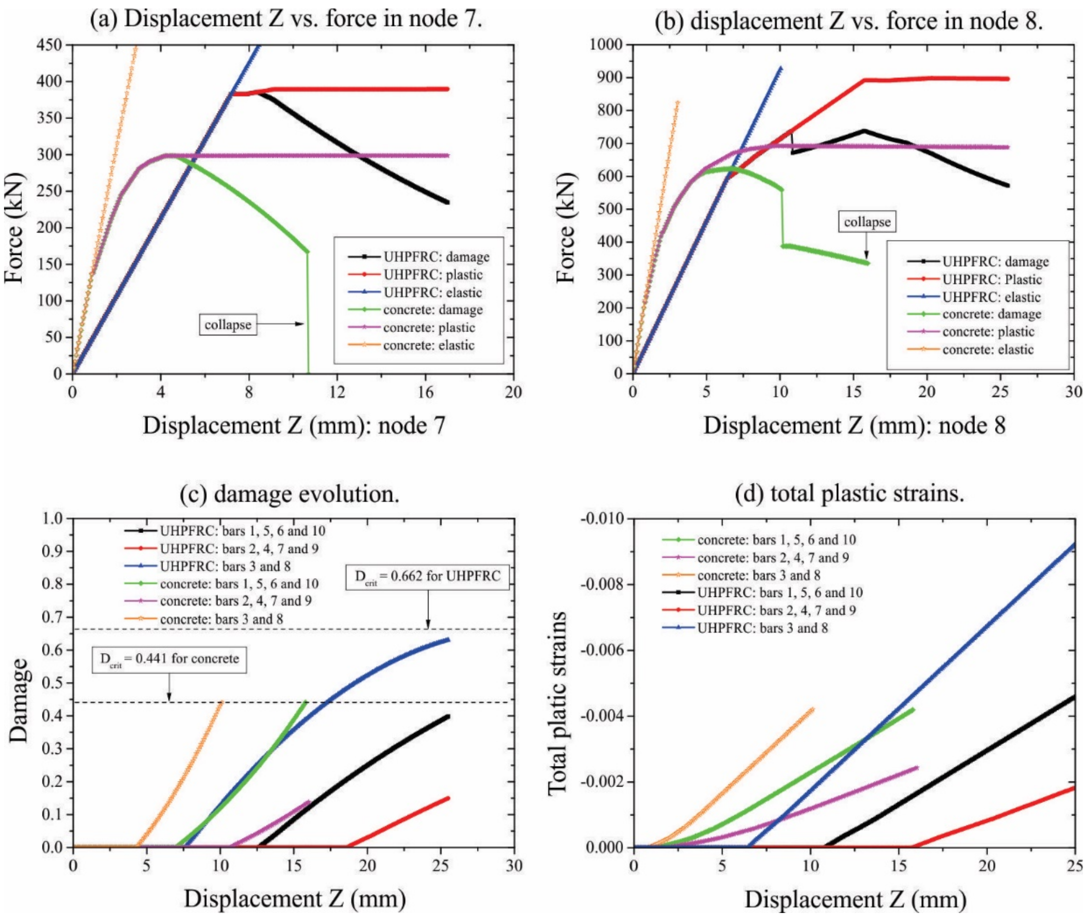

Figure 5. (a) Displacement Z *vs.* force in node 7; (b) displacement Z *vs.* force in node 8; (c) damage evolution in the bars and (d) total plastic strains in the bars.

In the context of plastic responses (Figure 5b), it is worth mentioning the loss of stiffness for displacements of 0.82 mm (conventional concrete) and 6.50 mm (UHPFRC), caused by plastic strains in elements 3 and 8 (Figure 5d). At displacements of Z=9.13 mm (conventional concrete) and Z=15.71 mm (UHPFRC), all elements (1 to 10) start yielding under constant stress in the plastic solution. Hence, the force vs. displacement curves become horizontal. For displacement levels higher than 9.13 mm (conventional concrete) and 15.71 mm (UHPFRC), the plastic response is singular (infinite displacement at constant force). In this case, softening behavior has not been accounted for in the pure plastic solution.

The proposed plastic damage model leads to consistent responses. For displacements of 0.82 mm (conventional concrete) and 6.50 mm (UHPFRC), one observes the plastic behavior of elements 3 and 8 (Figure 5d). For displacements of 4.36 mm (conventional concrete) and 7.65 mm (UHPFRC), elements 3 and 8 reach the initial damage threshold ($\varepsilon^{p}_{ln,d}$). Thus, softening behavior appears.

For conventional concrete at displacements of 10.12 mm, elements 3 and 8 reach critical damage (as seen in Figure 5c). Thus, these elements fail and a sudden drop in force is observed. To simulate the local failure of these elements, nearly zero Young's modulus is assumed for those bars that reach critical damage. The bars 1, 5, 6 and 10 reach the initial damage threshold at 6.99 mm of displacement, as seen in Figure 5c. At a displacement of 15.79 mm, these bars reach critical damage and fail. For displacement level equal to 10.69 mm, bars 2, 4, 7 and 9 starts damaging (Figure 5c). The complete collapse of the conventional concrete truss structure occurs for displacements of Z=10,69 mm (node 7) and Z=16.035 mm (node 8), as seen in Figure 5a and 5b.

For UHPFRC material and center node displacements in the range 10 mm to 15 mm, the truss structure experiences load redistributions, which lead to higher force values of elements 1, 5, 6, and 10. The bars 2, 4, 7 and 9 reach initial damage threshold for displacement level of 12.67 mm. None of the bars composed of UHPFRC reaches critical damage, as seen in Figure 5c. Consequently, the progressive collapse of the 3D truss structure composed of UHPFRC does not occur for this displacement level. Then, in addition to higher strength, UHPFRC provides an improvement on the post-failure structural behavior. This material avoided the total structural collapse, which cannot be avoided in the case of conventional concrete.

5. RELIABILITY ANALYSIS OF FAILURE PATHS

5.1 Basic formulation

Uncertainties are intrinsic to the progressive collapse problem. The abnormal loads which may trigger a collapse event are characterized by small probability of occurrence, large and random intensities, and extreme consequences [2]–[5]. Material degradation behavior (ductility, damage) is usually associated to larger variance than conventional (linear elastic) material behavior [34], [35]. Hence, it is natural to use reliability theory to study the progressive failure of structures.

Probabilistic formulations in the literature address the hazards, the loading scenarios, and their probabilities [2]–[7]. However, most papers addressing the mechanics of load transfer as structural damage progresses are deterministic [12], [13], [19]–[25]. Formulations addressing the reliability of structures in progressive failure scenarios are rare [6]–[8], [14]–[18]. Hence, application of the FLHB model to the reliability analysis of truss structures in progressive collapse analysis of hyperstatic trusses is the main contribution of this paper.

One relevant point to make, when applying any numerical model in reliability analysis (instead of deterministic analysis), is that the reliability algorithm tests the structure a large number of times, for very different values of the random parameters. Hence, the algorithm needs to be both efficient and stable. Any numerical floating-point instabilities are more likely to be revealed in reliability than in conventional mean value analysis.

Let $\mathbf{R} = \{R_1, R_2, \ldots, R_n\}$ be a vector of random variables describing the uncertainties of the structural problem, such as material yield and ultimate stresses, geometry, load magnitudes, etc. Let $\mathbf{R} = \mathbf{r}$ denote a specific outcome of the random variable vector. A limit state equation $g(\mathbf{r}) = 0$ is written, dividing the domain of $\mathbf{R}$ into a survival domain (Ω_s Os) and a failure domain (Ω_f), such that [35]:

$$\begin{cases} \Omega_s = \{r \mid g(\mathbf{r}) > 0\} \\ \Omega_f = \{r \mid g(\mathbf{r}) \leq 0\} \end{cases} \tag{5}$$

The fundamental problem in structural reliability is the assessment of the failure probability:

$$P_f = P\left[g(\mathbf{r}) \leq 0\right] = \int_{\Omega_f} f_{\mathbf{R}}(\mathbf{r}) d\mathbf{r} \tag{6}$$

where $P[\ ]$ is the probability operator, $f_{\mathbf{R}}(\mathbf{r})$ is the joint probability density function of the n-dimensional vector $\mathbf{R}$. If all random variables are independent, $f_{\mathbf{R}}(\mathbf{r})$ can be determined by:

$$f_{\mathbf{R}}(\mathbf{r}) = \prod_{i=1}^{n} f_{Ri}(r_i) \tag{7}$$

where $f_{Ri}(r_i)$ is the marginal probability density function (PDF) for random variable Ri.

Due to difficulties in multi-dimensional integration, Equation 6 cannot be solved analytically, unless for very simple problems [35]. Two lines of approaches have been developed for solving Equation 6: simulation methods and transformation methods [35]. In this paper, the brute force Monte Carlo Simulation (MCS) and the First Order Reliability Method (FORM) are considered, as follows.

The Monte Carlo Simulation (MCS) method is intuitive and of very simple numerical implementation. Samples of the random variables **R** are generated, following the joint density function $f_{\mathbf{R}}(\mathbf{r})$ [34], [35]. For each sample $\mathbf{r}_j$, the limit state function $g(\mathbf{r}_j)$ is evaluated. An indicator function $I(\mathbf{r})$ is introduced to identify points in the failure domain, such that $I(\mathbf{r}_j)=1$ if $I(\mathbf{r})\in\Omega_f$, and $I(\mathbf{r}_j)=0$ if $I(\mathbf{r})\notin\Omega_f$. The failure probability is evaluated as:

$$P_f = P\left[g(\mathbf{r})\leq 0\right] = \int_{\Omega} I(\mathbf{r}) f_{\mathbf{R}}(\mathbf{r})d\mathbf{r} = E\left[I(\mathbf{r})\right] \tag{8}$$

In Equation 8, the term $E\left[I(\mathbf{r})\right]$ is the mean or expected value of the indicator function, which can be estimated from a finite number of samples (n_s), as follows:

$$P_f = E\left[I(\mathbf{r})\right] \approx \hat{P}_f = \frac{1}{n_s}\sum_{j=1}^{n_s} I\left[\mathbf{r}_j\right] = \frac{n_f}{n_s} \tag{9}$$

where $\hat{P}_f$ is an estimate, and n_f is the number of points sampled in the failure domain. It can be shown [34], [35] that Equation 9 is an unbiased estimate of the true failure probability; hence, $\hat{P}_f \to P_f$ when $n_s \to \infty$. In practical terms, for a limited computational budget, the number of samples is limited, and the estimate $\hat{P}_f$ is subject to a statistical sampling error. Roughly speaking, to keep this error limited to about 10%, when evaluating a failure probability of the order $P_f = 10^{-p}$, requires the number of samples to be around $n_s \approx 10^{p+2}$ [34], [35]. Hence, the required number of samples also depends strongly on the order of magnitude of the failure probability being evaluated.

A more efficient way of computing small failure probabilities is by way of transformation methods, like the First Order Reliability Method (FORM). The random variables are initially mapped from the original design space to the standard Gaussian space, using a transformation $\mathbf{V} = T[\mathbf{R}]$. Transformation $T[\mathbf{R}]$ involves eliminating eventual correlation between the random variables [34], [35]. In standard Gaussian space, variables $\mathbf{V}$ have zero mean and unitary standard deviation, and the joint density function $f_{\mathbf{V}}(\mathbf{v})$ becomes radially symmetric w.r.t. the origin. The most probable point of the failure domain, $\mathbf{v}^*$, is found by solving a minimization problem:

$$\begin{cases} Find : \mathbf{v}^* \\ which\,minimizes : \mathbf{v} = \left(\mathbf{v}^t\mathbf{v}\right)^{1/2} \\ subject\,to : g(\mathbf{v}) = 0 \end{cases} \tag{10}$$

This minimization problem can be solved by the HLRF algorithm, proposed by [36], [37], or by other dedicated algorithms [34], [35]. The reliability index is the minimal distance between the limit state and the origin: $\beta = \mathbf{v}^*$. By approximating the limit state by a hyperplane, centered on $\mathbf{v}^*$, the first-order approximation to the failure probability is obtained as:

$$P_f \approx \Phi(-\beta) \tag{11}$$

where $\Phi(.)$ is the standard normal cumulative distribution function (CDF).

5.2 Reliability of truss structures, conditional on loading

In Section 5.1, the conventional formulation of structural reliability is presented. The formulation considers randomness in loads and/or strength variables.

In this paper, we focus on the strength of truss structures suffering progressive collapse. This is convenient since the numerical model is displacement-controlled. The prescribed displacement δ is the link between structural strength and the actual load effects. Truss strengths and conditional failure probabilities ($P[f|\delta]$) are evaluated for given δ, and as a function of δ. The actual displacement imposed on the structure is a function of actual load ($\delta(P)$), which is not addressed in the paper. This strategy is valid when only one independent load acts on the structure, or for a couple of dependent loads.

Hence, the failure probabilities in Section 5.1 are evaluated considering only strength random variables, leading to a conditional failure probability, $P[f|\delta]$. The (unconditional) probability of failure can be assessed through the total probability theorem, as follows:

$$P_f = \int_p P\left[f|\delta(p)\right] f_P(p)\,dp \tag{12}$$

where $f_P(p)$ is the density function of the random load. In this paper, we do not address the uncertainty in random loads; hence, we do not solve Equation 12, which is presented for completeness.

5.3 Conditional failure events during progressive failure

A failure path of a hyperstatic structure is the non-linear load-displacement response, from initial loading to complete loss of equilibrium. For a several-times hyperstatic structure, this includes a sequence of bar failures. When uncertainty in loading or in material response is considered, in principle, very different bar failure sequences can be observed. The number of failure sequences increases when independent loads act on the structure, or when independent material properties are assumed for different elements.

One significant difficulty in probabilistic analysis of progressive failure of several-times hyperstatic structures is handling the large number of possible conditional failure paths and branches, as illustrated in [6]–[8]. Analytical evaluation of the probabilities of each failure branch is quite involving, generally limited to a single or to fully dependent loads, or to the few more important failure paths and branches [38], [39]. One exception is the recent work of Feng et al. [18], which uses the probability density evolution method to evaluate failure path probabilities. The analytical addressing of failure paths allows one to consider “approximate” failure modes such as buckling of compressed members or simple rupture of tensile members.

In this paper, failure branch probabilities are handled by the Monte Carlo simulation and FORM algorithms. Individual and progressive bar failure events are handled by the non-linear material model. One acknowledged limitation of results presented herein in that either a single load is considered (Section 6.1), or fully dependent loads are considered (Section 6.2). Also, full dependence between material properties of different elements is considered, which is more realistic than assuming independence.

6. STRUCTURAL RELIABILITY EXAMPLES

6.1 von Mises truss with analytical solution

This section presents the reliability analysis of the von Mises truss. Results are presented in increasing order of complexity: linear elastic analysis is shown first, then geometrical nonlinearities are accounted for and, finally, geometrical and material nonlinearities are considered. Figure 6 illustrates the von Misses truss geometry and the constitutive models, typical of steel. Probabilities of failure are assessed through Monte Carlo Simulation (MCS) and the First Order Reliability Method (FORM). These solutions are compared and discussed in the following.

Table 5 describes the random variables and the assigned statistical properties. Nominal values for the parameters are as follows: the members are composed of tubular steel with circular cross-section of radius $r=5$ cm and cross-section area $A_0 = 78.5$ cm^2. Young`s modulus is E = 20500 KN/cm^2. Strength material parameters (for plastic analysis) are $\sigma_y = 10$ kN/cm^2 and $\varepsilon_y = 4.878 \times 10^{-4}$. The geometric parameters are: $x_0 = 200$ cm and $y_0 = 10$ cm. The vector of random variables is assembled as: $\mathbf{R} = \left\{E, \sigma_y, r, A_0, x_0, y_0\right\}$.

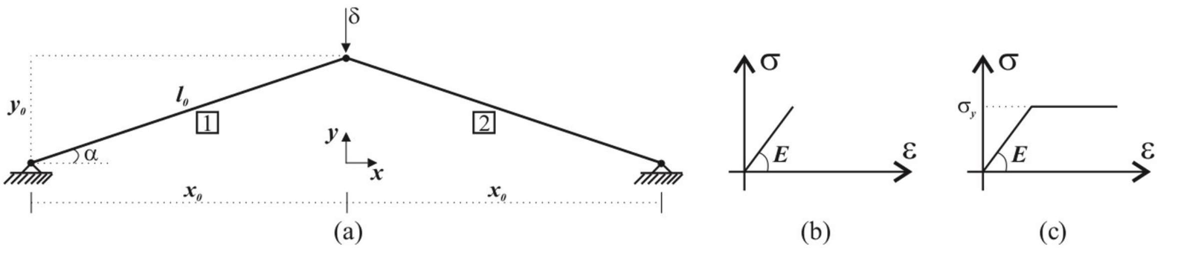

Figure 6. (a) geometric input data; (b) linear material response and (c) elastoplastic material response.

Table 5. Statistics for von Mises truss.

Variable	mean	cov	distribution	ref.
$\boldsymbol{E}$	1.00 E	0.03	Lognormal	[35]
$\boldsymbol{\sigma_y}$	1.00 σ_y	0.07	Lognormal	[35]
$\boldsymbol{A_0}$	1.01 A_0	0.04	Normal	[40]
$\boldsymbol{R}$	1.00 r	0.02	Normal	[40]
$\boldsymbol{x_0}$	1.00 x_0	0.02	Normal	[40]
$\boldsymbol{y_0}$	1.00 y_0	0.02	Normal	[40]

The analytical solution for this problem, accounting for linear response, is obtained by enforcing the equilibrium at the initial configuration. In this case, the normal force is as follows:

$$N_{bar} = -\frac{\delta E A_0}{\sqrt{x_0^2 + y_0^2}} sin\left[arctan\left(\frac{y_0}{x_0} \right) \right] \tag{13}$$

where δ is the prescribed displacement. Because material behavior is linear elastic and the bars are under compression, the limit state is written in terms of Euler buckling load as follows:

$$g(\mathbf{r}) = P_{cr} - N_{bar} = \frac{\pi^3 E r^4}{4\left(x_0^2 + y_0^2\right)} - \frac{\delta E A_0}{\sqrt{x_0^2 + y_0^2}} sin\left[arctan\left(\frac{y_0}{x_0} \right) \right] \tag{14}$$

Figure 7a shows the values for conditional probabilities of failure ($P[f|\delta]$ *vs*. δ) assessed by FORM and MCS for the analytical limit state (Equation 14). The probability of failure values are largely dependent on the prescribed displacement value, as expected. The responses provided by FORM and MCS are in excellent agreement. It illustrates the efficiency of FORM, which handled a non-linear limit state (Equation 14) properly. It is worth mentioning that MCS and FORM are complementary in this solution. The probabilities of failure are quite low for small values of prescribed displacements. Thus, MCS may become prohibitive because of the computational cost. The amount of MCS samples is $n_s = 10^6$; hence, MCS solutions are obtained for about $P[f|\delta] < 10^{-5}$.

As illustrated in Figure 7a, the target reliability index[1] of $\beta = 4.2$ ($P[f|\delta] \approx 10^{-5}$) leads to the maximum displacement in linear elastic analysis equal to 4 cm.

[1] JCSS [40], considering normal relative cost of safety measure and moderate consequences of failure.

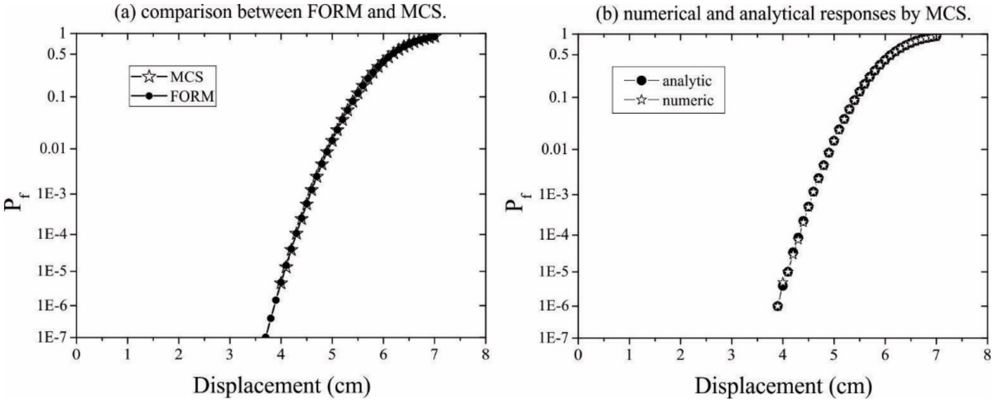

Figure 7. $P[f|\delta]$ *vs*. displacement curve. Linear elastic solution for buckling: (a) comparison between FORM and MCS and (b) comparison of numerical and analytical responses by MCS.

To demonstrate accuracy of the FLHB non-linear formulation, the model was employed in the numerical analysis of the von Mises truss. However, geometric and material linear elastic behavior have been assumed. In this case, the limit state equation is written as follows:

$$G(\mathbf{r}) = P_{cr} - N_{num} = \frac{\pi^3 E r^4}{4\left(x_0^2 + y_0^2\right)} - N_{num}(\mathbf{r}) \tag{15}$$

where N_{num} indicates the normal force value in the member from the numerical solution, which is a function of the random variables of the problem.

Figure 7b compares the analytical and numerical solutions assessed by MCS. The numerical scheme provides results in excellent agreement with the analytical approach, which confirms the accuracy of the implementation. Because the Euler buckling load governs the failure mode (which is determined in the initial configuration), the normal force in numerical analysis is equal to the normal force from the analytical response.

The analysis becomes realistic when geometrical and material nonlinearities are accounted for. The material behavior is initially assumed as elastoplastic, as illustrated in Figure 6c. One hundred load steps are applied in the central node, with displacement control, for the accurate mechanical description.

The analytical elastic solution, for this case, is determined by equilibrium in the current configuration, which leads to:

$$F_{an}(\mathbf{r},\delta) = 2EA_0 \left\{ 1 - \frac{\cos\left[\arctan\left(\frac{y_0}{x_0}\right)\right]}{\cos\left[\arctan\left(\frac{y_0-\delta}{x_0}\right)\right]} \right\} \sin\left[\arctan\left(\frac{y_0-\delta}{x_0}\right)\right] \tag{16}$$

where F_{an} is the force conjugate to the δ applied in the central node.

Figure 8 illustrates the numerical solutions obtained by the FLHB model, accounting for geometrical and material nonlinearities. The numerical and analytical responses are in excellent agreement. It is worth remarking the complex mechanical behavior of this two-truss bar problem, in which tensile and compression normal force values have been observed. The limit forces are 77.3 kN ($F_{lim,e}$) and 61.2 kN ($F_{lim,p}$), for the elastic and plastic materials, respectively. For such forces, the Hessian matrix determinant is nil. Notice that $F_{lim,p}$ is 26.3% smaller than the $F_{lim,e}$.

Also, a statistical analysis of $F_{lim,e}$, and $F_{lim,p}$ is performed. From samples of random variables in Table 5, samples of $F_{lim,e}$, and $F_{lim,p}$ are obtained. The EasyFit software is employed to find the probability distribution and parameters for these variables. One hundred samples are computed. Table 6 presents the results.

Table 6. Statistics for limit loads $F_{lim,e}$ and $F_{lim,p}$.

Variable	mean	Cov	distribution
$F_{lim,e}$	78.1	0.11	Lognormal
$F_{lim,p}$	59.3	0.09	Lognormal

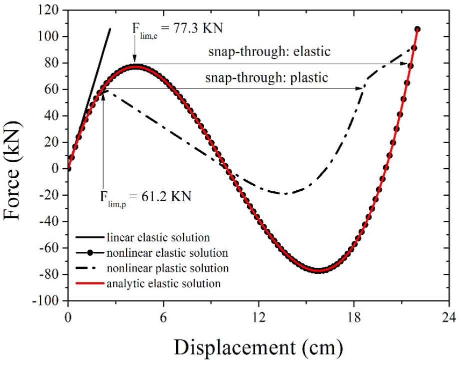

Figure 8. Load *vs*. displacement for geometrically nonlinear von Mises truss.

The limit state functions for non-linear analysis can be defined in terms of resistant forces and prescribed displacement δ. For the (semi-)analytical solution, one has:

$$g\left(\mathbf{r},\delta,F_{lim,e}\right)=F_{lim,e}-F_{an}\left(\mathbf{r},\delta\right)$$

$$g\left(\mathbf{r},\delta,F_{lim,p}\right)=F_{lim,p}-F_{an}\left(\mathbf{r},\delta\right) \tag{17}$$

The corresponding limit state equation in the proposed numerical formulation is given as follows:

$$g\left(\mathbf{r},\delta,F_{lim,e}\right)=F_{lim,e}-F_{num}\left(\mathbf{r},\delta\right)$$

$$g\left(\mathbf{r},\delta,F_{lim,p}\right)=F_{lim,p}-F_{num}\left(\mathbf{r},\delta\right) \tag{18}$$

where F_{num} is the force conjugate to the δ applied in the central node from the numerical solution, which is a function of the random variables of the problem.

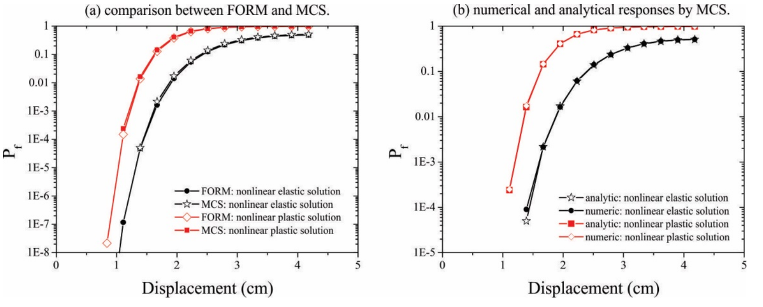

Figure 9. $P[f|\delta]$ *vs*. displacement curve: (a) comparison between FORM and MCS (b) comparison between numerical and analytical responses by MCS.

Figure 9a presents the $P[f|\delta]$ *vs.* displacement curves evaluated by FORM and MCS accounting for geometrical and material non-linearities. Notice the excellent agreement between the solutions even for the non-linear geometrical behavior. It is worth remarking that for the imposed displacement δ = 4 cm, the conditional failure probability is 0.5. In the linear elastic solution, such a probability of failure value has been achieved for δ = 6.1 cm, as illustrated in Figure 7. It confirms that the geometrical nonlinear assumption has major importance in the failure analysis of the von Mises truss. For the same target reliability value of $P[f|\delta]=10^{-5}$, the maximum prescribed displacement in geometrically nonlinear elastic solution is δ =1.39 cm, as illustrated in Figure 9a. As observed in Figure 9a, the assumption of non-linear material behavior increases the probability of failure, as expected. Hence, allowable displacements are much lower than in linear material and linear geometrical cases. For the target probability of failure $P[f|\delta]=10^{-5}$, the maximum prescribed displacement is 1.05 cm. Figure 9b compares the analytical and numerical responses computed by MCS, in which excellent agreement can be observed.

It is worth stressing that the evaluation of the previous statistics of limit loads $F_{lim,e}$ and $F_{lim,p}$ has been performed to facilitate the analysis for varying prescribed displacements δ. This problem separation is not usually required because random limit loads (strengths) could be evaluated within the FORM or MCS solutions directly from $F_{lim,e}(\mathbf{r})$ and $F_{lim,p}(\mathbf{r})$.

6.2 Elastoplastic twelve-member 3D truss structure

This example evaluates the reliability of the structure presented in Section 4. The 3D truss is composed of UHPFRC with nominal cross-sectional area A_0 = 1962.5 mm^2. The mean and coefficient of variation (COV) of the cross-sectional areas are E[A]=1.01A_0 and COV = 0.04. The damage model statistics are in Tables 3 and 4. The vector of random variables is assembled as: $\mathbf{R}=\left\{\aleph,\sigma_y,A,D_{crit},\varepsilon_{ln,d}^{p},\alpha_1^{p},\alpha_2^{p}\right\}$. Hence, limit state functions for each bar can be written in terms of the critical damage, as follows:

$$g_k\left(\mathbf{r},\delta,D_{crit}\right)=D_{crit}-D_{num}\left(\mathbf{r},\delta\right),\ k=1,2,\ldots,12. \tag{19}$$

where D^{num} is the bar damage given by the numerical solution, which is a function of the vector of random variables and the prescribed displacements δ.

Figure 10 shows the results for a deterministic (mean value) analysis, for which variables $\left\{\aleph,\sigma_y,A,D_{crit},\varepsilon_{ln,d}^{p},\alpha_1^{p},\alpha_2^{p}\right\}$ assume their values mean. Figures 10a and 10b show the displacement Z *vs.* force curves of nodes 7 and 8, respectively, considering the proposed model. At point 1 occurs the first loss of stiffness of the truss structure, due to plastification of bars 3 and 8. At point 2, bars 3 and 8 reach damage equal to 0.175 (see also Figure 10c), and a drop in force is observed (Figure 10b). This drop of force occurs because bars 3 and 8 enter the softening regime, under compression, as shown in Figure 2 for about the same damage level. Between points 2 and 3, the truss experiences load redistributions. Between points 3 and 4, all bars (except bars 11 and 12) are in the damage process; hence, softening behavior is observed. At point 4 bars 3 and 8 reach critical damage and fail, with a subsequent sudden drop in force (Figure 10b). Thus, these bars are removed to simulate local failure. At point 5 occurs the failure of bars 1, 5, 6 and 10, as they reach critical damage. This corresponds to the final collapse of this structure, which occurs under displacements Z=30.80 mm (node 7) and Z = 46.2 mm (node 8).

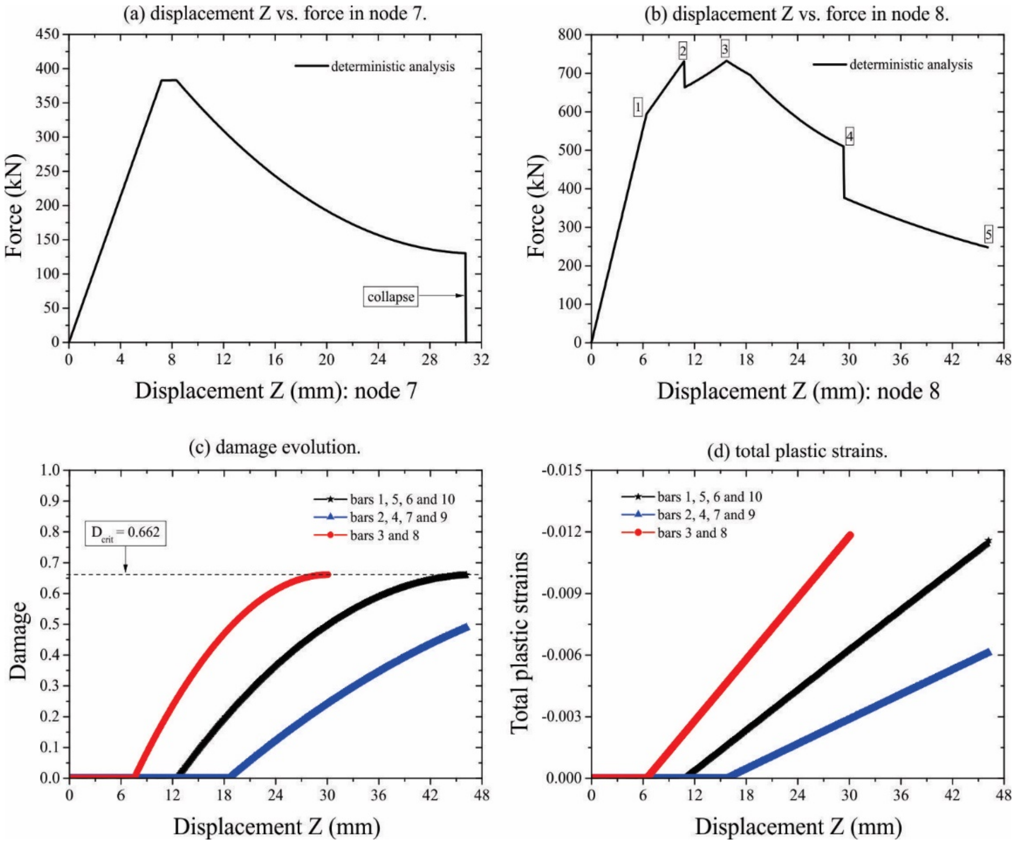

Figure 10. (a) Displacement Z *vs.* force in node 7; (b) displacement Z *vs.* force in node 8; (c) damage evolution and (d) total plastic strains in the bars: deterministic (mean value) analysis.

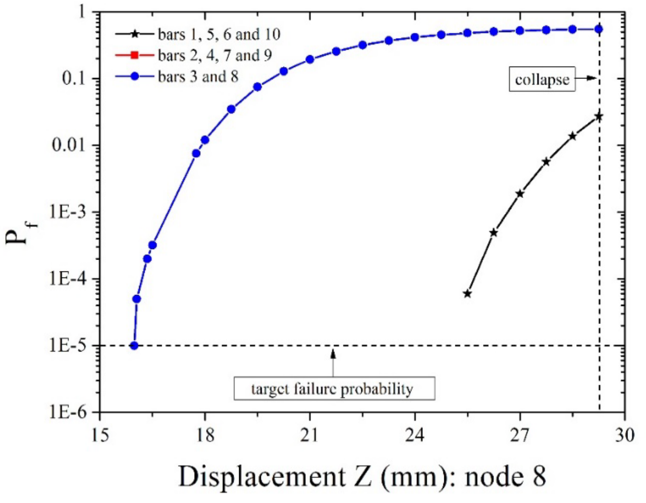

Figure 11. $P[f|\delta]$ *vs*. displacement curve by MCS.

Figure 11 shows the $P[f|\delta]$ *vs*. displacement curve considering non-linear geometric and material behavior, which has been evaluated by MCS with $n_s = 10^5$. The maximum allowable displacement is equal to 16.0 mm for the target failure probability of $P[f|\delta] = 10^{-5}$. In the deterministic analysis, and for displacements up to 29 mm, none of the members had reached critical damage (Figure 10b). However, considering the uncertainties of resistance variables, bars 3 and 8 achieve the target probability of failure for much smaller displacement values (around 16.0 mm). For a prescribed displacement of 26.25 mm, members 3 and 8 reach $P[f|\delta]$= 0.503, while bars 1, 5, 6 and 10 reach $P[f|\delta]$= $4.9 \cdot 10^{-4}$. Remark that $P[f|\delta]$= 0 for bars 2, 4, 7 and 10 at this displacement level.

Figure 12 shows the displacement Z *vs.* force curve in node 8 for one Monte Carlo sample leading to a full collapse of the truss. This curve was determined with $\mathbf{r}^* = \{\aleph, \sigma_y, A, D_{crit}, \varepsilon^p_{ln,d}, \alpha^p_1, \alpha^p_2\} = \{44692.42, 127.77, 2012.57, 0.729, 7.63\times 10^{-5}, -32863.1, 422.54\}$. In Figure 12b it is possible to note that for Z=18.5 mm (probabilistic analysis), bars 3 and 8 reach critical damage, leading to a sudden drop in force. Remark that in deterministic analysis those bars reach critical damage only for Z=30.11 mm. For this Monte Carlo sample, damage evolution presents a greater slope stronger than in the deterministic analysis, as illustrated in Figure 12c. This implicates that the displacement Z vs. force curve presents more pronounced softening behavior (see Figure 12a). Finally, for Z=29.25 mm the bars 1, 5, 6 and 10 reach critical damage, which conducts to the full collapse of this structure. This displacement level leads to $P[f|\delta] = 0.553$ (for bars 3 and 8) and $P[f|\delta] = 0.0273$ (for bars 1, 5, 6 and 10).

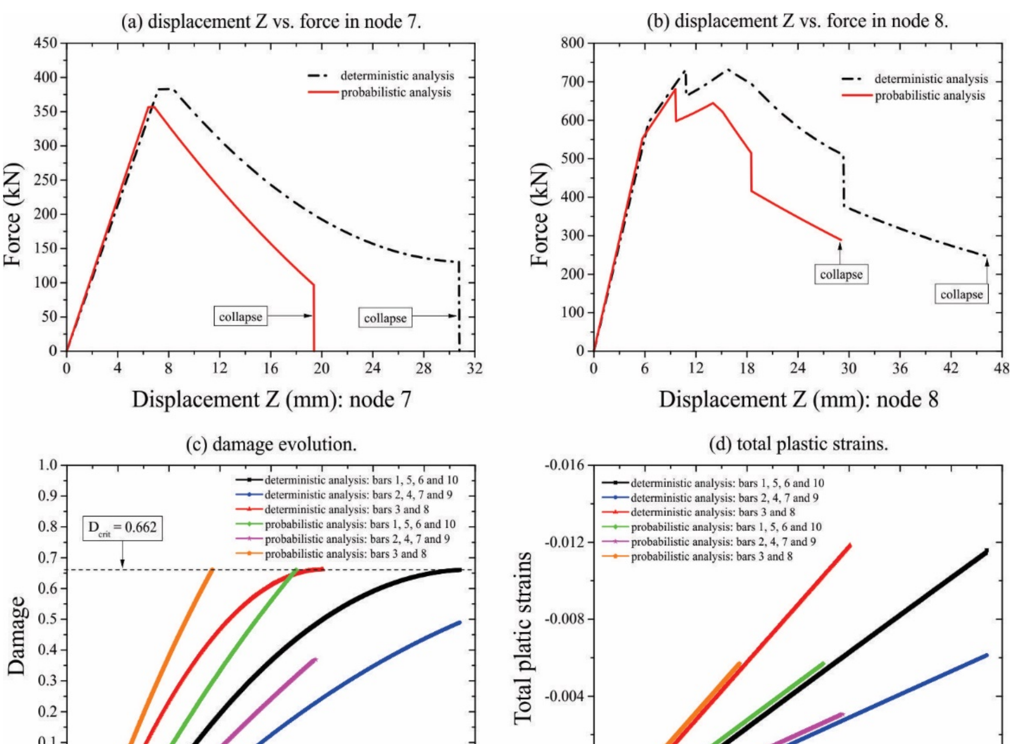

Figure 12. (a) Displacement Z *vs.* force in node 7; (b) displacement Z *vs.* force in node 8; (c) damage evolution and (d) total plastic strains in the bars: comparison between deterministic (mean value) and one sample of probabilistic analysis.

7 CONCLUSIONS

In this paper, the recently proposed [10] comprehensive ductile-damage FLHB model for truss structures has been employed to represent non-linear material responses of Ultra-High Performance Fiber Reinforced Concrete (UHPFRC). Based on a limited number of experimental curves, statistics of FLHB model parameters for UHPFRC have been obtained. These statistics were employed in the conditional reliability analysis of failure paths of truss structures, for imposed displacements.

It was demonstrated that the FLHB ductile-damage model accurately predicts the full stress-strain nonlinear response of UHPFRC, including the softening phase. Critical damage converges to the theoretical limit, avoiding numerical instabilities in element failures, leading to load redistributions until the complete structural collapse. An example problem has been presented comparing the failure paths of conventional concrete and UHPFRC trusses. Even being a fragile material, UHPFRC improves the structural ductility and leads to significant lower values of probability of failure in comparison with conventional concrete.

It was demonstrated, through two examples, that the FLHB model is both efficient and stable in the reliability analysis of complete truss structures experiencing progressive collapse. Load redistributions occur continuously after failure of individual members. The numerical model is non-linear but quite efficient, allowing even brute force Monte Carlo simulation for structures with moderate number of bars. Regardless of the significant non-linear geometrical and material behavior, it was shown that the First Order Reliability Method (FORM) provides accurate estimates of conditional failure probabilities, for prescribed displacements.

ACKNOWLEDGEMENTS

The authors acknowledge funding of this research project by Brazilian agencies CAPES (Brazilian Higher Education Council – Finance Code 001), CNPq (Brazilian National Council for Research, grant n. 306373/2016-5) and FAPESP (São Paulo State Research Foundation, grant n. 2017/01243-5). Valuable comments by the anonymous reviewers are also cheerfully acknowledged

REFERENCES

[1] J. M. Adam, F. Parisi, J. Sagaseta, and X. Lu, "Research and practice on progressive collapse and robustness of building structures in the 21st century," *Eng. Struct.*, vol. 173, pp. 122–149, 2019.

[2] B. R. Ellingwood, "Mitigating risk from abnormal loads and progressive collapse," *J. Perform. Constr. Facil.*, vol. 20, pp. 315–323, 2006.

[3] B. R. Ellingwood, "Strategies for mitigating risk to buildings from abnormal load events," *Int. J. Risk Assess. Manag.*, vol. 7, pp. 828–845, 2007.

[4] B. R. Ellingwood, E. V. Leyendecker, and J. T. P. Yao, "Probability of failure from abnormal load," *J. Struct. Eng.*, vol. 109, pp. 875–890, 1983.

[5] B. R. Ellingwood and D. O. Dusenberry, "Building design for abnormal loads and progressive collapse," *Comput. Aided Civ. Infrastruct. Eng.*, vol. 20, pp. 195–205, 2005.

[6] T. R. C. Felipe, V. G. Haach, and A. T. Beck, "Systematic reliability-based approach to progressive collapse," *ASCE ASME J. Risk Uncertain. Eng. Syst. A Civ. Eng.*, vol. 4, 04018039, 2018.

[7] R. K. Tessari, H. M. Kroetz, and A. T. Beck, "System reliability-based design optimization and risk-based optimization: a benchmark example considering progressive collapse," *Eng. Optim.*, vol. 51, pp. 1000–1012, 2016, http://dx.doi.org/10.1080/0305215X.2018.1502760.

[8] A. T. Beck, "Optimal design of hyperstatic redundant structural systems: fundamentals," *Eng. Struct.*, vol. 219, pp. 110542, 2020, http://dx.doi.org/10.1016/j.engstruct.2020.110542.

[9] H. B. Coda and R. R. Paccola, "A total-Lagrangian position-based FEM applied to physical and geometrical nonlinear dynamics of plane frames including semi-rigid connections and progressive collapse," *Finite Elem. Anal. Des.*, vol. 91, pp. 1–15, 2014.

[10] T. R. C. Felipe, E. D. Leonel, V. G. Haach, and A. T. Beck, "A comprehensive ductile damage model for 3D truss structures," *Inter J Non-Linear Mech*, vol. 112, pp. 13–24, 2019.

[11] J. Lemaitre, *A Course on Damage Mechanics*. New York: Springer, 1992.

[12] S. Yan, X. Zhao, K. J. R. Rasmussen, and H. Zhang, "Identification of critical members for progressive collapse analysis of single-layer latticed domes," *Eng. Struct.*, vol. 188, pp. 111–120, 2019.

[13] L. M. Tian, J. P. Wei, and J. P. Hao, "Optimization of long-span single-layer spatial grid structures to resist progressive collapse," *Eng. Struct.*, vol. 188, pp. 394–405, 2019.

[14] F. Miao and M. Ghosn, "Reliability-based dynamic analysis of progressive collapse of highway bridges," *Procedia Eng.*, vol. 199, pp. 1170–1174, 2017.

[15] F. Miao and M. Ghosn, "Reliability-based progressive collapse analysis of highway bridges," *Struct. Saf.*, vol. 63, pp. 33–46, 2016.

[16] Y. Ding, S. Song, and H. T. Zhu, "Probabilistic progressive collapse analysis of steel frame structures against blast loads," *Eng. Struct.*, vol. 147, pp. 679–691, 2017.

[17] Y. Ding, S. Song, and H. T. Zhu, "Probabilistic progressive collapse analysis of steel-concrete composite floor systems," *J. Construct. Steel Res.*, vol. 129, pp. 129–140, 2017.

[18] D.-C. Feng, S.-C. Xie, J. Xu, and K. Qian, "Robustness quantification of reinforced concrete structures subjected to progressive collapse via the probability density evolution method," *Eng. Struct.*, vol. 202, 109877, 2020.

[19] S. Szyniszewski and T. Krauthammer, "Energy flow in progressive collapse of steel framed buildings," *Eng. Struct.*, vol. 42, pp. 142–153, 2012.

[20] B. Asgarian and F. H. Rezvani, "Progressive collapse analysis of concentrically braced frames through EPCA algorithm," *J. Construct. Steel Res.*, vol. 70, pp. 127–136, 2012.

[21] M. Liu, "Progressive collapse design of seismic steel frames using structural optimization," *J. Construct. Steel Res.*, vol. 67, pp. 322–332, 2011.

[22] H. S. Kim, J. Kim, and D. W. An, "Development of integrated system for progressive collapse analysis of building structures considering dynamic effects," *Adv. Eng. Softw.*, vol. 40, pp. 1–8, 2009.

[23] J. W. Smith, "Structural robustness analysis and the fast fracture analogy," *Struct. Eng. Int.*, vol. 16, pp. 118–132, 2006.

[24] S. Gerasimidis and J. Sideri, "A new partial-distributed damage method for progressive collapse analysis of steel frames," *J. Construct. Steel Res.*, vol. 119, pp. 233–245, 2016.

[25] G. Kaewkulchai and E. Williamson, "Beam element formulation and solution procedure for dynamic progressive collapse analysis," *Comput. Struc.*, vol. 82, pp. 639–651, 2004.

[26] J. Lemaitre and R. Desmorat, *Engineering Damage Mechanics*. New York: Springer, 2005.

[27] A. L. Gurson, “Plastic flow and fracture behavior of ductile materials incorporating void nucleation, growth, and interaction,” Ph.D. dissertation, Brown Univ., Providence, RI, 1975.

[28] M. Greco, F. A. R. Gesualdo, W. S. Venturini, and H. B. Coda, "Nonlinear positional formulation for space truss analysis," *Finite Elem. Anal. Des.*, vol. 42, pp. 1079–1086, 2006, http://dx.doi.org/10.1016/j.finel.2006.04.007.

[29] T. M. Siqueira and H. B. Coda, "Total Lagrangian FEM formulation for nonlinear dynamics of sliding connections in viscoelastic plane structures and mechanisms," *Finite Elem. Anal. Des.*, vol. 129, pp. 63–77, 2017, http://dx.doi.org/10.1016/j.finel.2016.12.005.

[30] P. A. Krahl, R. Carrazedo, and M. K. El Debs, "Mechanical damage evolution in UHPFRC: Experimental and numerical investigation," *Eng. Struct.*, vol. 170, pp. 63–77, 2018.

[31] S. Krenk, *Non-linear Modeling Analysis of Solids and Structures*. Cambdrige: Cambridge University Press; 2009.

[32] S. Krenk and O. Hededal, "A dual orthogonality procedure for nonlinear finite element equations original research article," *Comput. Methods Appl. Mech. Eng.*, vol. 123, pp. 95–107, 1995.

[33] Y. B. Yang and L. J. Leu, "Constitutive laws and force recovery procedures in nonlinear analysis of truss," *Comput. Methods Appl. Mech. Eng.*, vol. 92, pp. 121–131, 1991.

[34] A. . T. Beck, *Reliability and Safety of Structures*. Rio de Janeiro: Elsevier Campus, 2019.

[35] R. E. Melchers and A. T. Beck, *Structural Reliability Analysis and Prediction*. New Jersey: John Wiley & Sons, 2018.

[36]. M. Hasofer and N. C. Lind, "Exact and invariant second moment code format," *J. Eng. Mech.*, vol. 100, pp. 111–121, 1974.

[37]. R. Rackwitz and B. Fiessler, "Structural reliability under combined random load sequences," *Comput. Struc.*, vol. 9, pp. 489–494, 1978.

[38] D. A. Onishchenko, "Analytical approach for estimating failure probability of multi-element structural systems with load-path history," *Procedia Mater. Sci.*, vol. 3, pp. 1994–1999, 2014.

[39] P. Thoft-Christensen and Y. Murotsu, *Application of Structural Systems Reliability Theory*. Berlin: Springer, 1986.

[40]. JCSS *Probabilistic Model Code, Joint Committee on Structural Safety 2001.* http://www.jcss.byg.dtu.dk/Publications/Probabilistic_Model_Code.aspx (accessed Jun 16, 2018).

Author contributions: TRCF: resources, computer programming, writing original draft; EDL, VGH: conceptualization, methodology, writing-review and editing; ATB: conceptualization, funding acquisition, methodology, supervision, writing original draft, writing-review and editing.

Editors: Bruno Breseghella, Guilherme Aris Parsekian.

IBRACON
IBRACON Structures and Materials Journal
Revista IBRACON de Estruturas e Materiais
ISSN 1983-4195 ismj.org
SciELO

ORIGINAL ARTICLE

Study of the influence of the foundation and the reservoir on the dynamic response in a concrete gravity dam profile

Estudo da influência da fundação e do reservatório na resposta dinâmica de um perfil de barragem gravidade

Iarly Vanderlei da Silveira[a]
Lineu José Pedroso[b]
Giuliano Santa Marotta[c]

[a]Instituto Federal da Paraíba, Departamento de Engenharia Civil, Cajazeiras, PB, Brasil
[b]Universidade de Brasília – UnB, Departamento de Engenharia Civil e Ambiental, Programa de Pós-graduação em Estruturas e Construção Civil – PECC, Grupo de Dinâmica e fluido-Estrutura – GDFE, Brasília, DF, Brasil
[c]Universidade de Brasília – UnB, Instituto de Geociências, Programa de Pós-graduação em Geociências Aplicadas e Geodinâmica, Brasília, DF, Brasil

Received 13 October 2020
Accepted 04 January 2021

Abstract: This work aims to verify the influence of the foundation and the reservoir on the dynamic behavior of concrete gravity dams in terms of the natural frequencies, vibration modes for a free vibration analysis; and in terms of maximum displacements and maximum stresses at singular points of the structure for a seismic excitation. The dam-reservoir-foundation interaction was investigated through modal and transient analysis by the finite element method via ANSYS APDL software. For this study, we used a typical Brazilian dam profile and compatible data from a Brazilian earthquake for the seismic excitation. The results showed the influence of the reservoir and the foundation on the natural frequencies in the coupled system, as well as its repercussions on the response of the dam under seismic excitation.

Keywords: dam-reservoir-foundation interaction, dynamic analysis, foundation flexibility, reservoir, ANSYS.

Resumo: Este trabalho tem o objetivo de verificar a influência da fundação e do reservatório no comportamento dinâmico em barragens gravidade de concreto, avaliando as frequências naturais e os modos de vibração para uma análise em vibração livre; assim como os deslocamentos máximos e as tensões máximas em pontos singulares da estrutura para uma excitação sísmica. A interação barragem-reservatório-fundação é investigada através da análise modal e transiente pelo método dos elementos finitos via software ANSYS APDL. Adotou-se um perfil de barragem típica brasileira e dados compatíveis de um sismo local para a excitação sísmica. Para o caso de vibração livre, os resultados mostraram a influência do reservatório e da fundação nas frequências naturais no sistema acoplado e a sua correlação com os resultados obtidos para o sistema desacoplado, já para a excitação sísmica houve modificações na resposta da estrutura com a alteração, em especial, do tipo de fundação.

Palavras-chave: interação barragem-reservatório-fundação, análise dinâmica, fundação flexível, reservatório, ANSYS.

How to cite: I. V. Silveira, L. J. Pedroso, and G. S. Marotta, "Study of the influence of the foundation and the reservoir on the dynamic response in a concrete gravity dam profile," *Rev. IBRACON Estrut. Mater.*, vol. 14, no. 4, e14403, 2021, https://doi.org/10.1590/S1983-41952021000400003

1 INTRODUCTION

The knowledge of the behavior of concrete gravity dams under dynamic load is an important issue in the evaluation of these structures stability. The assessment of the actual behavior of dams under dynamic loads is complex because it

Corresponding author: Iarly Vanderlei da Silveira. E-mail: iarly.silveira@ifpb.edu.br
Financial support: None.
Conflict of interest: Nothing to declare.

deals with a massive structure that presents non-linear characteristics and because it involves the interaction of three elements: the water of the reservoir, the soil of the foundation and the concrete of the dam.

Some studies in this field consider only the interaction between the fluid and the structure as preponderant in the dynamic assessment. However, recent research also shows the influence of the foundation [1], [2]. The study of soil-structure interaction (SSI) and fluid-structure interaction (FSI) in dams has advanced well over the last few years, in spite of requiring more refined investigations and more sophisticated models.

The SSI is an important factor to be considered and it requires special attention in dam constructions. It is also necessary to know the deformability of the foundations, the ration between the applied load and the resultant deformations, due to the potential differential settlements in the foundation.

The effects of the FSI are important in the coupled dam reservoir problems under seismic loads or in the case of fluid induced vibrations. The movement of the structure inevitably causes a movement of the fluid in contact with the structure walls. As a result, the fluid-structure assembly constitutes a coupled system for which it is often impossible to consider the responses and excitations separately.

Because the coupled system involves elements of different physical properties and requires a complex approach, an analytical treatment is often limited depending on the problem requirements. Thus, the finite element method (FEM) fits well in solving these problems due to its ability to discretize irregular geometries and solve cases involving the structure, the foundation and the reservoir fluid interacting with each other.

The methods used for the dynamic analysis of dam-gravity of concrete-reservoir were first developed by Westergaard [3], who obtained analytically, by using solution of the Laplace equation, the distribution of pressures along the fluid-structure interface.

Westergaard assumed that the hydrodynamic effect on a rigid dam during an acceleration is equivalent to an inertial force resultant from a mass distribution added to the dam body (additional mass), a method named pseudo static. Chopra [4] observed that the response of a dam when subjected to seismic loads was largely influenced by the fundamental mode of vibration, i.e., both the inertial and hydrodynamic forces depended on the fundamental mode of the structure vibration. Subsequently, Chopra and Chakrabarti [5], Hall and Chopra [6], Fenves and Chopra [7], Chopra and Zhang [8] and Ribeiro and Pedroso [9] evaluated other aspects that influenced the dam response under dynamic excitation, namely: fluid compressibility, fundamental vibration mode, foundation flexibility, as well as vertical and horizontal components of the earthquake. With the advancement of these studies and from the understanding of the problems involved, the researchers began to evaluate more complex geometries and problems, which mainly comprised the dam - reservoir - foundation coupled system. The pioneering SSI studies, Novak [10] and, Léger and Katsouli [11], evaluated the stability of the dam to landslide and tipping in a seismic analysis influenced by the variation of the foundation properties. In addition, Bougacha et al. [12] analyzed the effect of the sediments in the dam-reservoir-sediment-foundation interaction in the harmonic movements of the dam. In a more recent studies, Ghannat [13] highlighted factors that can affect dam stability and its foundation, such as overload, joint opening and failure modes. Inaudi et al. [14] evaluated the simplified linear methods for preliminary seismic analysis of dams, in particular, the influence of the foundation flexibility on the response. Lin et al. [15] analyzed the influence of the heterogeneity of the foundation that may cause an increase in the response of the dam; and Papazafeiropoulos et al. [16] presented a formulation based on finite elements for complex reservoir, foundation and dam geometries, evaluating the interaction of those elements and the influence of their characteristics, such as the thickness of the soil layer, the flexibility of the foundation and the presence of sediments. Burman et al. [17] showed in their study a free-field formulation used in dynamic analyzes involving SEI. Chopra [18] indicates that the flexibility of the foundation causes large displacements in the crest when studying the dam of Pine Flat submitted to a local earthquake. This author, in recent studies, has investigated the absorbent boundary conditions through damping elements for the foundation and the reservoir. Lokke and Chopra [1] it is presents a generalization for the conditions of non-return of the wave in the contour of a 3D arc dams involving a seismic excitation. A numerical formulation integrating dam-reservoir-foundation involving the three interacting media, which is based on the finite difference method (FDM) in a physical-intuitive manner, allowing the assemblage a complete matrix system to be solved, is presented in Pedroso [19].

This paper presents a discussion on the main aspects of a dynamic assessment in a concrete gravity dam, with typical dimensions in Brazil, which involves the study of free vibration and seismic excitation influenced by the foundation and the reservoir. Variables considered in the analyses include the variation of the modulus of elasticity of the foundation, and the influence in the reservoir of the distant boundary condition, evaluating the case of zero pressure and the case of the non-return condition of the wave (Sommerfield condition).

Simulations were run with the ANSYS program. An actual record of soil movements in Brazil, obtained through the partnership with the Seismological Observatory (OBSIS) of the University of Brasília (UnB), was considered in the analyses. It must be pointed out that few studies reproduce a real record on Brazilian soil.

2. PROBLEM DESCRIPTION

The dam-reservoir-foundation system consists of three sub-systems: the concrete dam; the rock of the foundation consisting as the structure support region, and the fluid domain having a border region with arbitrary geometry adjacent to the dam consisting of a uniform and infinite channel in the upstream direction.

For a dynamic analysis of gravity dams, these sub-systems are interacting with each other and may involve numerous variables such as local geological faults, seismic motions with wave propagation in all directions on the ground, non-linearities of materials and infinite contours in the soil and reservoir. Thus, the analyses of these structures can be extremely complex. In order to simplify, a 3D analysis can be seen in Figure 1a. By involving these problems, it is used, initially, the hypothesis that the structure can be represented by an 2D slice. (Figure 1b), in which the dam body behaves in the plane state of deformation, where the solicitations are, essentially within the x - z plane. Thus, the region of analysis of the dam-reservoir-foundation system is limited to a zone of finite domain for the problem, considering the entire linear, isotropic and homogeneous system. Figure 1b illustrates the simplified 2D system.

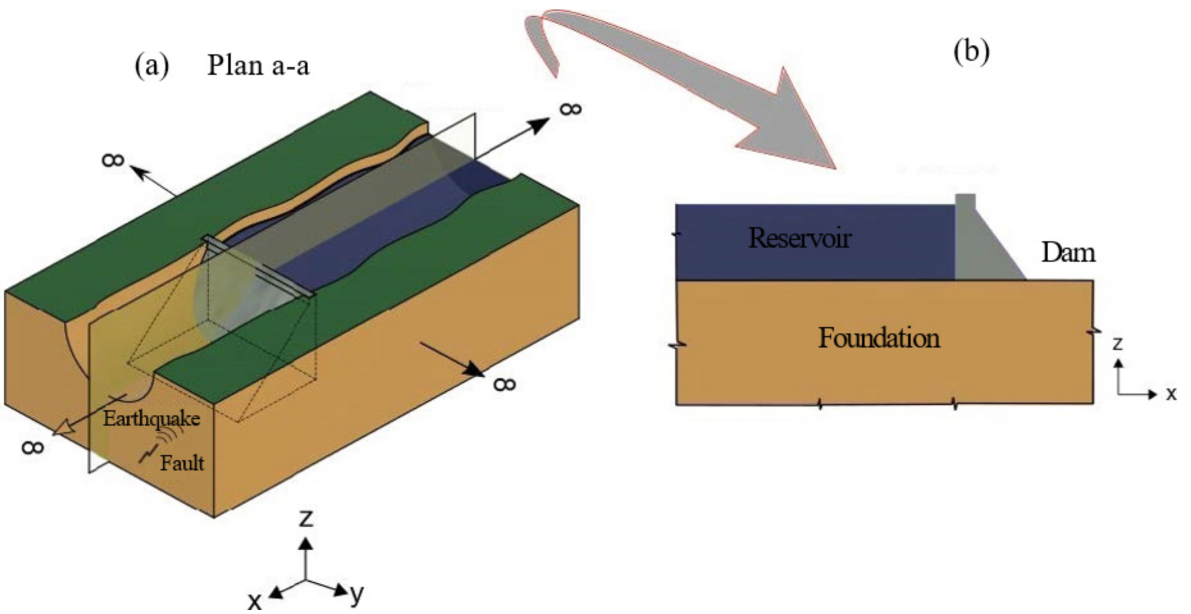

Figure 1. Dam gravity-reservoir-foundation coupled system: (a) 3D and (b) 2D.

3. THEORETICAL FORMULATION AND NUMERICAL MODEL

For the modeling of the coupled gravity-reservoir-foundation dam system involving, respectively, the interaction between concrete, water and soil in dynamic problems, a finite element formulation was used to discretize the equations of each means. Assuming some simplifications, namely:

- The dam structure and the foundation material are composed of linear, elastic and isotropic materials;
- The foundation is considered massless, to avoid the propagation and reflection problems of waves in the seismic analysis and;
- The fluid is considered quiescent (stagnant), inviscid (non-viscous) and incompressible. There is no flow, existing only vibration around a position of equilibrium (acoustic fluid).

The problem involving the dynamic effect between dam, reservoir and foundation must be studied together and integrated, since these means do not behave in isolation.

To include the effect of SSI, a formulation proposed by Burman et al. [17] was used, which the relates of the overlap of effects in terms of free field displacements.

In the formulation of the SSI dynamic equilibrium equations, the structure - foundation coupled system and interface zone are considered as shown in Figure 2, which shows the structure nodes, the foundation soil nodes and the common nodes at the soil-structure interface.

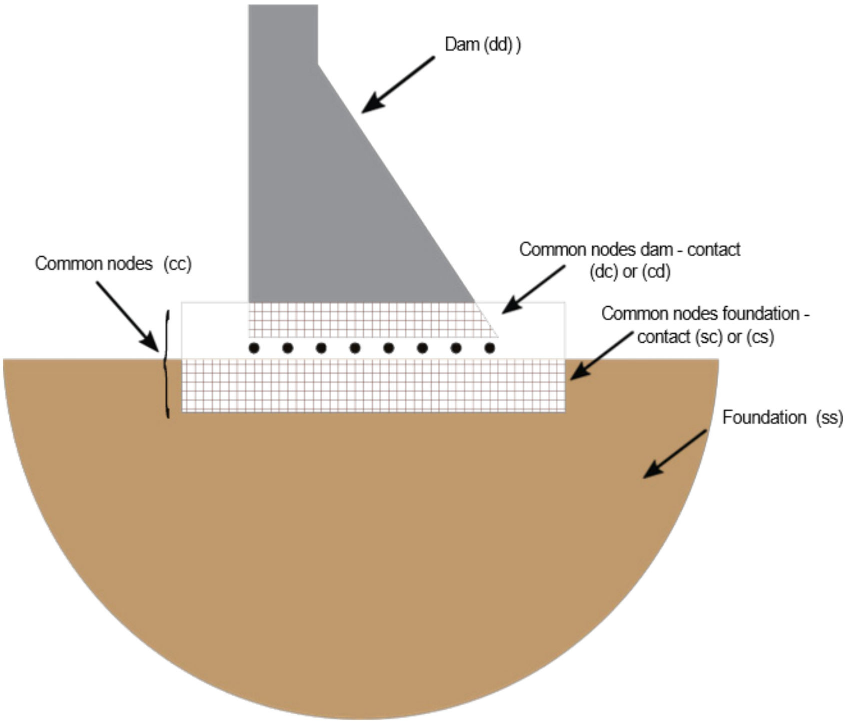

Figure 2. Interaction system foundation (s), dam (d) and the common interface zone (c).

The free field formulation leads to the following equation:

$$[M_{bs}]\left\{\ddot{U}_{bs}\right\}+[C_{bs}]\left\{\dot{U}_{bs}\right\}+[K_{bs}]\left\{U_{bs}\right\}=F=-[M_{bs}]\left\{\ddot{U}_{g}\right\} \tag{1}$$

in which the matrices M_{bs}, C_{bs}, K_{bs} represent, respectively, the mass, damping and stiffness of the complete dam - foundation system. The matrix $\ddot{U}_g$ represents the movement of the soil imposed by the seismic excitation, i.e., the vector F comprises the forces of seismic excitation acting at the base of the structure. The vector U_{bs} consists in the displacements of the nodes in relation to the base and the time derivatives, while $\dot{U}_{bs}$ and $\ddot{U}_{bs}$ are, respectively, the velocity and the acceleration on these nodes.

For the study of the FSI, without the influence of the foundation, a dam-reservoir coupling model was used, within the hypotheses of small displacements for the structure and the fluid. The domain of the fluid is ruled by the two-dimensional wave equation:

$$\nabla^2 p-\frac{1}{c^2}\ddot{p}=0 \tag{2}$$

The term ∇^2 corresponds to a stiffness operator, whereas $\frac{1}{c^2}$ is a mass operator, in which c is the velocity of the wave, p is the hydrodynamic acoustic pressure and t is the time. In order to solve the Equation 2, one must satisfy the boundary conditions that are shown in Figure 3. The boundaries of the reservoir comprise the interface with the dam (Γ_1), the bottom (Γ_2), the radiation at infinity (Γ_3) and the free surface (Γ_4).

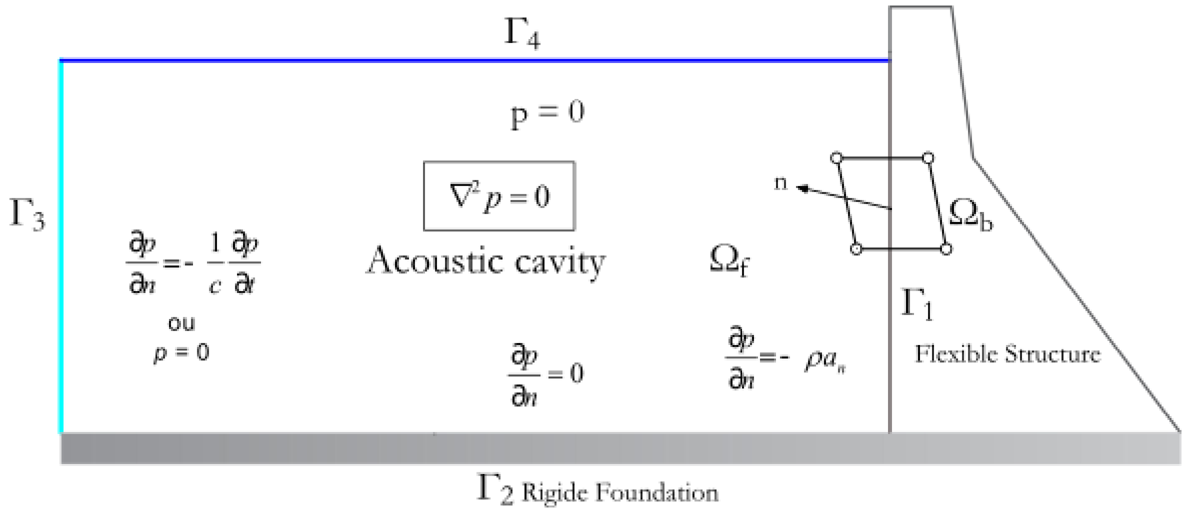

Figure 3. Fluid-structure interaction system.

The mathematical problem described by Equation 2, with the respective boundary conditions presented by the Figure 3 and discretization by the finite element method, leads to the equation of the movement of the reservoir (fluid) given by the matrix expression 3.

$$\left[M_f\right]\left\{\ddot{P}_f\right\}+\left[C_f\right]\left\{\dot{P}_f\right\}+\left[K_f\right]\left\{P_f\right\}-\rho\left[Q^T\right]\left\{\ddot{U}_{bs}\right\}=[0] \tag{3}$$

in which M_f, C_f, K_f, are respectively the mass matrices, damping and stiffness of the fluid, P_f and their derivatives represent the pressure and their variations, respectively. The term represents $\rho\left[Q^T\right]$ the coupling between the fluid and the structure.

A more complete development on the problem of acoustic cavities and fluid-structure interaction is found in Pedroso [20], [21].

The dynamic equation of the structure coupled to the foundation can be written similarly to Equation 1 by adding the term that represents the force associated with the hydrodynamic pressure produced by the reservoir, that is:

$$[M_{bs}]\left\{\ddot{U}_{bs}\right\}+[C_{bs}]\left\{\dot{U}_{bs}\right\}+[K_{bs}]\left\{U_{bs}\right\}=[M_{bs}]\left\{\ddot{U}_g\right\}+[Q]\left\{P_f\right\}=[0] \tag{4}$$

The global system soil-fluid-structure coupled is obtained by regrouping the two systems [1] and [4] into one as follows:

$$\begin{bmatrix} M_{bs} & 0 \\ \rho\left[Q^T\right] & M_f \end{bmatrix}\begin{Bmatrix} \ddot{U}_{bs} \\ \ddot{P}_f \end{Bmatrix}+\begin{bmatrix} C_{bs} & 0 \\ 0 & C_f \end{bmatrix}\begin{Bmatrix} \dot{U}_{bs} \\ \dot{P}_f \end{Bmatrix}+\begin{bmatrix} K_{bs} & -Q \\ 0 & K_f \end{bmatrix}\begin{Bmatrix} U_{bs} \\ P_f \end{Bmatrix}=\begin{Bmatrix} -M_{bs}\ddot{U}_g \\ 0 \end{Bmatrix} \tag{5}$$

The Equation 5 discretized by the MEF via ANSYS will be used for the analysis that will be object of our studies, involving the three media in question:

i) Modal analysis - decoupled and coupled free vibrations;
ii) Transient analysis - seismic excitation decoupled and coupled, as can be observed in Table 1.

Table 1. Cases analyzed in this work and their main characteristics

Cases (Dynamic Analysis)	System	Scheme	Foundation rock E_f/E_c	Reservoir boundary
Modal	DF	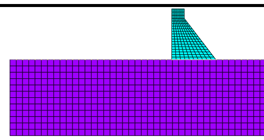	1, 2 e 5	---
	R	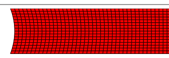	---	Zero pressure
	DRF	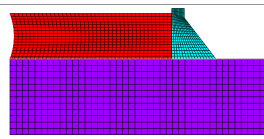	1, 2 e 5	Zero pressure
Transient	DF	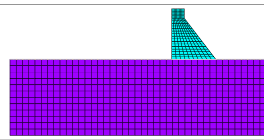	1, 2 e 5	---
	DRF	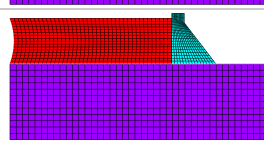	5	Zero pressure
	DRF		1, 2 e 5	Sommerfield condition

4 RESULTS AND DISCUSSIONS

4.1 Introduction

To obtain the dynamic response, modal and transient analyses were performed. In the first analysis, the natural modal frequencies and mode shapes were determined, whereas in the second, the history of displacements and stresses under seismic load were obtained.

In the modeling of the structure, the following physical properties were adopted for the concrete of the dam: specific mass equal to 2500 kg/m^3, Young's modulus equal to 25 GPa, Poisson's coefficient equal to 0,25. The physical properties of water are: velocity of sound 1440 m/s and specific mass 1000 kg/m^3. The soil of the foundation is assumed to be massless, in order to avoid the problems associated with propagation and wave reflections.

For a parametric soil-structure variation, it was used the relation between the modulus of elasticity of the foundation and the concrete: $\frac{E_f}{E_c} = 1$, 2 and 5. This variation can be found for different types of rock, from possible altered granites $\frac{E_f}{E_c} = 1$, gneiss $\frac{E_f}{E_c} = 2$ and shale $\frac{E_f}{E_c} = 5$. It should be noted that the modulus of elasticity of the foundation together with the Poisson's ratio and resistance to simple compression determine the modulus of deformability of the foundation, an important parameter for dam projects.

In the seismic excitation, the Rayleigh damping was considered with a value of 5% for the damping factor of the dam and soil coupled system.

For the structure and foundation, it was used the finite element - Plane 183 (plane strain). In the interface of the soil-structure interaction problem, it was utilized the elements 172 and TARGE 169, which make the connection between the nodes and the elements on the contact surfaces. For the reservoir it was used the FLUID29 element. At the far end of the reservoir, it was used the FLUID 129 element that is responsible for the absorption of waves in the boundary (non-return wave - Sommerfield condition).

The case studies analyzed in this work are oriented to the analysis of a typical 2 D profile of Brazilian dams, in accordance with the conditions and physical constants prescribed in this section.

Table 1 shows the simulation plan performed in this work for the different types of dynamic analysis (modal or transient) performed with the coupled and decoupled system. Also included in the simulations are the influence of the foundation: flexible $E_f/E_c = 1$; intermediary $E_f/E_c = 2$ and rigid ($E_f/E_c = 5$), as well as the boundary condition for the distant boundary of the reservoir (zero pressure and non-return condition of the wave or absorbent element - Sommerfield condition).

The dimensions of the system are presented in Table 2 and modelling of finite element mesh is shown in Figure 4. The distant dimensions for the reservoir and foundation were based on literature studies Løkke e Chopra [1]; Silveira and Pedroso [22]; Zeidan [23]; Huang [24]; Nascimento [25] and Gutstein [26], that have analogous and/or equivalent relations to represent the dimensions of the domain under study.

Table 2. Dimensions of the typical profile of a Brazilian dam, reservoir and foundation

Parameter	H	h_c	h_g	B	Hr
Value (m)	80	20	15	70	72

Therefore, the finite dimensions used to represent the model with ratios proportional to the height (H) of the dam are based on these well-founded previous studies.

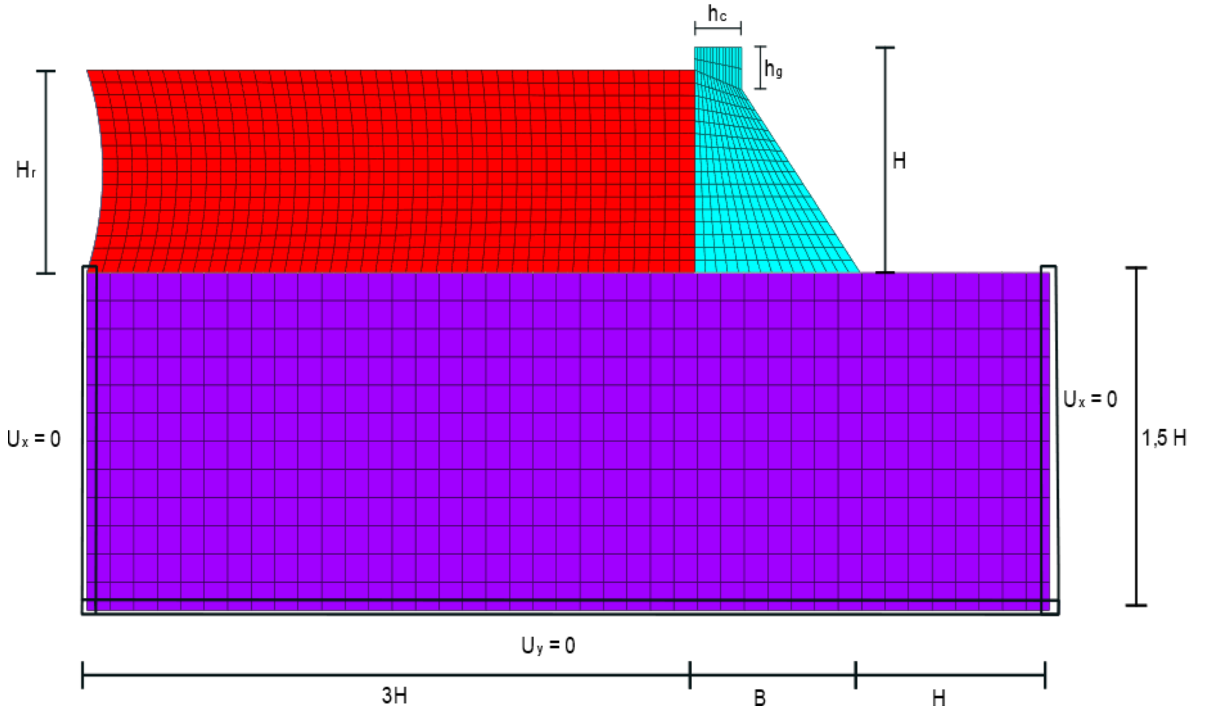

Figure 4. Modeling of the dam-reservoir-foundation system and its proper dimensions.

4.2 Free vibration study

- *Free vibrations: dam-foundation system (empty reservoir)*

In this case, the values of the natural frequencies and their modal deformations were determined as a function of the influence of the variation of the foundation stiffness, evaluating the magnitudes of the natural frequencies and the possible changes in the mode shape of the dam-foundation system.

The natural frequencies of the structure due the foundation flexibility is presented in Table 3. These results show that a decrease in the magnitudes of the frequencies occurs with the increase of the foundation flexibility.

Table 3 Alteration of the first 4 natural frequencies in Hertz for a variation between the elasticity modules of the foundation and the concrete.

Mode	E_f/E_c		
	1	**2**	**5**
1	3,57	4,02	4,38
2	7,99	9,48	10,64
3	8,79	9,91	11,17
4	15,83	17,51	19,25

Based in these results, it can be inferred that this reduction in the natural frequencies can take the structure to a zone of lower frequency, where the seismic load is more effective (low-frequency seismic frequency components that can coincide with the first frequencies of these structures).

In addition to modifying the frequency magnitudes of the system, the flexibility of the foundation also changes the mode shapes of the structure. This fact is observed in Figures 5 and 6 which present, respectively, the mode shape for the cases with more rigid foundation (Ef/Ec = 5) and flexible (Ef/Ec = 1), signaling that a more significant change occurs in the second and third modes in both cases, where in the first and fourth modes, the deformed are analogous.

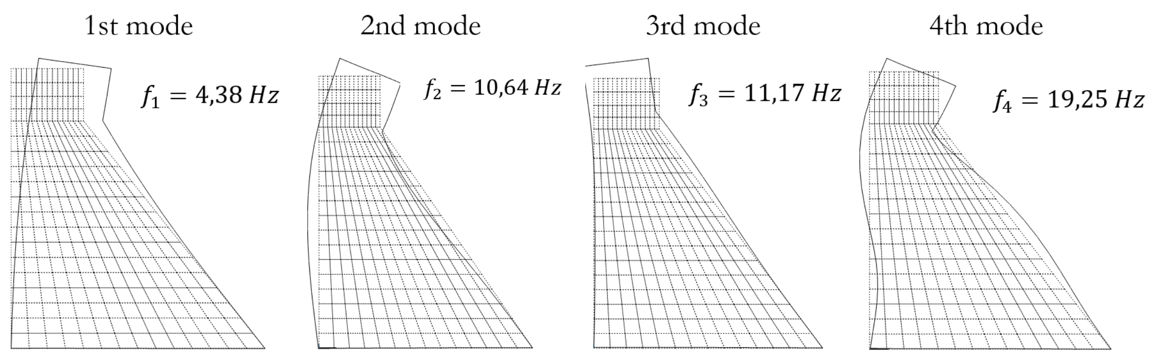

Figure 5. Vibration modes for the rigid foundation structure ($E_f/E_c = 5$).

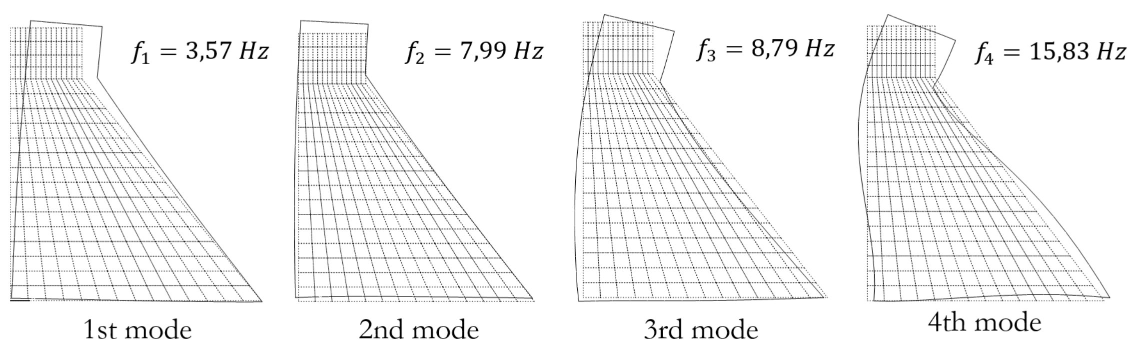

Figure 6. Modes of vibration for the structure with flexible foundation ($E_f/E_c = 1$).

Therefore, the effect of the foundation flexibility not only decreases the natural frequencies, but also can change the mode shapes, as can be observed in the comparison between Figures 5 and 6, for the 2nd and 3rd modes.

- *Free Vibration of the Decoupled Reservoir*

In the study of free vibrations for the decoupled reservoir, the zero-pressure condition was considered in the distant contour and the results of the natural frequencies were compared with an analytical expression which represents a closed-open acoustic cavity in the x and y directions. The analytical solution is given by Equation 6 for i and j = 1, 2, 3 ..., where c is the velocity of sound in the fluid, L is the length of the reservoir and H is the height of the fluid.

$$f_{anl.}^{i,j} = \frac{1}{2\pi}\sqrt{\left(\pi c^2\right)\left(\frac{(2i-1)^2}{4L^2}+\frac{(2j-1)^2}{4H^2}\right)} \tag{6}$$

The Figure 7 shows the first four mode shapes for the decoupled reservoir and their respective natural numerical and analytical frequencies. It is observed that the results show insignificant errors between the frequencies.

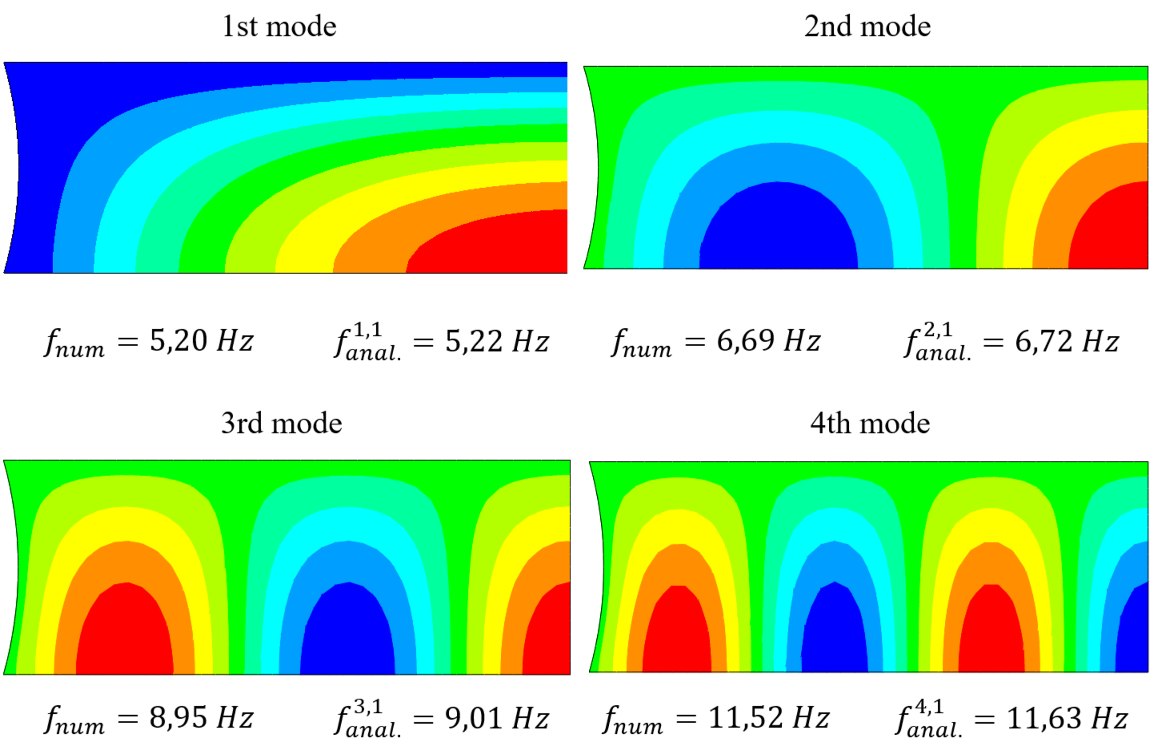

Figure 7. Vibration modes to the reservoir.

- *Free Vibration coupled: dam-reservoir-foundation system*

Considering the dam-reservoir-foundation coupled system, it was observed a reduction in the frequencies with the inclusion of the reservoir in relation to the previous case, when comparing the results presented in Table 4.

Table 4 Results of the first 4 natural frequencies in Hertz of the decoupled system (DS) and coupled (CS) dam-reservoir

	E_f/E_c						Reservoir	
Mode	1		2		5			
	(DS)	(CS)	(DS)	(CS)	(DS)	(CS)	Finite element	Analytical
1	3,57	3,05	4,02	3,48	4,38	3,85*	5,20	5,22
2	7,99	5,18	9,48	5,20	10,64	5,22	6,69	6,72
3	8,79	5,98	9,91	6,03	11,17	6,05	8,95	9,01
4	15,83	7,15	17,51	7,38	19,25	7,04	11,52	11,63

* additional mass mode

However, these results also showed a more preponderant influence of the foundation flexibility on the natural frequencies of the coupled system for the 1st mode in comparison to the presence of the reservoir.

Analyzing the coupled problem - Figure 8 - it is observed that the first mode is of dominant structure and represents the mode of additional mass, in which the fluid is incompressible and follows the movement of the structure.

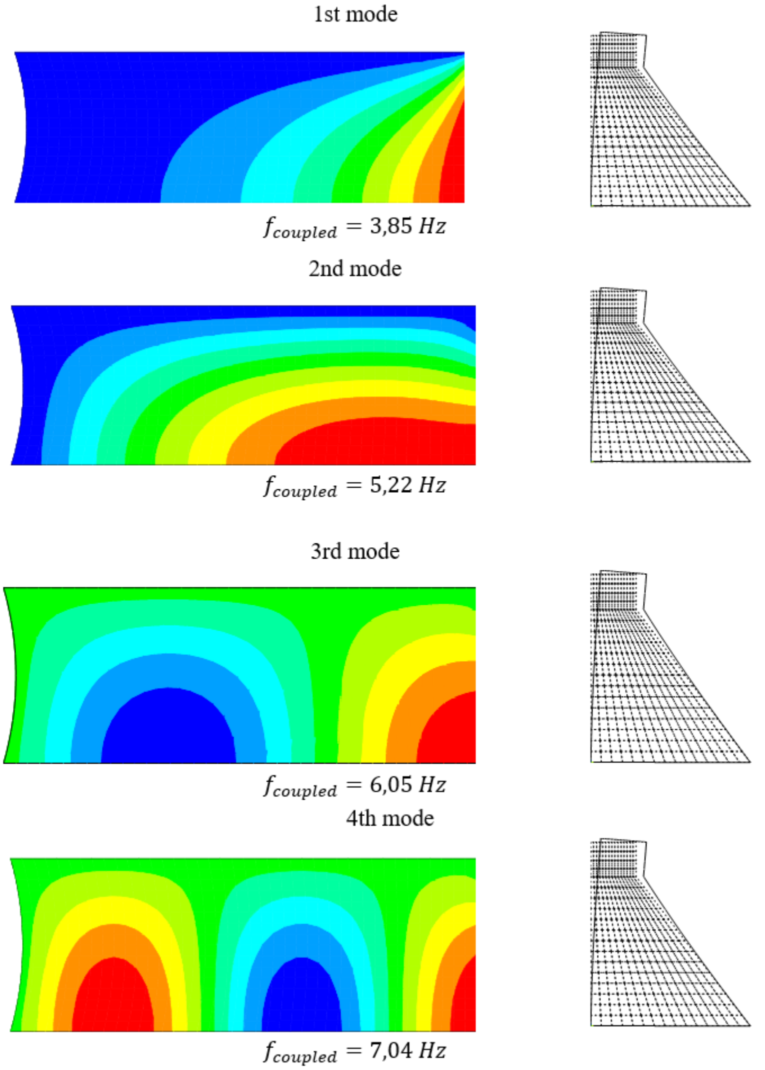

Figure 8. Vibration modes coupled in terms of pressure for the reservoir and displacements for the dam in the case of a rigid foundation.

However, the other modes (2 °, 3 ° and 4 °) are dominant in the reservoir and the mode shapes of the reservoir reproduce the same mode shapes of the decoupled case, but with slightly altered frequencies. The structure behaves practically as in a rigid wall, with a slightly flexible mode shape in its 1st decoupled mode.

- *Seismic Excitation*

For the study of the influence of dam-reservoir-foundation interaction under a seismic excitation, the system's response in terms of maximum principal displacements and stresses was verified at some points of the dam. For this seismic analysis, the two cases already studied in free vibrations were evaluated: 1) dam-foundation; 2) dam-reservoir-foundation.

For the transient analysis, it was used a historical seismic record of acceleration compatible with a region of Brazil with a maximum magnitude of 0,10 g; as shown in Figure 9. The frequency components of this accelerogram (frequency spectrum) are shown in Figure 10.

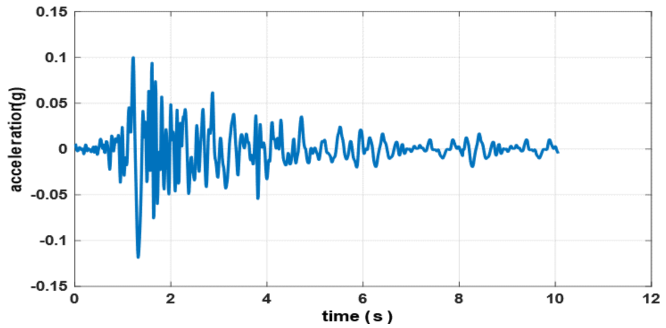

Figure 9. History of accelerations for a typical Brazilian earthquake under acceleration g.

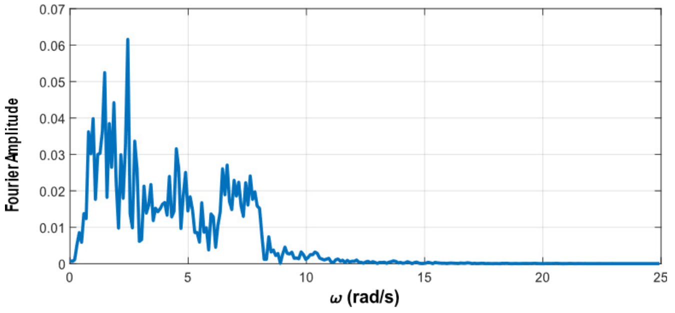

Figure 10. Spectral analysis of the Brazilian earthquake.

According to the proposal for the new seismic threat map in Brazil, shown in Figure 11, which improves the data of the anti-seismic standard (NBR-15421/2006), the earthquake assessed in this work has a probability of 2% probability to occur in most of Brazil for a period of 50 years.

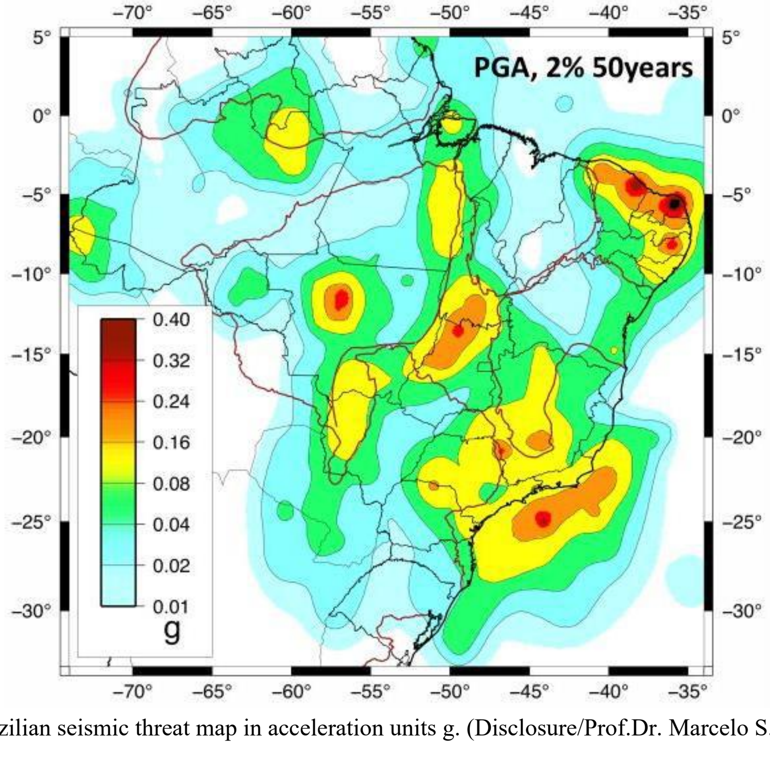

Figure 11. Brazilian seismic threat map in acceleration units g. (Disclosure/Prof.Dr. Marcelo S. Assumpção).

The inclusion of the earthquake in the cases studied is performed by the application of acceleration at the base of the structure (region of contact between the dam and the foundation).

In this analysis of seismic excitation, the structure response was studied in terms of maximum crest displacements and maximum stresses at three singular points of the dam: heel, finger and bottleneck (transition region), evaluating the influences of the foundation and of the reservoir. These points of analysis, whose denominations can be assimilated the parts of a human limb (foot), are best presented in Figure 12.

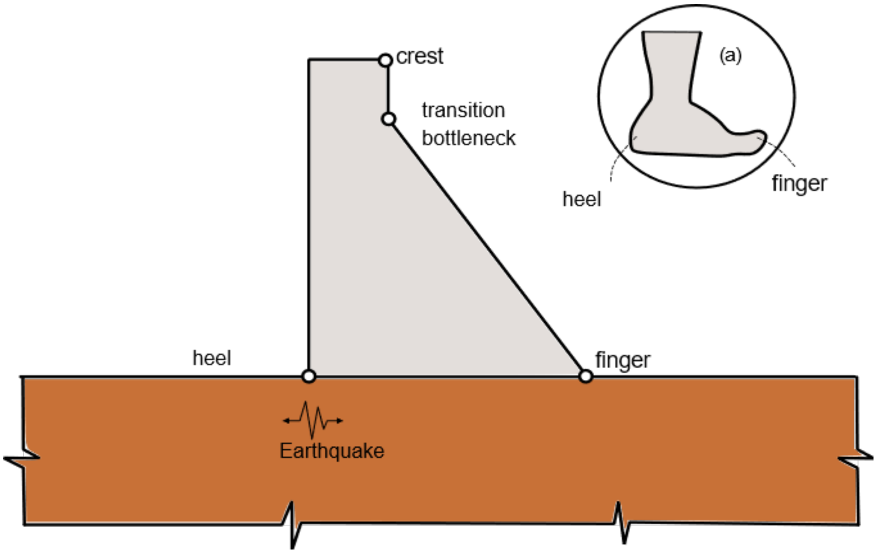

Figure 12. Points to be analyzed in the profile of the dam under seismic excitation.

1) Coupled system Dam-Foundation

For the dam-foundation system case, it was initially evaluated the displacement at the crest of the dam, shown in Figure 13, which shows a comparison between the maximum horizontal displacements (ordinate axis) versus the variation of the modulus of elasticity between foundation and concrete (abscissa axis). It can be observed that the maximum magnitudes close to 10 mm. Moreover, it is noted that the maximum displacements at the crest of the dam have decreased as the modulus of elasticity of the foundation increases.

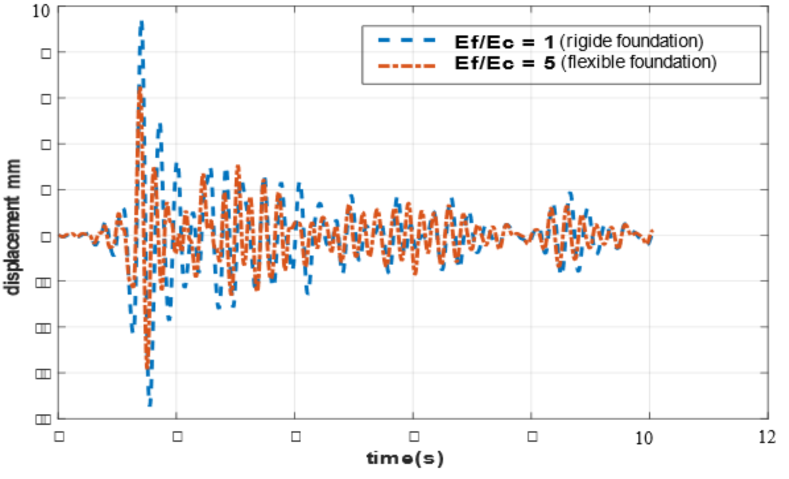

Figure 13. Variation in time of displacements on the crest of the dam as a function of the effect of the foundation.

The results obtained for the maximum principal stresses in the heel of the dam are shown in Figure 12, a region where the stresses normally reach its largest magnitudes. Figure 14 shows the change in the stresses with the change in the flexibility of the foundation, in which again it is observed that the increase of the modulus of elasticity of the foundation causes a substantial decrease in the effect of the seismic load in terms of tensile stresses.

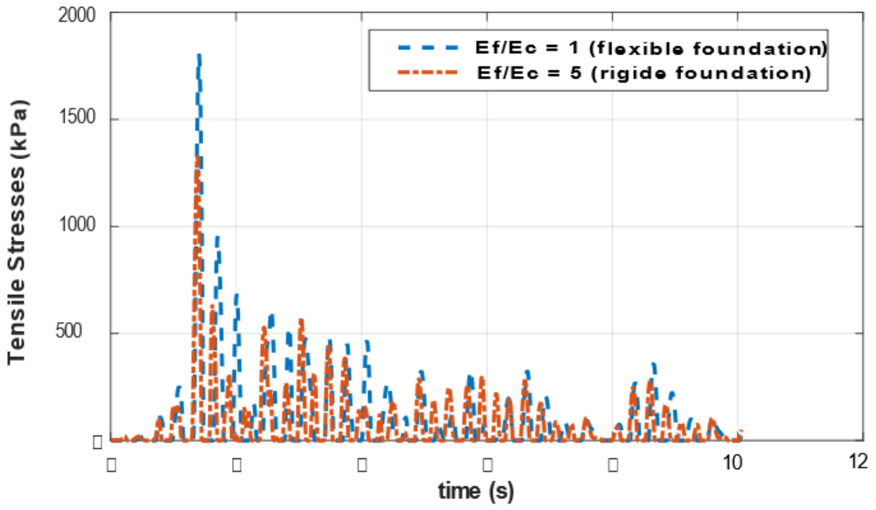

Figure 14. Variation in time of the maximum main stresses in the dam's heel according to the effect of the foundation.

When evaluating the history of maximum stresses in the three singular points: heel, bottleneck, and finger of the dam as a function of the flexibility of the foundation, it can be seen that it is in the region of the heel of the dam that the greatest stresses are found, followed by the bottleneck and the foot of the dam, respectively, as it can be verified in Figure 15. However, as the elasticity of the foundation increases, an increase in stresses occurs in the superior region of the structure (bottleneck), differently from what occurs in the heel and toe of the dam, where there is a tendency for reduction.

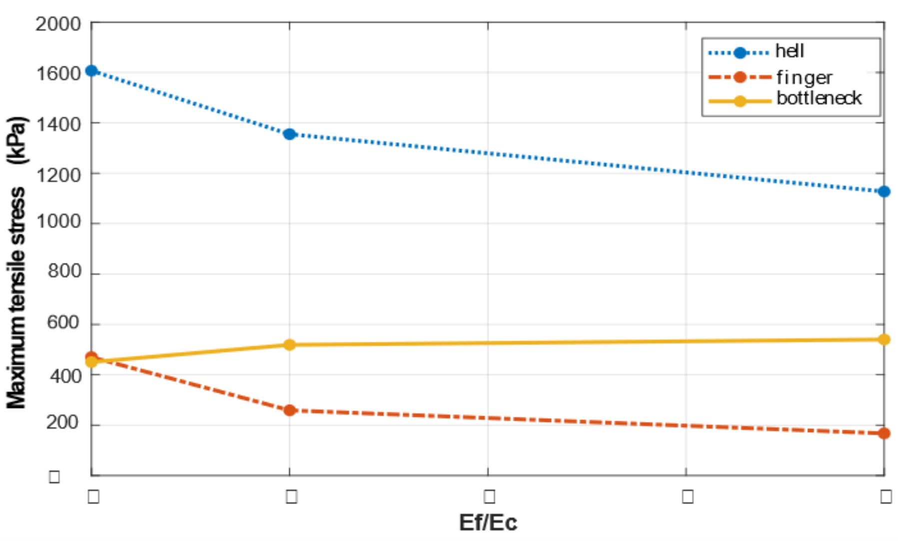

Figure 15. Variation of the maximum principal stresses in the heel, finger, and bottleneck of the dam according to the effect of the foundation.

2) Coupled system Dam-Foundation-Reservoir

For the evaluation of the effect of the presence of the reservoir in the coupled system, it was proposed a study similar to the one done in the previous item, in which the displacements and the maximum stresses in some singular points of the structure were evaluated. However, it was also considered in this step the verification of the influence of the distant boundary condition of the reservoir (zero pressure condition and the Sommerfield condition representing the wave absorption).

For the purpose of design, the zero-pressure condition is the simplest to be added, unlike the non-return condition of the wave, which has its peculiarities as a function of the analysis program. Thus, this study aims to verify the difference that exists in the results when considering these two different cases.

Figure 16 shows the results for the displacement at the crest of the dam considering these two cases and adopting the rigid foundation condition. It is observed from the figure that the displacements were equivalent both by the evaluation of the zero-pressure condition and the non-return condition (Sommerfield condition), with no significant differences in the results. The observed effects cannot be generalized, because the conditions of the presented case were favorable to this similarity in the results. However, with the change of certain conditions, to be seen in the next case, there is already a differentiation in the results.

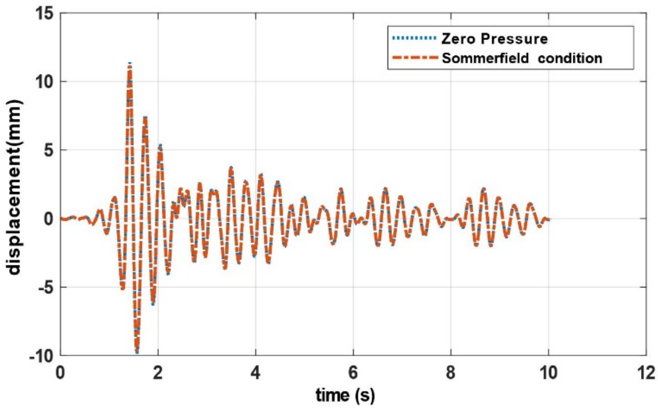

Figure 16. Variation in time of the displacement of the crest of the dam with the change of the boundary distant condition of the reservoir for a rigid foundation.

When assessing the influence of the foundation on the displacements at the dam crest for the cases in which is considered the rigid foundation (Ef/Ec = 1) and rigid (Ef/Ec = 5), shown in Figure 17, it was observed that the flexible foundation condition caused an increase in the magnitudes of the displacements. When comparing the results of the analysis in which only the dam-foundation interaction is considered (see Figure 13), there is an increase in the displacements with the inclusion of the reservoir effect.

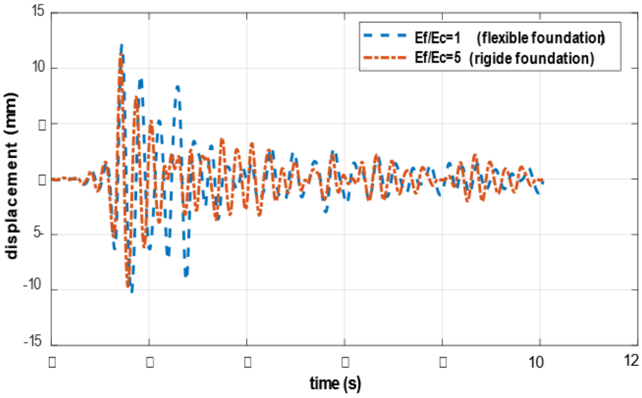

Figure 17. Variation in time of the displacement of the crest of the dam according to the effect of the foundation.

Similarly, for the heel stresses of the dam, an increase in the magnitudes of the maximum principal stresses was observed with the inclusion of the reservoir (Figure 18). This increase can cause problems in the structure since the tensile stresses that occur in the concrete approaching 2000 kPa tend to cause damage to the dam. It is also observed that in this case the flexibility of the foundation did not produce a result as significant as that seen in the item in which it was considered the dam-foundation system (see Figure 14).

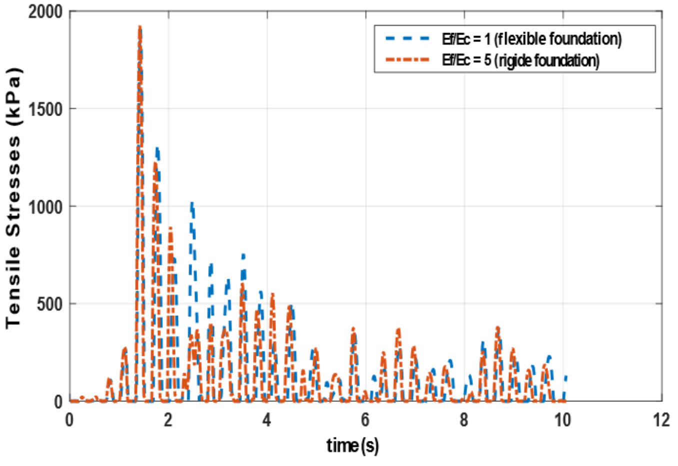

Figure 18. Variation of maximum stresses at the dam's heel.

The variation of the maximum tensile stresses was also evaluated in the other singular points of the structure, where the influence of the foundation was verified. It is observed in Figure 19 that the inclusion of the reservoir caused an increase in the level in the stresses in relation to the case without the reservoir (see Figure 15), as well as a decrease of these with the increase of the elasticity of the foundation to the heel and the finger of the structure.

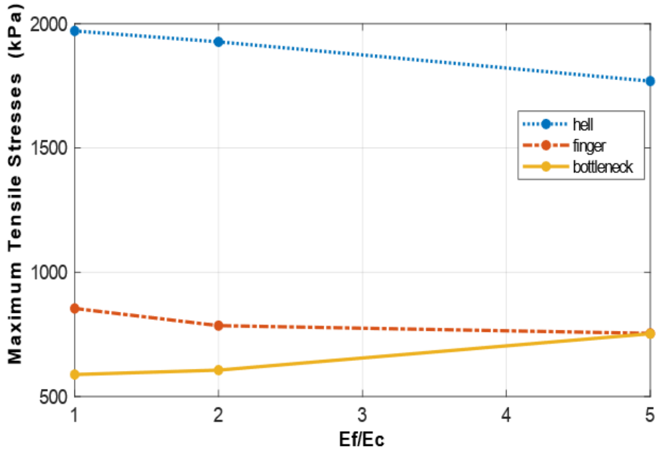

Figure 19. Variation of maximum stresses in the heel, finger, and bottleneck of the dam according to the effect of the foundation.

However, the bottleneck region was less susceptible to the presence of the reservoir, for the higher ratios Ef/Ec (rigid foundation). For the more flexible foundation there was even a slight decrease of stresses with the presence of reservoir, characterizing a behavior different from the standard of the other points analyzed.

It should be noted that the flexibility of the foundation altered the magnitudes of the stresses, especially in the interval in which the earthquake had its greatest intensity, see interval of 1 to 2s in Figure 9.

The seismic load causes a “come and go” movement in the structure and this causes the effects of stresses in different regions of the dam body to be different along the soil movement. This becomes clear when one observes Figure 20, which presents the mapping of the stresses at the dam for the instant of the maximum upstream and downstream forces for the case of the filled reservoir and rigid foundation (Ef/Ec = 5).

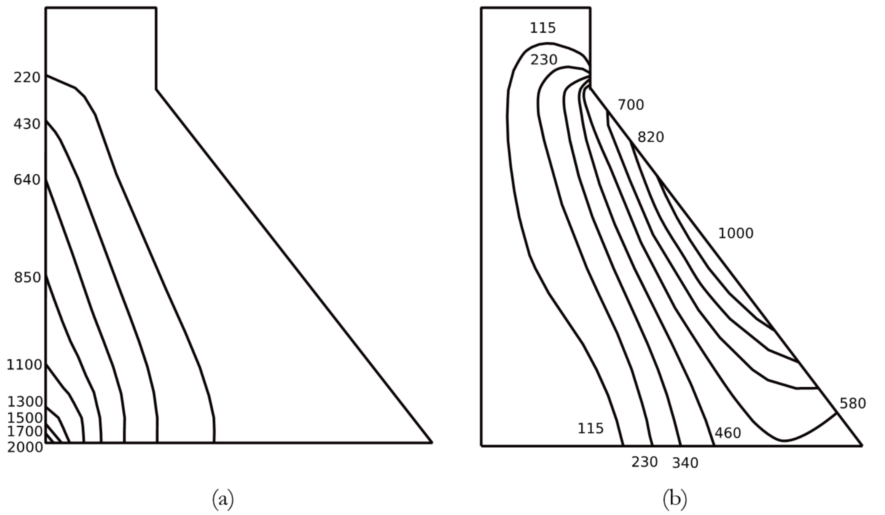

Figure 20. Time for maximum stresses of tensile in the dam body: (a) upstream t = 1,39 s and (b) downstream t = 1,50 s.

The heel region shows the highest stress concentrations as well as the structure bottleneck. And these effects can be amplified, as emphasized in this study, by changes in the elasticity of the foundation.

It is observed that the stresses along the heel region are much greater than those with respect to other points of the structure. At t = 1,39 s, a stress around 2000 kPa was obtained in this region, while at t = 1,50 s values of 1000 kPa occur in the intermediate region between the bottleneck and the finger on the downstream side of the dam. Thus, it is evident that the maximum stresses in the dam for a seismic excitation do not happen at the same instant, that is, there are intervals of time in which the upstream region is the most loaded, while in other time intervals the downstream of the structure is the most loaded region.

5 CONCLUSIONS

This work presented a dynamic study of the behavior of the dam - reservoir - foundation interaction in terms of free vibrations and under seismic load. For this, finite element models were developed through the ANSYS program in the APDL language. After the different simulations presented in this paper, some important conclusions were reached, namely:

- In the study of free vibrations, two systems were evaluated: 1) dam-foundation (BF) - empty reservoir; 2) dam-foundation-reservoir (BFR). For both cases, the influence of the foundation was observed, and it was verified that a reduction in the natural frequencies occurs for the more flexible foundations, fact that, in turn, also causes changes in the mode shape of the dam. In the case of the three coupled media, it was observed that the first mode is controlled by the dam (additional mass), and with the decrease of the stiffness of the foundation the reduction of this first natural frequency occurs more significantly, unlike the other higher modes which are controlled by the reservoir and in which this variation is not so striking in the magnitudes of the frequencies with the variation in the stiffness of the foundation.
- In the seismic analysis the displacements and the maximum stresses in some singular points of the dam were verified for a given acceleration history with a maximum intensity of 0.10 g. In the seismic analysis, also, a similar influence was observed in the previous item due to the influences of the foundation and the reservoir. For the crest displacements, and the stresses at the heel and foot of the dam, a reduction was observed with the increase of the stiffness of the foundation; on the contrary, an increase in the maximum stress variation was observed in the bottleneck.

- Another highlight corresponds to a comparison of the distant boundary conditions in the reservoir: the zero-pressure and the Sommerfield condition for rigid foundation. When considering both cases the results were similar, thus assuring us that the simpler condition (zero pressure) similarly reproduces the results for a rigid foundation seismic analysis.
- Finally, the authors recommend that in a dynamic analysis of dams, all the parameters involved should be analyzed in a way that is consistent with the conditions present in the dam-reservoir-foundation system, especially in the properties that influence the elasticity of the foundation. Regarding the reservoir, the simplified models of additional mass and zero pressure in the distant contours can be considered, in preliminary stages of design.

ACKNOWLEDGEMENTS

The authors thank the National Committee of Scientific and Technological Development (CNPq) and the University of Brasília (UnB), through the PECC.

REFERENCES

[1] A. Løkke and A. K. Chopra, "Direct finite element method for nonlinear earthquake analysis of 3-dimensional semi-unbounded dam-water-foundation rock systems," *Earthquake Eng. Struct. Dynam.*, vol. 47, no. 5, pp. 1309–1328, Apr 2018, http://dx.doi.org/10.1002/eqe.3019.

[2] N. B. Mendes, "Um estudo de propagação de ondas e lançamento do sismo na análise dinâmica acoplada barragem em arco - reservatório - fundação," Ph.D. dissertation, Univ. Brasilia, Brasília, 2018.

[3] H. M. Westergaard, "Water pressures on dams during earthquakes," *Trans. ASCE*, vol. 95, pp. 418–433, 1933. Accessed: Dec. 16, 2019. [Online]. Available: http://ci.nii.ac.jp/naid/10002935681/en/

[4] A. K. Chopra, "Earthquake resistant design of concrete gravity dams," *J. Struct. Div.*, vol. 104, no. 6, pp. 953–971, 1978.

[5] A. K. Chopra and P. Chakrabarti, "Earthquake analysis of concrete gravity dams including dam-water-foundation rock interaction," *Earthquake Eng. Struct. Dynam.*, vol. 9, no. 4, pp. 363–383, 1981, http://dx.doi.org/10.1002/eqe.4290090406.

[6] J. F. Hall and A. K. Chopra, "Hydrodynamic effects in the dynamic response of concrete gravity dams," *Earthquake Eng. Struct. Dynam.*, vol. 10, no. 2, pp. 333–345, Mar 1982, http://dx.doi.org/10.1002/eqe.4290100212.

[7] G. Fenves and A. K. Chopra, *Earthquake Analysis and Response of Concrete Gravity Dams*, 1st ed. Califórnia: Univ. California, 1984.

[8] A. K. Chopra and L. Zhang, "Earthquake-induced base sliding of concrete gravity dams," *J. Struct. Eng.*, vol. 117, no. 12, pp. 3698–3719, Dec 1991, http://dx.doi.org/10.1061/(ASCE)0733-9445(1991)117:12(3698).

[9] P. M. V. Ribeiro and L. J. Pedroso, "Dynamic response of dam-reservoir systems: review and a semi-analytical proposal," *Lat. Am. J. Solids Struct.*, vol. 14, no. 4, pp. 594–612, Mar 2017, http://dx.doi.org/10.1590/1679-78253500.

[10] M. Novak, "Dynamic soil-structure interaction, John P. Wolf, Prentice-Hall, Englewood Cliffs, N.J., 1985. No. of pages: £466. Price: £61.45," *Earthquake Eng. Struct. Dynam.*, vol. 14, no. 6, pp. 951, Nov 1986., http://dx.doi.org/10.1002/eqe.4290140610.

<jrn>[11] P. Léger and M. Katsouli, "Seismic stability of concrete gravity dams," *Earthquake Eng. Struct. Dynam.*, vol. 18, no. 6, pp. 889–902, Aug 1989, http://dx.doi.org/10.1002/eqe.4290180611.</jrn>

[12] S. Bougacha, J. L. Tassoulas, and J. M. Roësset, "Analysis of foundations on fluid-filled poroelastic stratum," *J. Eng. Mech.*, vol. 119, no. 8, pp. 1632–1648, Aug 1993, http://dx.doi.org/10.1061/(ASCE)0733-9399(1993)119:8(1632).

[13] Y. Ghanaat, "Failure modes approach to safety evaluation of dams," in *Proc. 13th World Conf. Earthq. Eng.*, Vancouver, 2004.

<jrn>[14] J. A. Inaudi, E. E. Matheu, R. L. Poeppelman, and A. Matusevich, *Foundation Flexibility Effects on the Seismic Response of Concrete Gravity Dams.* Tech. Memo. Public Works Res. Inst., 2005, pp. 269–289.</jrn>

[15] G. Lin, J. Du, and Z. Hu, "Earthquake analysis of arch and gravity dams including the effects of foundation inhomogeneity," *Front. Archit. Civ. Eng. China*, vol. 1, no. 1, pp. 41–50, Feb 2007, http://dx.doi.org/10.1007/s11709-007-0004-4.

[16] G. Papazafeiropoulos, Y. Tsompanakis, and P. N. Psarropoulos, "Dynamic interaction of concrete dam-reservoir-foundation: analytical and numerical solutions," in *Computational Methods in Earthquake Engineering*, M. Papadrakakis, M. Fragiadakis, N. D. Lagaros, Ed., Switzerland: Springer, 2011, pp. 455–488.

[17] A. Burman, P. Nayak, P. Agrawal, and D. Maity, "Coupled gravity dam-foundation analysis using a simplified direct method of soil-structure interaction," *Soil. Dyn. Earthquake Eng.*, vol. 34, no. 1, pp. 62–68, 2012, http://dx.doi.org/10.1016/j.soildyn.2011.10.008.

[18] A. K. Chopra, "Earthquake analysis of concrete dams: factors to be considered," in *Tenth U.S. Nat. Conf. Earthq. Eng.*, Anchorage, Alaska, 2014.

[19] L. J. Pedroso, *Fundamentos Teóricos-Numéricos para a Compreensão do Problema Acoplado Barragem-Reservatório-Fundação com Contornos Absorventes Longínquos, Superfície Livre, e Interação entre os Três Meios pelo Método das Diferenças Finitas.* Brasília, 2017.

[20] L. J. Pedroso, “Interação fluido-estrutura,” in *Notas de Curso e Apostila Didática*. Brasilia: Prog. Pós-grad. Estrut. Constr. Civ., 1992.

[21] L. J. Pedroso, “Formulações potencias para abordagens fluido-estrutura,” in *Notas do Curso de Interação Fluido-Estrutura e Apostila Didática*. Brasilia: Prog. Pós-grad. Estrut. Constr. Civ., 2004.

[22] I. V. Silveira and L. J. Pedroso, “Analysis of natural frequencies and modes of vibration involving interaction dam-reservoir-foundation for concrete gravity dams,” in *Third Int. Dam World Conf.*, 2018, p. 11.

[23] B. A. Zeidan, “Seismic analysis of dam-reservoir-foundation interaction for concrete gravity dams,” in *ICOLD2013*, 2014, Vience, Italy.

[24] J. Huang,“Seismic response evaluation of concrete gravity dams subjected to spatially varying earthquake ground motions,” Ph.D. dissertation, Drexel Univ., Drexel, 2011.

[25] C. A. Nascimento Jr.,“Um estudo comparativo analítico-numérico de tensões locais e globais em barragens gravidade de concreto,” M.S. thesis, Univ. Brasília, Brasília, 2016.

[26] D. Gutstein, “Estudo das tensões em fundações de barragens de gravidade de concreto por meio do método dos elementos finitos,” M.S. thesis, Univ. Santa Catarina, Florianópolis, 2003.

Author contributions: IVS: methodology, numerical modelling, investigation, formal analysis, writing - original draft; LJP and GSM: supervision, conceptualization, review, editing.

Editors: Bernardo Horowitz, José Luiz Antunes de Oliveira e Sousa, Guilherme Aris Parsekian.

IBRACON Structures and Materials Journal
Revista IBRACON de Estruturas e Materiais
ISSN 1983-4195 ismj.org

ORIGINAL ARTICLE

Rice husk ash as supplementary cementing material to inhibit the alkali-silica reaction in mortars

Uso da cinza de casca de arroz como adição mineral para inibir a reação álcali-sílica em argamassas

Eloise Aparecida Langaro[a]
Cleberson Adorno dos Santos[a]
Marcelo Henrique Farias de Medeiros[a]
Diego Souza de Jesus[b]
Eduardo Pereira[c]

[a]Universidade Federal do Paraná – UFPR, Programa de Pós-graduação em Engenharia Civil, Curitiba, PR, Brasil
[b]University of Ottawa, Department of Civil Engineering, Ottawa, Canada
[c]Universidade Estadual de Ponta Grossa – UEPG, Departamento de Engenharia Civil, Ponta Grossa, PR, Brasil

Received 14 January 2020
Accepted 09 November 2020

Abstract: Alkali-silica reaction (ASR) is one of the most harmful distress mechanisms that affects the durability of concrete worldwide. Yet, it has been found that ASR-induced expansion and distress may be prevented by the appropriate use of supplementary cementing materials (SCMs). Recent studies suggest that rice husk ash (RHA), a by-product of the rice production, may present promising performances as a pozzolanic material and to enhance the durability of blended mixtures. There are many controversial studies regarding the use of RHA and how its properties directly affect the performance and durability of concretes and mortars. The present study aims to evaluate the influence of the RHA on ASR through the accelerated mortar bar test (AMBT), X-Rays Diffraction (XRD), Thermogravimetric Analysis (TG), Mercury Intrusion Porosimetry (MIP) and Scanning Electron Microscopy (SEM). To validate the obtained data, the results were compared with mortars made of a well-known SCM (silica fume) which has distinguished behaviour against ASR. The results indicate that, besides the silica fume mortars have showed better results, the use of RHA suggests promising results to mitigate the ASR, yet, further analysis on concrete prims test should be carried out to fully validate the use of RHA to enhance the durability of the concrete. The RHA finesses and its particle size were the most important properties in the SCM performance.

Keywords: rice husk ash, pozzolanicity, alkali-silica reaction, particle size distribution.

Resumo: A reação álcali-sílica (RAS) é um dos mais nocivos mecanismos que afetam a durabilidade do concreto em todo o mundo. No entanto, já foi verificado que a expansão e a deterioração do concreto, devido a RAS, podem ser evitadas pelo uso de materiais apropriados, como adições minerais. Estudos recentes sugerem que a cinza da casca de arroz (CCA), um subproduto da produção de arroz, pode apresentar desempenho promissor como material pozolânico para aumentar a durabilidade de misturas com cimento Portland. Existem muitos estudos controversos a respeito do uso da CCA e como suas propriedades afetam diretamente o desempenho e a durabilidade de concretos e argamassas. O presente estudo teve como objetivo avaliar a influência da CCA na RAS através do teste acelerado de barras de argamassa (AMBT), Difração de Raios-X (DRX), Análise Termogravimétrica (TG), Porosimetria por Intrusão de Mercúrio (MIP) e Microscopia Eletrônica de Varredura (MEV). Para validar os dados obtidos, os resultados foram comparados com argamassas confeccionadas com uma reconhecida adição mineral (sílica ativa), a qual possui notável comportamento frente a RAS. Os resultados indicam que, além das argamassas de sílica ativa apresentarem melhores resultados, o uso de CCA pode sugerir resultados promissores para mitigar o RAS. Porém, análises adicionais a partir do ensaio de primas de concreto devem ser realizados para validar plenamente o uso desta cinza para aumentar a durabilidade do concreto. A finura

Corresponding author: Eloise Aparecida Langaro. E-mail: elolangaro@hotmail.com
Financial support: Coordenação de Aperfeiçoamento de Pessoal de Nível Superior – CAPES.
Conflict of interest: Nothing to declare.

o tamanho das partículas da CCA foram as características que mais tiveram impacto no desempenho da adição mineral.

Palavras-chave: cinza de casca de arroz, pozolanicidade, reação álcali-sílica, distribuição granulométrica.

How to cite: E. A. Langaro, C. A. Santos, M. H. F. Medeiros, D. S. Jesus, and E. Pereira, "Rice husk ash as supplementary cementing material to inhibit the alkali-silica reaction in mortars," *Rev. IBRACON Estrut. Mater.*, vol. 14, no. 4, e14404, 2021, https://doi.org/10.1590/S1983-41952021000400004

1 INTRODUCTION

Concrete is the most common construction material used in critical infrastructure worldwide. Portland cement (PC) is by far the most important ingredient of concrete, being the main responsible for its carbon-footprint and accounting for about 7% of the annual man-made CO_2 emission [1]. Which enhance the technical importance of finding cost-effective strategies to reduce the carbon-footprint associated with the production of PC. Moreover, one of the most adopted methods for reducing environmental impact of PC involves the use of supplementary cementing materials (SCMs) in concrete. Yet, major developments need to be constantly addressed in this area, specially aiming to the long-term behaviour of these materials when used in concrete structures.

Alkali-silica reaction (ASR) is one of the most harmful distress mechanisms that affects the durability of concrete worldwide. It is comprised of a chemical reaction between "unstable" silica mineral forms (from fine or coarse aggregates) and alkali hydroxides (e.g. Na^+, K^+ and OH^-) dissolved within the concrete pore solution [2]. It generates a secondary product, the ASR-gel, which has swelling properties and may generate internal stresses and cracking in the concrete [2]–[4]. One may notice, once the reaction takes place, there is any well stablished method or technique to complete stop the reaction; mostly, it's only delay the rate of occurrence [5], which reinforce that preventive measures are, in general, a better solution. For that, an adequate selection of material and well-proportioned concrete are best options. Moreover, it has been found that ASR-induced expansion and distress may be prevented by the appropriate use of supplementary cementing materials (SCMs) [6].

The technical importance binder composition with supplementary cementitious materials (SCMs) derives mainly from three aspects: 1) the reaction is slow, therefore, the release of heat due to the hydration reactions is also slow; 2) the reactions caused by these materials consume calcium hydroxide, rather than producing them, reducing the pH; 3) the interaction between amorphous silica, portlandite and water present in the concrete pores leads to further formation of C-S-H [3], [7]–[9]. The C-S-H formed from pozzolanic reactions has lower Ca/Si ratio than the commonly C-S-H; hence, enhancing the capacity of alkali bonding (Na+ and K^+) [9], [10].

Siliceous SCMs, such as Silica Fume (SF) and Rice Husk Ash (RHA), etc. consists nearly exclusively of SiO_2 of fine particle size and a relatively high pozzolanic activity. These materials, especially SF, are widely used to improve the compressive strength, abrasion resistance and durability of concrete [11], [12]. Moreover, the use of SF and RHA as part of the binder composition may mitigate or, at least, delay the development of ASR [3], [8]–[10]. Although, the effective performance of the RHA in cementitious materials is in function of several aspects, such as: the amount of silica, amorphous degree (dependent of the process of burning) and the average particle size distribution. De Souza et al. [13] presented an extensive review regarding the obtention of reactive silica from rice husk ash. The fabrication process implies in significant variations in the physical/morphological and chemical properties of the RHA grains; moreover, directly affecting the properties of cementitious materials made with RHA [13]–[17]. The controlled burning process of the RHA controls, besides the crystallinity of the RHA particles, the carbon content attached in the grains [18]–[20]. Moreover, depending of the amount of carbon on composition of RHA, some particle is able to present some hydrophilic behaviour leading to lack of available water for cement hydration reaction increasing rheological properties of the concrete [18]–[21]. Furthermore, also decreasing or slowing down the RHA reactivity with $Ca(OH)_2$ and affecting the amount of entrapped air in the concrete as well [21].

The RHA, a by-product of the rice production, constantly generated concerns regarding its disposal in nature, once currently RHA is used as land-filled disposal. Which enhance the importance of findings to validate its use as an alternative to replace the PC towards a greener and more durable future of the civil industry. Moreover, the present study aims to evaluate the influence of the RHA to suppress ASR in mortar bar specimens. To achieve the main objective, it will be conducted the accelerated mortar bar test (AMBT), X-Rays Diffraction (XRD), Thermogravimetric Analysis (TGA), Mercury Intrusion Porosimetry (MIP) and Scanning Electron Microscopy (SEM) analyses. To validate the obtained data, the results will be compared with mortars made of a well-known SCM (silica fume) which has distinguished behaviour against ASR.

2 MATERIALS AND EXPERIMENTAL PROGRAM

The reactive aggregate selected is from the region of Curitiba, Brazil. The aggregate has known potential ASR-reactivity; moreover, the aforementioned aggregate was used in the construction of different dams in Brazil and have been previously reported in research [22]. Furthermore, the mineralogical phases of the material were identified using the technique of X-Ray Diffraction (XRD) with variation range of 2θ from 5º to 75º. The aggregate was classified as a granite, according to ASTM C294 [23], and presented peaks of sanidine and albite (Figure 1).

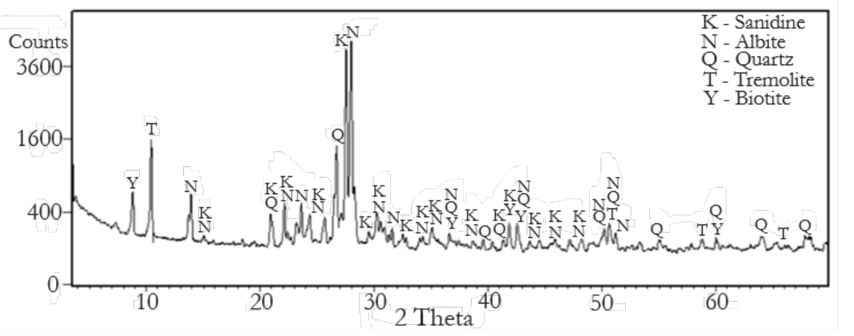

Figure 1. X-ray diffractogram of the reactive aggregate.

The chemical composition (Table 1), obtained through the semi-quantitative spectroscopy analysis (X-Rays Fluorescence-XRF), indicates significant amount of SiO_2 (i.e. 63.5%) and 8.74% of Na_2Oe_q. Besides the reactive phases of the aggregate, the amount of alkalis available may be released in the pore solution of the concrete accelerating the development of ASR, specially in the field [24], [25].

Table 1. Chemical composition (oxides %) of aggregate.

Aggregate	Chemical composition (%)							
	CaO	SiO_2	Al_2O_3	Fe_2O_3	K_2O	Na_2O	Na_2O_{eq}	Other oxides
	2.1	63.5	15.1	7.0	6.6	4.4	8.74	0.5

Portland cement with high early age strength CPV - ARI (PC), similar to PC type III as per ASTM C150 [26], was used as a control group and replaced partially (10% by weight) by the rice husk ash and silica fume [10], [18], [27]. Both supplementary cementitious materials are commercial products. The mixtures were proportioned following ASTM C1260 [28] recommendations (i.e. 1:2.25:0.47, cement to fine aggregate to water/binder ratio, by mass).

The particle size distribution (PSD) of the binder materials was obtained by laser diffraction and displayed in Figure 2. Silica fume shows the finest average PSD, D50 equal to 0.12 μm; which represents particles 52 times smaller than Portland cement (D50 of 6.24 μm). Rice husk ash displayed the highest average PSD among all binder materials with D50 of 7.89 μm.

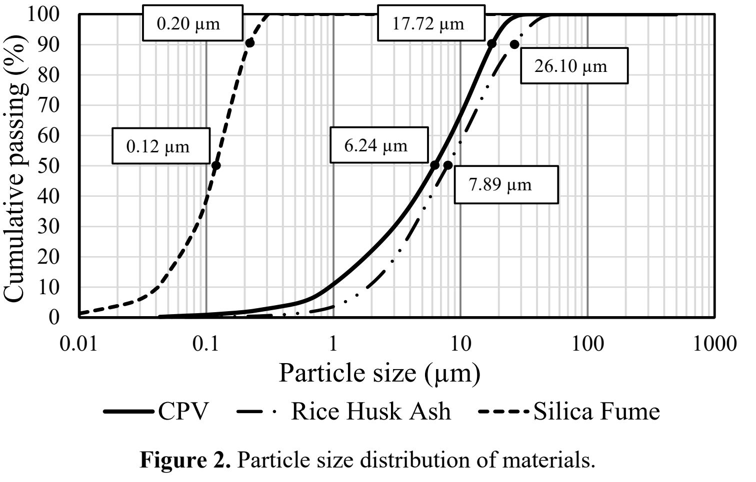

Figure 2. Particle size distribution of materials.

Table 2 reports the chemical compositions measured by XRF and the results of BET specific surface area, LOI and the specific gravity of the three binder materials. Moreover, the mineralogical composition obtained by the diffractometer RIGAKU Ultima IV X-ray Diffractometer, with range of 2θ between 5º and 75º are presented in Figure 3.

Table 2. Chemical composition (oxides %) and physical properties of materials.

Component	CPV (%)	Silica fume (%)	Rice husk ash (%)
CaO	59.36	0.19	0.43
SiO_2	16.27	92.35	88.47
Al_2O_3	5.06	2.21	2.72
Fe_2O_3	2.77	0.05	0.05
MgO	4.63	-	-
SO_3	5.30	1.52	1.55
K_2O	1.06	0.94	1.46
Other oxides	-	0.04	0.49
Na_2O_{eq}	0.697	0.619	0.961
Free lime*	1.46	-	-
Insoluble residue*	0.67	-	-
Loss on ignition	3.43	2.70	4.84
Specific gravity (g/cm^3)	3.13	2.12	2.18

* Data provided by the manufacturer

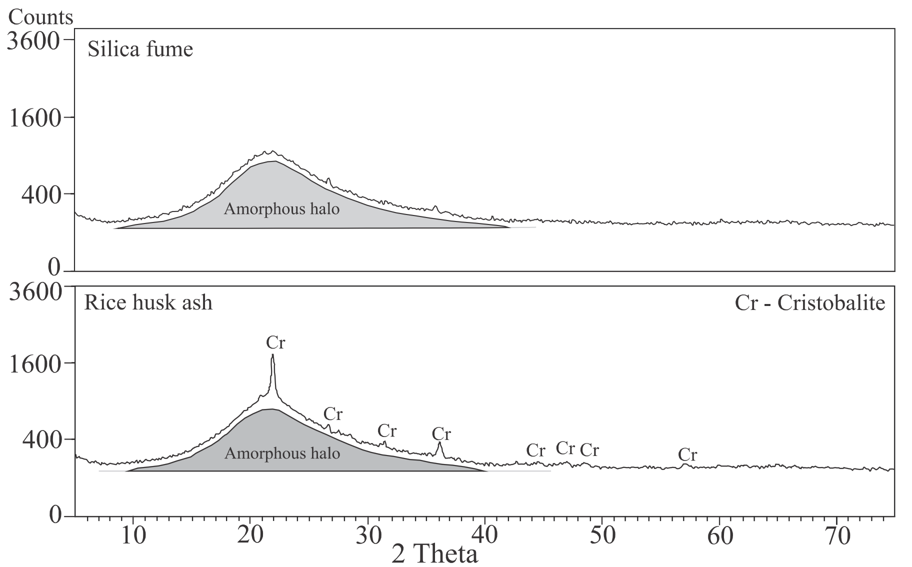

Figure 3. X-ray diffractograms of the silica fume and rice husk ash.

Firstly, the chemical composition (Table 2) indicates that both SCMs have significantly higher amount of SiO_2 than PC; which, SF has the highest value (92.35%), whereas RHA has 88.47%. Moreover, RHA indicates higher content of LOI and potassium (K); thus, LOI and K may negatively contribute to development of ASR. However, rice husk ash meets the requirements of ASTM C618 [29] with the limit of the specification LOI (6%) for ashes used in concrete. This material was obtained from the controlled combustion process by fluidized bed of rice husk ash and, thus, despite the temperature control, it is usual a small amount of carbon on its composition. Processes without temperature control led to higher amounts of carbon [30].

On the other hand, the diffractogram of RHA indicates that the material is composed basically by amorphous phases (indicated by the amorphous halo) and it has only a small crystal fraction organized as cristobalite. The silica fume did not exhibit peak in the diffractogram, presenting only a characteristic halo from an essentially amorphous microstructure, which may indicate higher pozzolanic reactivity. Moreover, to further understand the pozzolanic reactivity of the SCMs, modified Chapelle's test method was carried out as per NBR 15895 [31]. The obtained data suggests consumption of 1336 and 1542 mg of $Ca(OH)_2$/g of pozzolana for RHA and for SF, respectively. Indicating that both materials can be classified as highly reactive SCMs or super pozzolans.

2.1 Methods to evaluate ASR development

The efficiency of the SCMs in suppress ASR development was evaluated through the accelerated mortar bar test (AMBT) as per ASTM C1260 [28] and ASTM C1567 [32] on mortars was analyzed in general by two main groups samples. The mortars bars were designed as previously mentioned. After casting and moulding, all bars were subject to 24 h in the mould in moist cabinet; followed by placing the samples on deionized water at 80±2°C during the next 24 hours. Afterwards, the samples had their initial lengths measured and then, placed in a solution of sodium hydroxide (NaOH 1N) at 80±2°C during a period of 32 days. Moreover, the expansion measured was validated through statistical analysis, Variance Analysis (ANOVA) and Tukey's Test during the two main ages of evaluation (14 and 28 within the 32 days). One may notice that the AMBT was chosen once it allows faster and reliable answers to initially characterize binder mixtures and reactivity of aggregates; yet, concrete prism tests are more indicated to validate the effectiveness of SCMs in mitigate ASR, but the full procedure for CPT normally takes 2 years of development [3]. Which was a limiting factor in this research.

Additionally to AMBT, the well-known X-Ray diffraction (XRD), thermogravimetric analysis (TGA/DTG), mercury intrusion porosimetry (MIP) and scanning electron microscopy (SEM) test methods were also performed in the ASR-affected samples to further understand its development. For the XRD it was used was a diffractometer RIGAKU model Ultima IV with an X-ray tube with the copper anode, 40 kV/30 mA, and a divergence slit of 1°. The scanning range (2θ) used was from 3.5° to 70°, with angular step size of 0.017° and time interval of 10.16s by step; while the TGA analysis was performed in a TA Instruments SDT 2960, in dynamic nitrogen atmosphere (N_2) and flow rate of 100 mL/min with heating rate of 10°C/min, applied until the temperature of 1200°C. Besides that, SEM-EDS were performed in a FEG SEM Tescan, Mira 3 and analytical micro-probe of X-Rays Oxford X-Max 50 (EDX). The sample preparation consisted in a vacuum and metallization with gold. Finally, the mercury intrusion porosimetry the pressures applied were initial of 1.5 psi and final of 30 psi.

3 RESULTS AND DISCUSSIONS

3.1 Accelerated Mortar Bar Test (AMBT)

In this section, ASR expansion kinetics and amplitude results are presented for all 3 mortar bar mixtures. Figure 4 displays the results obtained through the Accelerated Mortar Bar Test (AMBT). The results indicate that, indeed, the finely crushed granite aggregate has potential reactivity for ASR development since the Control mortar mixture displayed expansion amplitudes in between 0.10% and 0.20% at 14 and 28 days. Moreover, this result is consistent with results found in the literature [22], in which is discussed the use of the granite aggregate in a Dam construction in Brazil that showed signal of ASR development.

The use both SCMs (for PC's replacement level of 10%) changed the ASR kinetics and expansion amplitudes. Mortar mixtures made of RHA showed at 14 days results slightly under the limit of 0.10%; yet, at 28 days this mixture developed 0.16% of expansion which classifies it as a potential mixture to develop ASR. Despite this behaviour, it worth noting that the use of RHA mitigate the reaction compared with the control group (as indicated through the statistical treatment displayed in Figure 5). On the other hand, replacing 10% of PC by SF, one may notice that granite reactivity was mitigated down to a non-reactive behaviour as per ASTM C 1260.

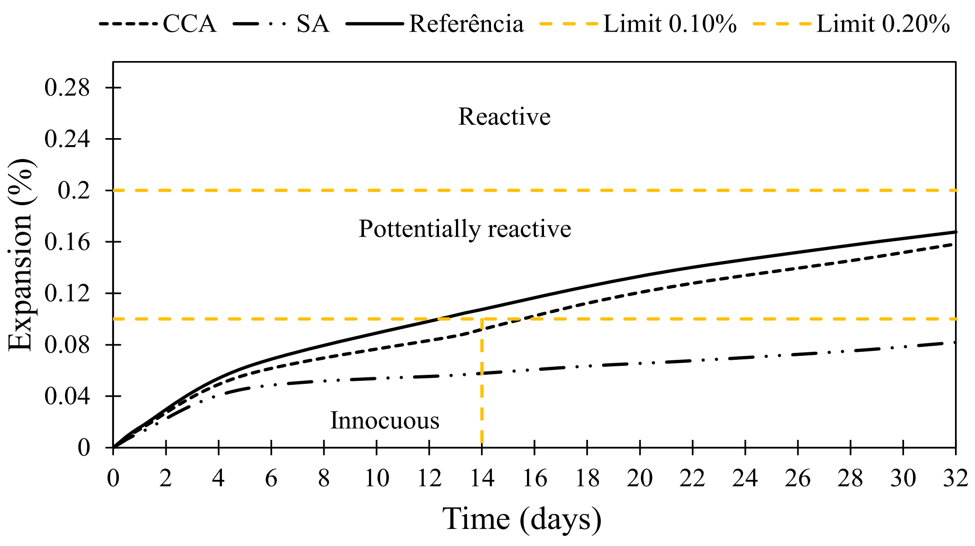

Figure 4. Evolution of the expansion of the mortar bars (AMBT) with 100% cement (Control) compared with 10% replacement of SCM (RHA e SF).

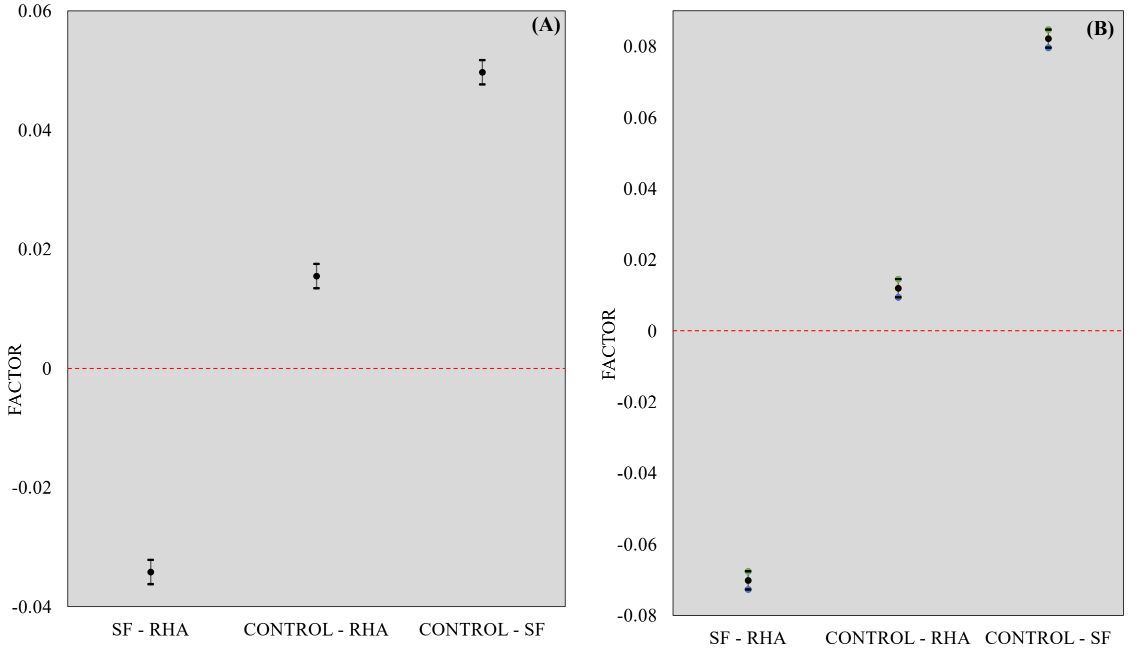

Figure 5. Comparative analysis of the averages, Tukey's test, for 14 (A) and 28 (B) days of exposure among the series studied, for a significance level of 5%.

Although the RHA is classified as material with high pozzolanic reactivity, as demonstrated in materials section through the modified Chapelle's test method. Interestingly, RHA indicates reactivity like SF; however, its behaviour was far different in the mortar bars exposed to ASR development. The particle morphology, chemical composition and particle size distribution showed the main differences between the two SCMs; which may explain the different behaviour measured. AMBT has been criticized in several documents [2], [33]–[35] since it can give "false positives" and "false negatives" answers due to the overly aggressive exposure conditions of the test. Finally, further concrete prism tests should be developed for a better characterization of the RHA in mitigate the ASR. Yet, this was possible to be done in the present study once CPT normally takes 2 years of development. Which was a limiting factor in this research.

3.2 X-ray Diffraction (XRD)

The main XRD peaks evaluated to identify the influence of the SF and RHA in the mortar bars exposed to ASR development are presented in Figure 6 (100% of intensity of the mineral Sanidine) and Figure 7 (100% of intensity of portlandite). It worth noting to mention that Sanidine ($KAlSi_3O_8$) is a mineral from the reactive aggregate used, in which have trend to be released and "consumed" along the development of ASR [36]. Therefore, variations on the main intensity peak of this material may indicate the occurrence of ASR in the mortar systems [37]. Clearly, the main peak of Sanidine was affected by the development of the reaction, moreover, the use of SF and RHA slowed down the mineral consumption indicating, indeed, that the reaction was mitigated.

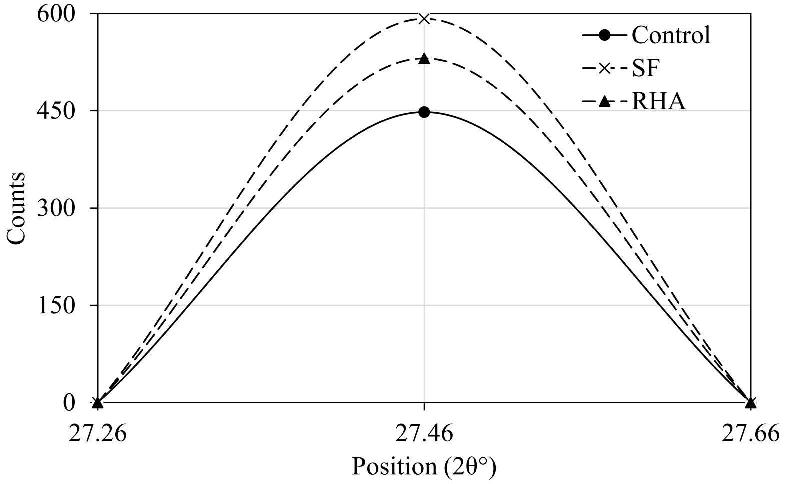

Figure 6. Peak of sanidine.

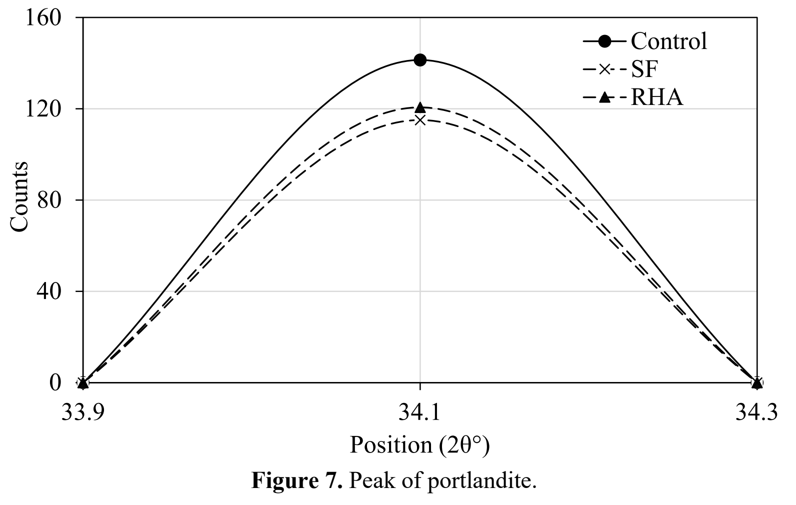

Figure 7. Peak of portlandite.

During the alkali-silica reaction, an electrical double layer of cations (sodium, potassium and/or calcium) develops at the silica surface to offset its negative charge. Later the interaction between both phases (amorphous silica and alkali layers) will initially form a colloidal suspension, then the aggregate will precipitate as ASR gel, depending on the availability of solvent, type of pore solution and its concentration, pore structure, and the conditions to which it is exposed [38]. It has been found that the formation of the outer layer of cations starts hindering the silica uptake over time. However, the diffusion of alkaline ions is barely affected, and thus the chemical reaction continues, especially within the aggregate particles. Moreover, different features (viscosity, mechanical properties, chemical composition, etc.) of the reaction products are found at different locations, i.e. alkali-silica gel within the aggregates and lime-alkali-silica gel in the surrounding cement paste [39]–[41].

As the reaction progresses, calcium ions diffuse into the silica particle as well, such that a cation exchange between Ca^{2+} and alkaline ions begins, releasing the Na^+ and K^+ to continue reacting with silica particles. The alkali-silica composition is significantly bulkier than the lime-alkali-silica compositions. As a result, the cracking caused by the ASR is initiated within the aggregates [41], [42].

Overall, cement is the main source of alkalis and portlandite (CH) within the concrete. Thus, it is convenient to use binder materials capable to reduce the final amounts of at least one of these compounds, which is the case of the SF and RHA, both highly reactive SCMs. Moreover, the main peak of portlandite (34.1° 2θ) analyzed through XRD indicates that, indeed, the pozzolanic reactivity of the SF and RHA affected the CH content. It worth noting that to evaluate the peak of portlandite in samples of SF and RHA, the total count of CH was "normalized" (divided by 0.9) to compare directly to Control group. The data normalization excludes alterations in the portlandite peak due to the simple replacement of the cement and only reactions consuming $Ca(OH)_2$ are being evaluated, enhancing that the SCMs, indeed consumed the CH, changing ASR kinetics.

Samples containing SCMs showed smaller portlandite peak, that indicates pozzolanic activity. Differences between total counts were close to 20% for control sample compared to SCMs samples. Medeiros et al. [43] reported similar results for concretes with Cement Portland and metakaolin and/or silica fume compared with control group (reference). The pozzolanic reaction of the SCMs improved the microstructure of the mortar bars and contributed to the reduction of porosity and permeability. This occurs due to the action of several mechanisms that contributes to the damage limit by ASR [3], [8]–[10], [44].

However, even if XRD results indicate the consume of portlandite due to pozzolanic reactivity, there are several factors regarding the characteristics of the materials that tend to influence the results of the samples expansion, besides the accelerated test itself. Different techniques are needed to provide a more conclusive evaluation.

3.3 Thermogravimetric Analysis (TGA)

Qualification and semi-quantification of hydration products through XRD analysis enhance the quality in identify those products formed during ASR; however, to quantify more precisely is necessary to adopted supplementary tests. In this case, the TG/DTG curves of the mortar's samples cured for 32 days. All test specimens present a significant mass reduction at the temperature around 105°C, 420°C and 660°C. It is acknowledged that heating hardened cement paste samples through room temperature to 1000 °C leads to loss of physically bound water, breakdown of $Ca(OH)_2$ and $CaCO_3$, respectively. The first broad peak between 50 and 200 °C in the DTG curve corresponds to the dehydration of C-S-H. Between 400–500°C, the intense peak seen in most of the samples corresponds to the decomposition of calcium hydroxide (CH). The temperature range of 600–800°C is considered as decarbonation or losses of carbon dioxide from samples. The amount of portlandite in relation to the loss of mass in the control sample was 4.32% (Figure 8). The determination of portlandite content $(Ca(OH)_2)$ consumed in the hydration of samples is indicated in Equation 1:

$$Ca(OH)_2(\%) = \frac{MM_{Ca(OH)_2}}{MM_{H_2O}} \times H_2O = 4.11 \times H_2O \tag{1}$$

Where $MM_{Ca(OH)_2}$ is the molecular mass of portlandite; MM_{H_2O} is the molecular mass of water and H_2O is loss of mass, in percentage obtained in test TGA.

Samples containing SCMs presented significantly lower portlandite amount (Figure 8A, 8B and 8C), which is mainly due to the pozzolanic reaction occurred between SCMs and portlandite during the cement hydration [17]. Figure 8D display the correlation between the expansion amplitudes and portlandite content measured through TGA. Abbas et al. [10] and Kandasamy and Shehata [45] obtained similar results for different supplementary cementitious materials (fly ash, rice husk ash and blast furnace slag) to mitigate ASR. Both studies reported a decrease in the amount of $Ca(OH)_2$ while the expansion due to ASR was reduced.

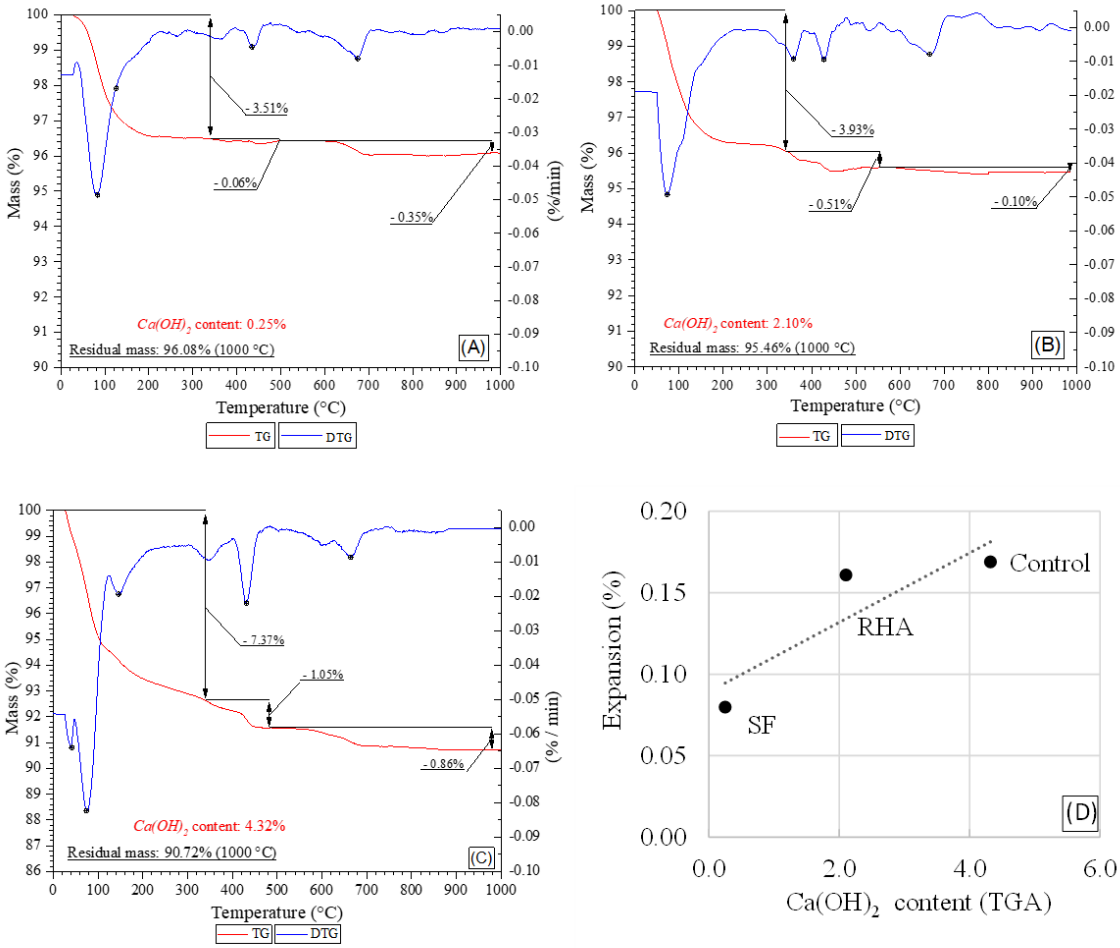

Figure 8. TGA and DTG (A) mortar with SF (B) mortar with RHA (C) Control mortar (D) Correlation between expansion (%) and portlandite content (%) (TGA).

The reactivity of the material, the average size of the particles and the amount or replacement are important characteristics that influence the development of the pozzolanic reaction. Although rice husk ash had high reactivity and an improvement in the performance of the mortar compared with the control series, the diffractogram (Figure 3) shows that the microstructure of RHA presented peaks of cristobalite, indicating lower reactivity than silica fume. Hoppe et al. [17] show in their results that the amount of amorphous silica of rice husk ash is an important aspect in the development of pozzolanic activity. Besides, cristobalite is a reactive mineral, potentially alkaline in terms of alkali-aggregate reaction [34], which could have affected the performance of the rice husk ash for mitigating ASR.

The optimized grinding of the material improves the pozzolanic characteristics increasing the specific surface area of grains [16]. According to De Souza et al. [13], impurities as inorganic compounds present in rice husk do not significantly modify the pozzolanic reaction. However, the particles must have a smaller size (micron or submicron). In the same context, Ahsan and Hossain [18] and Thanh et al. [46] showed that finer RHA particles are more efficient to mitigate ASR than the coarser ones. It is well known that smaller particles can quickly react due to the higher surface area that has an important influence of hydration process and on the kinetics of ASR. Coarser RHA particles reduce the packing density of the mixture, leading to a slightly more porous and permeable matrix with an easier percolation of alkaline ions.

PSD of materials showed that the particles of silica fume were 65.75 (D50) times smaller than RHA, and 52 times smaller than grains of Cement Portland. Besides, silica fume presented a higher amount of SiO_2 and reactivity, which is significantly influenced by PSD and specific surface area [16], [17], [30]. This indicates that the silica fume was able to significantly modify the microstructure of mortars due to its morphology, chemical composition and reactivity. It is important to consider the short-term evaluation (32 days) and the accelerated test of mortar bars. The particle size distribution and the packing density of the mortar presented more influence in the development of ASR than the pozzolanic reactivity by itself, as shown in results of XRD and TGA. The consumption of portlandite was higher for both SCMs compared to the control sample. However, results for induced expansion were significantly different, which may indicate that the physical properties of the silica fume are responsible for controlling the kinetics of ASR for the short-term evaluation used.

3.4 Mercury Intrusion Porosimetry (MIP)

Supplementary cementing material may contribute for the reduction of porosity and permeability of mortars, performing by physical effect (better refinement of voids, filling and points of heterogeneous nucleation in cement grains) and chemical effect (pozzolanic reactions). ASR demands water to start and continue the reaction. Thus, the porosity reduction contributes to reduction of expansion due to important points such as: diffusion of external alkalis, decrease of ASR propagation and water absorption by ASR-gel.

The objective of test of mercury intrusion porosimetry was evaluate two important aspects in mortars with SCMs. First, if the pore refinement occurs due to the partial substitution of cement by additions. Second, if the development of ARS may increase this property once crack might be formed along with higher expansion levels.

Samples with SCMs as part of the composition of the binder presented lower total porosity (Figure 9). SF mortar bars showed the best pore refinement according to porosity and pores distribution; moreover, lower coefficient of permeability (Figure 9).

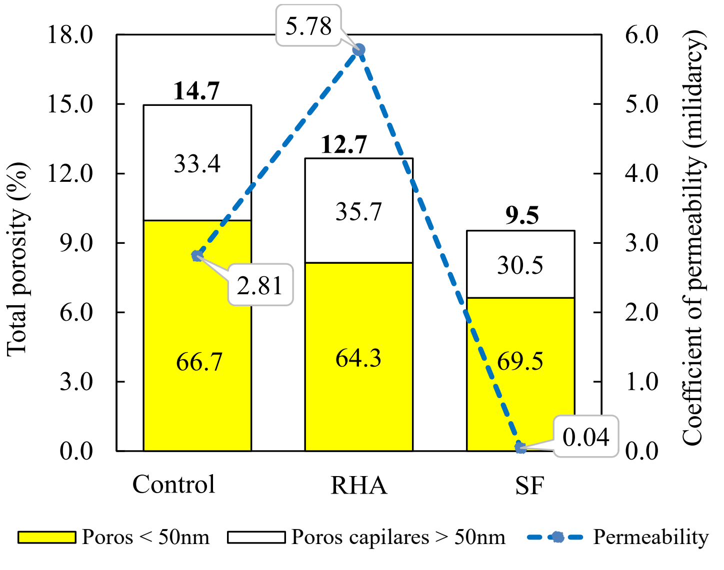

Figure 9. Porosity e permeability of mortars.

Results obtained for silica fume corroborate the results from other tests, showing a lower coefficient of permeability, lower total porosity, and lower expansion of mortar bars (AMBT). This result is consistent with Moser et al. [47], which presented that the use of supplementary cementitious materials in concrete exposed to occurrence of ASR shows lower permeability, contributing to mitigate the reaction and reduce the expansion of samples.

RHA mixtures had permeability coefficient of 5.78 mD, higher than SF and control, despite the lower porosity (in 2%) compared to control sample. Only because of physical aspects, rice husk ash was not able to increase the packing density. However, due to its high reactivity as SCM, that was pointed out by Chappell's modified method, the secondary products formed with the pozzolanic reaction contributes to filling some voids and in the interparticle space, which explains this small improvement in porosity. Considering the reactivity and formation of the particle of $C\text{-}S\text{-}H_{pozzolanic}$, rice husk ash was not able to totally access the thinner voids and to reduce the permeability of mortar bars. The distribution of the pore diameters demonstrated that 66.7% of the control samples pores were smaller than 50 nm (micropores). Mortar with silica fume and rice hunk ash presented 69.5% and 64.3% of pores, respectively.

3.5 SEM/EDX

Figure 10 displays the hydrated compounds, such as C-S-H, found in all samples. It is clear that mortar bars containing RHA and SF have higher amounts of SiO_2 and CaO than in control samples (Table 3), which may indicate pozzolanic activity and higher formation of C-S-H. Shafaatian et al. [48] demonstrated that the ratio CaO/SiO_2 of the hydrated material is a good parameter to indicate the mitigative potential for ASR development. Due to the pozzolanic reaction, the C-S-$H_{pozzolanic}$ has a small amount of Ca and, therefore, generates a ratio CaO/SiO_2 inferior to the C-S-H formed by hydrated cement without SCMs [10], [44], [49]. The absorption of alkalis by C-S-H changes due to its surface charge, and this depends on the CaO/SiO_2. At low ratios of CaO/SiO_2, the surface charge is negative and the C–S–H pozzolanic formed tends to bond alkalis [9].

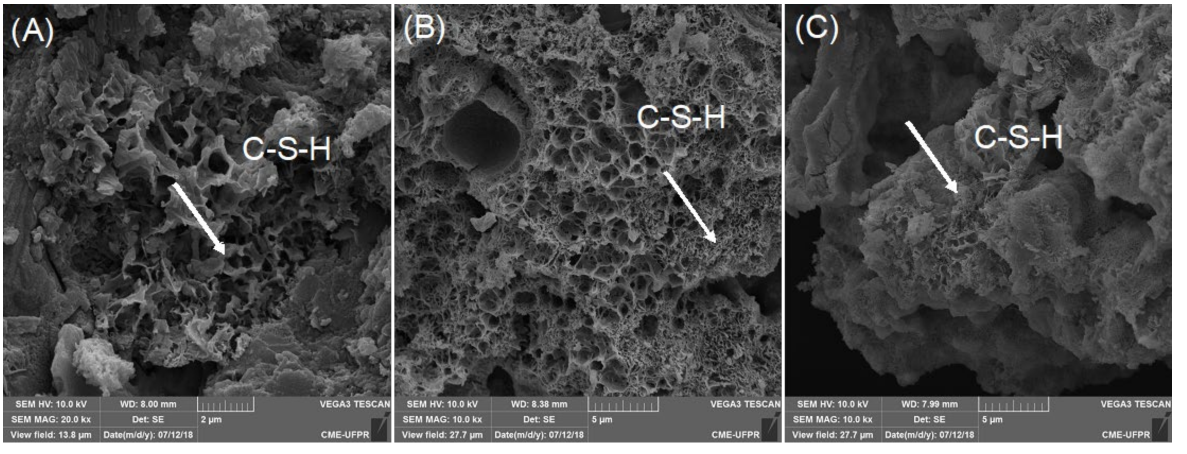

Figure 10. SEM of C-S-H (A) SF (B) RHA (C) Control.

Table 3 shows results from the analysis of EDX of mortars, based on the three points indicated in Figure 10, representing the analysis points.

Table 3. EDX of samples.

Sample	Mass present								Ratio of mass present
	SiO_2	CaO	Al_2O_3	Na_2O	K_2O	Na_2O_{eq}	MgO	Fe_2O_3	CaO/SiO_2
SF	33.16	49.53	3.21	0.00	1.69	1.11	1.99	11.72	1.49
RHA	50.01	42.54	6.42	6.60	1.69	7.71	0.00	0.00	0.85
Control	18.83	51.77	5.10	3.64	0.00	3.64	0.00	3.57	2.75

The smaller CaO/SiO_2 ratios were found in samples with SCMs (Table 3) and similar results were found on [10], [44], [49]. Samples containing RHA, although demonstrating smaller ratio CaO/SiO_2 than other samples, the amount of Na_2O_{eq} was higher (EDX analysis of C-S-H). Indicating that the smaller ratio of CaO/SiO_2 in C-S-H does not mean that is the best result regarding expansion. However, a small proportion contributes for the positive effect of the pozzolanic SCM. Besides, an analysis of the pore solution is necessary to understand the effects of alkalis present in the cement matrix mixed with different SCMs.

ASR is like the pozzolanic reaction [9]. The difference between both is in the time scale that ASR and pozzolanic reaction occur and regarding the pozzolanic reaction, there is no expansion due to its development mechanisms. The fineness of the SCM used provides a better distribution of C-S-H in the microstructure of the hydrated matrix. This does not happen in ASR, which the reactive silica is placed in discreet points generating a concentration of internal tension. Thus, the physical aspects supplementary cementitious materials are extremely important for their good performance in aspects regarding the alkali-aggregate reaction. In addition, the AMBT test contributes negatively to the pozzolanic reaction. This suggests that the classification of a material is performed using various techniques.

4 CONCLUSIONS

The main objective of this research was to evaluate the influence of the RHA to suppress ASR in mortar bar specimens comparing its behaviour with well-known SCM (silica fume) which has distinguished performance against ASR. The main findings of the current research are presented hereafter:

- Mortar bars made of silica fume demonstrated the best results, showing considerable reduction in damages and decelerating ASR kinetics. The use of SF significantly decreases the permeability and porosity of the mortar and reducing the diffusion of external alkali ions;
- Evaluation of XRD showed that mortars containing SCMs were able to retard the consumption of sanidine, that indicates a lower rate of ASR kinetics. The effect of a release of alkalis and other components (e.g. SiO_2 and Al_2O_3) on aggregates for the porous solution in the development of the reaction is still unknown. Further study is needed to evaluate how each type of reactive aggregate influences in ASR, depending upon the used materials and exposition environment.
- Although the rice husk ash presented high pozzolanic reactivity, its use was not able to reach the same efficiency to suppress ASR as silica fume. The physical properties of the SCM were crucial to on its performance according to the test conditions. Besides the process of controlled burning of ashes, an efficient grinding is required. In this study was used the particle size distribution, that is like the cement. It is also suggested that the test may be carried out in concrete, because AMBT may have inhibited a part of the performance of rice husk ash, due to its accelerated conditions.
- The ratio CaO/SiO_2 of the $C\text{-}S\text{-}H_{pozzolanic}$ found in mortar containing SCMs was smaller than the ratio C-S-H CaO/SiO_2 of the control mortar. This is an aspect related with the presence of the pozzolan reaction and the density of the hydration products, positively contributing to the reduction of expansion caused by ASR. However, the alkaline bond is not the only mechanism acting to contribute for the mitigation of ASR by SCMs. AMBT test can occult this aspect depending on the material used.

ACKNOWLEDGEMENTS

The authors would like to acknowledge the Post-graduation in Civil Construction Engineering (PPGECC) of Federal University of Parana and the financial support provided by CAPES (Coordination for the Improvement of Higher Education Personnel).

REFERENCES

[1] M. Limbachiya, S. C. Bostanci, and H. Kew, "Suitability of BS EN 197-1 CEM II and CEM V cement for production of low carbon concrete," *Constr. Build. Mater.*, vol. 71, pp. 397–405, Nov 2014, http://dx.doi.org/10.1016/j.conbuildmat.2014.08.061.

[2] B. Fournier and M. A. Bérubé, "Alkali-aggregate reaction in concrete: a review of basic concepts and engineering implications," *Can. J. Civ. Eng.*, vol. 27, no. 2, pp. 167–191, Apr 2000, http://dx.doi.org/10.1139/l99-072.

[3] N. P. Hasparyk, P. J. M. Monteiro, and H. Carasek, "Effect of silica fume and rice husk ash on alkali-silica reaction," *ACI Mater. J.*, vol. 97, no. 4, pp. 486–492, Jan 2001.

[4] J. M. Ponce and O. R. Batic, "Different manifestations of the alkali-silica reaction in concrete according to the reaction kinetics of the reactive aggregate," *Cement Concr. Res.*, vol. 36, no. 6, pp. 1148–1156, 2006, http://dx.doi.org/10.1016/j.cemconres.2005.12.022.

[5] P. Helene, M. Carvalho, and J. Pacheco, "Engineering field tests for alkali-aggregate reaction," *Struct. Concr.*, vol. 18, no. 2, pp. 349–355, Oct 2017, http://dx.doi.org/10.1002/suco.201600090.

[6] J. Lindgård, Ö. Andiç-Çakir, I. Fernandes, T. F. Rønning, and M. D. A. Thomas, "Alkali-silica reactions (ASR): Literature review on parameters influencing laboratory performance testing," *Cement Concr. Res.*, vol. 42, no. 2, pp. 223–243, Feb 2012, http://dx.doi.org/10.1016/j.cemconres.2011.10.004.

[7] J. Duchesne and Q. City, "Another look at the reaction mechanisms," *Cement Concr. Res.*, vol. 24, no. 2, pp. 221–230, 1994.

[8] W. Aquino, D. A. Lange, and J. Olek, "The influence of metakaolin and silica fume on the chemistry of alkali-silica reaction products," *Cement Concr. Compos.*, vol. 23, no. 6, pp. 485–493, Dec 2001, http://dx.doi.org/10.1016/S0958-9465(00)00096-2.

[9] M. Thomas, "The effect of supplementary cementing materials on alkali-silica reaction: a review," *Cement Concr. Res.*, vol. 41, no. 12, pp. 1224–1231, Dec 2011, http://dx.doi.org/10.1016/j.cemconres.2010.11.003.

[10] S. Abbas, S. M. S. Kazmi, and M. J. Munir, "Potential of rice husk ash for mitigating the alkali-silica reaction in mortar bars incorporating reactive aggregates," *Constr. Build. Mater.*, vol. 132, no. 1, pp. 61–70, Feb 2017, http://dx.doi.org/10.1016/j.conbuildmat.2016.11.126.

[11] M. H. Shehata and M. D. A. Thomas, "Use of ternary blends containing silica fume and fly ash to suppress expansion due to alkali-silica reaction in concrete," *Cement Concr. Res.*, vol. 32, no. 3, pp. 341–349, 2002, http://dx.doi.org/10.1016/S0008-8846(01)00680-9

[12] D. J. Souza, M. H. F. Medeiros, and A. N. D. J. Hoppe Fo., "Evaluation of external sulfate attack (Na_2SO_4 and $MgSO_4$): Portland cement mortars containing siliceous supplementary cementitious materials," *Rev. IBRACON Estrut. Mater.*, vol. 13, no. 4, pp. e13403, Sep 2020, http://dx.doi.org/10.1590/s1983-41952020000400003.

[13] M. F. De Souza, P. S. Batista, I. Regiani, J. B. L. Liborio, and D. P. F. Souza, "Rice hull-derived silica: applications in Portland cement and mullite whiskers," *Mater. Res.*, vol. 3, no. 2, pp. 25–30, Apr 2000, http://dx.doi.org/10.1590/S1516-14392000000200005.

[14] R. A. Bakar, R. Yahya, and S. N. Gan, "Production of high purity amorphous silica from rice husk," *Procedia Chem.*, vol. 19, pp. 189–195, 2016, http://dx.doi.org/10.1016/j.proche.2016.03.092.

[15] R. Zerbino, G. Giaccio, and G. C. Isaia, "Concrete incorporating rice-husk ash without processing," *Constr. Build. Mater.*, vol. 25, no. 1, pp. 371–378, Jan 2011, http://dx.doi.org/10.1016/j.conbuildmat.2010.06.016.

[16] J. H. S. Rêgo, A. A. Nepomuceno, E. P. Figueiredo, and N. P. Hasparyk, "Microstructure of cement pastes with residual rice husk ash of low amorphous silica content," *Constr. Build. Mater.*, vol. 80, pp. 56–68, Apr 2015, http://dx.doi.org/10.1016/j.conbuildmat.2014.12.059.

[17] J. Hoppe Fo., M. R. Garcez, E. O. Garcez, L. C. P. Silva Fo., and G. C. Isaia, "Evaluation of residual rice husk ash reactivity," *J. Aust. Ceram. Soc*, vol. 53, no. 2, pp. 917–924, 2017, http://dx.doi.org/10.1007/s41779-017-0106-y.

[18] M. B. Ahsan and Z. Hossain, "Supplemental use of rice husk ash (RHA) as a cementitious material in concrete industry," *Constr. Build. Mater.*, vol. 178, pp. 1–9, Jul 2018, http://dx.doi.org/10.1016/j.conbuildmat.2018.05.101.

[19] V. P. Della, I. Kühn, and D. Hotza, "Rice husk ash as an alternate source for active silica production," *Mater. Lett.*, vol. 57, no. 4, pp. 818–821, Dec 2002, http://dx.doi.org/10.1016/S0167-577X(02)00879-0.

[20] S. K. Antiohos, V. G. Papadakis, and S. Tsimas, "Rice husk ash (RHA) effectiveness in cement and concrete as a function of reactive silica and fineness," *Cement Concr. Res.*, vol. 61–62, pp. 20–27, 2014, http://dx.doi.org/10.1016/j.cemconres.2014.04.001.

[21] B. K. H. Obla, "Specifying fly ash for use in concrete," *Concr. Focus*, vol. 7, no. 1, pp. 60–66, 2008.

[22] L. Valduga, "Influência das condições de ensaio da ASTM C 1260 na verificação da reação álcali-agregado," Ph.D. dissertation, Prog. Pós-grad. Eng. Civ., Univ. Fed. Rio Grande do Sul, Porto Alegre, 2007.

[23] American Society for Testing and Materials, *Standard Descriptive Nomenclature for Constituents of Concrete*, ASTM C294-12, 2017.

[24] D. Constantiner and S. Diamond, "Alkali release from feldspars into pore solutions," *Cement Concr. Res.*, vol. 33, no. 4, pp. 549–554, Apr 2003, http://dx.doi.org/10.1016/S0008-8846(02)01001-3.

[25] F. Locati, S. Marfil, E. Baldo, and P. Maiza, "Na_2O, K_2O, SiO_2 and Al_2O_3 release from potassic and calcic – sodic feldspars into alkaline solutions," *Cement Concr. Res.*, vol. 40, no. 8, pp. 1189–1196, Aug 2010, http://dx.doi.org/10.1016/j.cemconres.2010.04.005.

[26] American Society for Testing and Materials, *Standard Specification for Portland Cement*, ASTM C150/C150M, 2019.

[27] A. Muthadhi and S. Kothandaraman, "Experimental investigations of performance characteristics of rice husk ash-blended concrete," *J. Mater. Civ. Eng.*, vol. 25, no. 8, pp. 1115–1118, 2013, http://dx.doi.org/10.1061/(ASCE)MT.1943-5533.0000656.

[28] American Society for Testing and Materials, *Standard Test Method for Potential Alkali Reactivity of Aggregates (Mortar-Bar Method)*, ASTM C1260-14, 2014.

[29] American Society for Testing and Materials, *Standard Specification for Coal Fly Ash and Raw or Calcined Natural Pozzolan for Use in Concrete*, ASTM C618, 2019.

[30] J. Hoppe Fo., M. R. Garcez, M. H. F. Medeiros, L. C. P. Silva Fo., and G. C. Isaia, "Reactivity assessment of residual rice-husk ashes," *J. Mater. Civ. Eng.*, vol. 29, no. 6, pp. 1–7, 2017, http://dx.doi.org/10.1061/(ASCE)MT.1943-5533.0001820.

[31] Associação Brasileira de Normas Técnicas, *Materiais Pozolânicos – Determinação do Teor de Hidróxido de Cálcio Fixado – Método Chapelle Modificado*, NBR 1589, 2010.

[32] American Society for Testing and Materials, *Standard Test Method for Determining the Potential Alkali-Silica Reactivity of Combinations of Cementitious Materials and Aggregate (Accelerated Mortar-Bar Method)*, ASTM C1567-13, 2013.

[33] F. Golmakani and R. D. Hooton, "Comparison of laboratory performance tests used to assess alkali-silica reactivity," in *Proc. Can. Soc. Civ. Eng. Conf., vol. 2*, 2016, pp. 1–7.

[34] R. A. Deschenes Jr. and W. Micah Hale, "Alkali-silica reaction in concrete with previously inert aggregates," *J. Perform. Constr. Facil.*, vol. 31, no. 2, 04016084, Apr 2017, http://dx.doi.org/10.1061/(ASCE)CF.1943-5509.0000946.

[35] M. Thomas, B. Fournier, K. Folliard, J. Ideker, and M. Shehata, "Test methods for evaluating preventive measures for controlling expansion due to alkali–silica reaction in concrete," *Cement Concr. Res.*, vol. 36, no. 10, pp. 1842–1856, Oct 2006, http://dx.doi.org/10.1016/j.cemconres.2006.01.014.

[36] Laboratório Nacional de Engenharia Civil, *Betões Metodologia para Prevenir Reacções Expansivas Internas*, LNEC E 461, 2007.

[37] M. A. T. M. Broekmans, "Deleterious reactions of aggregate with alkalis in concrete," *Rev. Mineral. Geochem.*, vol. 74, no. 1, pp. 279–364, 2012, http://dx.doi.org/10.2138/rmg.2012.74.7.

[38] M. Prezzi, P. J. M. Monteiro, and G. Sposito, "The alkali-silica reaction, part I: use of the double-layer theory to explain the behaviour of reaction-product gels," *ACI Mater. J.*, vol. 94, pp. 10–17, 1997, http://dx.doi.org/10.14359/280.

[39] S. Chatterji, "Chemistry of alkali-silica reaction and testing of aggregates," *Cement Concr. Compos.*, vol. 27, no. 7-8, pp. 788–795, 2005, http://dx.doi.org/10.1016/j.cemconcomp.2005.03.005.

[40] S. Chatterji, A. D. Jensen, N. Thaulow, and P. Christensen, "Studies of alkali-silica reaction. Part 3. mechanisms by which naci and $Ca(OH)_2$ affect the reaction," *Cement Concr. Res.*, vol. 16, no. 2, pp. 246–254, Mar 1986, http://dx.doi.org/10.1016/0008-8846(86)90141-9.

[41] T. Ichikawa and M. Miura, "Modified model of alkali-silica reaction," *Cement Concr. Res.*, vol. 37, no. 9, pp. 1291–1297, Sep 2007, http://dx.doi.org/10.1016/j.cemconres.2007.06.008.

[42] H. Wang and J. E. Gillott, "Mechanism of alkali–silica reaction and the significance of calcium hydroxide," *Cement Concr. Res.*, vol. 21, no. 4, pp. 647–654, Jul 1991, http://dx.doi.org/10.1016/0008-8846(91)90115-X.

[43] M. H. F. Medeiros, J. W. Raisdorfer, and J. Hoppe Fo., "Influência da sílica ativa e do metacaulim na velocidade de carbonatação do concreto: relação com resistência, absorção e relação a/c," *Ambient. Constr.*, vol. 17, no. 4, pp. 125–139, 2017, http://dx.doi.org/10.1590/s1678-86212017000400189.

[44] J. H. S. Rêgo, A. A. Nepomuceno, E. P. Figueiredo, N. P. Hasparyk, and L. D. Borges, "Effect of particle size of residual rice-husk ash in consumption of $Ca(OH)_2$," *J. Mater. Civ. Eng.*, vol. 27, no. 6, pp. 1–9, Jun 2015, http://dx.doi.org/10.1061/(ASCE)MT.1943-5533.0001136.

[45] S. Kandasamy and M. H. Shehata, "The capacity of ternary blends containing slag and high-calcium fly ash to mitigate alkali silica reaction," *Cement Concr. Compos.*, vol. 49, pp. 92–99, May 2014, http://dx.doi.org/10.1016/j.cemconcomp.2013.12.008.

[46] H. T. Le, K. Siewert, and H.-M. Ludwig, "Alkali silica reaction in mortar formulated from self-compacting high-performance concrete containing rice husk ash," *Constr. Build. Mater.*, vol. 88, pp. 10–19, Jul 2015, http://dx.doi.org/10.1016/j.conbuildmat.2015.04.005.

[47] R. D. Moser, A. R. Jayapalan, V. Y. Garas, and K. E. Kurtis, "Assessment of binary and ternary blends of metakaolin and Class C fly ash for alkali-silica reaction mitigation in concrete," *Cement Concr. Res.*, vol. 40, no. 12, pp. 1664–1672, Dec 2010, http://dx.doi.org/10.1016/j.cemconres.2010.08.006.

[48] S. M. H. Shafaatian, A. Akhavan, H. Maraghechi, and F. Rajabipour, "How does fly ash mitigate alkali-silica reaction (ASR) in accelerated mortar bar test (ASTM C1567)," *Cement Concr. Compos.*, vol. 37, no. 1, pp. 143–153, Mar 2013, http://dx.doi.org/10.1016/j.cemconcomp.2012.11.004.

[49] M. H. Shehata, M. D. A. Thomas, and R. F. Bleszynski, "The effects of fly ash composition on the chemistry of pore solution in hydrated cement pastes," *Cement Concr. Res.*, vol. 29, no. 12, pp. 1915–1920, Dec 1999, http://dx.doi.org/10.1016/S0008-8846(99)00190-8.

Author contributions: CAS, MHFM conceived the presented idea. EAL, CAS developed the written work presented in the paper. DSJ reviewed the English. CAS, EP performed the experimental analysis. All authors discussed the results and contributed to the final manuscript.

Editors: Fernando Soares Fonseca, José Luiz Antunes de Oliveira e Sousa, Guilherme Aris Parsekian.

IBRACON Structures and Materials Journal
Revista IBRACON de Estruturas e Materiais
ISSN 1983-4195 ismj.org

ORIGINAL ARTICLE

Behavior of composite beams with external prestressing in sagging moment regions

Comportamento de vigas mistas com protensão externa nas regiões de momento positivo

Karla Demoner Ribeiro[a]
Thiago Tononi Turini[a]
Lorenzo Augusto Ruschi e Luchi[a]
Adenilcia Fernanda Groberio Calenzani[a]

[a]Universidade Federal do Espírito Santo – UFES, Departamento de Engenharia Civil, Vitória, ES, Brasil

Received 08 October 2019
Accepted 14 December 2020

Abstract: Prestressed composite steel-concrete structures are scarcely used due to a lack of clear standardized design guidelines and formulations on the subject. The present research aims to present design methodologies for steel-concrete composite beams with external pretension applied via straight tendons. A computer program to perform structural analysis of such beams was developed based on two different methodologies: the first one is presented in ABNT NBR 8800:2008, in which the guidelines for the design of composite beams with compact webs are adjusted to include the effects of the pretension force. The second methodology is extracted from international literature and presents a structural design process based on stress distribution on the beam. Ninety prestressed and thirty non-prestressed beams were analyzed and designed with the aforementioned computer program to evaluate the influence of beam length, degree of symmetry of the steel profile and eccentricity of the pretension force on the mechanical resistance of the beams. It was observed that, although the prestressing force considerably improved resistance to bending, it introduced high compression stresses on the steel profile; hence, the pre-stressing of composite beams is proved efficient only for steel profiles with symmetrical cross-sections.

Keywords: prestressed composite beams. design methodology. external prestressing. computer program.

Resumo: A protensão em estruturas mistas de aço e concreto é pouco utilizada pela falta de normas e formulações claras sobre o assunto. Esse trabalho visa apresentar metodologias de análise e dimensionamento de vigas biapoiadas mistas de aço e concreto com protensão externa e cabo de traçado reto (pré-tração). Um programa computacional que efetua a análise e o dimensionamento dessas vigas foi elaborado com base em duas metodologias distintas: a da ABNT NBR 8800:2008, de vigas mistas compactas, ajustada para incluir os efeitos da força de protensão e uma segunda, extraída da literatura internacional, em que o dimensionamento é feito por meio da verificação das tensões atuantes. Noventa vigas mistas protendidas e trinta sem protensão foram calculadas por meio do programa computacional desenvolvido para avaliar a influência do comprimento do vão, do grau de monossimetria da seção transversal do perfil de aço e da excentricidade da força de protensão na capacidade resistente das vigas. Observou-se que embora a protensão gere uma melhora considerável no comportamento à flexão, a força de protensão introduz altas tensões de compressão no perfil de aço, por isso a eficiência da protensão foi comprovada apenas nos casos de vigas mistas com perfil de aço duplamente simétrico.

Palavras-chave: vigas mistas de aço e concreto protendidas. metodologias de dimensionamento. protensão externa. programa computacional.

How to cite: K. D. Ribeiro, T. T. Turini, L. A. R. Luchi, and A. F. G. Calenzani, "Behavior of composite beams with external prestressing in sagging moment regions," *Rev. IBRACON Estrut. Mater.*, vol. 14, no. 4, e14405, 2021, https://doi.org/10.1590/S1983-41952021000400005

Corresponding author: Adenilcia Fernanda Groberio Calenzani. E-mail: afcalenzani@gmail.com
Financial support: Foundation for Support of Research and Innovation of Espírito Santo (FAPES), with a master's scholarship of R$1,500.00 monthly to Karla Demoner Ribeiro.
Conflict of interest: Nothing to declare.

1 INTRODUCTION

External prestressing applied to steel-concrete composite beams results in elements of great structural efficiency, able to cover large spans and resist high loads with reduced structural weight. This technique is of interest for structural recovery and / or reinforcement of existing structures presenting severe pathologies caused by deterioration due to environmental agents or increases in service loads such as, for example, a bridge that experiences an increase in traffic or other loads throughout its lifespan.

Advantages of using external prestressing systems include: the absence of sheaths, which facilitates the building process, making construction more agile; possibility of reducing cross-sections, resulting in lighter and more efficient structural elements; reduction of prestressing losses due to friction, which may even be neglected when using unbonded tendons; external tendons with simpler lines and easier verification after installation; since tendons are external, they are easily inspected and can be re-prestressed or even replaced without interrupting the use of the structure. Figure 1 shows different cross-section types for composite beams with external prestressing tendons.

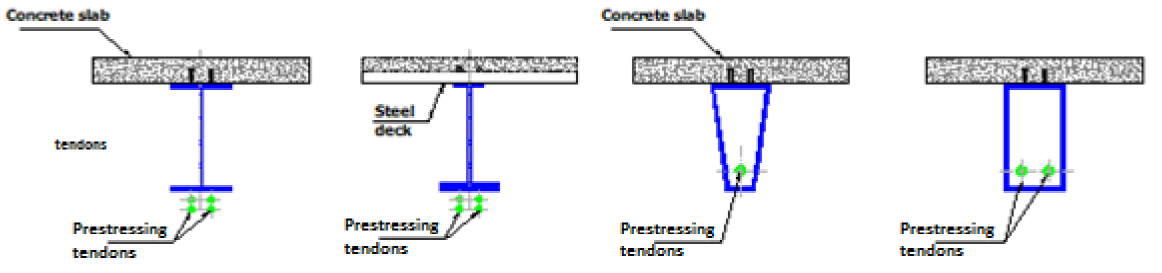

Figure 1. Possible profiles for external prestressing. Source: Troistky [1].

Studies indicate that the application of prestressing to composite steel-concrete structures is recent. Ayyub et al. [2] and Troitsky [1] state that in 1959, Szilard [3] suggested methods for the analysis and design of prestressed composite steel-concrete beams considering the effects of concrete shrinkage and creep. Hoadley [4], in 1963, investigated the behavior of simply supported steel and steel-concrete composite beams, prestressed with high resistance tendons and constant eccentricity along the beam. Strass [5], in the following year, developed an experimental study of composite steel-concrete beams subjected to positive bending moment. In 1966, Regan [6] analyzed the effects of variations in slab thickness, prestressing forces and load types on the behavior of simply supported composite steel-concrete beams.

Saadatmanesh et al. [7] to [8] published a series of analytical and experimental studies on prestressed composite beams in the regions of sagging and hogging bending moments. The authors reported some of the advantages of using prestressing in composite beams such as: reductions in the weight of structural steel; increases in the range of the linear elastic regime of the structure; increased strength; and improvements in fatigue and fracture behavior.

Saadatmanesh et al. [9] tested two composite beams, one subjected to positive bending moment and the other to negative bending moment. The steel beams were prestressed before concrete casting to prevent cracking of the slab. Force versus displacement graphs of the beams were plotted, as well as graphs of force versus strain of the concrete, steel beam and prestressing bars. The values measured experimentally correlated well with values predicted by Saadatmanesh et al. [7], who used internal force equilibrium equations and strain compatibility.

Chen and Gu [10] experimentally determined the strength of sagging moment regions in prestressed composite steel-concrete beams. In the first stage, the beams were tested without prestressing until the bottom flange of the steel beam began yielding, at which point the beams were unloaded. In the second stage, prestressing was applied to the composite beams before loading. The methodology adopted made it possible to analyze the behavior of the composite beams without prestressing. Additionally, based on the deformation compatibility of the tendons and the beam in the anchoring section and by balancing internal forces, the equation of the neutral axis is derived. A simplified expression to determine increases of stress on the tendons is developed, according to the method used to evaluate the capacity of the prestressed composite beam.

In Brazil, among studies on the use of external prestressing in composite beams, one can mention Nelsen [11] and Linhares [12]. Nelsen [11] presented a systematic approach for the analytical design procedure of simply supported and externally prestressed composite steel-concrete I-beams based on requirements from ABNT NBR 8800: 2008 [13], with emphasis on ultimate limit states (ULS). The author studied the influence of prestress force levels, eccentricity of the tendons and constructive methodology (pre-tensioning or post-tensioning) on the strength of structural elements, using spreadsheets developed with the software MathCAD.

Linhares [12] carried out a case study of an externally prestressed composite box-girder bridge featuring two continuous spans, proceeding to an analytical verification following design criteria from AASHTO-LRFD. An initial model consisting of spatial frame bars was developed with the software STRAP for the structural analysis of the system, followed by the creation of a more refined finite element model featuring shell elements with the aid of the computer program SAP2000, to confront and validate the results of the initial model, especially in terms of stresses and displacements. The author concluded that prestressing the composite beam resulted in a small increase in flexural strength in the region subjected to positive bending moment, proving to be of little advantage, according to the AASHTO design criteria. The calculation of prestress force losses due to friction resulted in a small value, since the span only presented two inflection points.

Recently, Lou et al. [14] developed a FE model to analyze composite steel and concrete beams with external prestressing under short and long-term loads, aiming to compare results with composite steel and concrete beams without prestressing. The effect of geometric non-linearity was added by considering the flexural and axial interaction in the finite element formulation, updating the eccentricities of the tendons in the numerical procedure. Results confirmed that prestressing composite beams considerably improved their behavior under short loads. However, there was no noticeable difference on the response to time-dependent effects.

Liban and Tayşi [15], on the other hand, performed a numerical analysis of a simply supported pre-tensioned composite beam with overhangs, in order to observe the behavior of regions subjected to positive and negative bending moments, and also assess the influence of tendon position on the behavior of the structure. Results show that it is more beneficial for the structure to place the straight tendon near the top flange of the profile, thus obtaining an ultimate load approximately 22% larger than if the straight tendon was positioned near the bottom flange of the profile.

On this research, a computer program was developed using Microsoft Office Excel [16] with an interface in Visual Basic language, in the Microsoft Visual Basic Express environment [17]. The program performs the analysis and design of simply supported composite steel and concrete beams with external prestressing and straight tendons (pre-tension), checking safety conditions for ultimate limit states and the serviceability limit state (SLS) of excessive deflection.

1.1 Theoretical formulation

The Brazilian standard NBR 8800: 2008 [13] addresses the design of composite steel and concrete beams without prestressing. Thus, for this research, the design equations were adjusted to include the effects of prestressing forces. This force is estimated according to Nunziata [18], considering that the maximum compressive stress in the central section of the steel profile at the time of prestressing cannot exceed the design yield strength of steel, according to Equation 1.

$$\frac{M_g}{W_a}-\frac{P\beta_n\gamma_p}{A_a}-\frac{P\beta_n\gamma_p e_{p\_a}}{W_a}=-f_{yd} \tag{1}$$

It is worth mentioning that at first, since the element is subjected to pre-tensioning with prestressing occurring before the application of the construction loads, the steel beam must resist all the stresses introduced by prestressing. As such, the formulation of Equation 1 uses the properties of the steel profile. Isolation of the prestressing force P results in Equation 2:

$$P=\frac{\dfrac{M_g}{W_a}+f_{yd}}{\dfrac{\beta_n\gamma_p}{A_a}+\dfrac{\beta_n\gamma_p e_{p\_a}}{W_a}} \tag{2}$$

Where: P is the prestressing force, f_{yd} is the design yield strength of the steel of the profile, M_g is the maximum bending moment caused by the weight of the profile, W_a is the elastic section modulus of the steel profile, e_{p_a} is the eccentricity of the prestressing tendon in relation to the center of gravity of the steel cross-section, A_a is the cross-sectional area of the steel profile, γ_p is a safety factor applied to the prestressing force and β_n is the amplification factor of the prestressing force, introduced to compensate for losses in prestress force, taken as 1.1.

Equation 2 was adjusted to fit the flexo-compression interaction curve of NBR 8800: 2008 [13]. Assuming that the design axial force is greater than 20% of the design resistance to axial force, Equation 3, the prestressing force value is obtained according to Equation 5. Furthermore, the term related to the bending moment due to the weight of the steel beam cannot be considered when the tendon layout is straight, since the effects favoring structural safety do not occur at the supported cross-sections in this case.

$$\frac{N_{Sd}}{N_{Rd}}+\frac{8M_{Sd}}{9M_{Rd}}\leq 1 \text{ to } \frac{N_{Sd}}{N_{Rd}}>0.2 \tag{3}$$

$$\frac{\gamma_p\beta_nP}{N_{Rd}}+\frac{8\gamma_p\beta_nPe_{p\_a}}{9M_{Rd}}\leq 1 \tag{4}$$

$$P=\frac{1}{\frac{\gamma_{p\beta_n}}{N_{Rd}}+\frac{8\gamma_p\beta_ne_{p\_a}}{9M_{Rd}}} \tag{5}$$

where M_{Rd} is the design resistance to bending moment of the steel beam, γ_p is the load factor of prestressing force, N_{Rd} is the design resistance to axial force of the steel beam and e_{p_a} is the eccentricity of the tendon in relation to the centroid of the beam cross-section. Remaining variables are defined according to Equation 2.

With the application of the gravitational loads of construction, an increase in the value of the initial prestressing force is assumed, which varies according to the configuration of the prestressing tendon and the distribution of the load. This increase in the value of the initial prestressing force, called force increment, can be calculated in several ways, such as: with the application of the principle of virtual work (Troitsky [1]); deformation increment method or finite element method. If a straight tendon is considered, the expressions to determine the increase in prestressing force ΔP are Equation 6 for uniformly distributed load q and Equation 7 for two symmetrically placed concentrated loads F of same magnitude, at a distance a from supports.

$$\Delta P=\frac{qL^2e_{p\_tr}}{12\left(e_{p\_tr}^2+\frac{I_{tr}}{A_{tr}}+\frac{E_aI_{tr}}{E_pA_p}\right)} \tag{6}$$

$$\Delta P=\frac{e_{p\_tr}Fa\left(L-a\right)}{L\left(e_{p\_tr}^2+\frac{I_{tr}}{A_{tr}}+\frac{E_aI_{tr}}{E_pA_p}\right)} \tag{7}$$

where E_a is the modulus of elasticity of the steel profile, E_p is the modulus of elasticity of the prestressing tendon, L is the length of said tendon, equal to the length of the beam, I_{tr} is the moment of inertia of the composite section, A_p is the area of active reinforcing steel, A_{tr} is the area of the transformed composite section, e_{p_tr} is the eccentricity of the prestressing tendon in relation to the centroid of the composite section and q is the uniformly distributed load. Remaining variables are defined according to Equation 5.

1.2 Simplifying assumptions

The present study was limited to the verification of simply supported composite steel and concrete beams with external prestressing (pre-tension) in regions of positive moment. The steel section and the prestressed composite section were designed with procedures defined in the standards: ABNT NBR 8800: 2008 [13], ABNT NBR 6118: 2014

[19], ABNT NBR 7482: 2008 [20] and ABNT NBR 7483: 2008 [21]. Some premises that simplify the analysis and limit the scope of the study were adopted, namely:

- Compact steel section, that is, local flange or web buckling is not expected, meaning that $Q_a = Q_s = Q = 1$;
- Complete interaction between steel and concrete materials, guaranteed by the proper design of stud bold shear connectors;
- Unshored construction;
- Solid reinforced-concrete slab;
- Tensile strength of concrete is neglected;
- Straight line tendon;
- Verification is limited to the mid-span section, where the largest bending moment is expected;
- Shear force is resisted only by the steel profile.

2 PRESENTATION OF THE PROGRAM

The program verifies the ultimate resistance to bending of the prestressed composite beam according to the methodology adopted by ABNT NBR 8800: 2008 [13] but with the modifications proposed in item 1.1 of this paper. Doubly and monosymmetric steel profiles are accepted by the program. There is also the option of using the procedure proposed by Nunziata [18], which checks the stresses on steel and concrete.

Design routines were developed in the form of flowcharts to systematize the entire script and assist in the elaboration of the program. The routines illustrate the procedures performed, clarifying the sequence of calculations, indicating the design equations used and the basic commands needed such as decision and data selection. In total, 11 routines were developed. Routine 1 calculates the position of the elastic neutral axis, ENA, and the moment of inertia of the homogenized composite section.

Routines 2 and 3 calculate the design resistance to compression and the design resistance to bending moment of the steel profile, respectively. Routines 4 and 5 are intended, respectively, for calculating the prestressing force and its increase. Routine 6 verifies the combined bending and axial stresses of the steel profile.

Routine 7 calculates the position of the plastic neutral axis, PNA, measured from the top of the slab, symbolized by the letter a when it passes through the slab and by y_{LNP} when it crosses the steel profile. This routine also provides an expression for the ultimate bending moment of the composite section.

Routine 8 calculates the ultimate shear force, routine 9 determines the midspan deflection of the prestressed composite section and in routine 10, the calculation of stresses on steel and concrete is presented. Finally, routine 11 includes the calculation of the number of shear connectors needed for full interaction. The complete flowcharts for routines 1 to 11 are presented in Ribeiro [22].

The logic used in the program, enumerated below, performs the design in three stages of the lifespan of the structure: phase 1, during construction, when the steel profile resists the construction loads and the prestressing force; phase 2, when composite behavior is developed and the composite beam supports immediate loads such as live loads attributed to occupation and finally phase 3, when long-term effects are considered. Table 1 shows the loads considered in the structural analysis and Table 2 shows the load factors according to ABNT NBR 8800: 2008 [13] for construction load combination (before curing) and for normal load combination (after curing). Applied loads are calculated using construction combinations in phase 1 and normal combinations in phases 2 and 3.

Table 1. Load considered in structural analysis

(1)	g_1 – Weight of the steel beam
(2)	P – Prestressing force on steel tendons
(3)	g_3 – Weight of the concrete slab
(4)	ΔP_4 - Increment of prestressing force due to the weight of the concrete slab
(5)	g_5 – Serviceability dead load
(6)	q_6 – Serviceability live load
(7)	ΔP_7 - - Increment of prestressing force due to serviceability dead load
(8)	ΔP_8 - - Increment of prestressing force due to serviceability live load
(9)	P_9 – Concrete slab shrinkage

Table 2. Loads safety fator (γ)

Loads	Before Concrete Casting	After Concrete Casting
Weight of the steel beam (g_1)	$\gamma'_{g1} = 1.15$	$\gamma_{g1} = 1.25$
Prestressing force on steel tendons (P)	$\gamma'_{g2} = 1.20$	$\gamma_{g2} = 1.20$
Weight of the concrete slab (g_3)	$\gamma'_{g3} = 1.25$	$\gamma_{g3} = 1.35$
Serviceability dead load (g_5)	-	$\gamma_{g5} = 1.35$
Serviceability live load (q_6)	-	$\gamma_{g6} = 1.50$

1) Data input, calculation of geometric properties and ultimate forces of the steel profile and calculation of prestressing force:
• Calculation of the geometric properties of the cross-section of the steel profile;
• Calculation of the PNA of the steel profile section;
• Calculation of the number of stud bolts;
• Call Routine 1 - Calculation of the ENA of the homogenized section;
• Call Routine 2 - Calculation of the design resistance to compression (N_{Rd}) of the steel profile;
• Call Routine 3 - Calculation of the design resistance to negative moment (M^{-}_{Rd}) of the steel profile;
• Call Routine 4 - Calculation of the initial prestressing force (P);
2) Design according to NBR 8800:2008 [13]:
2.1) Verification in phase 1 – Steel beam
• Loads: (1) + (2) + (3) + (4);
• Call Routine 5 - Calculation of increases in prestressing force (ΔP_4) due to the weight of the concrete slab and verification of maximum stress on the tendons after force increments;
• Calculation of the design compression force (N_{Sd_1}) of phase 1:

$$N_{Sd\_1} = \gamma_{g2} \cdot \beta_n \cdot P + \gamma_{g2} \cdot \beta_n \cdot \Delta P_4 \tag{8}$$

• Calculation of the design bending moment (M_{Sd_1}) of phase 1:

$$M_{Sd\_1} = \frac{\gamma'_{g1} \cdot g_1 \cdot L_v^2}{8} + \gamma_{g2} \cdot \beta_n \cdot P \cdot e_{p\_a} + \frac{\gamma'_{g3} \cdot g_3 \cdot L_v^2}{8} + \gamma_{g2} \cdot \beta_n \cdot \Delta P_4 \cdot e_{p\_a} \tag{9}$$

• Call routine 3 – Calculation of the resistance to bending of the steel profile, M_{Rd_1}, resistance to negative (M^{-}_{Rd}) or positive (M^{+}_{Rd}) bending moment, depending on the value of M_{Sd_1};
• Call routine 6 – Flexo-compression design:

$$\frac{N_{Sd\_1}}{N_{Rd\_1}} + \frac{8 \cdot M_{Sd\_1}}{9 \cdot M_{Rd\_1}} \leq 1 \tag{10}$$

• Calculation of the design shear force (V_{Sd_1}) of phase 1:

$$V_{Sd\_1} = \frac{\gamma'_{g1} \cdot g_1 \cdot L_v}{2} + \frac{\gamma'_{g3} \cdot g_3 \cdot L_v}{2} \tag{11}$$

• Call routine 8 – Calculation of the design resistance to shear force (V_{Rd}) of the steel profile;

• Verification $V_{Sd\_1} \leq V_{Rd}$;

2.2) Verification in phase 2 – Steel-concrete composite beam, t=0 and $n = \frac{E_a}{E_c}$

• Loads: (1) + (2) + (3) + (4) + (5) + (6) + (7) + (8);

• Call routine 5 – Calculation of increments in prestressing force due to applied loads. Calculates increments due to dead loads (ΔP_7) and live loads (ΔP_8) and verifies maximum stresses on the tendons after the increments;

• Calculation of the design axial force (N_{Sd_2}) in phase 2:

$$N_{Sd\_2} = N_{Sd\_1} + \gamma_{g2} \cdot \beta_n \cdot \Delta P_7 + +\gamma_{g2} \cdot \beta_n \cdot \Delta P_8 \tag{12}$$

• Calculation of the design bending moment (M_{Sd_2}) of phase 2:

$$M_{Sd\_2} = M_{Sd\_1} + \frac{\gamma_{g5} \cdot g_5 \cdot L_v^2}{8} + \frac{\gamma_{g6} \cdot q_6 \cdot L_v^2}{8} + \gamma_{g2} \cdot \beta_n \cdot \Delta P_7 \cdot e_{p\_tr} + \gamma_{g2} \cdot \beta_n \cdot \Delta P_8 \cdot e_{p\_tr} \tag{13}$$

• Call routine 7 – Calculation of PNA and design resistance to bending moment (M_{Rd_2}) of the prestressed composite section;

• Call routine 6 – Flexo-Compression verification:

$$\frac{N_{Sd_2}}{N_{Rd}} + \frac{8 \cdot M_{Sd\_2}}{9 \cdot M_{Rd\_2}} \leq 1 \tag{14}$$

For simplification, it is assumed that only the steel profile resists axial forces.

• Calculation of the design shear force (V_{Sd_2}) of phase 2:

$$V_{Sd\_2} = V_{Sd\_1} + \frac{\gamma_{g5} \cdot g_5 \cdot L_v}{2} + \frac{\gamma_{g6} \cdot q_6 \cdot L_v}{2} \tag{15}$$

• Verifies if $V_{Sd\_2} \leq V_{Rd}$;

2.3) Verification in phase 03 – Steel-concrete composite beam, t=∞ and $n = \frac{3E_a}{E_c}$

• Loads: (1) + (2) + (3) + (4) + (5) + (6) + (7) + (8) + (9);

• Call routine 1 – Calculation of the ENA of the homogenized section for t=∞ and $n = \frac{3E_a}{E_c}$;

• Calculation of forces due to concrete shrinkage (P9):

$$P_9 = \gamma_{g3} \cdot \frac{E_c}{3} \cdot \varepsilon_{cs,\infty} \cdot A_c \tag{16}$$

$\varepsilon_{cs,\infty}$ is the strain caused by shrinkage.

• Calculation of the design axial force (N_{Sd_3}) of phase 3:

$$N_{Sd\_3} = N_{Sd\_2} + P_9 \tag{17}$$

• Calculation of the design bending moment (M_{Sd_3}) of phase 3:

$$M_{Sd\_3} = M_{Sd\_2} + \gamma_{g3} \cdot P_9 \cdot \left(y_{tr}^{'} - \frac{t_c}{2} \right) \tag{18}$$

• Flexo-compression verification:

$$\frac{N_{Sd3}}{N_{Rd}} + \frac{8 \cdot M_{Sd\_3}}{9 \cdot M_{Rd\_2}} \leq 1 \tag{19}$$

For simplification, it is assumed that only the steel profile resists axial forces. Also, the design resistance to bending of phase 3 is the same as in phase 2.
3) Call routine 9 – Calculation of deflection.
4) Design according to Nunziata [18]:
• Calls design routine 10 by verification of stresses.

3 EXPERIMENTAL VALIDATION

To validate the changes proposed to the formulations of ABNT NBR 8800: 2008 [13], two experiments on pre-tensioned prestressed composite beams were used, one tested by Ayyub et al. [2] and the other tested by Chen and Gu [10].

3.1 Experiment performed by Ayyub et al. [2]

The prestressed composite beam tested by Ayyub et al. [2], named *Specimen* A, Figure 2, consists of a simply supported element with a span length of 4.575 m, subjected to concentrated loads of equal magnitude applied at two symmetrical points in relation to midspan at a distance of 0.915 m from supports. The cross-section features a steel profile W360 x 45 with f_y equal to 345 MPa, a concrete slab with a thickness of 76mm and f_{cj} equal to 33.4 MPa defined by compressive tests of three specimens cured for 90 days. The slab presents a width of 915mm. Prestressing was performed via steel tendons of grade 150 DYWIDAG Threadbars of 16mm, with f_{pyk} of 910 MPa and f_{ptk} of 1100 MPa, at a distance of 57mm from the lower surface of the bottom flange of the steel profile, and a prestressing force of 98kN applied to each tendon.

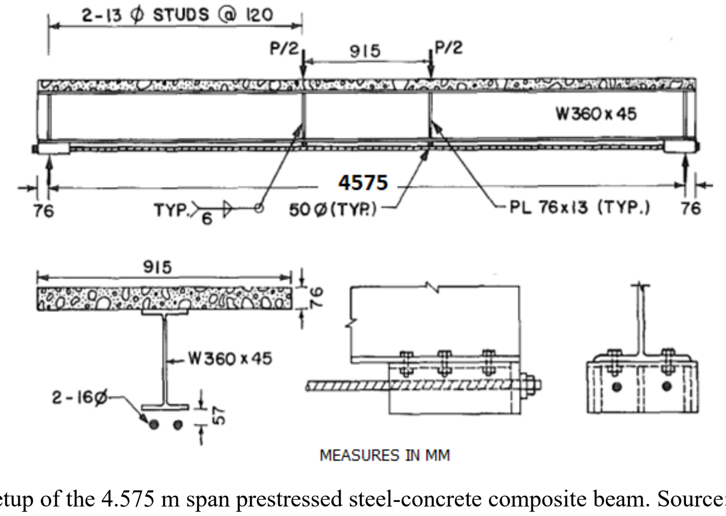

Figure 2. Test setup of the 4.575 m span prestressed steel-concrete composite beam. Source: Ayyub et al. [2].

Since prestressing was carried out before concreting the slab, increments in prestressing force were determined using the weight of fresh concrete and the experimental load, totaling an increase of 74.92 kN at the end of the test. Thus, the prestressing force at the moment of collapse is equal to 270.92 kN.

The ultimate limit state observed for the beam studied was the crushing of the concrete slab, which occurred for a bending moment of 586.51 kN.m. Calculating the characteristic resistance to bending moment according to the methodology proposed herein resulted in a value of 515.7 kN.m, 12.07% less than the ultimate load observed experimentally, showing that the proposed methodology favors structural safety.

3.2 Experiment performed by Chen and Gu [10]

The prestressed composite beam tested by Chen and Gu [10], named BS2, Figure 3, consists of a simply supported element with a span of 5 m, subjected to concentrated loads of equal magnitude applied at two symmetrical points in relation to midspan at a distance of 1.4 m from supports. The cross-section is composed using steel plates of 120 x 10 mm for the flanges and 250 x 6 mm for the web, with f_y equal to 367 MPa, a concrete slab with a thickness of 90 mm and f_{cj} equal to 30 MPa defined by compressive tests of three specimens cured for 30 days. The slab presents a width of 1100 mm. Prestressing was introduced by two steel tendons with a cross-sectional area of 137.4 mm^2, with f_{pyk} of 1680 MPa and f_{ptk} of 1860 MPa, at a distance of 30 mm from the lower surface of the bottom flange of the steel profile, and a prestressing force of 112.6 kN applied to each tendon.

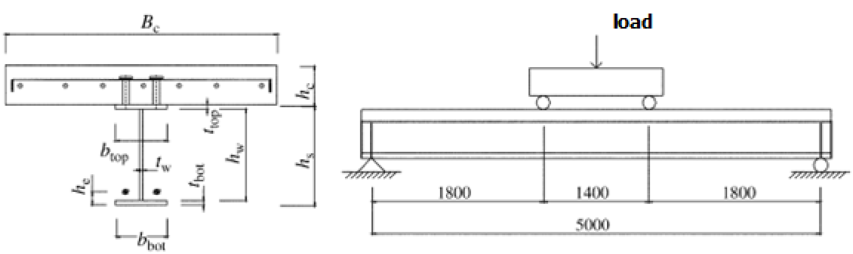

dimensions in mm

B_c	h_c	b_{top}	t_{top}	h_w	t_w	b_{bot}	t_{bot}	h_e
1100	90	120	10	250	6	120	10	30

Figure 3. Test setup of the 5 m span prestressed steel-concrete composite beam. Source: Chen and Gu [10].

In this test, prestressing was carried out after concreting the slab, therefore only the test load was considered in the calculation of the prestressing force, totaling an increase of 72.1 kN at the end of the test, thus obtaining a prestressing force at collapse of 297.3 kN.

The ultimate limit state of the beam studied was the crushing of the concrete slab, which occurred for a bending moment of 373.2 kN.m. The characteristic resistance to bending moment, according to the methodology proposed herein, was 351.67 kN.m, therefore 5.77% less than the ultimate load verified experimentally, showing that the proposed methodology once again favors structural safety.

4 PARAMETRIC STUDY

4.1 Parametrization models

In the parametrized models, the composite beams analyzed feature double or monosymmetric steel profiles with smaller top flanges. The profiles are made of structural steel ASTM A572 gr. 50 (f_y equal to 345 MPa and f_u equal to 450 MPa). According to ABNT NBR 8800:2008 [13], monosymmetric cross-sections must meet the criteria given in Equations 20 and 21.

$$\frac{1}{9} \leq \alpha_y \leq 9 \text{ com } \alpha_y = \frac{I_{yc}}{I_{yt}} \tag{20}$$

$$A_{fs} + A_w > A_{fi} \tag{21}$$

where: I_{yc} is the moment of inertia of the compressed flange in relation to the axis that crosses the web at mid-thickness; I_{yt} is the moment of inertia of the tensioned flange in relation to the axis that crosses the web at mid-thickness; A_{fs} is the area of the upper flange, A_w is the area of the web and A_{fi} is the area of the bottom flange of the steel profile. In this study, the inverse of the coefficient α_y is called degree of monosymmetry, α_m, which may vary from 1 (for doubly symmetric sections) to a maximum value of 9.

$$\alpha_m = \frac{1}{\alpha_y} \text{ and } 1 \leq \alpha_m \leq 9 \tag{22}$$

To assess the influence of the degree of monosymmetry, profiles with the same cross-section area, equal to 178.00 cm^2, were selected. The weight of the steel I-beams is chosen as the same for all models on purpose, to allow an analysis of which geometric configuration provides the most resistant prestressed composite beam with the same cost. The height of the profiles was fixed at 550 mm, the thickness of the web at 12.50 mm and the width of the lower flange at 300 mm. The other parameters of the profiles were chosen to meet the specified steel area and provide variations in the degree of monosymetry (α_m).

Values of beam length include 9, 10.5, 12, 13.5, 15 and 17 meters, consequently, the ratios between beam length and profile height studied are equal to approximately 16, 19, 22, 25, 27 and 31. The maximum free-span is 3.0 meters, equal to the distance between the beams perpendicular to the element under analysis. The distance of the beams adjacent to the beam studied is 5.0 meters.

Three eccentricity values (e_p) 630, 730 and 780 mm, were adopted for the beams as shown in Figure 4. For all models, the tendon path, formed by steel tendons CP-190 RB, is straight throughout the entire length of the beam.

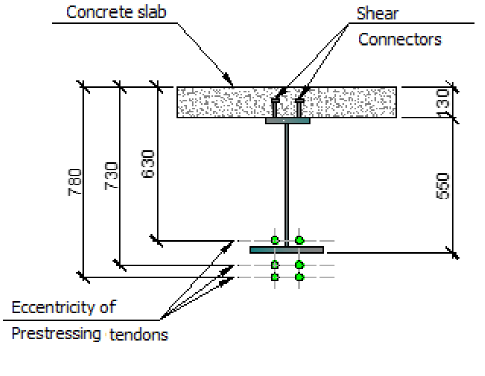

Figure 4. Profile scheme.

In total, one hundred and twenty composite steel and concrete beams were designed by the program, 90 of which are prestressed composite beams with eccentricity values of 630, 730 or 780mm. The remaining 30 models do not feature prestressing tendons. The models were named according to the presence or absence of prestressing using the acronyms VMP and VM, respectively. The prefixes VMP and VM are followed by the eccentricity values of prestressing tendons in relation to the top of the concrete slab, in turn followed by span length and the model number. Thus, the VMP 730x9x1 model indicates a prestressed composite beam with tendons located at 730mm from the top of the concrete slab, beam span equal to 9m and model number 1.

4.2 Methodology

Ultimate limit state verifications related to bending moment and shear force were performed along with checks of the serviceability limit state of excessive deformation. The verification of the interaction between axial and flexural forces was also performed. Tables 3 and 4 present the necessary checks for each of the aforementioned phases, considering the pre-tension method, that is, tendons are prestressed before casting the concrete slab.

Table 3. Design verifications of prestressed steel-concrete composite beam – ULS.

Verification phase	Loads	U.L.S Verification
1st Phase: Steel Beam	q_1 – Weight of the steel beam	- Compression $(N_{Sd\,1} \le N_{Rd\,1})$;
	P – Prestressing force on tendons	- Bending Moment $(M_{Sd\,1} \le M_{Rd\,1})$;
	q_3 – Weight of the concrete slab	- Shear force $(V_{Sd\,1} \le V_{Rd\,1})$;
	ΔP_4 - Increment of prestressing force due to concrete the weight of the concrete slab	- Flexure-compression Interaction
2nd Phase: Prestressed steel-concrete composite beam t = 0	Including 1st phase loads	
	q_5 – Serviceability dead load	- Compression $(N_{Sd\,2} \le N_{Rd\,2})$;
	q_6 – Serviceability live load	- Bending Moment $(M_{Sd\,2} \le M_{Rd\,2})$;
	ΔP_7 - Increment of prestressing force due to serviceability dead load	- Shear force $(V_{Sd\,2} \le V_{Rd\,2})$;
$n = \frac{E_a}{E_c}$	ΔP_8 - Increment of prestressing force due to serviceability live load	- Flexure-compression Interaction
3rd Phase: Prestressed steel-concrete composite beam t = ∞	Including 1st and 2nd phase loads	- Compression $(N_{Sd\,3} \le N_{Rd\,3})$;
	q_9 – Concrete slab shrinkage	- Bending Moment $(M_{Sd\,3} \le M_{Rd\,3})$;
$n = \frac{3E_a}{E_c}$		- Flexure-compression Interaction

Table 4. Verification phases of Prestressed steel-concrete composite beam – SLS.

Verification phase	1st Fase: Steel Beam	2nd Fase: Prestressed steel-concrete composite beam	
		t = 0 and $n = \frac{E_a}{E_c}$	**t = ∞ and** $n = \frac{3E_a}{E_c}$
Loads	q_1 – Weight of the steel beam	q_6 – Serviceability live load	q_5 – Serviceability dead load
	P – Prestressing force on tendons	ΔP_8 - Increment of prestressing force due to serviceability live load	ΔP_7 - Increment of prestressing force due to serviceability dead load
	q_3 – Weight of the concrete slab		
	ΔP_4 - - Increment of prestressing force due to the weight of the concrete slab		
Verifications S.L.S	Immediate deflection: (δ_1)	Short term deflection: (δ_2)	Long term deflection: (δ_3).
	Total deflection: $\delta_{total} = \delta_1 + \delta_2 + \delta_3 \le L/350$		

To proceed with the analysis of the results, the values of applied and resistant bending moment are presented for the cross section at the middle of the beams, for phase 2. This is because these forces refer to the methodology from ABNT NBR 8800: 2008 [13] which does not address the effects of creep and shrinkage in ULS analyses, only in the calculation of deflection. The design stresses acting on the elements are presented for phase 3 because calculations are based on Nunziata [18], which considers the effects of shrinkage and creep in ULS verifications.

5 RESULT ANALYSIS

5.1 Influence of the ratio between span length and profile height

Regarding the flexural strength of composite beams without prestressing (VM), the analysis of the graph in Figure 5 allows us to observe that, when the L/d ratio goes from 16 to 31, there is an increase in the resistance to bending moment of 10.9% for doubly symmetric section and approximately 10.1% for the section with a degree of symmetry of 2.07 and approximately 9.0% for sections with a degree of symmetry of 2.83, 3.88 and 5.22. This increase in strength is a result of the increase in the effective width of the beam, in turn due to a larger span length.

In Figure 6, the composite steel and concrete beams without prestressing (VM) and the prestressed (VMP) with L/d ratio equal to approximately 31 did not meet the design criteria for flexural and axial interaction, since the utilization index (i_{a2}) was greater than 1. For L/d ratios of 16 to 25, the beams met the design criteria with clearance. As such, for the studied load type, it is noted that an L/d ratio equal to 27 would be the most advantageous in economic terms, since the utilization index (i_{a2}) was the closest to 1.

Regarding the flexural strength of prestressed beams (VMP), it is observed that the ultimate bending moment increases practically linearly as the L/d ratio increases from 16 to 27 for all degrees of monosymetry. It is also observed that the beams with monosymmetric sections present the highest resistance to bending moment, reaching an increase of 35.6% when the L/d ratio grows from 16 to 27 for the sections with a monosymmetry index of 2.83, 3.88 and 5.22; 38.12% for the section with a degree of monosymmetry equal to 2.07 and 38.75% for the doubly symmetrical section. For values of L/d ratio equal to 27 and larger, the increase in resistance to bending moment is small for both monosymmetric sections (about 1%) and for the doubly symmetric section (about 3%).

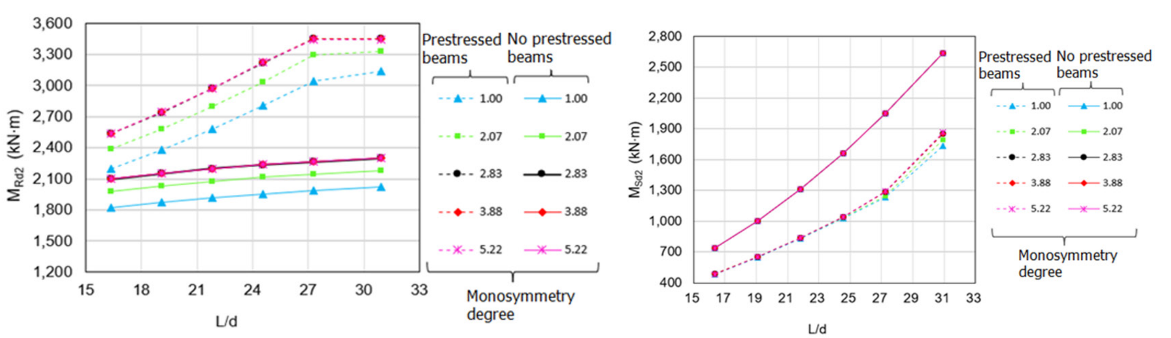

Figure 5. M_{Rd} and M_{Sd} versus L/d ratio graphs for e_p = 730mm.

The ratio between the resistance to bending moment of the prestressed composite beams and that of the unstressed composite beams, $M_{Rd2\ VMP} / M_{Rd2\ VM}$ shows that the ultimate bending moment of the prestressed composite beams is much higher than that of the composite beams without prestressing tendons; 21% and 55% greater for L/d ratios of 16 and 31, respectively in the case of doubly symmetrical section; and 21% and 49% higher for the L/d ratio equal to 16 and 31, respectively, in the case of the section with the highest monosymmetry degree. Larger spans have a higher $M_{Rd2\ VMP} / M_{Rd2\ VM}$ ratio because as the span increases, in addition to the increase in the effective width, the value of the prestressing force also increases, which contributes to a significant portion of the ultimate bending moment.

From Figure 5 it should be noted, as expected, that the bending moment acting on the prestressed composite beams is much lower than that of the conventional beams, being 35% and 34% lower for L/d ratios equal to 16 and 31 respectively for doubly symmetrical sections; and 34% and 29% higher for the L/d ratio equal to 16 and 31 respectively for the section with the highest monosymmetry degree. The bending moment resulting from the application of the prestressing force reduces the bending moment acting on the prestressed composite beams. The ratio between the bending moment of the composite beams with prestressing and that of the composite beams without prestressing was almost constant, around 38%, which shows that prestressing considerably reduces bending effects regardless of span length.

Although prestressing presented considerable benefits, reducing the magnitude of bending moments and increasing flexural strength, improvements in beam utilization index (i_{a2}) is less evident, as seen in Figure 6, because the compression force on the profile due to the prestressing force introduces compression stresses that add to the stresses arising from bending. Significant improvements in the utilization index only occur for the doubly symmetrical section, for all L/d ratios. For sections with a lower degree of monosymmetry (2.07 and 2.83), the benefits of prestressing are only observed in smaller spans. In cross-sections with a higher degree of monosymmetry (3.88 and 5.22), prestressing was not advantageous, resulting in a lower utilization rate.

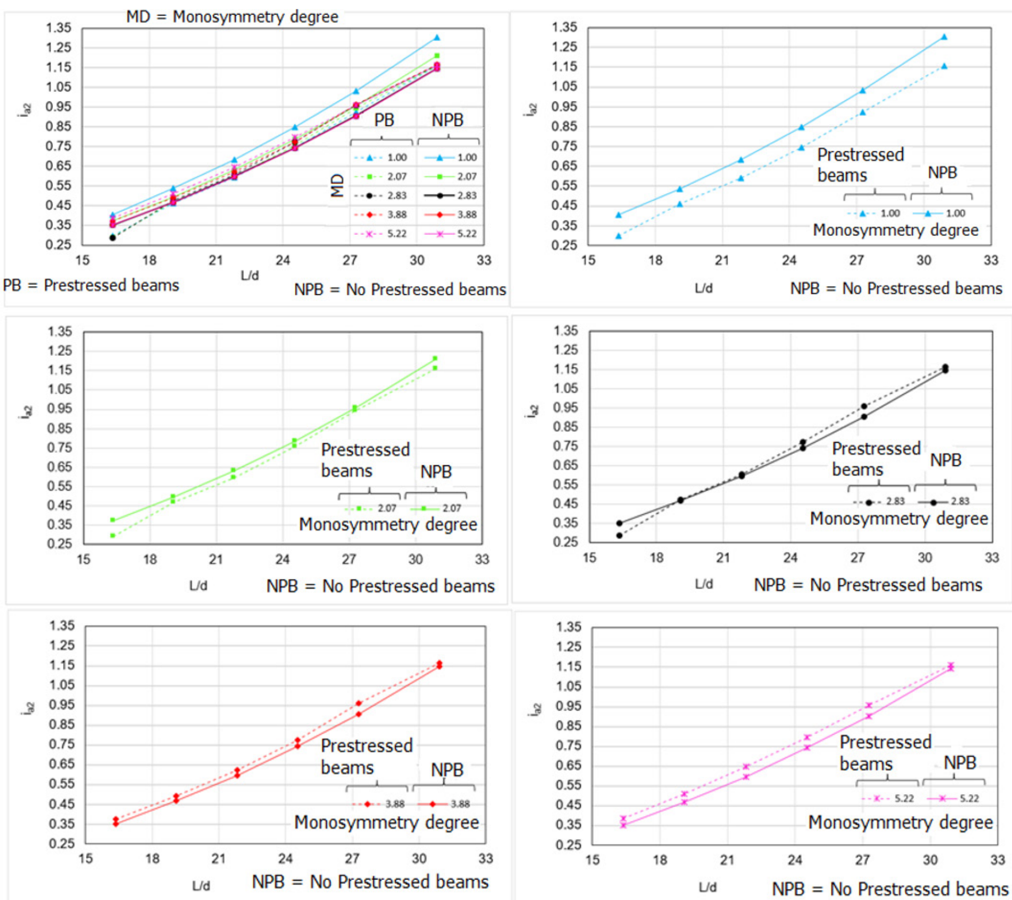

Figure 6. i_{a2} versus L/d ratio for e_p = 730mm.

If NBR 8800: 2008 [13] included the effects of shrinkage and creep in the calculation of design loads, there would be an average increase of approximately 4.1% to 10.7% for L/d ratios of 31 to 16, respectively. The ultimate bending moment of phase 3 is the same as that of phase 2.

5.2 Influence of the degree of monosymmetry

According to Figure 7, the composite beams without prestressing show an increase in the ultimate bending moment (M_{Rd2}) as the monosymetry index (α_m) increases from 1.0 to 2.83 (on average 14.4%). Thereafter the resistance to bending moment is practically constant. For each degree of monosymmetry, there is little difference between the values of flexural strength for the spans analyzed, with the beam with the largest span being the most resistant.

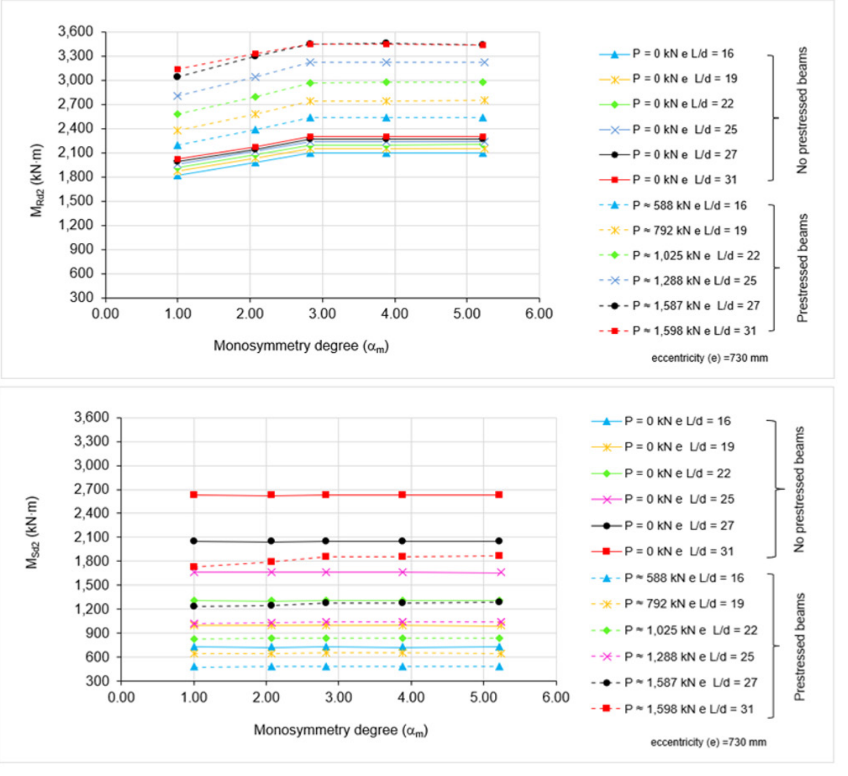

Figure 7. M_{Rd} and M_{Sd} versus monosymmetry degree graphs for e_p = 730mm.

It is observed that in the prestressed composite beams the ultimate moment also increases if the degree of monosymmetry is increased from 1.0 to 2.83 for all beams. There is an increase of approximately 15.4%, 15.1%, 14.9%, 14.8%, 13.3 and 10.0% in flexural strength for L/d ratios of 16, 19, 22, 25, 27 and 31, respectively. For monosymmetry index values larger than 2.83, the flexural strength is practically constant. For each monosymmetry index (α_m), there is a more noticeable difference between the values of flexural strength of the analyzed spans if compared to beams without pre-tension.

The second graph in Figure 7 illustrates the influence of monosymetry index (α_m) on the value of the design bending moment (M_{Sd2}) for an eccentricity (e_p) of 730mm. Composite beams without prestressing show no dependence between internal bending moment and the monosymmetry index (α_m). As for the prestressed composite beams, there is a slight dependence between the design bending moment and the monosymetry index (α_m) when the latter varies from 1.0 to 2.83. There is a small increase of 2.2%, 2.7%, 0.37%, 0.40%, 2.3% and 9.3% in design bending moment for L/d ratios equal to 16, 19, 22, 25, 27 and 31, respectively, when the monosymetry index increases from 1.0 to 2.83. This is a result of the prestressing force taking the properties of the cross section and the span length into account. For monosymmetry index values greater than 2.83, (from 2.83 to 5.22) variations in design load are small.

As shown in Figure 8, the use of monosymmetric profiles is only interesting from an economic point of view for composite beams without prestressing, in which a reduction in utilization rate is observed when the monosymetry degree increases from 1.0 to 2.83.

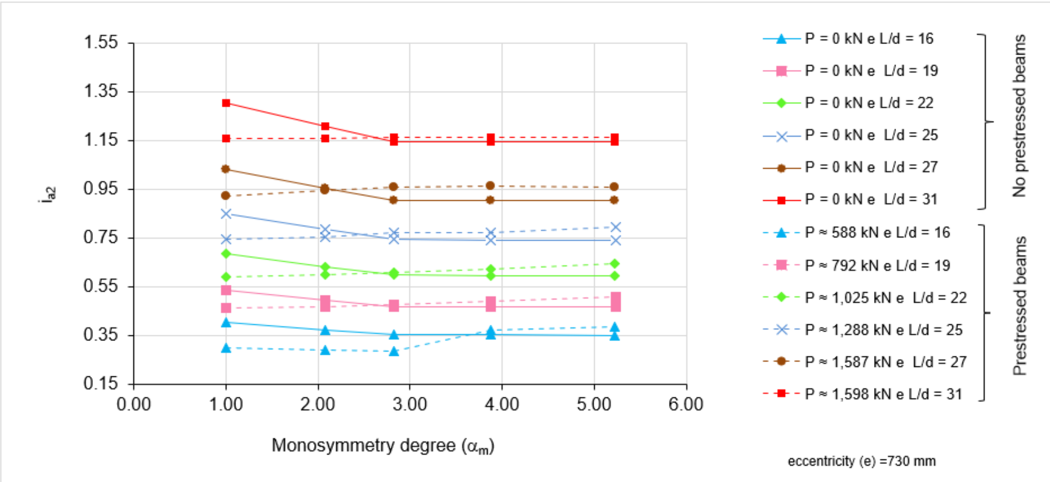

Figure 8. i_{a2} versus monosymmetry degree (α_m) graph for e_p = 730mm.

5.3 Influence of eccentricity

Figures 9 to 14 present the influence of eccentricity (e_p) on the design resistance to bending moment (M_{Rd2}) of the prestressed beams for L/d ratios equal to 16, 19, 22, 25, 27 and 31, respectively.

Figure 9 indicates that, for an L/d ratio of 16, there are variations in flexural strength if (e_p) also varies, regardless of the degree of monosymmetry (α_m) of the beam. Regarding the smallest eccentricity value (e_p = 630mm), the resistance to bending moment is reduced by an average of 5.20% when eccentricity increases 100 mm (e_p =730 mm) and an average of 6.73% when eccentricity increases 150 mm (e_p = 780 mm) for all monosymmetry degree values (α_m) .

Models			e_p (mm)	Ratio L/d	α_m	Prestressing Force (kN)	M_{Rd2} (kN)	$\frac{M_{Rd2} - M_{Rd2\,(e_p=630)}}{M_{Rd2\,(e_p=630)}}$ (%)	M_{Sd2} (kN)	$\frac{M_{Sd2} - M_{Sd2\,(e_p=630)}}{M_{Sd2\,(e_p=630)}}$ (%)
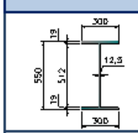	41	VMP$_{630x9x41}$	630			802.30	2,288.86	-	474.31	-
	1	VMP$_{730x9x1}$	730	16	1.00	533.15	2,195.59	-4.08%	482.00	1.62%
	21	VMP$_{780x9x21}$	780			452.36	2,165.75	-5.38%	485.69	2.40%
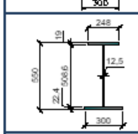	42	VMP$_{630x9x42}$	630			912.62	2,509.54	-	476.62	-
	2	VMP$_{730x9x2}$	730	16	2.07	581.39	2,386.94	-4.89%	484.46	1.64%
	22	VMP$_{780x9x22}$	780			487.26	2,350.05	-6.36%	488.17	2.42%
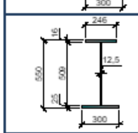	43	VMP$_{630x9x43}$	630			1,015.67	2,688.19	-	478.68	-
	3	VMP$_{730x9x3}$	730	16	2.83	622.06	2,534.66	-5.71%	486.75	1.69%
	23	VMP$_{780x9x23}$	780			515.70	2,490.95	-7.34%	490.49	2.47%
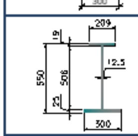	44	VMP$_{630x9x44}$	630			1,018.43	2,688.38	-	478.41	-
	4	VMP$_{730x9x4}$	730	16	3.88	623.71	2,535.54	-5.69%	486.35	1.66%
	24	VMP$_{780x9x24}$	780			517.09	2,492.00	-7.30%	490.03	2.43%
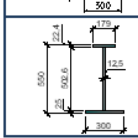	45	VMP$_{630x9x45}$	630			1,021.85	2,688.81	-	478.00	-
	5	VMP$_{730x9x5}$	730	16	5.22	626.17	2,536.99	-5.65%	485.63	1.60%
	25	VMP$_{780x9x24}$	780			519.35	2,493.74	-7.26%	489.17	2.34%

Figure 9. Eccentricity influence - L/d ratio = 16.

The design bending moment is slightly influenced by eccentricity. For the smallest value of eccentricity, (e_p = 630mm), the design bending moment increases an average of 1.64% when eccentricity increases 100 mm (e_p =730 mm) and 2.41% when eccentricity increases 150 mm (e_p = 780 mm).

Figures 10, 11 and 12 show that the L/d ratios equal to 19, 22 and 25 present a behavior similar to that of the models with L/d ratios of 16, regarding variations in flexural strength as a function of eccentricity. For the lowest eccentricity value (e_p = 630mm), the ultimate bending moment decreases by an average of 9.09% (Figure 10), 7.66% (Figure 11) and 6.72% (Figure 12) when the eccentricity increases 100 mm (e_p = 730 mm) and decreases on average 10.92% (Figure 10), 9.91% (Figure 11) and 9.39% (Figure 12) when the eccentricity increases 150 mm (e_p = 780 mm).

Models			e_p (mm)	Ratio L/d	α_m	Prestressing Force (kN)	M_{Rd2} (kN)	$\frac{M_{Rd2}-M_{Rd2\,(ep=630)}}{M_{Rd2\,(ep=630)}}$ (%)	M_{Sd2} (kN)	$\frac{M_{Sd2}-M_{Sd2\,(e_p=630)}}{M_{Sd2\,(e_p=630)}}$ (%)
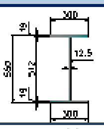	111	VMP$_{630x10,5x111}$	630			1,081.36	2,506.88	-	636.80	-
	101	VMP$_{730x10,5x101}$	730	19	1.00	718.72	2,380.19	-5.05%	646.55	1.53%
	106	VMP$_{780x10,5x106}$	780			609.86	2,339.62	-6.67%	651.14	2.25%
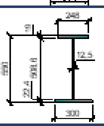	112	VMP$_{630x10,5x112}$	630			1,229.24	2,750.54	-	640.34	-
	102	VMP$_{730x10,5x102}$	730	19	2.07	783.09	2,583.93	-6.06%	650.64	1.61%
	107	VMP$_{780x10,5x107}$	780			656.29	2,533.74	-7.88%	655.34	2.34%
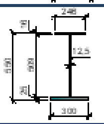	113	VMP$_{630x10,5x113}$	630			1,368.05	3,100.27	-	635.20	-
	103	VMP$_{730x10,5x103}$	730	19	2.83	837.85	2,741.76	-11.56%	653.98	2.96%
	108	VMP$_{780x10,5x108}$	780			694.57	2,682.31	-13.48%	658.78	3.71%
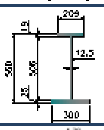	114	VMP$_{630x10,5x114}$	630			1,371.79	3,098.90	-	634.92	-
	104	VMP$_{730x10,5x104}$	730	19	3.88	840.09	2,743.96	-11.45%	653.40	2.91%
	109	VMP$_{780x10,5x109}$	780			696.46	2,684.64	-13.37%	658.12	3.65%
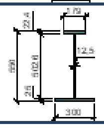	115	VMP$_{630x10,5x115}$	630			1,376.97	3,097.42	-	634.49	-
	105	VMP$_{730x10,5x105}$	730	19	5.22	843.61	2,747.16	-11.31%	652.38	2.82%
	110	VMP$_{780x10,5x110}$	780			699.66	2,688.10	-13.21%	656.90	3.53%

Figure 10. Eccentricity influence - L/d ratio = 19.

Once again, the internal moment suffers little influence from the eccentricity. In relation to the lower eccentricity value (e_p = 630mm), the design bending moment increases on average 2.37% (Figure 10) and 1.6% (Figure 11) and decreases on average 2.0% (Figure 12) when the eccentricity increases by 100 mm (e_p = 730 mm). When the eccentricity increases by 150 mm (e_p = 780 mm), the design bending moment increases on average 3.1% (Figure 10), 2.28% (Figure 11) and decreases on average 1.39% (Figure 12).

In short, for L/d ratios equal to 16, 19, 22 and 25, the eccentricity of 630 mm provides the greatest flexural strength for all degrees of monosymmetry and, also, the lowest bending moment in most cases, thus this eccentricity would be ideal for designs featuring the aforementioned L/d ratios.

Models			e_p (mm)	Ratio L/d	α_m	Prestressing Force (kN)	M_{Rd2} (kN)	$\frac{M_{Rd2}-M_{Rd2\,(e_p=630)}}{M_{Rd2\,(e_p=630)}}$ (%)	M_{Sd2} (kN)	$\frac{M_{Sd2}-M_{Sd2\,(e_p=630)}}{M_{Sd2\,(e_p=630)}}$ (%)
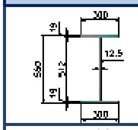	46	$VMP_{630x12x46}$	630	22	1.00	1,402.70	2,748.78	-	817.21	-
	6	$VMP_{730x12x6}$	730			932.77	2,583.52	-6.01%	828.88	1.43%
	26	$VMP_{780x12x26}$	780			791.64	2,530.55	-7.94%	834.23	2.08%
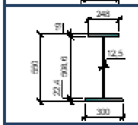	47	$VMP_{630x12x47}$	630	22	2.07	1,592.80	3,018.02	-	822.59	-
	7	$VMP_{730x12x7}$	730			1,014.90	2,800.60	-7.20%	835.49	1.57%
	27	$VMP_{780x12x27}$	780			850.62	2,734.98	-9.38%	841.15	2.26%
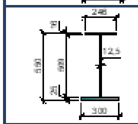	48	$VMP_{630x12x48}$	630	22	2.83	1,772.51	3,241.83	-	826.15	-
	8	$VMP_{730x12x8}$	730			1,085.74	2,969.99	-8.39%	840.21	1.70%
	28	$VMP_{780x12x28}$	780			900.12	2,892.33	-10.78%	846.08	2.41%
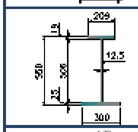	49	$VMP_{630x12x49}$	630	22	3.88	1,776.57	3,244.15	-	825.82	-
	9	$VMP_{730x12x9}$	730			1,087.93	2,972.77	-8.37%	839.71	1.68%
	29	$VMP_{780x12x29}$	780			901.90	2,895.15	-10.76%	845.51	2.38%
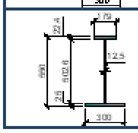	50	$VMP_{630x12x50}$	630	22	5.22	1,782.59	3,247.61	-	825.00	-
	10	$VMP_{730x12x10}$	730			1,092.25	2,977.22	-8.33%	838.32	1.62%
	30	$VMP_{780x12x30}$	780			905.87	2,899.83	-10.71%	843.86	2.29%

Figure 11. Eccentricity influence - L/d ratio = 22.

Models			e_p (mm)	Ratio L/d	α_m	Prestressing Force (kN)	M_{Rd2} (kN)	$\frac{M_{Rd2}-M_{Rd2\,(e_p=630)}}{M_{Rd2\,(e_p=630)}}$ (%)	M_{Sd2} (kN)	$\frac{M_{Sd2}-M_{Sd2\,(e_p=630)}}{M_{Sd2\,(e_p=630)}}$ (%)
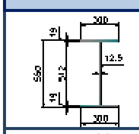	91	$VMP_{630x13,5x91}$	630	25	1.00	1,765.94	3,014.63	-	1,013.11	-
	81	$VMP_{730x13,5x81}$	730			1,175.01	2,805.65	-6.93%	1,026.46	1.32%
	86	$VMP_{780x13,5x86}$	780			997.46	2,738.56	-9.16%	1,032.39	1.90%
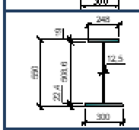	92	$VMP_{630x13,5x92}$	630	25	2.07	1,994.87	3,307.42	-	1,023.49	-
	82	$VMP_{730x13,5x82}$	730			1,278.27	3,038.28	-8.14%	1,035.75	1.20%
	87	$VMP_{780x13,5x87}$	780			1,071.63	2,955.11	-10.65%	1,042.20	1.83%
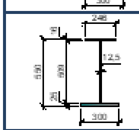	93	$VMP_{630x13,5x93}$	630	25	2.83	2,036.95	3,451.35	-	1,079.00	-
	83	$VMP_{730x13,5x83}$	730			1,367.48	3,220.94	-6.68%	1,042.13	-3.42%
	88	$VMP_{780x13,5x88}$	780			1,133.97	3,122.56	-9.53%	1,048.94	-2.79%
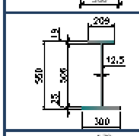	94	$VMP_{630x13,5x94}$	630	25	3.88	2,035.75	3,451.37	-	1,080.21	-
	84	$VMP_{730x13,5x84}$	730			1,368.19	3,223.03	-6.62%	1,042.37	-3.50%
	89	$VMP_{780x13,5x89}$	780			1,134.31	3,124.54	-9.47%	1,049.20	-2.87%
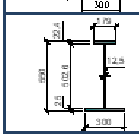	95	$VMP_{630x13,5x95}$	630	25	5.22	1,958.26	3,407.24	-	1,102.96	-
	85	$VMP_{730x13,5x85}$	730			1,372.98	3,228.21	-5.25%	1,040.96	-5.62%
	90	$VMP_{780x13,5x90}$	780			1,138.63	3,129.80	-8.14%	1,047.48	-5.03%

Figure 12. Eccentricity influence - L/d ratio = 25.

Figures 13 and 14, for L/d ratios equal to 27 and 31, respectively, show a quite different behavior from that observed in L/d ratios equal to 16, 19, 22 and 25. There is no significant variation of ultimate bending moment when eccentricity value changes. More specifically, for the L/d ratio equal to 27, Figure 13, the ultimate bending moment is reducing on average 0.62% when the eccentricity increases by 100 mm (e_p = 730 mm) and 3.07% when the eccentricity increases by 150 mm (e_p = 780 mm). The design moment is reduced with the eccentricity, varying from - 7.89% to -12.37% when the eccentricity increases by 100 mm (e_p = 630 mm to e_p = 730 mm), in similar fashion to when the eccentricity increases by 150 mm (e_p = 630 mm for e_p = 780 mm), showing reductions of about -7.43% to -14.14%.

Models			e_p (mm)	Ratio L/d	α_m	Prestressing Force (kN)	M_{Rd2} (kN)	$\frac{M_{Rd2} - M_{Rd2\,(e_p=630)}}{M_{Rd2\,(e_p=630)}}$ (%)	M_{Sd2} (kN)	$\frac{M_{Sd2} - M_{Sd2\,(e_p=630)}}{M_{Sd2\,(e_p=630)}}$ (%)
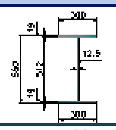	51	$VMP_{630x15x51}$	630	27	1.00	1,847.12	3,113.36	-	1,342.33	-
	11	$VMP_{730x15x11}$	730			1,445.82	3,047.02	-2.13%	1,236.36	-7.89%
	31	$VMP_{780x15x31}$	780			1,227.68	2,963.39	-4.82%	1,242.62	-7.43%
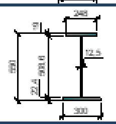	52	$VMP_{630x15x52}$	630	27	2.07	1,922.03	3,316.90	-	1,407.31	-
	12	$VMP_{730x15x12}$	730			1,572.66	3,296.90	-0.60%	1,249.01	-11.25%
	32	$VMP_{780x15x32}$	780			1,318.81	3,193.72	-3.71%	1,256.04	-10.75%
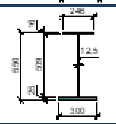	53	$VMP_{630x15x53}$	630	27	2.83	1,957.63	3,457.32	-	1,464.25	-
	13	$VMP_{730x15x13}$	730			1,626.08	3,454.36	-0.09%	1,283.20	-12.37%
	33	$VMP_{780x15x33}$	780			1,395.54	3,372.72	-2.45%	1,265.01	-13.61%
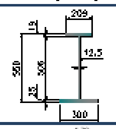	54	$VMP_{630x15x54}$	630	27	3.88	1,956.12	3,458.04	-	1,465.54	-
	14	$VMP_{730x15x14}$	730			1,624.61	3,455.06	-0.09%	1,284.52	-12.35%
	34	$VMP_{780x15x34}$	780			1,395.98	3,374.82	-2.41%	1,265.29	-13.66%
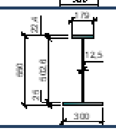	55	$VMP_{630x15x55}$	630	27	5.22	1,934.32	3,447.03	-	1,472.79	-
	15	$VMP_{730x15x15}$	730			1,601.18	3,440.36	-0.19%	1,295.93	-12.01%
	35	$VMP_{780x15x35}$	780			1,398.30	3,378.61	-1.98%	1,264.57	-14.14%

Figure 13. Eccentricity influence - L/d ratio = 27.

For the L/d ratio equal to 31, Figure 14, in relation to the lowest eccentricity value (e_p = 630mm), the design resistance to bending moment increases on average 0.27% when the eccentricity increases 100 mm (e_p = 730 mm) and increases by an average of 2.94% when the eccentricity increases by 150 mm (e_p = 780 mm). The design bending moment decreases on average 9.30% when the eccentricity increases by 100 mm (e_p = 730 mm) and decreases on average 5.81% when the eccentricity increases by 150 mm (e_p = 780 mm).

Models			e_p (mm)	Ratio L/d	α_m	Prestressing Force (kN)	M_{Rd2} (kN)	$\frac{M_{Rd2} - M_{Rd2\,(e_p=630)}}{M_{Rd2\,(e_p=630)}}$ (%)	M_{Sd2} (kN)	$\frac{M_{Sd2} - M_{Sd2\,(e_p=630)}}{M_{Sd2\,(e_p=630)}}$ (%)
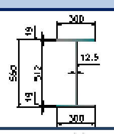	56	$VMP_{630x17x56}$	630	31	1.00	1,750.83	3,116.60	-	1,916.80	-
	16	$VMP_{730x17x16}$	730			1,496.04	3,138.89	0.72%	1,734.57	-9.51%
	36	$VMP_{780x17x36}$	780			1,839.60	3,450.97	10.73%	2,045.06	6.69%
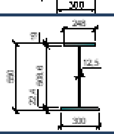	57	$VMP_{630x17x57}$	630	31	2.07	1,815.04	3,314.92	-	1,984.71	-
	17	$VMP_{730x17x17}$	730			1,537.29	3,328.42	0.41%	1,796.81	-9.47%
	37	$VMP_{780x17x37}$	780			1,819.66	3,440.89	3.80%	2,052.11	3.40%
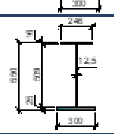	58	$VMP_{630x17x58}$	630	31	2.83	1,841.53	3,450.38	-	2,043.66	-
	18	$VMP_{730x17x18}$	730			1,545.17	3,453.59	0.09%	1,854.32	-9.26%
	38	$VMP_{780x17x38}$	780			1,430.10	3,454.32	0.11%	1,774.28	-13.18%
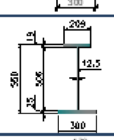	59	$VMP_{630x17x59}$	630	31	3.88	1,839.60	3,450.97	-	2,045.06	-
	19	$VMP_{730x17x19}$	730			1,543.42	3,454.06	0.09%	1,855.78	-9.26%
	39	$VMP_{780x17x39}$	780			1,428.42	3,454.75	0.11%	1,775.76	-13.17%
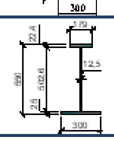	60	$VMP_{630x17x60}$	630	31	5.22	1,819.66	3,440.89	-	2,052.11	-
	20	$VMP_{730x17x20}$	730			1,521.80	3,440.26	-0.02%	1,866.94	-9.02%
	40	$VMP_{780x17x40}$	780			1,406.68	3,439.50	-0.04%	1,788.89	-12.83%

Figure 14. Eccentricity influence - L/d ratio = 31.

In summary, it is concluded that a more comprehensive analysis is necessary to determine the ideal value of design eccentricity for prestressed composite beams, since the flexural behavior, in terms of resistant and applied bending moment, differs in relation to eccentricity changes according to the selected L/d ratio. It is important to note that, in the methodology used herein, the variation in the eccentricity of the tendon implies a variation in the value of the initial prestressing force, according to the flexo-compression interaction equation (Equation 5). Therefore, an increase in eccentricity does not always cause an increase in bending resistance, since the initial prestressing force is reduced to meet the conditions given in Equation 5.

5.4 Analysis of stresses

The stresses were determined considering the interaction of axial forces and bending moment for phase 3, according to the methodology of Nunziata [18].

Figure 15 shows that the design stresses on the upper flange of the steel profile are smaller than the design yield stress of steel ($f_{yd} = 31.4$ kN / cm^2) in all models studied, except for the composite beams without prestressing with an L/d ratio equal to 31 and prestressed composite beams with an L/d ratio equal to 31 and eccentricity of 630 mm. The composite beams without prestressing present compressive stresses on the upper flange that are considerably larger than the values observed for prestressed composite beams. It is also observed that the variation in the eccentricity (e_p) of the tendon influences the stress distribution on the upper flange of the steel profile. For this graph, the models with eccentricity of 780 mm and doubly symmetrical section presented the lowest stress values.

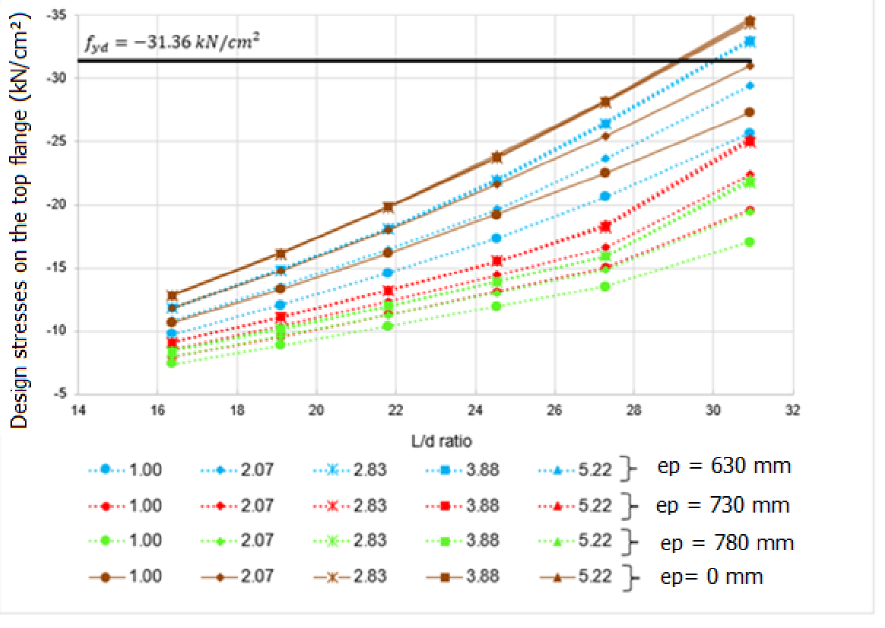

Figure 15. Graph of design stresses on the top flange of the profile.

From the graph in Figure 16, regarding the stresses on the bottom flange of the steel profile, it is noted that the models of composite beams without prestressing do not meet criteria for the design yield stress of steel, except for the models with an L/d ratio equal to 16 and in some models with an L/d ratio of 19. Thus, many of the beams without prestressing that do not pass the Nunziata methodology [18] meet the criteria of ABNT NBR 8800: 2008 [13]. This is due to the former being more conservative since it considers the beginning of yield at a point on the cross-section as the failure criteria, while the criteria of ABNT NBR 8800: 2008 [13] considers the plastic hinge formation as the ULS.

Still concerning stresses on the lower flange of the steel profile, most of the prestressed composite beams meet the criterion for yield stress limits, except for models with an L/d ratio equal to 31. According to the graph presented in ABNT NBR 8800: 2008 [13], the models with eccentricity of 680 mm and monosymmetry indexes equal to 2.83; 3.88 and 5.22 present the smallest stresses.

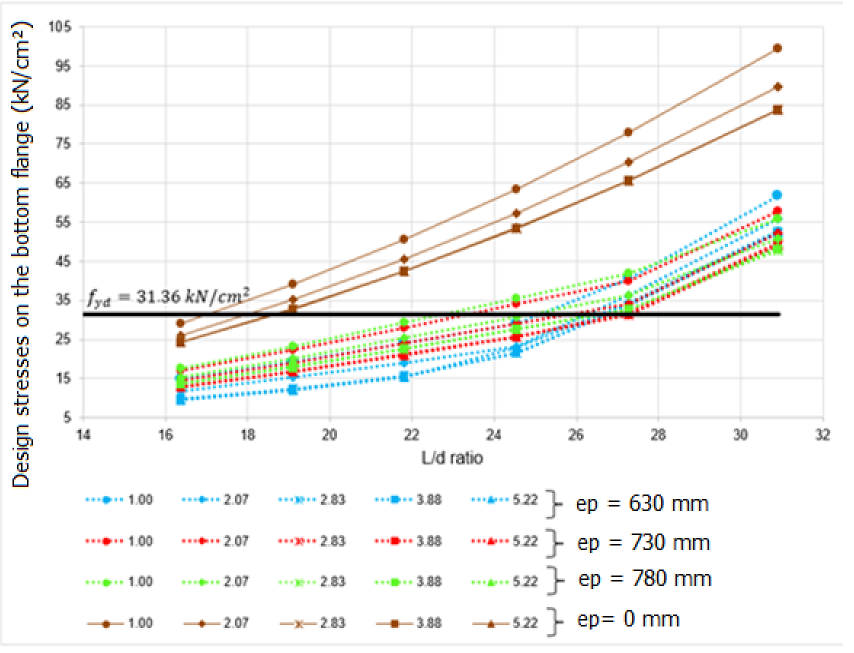

Figure 16. Graph of design stresses on the bottom flange of the profile.

Figure 17 shows the normal design stress on the top surface of the concrete slab as a function of the L/d ratio. It is observed that the design stress on the concrete portion of the models without prestressing is less than that of prestressed composite beams. No case exceeded the ultimate stress of $0.85 f_{cd}$, equal to 1.51 kN / cm^2. Input data used to calculate each model is given in Table 3.

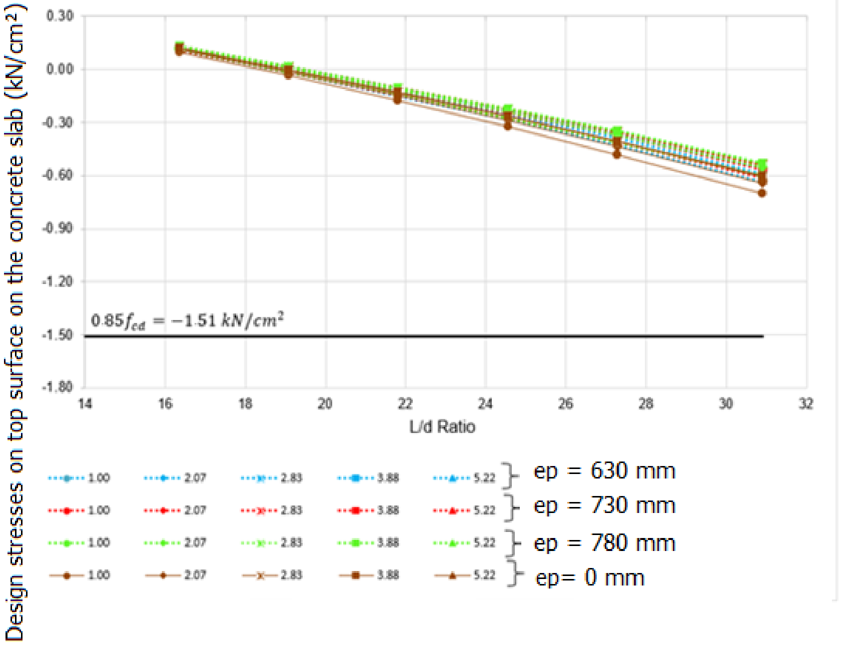

Figure 17. Graph of stresses on the top surface of the concrete slab.

5.5 Analysis of displacements

The maximum deflection of the prestressed composite beams and of composite beams without prestressing was determined by homogenizing the composite section according to the computer routine from which the displacements at midspan are obtained. Figure 18 shows the maximum deflection value of the beams for different L/d ratios.

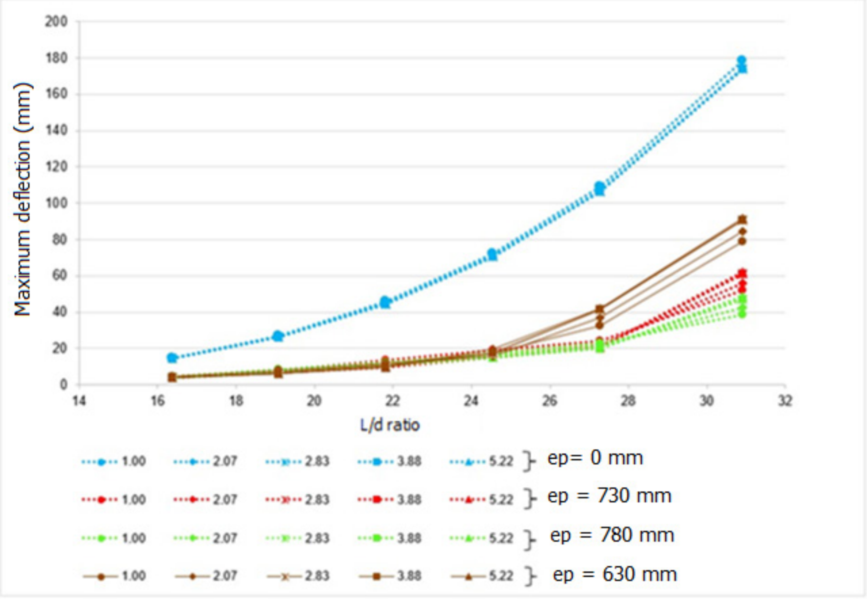

Figure 18. Maximum deflection of the beams at midspan.

It is noted that prestressing has a significant influence on the Serviceability Limit State of excessive deformation when analyzing the reduction of the midspan deflection of the prestressed composite beam in relation to the non-prestressed composite beams, percentage-wise [$(d_{VM} - d_{VMP})/d_{VM}$, (%)]. According to Figure 18, for an L/d ratio of 31 and eccentricity of 630 mm, the midspan deflection of the prestressed composite beam (d_{VMP} = 78.92 mm) is less than half the value found for the composite beam without prestressing (d_{VM} = 178.42 mm), with a reduction of 56%. The midspan deflection reduction reaches 72% for an L/d ratio of 19 and eccentricity of 630 mm, where the deflection is reduced from 27.16 mm to 7.69 mm.

It is also noted that for L/d ratios smaller than 25, there is no significant change in the midspan deflection of prestressed beams when the eccentricity value is changed. For L/d ratios equal to 27 and 31, however, higher values of eccentricity of the prestressing force presented smaller displacements. A deflection reduction percentage of 34% is achieved between eccentricity values of 730mm and 630mm and 25% between the eccentricities of 730mm and 780 mm.

In summary, the analysis of results allowed an assessment of the benefits of applying external prestressing in composite beams for controlling both ULS and SLS, since there was an increase in strength and stiffness of the beams.

6 CONCLUSION

The main objective of this research was to study the behavior of composite steel and concrete beams with external prestressing using the pre-tensioning technique with straight tendons. A computer program was developed to calculate design forces and design cross-sections as regions of positive bending moment of the beams following two design methodologies: one based on ABNT NBR 8800: 2008 [13] and the other according to Nunziata [18]. In both methodologies, the prestressing strength is estimated according to Nunziata [18]. The program checks safety conditions for Ultimate Limit States and the Serviceability Limit State of excessive deformation.

A parametric study, using the computer program developed, was implemented in 120 composite steel and concrete beams of different characteristics, 90 of them with external prestressing and 30 of them without prestressing. The influence of the following parameters was evaluated: ratio between the length of the beam and the height of the steel profile; monosymmetry degree of the steel profile and eccentricity of the prestressing force. The latter was restricted to two different locations for prestressing tendons, above and below the bottom flange of the steel profile.

Results indicate that the composite beams of steel and concrete without prestressing (VM) and prestressed (VMP) with an L/d ratio of approximately 31 do not meet the combined bending-compression design criteria for the load applied, 5 kN/m^2 of live load, since the utilization rate was larger than 1. For L/d ratios ranging from 16 to 25, the beams meet the design criteria with clearance. It should be noted that the L/d ratio equal to 27 would be the most advantageous in economic terms since the utilization rate was the closest to 1.

Although prestressing has generated a considerable improvement in the behavior of the composite beams under bending, reducing the design bending moment and increasing the ultimate bending moment, its improvement in the rate of utilization of the beam was less noticeable, because the compression force on the steel profile due to the prestressing force introduces compressive stresses that are added to stresses arising from bending. Significant improvements in the utilization index only occur for the doubly symmetrical section. For sections with a lower monosymmetry (2.07 and 2.83), the beneficial effects of prestressing are only observed in smaller spans. In cross-sections with a higher monosymmetry degree (3.88 and 5.22), prestressing is not advantageous, resulting in smaller utilization rates when compared to beams without prestressing.

It was also concluded that the use of monosymmetric profiles in composite beams is only interesting from an economic point of view for beams without prestressing a with monosymmetry index smaller than 2.83.

For the three cases of tendon eccentricity (630, 730 and 780 mm) studied, it was observed, for L/d ratios equal to 16, 19, 22 and 25, that the 630 mm eccentricity provides the greatest flexural strength and the smallest design bending moment, so this eccentricity would be ideal for the design. For L/d ratios equal to 27 and 31, it was not possible to establish the ideal design eccentricity, since the eccentricity that provides the largest bending resistance also provides the highest value of design bending moment.

Finally, it is observed that prestressing has a significant influence on the control of the SLS of excessive displacement when analyzing reductions in deflection at the midspan of prestressed composite beams in relation to unstressed composite beams. The result analysis allowed the observation of the benefits of applying external prestressing in composite beams for controlling ULS and SLS, since there was an increase in both strength and stiffness of the beams.

Although underutilized in Brazil due to little knowledge of the system and its design methods, it is clear that prestressed composite steel and concrete beams have great relevance for maintenance projects, recovery of existing structures and design of large new structures. International scientific literature presents theoretical and experimental studies aimed at understanding the structural behavior of this type of beam, and this research contributed to a greater understanding of design methodologies for these structural elements.

ACKNOWLEDGEMENTS

The authors would like to acknowledge the Foundation for Support of Research and Innovation of Espírito Santo (FAPES) for the support during the development of this research.

REFERENCES

[1] M. S. Troitsky, *Prestressed Steel Bridges: Theory and Design.* 16th ed. New York, USA: Van Nostrand Reinhold, 1990.

[2] B. M. Ayyub, Y. G. Sohn, and H. Saadatmanesh, "Prestressed composite girders under positive moment," *J. Struct. Eng.*, vol. 116, no. 11, pp. 2931–2951, 1990. http://dx.doi.org/10.1061/(ASCE)0733-9445(1990)116:11(2931).

[3] R. Szilard, “Design of prestressed composite steel structures," *J. Struct. Div.*, vol. 85, no. 9, pp. 97–123, 1959.

[4] P. G. Hoadley, "Behavior of prestressed composite steel beams," *J. Struct. Div.*, vol. 89, no. 3, pp. 21–34, 1963.

[5] J. C. Strass “An experimental and analytical study of prestressed composite beams,” M.S thesis, Rice Univ., Houston, TX, 1964.

[6] R. S. Regan, “An analytical study of the behavior of prestressed composite beams,” M.S thesis, Rice Univ., Houston, TX, 1966.

[7] H. Saadatmanesh, P. Albrecht, and B. M. Ayyub, “Analytical study of prestressed composite beams,” *J. Struct Eng.*, v. 115, n. 9, p. 2364–2381, 1989. https://doi.org/10.1061/(ASCE)0733-9445(1989)115:9(2364).

[8] H. Saadatmanesh, P. Albrecht, and B. M. Ayyub, “Guidelines for flexural design of prestressed composite beams,” *J. Struct Eng.*, v. 115, n. 11, p. 2944–2961, 1989. https://doi.org/10.1061/(ASCE)0733-9445(1989)115:11(2944).

[9] H. Saadatmanesh, P. Albrecht, and B. M. Ayyub, “Experimental study of prestressed composite beams,” *J. Struct Eng.*, v. 115, n. 9, p. 2348–2363, 1989. https://doi.org/10.1061/(ASCE)0733-9445(1989)115:9(2348).

[10] S. Chen and P. Gu, "Load carrying capacity of composite beams prestressed with external tendons under positive moment," *J. Construct. Steel Res.*, vol. 61, pp. 515–530, 2005. http://dx.doi.org/10.1016/j.jcsr.2004.09.004.

[11] A. C. H. Nelsen, "Comportamento estrutural de beams mistas de aço and concreto com protensão externa," M.S. thesis, Centr. Ciênc. Exat. Tec., Univ. Fed. São Carlos, São Carlos, SP, 2013.

[12] B. T. Linhares "Análise de pontes em estruturas mistas de aço-concreto de seção caixão com protensão externa," M.S thesis, Dep. Eng. Civil, Univ. Fed. Rio Grd. Sul, Porto Alegre, RS, 2015.

[13] Associação Brasileira de Normas Técnicas, *Projeto de Estrutura de Aço e de Estrutura Mista de Aço e Concreto de Edifícios*, ABNT NBR 8800:2008, 2008.

[14] T. Lou, S. M. R. Lopes, and A. V. Lopes, "Numerical modeling of externally prestressed steel-concrete composite beams," *J. Construct. Steel Res.*, vol. 61, pp. 226–236, 2016. http://dx.doi.org/10.1016/j.jcsr.2016.02.008.

[15] R. T. Liban and N. Tayşi, "Nonlinear finite element analysis of composite cantilever beam with external prestressing," *Int. J. Civ. Environ. Eng.*, vol. 11, no. 4, pp. 511–517, 2017., http://dx.doi.org/10.5281/zenodo.1130935.

[16] Microsof, "Microsoft Office Excel," USA: Microsoft Corporation, 2013.

[17] Microsoft, "MicrosoftVisual Basic Express," USA: Microsoft Corporation, 2013.

[18] V. Nunziata, *Strutture in Acciaio Precompresso*, 2nd ed. Palermo, Italy: Dario Flaccovio, 2004.

[19] Associação Brasileira de Normas Técnicas, *Projeto de Estruturas de Concreto – Procedimento,* ABNT NBR 6118:2014, 2014.

[20] Associação Brasileira de Normas Técnicas, *Fios de Aço para Concreto Protendido – Especificação,* ABNT NBR 7482:2008, 2008

[21] Associação Brasileira de Normas Técnicas, *Cordoalhas de Aço para Estruturas de Concreto Protendido – Especificação,* ABNT NBR 7483:2008, 2008

[22] K. D. Ribeiro, "Análise and dimensionamento de beams mistas de aço and concreto com protensão externa," M.S thesis, Dep. Eng. Civ., Univ. Fed. Esp. Sto., Vitória, ES, 2018.

Author contributions: KDR: conceptualization, funding acquisition, methodology, writing; TTT: conceptualization, experimental proof, methodology, writing; LARL and AFGC: supervision, formal analysis.

Editors: Maurício de Pina Ferreira, José Luiz Antunes de Oliveira e Sousa, Guilherme Aris Parsekian.

Rev. IBRACON Estrut. Mater., vol. 14, no. 4, e14406, 2021

IBRACON Structures and Materials Journal
Revista IBRACON de Estruturas e Materiais
ISSN 1983-4195 ismj.org

ORIGINAL ARTICLE

Experimental evaluation of induced human walking vibrations on steel-concrete composite floors

Avaliação experimental do comportamento dinâmico de pisos mistos (aço-concreto) submetidos ao caminhar humano

Bárbara Elisa Ferreira[a]
Hermes Carvalho[a]
José Guilherme Santos da Silva[b]
Rodrigo Barreto Caldas[a]
Jefferson Viana Aguiar[b]

[a]Universidade Federal de Minas Gerais – UFMG, Departamento de Engenharia de Estruturas, Belo Horizonte, MG, Brasil
[b]Universidade do Estado do Rio de Janeiro – UERJ, Faculdade de Engenharia, Rio de Janeiro, RJ, Brasil

Received 23 September 2020
Accepted 06 November 2020

Abstract: This work presents the experimental evaluation of the dynamic behavior of Steel and concrete composite floors, from a human comfort point of view, when submitted to human walking. The structural model investigated was a real composite floor system under construction, with a total area of approximately 1300 m^2. A preliminary numerical model was developed in order to guide the ideal positioning of excitation and instrumentation to be adopted in the experimental "in situ" evaluation. Next, free vibration tests were carried out to obtain the modal parameters of the structure. More than 180 forced vibration tests with excitation caused by a person walking at different step frequencies and directions were performed to determine de maximum structure's response. The results found were compared with human comfort criteria recommended by national and international standards and design guides. Subsequently, a people quantity influence analysis on the dynamic response of the floor was carried out, where it was noticed that the increase in the number of users walking on the floor also increased the peak acceleration value. This fact emphasizes the need to carry out experimental evaluations considering the variation of people quantity on floor activity in order to evaluate the real scenario of human vibrations induced in the structure under service.

Keywords: experimental dynamic analysis, human comfort assessment, steel-concrete composite floor, numerical modeling.

Resumo or Resumen: O presente trabalho apresenta a avaliação experimental do comportamento dinâmico de pisos mistos (aço-concreto), sob o ponto de vista do conforto humano, quando submetidos ao caminhar humano. O modelo estrutural investigado foi um sistema de piso misto (aço-concreto) real e em fase de construção, com área total aproximada de 1300 m^2. Um modelo numérico preliminar foi elaborado visando nortear o posicionamento ideal da excitação e instrumentação a ser adotada no ensaio experimental in loco. A partir do programa experimental definido, testes de vibração livre foram realizados para determinar os parâmetros modais da estrutura. Cerca de 180 ensaios de vibração forçada sob a excitação causada pelo caminhar de uma pessoa em diferentes frequências de passo e direções foram realizadas para determinar as respostas máximas do piso. Os resultados encontrados foram comparados com critérios de conforto humano recomendados por normas e guias de projeto nacionais e internacionais. Posteriormente, realizou-se uma análise da influência do número de pessoas na resposta dinâmica do piso, sendo observado que o aumento da quantidade de usuários caminhando sobre o piso acarretou no acréscimo do valor da aceleração de pico. Tal fato enfatiza a necessidade da realização de avaliações experimentais considerando a variação da quantidade de pessoas exercendo atividades sobre o piso, de forma a representar as vibrações induzidas nas situações reais de serviço da estrutura.

Palavras-chave: análise dinâmica experimental, conforto humano, pisos mistos (aço-concreto), modelagem numérica.

How to cite: B. E. Ferreira, H. Carvalho, J. G. S. Silva, R. B. Caldas, and J. V. Aguiar, "Experimental evaluation of induced human walking vibrations on steel-concrete composite floors," *Rev. IBRACON Estrut. Mater.*, vol. 14, no. 4, e14406, 2021, https://doi.org/10.1590/S1983-41952021000400006

Corresponding author: Barbara Elisa Ferreira. E-mail: barbara.elisaf@gmail.com
Financial support: None.
Conflict of interest: Nothing to declare.

1 INTRODUCTION

Steel and concrete composite structures have been consolidated as a strong technological alternative in the Brazilian civil construction scenario, being increasingly adopted in commercial, parking, and residential buildings. On the other hand, with the emergence of materials with greater resistance, it has become increasingly feasible to reduce the total height of a composite floor system, seeking useful space improvement. However, this trend implies in reducing the system's stiffness, making these structures increasingly susceptible to the effects of dynamic loads induced by human activities, causing discomfort to users or even structural problems. For this reason, several authors [1]–[10] have developed important research with consistent and qualified investigations regarding the consideration of dynamic actions in the design of structures for human comfort assessment, based on experimental data and finite element models. Dynamic tests are a convenient way for the evaluation of existing or under construction structures due to their non-destructive character, and, therefore, allows to obtain real modal parameters in multiple regions. Based on real values for such parameters, the structure evaluation in relation to acceptable vibration levels is performed with greater reliability.

Varela and Battista [6] related problems with excessive vibration in steel and concrete composite floor and discomfort to users even when the structures met the criteria established in structural design standards. Dallard et al. [11] argues in his work that excessive structural vibration disturbs users in their activities and that the structures may even be rendered unusable or considered unsafe due to panic caused among people due to vibrations. Varela [12] found experimentally that problems due to dynamic excitations produced by human activities are more acute and frequent in continuous slab panels, as they have multi-vibration modes.

Most studies and standards report that human discomfort occurs in structures with a natural frequency below 8 Hz, however, Brownjohn and Middleton [13] analysed in their study that structures with a frequency above 10 Hz also presented significant dynamic responses. Araújo and Costa [14] also came to similar findings. The authors studied the dynamic behavior of three concrete slabs and realized that, despite the displacements found in these structures meeting the recommendations of ABNT NBR 6118 [15], the peak accelerations for models with a natural frequency greater than 10 Hz exceeded the imposed limits for human comfort. Gaspar [16] experimentally evaluated the structural system flexibility influence during the practice of rhythmic activities, concerning human comfort, performing tests on rigid and flexible floors. The author noted, as expected, the accelerations in time tended to decrease as the frequencies of activity and their respective harmonics moved away from the floor fundamental frequency. However, the values found for these cases were higher than the human comfort limits imposed in the literature, indicating that the comfort assessment for frequencies further from resonance should not be neglected. These facts demonstrate that the influence and contribution of the highest harmonics of human walking should not be underestimated with regard to human comfort.

People and structure movement synchronization is a case of human-structure interaction and this behavior has been studied at different times as reported by Nakamura et al. [17] and Matsumoto and Griffin [18]. Shahabpoor et al. [19] analysed the human presence influence in altering the structure modal parameters, concluding that the actions exercised by people tend to considerably increase structural damping, but cause small changes in natural frequencies. The authors also found that the change in the structure modal parameters becomes more significant as the number of people involved in the activities increases. Venuti et al. [21] demonstrated that, in addition to the dynamic structure-pedestrian interaction, it is also important to analyse the different walking paths that can be performed by users, as well as speed and step length. Following this same line of study, Zhang and Xu [22] carried out a parametric analysis in order to determine the difference in floor responses associated with four walking paths: parallel and perpendicular to the floor beams, diagonal and circular. The authors concluded that the path leads to the greatest responses depends on the floor attachment conditions.

Therefore, in view of the growing number of human comfort problems reported in composite structures, this study aims to study a real composite floor (steel-concrete) dynamic response, located in Belo Horizonte city, when subjected to human walk loads. The structure modal properties are determined by experimental and numerical analysis, with subsequent comparison between them. In the floor experimental analysis, different dynamic actions are evaluated, thus allowing the structure peak accelerations determination, as well as the dependence of these responses on the excitations imposed on the structure. Finally, this work also presents the objective of evaluating the human comfort levels of the floor regarding the vibration acceptable limits.

2 STRUCTURE DESCRIPTION

The investigated structure corresponds to an existing building, which is under construction and was designed to be a teaching hospital for a private University in the city of Belo Horizonte / MG, Brazil (Ferreira [23]). Its structural system is based on composite floors (steel-concrete), composed of concrete slabs supported by steel beams, with twelve floors. Each building floor has a total area of approximately 1300 m^2. Figure 1 shows a standard floor (8th floor), with typical height between occupable floors of 3.40 meters. Three floors between axes A and C and two floors located between axes 1' and 3' were studied.

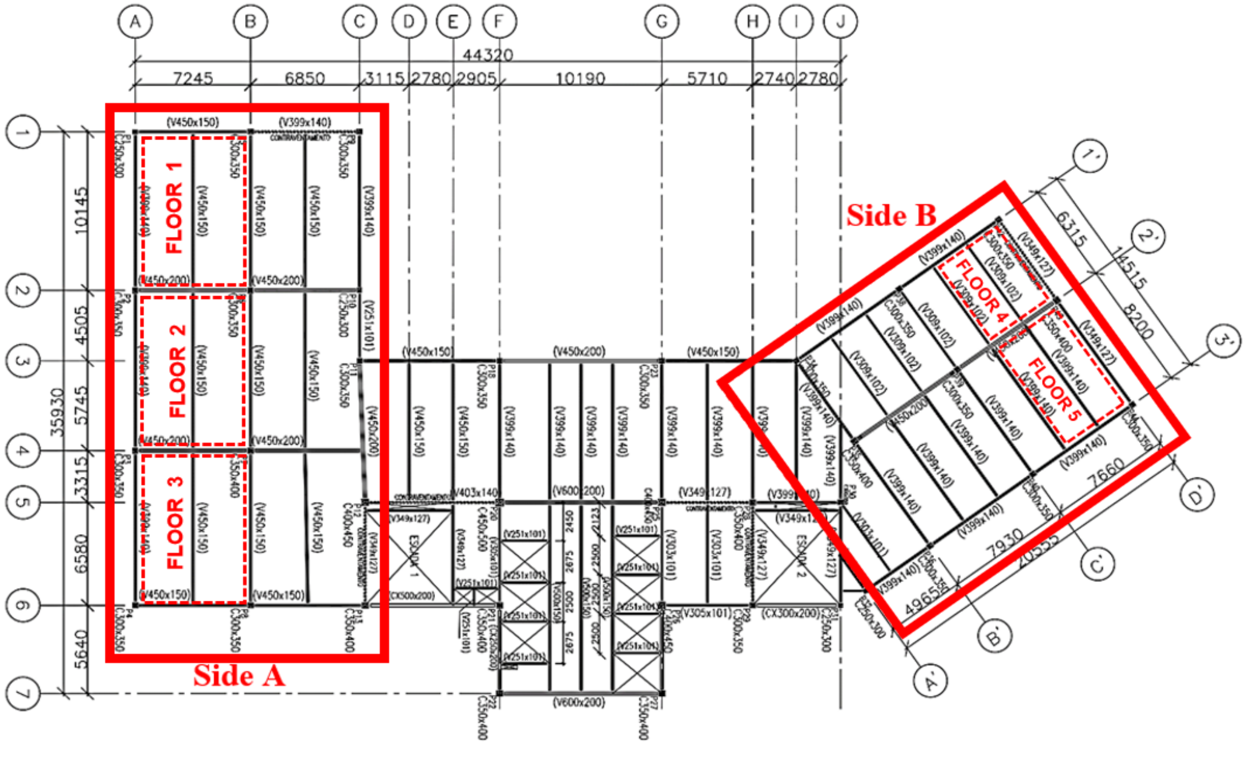

Figure 1. Composite floor (steel-concrete) investigated: 8th floor [mm].

The building columns and beams are made of welded steel profiles, with geometric dimensions and properties according to the project and the columns are made up of welded box-shaped profiles, filled with concrete (Figure 2 and Figure 3). The composite slabs are of steel deck type with total thickness of 150 mm, mold by Metform type MF75 and thickness of 0.85 mm or 0.95 mm. In addition, the floor has a 1.5-meter-high masonry throughout the perimeter, stairway boxes and elevator boxes, aspects that should be considered in the numerical modelling of the structure. The structural masonry was built with a 14x19x29 cm structural ceramic block and filled with grout and steel bars, in addition to concrete strapping.

In relation to the materials physical characteristics, the concrete has a characteristic compressive strength (f_{ck}) equal to 30 MPa, Young's modulus (E_c) of 38 GPa, Poisson's ratio (v_c) equal to 0.2 and specific weight (γ_c) of 2500 kgf/m^3; and the steel has a yield strength (f_y) of 345 MPa, Young's modulus (E_s) of 200 GPa, Poisson's ratio (v_s) equal to 0.3 and a specific weight (γ_s) of 7849.05 kgf/m^3. The material properties were obtained in the building's original structural drawings, made available by Codeme Engenharia S/A, the company responsible for the structure execution. For the structural masonry, a module of longitudinal elasticity (E_a) of 20.4 GPa was adopted, Poisson's ratio (v_a) equal to 0.15 and specific weight (γ_a) of 1250 kgf/m^3, according to the criteria established by ABNT NBR 15812-1 standard [24], due to absence of tests or accurate information about the characteristics of the block.

Figure 2. Identification of floors 1, 2 and 3 (Side A).

Figure 3. Identification of floors 4 e 5 (Side B).

3 NUMERICAL MODEL

The numerical model developed for composite floors (steel-concrete) modal analysis adopted the usual discretization techniques associated with the Finite Element Method (FEM), based on the computer program ANSYS [25]. In this computational model, all beams and columns were represented by the element BEAM44, where the effects of bending and torsion are considered. The BEAM44 corresponds to a uniaxial element composed of two nodes and each one with six degrees of freedom: translations and rotations in X, Y and Z. This element allows considering the nodes to be separated from the centroid axis. This eccentricity should be considered in the beams modelling, since the slab and beam are not positioned on the same axis and affects directly the structure's natural frequencies. Reinforced concrete slabs and masonry were simulated using shell elements type SHELL63, based on thin plate theory and defined by four nodes with six degrees of freedom in each node, three of translation and three of rotation in directions X, Y and Z.

The numerical model showed 8089 nodes, 9338 elements, and 48294 degrees of freedom, as can be seen in Figure 4. The complete interaction between the concrete slabs and the steel beams was considered in the study through knot coupling of the three-dimensional shell and beam elements, simulating the behaviour of a composite structural system. Linear, elastic and isotropic behaviour was considered for steel and concrete materials, and all sections of the structural model remained flat in the deformed state. The boundary conditions considered restricted the columns' base and top nodes over half high above and below the analysed system floor, so that they are prevented from moving translationally, in the horizontal and vertical plane. The secondary beams connection nodes with the main beams were modelled as rigid nodes.

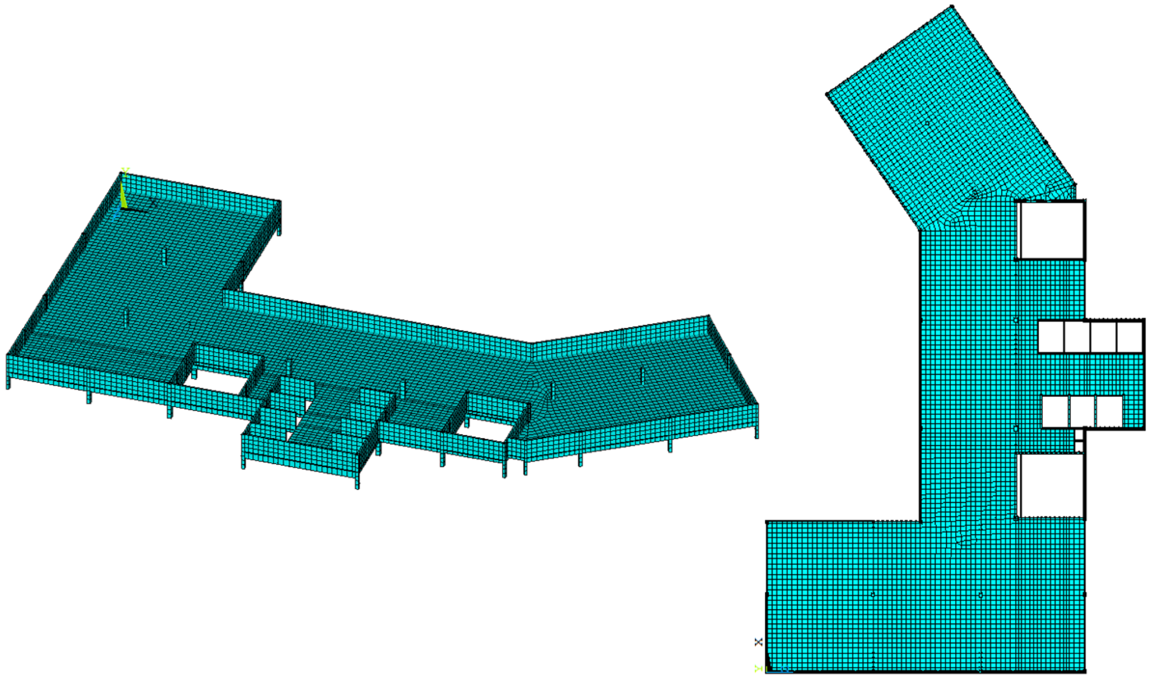

Figure 4. Investigated composite floor (steel-concrete) finite element model.

4 EXPERIMENTAL ANALYSIS

The on-site experimental program was divided into two stages. Firstly, free vibration tests were carried out to obtain the modal parameters of the structure - natural frequencies, modal shapes and modal damping rate. Secondly, forced vibration tests were performed, represented by the walking of a person in a controlled manner, to obtain the dynamic responses of the floors. The tests were carried out on previously defined floors and their results provided real parameters for the FEM model evaluation in terms of its dynamic and users' comfort characteristics, using national and international standards criteria and practical guides.

The floors experimental modal analysis was carried out by means of "in situ" dynamic monitoring, through the installation of PCB Piezotronics seismic accelerometers, model 393B04, connected to a data acquisition system from Bruel and Kjaer, model 3050-A-060. The free vibration test was carried out in such a way that the floors were excited by the impact of a 106.2 kg person, using boots with flexible plastic soles, jumping in their respective centres at a height of 0.48 m. Each floor was excited by three impacts, with sufficient time intervals between each one to dampen vibrations in the dominant modes. Each test procedure was repeated three times on each floor, totalling fifteen tests on the entire floor, and only the most relevant results are presented in this paper. Modal analysis tests were performed to obtain natural frequencies, time functions associated with accelerations in relevant structural sections of the structure and damping coefficients. The method used in this work was Single Input Multiple Output data (SIMO), a technique commonly used in experimental dynamic monitoring of structures (Brandt [26], Cunha and Caetano [27]).

Before the experimental modal tests, the main structure's vibration modes behaviour was investigated through the numerical model, aiming to find common floor points that would excite the largest number of modes. Then, five points were chosen in this analysis, in order to obtain the investigated system floor modal parameters. These points of interest are illustrated in Figure 5.

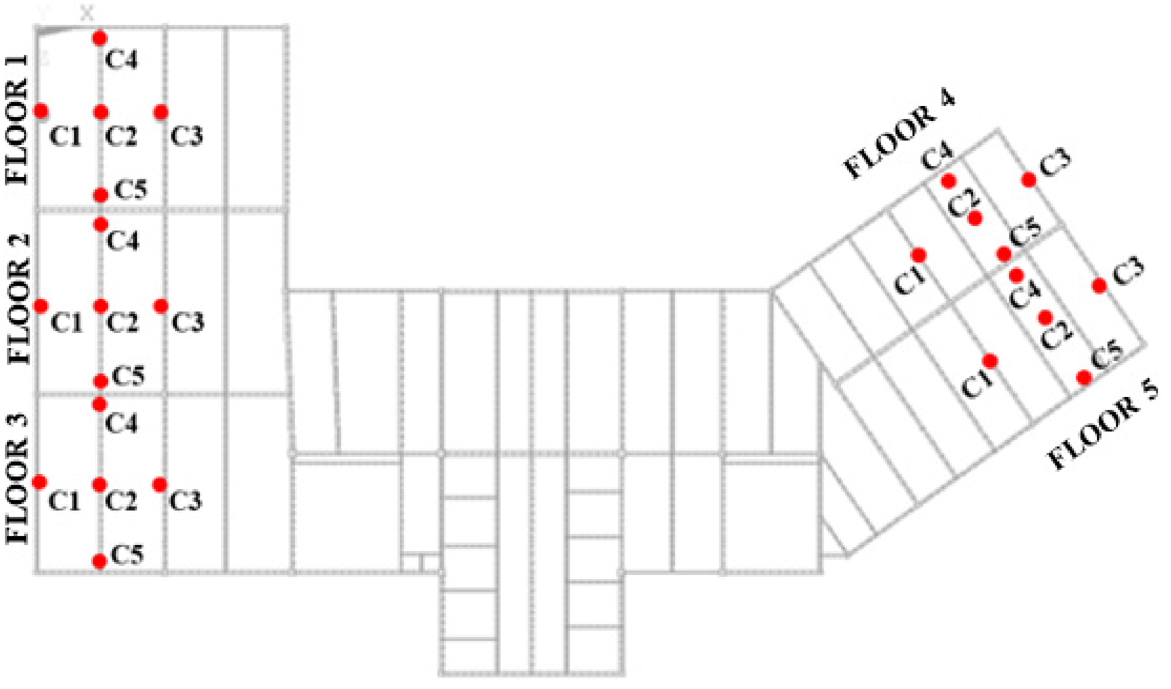

Figure 5. Instrumentation points over the five tested floors.

The dynamic responses of the floor were obtained when a person walked on the structure, with step frequencies controlled in previously defined or random directions. Figure 6 illustrates typical walking paths. Each of these trajectories was executed three times on each floor, with a complete execution characterized by three back and forth walks. Table 1 summarizes the performed tests, with 36 tests per floor and 180 tests on the system floor. A metronome was used to control step frequency and maintain the pace of human walking on the structure. The representative unit for metronome is "bpm" (beats per minute). Thus, each sound beat corresponds to the contact of each step in the structure. The metronome was set at 102 bpm (fp = 1.7 Hz) to induce a slow walk, 120 bpm (fp = 2.0 Hz) to induce a normal walk and 138 bpm (fp = 2.3 Hz) to lead to a fast walk.

In order to assess the number of people walking on the floor dynamic response influence, the monitoring of floor 1 was also carried out considering the walking of four people, with different biotypes and weights, in a slow (fp = 1.7 Hz), normal (fp = 2.0 Hz) and fast (fp = 2.3 Hz) step frequency. All types of walking took place in a random trajectory, as it better represents the situation of daily use. For this test, only one accelerometer was used, fixed in the centre of the slab (accelerometer C2), which represents the point of floor 1 fundamental modes greatest vibration amplitude, especially the first three modes. The results obtained from the tests were compared with those obtained for floor 1 excited by only one person and used in the floor in-service assessment with regard to human comfort, through the application of AISC DG 11 [1] and ISO 2631-2 [28].

Table 1. Total tests performed per floor.

Direction	Slow	Normal	Fast	Total by direction
	1.7 Hz	2.0 Hz	2.3 Hz	
Perpendicular	3	3	3	9
Parallel	3	3	3	9
Diagonal	3	3	3	9
Random	3	3	3	9
Total by frequency	12	12	12	**36**

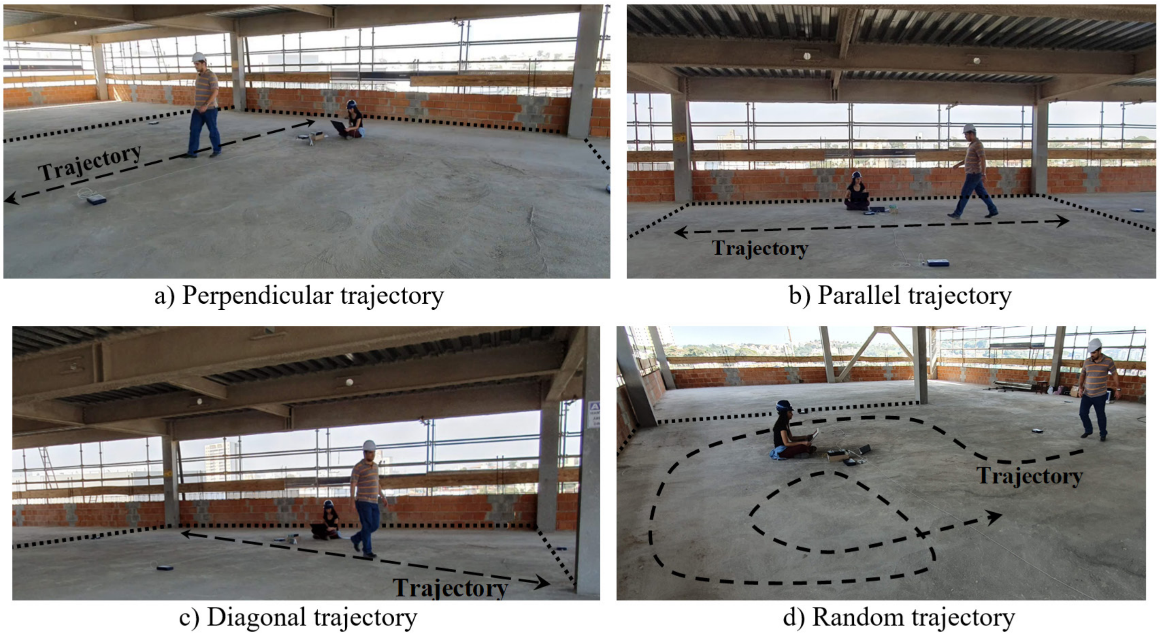

Figure 6. Walking paths illustration.

5 RESULTS AND DISCUSSIONS

The results obtained in the "*in situ*" free and forced experimental vibration tests were processed and treated with MatLab platform, where signal filters recommended by ISO 2631-1 [29] and ISO 2631-2 [28] were applied.

5.1 Free vibration

The structure modal parameters - natural frequencies, vibration modes and modal damping rate - were determined by processing the vertical acceleration signals at the five points monitored in the free vibration experimental tests. Three free vibration tests were performed per floor, with three impacts in each test, totalling nine excitations per floor. The nine responses were grouped, and the graph obtained in the time domain for floor 1 is illustrated in Figure 7. It is observed that the series of impacts were carried out in sufficient time intervals to cushion the dominant modes amplitudes. The greatest acceleration amplitude occurred in the floor centres, close to the impact point as expected.

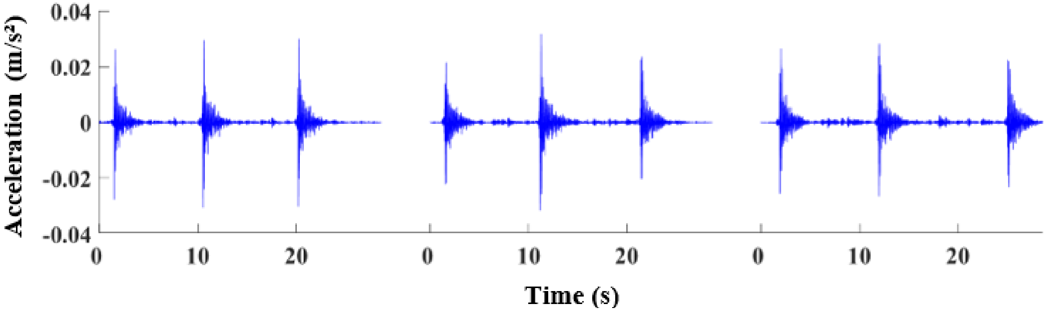

Figure 7. Acceleration x time recorded by channel 2, located at floor 1 centre.

Figure 8 presents the experimental results obtained in the frequency domain from the performed readings, in order to identify the eigenvalues that most collaborated with the chosen floor vibrations, with regard to the energy transfer for the system dynamic response. Analysing the results, it appears that the first three natural frequencies corresponding to the structure's first, second and third vertical vibration modes are 5.9 Hz, 6.5 Hz and 6.9 Hz, respectively.

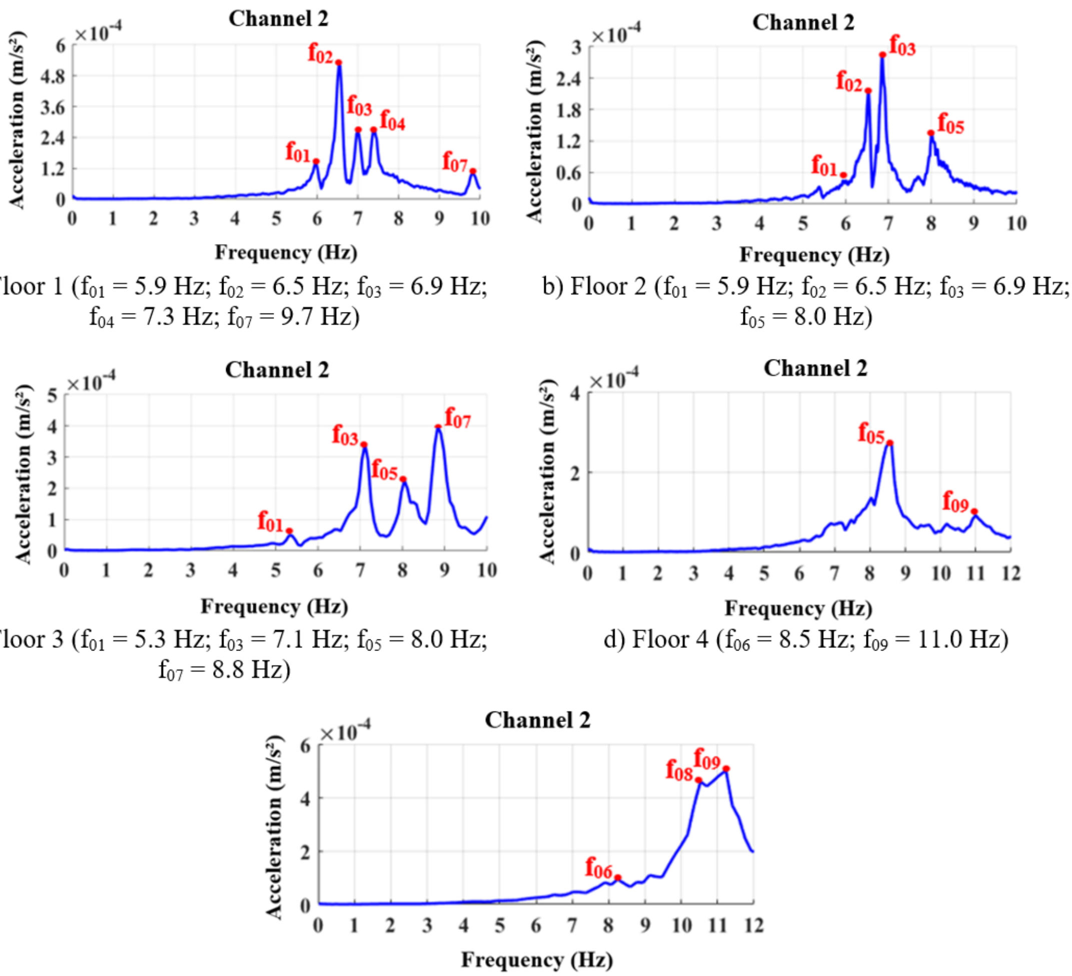

a) Floor 1 (f_{01} = 5.9 Hz; f_{02} = 6.5 Hz; f_{03} = 6.9 Hz; f_{04} = 7.3 Hz; f_{07} = 9.7 Hz)

b) Floor 2 (f_{01} = 5.9 Hz; f_{02} = 6.5 Hz; f_{03} = 6.9 Hz; f_{05} = 8.0 Hz)

c) Floor 3 (f_{01} = 5.3 Hz; f_{03} = 7.1 Hz; f_{05} = 8.0 Hz; f_{07} = 8.8 Hz)

d) Floor 4 (f_{06} = 8.5 Hz; f_{09} = 11.0 Hz)

c) Floor 5 (f_{06} = 8.4 Hz; f_{08} = 10.6 Hz; f_{09} = 11.2 Hz)

Figure 8. Floor's vibration modes experimental FFT magnitudes.

It is worth mentioning that the system floor's first three natural frequencies are within the range of 5 Hz to 8 Hz, which according to experimental studies related to human sensitivity is the interval people react in a particularly adverse way to vibrations. In addition, the fundamental frequency range of human walking presents values between 1.7 Hz and 2.3 Hz, so the third or fourth harmonics of walking could coincide, or be quite close, to the first three floor's natural frequencies, leading to amplification of vibration amplitudes. Thus, the importance of carrying out forced vibration tests to assess the accelerations resulting from floor conditions for future users' human comfort analysis is evident.

The accelerations in the time domain were filtered in the first three vibration modes to determine modal damping (shown in Table 2) using the logarithmic decrement method. Figure 9 shows an example of the time-acceleration graphs filtered in the interest mode.

Most of the standards, design guides and relevant literature work estimate that the damping rate for finished offices' composite floors (steel-concrete) is in the range of 2% to 5% [1],[2],[4]. The damping rates of the floor under study were found outside this range, which was already expected and justified by the construction phase in which the building was at the time of the experimental tests, with the absence of non-structural elements that contribute to the increase in floor cushioning, such as: windows, partitions, furniture, coverings, among others.

Figure 10 illustrates, respectively, the first nine floor vibration modes obtained through the finite element model. It is observed that floors 1, 2 and 3, as they are structures with continuous slabs, present some similar vibration modes and natural frequencies with very close values, which makes it difficult to identify them in the experimental results.

Table 2. Evaluated floor's natural frequencies comparison.

Mode Shape	Natural Frequency (Hz)		Difference (%)	Damping Coefficient (%)
	Finite Element Model	Experimental Tests		
1º	5.71	5.90	3.2	1.26 (± 0.13)
2º	6.49	6.50	0.2	1.03 (± 0.19)
3º	6.87	6.97 (± 0.12)	1.4	1.19 (± 0.21)
4º	7.61	7.67 (± 0.35)	0.7	-
5º	8.17	8.45 (± 0.21)	3.3	-
6º	8.71	8.40 (± 0.57)	3.7	-
7º	9.24	9.75 (± 0.07)	5.2	-
8º	10.08	10.40 (± 0.28)	3.1	-
9º	10.69	11.10 (± 0.14)	3.7	-

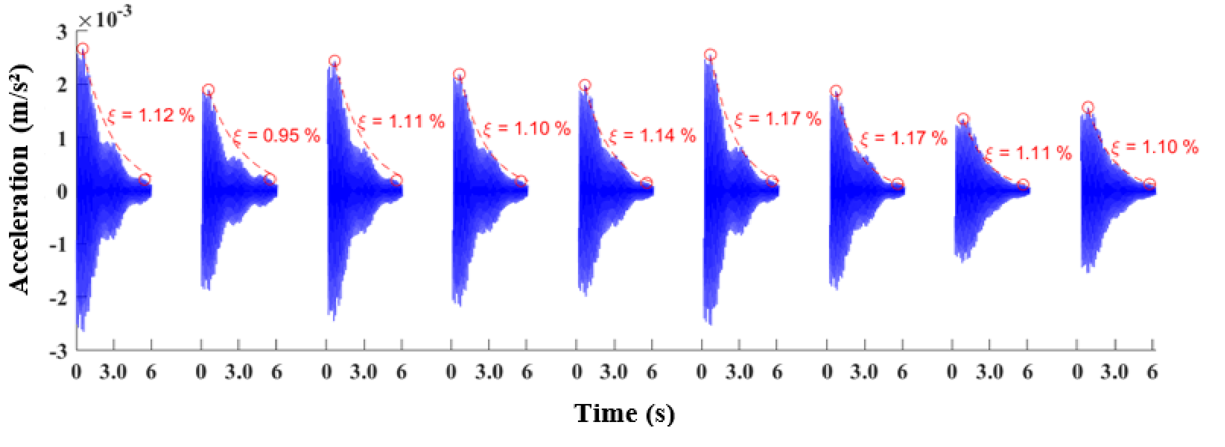

Figure 9. Example of the acceleration graph in the time domain filtered at the third mode.

Table 2 shows the comparison between the real structure tested natural frequencies and the respective numerical model. It is noted that the experimental results obtained for the five floors show a satisfactory agreement with each other, as well as when compared to the numerical results, with differences between 0.2% and 5.2%, which indicates that the structural model under study is well calibrated and able to represent the structure behaviour. It is also worth mentioning that the agreement between the investigated floors dynamic structural responses obtained experimentally indicates a positive validation of the experimental tests developed.

5.2 Forced vibration

The experimental results associated with the greater dynamic structural response of each floor (vertical accelerations) are shown in Figures 11 to 16. These results were obtained in the time and frequency domains, respectively, corresponding to the output response associated with the accelerometers fixed in the floors centres (see Figure 5).

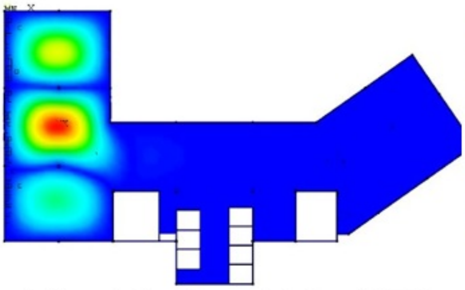

a) 1st mode (bending mode): $f_{01} = 5.71$ Hz

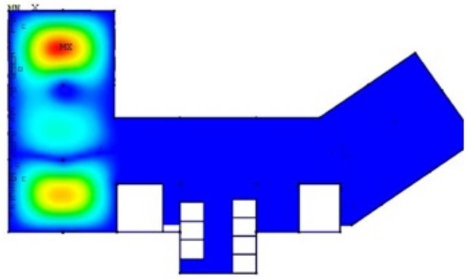

b) 2nd mode (bending mode): $f_{02} = 6.49$ Hz

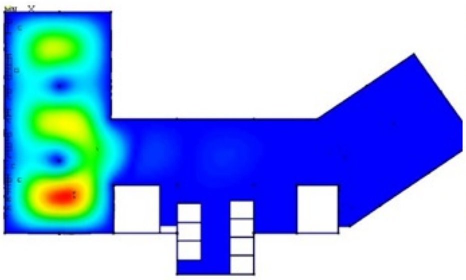

c) 3rd mode (bending mode): $f_{03} = 6.87$ Hz

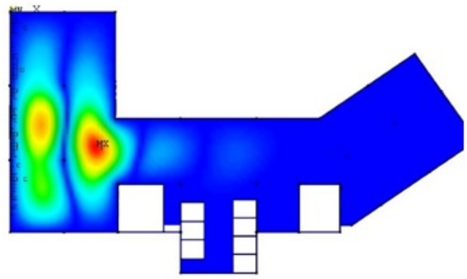

d) 4th mode (bending mode): $f_{04} = 7.61$ Hz

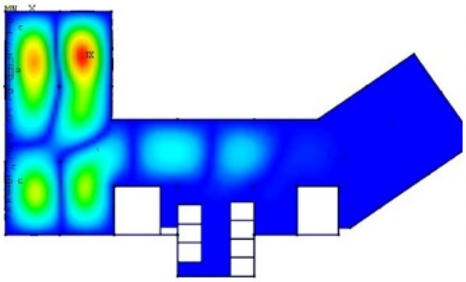

e) 5th mode (bending mode): $f_{05} = 8.07$ Hz

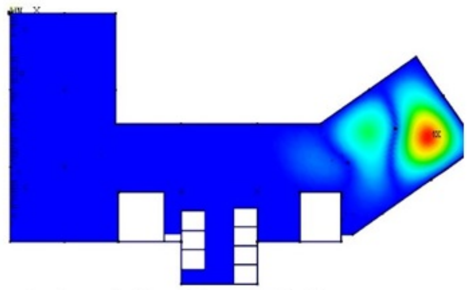

f) 6th mode (bending mode): $f_{06} = 8.17$ Hz

g) 7th mode (bending mode): $f_{07} = 9.24$ Hz

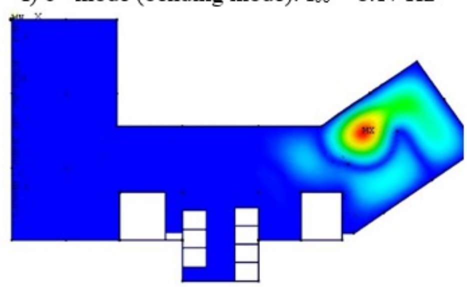

h) 8th mode (bending mode): $f_{08} = 10.08$ Hz

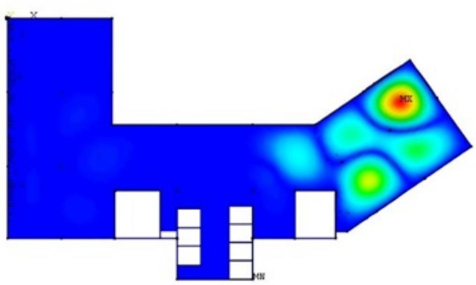

i) 9th mode (bending mode): $f_{09} = 10.69$ Hz

Figure 10. Vertical bending vibration modes of the floors under study.

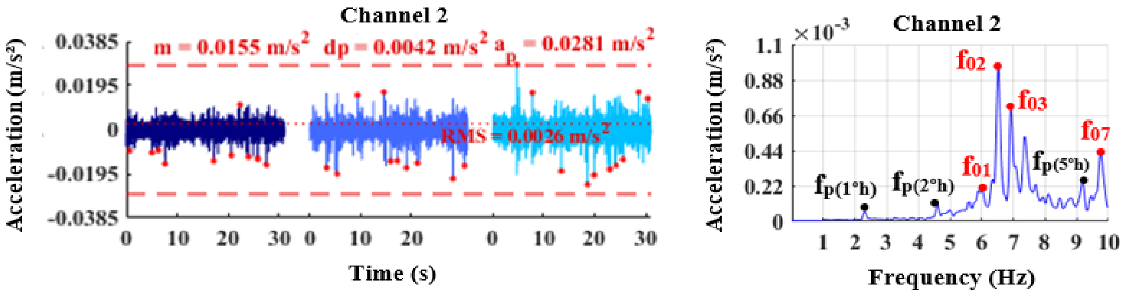

Figure 11. Dynamic response from floor 1 for fast walking on a random trajectory.

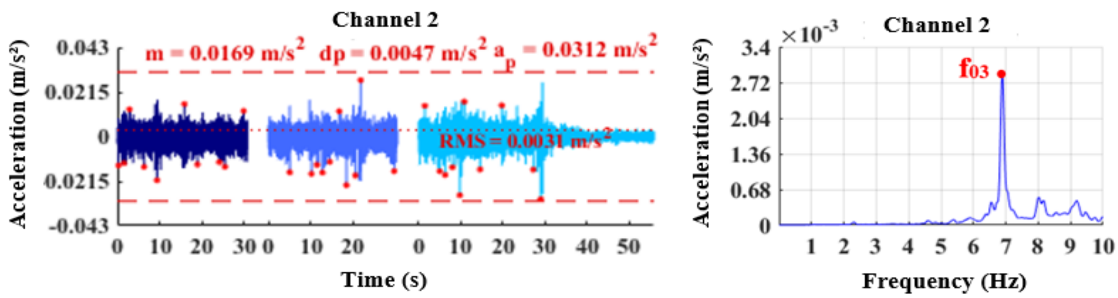

Figure 12. Dynamic response from floor 2 for fast walking on a random trajectory.

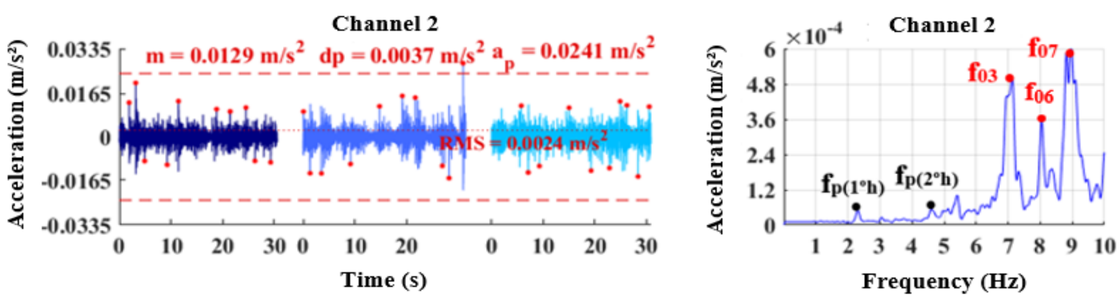

Figure 13. Dynamic response from floor 3 for fast walking on a random trajectory.

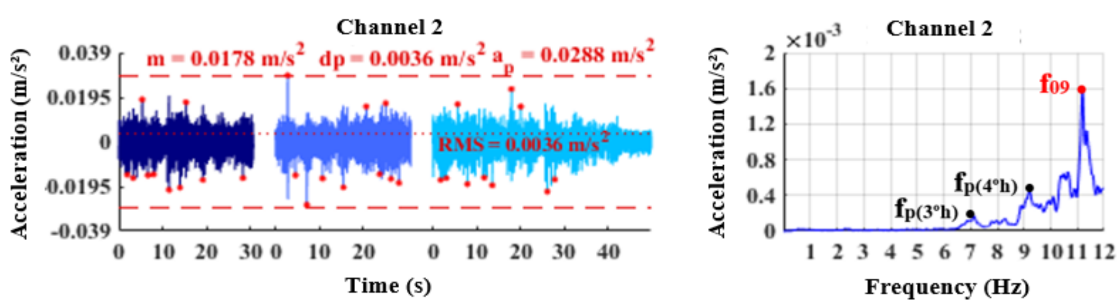

Figure 14. Dynamic response from floor 4 for fast walking on a random trajectory.

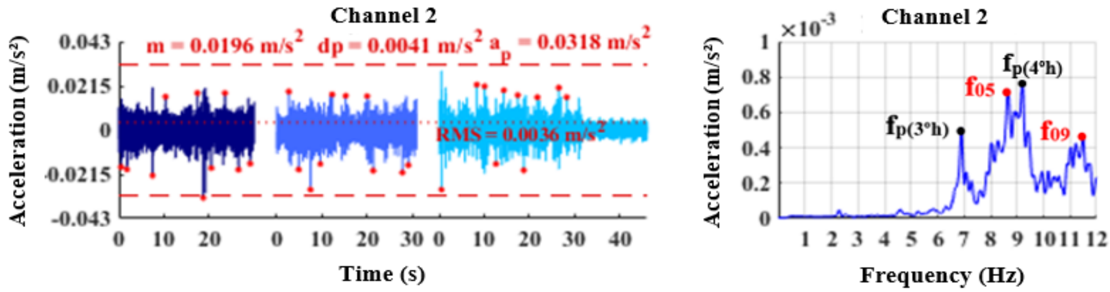

Figure 15. Dynamic response from floor 5 for fast walking on a random trajectory.

Three tests were performed for each direction and step frequency. The shades of blue shown in Figures 11 to 15 represent each of the three tests performed. The maximum peak acceleration that could occur on each floor, for each direction and step frequency, was determined from a probabilistic analysis, considering a confidence level equal to 99.7% (3σ). To calculate mean peak acceleration, the ten highest values obtained in each test (in module) were used, totalling thirty values, identified in Figures 11 to 16 by the red dots, followed by the standard deviation calculation. The results found for mean (m), standard deviation (d_p) and peak acceleration (a_p) are shown in the graphs above the red dashed line. The red dashed lines in Figures 11 to 16 indicate a confidence interval of 3σ, thus indicating that in 99.7% of cases maximum peak acceleration would occur within this range.

The maximum peak acceleration values and RMS found in this experimental investigation are summarized in Table 3. The results demonstrate that the maximum value of peak acceleration occurred when the user was walking fast (fp = 2.3 Hz). In tests performed on floor 1 considering the walking of four people, the greatest acceleration responses were also obtained for the fast-walking situation (see Figure 16).

Table 3. Comparison of the accelerations obtained on the five floors with normative limits.

Floor	People quantity	Maximum Peak Acceleration (m/s²)	Human Comfort AISC	Maximum RMS Acceleration (m/s²)	Human Comfort ISO 2631-2
1	1	0.028	Acceptable	0.0026	Acceptable
2	1	0.031	Acceptable	0.0031	Acceptable
3	1	0.024	Acceptable	0.0024	Acceptable
4	1	0.029	Acceptable	0.0036	Acceptable
5	1	0.032	Acceptable	0.0036	Acceptable
1	4	0.061	Unacceptable	0.0045	Acceptable

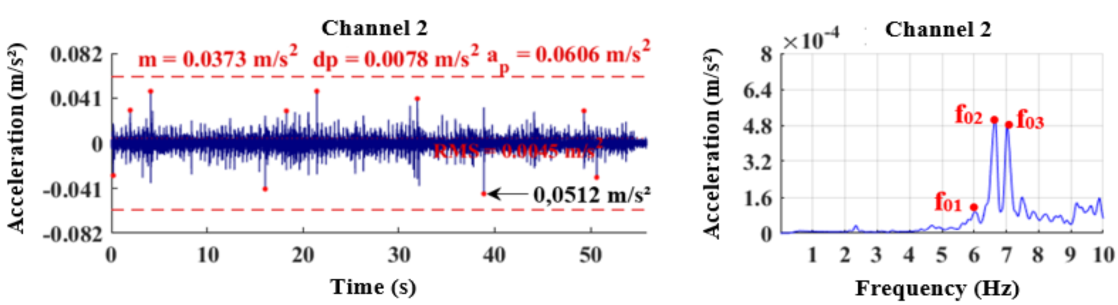

Figure 16. Dynamic response from floor 1 for four fast walking people on a random trajectory.

5.3 Human comfort

The suitability of the floor under study was verified when subjected to human walking in terms of discomfort related to vibrations. In this way, the dynamic responses found in the experimental dynamic analysis for the five floors were compared with the limit values proposed by technical literature of AISC DG 11 [1], of ISO 2631-2 [28] and Brazilian standards ABNT NBR 8800:2008 [30] and ABNT NBR 6118:2014 [15].

It is worth mentioning that the structure, during monitoring, was not finalized, pending the finishes, internal partitions, external closings, installations, among others. The inclusion of these components increases the damping rates and attenuates the structure vibration levels, being therefore favourable to the comfort of users.

According to the recommendations of ABNT NBR 8800:2008 [30], in the case of structures subject to constant walking actions such as offices and similar structures, the value of 4 Hz is indicated as the lower limit for the floor fundamental frequency. Thus, as the first natural frequency of the system floor is 5.90 Hz, it is concluded that this structure meets the criteria adopted by this standard. However, it is emphasized that, according to ABNT NBR 8800:2008 [30], these criteria start from the assumption of a simplified assessment of vibration generated by human activities and may not represent an ideal solution to the problem. Thus, it is recommended that structural designs assess the problems of floor vibrations through a dynamic analysis.

Floors comfort was also analysed according to the recommendations of NBR 6118:2014 [15]. For structures intended for office occupation, a most compatible case for the destination of the floors under study, this standard recommends that the structure fundamental frequency be 20% away from the critical frequency (4 Hz). Thus, as the floor's first natural frequency is 5.90 Hz, it may be concluded that this structure meets the criteria recommended by this standard. The criteria recommended by ABNT NBR 6118:2014 [15] assume that removing the first natural frequency from the resonance structure with the first two harmonics of human walking is sufficient. However, cases of resonance even with the fourth harmonic of walking are observed, as concluded by other authors. Thus, the critical frequency for the office cases, for example, should be at least 8Hz. It is also noteworthy that a method of assessing excessive vibration based only on analysis of minimum frequencies is not advisable, as the structure can present uncomfortable vibrations to its users even if there is no resonance with the excitation source (Varela [12]). In this way, the structure under study was also evaluated according to international standards and design guides, based on acceleration limits.

The AISC DG 11 [1] recommends that peak accelerations on a floor be limited to 0.5% g (0.049 m/s^2) and, ISO 2631-2 [28] suggests a limit for RMS acceleration equal to 0.02 m/s^2. In both codes, the limits related to office occupation were chosen, since this is the activity that most resembles future building destination. The results of peak acceleration and RMS found for the five floors are summarized in Table 3, where they are compared to the limits proposed by the cited codes. It can be noted that the proposed human comfort criteria AISC DG 11 [1] and ISO 2631-2 [28] were met in all walking situations considering a person action over the five studied floors. Thus, it can be inferred that the investigated structural system, due to a person's walk, will not present human comfort problems.

However, analysing only the results obtained for floor 1, it is observed that the walking of four people at a frequency of 2.3 Hz resulted in a peak acceleration of 0.061 m/s^2, above the limit recommended by AISC DG 11 [1], while in the test with a person walking on floor 1, with the same step frequency and the same trajectory, the value found was 0.028 m/s^2. From this analysis it is concluded that the increase in the number of people walking causes the increase in peak acceleration amplitudes. The increase, for floor 1, exceeded the limit established by AISC DG 11 [1] for human comfort.

It is evident that the number of users that make up the loading significantly affects the composite floor dynamic response investigated in this work. In this way, the relevance of carrying out tests is clear considering the variation in the number of people on the floor so that this activity is as close as possible to the real structure use situation. This fact must also be considered when designing such structures.

All the results obtained through the analyses refer to the structure's behaviour during its construction phase. Thus, the damping ratio found is not the final and it will undergo changes after the introduction of non-structural elements, such as ceilings and internal partitions. Another important point to note in the finished structure is the architecture layout, which will pre-determine the path users will take on the floor, which is an important factor for the development and analysis of the excitation.

6 CONCLUSIONS

The present work aimed to evaluate the experimental dynamic response of a real composite floor system under construction, located in Belo Horizonte/MG city, when subjected to dynamic excitations arising from human activities.

Five typical floor panels of a building with a total area of 1300 m^2 were instrumented, which, after completion, will be used as a teaching hospital of a medical school.

The investigated structure modal analysis was performed experimentally and numerically. The modal testing of the floors was carried out by dynamic monitoring using five seismic accelerometers installed on the slabs. Then, these results were calibrated with a finite element model developed in the ANSYS program. A good agreement was obtained between the experimental and numerical results, with differences between 0.2% and 5.2%. Having in mind structural systems of multiple floors (several slab panels) with a relatively uniform stiffness distribution, as in this case, it was noted that the first natural frequencies are very close, showing the phenomenon of mode concentration, easily excited under human walking.

Forced vibration tests were carried out on the structure and each of the five floor panels were excited by human walking, considering three different step frequencies (1.7 Hz, 2.0 Hz and 2.3 Hz), and in different directions, aiming to guarantee the possible trajectory variability of future use of the floor by the occupants. The investigated five floor panels were evaluated according to the ABNT NBR 8800:2008 [30] and ABNT 6118:2014 [15] recommendations, and the results, based on the peak accelerations values, have indicated that the recommended limits were not violated. However, these criteria are overly simplistic and, in this research work it is suggested that these results can be used only for initial assessments and conceptual project of the floor, when subjected to human activity. It is recommended that slabs subjected to people activity can be evaluated by means of dynamic analysis considering the characteristics and nature of excitations, limits for human comfort depending on the use and occupation, structure natural frequencies, modal damping ratios and the effective mass.

Considering the vibration caused by walking, none of the slabs of the investigated steel-concrete composite floor violated the human comfort criteria proposed by AISC DG 11 [1] and ISO 2631-2 [28]. However, it must be emphasized that there are studies in the technical literature that aim to represent the influence of simultaneous multi-person walking scenarios on the dynamic behaviour of floors. Živanović et al. [31] and Chen et al. [32] have developed a research work comparing the vibration responses measured on an office floor, due to the single person walking and the simultaneous multi-person walking scenario on the same floor. The results found by Živanović et al. [31] have shown that occupants were exposed to lower vibrations during simultaneous multi-person walking when compared to those obtained when a single person was considered to all walking paths. On the other hand, the response obtained by Chen et al. [32] has shown that simultaneous walking scenarios considering two people resulted in higher peak acceleration values than those obtained in single person walking scenarios. It is crystal clear that the obtained results in different research works are conflicting and in the authors' point of view this is an indicative that the research associated to the dynamic structural behaviour and human comfort assessment of floors requires more investigation.

In this research work, the situation associated with multiple individuals walking on the structure was also investigated. This way, Floor 1 was subjected to the dynamic actions of four people walking freely, with different step velocities, which resulted in a significant increase in the peak acceleration and RMS values. This fact has indicated that the walking induced by a group of people can produce excessive vibrations on the floor. In this situation, the human comfort limits of AISC DG 11 [1] were surpassed. Thus, it must be emphasized that the dynamic structural behaviour of the studied steel-concrete composite floor presents strong relation with the number of people walking on the structure, and the relevance of carrying out more studies about this effect is evident. On the other hand, it is worth to mention that the structural system is in the final construction phase and certainly the damping ratio associated to the non-structural elements, for example, can improve the floor's dynamic performance.

In general, the human comfort analysis in terms of peak accelerations can lead to conservative values, since an isolated acceleration peak can compromise a floor that, in fact, during all the excitation, is hardly subject to this peak of vibration. However, considering the future use of the investigated building, as a teaching hospital, it is important to highlight that considering the floors where a high degree of comfort is required, such as operating rooms and precision instrument rooms, peak acceleration would have an adverse and considerable effect. The main criticism regarding the use of the RMS value is because this value presents little sensitivity to eventual shocks that occurred during the measurement time, since the sparse peaks have little influence on the final RMS values. Thus, the importance of analysing the structure according to the different criteria, having in mind the maximum acceleration values which occurred during experimental tests with their corresponding frequencies and RMS values is highly evident.

It should be noted that the study is instructive and does not aim to affirm that a design guide is more accurate than other. This way, a contribution is presented based on the assess the steel-concrete composite floors structural behaviour when subjected to dynamic excitations associated with people's walking. Finally, this investigation emphasizes the importance of the structural engineers to be knowledgeable about the activities performed on the structural system, aiming the development of a rational and optimized project, according to current procedures foreseen in the standards and design recommendations based on human comfort criteria.

ACKNOWLEDGEMENTS

The authors gratefully acknowledge the support and information provided by the company CODEME S.A. and the financial support for this research work provided by the Brazilian Science Foundation's CNPq, CAPES and FAPERJ.

REFERENCES

[1] T. M. Murray, D. E. Allen, E. E. Ungar, and D. B. Davis, *Vibrations of Steel-Framed Structural Systems Due to Human Activity*, 2nd ed. USA: AISC, 2016.

[2] M. Willford and P. A. Young, *Design Guide for Footfall Induced Vibration of Structures* (Steel Design Guide Series). Trowbridge, UK: The Concrete Society Publication, 2006.

[3] M. Feldmann, C. Heinemeyer, and C. Butz, *Design of Floor Structures for Human Induced Vibrations* (JRC Scientific and Technical Reports). Brussels: European Comission, 2009.

[4] A. Smith, S. Hick, and P. Devine, *Design of Floors for Vibration: A New Approach* (*SCI Publication*). Ascot, UK: The Steel Construction Institute, 2009. https://doi.org/10.13140/RG.2.2.29342.95048.

[5] S. J. Hicks and A. L. Smith, "Design of floor structures against human induced vibrations," *Steel Constr.*, vol. 4, no. 2, pp. 114–120, 2011. http://dx.doi.org/10.2788/4640.

[6] W. D. Varela and R. C. Battista, "Control of vibrations induced by people walking on large span composite floor decks," *Eng. Struct.*, vol. 33, pp. 2485–2494, 2011. http://dx.doi.org/10.1016/j.engstruct.2011.04.021.

[7] H. A. T. Nguyen, "Walking induced floor vibration design and control," Ph.D. thesis, Fac. Eng. Ind. Scienc. Swinburne Univ. Tec., Melbourne, Australia, 2013.

[8] A. Pavic and P. Reynolds, "Experimental assessment of vibration serviceability of existing office floors under human-induced excitation," *Exp. Tech.*, vol. 23, pp. 41–45, 1999. http://dx.doi.org/10.1111/j.1747-1567.1999.tb01305.x.

[9] S. M. Homem, *Control of Human Induced Floor Vibrations*. Cambridge: Massachusetts Institute of Technology, 2014.

[10] S. Berczynsky and T. Wroblewski, "Experimental verification of natural vibration models of steel-concrete composite beams," *J. Vib. Control*, vol. 16, pp. 2057–2081, 2010. http://dx.doi.org/10.1177/1077546309350552.

[11] P. Dallard et al., "The London Millennium Footbridge,"" *Struct. Eng.*, vol. 79, pp. 17–33, 2001.

[12] W. D. Varela, "Modelo teórico-experimental para análise de vibrações induzidas por pessoas caminhando sobre lajes de edifícios," Ph.D. thesis, Univ. Estad. Rio Jan., Rio de Janeiro, Brasil, 2004.

[13] J. M. W. Brownjohn and C. Middleton, "Efficient dynamic performance assessment of a footbridge," *J. Bridge Eng.*, vol. 158, no. 4, pp. 185–192, 2005.

[14] T. D. Araújo, and Y. C. V. Costa, "Evaluation of dynamic behaviour of waffle slab to gym center," *Lat. Am. J. Solids Struct.*, vol. 11, pp. 1114–1131, 2014. http://dx.doi.org/10.1590/S1679-78252014000700004.

[15] Associação Brasileira de Normas Técnicas. *Projeto de Estruturas de Concreto*, NBR 6118, 2014.

[16] C. M. R. Gaspar "Avaliação do efeito da interação humana sobre pisos de edificações submetidos a atividades humanas rítmicas," Ph.D. thesis, Univ. Estad. Rio Jan., Rio de Janeiro, Brasil, 2018.

[17] S. Nakamura, T. Kawasaki, H. Katsuura, and K. Yokoyama, "Experimental studies on lateral forces induced by pedestrians," *J Constr Steel Res*., vol. 64, no. 2, pp. 247–252, 2008.

[18] Y. Matsumoto and M. J. Griffin, "Comparison of biodynamic responses in standing and seated human bodies," *J. Sound Vibrat.*, vol. 238, pp. 691–704, 2000. http://dx.doi.org/10.1006/jsvi.2000.3133.

[19] E. Shahabpoor, A. Pavic, and V. Racic, "Interaction between walking humans and structures in vertical direction: a literature review," *Shock Vib.*, vol. 2016, pp. 1–22, 2016. http://dx.doi.org/10.1155/2016/3430285.

[21] F. Venuti, V. Racic, and A. Corbetta, "Pedestrian-structure interaction in the vertical direction: coupled oscillator-force model for vibration serviceability assessment", in *Proc. 9th Internat. Conf. Struct. Dynam, EURODYN 2014*, Porto, Portugal, 2014, pp. 915–920.

[22] S. Zhang and L. Xu, "Human-induced vibration of cold-formed steel floor systems: Parametric studies," *Adv. Struct. Eng.*, vol. 23, no. 10, pp. 2030–2043, 2020. http://dx.doi.org/10.1177/1369433220904013.

[23] B. E. Ferreira, "Análise numérico-experimental de vibrações induzidas pelo caminhar humano sobre pisos mistos (aço-concreto)," M.S. thesis, Univ. Fed. Minas Ger., Belo Horizonte, Brasil, 2020.

[24] Associação Brasileira de Normas Técnicas. *Alvenaria Estrutural – Blocos Cerâmicos. Parte 1: Projetos*, ABNT NBR 15812-1, 2010.

[25] ANSYS Swanson Analysis Systems Inc. "Theory reference (version 12.1)", USA: ANSYS, Inc., 2009.

[26] A. Brandt, *Noise and Vibration Analysis. Signal Analysis and Experimental Procedures*, Hoboken: John Wiley & Sons, Inc., 2011.

[27] A. Cunha and E. Caetano, "Experimental modal analysis of civil engineering structures," *J. Sound Vibrat.*, vol. 40, pp. 12–20, 2006.

[28] International Standard Organization. *Mechanical Vibration and Shock - Evaluation of Human Exposure to Whole-body Vibration – Part 2: Vibration in Buildings (1 Hz to 80 Hz)*, ISO 2631-2, 2003.

[29] International Standard Organization. *Evaluation of Human Exposure to Whole-body Vibration: General Requirements*, ISO 2631-1, 1997.

[30] Associação Brasileira de Normas Técnicas. *Projeto de Estruturas de Aço e de Estruturas Mistas de Aço e Concreto de Edifícios*, NBR 8800, 2008.

[31] S. Živanović, A. Pavic, and V. Racic "Towards modelling in-service pedestrian loading of floor structures," in *Proc. 30th IMAC, A Conf on Struct. Dynam.: Top. Dynam. Civ. Struct.*, New York, pp. 85–94, 2012. https://doi.org/10.1007/978-1-4614-2413-0

[32] S. Chen, J. Zhang, and R. Zhang "Human-induced vibration of steel–concrete composite floors," in *Proc. Inst. Civ. Eng: Struct. Build.*, pp. 50–63, 2018. https://doi.org/10.1680/jstbu.16.00179.

Author contributions: BEF: conceptualization, writing, data acquisition, formal analysis, methodology; HC and JGSS: supervision, formal analysis; RBC: supervision; JVA: data acquisition.

Editor: Ricardo Carrazedo, Guilherme Aris Parsekian.

IBRACON Structures and Materials Journal
Revista IBRACON de Estruturas e Materiais
ISSN 1983-4195 ismj.org

ORIGINAL ARTICLE

Experimental assessment of accelerated test methods for determining chloride diffusion coefficient in concrete

Avaliação experimental de métodos acelerados de determinação do coeficiente de difusão de cloretos no concreto

Félix Krolow Sell Junior[a]
Gustavo Bosel Wally[b,c]
Fernando Ritiéle Teixeira[a,c]
Fábio Costa Magalhães[c,d]

[a]Universidade Federal de Pelotas – UFPel, Centro de Desenvolvimento Tecnológico, Programa de Pós-graduação em Ciência e Engenharia de Materiais, Pelotas, RS, Brasil
[b]Universidade Federal do Rio Grande do Sul – UFRGS, Programa de Pós-graduação em Engenharia Civil, Porto Alegre, RS, Brasil
[c]Instituto Federal de Ciência e Tecnologia do Rio Grande do Sul – IFRS, Laboratório de Estruturas e Materiais de Construção Civil, Rio Grande, RS, Brasil
[d]Universidade Federal de Rio Grande – FURG, Escola de Engenharia, Programa de Pós-graduação em Engenharia Oceânica, Rio Grande, RS, Brasil

Received: 08 May 2020
Accepted: 14 September 2020

Abstract: The performance of accelerated test methods to determine the chloride diffusion coefficient in concrete is an important tool in the evaluation of the durability-related properties of the material and in the service life prediction of structures. In this way, this paper presents an experimental assessment of three standardized test methods for determining chloride diffusion coefficient. The migration-based tests presented by NT Build 492 and UNE 83987 and the diffusion-based test presented by ASTM C1556 were carried out. Six concrete mixes were produced: three with different water/binder ratios (0.45, 0.55, and 0.65) and three with replacement of cement by silica fume in the levels of 5, 10, and 20%. The results indicate that the method standardized by NT Build 492 has the best correlation with the diffusion test, in addition to being the one that requires the shortest execution time and has the lowest coefficient of variation of the results.

Keywords: chloride diffusion coefficient, accelerated test methods, concrete durability.

Resumo: A realização de ensaios acelerados de determinação do coeficiente de difusão de cloretos no concreto é uma importante ferramenta na avaliação das características relacionadas à durabilidade do material e na previsão da vida útil das estruturas. Nesse sentido, este trabalho apresenta uma avaliação experimental de três metodologias normatizadas de determinação do coeficiente de difusão do concreto. Foram realizados os ensaios de migração iônica apresentados pela NT Build 492 e pela UNE 83987 e o ensaio de difusão regido pela ASTM C1556. Seis traços de concreto foram produzidos, sendo três com diferentes relações água/aglomerante (0,45, 0,55 e 0,65) e três com substituição de cimento por sílica ativa nos teores de 5, 10 e 20%. Os resultados indicam que o método normatizado pela NT Build 492 apresenta a melhor correlação com o ensaio de difusão, além de ser o que requer menor tempo de execução e apresentar menor coeficiente de variação dos resultados.

Palavras-chave: coeficiente de difusão de cloretos, métodos acelerados, durabilidade do concreto.

How to cite: F. K. Sell Junior, G. B. Wally, F. R. Teixeira, and F. C. Magalhães, "Experimental assessment of accelerated test methods for determining chloride diffusion coefficient in concrete", *IBRACON Struct. Mater. J.*, vol. 14, no. 4, e14407, 2021, https://doi.org/10.1590/S1983-41952021000400007

Corresponding author: Gustavo Bosel Wally. E-mail: gustavo.wally@gmail.com
Financial support: This study was financed in part by the Coordenação de Aperfeiçoamento de Pessoal de Nível Superior – Brasil (CAPES) – Finance Code 001.
Conflict of interest: Nothing to declare.

1 INTRODUCTION

The determination of the chloride diffusion coefficient in concrete is a common practice, since the diffusivity can be taken as an indicator of the resistance of concrete to the chloride penetration, as well as used as an input parameter in service life prediction models. The transport of chloride ions through concrete, however, is a complex issue, implying the development of a wide range of tests aimed at determining the diffusion coefficient, each having its own particularities and limitations [1], [2].

In parallel, the importance of the performance-based approach for concrete durability has recently been promoted and discussed worldwide [3], [4]. This is because the prescriptive approach traditionally adopted in durability design is limited to stipulating parameters such as minimum cement content, minimum compressive strength, and maximum water/binder (w/b) ratio [5]. It should be noted that NBR 6118 [6] presents the idea of a performance-based approach, however, without mentioning any test method, not even reference values for the validation of the results. In the performance-based approach, it is desirable to evaluate at least one parameter that reflects the general durability-related properties of concrete when in its early ages, such as the diffusion coefficient, in a similar way to the compressive strength assessed at 28 days, which is a simple and relative index that reflects the compressive strength and general mechanical properties of concrete [7]. However, although quick results are always desirable in engineering applications, it is known that the chloride penetration into concrete occurs at very low rates [8].

In this sense, steady state and non-steady state migration test methods, as well as methods based on the electrical resistivity of the material, have been widely used internationally as accelerated tests to evaluate the chloride diffusivity in concrete [9]. These tests, despite not imposing real exposure conditions on concrete, in which a multiplicity of actions occurs simultaneously and randomly, make it possible to obtain results in less time and involve lower operating costs [10]. However, due to the complexity of the transport mechanisms involved in the chloride penetration process, there is still a lack of data on correlations between the results obtained from different test methods, whether based on migration, resistivity, or diffusion. In the literature, experimental data to establish these correlations are also limited [11].

In this context, this paper evaluates the characteristics, results and correlations of three different standardized test methods for determining chloride diffusion coefficient in concrete. The migration tests standardized by NT Build 492 [12] and UNE 83987 [13] and the diffusion test governed by ASTM C1556 [14] were carried out. For the analysis, six different concrete mixes were produced: three with different w/b ratios (0.45, 0.55, and 0.65), and three with partial replacement of cement by silica fume in the levels of 5, 10, and 20%.

2 METHODOLOGY

2.1 Materials

Brazilian Portland cement CP II Z-40, natural quartz sand, gravel, silica fume, polyfunctional additive, and potable water were used to produce the concretes. The aggregates used are in accordance with the NBR 7211 [15] and their physical characteristics are shown in Table 1.

Table 1. Physical characterization of the aggregate.

Parameter	Fine sand	Medium sand	Coarse aggregate
Fineness modulus	1.64 [a]	2.42 [a]	6.71 [a]
Maximum diameter (mm)	2.40 [a]	2.40 [a]	12.50 [a]
Specific gravity (g/cm^3)	2.67 [b]	2.65 [b]	2.65 [c]
Loose unit mass (g/cm^3)	1.39 [d]	1.53 [d]	1.46 [d]

[a] –NBR NM 248 [16], [b] –NBR NM 52 [17], [c] –NBR NM 53 [18], [d] –NBR NM 45 [19].

The choice of CP II Z-40 cement was because it is the type of cement most easily found in the local market for use in structural elements, has a low content of pozzolanic addition and presents a better performance to Portland cement without additions in terms of durability. The polyfunctional additive adopted is free of chlorides and its specific gravity can vary between 1.14 and 1.20 g/cm^3. The silica fume, in turn, was chemically characterized by means of energy dispersive X-ray analysis (EDX) and its composition is shown in Table 2.

Table 2. Chemical characterization of silica fume.

Component	SiO_2	K_2O	CaO	Fe_2O_3	MnO	Others
Content (%)	88.32	6.14	4.35	0.68	0.39	0.12

2.2 Mix design and concrete production

The concrete mix design was performed using the IPT/EPUSP [20] methodology. Through the experimental procedure, the ideal dry mortar content was defined at 52% ($\alpha = 0.52$). The proportion of 1:1.6:2.4 (cement: sand: gravel) was defined. The value of 100 ± 10 mm was adopted for concrete slump. The composition of concretes is shown in Table 3.

Table 3. Material consumption of the concrete mixes.

Mix	w/b ratio	Material consumption (kg/m^3)				
		Cement	Silica fume	Fine sand	Medium sand	Coarse aggregate
R 45	0.45	400.00	0.00	128.00	512.00	960.00
SF 5	0.45	380.00	20.00	128.00	512.00	960.00
SF 10	0.45	360.00	40.00	128.00	512.00	960.00
SF 20	0.45	320.00	80.00	128.00	512.00	960.00
R 55	0.55	383.00	0.00	122.56	490.24	919.20
R 65	0.65	367.00	0.00	117.44	469.76	880.80

The mixing of the concrete was carried out in accordance with NBR 5738 [21]. Sixteen specimens (ϕ 100 x 200 mm) of each mix were produced. After molding, the specimens were subjected to submerged curing in a water tank saturated with lime and controlled temperature, according to the specifications of NBR 5738 [21], until the age of 120 days.

2.3 Preparation and selection of samples

The specimens intended for the tests to determine the chloride diffusion coefficient had to be cut to obtain samples with the dimensions recommended in the standard that governs each test method. The cut was performed on a water-cooled diamond saw. The scheme of the cut of the specimens and the dimension of the samples destined for each test are presented in Figure 1. After being cut, all the slices had their sides waterproofed with epoxy paint. The samples used in the immersion test (ASTM C1556 [14]) also received the application of a thin layer of plastic mass and waterproofing the face opposite to the cut.

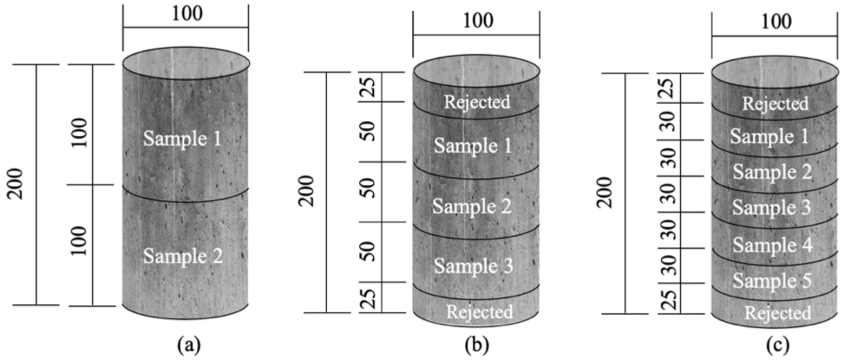

Figure 1. Sample cut scheme (dimensions in mm): (a) for ASTM C1556 [14] test method; (b) for NT Build 492 method; (c) for UNE 83987 [13] method.

To avoid the use of samples with very different gravel and paste content, the mortar content of the samples was also determined. For this, an adaptation of ASTM E562 [22] was used, as proposed by Ribeiro [23]. Through this methodology it is possible to estimate the relative amount of a phase (coarse aggregate or mortar, for example) by overlaying a mesh on the sample and quantifying the nodes that appear on the evaluated phase. Nodes located on the transition zone are given 0.5 points, while nodes positioned on the analyzed phase receive 1 point. Finally, the percentage of the phase in the sample is obtained by the relationship between the number of points and the total knots of the mesh used. Figure 2 presents this methodology schematically.

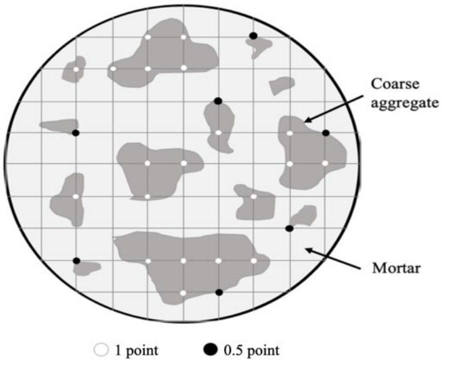

Figure 2. Methodology proposed by Ribeiro [23] to determine the relative percentage of a phase in the sample.

2.4 Methods

2.4.1 Compressive strength and capillary water absorption

Initially, to obtain preliminary data about the physical and mechanical characteristics of the concretes, the tests of compressive strength and capillary water absorption were carried out, following, respectively, the codes NBR 5739 [24] and NBR 9779 [25]. Both tests were performed 126 days after casting the concretes and in each test three specimens from each concrete mix were used.

2.4.2 Apparent diffusion coefficient – Immersion test

The test method standardized by ASTM C1556 [14] consists of immersing specimens in saline solution for a minimum period of 35 days. In this test, there is no imposition of a electric potential difference, with the ions entering the concrete given mostly by diffusion. Thus, among the tests covered in this study, this method is the closest to the exposure conditions imposed by a chloride-rich environment.

For the test, three samples of ϕ 100 x 100 mm from each concrete mix were used. Before carrying out the test, all samples were saturated in calcium hydroxide solution for a minimum period of 24 h, until mass constancy. During the test, which started 126 days after casting the concrete, all specimens were submerged for 112 days in saline solution with a concentration of 165 g de NaCl per liter of water and at a temperature of 23 ± 2 ºC. After the immersion period, the samples were dried in air, at a controlled temperature of 23 ± 2 ºC for 24 h.

After drying, the concrete powder was extracted for later determination of the chloride profiles. A vertical drill was used with an adjustable drill stop and an 8 mm drill. In each specimen, the extractions were performed at 7 different depths, as shown in Table 4.

Table 4. Extraction depths to determine chloride content.

Point	P1	P2	P3	P4	P5	P6	P7
Depth (mm)	0-2	2-5	5-8	8-11	11-14	14-17	17-20

The determination of chloride content was carried out through potentiometry using a silver/silver chloride electrode, with an accuracy of 0.01%. From the chloride profile, the apparent diffusion coefficient (D_a) can be determined by adjusting Equation 1 to the chloride content values measured by non-linear regression using the least square method.

$$C(x,t) = C_S - (C_S - C_i)\, erf\left(\frac{x}{\sqrt{4 D_a t}}\right) \tag{1}$$

where $C(x,t)$ = chloride concentration at the depth x after the time t (%); C_S = chloride content on the concrete surface (%); C_i = initial chloride content in concrete (%); erf = Gauss error function; x = distance between the concrete surface and the mid-layer depth (m); D_a = apparent diffusion coefficient (m^2/s); and t = exposure time (s).

2.4.3 Non-steady-state diffusion coefficient – Rapid chloride migration test

The non-steady-state diffusion coefficient (D_{nssm}) was determined based on the method proposed by Tang [26] and later standardized by NT Build 492 [12]. Among the test methods adopted in this paper, this is the one that requires less time, with a duration that can vary between 6 and 96 h, according to the concrete characteristics. Although this method is widely disseminated and consolidated, it should be noted that the determination of the D_{nssm} depends on the depth of chloride penetration using silver nitrate ($AgNO_3$) spray. The colorimetric method using $AgNO_3$ is a recurring reason for divergences in the literature, as it can present false-positive results in case of concrete carbonation [27], [28]. However, false-positive results due to carbonation tend to be observed close to the surface of the concrete sample, at depths significantly less than the chloride penetration depths recorded in the method prescribed by NT Build 492 [12].

To perform the test, four samples of ϕ 100 x 50 mm from each concrete mix were used. Initially the specimens were subjected to a voltage of 30 V, which was adjusted according to the current measured initially, which could vary between 10 and 60 V. The temperatures of the anodic solution were also measured at the beginning and at the end of the procedure. Figure 3 shows the realization of the first stage of the test, in which the concretes are exposed to chlorides. After being subjected to ionic migration, the samples were diametrically broken and 0.1 M $AgNO_3$ solution was sprayed on them to check the chloride penetration depth.

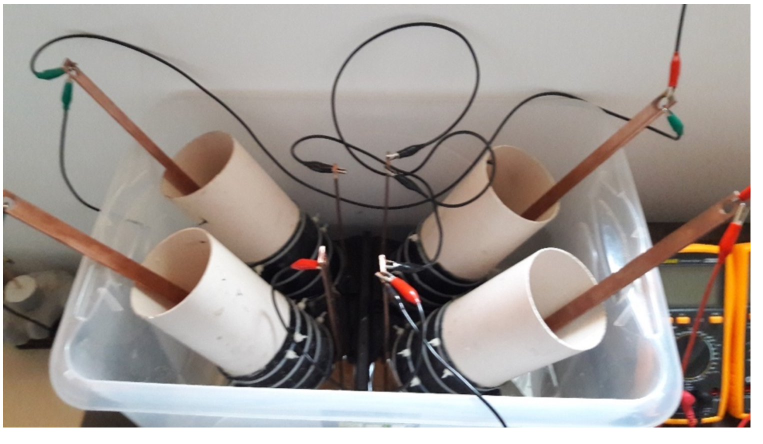

Figure 3. Execution of the NT Build 492 test method.

Lastly, the D_{nssm} was calculated using Equation 2

$$D_{nssm} = \frac{0.0239(273+T)L}{(U-2)t}\left(x_D - 0.0238\sqrt{\frac{(273+T)L x_D}{U-2}}\right) \tag{2}$$

where D_{nssm} = non-steady state diffusion coefficient ($\times$ 10^{-12} m^2/s); T = average value of the initial and final temperatures in the anolyte solution (ºC); L = thickness of the specimen (mm); U = absolute value of the applied voltage (V); x_D = average value of the penetration depths (mm); and t = test duration (h).

2.4.4 Chloride diffusion coefficient – Multiregime test method

The multiregime test method, initially proposed by Castellote et al. [29] and consolidated by UNE 83987 [13], was used to determine the steady state and the non-steady state diffusion coefficients of concretes. Three samples of ϕ 100 x 30 mm from each concrete mix were used. Due to an operational problem, it was not possible to evaluate SF 20 concrete when this test was performed.

This method consists of the evaluation of chloride migration between two chambers with different chloride concentrations, under the application of a 12 V electric potential difference. One of the cells was filled with 1 M NaCl solution and the other filled with distilled water. Figure 4 shows the performance of the test.

Figure 4. Execution of the multiregime test method.

The chloride concentration in the anodic cell was determined through the relationship between the conductivity of water and the chloride concentration, as shown in Figure 5. The values shown in Figure 5 were obtained in a laboratory environment, at a temperature of 23 ± 2 ºC, using distilled water and NaCl.

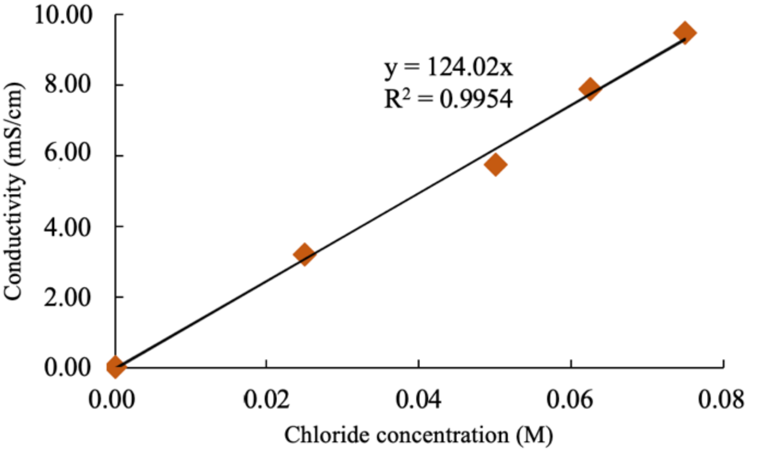

Figure 5. Adjustment for determining chloride concentration based on water conductivity.

The measurement of water conductivity was performed periodically using a digital conductivity meter. In the first moments of the test, the chloride concentration in the anodic cell is low and increases slowly, characterizing the non-steady state. Then, the ions flux becomes constant, indicating the steady state. The *time-lag* (τ), for the case of chlorides transport, is defined as the time required for ionic flow through the concrete to become constant [30], [31]. Figure 6 schematically presents the methodology for determining the *time-lag*.

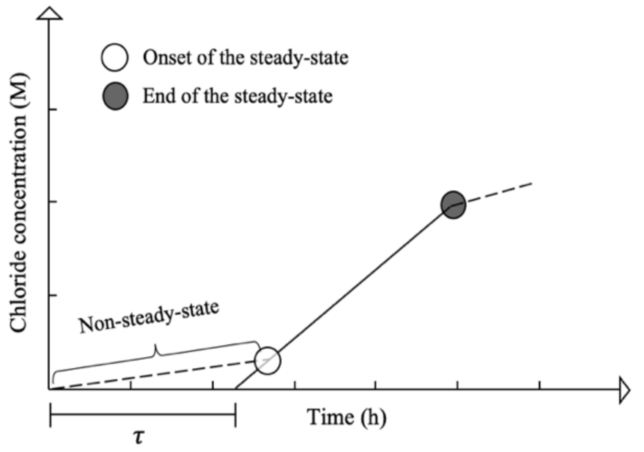

Figure 6. Scheme for determining the time-lag (τ), the steady-state, and non-steady-state (Adapted from Ribeiro *et al.* [30]).

The non-steady state diffusion coefficient (D_{ns}) was determined based on Equation 3. In turn, the steady state diffusion coefficient was calculated using the modified Nernst-Planck equation, presented in Equation 5.

$$D_{ns} = \frac{2l^2}{\tau v^2}\left[v \coth\frac{v}{2} - 2\right] \tag{3}$$

where D_{ns} = non-steady-state diffusion coefficient (cm^2/s); l = thickness of the sample (cm); τ = *time-lag* (s); and v is calculated according to Equation 4.

$$v = \frac{ze\Delta\Phi}{kT} \tag{4}$$

where z = valence of ions (= 1 for chlorides); e = elementary charge (C); $\Delta\Phi$ = average voltage (V); k = Boltzmann constant (J/K); and T = temperature (K).

$$D_s = \frac{J_{Cl} RTl}{zFC_{Cl}\gamma\Delta\theta} \tag{5}$$

where D_s = steady state diffusion coefficient (cm^2/s); J_{Cl} = ions flux, calculated according to Equation 6 (mol/(cm^2 $\times$ s); R = gas constant (cal/(mol $\times$ K)); T = temperature (K); l = thickness of the sample (cm); z = valence of ions (= 1 for chlorides); F = Faraday constant (cal/(volt $\times$ eq)); C_{Cl} = chloride concentration in the cathode cell (mol/cm^3); γ = coefficient of activity of the cathodic cell solution (= 0.657 for chloride); and $\Delta\theta$ = average voltage across de sample (V).

$$J_{Cl} = \frac{V}{A}\frac{dC}{dt} \tag{6}$$

where J_{Cl} = ions flux (mol/(cm^2 $\times$ s)); V = cathode cell volume (cm^3); A = sample section area exposed to ions (cm^2); e dC/dt = slope of the linear part of the chloride concentration *vs*. time graph.

3 RESULTS AND DISCUSSIONS

3.1 Compressive strength and water absorption by capillarity

The results obtained in the tests of compressive strength and capillary water absorption, performed at 126 days, are shown in Table 5.

Table 5. Compressive strength (f_{cm}) and capillary water absorption of concretes.

Mix	f_{cm} (MPa)	Capillary water absorption after 72 h (g/cm^2)
R 45	63.22	1.15
SF 5	63.46	1.04
SF 10	70.88	1.01
SF 20	74.51	0.91
R 55	46.57	1.35
R 65	40.60	1.77

It can be seen, based on the data presented in Table 5, that, in general, silica fume increased the compressive strength and reduced the capillary water absorption of concretes. These improvements occur due to the pozzolanic reaction between $Ca(OH)_2$ from cement hydration and SiO_2 present in silica fume, providing the formation of secondary CSH. Also, silica fume acts as filler, modifying the concrete microstructure and making the paste more homogeneous. Similar results were observed by Meddah et al. [32], Poon et al. [33], and Shekarchi et al. [34].

It should be noted that the variation in compressive strength between some concretes is quite small (less than 1 MPa in the case of R 45 and SF 5 concretes). This difference is quite small when analyzing the degree of precision of the test method in question.

3.2 Apparent diffusion coefficient – Immersion test

Figure 7 shows the chloride penetration profiles obtained from the powder extracted from the specimens submitted to the diffusion test standardized by ASTM C1556 [14]. These profiles are necessary for the calculation of D_a . The values of D_a , in turn, are shown in Table 6. Since the standard that governs this method does not present any classification of the penetrability of chlorides in concrete based on the diffusion coefficient, the classification proposed by Nilsson et al. [35] were used.

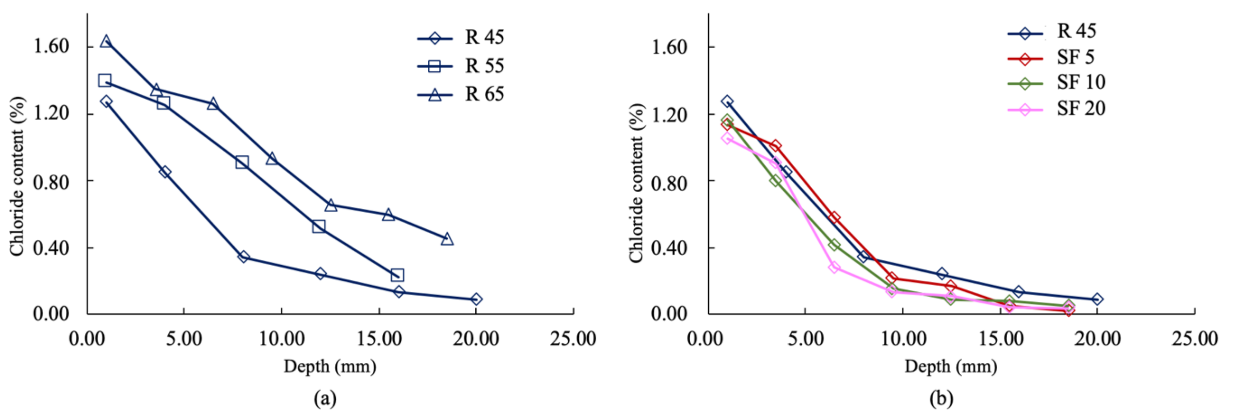

Figure 7. Chloride profiles obtained through potentiometry: (a) influence of the w/b ratio; (b) influence of the silica fume content.

Table 6. Apparent diffusion coefficients (D_a) obtained through ASTM C1556 [14] test method.

Mix	D_a ($\times$ 10^{-12} m^2/s)	Resistance to chloride penetration [35]
R 45	3.23	Very high
SF 5	2.85	Very high
SF 10	1.91	Extremely high
SF 20	1.81	Extremely high
R 55	7.99	High
R 65	13.48	Moderate

It is noteworthy that the results obtained in the immersion test method are those that best represent the real conditions of exposure of the concrete to chloride-rich environments, since the ions penetrate the material mainly by diffusion. However, to obtain chloride profiles with a penetration depth that would allow a satisfactory evaluation, 112 days of immersion were necessary, which is, therefore, a considerably slower test than the other tests covered in this paper.

3.3 Non-steady-state diffusion coefficient – Rapid chloride migration test

The D_{nssm} values obtained and the classification of the concretes in terms of resistance to chloride penetration are shown in Table 7. It is noteworthy that all the concretes evaluated in this paper required tests lasting no longer than 48 h. Thus, this is a test method capable of providing information about the durability-related characteristics of concrete in its early ages.

Table 7. Non-steady-state diffusion coefficient (D_{nssm}) obtained through NT Build 492 [12] test method.

Mix	D_{nssm} ($\times$ 10^{-12} m^2/s)	Resistance to chloride penetration [35]
R 45	2.85	Very high
SF 5	1.75	Extremely high
SF 10	0.90	Extremely high
SF 20	0.20	Extremely high
R 55	4.76	Very high
R 65	6.02	High

3.4 Chloride diffusion coefficient – Multiregime test method

Figure 8 shows the evolution of the chloride concentration in the anodic cell over time. Although it does not directly express the steady state and non-steady state diffusion coefficients, the analysis of the evolution of the chloride concentration allows to infer in a comparative way about the resistance of concretes to the penetration of ions. In this case, the more attenuated the curve is, the greater the difficulty imposed by the concrete on the passage of the ions.

The values of *time-lag*, ions flux, D_s e D_{ns}, calculated from the data presented in Figure 8, are presented in Table 8. Attention should be paid to the fact that, in Table 8, the classification of concretes in terms of resistance to chloride penetration was performed considering only the values of D_{ns}, since the classification in question was originally proposed to be related to non-steady state diffusion coefficients.

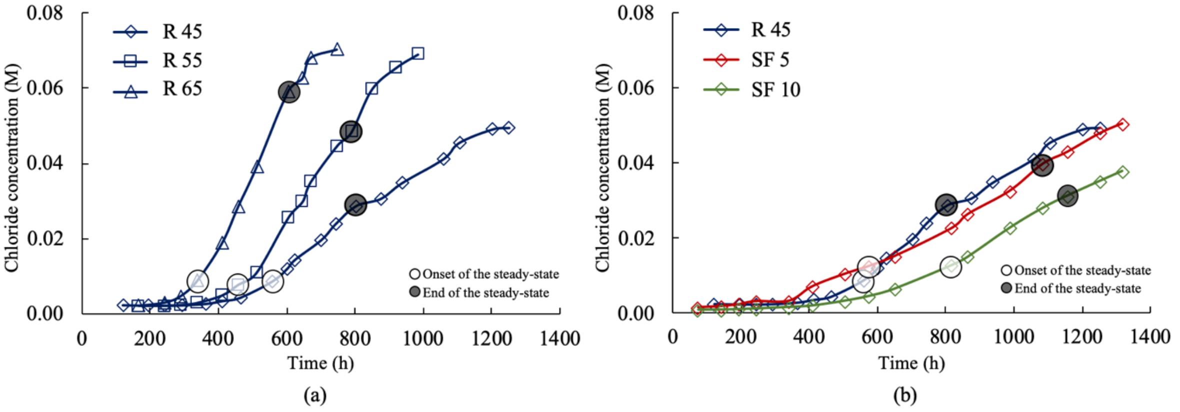

Figure 8. Evolution of chloride concentration in the anodic cell: (a) influence of the w/b ratio; (b) influence of the silica fume content.

Table 8. Chloride diffusion coefficients (steady-state and non-steady-state) obtained through UNE 83987 [13] test method.

Mix	*Time-lag* (h)	Ions flux ($\times$ 10^{-10} mol/(cm^2 $\times$ s))	D_s ($\times$ 10^{-12} m^2/s)	D_{ns} ($\times$ 10^{-12} m^2/s)	Resistance to chloride penetration (D_{ns}) [35]
R 45	465	4.37	0.83	2.26	Extremely high
SF 5	485	3.32	0.63	2.17	Extremely high
SF 10	585	2.88	0.55	1.80	Extremely high
R 55	410	6.01	1.15	2.57	Very high
R 65	315	9.54	1.82	3.34	Very high

When evaluating the data presented in Table 8, it is necessary to note the difference between the values of D_s and D_{ns}. Castellote and Andrade [2] point out that it is of great importance to understand the difference between the coefficients measured in steady state and non-steady state, especially when these will be adopted as an input parameter in service life prediction models. In the case of the concretes evaluated in this paper, the values of D_{ns} are noted, on average, 2.7 times higher than the values of D_s.

3.5 General evaluation of the test methods for determining chloride diffusion coefficient

The results obtained through the three test methods and the classification of the concretes in terms of their resistance to chloride penetration are shown in Figure 9. The values of D_a, D_{nssm} e D_{ns}, previously presented in Tables 6, 7, and 8, respectively, were omitted for a better overview of the results.

It can be seen, based on Figure 9, that the test methods prescribed by NT Build 492 [12] and UNE 83987 [13] show lower results than those obtained using the method standardized by ASTM C1556 [14]. This fact was also observed by Castellote and Andrade [2]. Yuan and Santhanam [8], in turn, observed higher diffusion coefficients for the same concrete when using migration methods. These facts may be related to the type or content of mineral addition used and the curing process adopted since, according to Yuan [36], the migration-based test methods appear to be quite sensitive to the resistivity of concrete, with the diffusion coefficient being linked to the initial current. Even so, it is emphasized again that the immersion method, even though it is an accelerated test, is what tends to present results closer to those obtained in real structures, since there is no imposition of electric potential difference. The multiregime test method, in turn, is the one with the lowest average diffusion coefficient.

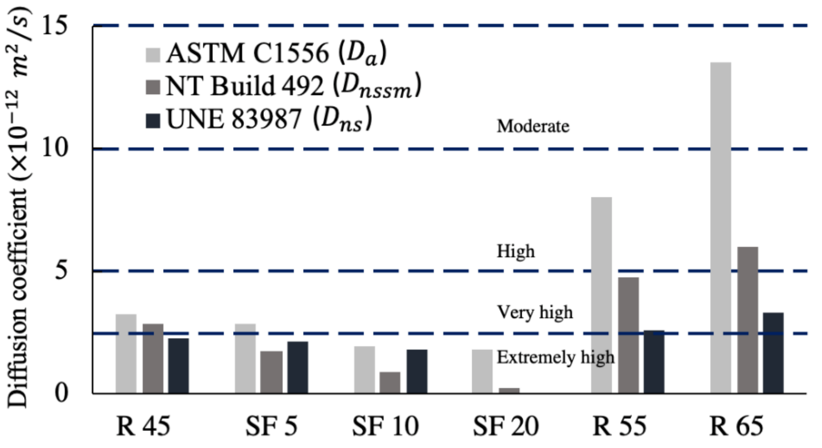

Figure 9. Panorama of the diffusion coefficients obtained through the three test methods.

It is also noted that, in general, the difference between the diffusion coefficients determined by the three methods is significantly greater when evaluating the concretes that tend to have greater penetrability – namely, R 55 and R 65. As for the concretes that follow prescriptive parameters related to chloride environments (case of the mixes R 45, SF 5, SF 10, and SF 20), the values of D_a, D_{nssm} and D_{ns} are closer.

When analyzing the classification of concretes in terms of diffusivity, it is observed that, because of variations in diffusion coefficients, there are also differences in this parameter. It appears that only SF 10 has the same classification (extremely high) when evaluated by the three methodologies. The mix R 65, however, presented three different classifications, because of the wide variation in the diffusion coefficients obtained for this concrete.

In general, the partial replacement of cement by silica fume significantly reduced the diffusion coefficients determined through the three methods. This fact was already expected due to the physical and chemical performance of the fine particles of silica fume, refining the microstructure of the concrete and reducing its diffusivity, as also reported by several authors [32]-[34],[37]. When evaluating concretes with different w/b ratios, the expected increase in the penetrability of concretes due to the increase in the w/b ratio is also confirmed. It is noteworthy, however, that the R 65, with the highest w/b ratio, was the one that showed the greatest divergence in the diffusion coefficients measured experimentally.

Finally, Figure 10 shows the correlation between the three tests performed. The ASTM C1556 [14] test method was taken as a reference because this is an assay in which the chloride penetration occurs mainly by diffusion.

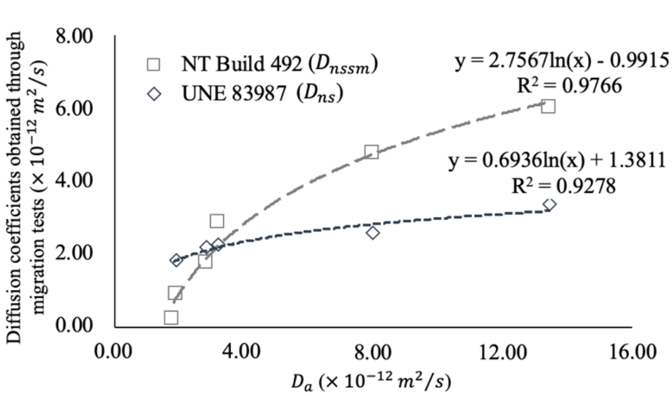

Figure 10. Correlation between the results obtained through the different test methods performed.

It can be seen, from Figure 10, that the test method standardized by NT Build 492 [12], despite being the method that uses the greatest electric potential differences and depending on the colorimetric test with silver nitrate spray, is the one that has the best correlation with the diffusion test ($R^2 = 0.9766$). It is noteworthy that this method presents the simplest basis for its realization, requires less equipment, and demands less time than the other tests. In addition, the D_{nssm} values presented a coefficient of variation (COV) lower than that obtained in the multiregime test method – namely, $COV_{Dnssm} = 9.98\%$; $COV_{Dns} = 19.95\%$.

4 CONCLUSIONS

In this paper, three standardized test methods for determining concrete chloride diffusion coefficient and their correlations were evaluated. The main conclusions stand out:

- The test methods for determining concrete chloride diffusion coefficient analyzed in this study showed a good correlation, with R^2 greater than 0.90. It should be noted that the method described in NT Build 492 [12] has a greater correlation with the diffusion test, with $R^2 = 0.9766$. In addition, it was inferred that, when analyzing concrete less resistant to chloride penetration, the greater the discrepancy between the values presented by the three methods;
- In general, the multiregime test method showed the lowest non-steady state diffusion coefficients and the lowest correlation with the immersion test. This fact must be considered because the consideration of a very low diffusivity can induce structural designers to reduce the requirements regarding other aspects that contribute to the concrete durability, such as the cover depth and, thus, accentuate the reduction of the performance of the structural element over time;
- The use of chloride diffusion coefficients in service life prediction models needs special attention, since variations in diffusion coefficients, such as those presented in this paper, can significantly influence the service life prediction, the durability design, and the maintenance plan of the structures, especially when exposed to harsh environments;
- The use of silica fume in partial replacement of cement, in turn, corroborating with the data of several authors, generated reductions in the diffusivity of concretes when using the three test methods;
- Finally, the importance of using the durability indicators and the performance-based approach for concrete durability is highlighted. It was found that concretes that follow the same prescriptive parameters, such as w/b ratio and compressive strength, as observed in the mixes R 45 and SF 5, can show significantly different performances when evaluated from the perspective of durability.

ACKNOWLEDGEMENTS

The authors thank the Laboratório de Química dos Materiais (LQM) at the Universidade Federal do Rio Grande (FURG) for its assistance in carrying out the potentiometry test to determine the chloride profiles.

REFERENCES

[1] M. G. Alexander, "Service life design and modelling of concrete structures–background, developments, and implementation," *Rev. ALCONPAT*, vol. 8, no. 3, pp. 224–245, Sep 2018. http://dx.doi.org/10.21041/ra.v8i3.325.

[2] M. Castellote and C. Andrade, "Round-Robin test on methods for determining chloride transport parameters in concrete," *Mater. Struct.*, vol. 39, no. 10, pp. 955, Oct 2006. http://dx.doi.org/10.1617/s11527-006-9193-x.

[3] V. Baroghel-Bouny et al., "Easy assessment of durability indicators for service life prediction or quality control of concretes with high volumes of supplementary cementitious materials," *Cement Concr. Compos.*, vol. 33, no. 8, pp. 832–847, Sep 2011. http://dx.doi.org/10.1016/j.cemconcomp.2011.04.007.

[4] H. Beushausen, R. Torrent, and M. G. Alexander, "Performance-based approaches for concrete durability: State of the art and future research needs," *Cement Concr. Res.*, vol. 119, pp. 11–20, May 2019. http://dx.doi.org/10.1016/j.cemconres.2019.01.003.

[5] G. B. Wally, et al., "Avaliação de indicadores de durabilidade de concretos com sílica ativa", in *61° Cong. Bras. Concr.*, Fortaleza, Oct., 2019.

[6] Associação Brasileira de Normas Técnicas, *Projeto de estruturas de concreto – Procedimento*, NBR 6118, 2014.

[7] G. B. Wally, F. C. Magalhães, and L. C. P. Silva Fo., "Conceitos e aspectos da abordagem com base no desempenho na avaliação da durabilidade de estruturas de concreto armado expostas a ambientes agressivos", *Rev. Concreto & Construções*, vol. 100, pp. 81–85, Dec., 2020. http://dx.doi.org/10.4322/1809-7197.2020.100.0006.

[8] Q. Yuan and M. Santhanam, "Test methods for chloride transport in concrete", in *Performance of Cement-based Materials in Aggressive Aqueous Environments – State-of-the-art Report, RILEM TC 211-PAE*, M. Alexander, A. Bertron, N. de Belle, Eds., New York, USA: Springer, 2013, ch. 13, pp. 319–343.

[9] L. Tong and O. E. Gjørv, "Chloride diffusivity based on migration testing," *Cement Concr. Res.*, vol. 31, no. 7, pp. 973–982, Jul 2001. http://dx.doi.org/10.1016/S0008-8846(01)00525-7.

[10] G. R. Meira and P. R. R. Ferreira, "Revisão sobre ensaios acelerados para indução da corrosão desencadeada por cloretos em concreto armado," *Amb. Cons.*, vol. 19, no. 4, pp. 223–248, Oct 2019. http://dx.doi.org/10.1590/s1678-86212019000400353.

[11] D. V. Ribeiro, J. A. Labrincha, and M. R. Morelli, "Chloride diffusivity in red mud-ordinary Portland cement concrete determined by migration tests," *Mater. Res.*, vol. 14, no. 2, pp. 227–234, May 2011. http://dx.doi.org/10.1590/S1516-14392011005000026.

[12] Nordtest, *Concrete, Mortar and Cement-based Repair Materials: Chloride Migration Coefficient from Non-steady-state Migration Experiments*, NT Build 492, 1999.

[13] Asociación Española de Normalización, *Determinación de los Coeficientes de Difusión de los Iones Cloruro en el Hormigón Endurecido - Método multiregimen*, UNE 83987, 2012.

[14] American Society for Testing and Materials, *Standard Test Method for Determining the Apparent Chloride Diffusion Coefficient of Cementitious Mixtures by Bulk Diffusion*, ASTM C1556, 2016.

[15] Associação Brasileira de Normas Técnicas, *Agregados para Concreto – Especificação*, NBR 7211, 2009.

[16] Associação Brasileira de Normas Técnicas, *Agregados – Determinação da Composição Granulométrica*, NBR NM 248, 2003.

[17] Associação Brasileira de Normas Técnicas, *Agregado Miúdo – Determinação da Massa Específica e Massa Específica Aparente*, NBR NM 52, 2009.

[18] Associação Brasileira de Normas Técnicas, *Agregado Graúdo – Determinação da Massa Específica, Massa Específica Aparente e Absorção de Água*, NBR NM 53, 2009.

[19] Associação Brasileira de Normas Técnicas, *Agregados – Determinação da Massa Unitária e do Volume de Vazios*, *NBR NM 45*, 2006.

[20] P. R. L. Helene and P. Terzian, *Manual de Dosagem e Controle do Concreto*. São Paulo, SP: Pini, 1992.

[21] Associação Brasileira de Normas Técnicas, *Concreto – Procedimento para Moldagem e Cura de Corpos de Prova*, NBR 5738, 2016.

[22] American Society for Testing and Materials, *Standard Test Method for Determining Volume Fraction by Systematic Manual Point Count*, ASTM E562, 2011.

[23] D. V. Ribeiro, "Influência da adição de lama vermelha nas propriedades e na corrosibilidade do concreto armado," Ph.D. thesis, Prog. Pós-grad. Ciênc. Eng. Mat., Univ. Fed. S. Carlos, São Carlos, Brasil, 2010.

[24] Associação Brasileira de Normas Técnicas, *Concreto – Ensaio de Compressão de Corpos de Prova Cilíndricos*, NBR 5739, 2018.

[25] Associação Brasileira de Normas Técnicas, *Argamassa e Concreto Endurecidos – Determinação da Absorção de água por Capilaridade*, NBR 9779, 2012.

[26] L. Tang, "Electrically accelerated methods for determining chloride diffusivity in concrete," *Mag. Concr. Res.*, vol. 48, no. 176, pp. 173–179, Sep 1996. http://dx.doi.org/10.1680/macr.1996.48.176.173.

[27] L. V. Real et al., "Método colorimétrico por aspersão de nitrato de prata para avaliação da penetração de cloretos em concreto: estado da arte," *Rev. ALCONPAT*, vol. 5, no. 2, pp. 149–159, May 2015. http://dx.doi.org/10.21041/ra.v5i2.84.

[28] M. H. F. Medeiros, G. C. Réus, and C. V. Pontes, "Nitrato de prata como método colorimétrico para detecção da penetração de cloretos: análise crítica," in *3º Simp. Paranaense de Patologia das Construções*, Curitiba, 2018, pp. 186–197. http://dx.doi.org/10.4322/2526-7248.017.

[29] M. Castellote, C. Andrade, and C. Alonso, "Measurement of the steady and non-steady-state chloride diffusion coefficients in a migration test by means of monitoring the conductivity in the anolyte chamber – Comparison with natural diffusion tests," *Cement Concr. Res.*, vol. 31, no. 10, pp. 1411–1420, Oct 2001. http://dx.doi.org/10.1016/S0008-8846(01)00562-2.

[30] D. V. Ribeiro, J. A. Labrincha, and M. R. Morelli, "Effect of the addition of red mud on the corrosion parameters of reinforced concrete," *Cement Concr. Res.*, vol. 42, no. 1, pp. 124–133, Jan 2012. http://dx.doi.org/10.1016/j.cemconres.2011.09.002.

[31] N. S. Amorim Jr., et al., "Concrete containing recycled aggregates: Estimated lifetime using chloride migration test," *Constr. Build. Mater.*, vol. 222, pp. 108–118, Oct 2019. http://dx.doi.org/10.1016/j.conbuildmat.2019.06.136.

[32] M. S. Meddah et al., "Performance evaluation of binary concrete designed with silica fume and metakaolin," *Constr. Build. Mater.*, vol. 166, pp. 400–412, Mar 2018. http://dx.doi.org/10.1016/j.conbuildmat.2018.01.138.

[33] C. S. Poon, S. C. Kou, and L. Lam, "Compressive strength, chloride diffusivity and pore structure of high performance metakaolin and silica fume concrete," *Constr. Build. Mater.*, vol. 20, no. 10, pp. 858–865, Dec 2006. http://dx.doi.org/10.1016/j.conbuildmat.2005.07.001.

[34] M. Shekarchi, A. Rafiee, and H. Layssi, "Long-term chloride diffusion in silica fume concrete in harsh marine climates," *Cement Concr. Compos.*, vol. 31, no. 10, pp. 769–775, Nov 2009. http://dx.doi.org/10.1016/j.cemconcomp.2009.08.005.

[35] L. Nilsson, M. H. Ngo, and O. E. Gjørv, "High-performance repair materials for concrete structures in the port of Gothenburg", in *Proc. 2nd Int. Conf. Concr. Under Severe Conditions: Environment and Loading*, Sapporo, 1995, pp. 1193–1198.

[36] Q. Yuan, "Fundamental studies on test methods for the transport of chloride ions in cementitious materials," Ph.D. thesis, Dept. Struct. Eng., Ghent Univ., Ghent, 2009.

[37] M. I. Khan and R. Siddique, "Utilization of silica fume in concrete: Review of durability properties," *Resour. Conserv. Recycling*, vol. 57, pp. 30–35, Dec 2011. http://dx.doi.org/10.1016/j.resconrec.2011.09.016.

Author contributions: FKSJ: conceptualization, methodology, formal analysis, writing; GBW: methodology, data curation, formal analysis, writing; FRT: conceptualization, methodology; FCM: conceptualization, methodology, formal analysis, writing, supervision;

Editors: Fernando Pelisser Guilherme Aris Parsekian.

IBRACON Structures and Materials Journal
Revista IBRACON de Estruturas e Materiais
ISSN 1983-4195 ismj.org

ORIGINAL ARTICLE

Experimental investigation on structural concrete masonry in fire: emphasis on the thermal behavior and residual strength

Análise experimental sobre alvenaria estrutural de blocos de concreto em situação de incêndio: ênfase no comportamento térmico e na resistência residual

Davi Fagundes Leal[a,b]
Rafael Henrique Dupim[a]
Jorge Munaiar Neto[a]
Márcio Roberto Silva Corrêa[a]

[a]Universidade de São Paulo – USP, Escola de Engenharia de São Carlos, Departamento de Engenharia de Estruturas, São Carlos, SP, Brasil
[b]Instituto Federal de Educação, Ciência e Tecnologia Fluminense, Campos dos Goytacazes, RJ, Brasil

Received 17 June 2020
Accepted 15 October 2020

Abstract: This paper aims to analyze the thermal behavior and residual mechanical properties of concrete hollow-blocks structural masonry and its component materials in fire situation using experimental investigation. Compression tests were carried out on blocks, prisms and small walls at room temperature and after being exposed for 70 minutes to the ISO 834 Standard Fire. The test at high temperatures was run using a furnace powered by natural gas and instrumented with thermocouples to measure temperatures in the specimens. The influence of the initial concrete strength on masonry behavior was evaluated considering the use of blocks with different strengths at room temperature. In addition, exposure to fire was also investigated considering masonry elements with no coverings and submitted to two different fire exposure conditions: one or both sides. The results indicate a substantial loss in the masonry load capacity at high temperatures, especially in cases of fire exposure on both sides, where the residual compressive strength resulted, on average, between 20% and 27% for the blocks and approximately 14% for prisms and small walls. Its performance with fire heating up on only one face is much higher, with an average residual masonry strength equal to 46% compared to its strength at room temperature. The obtained results are also useful for evaluating masonry regarding the integrity and thermal insulation criteria, the latter achieved with little over 60 minutes of testing.

Keywords: structural masonry, concrete, fire, residual strength, thermal behavior.

Resumo: O presente trabalho tem como objetivo investigar, por meio de análises experimentais, o comportamento térmico e as propriedades mecânicas residuais da alvenaria estrutural de blocos vazados de concreto e seus materiais componentes em situação de incêndio. Foram realizados ensaios de compressão com elementos representativos da alvenaria (blocos, prismas e pequenas paredes) antes e após serem expostos por 70 minutos ao Incêndio-Padrão proposto na ISO 834-1:1999, o qual foi aplicado por meio de um forno a gás natural instrumentado com termopares para a medição das temperaturas em seu interior e também nos corpos de prova. A influência da resistência inicial do concreto no comportamento da alvenaria foi avaliada considerando-se blocos com diferentes resistências características à temperatura ambiente. Além disso, a forma de exposição ao incêndio foi também investigada, sendo ensaiados elementos sem revestimento e com fogo atuando em uma ou em ambas as faces. Os resultados apontam significativa perda de capacidade resistente da alvenaria quando em temperaturas elevadas, principalmente nos casos em que o fogo atua em ambas as faces, onde a resistência residual à compressão resultou entre 20% e 27% para os blocos e em torno de 14% para prismas e pequenas paredes, em média. Seu desempenho com fogo atuando em apenas uma face se mostra bem melhor, com resistência residual média da alvenaria igual a 46% em relação à sua resistência à temperatura ambiente. Os resultados encontrados também são úteis para a avaliação da alvenaria quanto aos critérios de estanqueidade e isolamento térmico, este último atingido com pouco mais de 60 minutos de ensaio.

Palavras-chave: alvenaria estrutural, concreto, incêndio, resistência residual, comportamento térmico.

Corresponding author: Davi Fagundes Leal. E-mail: daviusp@sc.usp.br
Financial support: This study was funded by the São Paulo Research Foundation (FAPESP – grant number 2017/20255-4). Author Rafael Henrique Dupim received a research scholarship from the National Council for Scientific and Technological Development (CNPq).
Conflict of interest: Nothing to declare.

How to cite: D. F. Leal, R. H. Dupim, J. Munaiar Neto, and M. R. S. Corrêa, "Experimental investigation on structural concrete masonry in fire: emphasis on the thermal behavior and residual strength," *Rev. IBRACON Estrut. Mater.,* vol. 14, no. 4, e14408, 2021, https://doi.org/10.1590/S1983-41952021000400008

1. INTRODUCTION

Structural masonry elements are an assembly of blocks bonded together with mortar joints. In this type of construction, in addition to being an important part in the architectural layout, walls also fulfill the structural function. Therefore, structural masonry buildings generally do not need columns and beams as slabs consider masonry walls as support. This construction system has been widely used in many countries, especially in Brazil, where it can be found from small houses to multi-storey buildings with about twenty floors, as presented in Corrêa [1].

Nowadays, the behavior of structural masonry at room temperature is relatively well known as there is a large body of research and a consolidated set of codes for design and construction control. However, regarding its behavior at elevated temperatures, there is still a gap in the literature concerning a clear understanding of masonry wall performance in fire situations, as discussed in Russo and Sciarretta [2].

Among the main codes, Eurocode 6 [3], as well as the American and the Australian codes ([4] and [5]), are worth mentioning, which provide methodologies for the design of structural concrete masonry in fire situations. Their design procedures include performance requirements for determining fire resistance of masonry walls, which are based on three criteria called *R* (mechanical resistance), *E* (integrity) and *I* (thermal insulation). According to Eurocode 6, these criteria are assumed to be met in the following conditions:

- Criterion *R* - when the loadbearing function is maintained throughout the required time of fire exposure;
- Criterion *I* - when the mean temperature of the unexposed face does not rise by more than 140 ºC, and the maximum temperature rise at any point of that surface does not exceed 180 ºC;
- Criterion *E* - when the passage of flames and hot gases through the member is prevented.

For the standard fire exposure, members shall comply with criteria according to their function in the building, as follows: Criterion *R*, for loadbearing function only (non-separating walls); Criteria *EI*, for separating function only (non-loadbearing walls); and Criteria *REI*, for both separating and loadbearing functions.

A small number of experimental and theoretical studies aimed at evaluating the performance of masonry walls in relation to these criteria is available in the literature. Nahhas et al. [6] present experimental results of a masonry wall constructed by assembling concrete hollow blocks with three partitions and two vertical cells throughout the wall's thickness, which took more than 120 minutes to reach 200 °C on the unexposed face once subjected to the ISO 834 Standard Fire [7]. On the other hand, blocks with only one cell in the wall thickness direction tend to present a much lower performance with respect to the thermal insulation criterion, as observed in Lopes et al. [8], whose tests resulted in values between 67 and 80 minutes of fire resistance.

Based on experimental investigation, Harmathy and Allen [9] observed that a 25 mm thick air layer inside a concrete wall can improve its thermal insulation by up to 10% compared to solid walls with the same volume. However, as heat transfer through an air gap is practically independent of its thickness, there is no major insulation gain increasing this layer. In addition, the authors conclude that increasing the shells' thickness of hollow blocks is more efficient for the thermal insulation of masonry than increasing their webs.

Regarding the mechanical resistance, Russo and Sciarretta [2] point out that real events often demonstrate that masonry walls and structures can excellently withstand the action of fire and high temperatures. However, the wide variety of geometries and materials commonly used in blocks and joints, as well as the different possible boundary conditions, have motivated various studies to have a clearer understanding about the behavior of masonry elements in fire, such as [10]–[17].

Over the last three decades, structural masonry has been consolidated as an important part of the construction market in Brazil due to its advantages compared to reinforced concrete and steel structures, mainly because of the reduction in construction costs. Hollow concrete blocks and cement-lime based mortar joints have been widely used in structural masonry elements in both low and tall buildings, where 14 cm thick walls are commonly used in structural design. However, Brazilian standards do not currently provide procedures for structural masonry design at high temperatures, which represents a potential risk to the safety of masonry buildings in fire situations. In addition, few studies have been carried out in the specific field of post-fire safety of masonry structures, as pointed out in Russo and Sciarretta [2].

Thus, this paper aims to analyze aspects related to concrete hollow-blocks structural masonry, which have been underexplored in the literature, using experimental tests. Examples include performance differences between representative masonry elements (blocks, prisms and small walls) at elevated temperatures, the influence of the initial strength of blocks on the masonry behavior in fire situations, the fire exposure on one or both faces of walls and the residual strength of these elements after the action of fire.

2. MATERIALS AND EXPERIMENTAL PROGRAM

In order to evaluate the residual strength and thermal behavior of masonry, the experimental program was carried out at the Structures Laboratory at the São Carlos School of Engineering (LE/EESC/USP). It is divided into the three following stages:

1) Characterization tests at room temperature;
2) Thermal test (at elevated temperatures);
3) Post-fire compression tests.

In each of these steps, blocks, prisms and five-row small walls were tested (Figure 1), as well as mortar specimens. Hollow concrete blocks with a width equal to 14 cm (wall thickness) and two different nominal compression strengths equal to 4.0 MPa and 10.0 MPa were considered (nominal strengths related to the gross cross-section, which correspond to a net strength of about 7.7 MPa and 19.2 MPa, respectively). The blocks and half-blocks were manufactured by a Brazilian company specialized in precast concrete elements for civil construction (*Tatu Pré-Moldados Ltda*), and were produced from high-early-strength Portland cement, water, crushed diabase coarse aggregate of maximum size 12.5 mm and natural quartz sand as fine aggregate (siliceous aggregates). A company specialized in civil construction was hired to build the specimens at the laboratory (LE/EESC/USP), therefore all masonry elements included in this experimental investigation were built by an experienced mason.

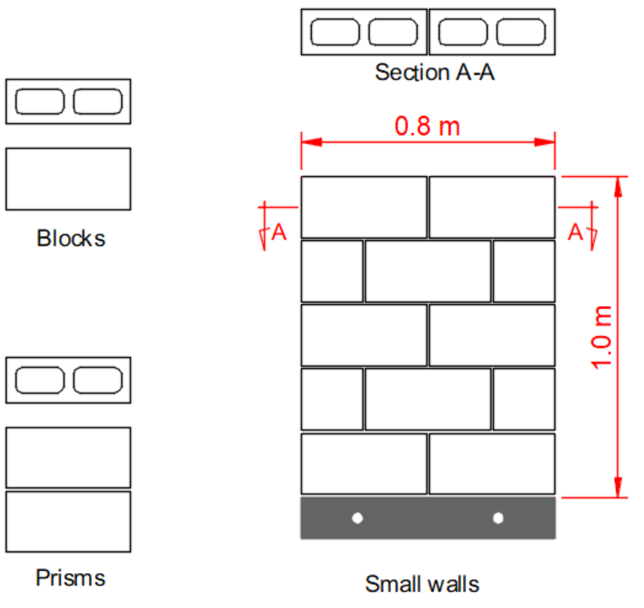

Figure 1. Test specimens: blocks, prisms and small walls.

The mortar was made of Portland cement, lime and river sand produced in a concrete mixer at the laboratory, following 1:0.5:4.5 as volume and water/cement ratio equal to 1.23 (average consistence index equal to 248.2, which was obtained according to Associação Brasileira de Normas Técnicas [18]). Prisms and small walls were assembled with full bedding with 1 cm thick joints. In order to ensure the accuracy of the joints' thickness, 10 mm diameter steel bars were used as a template between blocks while constructing the samples and were removed as soon as mortar had sufficient strength to support the blocks above. All prisms and small walls were stored in the laboratory and were submitted to air curing in a covered environment until testing. For each type of element tested, 6 blocks, 6 half-blocks, 6 prisms, 3 small walls and 6 mortar specimens were used according to the sampling defined in standards [19]–[21], as detailed in Table 1.

Table 1. Sampling and tests.

Specimen		Room temperature		Furnace	Post fire
		Physical - geometric	Compression	Fire	Compression
4 MPa (7.7 MPa*)	Block	6	6	6	6
	Half-block	6	6	-	-
	Prism	-	6	6	6
	Small wall	-	3	3	3
	Trio**	-	-	3	3
10 MPa (19.2 MPa*)	Block	6	6	6	6
	Half-block	6	6	-	-
	Prism	-	6	-	-
	Small wall	-	3	3	3
Mortar cylinders		-	6	6	0***

*nominal compression strength considering the net cross-section. **group of three small walls, as presented in Item 2.2. ***no post-fire tests were carried out with the mortar specimens due to their degradation, as presented in Item 3.2.

The experiments were planned according to the laboratory schedule and the activities related to the preparation of the tests, such as transporting samples, curing, instrumentation and thermal insulation of specimens' parts with a ceramic fiber blanket. Thus, the tests using blocks, prisms and small walls were carried out at room temperature between 60 and 72 days after constructing of the specimens; mortar specimens were then tested at 91 days of age. Finally, the masonry specimens were tested at elevated temperatures 104 days after being constructed, followed by the post-fire tests seven days after fire exposure.

2.1 Characterization tests at room temperature

Table 2 presents the physical and geometric properties of blocks and half blocks used, obtained through tests prescribed in Associação Brasileira de Normas Técnicas [19] and [20].

Table 2. Physical and geometric properties of blocks and half blocks.

Block	External dimensions			Thickness			Areas			Absorption (%)
	L (mm)	B (mm)	H (mm)	e_L (mm)	e_T (mm)	e_S (mm)	Gross (mm^2)	Net (mm^2)	A_{Gross}/A_{Net} (%)	
4 MPa block	390	139	190	25.6	25.5	26.5	54337	28221	52	6.6
10 MPa block	390	139	190	25.6	25.6	26.4	54359	28356	52	4.4
4 MPa half-block	191	138	188	25.3	25.3	-	26338	14708	56	6.0
10 MPa half-block	191	138	191	25.5	25.5	-	26430	14913	56	5.0

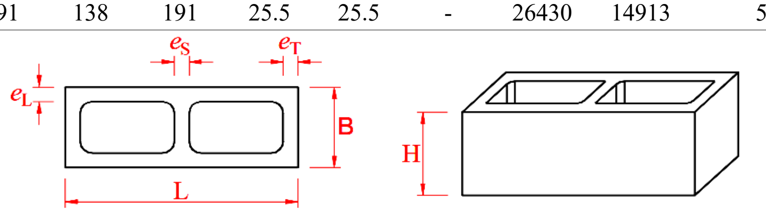

In order to evaluate the residual compressive strength (post-fire) of the masonry, compression tests were initially performed at room temperature (elements presented in Figure 1), whose results are taken as a reference in subsequent analyses at elevated temperatures.

For testing blocks, half blocks and prisms, a servo-controlled Instron 300 HVL machine was used, with a maximum load capacity of 1500 kN (Figure 2a). After initial accommodation cycles, loading was progressively applied at a rate of 0.02 mm/s (displacement control) until specimen rupture was achieved. In order to reduce stress concentration and the influence of the loading platens on the results, the compression tests were carried out with 50 mm thick platens and 20 mm mineral fiber capping boards at the top and bottom of the specimens, as also used in Oliveira [22] and Izquierdo [23].

In the case of small walls, an Instron 8506 servo-controlled device was used (Figure 2b), which has a load capacity of up to 2500 kN. Loading was also applied with displacement control at a rate of 0.01 mm/s. In order to obtain the stress-strain curve and the modulus of elasticity of the assembly, four LVDT displacement transducers were fixed by pairs on both faces of the small walls, as illustrated in Figure 2c.

Cylindrical specimens of 50 mm diameter and 100 mm height were cast to determine the compression and tensile strength of the mortar. The samples were removed from the molds after 24 hours and then transferred to air curing in the same place where the blocks, prisms and small walls were stored (covered environment and temperature between 20 and 30 °C) to avoid the influence of humidity on the results. Instron 300 HVL was also used for the compression tests considering a loading rate of 0.01 mm/s (Figure 3a). Two clip-gages were fixed on the specimens in order to determine the modulus of elasticity, which were calculated according to American Society for Testing and Materials [24], i.e. the secant modulus referring to 5% and 33% of the peak stress. The average results of compression strength and modulus of elasticity were, respectively, 4.90 MPa (coefficient of variation CV = 8.15%) and 10.99 GPa (CV = 16,33%), with an average peak strain equal to 1.10‰.

An ELE Autotest 2000 machine was used to determine the mortar tension strength by means of diametrical compression tests on 6 cylindrical specimens (Figure 3b), which were carried out as prescribed in Associação Brasileira de Normas Técnicas [25]. The average result was equal to 0.63 MPa, with a CV = 17.51%.

2.2 Experimental program at elevated temperatures

The elements shown in Figure 1 were analyzed at elevated temperatures using a gas-fueled furnace, as shown in Figure 4, which has internal dimensions of 4 m x 3 m x 1.5 m and can simulate the ISO 834 Standard Fire curve [7]. This heating device has eight burners that work under the control of a control center to reproduce the temperature-time curve specified for the test. Temperature evolution is controlled by nine thermocouples (named TP1 to TP9), which are evenly distributed in the furnace's internal space.

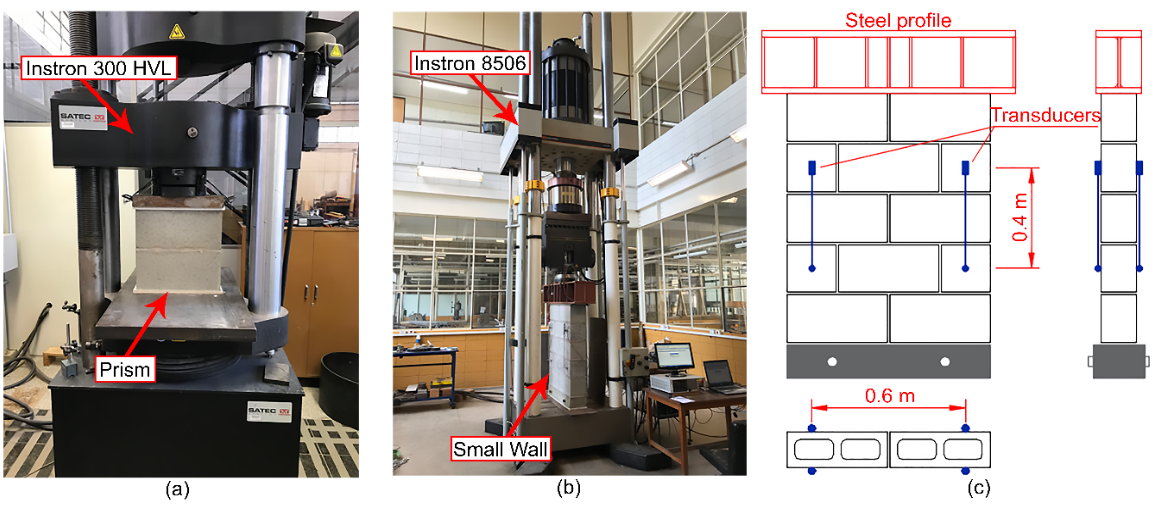

Figure 2. Compression tests of blocks, prisms and small walls at room temperature.

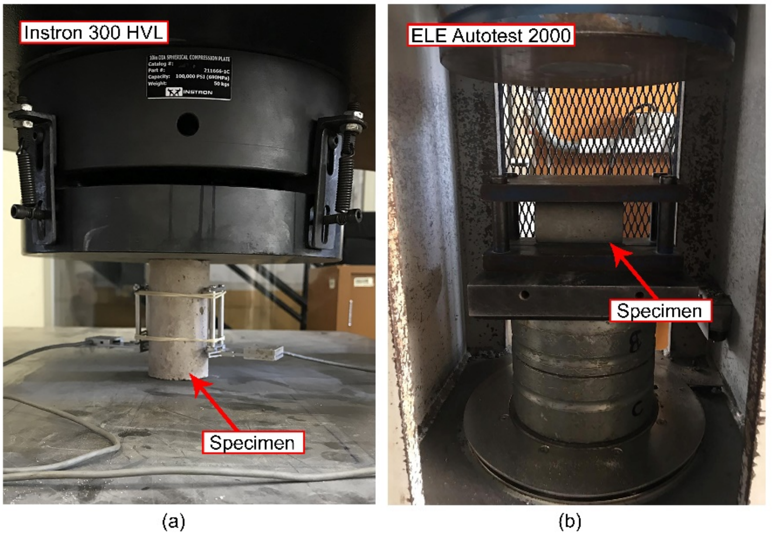

Figure 3. Bedding mortar: (a) compression and (b) tensile tests.

Figure 4. External view of the furnace used in the test.

Figure 5 shows the distribution of specimens inside the furnace, which were positioned far enough away from the burners so that there was no direct contact with flames. The experiment was performed with unloaded elements inside the furnace, i.e., blocks, prisms and small walls were initially exposed only to the action of fire. In addition, the separating function of masonry was investigated by the trio of small walls shown in Figure 5, which were exposed to fire on only one of their faces.

A 50 mm thick and 128 kg/m^3 density ceramic fiber blanket was used on the top and bottom sections of all specimens to ensure the thermal insulation of the interior of blocks in the furnace. In addition, the same type of blanket was used to insulate the internal space of the trio of small walls and their vertical interfaces, as can be seen in Figure 5.

The instrumentation of specimens was made using type K thermocouples, which were fixed at various points along the mid-height cross section of the elements: firstly, small holes were drilled in the blocks using a 4.0 mm diameter drill and then thermocouples were fixed with cement paste at the desired depths to obtain temperature measurements. Cement paste was chosen to fix the thermocouples due to the similarity between the thermal properties of both materials (concrete and cement paste), as well as its easy handling. In order to assess the reliability of measurements, two specimens of each type were instrumented (i.e, four blocks, four small walls, two small walls of the trio and two prisms), totaling 47 thermocouples. Temperature measurements were logged at each second of fire exposure during the test.

The moisture content of blocks was also determined before the test. The mass of six blocks were measured in moist condition and after drying for 24 hours in a chamber at (110 ± 5)°C; the blocks were inserted into the chamber for another two hours to assess further changes in mass. Thus, the moisture content was then determined from the difference between the moist and dry mass, resulting in 1.2% for 4 MPa blocks and 1.7% for 10 MPa blocks.

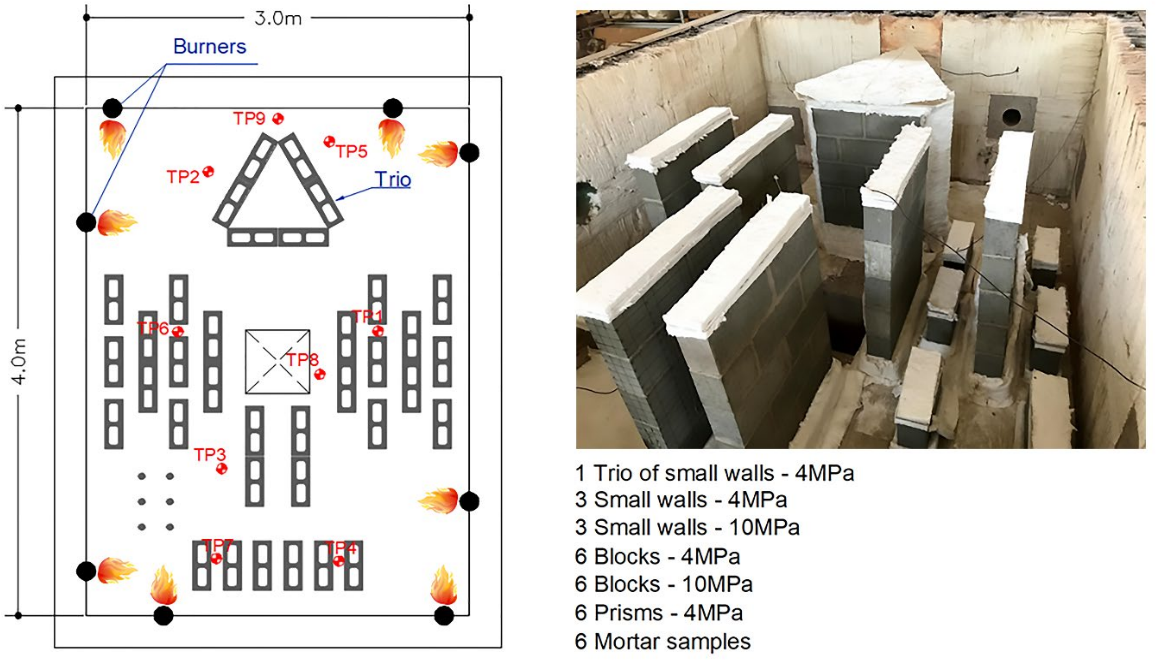

Figure 5. Test at elevated temperature: distribution of the specimens inside the furnace.

2.3 Post-fire compression tests

After exposure to fire, specimens were slowly cooled while still in the furnace, taking approximately 20 hours to cool completely. The residual strength of elements was then obtained by compression tests similar to those described in Item 2.1 and were performed seven days after the furnace test.

3. RESULTS AND DISCUSSION

3.1 Temperature level values

Specimens were submitted to the ISO 834 Standard Fire [7] for 70 minutes, where the maximum average temperature reached inside the furnace was 972 °C. Figure 6 shows the results of small walls exposed to fire on all their external faces, in which masonry does not act as a separating element. The measurements indicated in the captions refer to the distance from the analyzed point to the nearest fire exposed face, both for walls built with 4 MPa blocks (continuous lines) and for 10 MPa blocks (dashed lines). These curves correspond to the average results of two specimens for each point investigated as there were no large differences in the results of the thermocouples at any point. In addition, "Mort.13mm" represents the temperature evolution at 13 mm depth in the mortar joints; this curve corresponds to the average results of four thermocouples located at the mid-height horizontal joint of four different small walls.

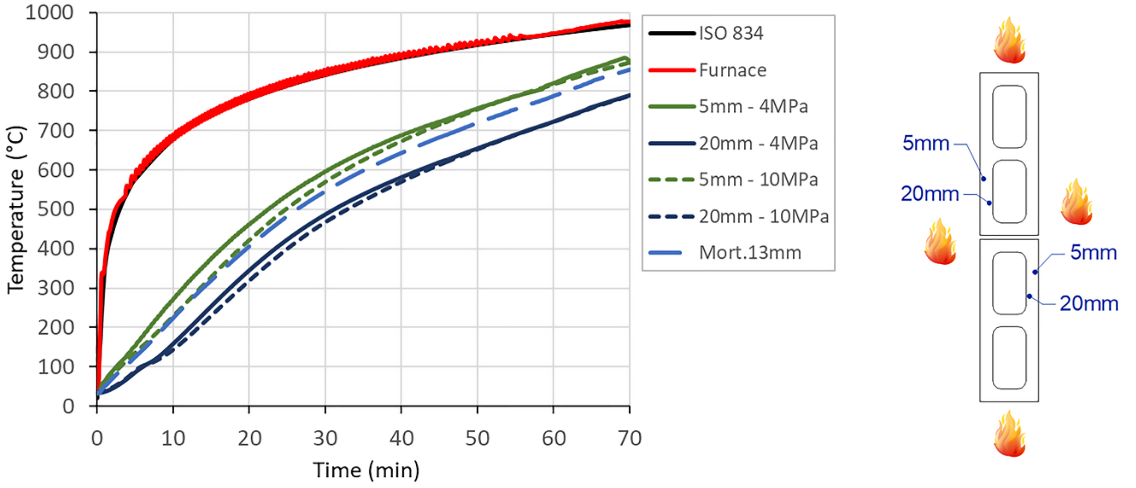

Figure 6. Small walls with fire acting on all their faces.

As expected, an important difference in slope can be noted when comparing the beginning of the 5mm and 20mm depth curves. This delay in the temperature rise in deeper sections within concrete members depends on the thermal properties of the material and increases considerably as a function of the moisture content of the concrete, as mentioned in Buchanan and Abu [26].

Although the temperature evolution in 10 MPa block walls was lower than in 4 MPa block walls throughout the test, there was a close proximity between the results, as can be seen when comparing the dashed curves with the continuous ones at each investigated point. Thus, the results indicate a small variation of thermal properties as a function of the block strength or, in other words, the difference between the thermal properties of both concretes (4 MPa and 10 MPa blocks) does not strongly influence the temperature rise through the masonry cross section. In addition, the curve for the mortar joint ("Mort.13mm") shows a similar trend when compared to those of blocks. Therefore, although the materials of the blocks and joints studied here may present different values of thermal and physical properties (specific heat, thermal conductivity and density), when considered simultaneously, these properties led to similar temperature rises in the masonry elements tested, which means that their materials have similar thermal diffusivities.

As shown in Table 2, the analyzed blocks have shells with an average thickness of 25 mm. In this case, it was observed that practically the entire wall thickness was submitted to temperatures above 500°C in less than 40 minutes when exposed to the standard fire on both faces, a temperature at which concrete already has a large reduction in its residual strength (about 40%, according to European Standards [27]). At 70 minutes, the maximum temperatures reached at points of 5 mm and 20 mm deep were around 875°C and 800°C, respectively, which is critical for concrete in terms of loss of strength: between 85% and 92% considering siliceous aggregate concrete [27].

Aiming to assess any possible differences in the temperature evolution in individual blocks and prisms when compared to walls (which would result in different percentage losses in terms of residual strength between these elements), four blocks and two prisms were also instrumented with thermocouples. Figure 7 shows the average temperature-time curves obtained at the indicated instrumentation points, where continuous lines refer to blocks with nominal strength of 4 MPa and dashed lines to 10 MPa blocks.

As in the small walls, 10 MPa blocks presented lower temperatures than 4 MPa blocks, but with few marked differences. The same pattern can be observed in mortar joints ("Mort.13mm"), whose temperature-time curve shows a similar trend when compared to the same measurement point in the block (point at 13 mm deep). Therefore, the results indicate that, depending on the mortar properties, the use of simpler specimens (such as blocks and prisms) may lead to satisfactory results when the focus is the representation of heat transfer along the thickness of masonry walls.

When analyzing curves for webs and cores, it is apparent that the preferred heat flow path is through blocks' cells rather than solid parts, since the temperature increase in the cells is greater than in their webs (at least up to 43 minutes, when thermocouples fixed at this those points have measurement problems), as can be seen by comparing the "Void" and "Web" curves in Figure 7. This finding is consistent with observations presented in Harmathy and Allen [9], which concluded that the presence of cavities is more beneficial for the thermal insulation of masonry the higher the thermal conductivity of concrete.

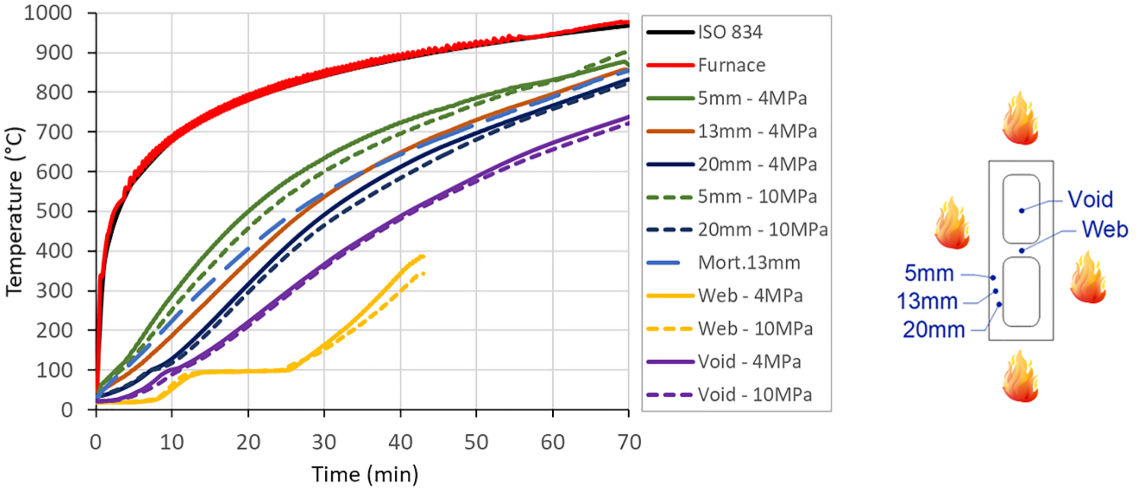

Figure 7. Blocks with fire acting on all their faces.

Figure 8 presents the average results of temperature rise at some points along the cross section related to the trio of small walls (fire acting on only one face), where the indicated measurements refer to the distance from the analyzed point to the exposed face and "Internal" refers to the air temperature measurements within the trio of small walls. Due to the presence of hollow cores in blocks, a large temperature difference can be observed between the exposed and unexposed masonry faces, with a maximum difference of around 680°C at the end of the test.

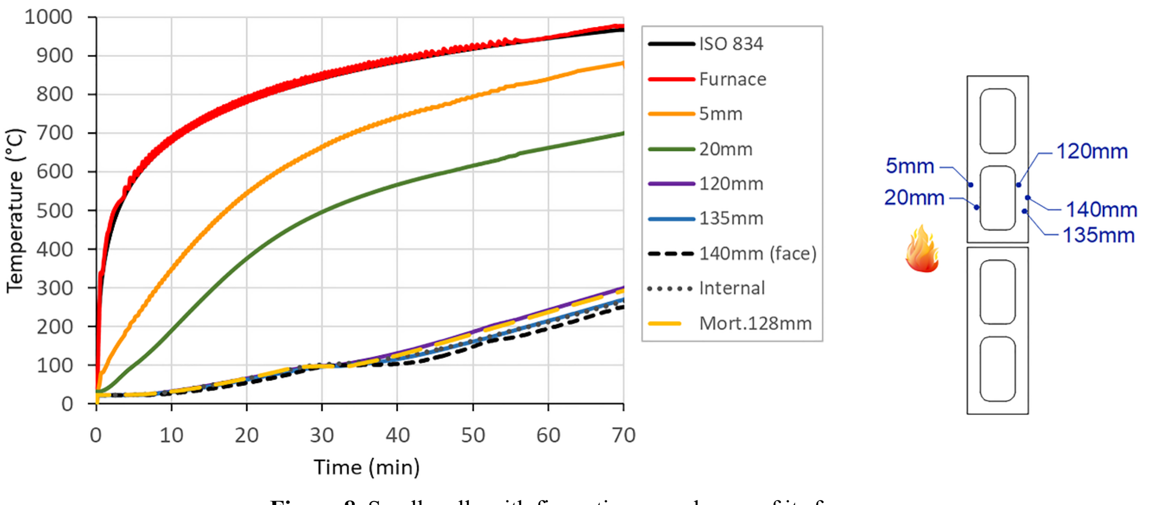

Figure 8. Small walls with fire acting on only one of its faces.

In this context, the thermal insulation criterion was evaluated based on the thermocouple measurements fixed on the unexposed face (point at 140 mm), resulting in a fire resistance time of approximately 62 minutes (the time when the maximum temperature on the unexposed surface reached 180 °C plus the initial test temperature). Considering, for example, requirements of Associação Brasileira de Normas Técnicas [28] and British Standards Institution [29] for minimum periods of fire resistance, this time would only be suitable for residential buildings with a maximum height of 23 m and 18 m, respectively.

As also found in Nahhas et al. [6] and Lopes et al. [8], a plateau was observed at 100 °C in some of the curves, especially at points furthest from the exposed face, also observed in Figure 7, where the same temperature remains constant for a few minutes. This phenomenon is a result of moisture content in concrete, which tends to absorb a large amount of energy due to free water vaporization and, consequently, sharply increases the specific heat of the material at this temperature level. Therefore, a delay is observed in temperature evolution on the unexposed face (see the “140mm (face)” curve in Figure 8), contributing to the increase in the fire resistance time according to the thermal insulation criterion.

Considering that the blocks' shells are about 25 mm thick (see Table 2), it can be inferred that the entire thickness of the exposed shells reached temperatures above 500°C during the 70 minutes of fire exposure based on the measurements of the thermocouples located at 20 mm deep. This result directly impacted the residual strength of the walls (as will be seen next), although the temperature on the unexposed side remained below 250°C during heating.

It is noteworthy that the evolution of the temperature inside the furnace precisely reproduced the Standard Fire, as can be seen in Figures 5 to 7, where the average temperature curve of the furnace is similar to the ISO 834 curve. The efficiency of the ceramic fiber blanket can be noted in Figure 8, where the temperatures reached inside the trio of small walls (“Internal curve”) remained much lower than the furnace temperature during the test, indicating a good thermal insulation effect provided by the ceramic blanket. After turning off the furnace, the trio of walls continued to heat up, as the furnace temperature remains higher when compared to the temperature inside the trio for a while, reaching a maximum temperature of 449°C on the unexposed face.

3.2 Degradation of materials

The obtained results signalize that masonry tends to experience different kinds of damage according to concrete strength, as shown in Figure 9. Due to the thermal expansion, higher compressive strength blocks present substantial cracks during heating, although their material remained in an adequate apparent condition at the end of the test. On the other hand, less resistant blocks showed only discrete superficial cracks, but showing evidence of considerable material degradation, given that 4 MPa blocks could be easily broken when handled after fire exposure.

(a) (b)

Figure 9. Blocks with nominal strength of (a) 4 MPa and (b) 10 MPa after heating.

An analogue situation was also observed on prisms and small walls, emphasizing the tendency of crack formation on the lateral face along the height of the walls (Figure 10a). In addition, a crack pattern was observed on both front faces of the elements, where slightly curved vertical cracks close to the blocks’ webs can be noted (Figure 10a). In the small walls, the observed amount of cracks was much lower than in the individual blocks, especially in lower rows, suggesting that compressive loading (in this case, the self-weight of upper on lower blocks) and the confinement effect of joints and adjacent blocks tend to reduce the occurrence of cracks due to thermal expansion, hence also contributing to the performance of walls with respect to the integrity criterion.

Regarding walls with fire heating up on only one face (in this case, the trio), the temperature gradient along the section resulted in the curving of walls, with an average top displacement of around 2.8 cm in relation to the base (Figure 10b). This measurement was performed after cooling the specimens, given that transducers do not resist the high temperatures inside the furnace during the experiment. Despite this thermal bowing, no cracks were observed at the block-joint interfaces, possibly because of the absence of loads and restraints to thermal expansion on the walls, which tend to increase deflections due to second-order effects. No spalling was observed in any of the samples.

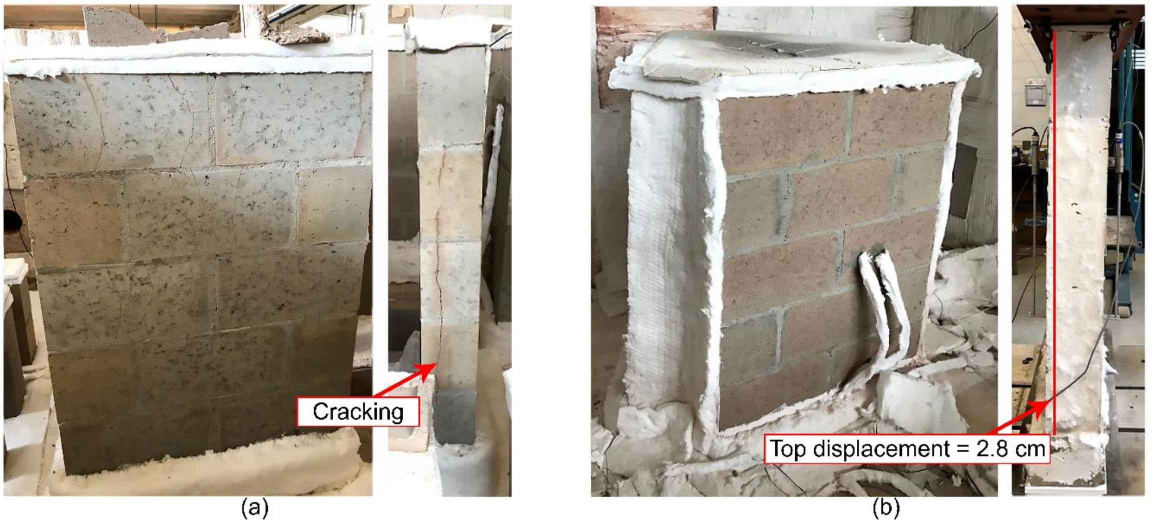

Figure 10. Small walls after the test: fire on (a) all faces and (b) one face (trio).

Figure 11 shows the mortar specimens immediately after cooling and seven days after the test. For the first situation, the material only had a few discrete and apparently superficial cracks (Figure 11a). One week later, mortar samples presented considerable degradation, showing evidence of a large number of deep cracks and, also, with no residual strength (Figure 11b). This is due to changes that occurred in the lime used in mortar at high temperatures, which turns calcium hydroxide ($Ca(OH)_2$) into calcium oxide (CaO) between 400-500 °C; upon cooling, this compound reacts with atmospheric carbon dioxide (CO_2) and gives rise to calcium carbonate ($CaCO_3$), resulting in an expansion of the material [30], [31].

This cracking behavior did not happen in mortar joints of small walls, even though it was the same material. It appears that the confinement between blocks ultimately results in a beneficial effect on the mortar joints and restricts the crack formation (see Figure 10), contrary to what happens to cylindrical specimens shown in Figure 11b. Therefore, further investigations are needed to evaluate the performance of cement and lime-based mortars in bedding joints of masonry structures in fire situations, especially in cases of load-bearing walls.

Figure 11. Bedding mortar specimens (a) one day after the test and (b) seven days after the test.

3.3 Residual Mechanical Properties

Figure 12 presents the results of the compression tests performed before and after the exposure to standard fire. Values refer to the characteristic and average strengths in relation to the gross section area (f_k and f_m,) and the average strength in the net section area ($f_{m,liq}$), which are calculated according to the requirements of Brazilian standards [19] and [21]. Table 3 summarizes the post-fire results, highlighting the residual strength as a percentage of the average strength at room temperature.

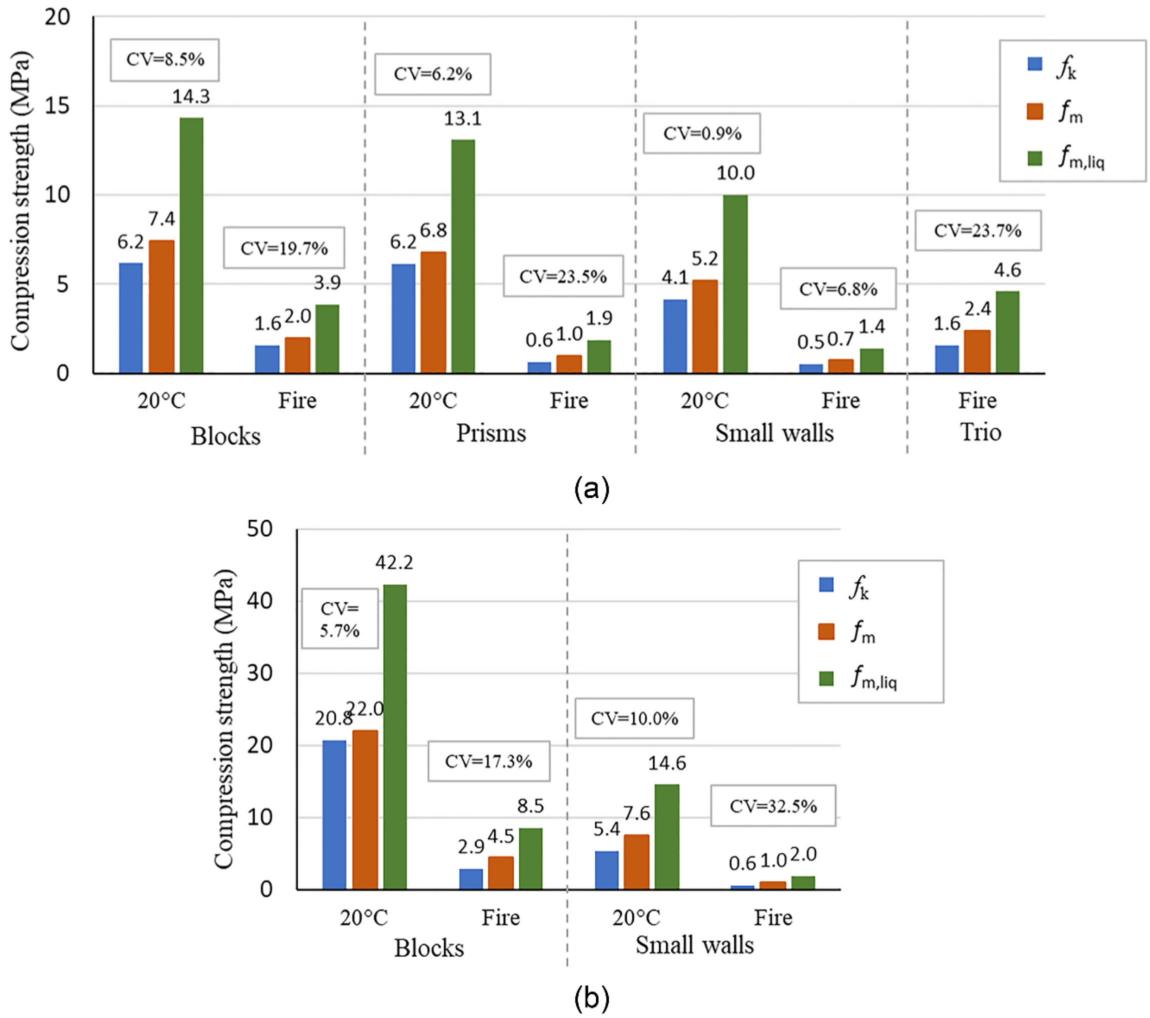

Figure 12. Compressive strength before and after fire: (a) 4 MPa blocks and (b) 10 MPa blocks (nominal).

Table 3. Residual compression strength after 70 minutes under the ISO 834 Standard Fire.

Blocks' nominal strength	Blocks		Prisms		Small walls		Trio	
	F_{fire} (kN)	F_{fire}/F_{room}	F_{fire} (kN)	F_{fire}/F_{room}	F_{fire} (kN)	F_{fire}/F_{room}	F_{fire} (kN)	F_{fire}/F_{room}
4 MPa	108.7	**27%**	52.8	**14%**	79.3	**14%**	259.0	**46%**
10 MPa	242.3	**20%**	-	-	111.5	**13%**	-	-

F_{fire} – average compression strength after cooling (residual strength). F_{room} – average compression strength at room temperature (before fire exposure).

Room-temperature tests indicate that the characteristic strength of blocks is much higher than the nominal strengths specified by the manufacturer: 6.2 MPa and 20.8 MPa instead of 4 MPa and 10 MPa. In addition to the results shown in Figure 12, half-blocks were also tested at room temperature according to the sampling presented in Table 1, resulting in average compression strengths in the gross section area equal to 10.7 MPa and 18.4 MPa (characteristic strength equal to 9.4 MPa and 14.1 MPa), with a coefficient of variation of 8.6 and 10.8, respectively.

After the furnace test, a large loss of masonry strength was observed, especially for elements exposed to fire on both faces, where the residual strength resulted in less than a quarter for most tested elements. In addition, there is a considerable increase in the coefficient of variation (CV) on individual results of specimens around the mean, which influences the characteristic strength of elements.

Higher strength blocks presented considerable percentage strength reduction when compared to lower strength blocks, probably due to the higher incidence of cracking during heating. Additionally, the results show that prisms and small walls tend to experience an expressive loss of strength when compared to the blocks, indicating an influence of the mortar joints on the residual masonry strength, as expected. In this context, it was observed that, in percentage, prisms and small walls showed the same strength as post-fire compression (around 14%), which may be an indication that using simpler specimens (such as two-block prisms) can lead to satisfactory results in the evaluation of the residual compressive masonry strength as a whole, considering the slenderness effects separately.

The results of the trio of small walls indicate that this type of structural masonry performs much better when exposed to fire on only one face (wall acting as a separating element during fire), resulting in residual strength about three times higher than fire exposure to both faces (considering similar boundary conditions in both cases). However, it is noteworthy that the test lasted 70 minutes, and therefore elements did not reach the most critical fire exposure predicted in design codes such as Associação Brasileira de Normas Técnicas [28] and British Standards Institution [29], which would be that corresponding to required periods of fire resistance of 120 minutes. In this case, the results point to the need to find ways to protect masonry against fire in order to ensure safety of the structure in taller buildings.

It is noteworthy that the conditions established for these tests are the most critical regarding the strength of materials (concrete and mortar), as their resistance after cooling is lower than with the specimen still heated or even when there is simultaneous mechanical and thermal actions (considering samples heated up to the same maximum temperature), as can be observed in Abrams [32].

Figure 13 shows the stress-strain curves (relative to gross section area) of small walls before and after fire exposure, where dashed lines refer to individual specimen results and continuous lines with markers correspond to the average results.

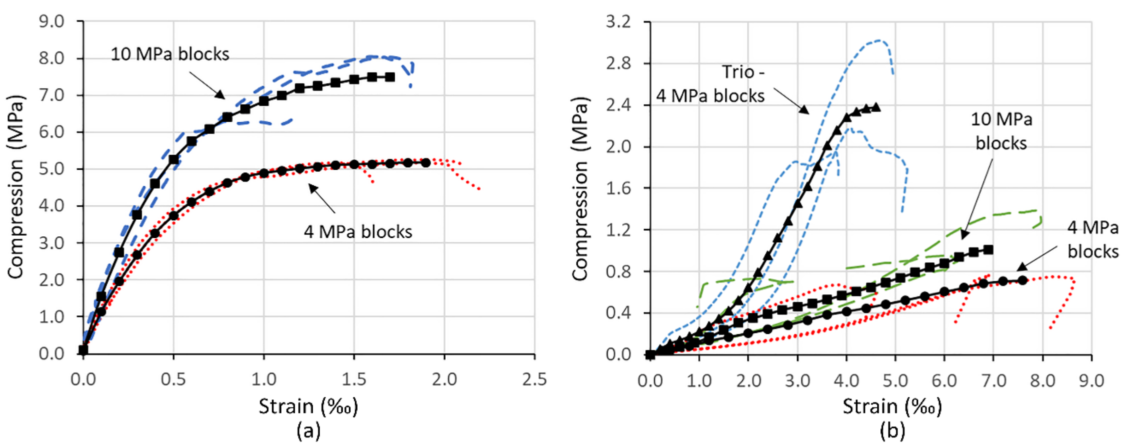

Figure 13. Stress-strain curves of small walls: (a) at room temperature; (b) after fire.

Unlike tests performed at room temperature (Figure 13a), where individual results of specimens followed a similar trend, after exposure to fire, masonry tends to show important variability in its behavior under compression (Figure 13b). Such variations are directly related to the presence of cracks, resulting from thermal expansion, which are randomly distributed along the masonry surface.

In addition to impacts on strength, exposure to high temperatures also significantly reduces the modulus of elasticity of the materials involved, resulting in reduced masonry stiffness as a whole. Table 4 presents the modulus of elasticity (E_p) values of masonry before and after fire exposure, evaluated according to requirements of Associação Brasileira de Normas Técnicas [21], that is, in the range corresponding to 5% and 30% of the failure stress.

Table 4. Modulus of elasticity of small walls before and after the ISO 834 Standard Fire [7].

Blocks' nominal strength	At room temperature				After 70 min of fire exposure				$\frac{E_{p,Fire}}{E_{p,20°C}}$ (%)
	f_m (MPa)	ε_u (‰)	$E_{p,20°C}$ (GPa)	CV (%)	f_m (MPa)	ε_u (‰)	$E_{p,Fire}$ (GPa)	CV (%)	
4 MPa	5.20	1.9	**9.50**	8.6	0.73	7.6	**0.12**	76.5	**1.3**
10 MPa	7.61	1.6	**13.69**	14.2	1.03	6.9	**0.16**	43.5	**1.2**
4 MPa - Trio	5.20	1.9	**9.50**	8.6	2.38	4.6	**0.40**	22.4	**4.2**

f_m – average compression strength of the small walls (in the gross area). ε_u – strain corresponding to the maximum stress (f_m). $E_{p,20°C}$ – modulus of elasticity at room temperature (before fire exposure). $E_{p,Fogo}$ – modulus of elasticity after cooling (residual). CV – coefficient of variation of individual results of the specimens around the mean.

Regardless of block strength, the modulus of elasticity of the masonry decreases dramatically after fire exposure on both faces, resulting in just over 1% compared to its value at room temperature. Although it showed less reduction in its stiffness, this fact is also observed in walls with only one face exposed to fire, where the post-fire modulus of deformation resulted in only 4.2% compared to results at room temperature.

In this context, it is important to point out that, in addition to the time of fire exposure, the different types of mortar commonly used in bed and vertical joints tend to directly influence the residual stiffness of the assembly, as its degradation at high temperatures depends on its component materials, as discussed in Andreini et al. [15].

4. CONCLUSIONS

Considering the particular case investigated here (i.e, characteristics of the specimens regarding their geometry and materials, as well as the boundary conditions imposed in the tests), the following conclusions can be drawn:

- Variation in block strength (concretes with the same aggregate type) does not significantly change the temperature evolution along the masonry cross section.
- However, masonry tends to experience different kinds of damage according to the initial strength of block concretes. Due to thermal expansion, higher strength blocks are more susceptible to cracking; in contrast, lower strength blocks tend to show greater degradation in the mechanical properties of the material at elevated temperatures.
- Masonry has a considerable reduction in its compressive strength after exposure to fire (Standard Fire) on both faces, with residual strength around 14% compared to its strength at room temperature, after 70 minutes of exposure.
- Its performance is much better by exposure to fire on only one face, where the average residual strength resulted in the triple of walls without separating function.
- Considering the geometry of blocks analyzed, the thermal insulation criterion is reached just over 60 minutes under the ISO 834 Standard Fire [7], which can be critical for tall buildings.
- Therefore, considering the criteria of mechanical resistance and thermal insulation, the experimental results presented here indicate the need to study ways to protect masonry against fire, especially in cases of multi-storey buildings.
- Due to the proximity of the results of blocks, prisms and small walls, it can be concluded that mortar joints made with cement, lime and sand up to 1 cm thick do not significantly change the temperature gradient in the section compared to blocks. However, they have a considerable influence on the residual mechanical properties of masonry after fire exposure.
- Considering the good agreement between the results of prisms and small walls, the use of simpler specimens, such as two-block prisms, may lead to satisfactory results in the evaluation of temperature rise and the residual strength of masonry as a whole, taking into consideration the slenderness effects separately.

5. ACKNOWLEDGEMENTS

The authors acknowledge the São Paulo Research Foundation (FAPESP – grant #2017/20255-4) for the financial support. Moreover, we acknowledge the Structural Engineering Department at the University of Sao Paulo (USP-

EESC) for the facilities and technical support for this research and the National Council for Scientific and Technological Development (CNPq) for the research scholarship.

6. REFERENCES

[1] M. R. S. Corrêa "Masonry engineering in brazil past development, current overview, future improvements", in *15th Inter. Brick and Block Masonry Conf.*, Florianópolis, Brazil, 2012.

[2] S. Russo and F. Sciarretta, "Masonry exposed to high temperatures: Mechanical behaviour and properties - An overview," *Fire Saf. J.*, vol. 55, pp. 69–86, Jan 2013. http://dx.doi.org/10.1016/j.firesaf.2012.10.001.

[3] European Standards, *Eurocode 6 - Design of Masonry Structures - Part 1.2: General Rules - Structural Fire Design*, EN 1996-1-2:2005, 2005.

[4] American Concrete Institute, *Code Requirements for Determining Fire Resistance of Concrete and Masonry Constructions Assemblies*, ACI/TMS 216.1-14, 2014.

[5] Standards Australia, *Australian Standard - Masonry Structures*, AS 3700-2018, 2018.

[6] F. A. Nahhas, R. A. Saada, G. Bonnet, and P. Delmotte, "Resistance to fire of walls constituted by hollow blocks: experiments and thermal modelling," *Appl. Therm. Eng.*, vol. 27, pp. 258–267, Jan 2007. http://dx.doi.org/10.1016/j.applthermaleng.2006.04.017.

[7] International Organization for Standardization, *Fire Resistance Tests – Elements of Building Construction – Part 1: General Requirements*, ISO 834-1:1999, 1999.

[8] R. F. R. Lopes, J. P. C. Rodrigues, J. M. Pereira, and P. B. Lourenço, "Análise experimental de uma parede de alvenaria estrutural de blocos de concreto de três células em situação de incêndio," *Concreto Construcoes*, vol. 90, pp. 86–94, Apr-Jun 2018.

[9] T. Z. Harmathy and L. W. Allen, "Thermal performance of concrete masonry walls in fire," *Fire Technol.*, vol. 8, pp. 142–148, May 1972. http://dx.doi.org/10.1007/BF02590578.

[10] A. Nadjai, M. O'Garra, F. A. Ali, and D. Laverty, "A numerical model for the behaviour of masonry under elevated temperatures," *Fire Mater.*, vol. 27, pp. 163–182, Aug 2003. http://dx.doi.org/10.1002/fam.824.

[11] A. Nadjai, M. O'Garra, F. A. Ali, and R. Jurgen, "Compartment masonry walls in fire situations," *Fire Technol.*, vol. 42, pp. 211–231, Apr 2006. http://dx.doi.org/10.1007/s10694-006-7509-6.

[12] M. Andreini and M. Sassu, "Mechanical behaviour of full unit masonry panels under fire action," *Fire Saf. J.*, vol. 46, pp. 440–450, Oct 2011. http://dx.doi.org/10.1016/j.firesaf.2011.07.004.

[13] T. Nguyen and F. Meftah, "Behavior of clay hollow-brick masonry walls during fire. Part 1: Experimental analysis," *Fire Saf. J.*, vol. 52, pp. 55–64, Aug 2012. http://dx.doi.org/10.1016/j.firesaf.2012.06.001.

[14] T. Nguyen and F. Meftah, "Behaviour of hollow clay brick masonry walls during fire. Part 2: 3D finite element modelling and spalling assessment," *Fire Saf. J.*, vol. 66, pp. 35–45, May 2014. http://dx.doi.org/10.1016/j.firesaf.2013.08.017.

[15] M. Andreini, A. D. Falco, and M. Sassu, "Stress-strain curves for masonry materials exposed to fire action," *Fire Saf. J.*, vol. 69, pp. 43–56, Oct 2014. http://dx.doi.org/10.1016/j.firesaf.2014.08.005.

[16] S. Russo and F. Sciarretta, "Numeric research on the mechanical properties of different masonry units during and after fire", in *Proc. Brick and Block Masonry: Trends, Innovations and Challenges*, Modena, 2016, pp. 999–1005.

[17] W. Khaliq and M. F. Bashir, "High temperature mechanical and material properties of burnt masonry bricks," *Mater. Struct.*, vol. 49, pp. 5195–5208, Mar 2016. http://dx.doi.org/10.1617/s11527-016-0854-0.

[18] Associação Brasileira de Normas Técnicas, *Argamassa para assentamento e revestimento de paredes e tetos — Determinação do índice de consistência*, ABNT NBR 13276, 2016.

[19] Associação Brasileira de Normas Técnicas, *Blocos vazados de concreto simples para alvenaria — Requisitos*, ABNT NBR 6136, 2016.

[20] Associação Brasileira de Normas Técnicas, *Blocos vazados de concreto simples para alvenaria — Métodos de ensaio*, ABNT NBR 12118, 2013.

[21] Associação Brasileira de Normas Técnicas, *Alvenaria de blocos de concreto — Métodos de ensaio*, ABNT NBR 16522, 2016.

[22] L. M. F. Oliveira, "Estudo teórico e experimental do comportamento das interfaces verticais de paredes interconectadas de alvenaria estrutrural," Ph.D. thesis, Univ. S. Paulo, São Carlos, SP, Brasil, 2014. [Online]. Available: https://teses.usp.br/teses/disponiveis/18/18134/tde-30072014-085747/publico/2014DO_LucianaMarcelaFilizoladeOliveira.pdf

[23] O. S. Izquierdo, "Estudo da interface bloco/graute em elementos de alvenaria estrutural," Ph.D. thesis, Univ. S. Paulo, São Carlos, SP, Brasil, 2015. [Online]. Available: http://web.set.eesc.usp.br/static/media/producao/2015DO_OrietaSotoIzquierdo.pdf

[24] American Society for Testing and Materials, *Standard Test Method for Static Modulus of Elasticity and Poisson's Ratio of Concrete in Compression*, ASTM C469/C469M-14, 2014.

[25] Associação Brasileira de Normas Técnicas, *Concreto e argamassa — Determinação da resistência à tração por compressão diametral de corpos de prova cilíndricos*, ABNT NBR 7222, 2011.

[26] A. H. Buchanan and A. K. Abu, *Structural design for fire safety*, 2nd ed. Chichester, West Sussex, United Kingdon: John Wiley & Sons, 2018.

[27] European Standards, *Eurocode 2 - Design of Concrete Structures. Part 1.2: General Rules for – Structural Fire Design*, EN 1992-1-2:2004, 2004.

[28] Associação Brasileira de Normas Técnicas, *Exigências de resistência ao fogo de elementos construtivos de edificações - Procedimento*, ABNT NBR 14432, 2001.

[29] British Standards Institution, *Fire Safety in the Design, Management and Use of Residential Buildings – Code of Practice*, BSI BS 9991, 2015.

[30] M. Henry, M. Suzuki, and Y. Kato, "Behavior of fire-damaged mortar under variable re-curing conditions," *ACI Mater. J.*, vol. 108, pp. 281–289, Jan 2011. http://dx.doi.org/10.14359/51682493.

[31] V. Pachta, S. Triantafyllaki, and M. Stefanidou, "Performance of lime-based mortars at elevated temperatures," *Constr. Build. Mater.*, vol. 189, pp. 576–584, Nov 2018. http://dx.doi.org/10.1016/j.conbuildmat.2018.09.027.

[32] M. S. Abrams, "Compressive strength of concrete at temperatures to 1600F," *Am. Concr. Inst.*, Temperature and Concrete, vol. 25, pp. 33–58, 1971. ACI Special Publication.

Author contributions: DFL: Conceptualization, Data curation, Formal analysis, Funding acquisition, Investigation, Methodology, Project administration, Validation, Visualization, Writing-original draft, Writing-review & editing; RHD: Conceptualization, Data curation, Formal analysis, Investigation, Methodology, Project administration, Validation, Visualization; JMN: Conceptualization, Data curation, Formal analysis, Funding acquisition, Investigation, Methodology, Project administration, Supervision, Validation, Visualization, Writing-review & editing; MRSC: Conceptualization, Data curation, Formal analysis, Funding acquisition, Investigation, Methodology, Project administration, Supervision, Validation, Visualization, Writing-review & editing.

Editors: Nigel G. Shrive, Guilherme Aris Parsekian.

IBRACON
IBRACON Structures and Materials Journal
Revista IBRACON de Estruturas e Materiais
ISSN 1983-4195 ismj.org
SciELO

ORIGINAL ARTICLE

Contributions to the design of precast concrete culverts with unusual cross sections

Contribuição ao projeto estrutural de galerias de concreto pré-moldado com seções transversais não usuais

Aline Bensi Domingues[a]
Mounir Khalil El Debs[a]

[a]Universidade de São Paulo – USP, Escola de Engenharia de São Carlos, Departamento de Engenharia de Estruturas, São Carlos, SP, Brasil

Received 05 September 2019
Accepted 01 September 2020

Abstract: Culverts are structures used in road and railway infrastructure works such as underpasses. Among the several forms of cross-sections, the rectangular one (box culvert) has been mostly employed. However, when installed at high embankments, this structure shows high values of bending moment and shear force, which tend to be amplified by the soil arching. This paper addresses a study of section culvert with an arc cover, called modified, and a section defined by three arches, with a flat base. Such cross-section forms reduce the bending moment due to their geometry, and efforts can be decreased with the use of reduced thicknesses by mechanisms of soil-structure interaction. Analyses were performed in the plane-strain deformation with finite elements towards considering soil-structure interaction, and the results proved the influence of the geometry shape on the soil-culvert interaction behavior. A comparative analysis of the material cost index (ICM) values for 25 geometries (12 modified culverts, 12 culverts defined by three arcs and 1 box culvert) was used for estimating the economic viability of each unusual section culvert. The results showed 27 and 54% economy in materials for modified culvert and culvert defined by three arcs, respectively, in comparison with the rectangular section.

Keywords: precast concrete, culvert, section arch, soil-structure interaction, soil arching effect.

Resumo: As galerias são estruturas utilizadas em obras de infraestrutura rodoviária e ferroviária como passagens inferiores ou para transposição de talvegues. Embora existam várias formas de seções transversais, a seção transversal retangular (box culvert) é a mais empregada. No entanto, à medida que esta estrutura é instalada em elevadas alturas de terra, a forma retangular apresenta altos valores de momento fletor e força cortante. Este efeito tende a ser ampliado com o arqueamento do solo em grandes alturas de aterro. Neste artigo apresenta-se um estudo de galeria de seção com cobertura em arco, chamada modificada, e de seção definida por três arcos, com uma base plana. Com estas formas de seções transversais têm-se a diminuição dos esforços de flexão, devido à geometria. Além disto, pode-se reduzir ainda mais esses esforços com o emprego de espessuras reduzidas considerando os mecanismos de interação solo-estrutura. Para considerar a interação solo-estrutura foram realizadas análises no estado plano de deformação com elementos finitos. Os resultados comprovaram a influência significativa do formato das geometrias no comportamento da interação solo-galeria. Além disso, a análise comparativa do índice de custo de material (ICM) foi utilizada para estimar a viabilidade econômica de cada galeria não-usual. Os valores índice de custos de material foram analisados para 25 geometrias (12 galerias modificadas, 12 galerias definidas por três arcos e 1 galeria retangular), para as situações representativas preestabelecidas, os resultados mostram que a maior economia com material é de 29 e 54% para modificada e definida por três arcos, respectivamente, em comparação com a seção retangular.

Palavras-chave: concreto pré-moldado, galeria enterrada, seção transversal não usual, interação solo-estrutura.

How to cite: A. B. Domingues and M. K. El Debs, “Contributions to the design of precast concrete culverts with unusual cross sections,” *Rev. IBRACON Estrut. Mater.*, vol. 14, no. 4, e14409, 2021, https://doi.org/10.1590/S1983-41952021000400009

Corresponding author: Aline Bensi Domingues. E-mail: alinebensi@usp.br
Financial support: This study was partially financed by the Coordenação de Aperfeiçoamento de Pessoal de Nível Superior - Brasil (CAPES) - Finance Code 001.
Conflict of interest: Nothing to declare.

1 INTRODUCTION

Culverts are normally used for sewage, water or gas distribution, urban drainage and underpasses, and, in a smaller proportion, but high potential, passage of electricity, telephony and data transmission cables. Precast concrete culverts are widely employed in streams and rainwater under highways or railways, or even as underpass for vehicles and pedestrians, with no effect on their superstructure. Their efficiency has been recognized both technically and economically.

In general, circular section tubes are the most common type of buried structures, and small cross-section tubes are constructed almost in this shape. However, the use of trapezoidal, arc, elliptical or ovoid sections is common when larger diameters or spans are required [1]. The rectangular section of precast concrete, known as box culvert, is used in cases of larger spans, often for vehicle or pedestrian traffic crossing waterways, while promoting an adequate water passage, with up to 4.0-meter span.

A survey on total highway budgets conducted with data provided by DNIT [2] revealed the cost of culvert represented 11.7% of the overall value of the highway construction. Another survey based on a feasibility study for the implementation of VALEC railway sections [3] reported three budget alternatives for the same stretch, evidencing the costs for the implementation of culverts represented 13.44%, 15.19% and 15.73% (for alternatives 1, 2 and 3, respectively) of the total budgets for the railway. Such exemplified values are in agreement with other data from the literature that indicate approximately 10 to 15% of the budget refer to the construction of culverts for roadways [4].

Despite the applicability of precast concrete box culverts, they may not be suitable in situations of, for instance, installation under high embankment. Like any buried structure, culverts cause an intense redistribution of stresses in the surrounding soil, which affects the stresses applied to the structure itself. Great depths of soil show even higher concentrations of stresses, thus increasing the internal forces in the structure, especially the shear force. Kim and Yoo [5], Pimentel et al. [6] and Abuhajar [7] observed the arching effect of the soil around the box culverts under high embankments is more significant and may lead to serious failures in the structures. Therefore, improvements in the structural performance of different processes can offer greater security and important savings, in comparison to the most used culverts, i.e., those of circular or rectangular shapes.

As an alternative to usual cross sections, this article reports on a study of a precast concrete culvert with modified cross-section (Figure 1a); its cover slab displays the shape of an arch, and the cross-section is defined by three arches (Figure 1b). The structural behavior of the construction is improved in the sections by the arc segments, thus reducing both bending moments and shear force.

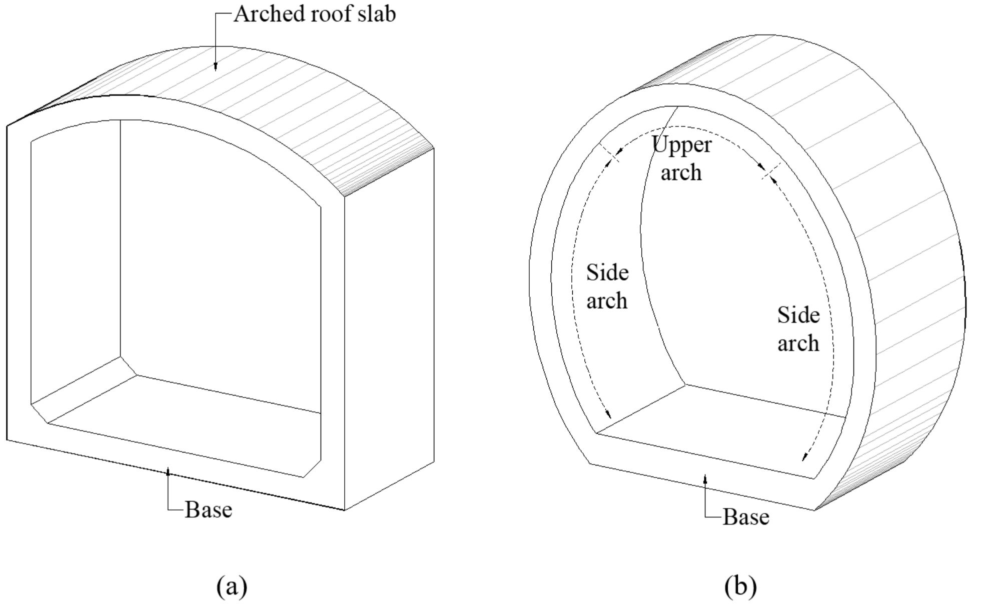

Figure 1. Cross section of the proposed culvert.

Modified culvert is the main option for box culvert for installation under high embankments. In this section format, the combination of the arc coverage favors the distribution of bending moments, similarly to the behavior of three-sided precast concrete arch sections [8], [9]. The percentage of arc slope ($i = h_a/b$) of the roof slab affects the stress distribution. The advantage of the section with arch cover is its better construction details such as bedding and compaction. The flat geometry of the base favors the compaction of the foundation. The backfill quality around the proposed culverts is higher than that of circular section tubes, since the latter may provide poor compaction in the base, leading to complex stresses, uneven settlement over the culvert, and its possible structural distress.

On the other hand, the shape of the section defined by three arcs varies regarding the proportions between the radii of the circumference arcs. If the radius of the side arc is greater than that of the roof arc, an "ellipse" section is created; if the lateral and coverage radii are the same, the section configuration is called "horseshoe". Finally, if the radius of the lateral arc is smaller than the radius of the roof arc, a "lenticular" section is formed.

The benefit of the culvert defined by the three arches tends to increase with the installation depth due to the interaction process established between the surrounding soil and the structure - great depths undergo tension changes from the contribution of soil confinement and mobilization of the arching effect. High embankment is estimated when the soil height is over 3 meters, or when the relationship between the installation depth (H) and the span (B_c) is greater than 1 ($H/B_c > 1$), i.e., the largest of two values. Under large backfill heights, the structure is not affected by the cyclic traffic loading, whose interference is rapidly reduced with an increase in the landfill height over the culvert.

Arc sections show an alteration in the distribution of internal forces, and the soil-culvert interaction is established with higher intensity in great depths, which, in some situations, increases the loads on the structure, and decreases them in others. This behavior can be affected by both type of installation of the culvert and relative stiffness of the system, i. e., relative stiffness between box culvert and surrounding soil (e.g., rigid, semi-rigid, flexible). In general, precast concrete culverts behave like rigid ducts, i.e., they support the loads imposed by themselves. Culverts defined by three arches can be dimensioned in such a way as to behave as semi-rigid ones, reducing the thickness of the walls and, therefore, affecting the soil-culvert interaction and mobilizing resistant soil mechanisms that support more loads according to the structure's flexibility - the thinner the culvert wall, the stronger the interaction of the structure with the soil. On the other hand, the soil will support loads imposed on the system. In this case, the stress capacity of the soil is more demanding, thus inducing reductions in the values of the internal forces in the culvert. Another important aspect is both thickness reduction and increased flexibility of the culvert contribute to the arching effect of the soil; consequently, evaluations of culverts with such characteristics must consider the mechanism of soil-structure interaction through numerical simulations.

The characteristics of the modified culvert and culvert defined by three arcs of circumference are better than those of preexisting culverts (box culvert or pipes tubes) in installation conditions under high embankments. For example, a reduction in weight due to a reduction in thicknesses not only saves material, but also facilitates transportation and assembly phase. Among the favorable characteristics is the ease of construction of the bedding, since the soil of foundation can be well compacted and the reactions at the bottom of the structure become uniform, thus reducing the concentrated stresses. On the other hand, both bending moments and thickness of the bottom can also increase. The installation of the section defined by three arches promotes an easier construction of the lateral embankment near the base; therefore, differently from circular sections, the well-consolidated compaction of the lateral soil prisms contributes to containment.

2 STRUCTURAL BEHAVIOR AND NUMERICAL MODELING

The action of soil pressure distribution on buried structures is essential for their design. In general, culverts are subject to vertical and horizontal pressures. The former is balanced by the reaction of the soil in the bottom slab. Stresses in buried structures are mainly due to actions such as own weight, soil load, fluid pressures inside the duct, loads produced by overloads on the surface, depending on the nature of the traffic (road, rail, air|), actions by construction overloads, lateral pressures produced by the soil, actions from compaction equipment during the construction of the backfill, and actions produced by driving and during the handling, transport, and assembly of a culvert [10].

In simplified cases, the stresses acting on a culvert are equivalent to geostatic pressures. In this hypothesis, the calculation of uniform vertical pressures (P_v) produced by the soil is a linear function of the height of the soil over the culvert (h_{soil}) and the specific weight of the soil (γ_{soil}). The horizontal pressures (P_h) are calculated with a coefficient of passive earth pressure ($P_h = kP_v$). However, in some cases, simplified models lead to uneconomical solutions, or unsafe solutions, with cracks emerging above desirable limit values [6], [11]. Although culverts are relatively simple structures, the stress applied to them during their construction and subsequent useful life is complex.

A reduction or increase in the load applied to a duct due to the characteristics of the soil, geometry, rigidity of the structure, and consequent relative movement between the structure and the adjacent soil can be positive or negative arching. In active (positive) arching, the structure in a soil mass is more compressible than the surrounding soil. When pressure is applied to this system due to the soil's own weight or overload, the structure deforms more than the soil. Stresses in the structure are lower than geostatic stresses, whereas those of the adjacent soil are greater. This phenomenon, which normally occurs in flexible culverts, resembles a distribution of the soil pressures acting above the culvert to the sides.

For passive (negative) arching, the soil is more compressible than the structure, and, therefore, undergoes greater displacements, mobilizing shear stresses that increase the total pressure on the structure and decrease the pressure on the adjacent soil. Initially, since the structure deforms uniformly, the stresses are higher at the edges and lower at the center line.

However, the material of real structures exhibits a nonlinear behavior and does not deform uniformly, causing stress distributions to be more complex. According to Evans [12], a structure of more flexible central portion of the spans can experience simultaneous active and passive arching on its faces, as shown in Figure 2. Therefore, the evaluation of the behavior and efficiency of each proposed culvert requires the incorporation of soil-structure interaction.

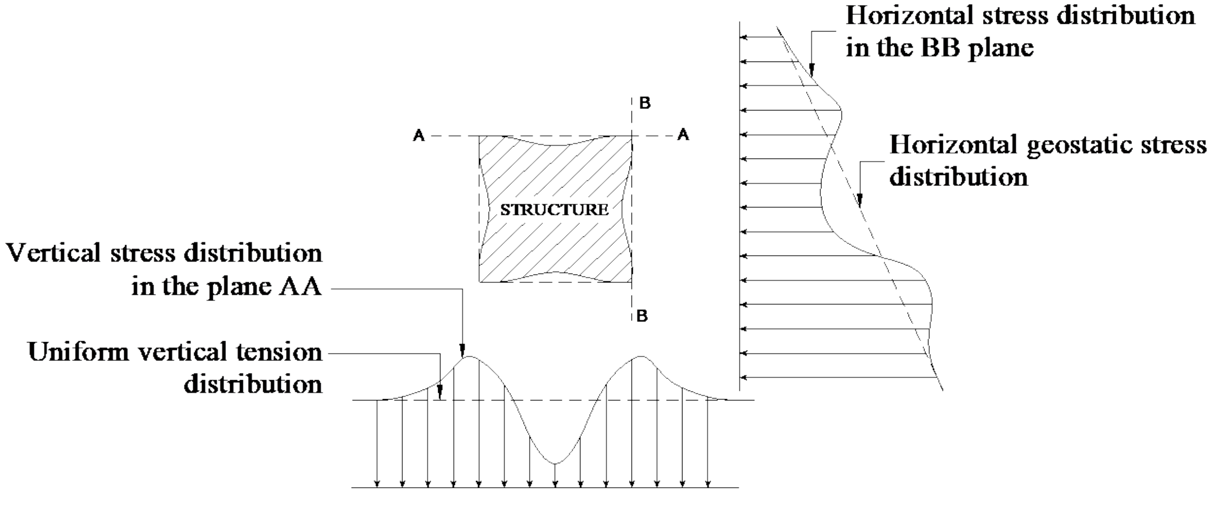

Figure 2. Stress distribution in a flexible rectangular structure.

The behavior of the culvert is affected by the conditions of the surrounding soil and the characteristics of the structure itself. The soil-culvert interaction influences the behavior of the pressure distribution, hence, the stresses acting on the structure. A more complete assessment of a buried structure, especially over great depths, considers the non-linearity of the geotechnical conditions, the structure itself and the interfaces. The finite element numerical modeling is a suitable process; therefore, it simulated the soil-culvert interaction system. The culvert model is characterized as a plane strain deformation; consequently, Finite Element Method (FEM) assessed the behavior and efficiency of each proposed culvert. FEM analysis with GeoStudio computational package [13] was used because it is suitable for geotechnical analyses.

The model of each evaluated section consists of three main parts, namely culvert, foundation, and backfill. A 5m high foundation soil was assumed, and the backfill was divided into several layers towards simulating a construction process. The maximum backfill height above the culvert was set to 20 meters and the number of phases corresponding to the simulation of the backfill construction process was 45. The outer limits of the model were restricted with simple supports, which were considered fixed supports at the lower limit, thus preventing displacements on the vertical and horizontal axis, as shown in Figure 3.

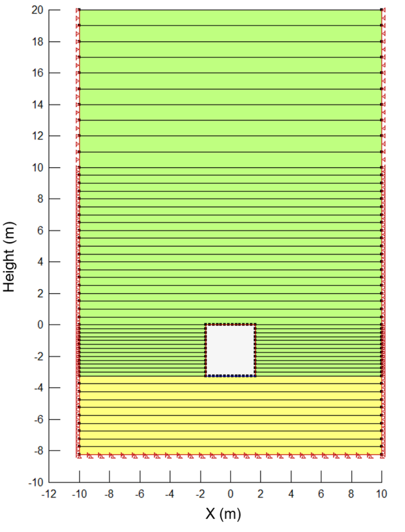

Figure 3. Layers of soil in the construction stages.

The culvert was modeled with bar elements for approximating the third-degree displacements and Euler-Bernoulli cinematic hypothesis in a linear elastic analysis. The soil material was considered perfectly plastic elastic by the Mohr-Coulomb rupture criterion. The finite element mesh that simulates the soil was comprised of triangular or quadrangular elements of approximately 12.5 cm (Figure 4).

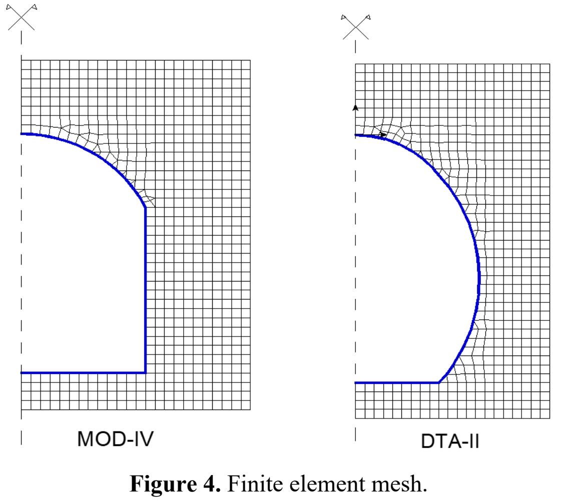

Figure 4. Finite element mesh.

Regarding soil parameters, dilation angle ψ_s was 0 °, according to sensitivity analyses conducted by Pimentel [6], which revealed a 0 ° to 15 ° variation in the dilation angle did not significantly affect the results of load capacity of the structure. Abuhajar [7] used a small cohesion value (c_s = 5kPa) for avoiding numerical instabilities. Poisson's ratio (ν) influences horizontal pressures, since the formulation for the coefficient of passive earth pressure (k) is a function of it. For k = 0.5, the average representative value of ν is 0.334. The specific weight and Young's modulus of the soil, i.e., 19 kN/m^3 and 5000 kPa, respectively, were adopted.

3 MATERIALS AND EXPERIMENTAL PROGRAM

Some criteria were established and defined by three arcs (DTA), with a usual rectangular section (RET) for a comparative evaluation of the behavior of the modified culvert (MOD).

Four main sections (MOD I, MOD II, MOD III and MOD IV) were characterized for the culverts. Figure 5 displays the configuration of the cross sections and the main parameters adopted for the culverts, and Table 1 shows each variation established. The modified culverts analyzed maintained the same dimensions for the base (bl) and the total height (h). The first variation between them was related to a reduction in the coverage arc; consequently, the arrows (i) varied 15, 30, 45 and 60%. The second variation referred to the thickness of the walls, and the following three series were established: Series “a”, of 0.25m thicknesses for both side walls, bottom slab and cover, Series “b”, of 0.17m thick bottom slab, walls and cover, and Series “c”, of 0.25m thick bottom slab and 0.15m thick side walls and cover slab. Regarding the material´s properties, the use of a conventional C40 concrete was estimated adopting 30 GPa Young’s modulus and 0.2 Poisson's ratio.

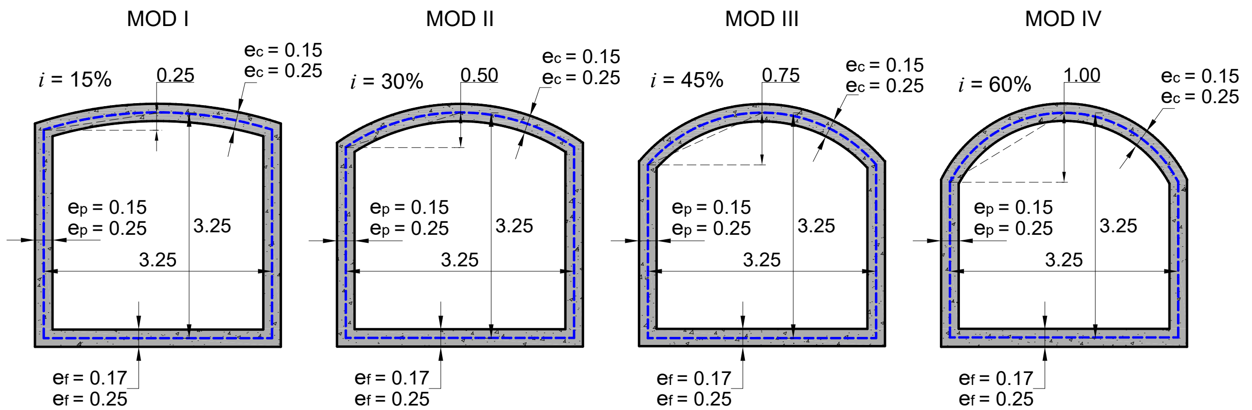

Figure 5. Representation of the cross section of the modified culverts.

Table 1. Geometric parameters of the modified culverts.

Sigla	b_{ext} (mm)	h_{ext} (mm)	h_a (mm)	h_r (mm)	R_{ext} (mm)	r_{int} (mm)	e_c (mm)	e_p (mm)	e_f (mm)
MOD I-a	3500	3500	250	3250	5530	5280	250	250	250
MOD II-a			500	3000	3020	2770			
MOD III-a			750	2750	2260	2010			
MOD IV-a			1000	2500	1950	1700			
MOD I-b	3400	3410	250	3160	5480	5330	150	150	170
MOD II-b			500	2910	2970	2820			
MOD III-b			750	2660	2210	2060			
MOD IV-b			1000	2410	1900	1750			
MOD I-c	3400	34500	250	3200	5480	5330	150	150	250
MOD II-c			500	2950	2970	2820			
MOD III-c			750	2700	2210	2060			
MOD IV-c			1000	2450	1900	1750			

The criteria for comparisons between the culverts defined by three arches are associated with the same internal area. Four proportions were chosen for the culvert defined by three arches (DTA I, DTA II, DTA III and DTA IV). Figure 6 displays a representation of the cross sections of the culverts and Table 2 shows each variation established.

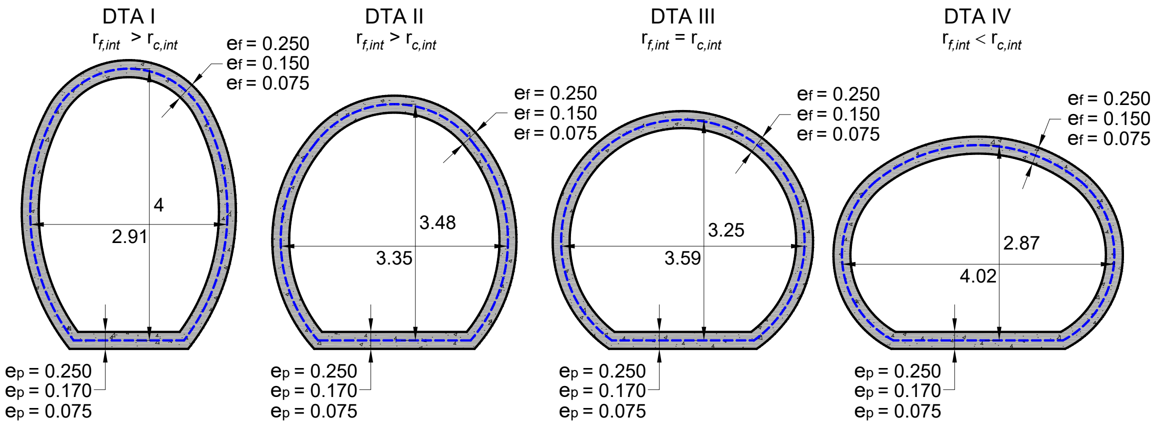

Figure 6. Representation of the cross section of the culvert defined by three arches.

Table 2. Geometric parameters of the culvert defined by three arcs.

Sigla	h_{ext} (mm)	b_{ext} (mm)	b_b (mm)	$R_{f,ext}$ (mm)	$r_{f,int}$ (mm)	$R_{c,ext}$ (mm)	$r_{c,int}$ (mm)	e_p (mm)	e_f (mm)
DTA I-a	4250	3160	1750	3230	2980	1360	1120	250	250
DTA II-a	3725	3600	2360	2380	2130	1590	1340		
DTA III-a	3500	3840	2170	1920	1670	1920	1670		
DTA IV-a	3125	4270	2560	1550	1300	2530	2280		
DTA I-b	4160	3060	1700	3180	3030	1310	1160	150	170
DTA II-b	3635	3500	2320	2330	2180	1540	1390		
DTA III-b	3410	3740	2140	1870	1720	1870	1720		
DTA IV-b	3035	4170	2540	1500	1350	2480	2330		
DTA I-c	4200	3060	1700	3180	3030	1310	1160	150	250
DTA II-c	3675	3500	2320	2330	2180	1540	1390		
DTA III-c	3450	3740	2140	1870	1720	1870	1720		
DTA IV-c	3075	4170	2540	1500	1350	2480	2330		
DTA II-d	3550	3420	2280	2290	2210	1500	1430	75	75

As in the analysis of modified culverts, variations in thickness were established for the culvert defined by three arches. The following four types of thickness were applied in the analysis: Series “a”, of 0.25m thicknesses for both bottom slab and arched stretches, Series “b”, of 0.17m thick bottom slab and 0.15m arc sections, Series “c”, of 0.25m thick bottom slab and 0.15m arc sections, and Series “d”, of 0.75m thick base and arc sections. The Young’s modulus was the same for the first three series (“a”, “b” and “c”), i.e., E_c = 30 GPa, and Poisson's ratio (ν = 0.2) was equal to that of the modified culvert. Series “d” was comprised of ultra high-performance concrete (UHPC) of 100MPa (C100) compressive strength and 47.5 GPa Young's modulus (E_c) [14].

A standard box culvert was used for a comparison with the other variations in the modified culvert and the culvert defined by three arcs, as shown in Table 3. The values of the internal forces used in the analyses and designs of the culverts are multiplied by coefficient γ = 1,4.

3.1 Analysis of changes in the geometry

The values of the internal forces in the models analyzed showed an approximately linear variation as the pressure in the structures increased; consequently, their height was 10m. Figure 7 illustrates an example of redistribution of vertical pressures in the soil around modified culverts and culvert defined by three arches, respectively.

Table 3. Geometric parameters of the reference **box cul**vert.

Box culvert - RET I-a	
Parameter/Culvert type	Simple
Width (b_{int})	3.00 m
Height (h_{int})	3.00 m
Length (l_c)	1.00 m
Wall thickness (e_p)	0.25 m
Concrete cross section area (A_c)	0.25 m^2
Wall's Moment of inertia (I_p)	0.00130 m^4
Poisson's ratio (ν)	0.30
Young's Modulus (E_c)	30 GPa

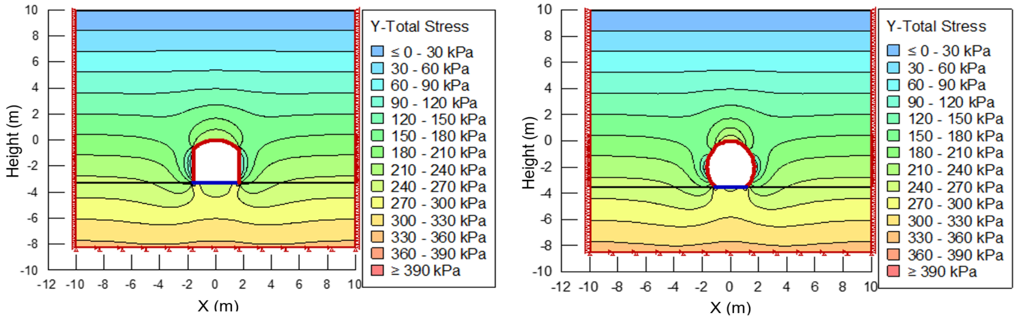

Figure 7. Vertical pressure distributions.

The modified culvert showed a tendency for a better distribution of bending moments and shear forces due to the inclination of the arc cover. Figure 8 displays the variation in the bending moments of the modified culverts. The variation in the bending moments in the middle sections of the cover slab (MLC) and upper corner (CSQ) decreased between 9 and 10% for each 15% increment in the roof arrow. However, such variations are less significant at the bottom of the culvert, and the bending moment values are up to 7% higher in the middle section of the bottom slab (MLF) than in the same section of the box culvert.

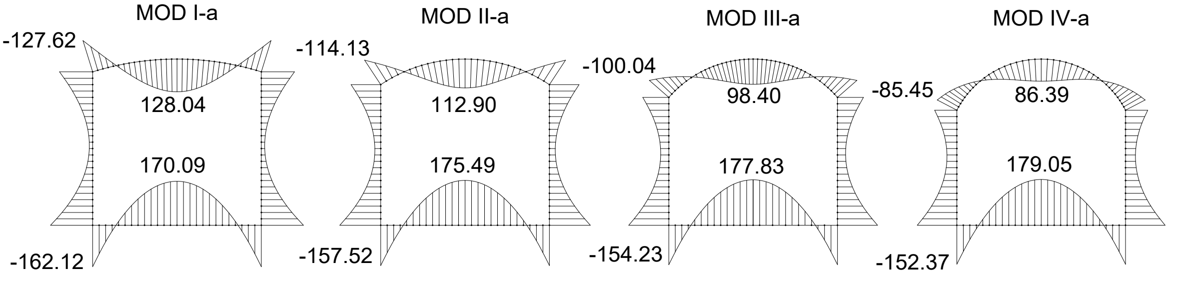

Figure 8. Bending moment diagrams (kN·m) for the modified culvert - Serie a (H = 10m).

Regarding the shear force in the modified culvert, a change occurred in the distribution of values and in the values of bending moments. Figure 9 displays the values of the shear force in the roof for the modified culvert: MOD I-a, MOD II-a, MOD III-a and MOD IV-a. The upper critical sections (CSC and CSQ) show a greater reduction in the shear force.

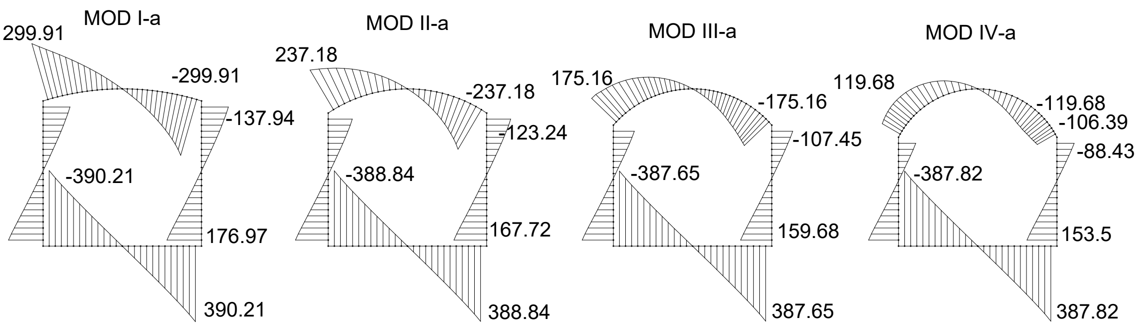

Figure 9. Diagrams of shear force (kN) for the modified culvert - Series a (H = 10m).

The comparison among the different types of culverts defined by three arches considered four geometric proportions; however, all models analyzed had the same internal size. Regarding the distribution of flexion efforts, the more elongated the culvert format, the lower the h_{ext}/b_{ext} ratio, and the lower the effort values. This is due to the stronger influence of horizontal pressures in relation to vertical ones, which can even equal and exceed in magnitude. The more flattened the culvert defined by three arches (horseshoe), the heavier the vertical load on it, and the less significant the benefit of lateral pressures, thus causing greater bending moments. Since vertical pressures tend to be higher than horizontal ones, the advantage in relation to the structural behavior is greater in the "ellipse" section, and gradually decreases in the "lenticular" one [15]. The results of the numerical simulations shown in Figures 10 and 11 confirm this behavior. The analysis of the culverts defined by three arches revealed the most elongated shape culvert (vertical ellipse type) exhibits the best structural behavior; therefore, the lowest internal forces were observed in gallery DTA-I.

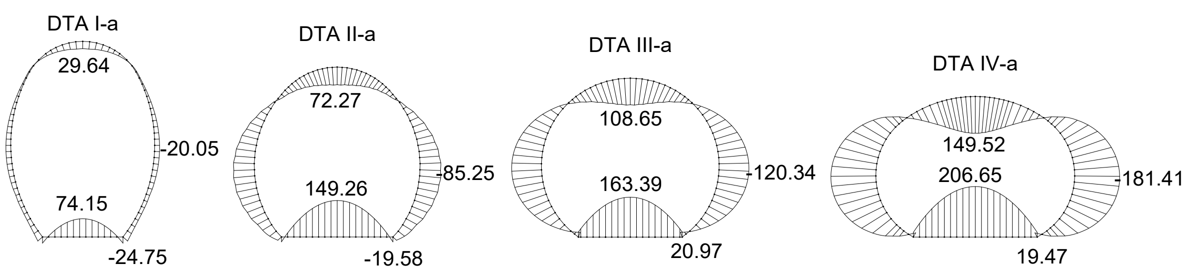

Figure 10. Diagrams of bending moments (kN·m) for culverts defined by three arcs.

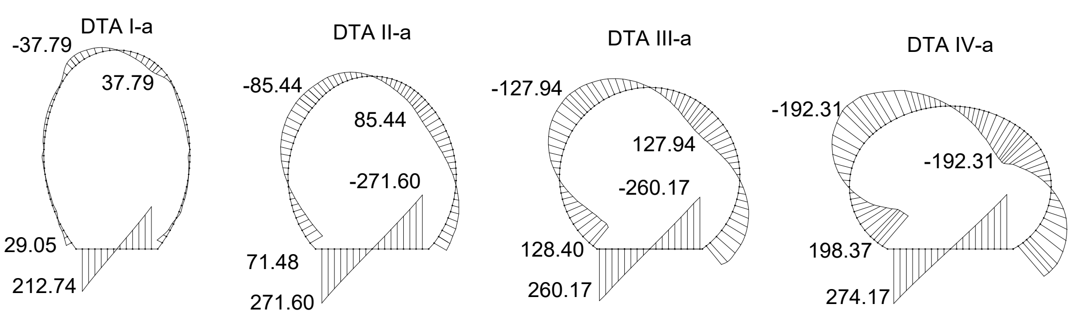

Figure 11. Diagrams of shear force (kN) for culverts defined by three arcs.

3.2 Analysis of thickness change

The thickness of the culverts affects the stress distribution, so that their reduction also decreases the requests acting on the structure, since, as addressed elsewhere, the soil-culvert interaction mobilizes resistant soil mechanisms that support heavier or lighter loads, depending on the flexibility of the structure. The thinner the culvert wall, the stronger its interaction with the ground for supporting important loads. In this case, the strength capacity of the soil is more demanding, which leads to reductions in the values of internal forces. In buried culverts, the materials deformations and soil-structure interaction affect not only the stresses and internal forces, but also the flexural stiffness of the walls of the culverts. The analysis of the proposed series (Series "a", "b" and "c") revealed culverts of thickest base (Serious "c"), therefore, higher flexion stiffness (EI) induces concentrations of stress in this region.

Figure 12 shows an example of variation in the bending moment in modified culverts MOD III-a (Series "a", of 0.25m thickness), MOD III-b (Series "b", of 0.15 m wall thickness and crowning slab, and 0.17m base), and MOD III-c (Series "c", of 0.25m base and side walls thickness and 0.15m equal coverage). The value in parentheses indicates percentage of increase or decrease in the bending moments in relation to MOD III-a of 0.25m thickness.

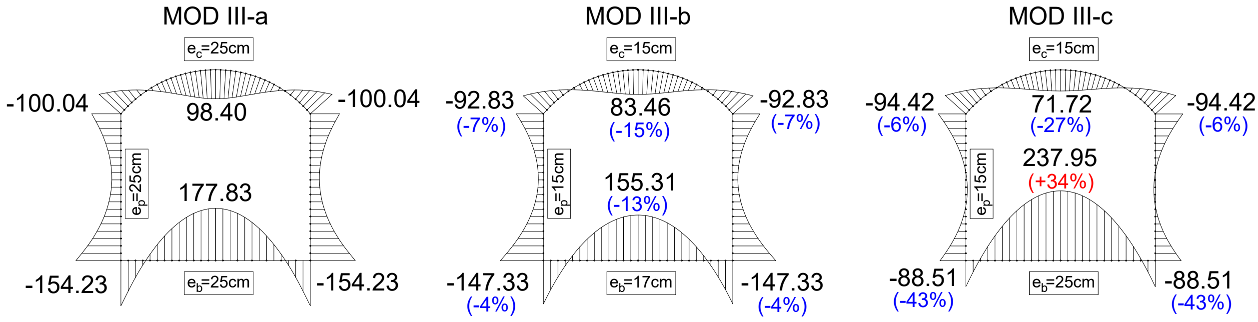

Figure 12. Bending moments (kN·m) for different wall thicknesses in the modified culvert (H = 10m).

When the thickness of Series "a" was reduced to that of Series "b", the value of the moments of all critical sections were reduced, reaching 15% in the critical MLC section. The thinnest wall provided the strongest interaction between the structure and the soil. However, when the 0.25 m thickness in the bottom slab was maintained and the thickness of the side walls and roof slab was reduced to 0.15 m (Series "c"), the rearrangement of the bending moments in MOD III- c displayed unique characteristics. The higher flexural stiffness (EI) caused the bottom slab to concentrate greater bending moment (34% increase in the MLF section compared to the MOD III-a culvert), but the bending moment in the middle of the roof slab (MLC) and in the lower corners (CIQ) significantly decreased, showing 27% and 43% reductions, respectively.

The increased interaction with the ground also mobilizes greater horizontal pressures when the thickness of the walls is reduced. The analysis of the shear force diagrams in Figure 13 shows this increase in the horizontal reaction increases the shear force in the side walls of the thinner culvert (MOD III-b).

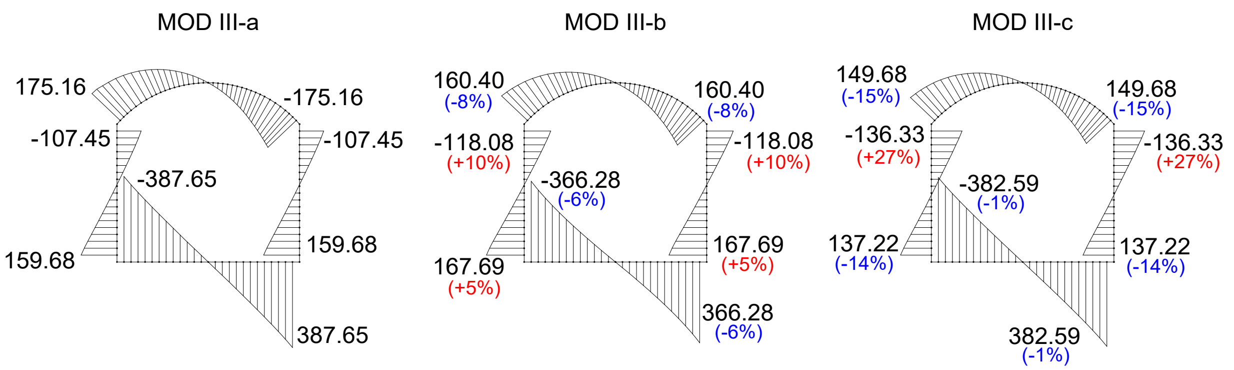

Figure 13. Shear force (kN) for different wall thicknesses in modified culvert (H = 10m)

In general, precast concrete culverts behave as rigid conduits; however, an alternative and relatively simple approach known as relative stiffness (RS) and designed by Gumbel et al. [16] shows some pipes may fall into either category (a flexible or a semi-rigid pipe). The “relative stiffness” criterion refers to the stiffness of the whole system (soil and buried conduit). Regarding the approximation of the sections defined by three arches in a circular section of the same area, only the thickest culverts (Series a) are considered rigid, with values of RS around 7.0. In series “b” and “c”, the systems behave with intermediate relative stiffness, with RS values between 30 and 33, and in the culvert defined by three arcs (Series “d”), the calculation of the relative stiffness provided values of the order of 155 for RR. According to the limits established by Gumbel et al. [16], Series “d” corresponds to a structure that supports 78% of the load imposed on the system. The result shows good measurements of the system for changes in the structure´s stiffness, although this verification is not ideal for other cross-sections, including circular ones.

Figures 14 and 15 show the variations in the bending moments and the shear force, respectively, for DTA II culvert in the analyzed series (Serious “a”, “b “,” c “and” d “), with 10m high embankment (H), illustrating the way a change in thickness affects the efforts in the culvert defined by three arcs.

Similarly to the modified culverts, the results for culverts defined by three arches showed the reduction in the wall thicknesses and increase in the flexibility of the structure reduce the internal forces, due to the greater interaction established with the soil. However, the reductions in the culverts defined by three arches are even more significant than those in the modified culverts, mainly in relation to shear force.

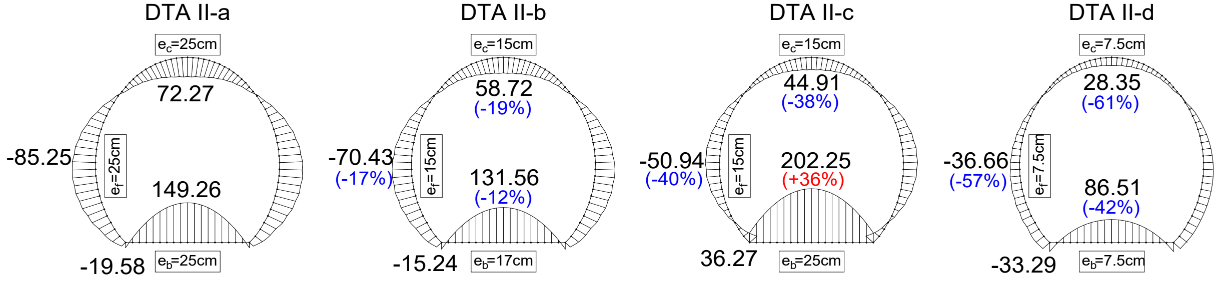

Figure 14. Comparison of the bending moments (kN·m) for DTA II culvert (H = 10m)

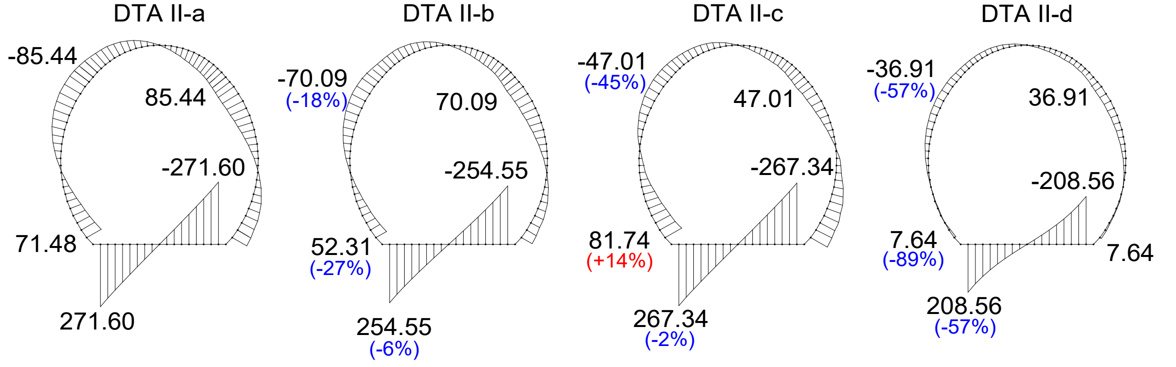

Figure 15. Comparison of the shear force (kN) for DTA II culvert (H = 10m)

The concrete Young’s modulus in Series “d” is higher due to the use of ultra-high performance concrete, but its thickness is small (e = 0.075 m). Therefore, flexural stiffness (EI) is approximately half of that of Series “a”. According to the diagrams of DTA II-d (Figures 14 and 15), the stresses in the structure can suffer a more than 50% reduction in the most requested sections compared to DTA II-a. Moreover, in several less requested regions, the internal forces in the Series “d” culverts show low values, including proportionality between the negative and positive bending moments.

4 COMPARISON OF MATERIAL COSTS

The main comparison in this research is expressed in the Material Cost Index (ICM) per culvert unit - each culvert unit is 1m long in the longitudinal direction. The costs of formwork, factory operations, transportation and assembly do not change among the different alternatives; therefore, the model adopted for the calculation of ICM takes into account the consumption of materials, obtained according to structural design, and the costs of concrete and steel bars. Equation 1 gives the material consumption and cost breakdown for the ICM evaluation:

$$ICM = C_{ba} \cdot R_{ba} + C_{te} \cdot R_{te} + C_{tr} \cdot R_{tr} + C_{C30} \cdot R_{C30} \quad (1)$$

where C_{ba} is the consumption of cut and bent rebar per m^3 of concrete, C_{te} is the consumption of reinforcement welded wire mesh per m^3 of concrete, C_{tr} denotes the consumption of transverse reinforcement per m^3 of concrete, and C_{C30} represents the total consumption of concrete. Resistance class C30 was taken as a reference.

The analysis involved the costs for each type of material, i.e., bent rebar (R_{ba}), reinforcement welded wire mesh (R_{te}), and transverse reinforcement (R_{tr}), all affected, respectively, by coefficients α, β, γ, which consider the reinforcement bar cuttining and bending workmanship, and assembling or welding of each type of reinforcement in relation to the cost of straight steel bars $R_{bar,ret}$ (straight rebar), as shown in Table 4. δ coefficient affects the cost increment in relation to other strength classes for the concrete.

Table 4. Coefficients for the ICM calculation.

Type of cost	Abbreviation	Standard coefficient
Cost of steel rebars	$R_{bar,ret}$	-
Cost of steel rebars (cut and bent rebar)	R_{ba}	$\alpha \cdot R_{bar,ret}$ (steel)/kg
Cost of reinforcement welded wire mesh	R_{te}	$\beta \cdot R_{bar,ret}$ (steel)/kg
Cost of transverse reinforcement	R_{tr}	$\gamma \cdot R_{bar,ret}$ (steel)/kg
Cost of concrete m^3 (relative)	R_{Con}	$\delta \cdot R_{C30}$ (concrete/m^3)

Ratio μ (Equation 2) shows the relationship between the cost of C30 concrete (R_{C30}) and the cost of straight rebar ($R_{bar,ret}$). The expression for the ICM/R_{C30} calculation is given by Equation 3 and should consider the coefficients indicated in Table 4.

$$\mu = \frac{R_{C30}}{R_{bar,ret}} (kg / m^3) \quad \frac{(\text{C30 Cost per m}^3)}{(\text{Rebar Cost per kg})} \quad (2)$$

$$\frac{ICM}{R_{C30}} = \frac{C_{ba} \cdot \alpha}{\mu} + \frac{C_{tel} \cdot \beta}{\mu} + \frac{C_{trans} \cdot \gamma}{\mu} + 1.0 \cdot \delta \quad (3)$$

4.1 Guidelines for design

The verification of the material cost index is based on the consumption of materials according to structural design. Regarding the structural design of reinforced concrete culvert, the internal forces in its walls are characterized by high bending moment values in comparison to normal force (compression), thus configuring a problem of high eccentricity flexure and axial compression load. In this case, the design of reinforcements for sections subjected to axial compression and flexure of high eccentricity presented in Fusco [17] was employed. Table 5 shows the magnitude of the longitudinal reinforcements calculated in the MLF and MLC sections for the design of the analyzed culverts d" = 3.5 cm and 4.5 cm for the inside and outside of the culvert, respectively.

The evaluation of the shear force verification is similar to that of concrete slab. When the transversal reinforcement is not dispensed, the thickness of the wall can be increased, or a transverse reinforcement area can be calculated to resist to the shear force. In this case, the reinforcement area will be calculated like beams (model I), as specified by ABNT NBR 6118 [18]. Table 6 shows the transverse reinforcement value calculated in the MLF and MLC sections for the analyzed culverts.

Table 5. Longitudinal reinforcement for critical sections MLF and MLC.

				Concrete					
				C30		C40		C50	
Culvert	Section(1)	M_d (kN.m)	N_d (kN)	$A_{s,cal}^{(2)}$ (cm²/m)	$A'_{s,cal}^{(2)}$ (cm²/m)	$A_{s,cal}^{(2)}$ (cm²/m)	$A'_{s,cal}^{(2)}$ (cm²/m)	$A_{s,cal}^{(2)}$ (cm²/m)	$A'_{s,cal}^{(2)}$ (cm²/m)
RECTANGULAR (reference)	MLF	167.36	200.29	12.24	3.7	11.81	4.94	11.58	6.17
	MLC	165.44	200.3	12.06	3.7	11.63	4.94	11.4	6.17
MOD I-a	MLF	170.09	189.87	12.78	3.7	12.25	4.94	12.02	6.17
	MLC	128.04	176.89	8.6	3.7	8.4	4.94	8.26	6.17
MOD II-a	MLF	175.49	180.45	13.47	3.7	13.01	4.94	12.68	6.17
	MLC	112.91	193.95	6.78	3.7	6.63	4.94	6.55	6.17
MOD III-a	MLF	177.83	172.34	13.92	3.7	13.38	4.94	13.12	6.17
	MLC	98.44	207.41	5.17	3.7	5.04	4.94	6.17	6.17
MOD IV-a	MLF	179.05	166.13	14.15	3.7	13.61	4.94	13.35	6.17
	MLC	86.38	217.03	3.82	3.7	4.94	4.94	6.17	6.17
MOD I-b	MLF	150.58	185.02	22.42	8.56	21.82	3.36	20.66	4.20
	MLC	112.17	179.97	19.82	8.43	18.96	2.96	17.94	3.70
MOD II-b	MLF	153.35	175.45	23.1	9.07	22.5	3.36	21.4	4.20
	MLC	97.39	200.08	16.07	5.04	15.14	2.96	14.24	3.70
MOD III-b	MLF	155.31	167.2	23.61	9.43	23.01	3.36	21.99	4.20
	MLC	83.46	215.13	12.6	2.22	11.55	2.96	10.98	3.70
MOD IV-b	MLF	156.44	160.86	23.93	9.63	23.33	3.36	22.28	4.20
	MLC	72.17	225.34	9.74	2.22	8.95	2.96	8.55	3.70
MOD I-c	MLF	225.08	168.83	19.48	3.7	18.3	4.94	17.84	6.17
	MLC	104.25	196.58	17.7	6.62	16.84	2.96	15.75	3.70
MOD II-c	MLF	232.59	157.12	20.56	3.7	19.36	4.94	18.87	6.17
	MLC	87.34	218.75	13.42	2.74	12.37	2.96	11.75	3.70
MOD III-c	MLF	237.95	147.28	21.4	3.7	20.16	4.94	19.55	6.17
	MLC	71.72	235.29	9.47	2.22	8.69	2.96	8.29	3.70
MOD IV-c	MLF	241.07	139.95	21.97	3.7	20.59	4.94	19.97	6.17
	MLC	59.29	246.45	6.38	2.22	5.96	2.96	5.73	3.70
DTA I-a	MLF	74.15	256.14	3.7	3.7	4.94	4.94	6.17	6.17
	MLC	29.64	238.6	3.7	3.7	4.94	4.94	6.17	6.17
DTA II-a	MLF	149.26	201.75	10.33	3.7	9.97	4.94	9.83	6.17
	MLC	72.27	222.04	3.7	3.7	4.94	4.94	6.17	6.17
DTA III-a	MLF	163.39	196.96	11.92	3.7	11.42	4.94	11.27	6.17
	MLC	108.65	197.85	6.32	3.7	6.18	4.94	6.17	6.17
DTA IV-a	MLF	206.66	167.4	17.26	3.7	16.47	4.94	16.05	6.17
	MLC	149.85	177.6	10.83	3.7	10.46	4.94	10.33	6.17
DTA I-b	MLF	67.02	261.18	5.41	2.52	5.09	3.36	4.94	4.20

Table 5. Continue ...

	MLC	22.77	244.43	2.22	2.22	2.96	2.96	3.7	3.70
DTA II-b	MLF	131.56	205.31	18.56	5.07	17.78	3.36	16.75	4.20
	MLC	58.72	229.14	6.52	2.22	6.05	2.96	5.83	3.70
DTA III-b	MLF	141.1	202.01	20.37	6.82	19.77	3.36	18.62	4.20
	MLC	89.85	207.2	14.21	3.32	13.22	2.96	12.49	3.70
DTA IV-b	MLF	173.13	169.05	24.31	8.88	23.82	3.55	22.43	4.20
	MLC	123.16	188.85	17.32	3.53	16.31	3.36	15.56	4.20
DTA I-c	MLF	89.55	252.52	3.7	3.7	4.94	4.94	6.17	6.17
	MLC	19.76	247.44	2.22	2.22	2.96	2.96	3.7	3.70
DTA II-c	MLF	202.25	182.48	16.45	3.7	15.67	4.94	15.27	6.17
	MLC	44.91	247.74	3.4	2.22	3.19	2.96	3.7	3.70
DTA III-c	MLF	220.41	175.28	18.78	3.7	17.74	4.94	17.28	6.17
	MLC	75.76	229.65	10.57	2.22	9.66	2.96	9.18	3.70
DTA IV-c(3)	MLF	292.09	129.19	-	-	-	-	-	6.17
	MLC	104.78	226.15	-	-	-	-	-	6.17

(1) Critical sections for design of culverts are given as shown below:

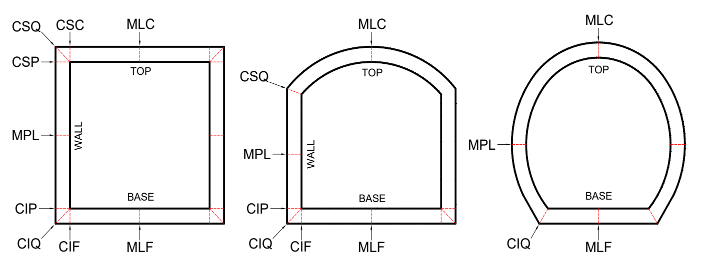

MLC - midspan of the top slab
CSC - superior corner of the top slab
CSQ - top corner
CSP - top corner of wall
MPL - midspan of the side wall
CIP - bottom corner of wall
CIQ - bottom corner
CIF - bottom corner of the bottom slab
MLF - midspan of the bottom slab

(2) Values calculated for CA-60.

(3) DTA IV-c section culvert presented design outside limits.

Note: other information about the design process can be consulted in Domingues [19].

Table 6. Transverse reinforcement for critical sections CIF and CSC of the analyzed culverts.

				Concrete					
				C30		C40		C50	
Culvert	Section(1)	Hn(2)	V_d (kN)	A_{sw}(3) (cm²/m/m)	Stirrups region (m)	A_{sw}(3) (cm²/m/m)	Stirrups region (m)	A_{sw}(3) (cm²/m/m)	Stirrups region (m)
REC. (reference)	CIF		391.79	27.25	0.63	20.51	0.38	14.32	0.25
	CSC		336.11	19.17	0.50	12.50	0.25	6.37	0.13
MOD I-a	CIF		390.21	27.13	0.63	20.41	0.38	14.24	0.25
	CSC		299.91	14.21	0.30	7.26	0.10	0.88	0.05
MOD II-a	CIF		388.84	27.01	0.63	20.32	0.38	14.17	0.25
	CSC		237.18	4.75	0.11	0.00	0.00	0.00	0.00
MOD III-a	CIF		387.65	26.91	0.63	20.23	0.38	14.09	0.25

Table 6. Continue...

	CSC		175.16	0.00	0.00	0.00	0.00	0.00	0.00
MOD IV-a	CIF		386.82	26.83	0.63	20.17	0.38	14.04	0.25
	CSC		106.39	0.00	0.00	0.00	0.00	0.00	0.00
MOD I-b	CIF	X	370.01	36.64	0.88	64.80	0.75	57.00	0.63
	CSC	X	285.68	35.71	0.91	62.02	0.70	53.28	0.60
MOD II-b	CIF	X	367.91	36.37	0.88	64.27	0.75	56.48	0.63
	CSC	X	221.98	24.37	0.80	38.77	0.57	29.77	0.34
MOD III-b	CIF	X	366.28	36.15	0.88	63.85	0.75	56.09	0.63
	CSC	X	160.40	13.46	0.56	16.61	0.28	7.36	0.19
MOD IV-b	CIF	X	365.28	36.02	0.88	63.61	0.75	55.85	0.63
	CSC	X	103.60	0.00	0.00	0.00	0.00	0.00	0.00
MOD I-c	CIF		385.46	26.85	0.63	20.23	0.38	14.14	0.25
	CSC	X	284.37	35.48	0.81	61.59	0.70	52.73	0.60
MOD II-c	CIF		383.85	26.70	0.63	20.10	0.38	14.03	0.25
	CSC	X	216.10	23.22	0.68	36.44	0.45	27.27	0.34
MOD III-c	CIF		382.59	26.58	0.63	19.99	0.38	13.94	0.25
	CSC	X	149.68	11.51	0.37	12.73	0.19	3.40	0.06
MOD IV-c	CIF		381.79	26.51	0.63	19.93	0.38	16.29	0.25
	CSC		92.44	0.00	0.00	0.00	0.00	0.00	0.00
DTA I-a	CIF		212.74	0.00	0.00	0.00	0.00	0.00	0.00
	PI_{Vmax}		37.79	0.00	0.00	0.00	0.00	0.00	0.00
DTA II-a	CIF		271.60	8.90	0.13	2.12	0.13	0.00	0.00
	PI_{Vmax}		85.44	0.00	0.00	0.00	0.00	0.00	0.00
DTA III-a	CIF		260.17	7.36	0.13	0.61	0.13	0.00	0.00
	PI_{Vmax}		127.94	0.00	0.00	0.00	0.00	0.00	0.00
DTA IV-a	CIF		274.18	9.97	0.25	3.33	0.13	0.00	0.00
	PI_{Vmax}		192.31	0.08	0.13	0.00	0.00	0.00	0.00
DTA I-b	CIF		204.55	19.69	0.13	10.60	0.13	2.25	0.13
	PI_{Vmax}		31.44	0.00	0.00	0.00	0.00	0.00	0.00
DTA II-b	CIF		254.55	37.54	0.38	28.98	0.25	21.11	0.25
	PI_{Vmax}		70.08	0.00	0.00	0.00	0.00	0.00	0.00
DTA III-b	CIF		208.91	23.70	0.25	15.17	0.13	7.33	0.13
	PI_{Vmax}		106.49	4.08	0.63	0.00	0.00	0.00	0.00

Table 6. Continue ...

DTA IV-b	CIF	240.03	33.71	0.38	25.28	0.25	17.53	0.13
	PI_{Vmax}	161.45	20.46	2.69	12.70	2.56	5.62	2.06
DTA I-c	CIF	209.05	0.00	0.00	0.00	0.00	0.00	0.00
	PI_{Vmax}	30.64	0.00	0.00	0.00	0.00	0.00	0.00
DTA II-c	CIF	267.34	8.83	0.13	2.16	0.13	0.00	0.00
	PI_{Vmax}	59.39	0.00	0.00	0.00	0.00	0.00	0.00
DTA III-c	CIF	253.76	6.91	0.13	0.27	0.05	0.00	0.00
	PI_{Vmax}	95.22	0.00	0.00	0.00	0.00	0.00	0.00
DTA IV-c	CIF	263.33	0.00	0.00	2.26	0.00	0.00	0.00
	PI_{Vmax}	143.48	16.81	2.56	9.21	2.38	2.25	0.44

(1) Critical sections for design of culverts are given as shown below::

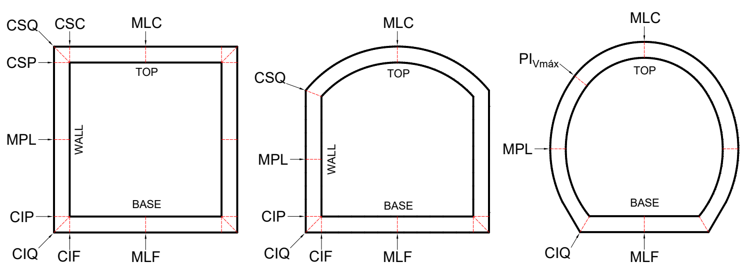

MLC - midspan of the top slab

CSC - superior corner of the top slab

CSQ - top corner

CSP - top corner of wall

MPL - midspan of the side wall

CIP - bottom corner of wall

CIQ - bottom corner

CIF - bottom corner of the bottom slab

MLF - midspan of the bottom slab

$PI_{Vmáx}$ - intermediate point of shear

(2) Haunch must be specified at the designer's discretion.

(3) The transverse reinforcement for the culverts are usually arranged in 4-legged, 6-legged or 8-legged stirrups.

Note: other information about the design process can be consulted in Domingues [19].

Concrete reduction coefficients $\gamma_c = 1.3$ and steel $\gamma_s = 1.1$ were adopted for the proposed culverts, considering a strict quality control. Apart from the checks performed, the culverts required the checking of fatigue, unacceptable cracking, handling, and stresses from changes in the direction of the longitudinal reinforcements. In the curved segments, possible stresses tend to rectify the longitudinal rebar. The curved rebar is checked according to the recommendations of Leonhardt and Mönnig [20] and Fusco [21]. Additional transverse reinforcements are provided in cases of significant angular deviations that can cause intense transverse tensile stresses in the concrete.

Figure 16 illustrate the steel rebar arrangement for the modified culvert and culvert defined by three arches, respectively. An assembly reinforcement consisting of a reinforcement welded wire mesh made of CA-60 steel is provided, and a more longitudinal CA-50 steel rebar is supplied in regions of greatest stresses. When the structural design imposes transverse reinforcement on the shear force, the stirrups must be allocated in regions of maximum shear force, or other verification with haunches can be performed.

For more information on the structural design of precast concrete culverts, reader can refer to the technical manual “Projeto estrutural de galerias e canais com aduelas de concreto pré-moldadas” from the ABTC (Associação Brasileira dos Fabricante de Tubos de Concreto) [22].

4.2 Evaluation of the cost index

The analysis based on the material cost index (ICM) takes into account the total costs for the production of the culverts (e.g., labor for assembly) and amount of materials consumed for each culvert. Value changes are established according to the coefficients of Equation 3.

μ was set to 71.55m^3/kg, according to the cost per cubic meter (m^3) of C30 concrete and cost per kilo (kg) of straight steel rebar [23]. The other cost index adopted are shown in Tables 7 and 8.

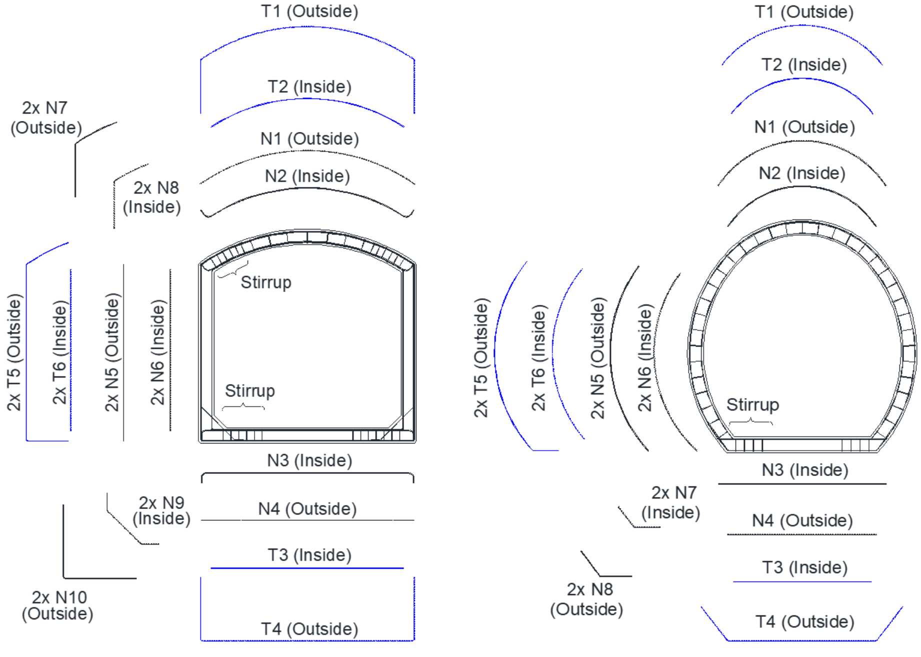

Figure 16. Reinforcement arrangement in culverts modified and defined by three arches.

Table 7. Steel cost index.

Coefficient	Value adopted	Additional consideration
α	1.5	Includes the cost of cutting, bending and assembly
β	1.2	Includes the cost of welding, bending and assembly
γ	2.0	Includes the cost of cutting, bending and assembly

Table 8. Concrete cost index.

Concrete strength class	δ adopted	Additional consideration
C30	1.1	Includes placement
C40	1.2	Includes placing and increasing cement consumption
C50	1.4	Includes placement, increased cement consumption and higher technological control

The analysis of the material cost index (ICM) of the modified culverts verified the ICM/RC30 values per unit and compared them for the three-thickness series (Series a, b and c), according to Figures 17a, respectively. Each unit was dimensioned for landfill height H = 10 m. The dotted line indicates the value of ICM/RC30 for the box culvert (RET I-a) dimensioned with C30 concrete, kept as a reference for all comparisons. The influence of the characteristic strength of concrete to compression was also verified for each series, and the design verification was calculated for C30, C40 and C50 concretes.

The analysis of the material cost index revealed the proposed modified culverts are economically viable for “a” and “c” series. Regarding Series “b”, despite the improvement in relation to the internal forces in the upper section of the culvert, the base region kept the same proportion of strength, and, therefore, no gain is acquired if the thickness of the bottom slab of the modified culverts is reduced.

The material cost index (ICM) of the standard box culvert is 7.59. On the other hand, the ICM of the modified culvert (MOD IV-c) is 5.54, which represents 27% savings. A design optimization for C30 concrete with 25cm thickness (Series a) is observed, since the soliciting efforts were adequately covered in the design with the C30 concrete. Many regions after structural design are calculated as minimum reinforcement areas, therefore, the increase in the concrete strength led to an increase in the minimum reinforcement rates. Another implication is the cost of the manufacture of more resistant concrete is also higher (e.g., C40 concrete is 20% more expensive ($\delta = 1.20$) than the reference concrete). In other loading situations, however, an opposite effect is observed, proving the importance of assessing ICM in each case.

The graphs in Figure 17b show the material cost indices (ICM/R_{C30}) of the culverts defined by three arcs for Series “a”, “b” and “c”.

The culverts defined by three arches exhibit an excellent behavior regarding thickness reduction, if proportions are maintained in an elliptical or horseshoe shape. The cost index in the culverts defined by three arcs shows, therefore, up to 54% savings, relative to the ICM of culvert DTA I-c, with a value of 3.22. As shown in Figures 17b, DTA IV could not be dimensioned - such a specific culvert of lenticular-type format was dimensioned outside the limits of the composite flexion model used.

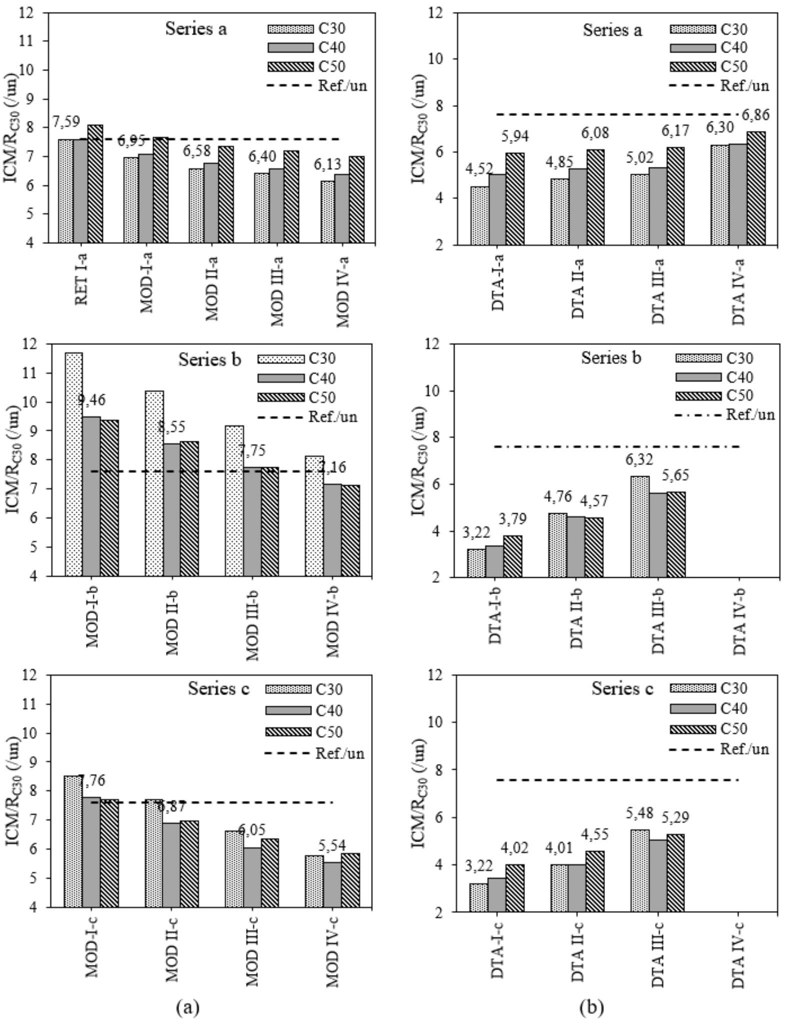

Figure 17. Cost index for (a) modified culverts and (b) culvert defined by three arcs.

According to the ICM values and the results shown in Tables 5 and 6, an increase in the concrete fck, despite reducing the reinforcement calculated in certain regions, increases the minimum reinforcement areas, thus leading to a slightly higher ICM of higher strength concretes in comparison to reference C30 concrete.

The ICM indications do not consider expenses with molds and that the coefficients adopted in the expression for their calculation may vary according to the market or region.

5 CONCLUSIONS

This article has reported a numerical investigation on the behavior of culverts at great depths (H> B_c), and, according to the results for the box culvert and the proposed culverts with unusual cross sections, the following conclusions can be drawn:

a) The analysis of the diagrams showed changes in the geometries of the cross sections significantly changed the requesting strength. In modified culverts, larger arrows in the coverage arc decrease the stress in the upper part in both bending moments and shear force, with no changes in the lower part. Regarding culverts defined by three arches, cross sections of ellipse shape promote the best distribution of strength, and the greater the radius of the lateral arc (r_f) in relation to the radius of the coverage arc (r_c), the lesser the strength. Moreover, a decrease in the width of the bottom slab (b) also reduces the stress at the base.

b) The stress acting on the culverts is lower when the thicknesses of the walls are reduced, due to a stronger interaction established with the soil, thus mobilizing a higher strength capacity of the surrounding soil, and a change in the flexural rigidity (EI) of the bottom slab in relation to the EI adopted for the side walls and roof affects the stress distribution.

c) The dimensions demonstrated the viability of the proposed cross sections for installation under elevated embankments. The cost index enabled the quantification of the materials savings for the modified culverts, which represent 5% to 27% in the analyzed models in comparison to the box culverts, according to the thickness of the walls and the proportion in the abatements of the arch roof. Moreover, an analysis of the cost index for the culvert defined by three arches proved even more optimistic, with material savings ranging from 17 to 54% in comparison to the box culvert. The analysis of the dimensions for the culvert defined by three arches also revealed a reduction in the thickness of the walls is quite efficient for sections of “ellipse” and “horseshoe” types; however, the thickness of “lenticular” culverts should not be reduced if rf is much lower than r_c.

The replacement of the box culvert for the unusual cross-sectional culvert reduces the requesting stress. Regarding the reduction in the thicknesses usually employed, the greater the interaction between the structure and the soil, the smaller the bending moments, due to the greater participation of the resistant mechanism of the soil. A reduction in thickness causes the structure to become less resistant to the stress produced by high localized pressures.

ACKNOWLEDGEMENTS

The authors acknowledge the Coordenação de Aperfeiçoamento de Pessoal de Nível Superior - Brazil (CAPES) – [Código de Financiamento 001] for the financial support, and the Brazilian Association of Concrete Pipe (ABTC - Associação Brasileira dos Fabricantes de Tubos de Concreto). The first author is indebted to the School of Engineering of São Carlos and CNPq, for the financial support for the continuation of the research through the granting of a doctoral scholarship.

REFERENCES

[1] B. D. S. Bueno and Y. D. J. Costa, *Dutos Enterrados: Aspectos Geotécnicos*. São Carlos: EESC-USP, 2009.

[2] Departamento Nacional de Infraestrutura de Transportes, *Planilha de Preços Unitários da Rodovia BR-242/TO: Trecho Divisa BA/TO a Divisa TO/MT.* Brasília, 2012.

[3] VALEC Engenharia, Construções e Ferrovias S.A., *Estudo de Viabilidade Técnica, Econômica e Ambiental (EF-151): Trecho Itumbiara/GO – Goiânia/GO – Brasília/DF.* Brasília, 2012.

[4] M. K. El Debs, “Contribuição ao projeto de galerias enterradas: alternativas em argamassa armada,” Ph.D. dissertation, SET-EESC, São Carlos, 1984.

[5] K. Kim and C. H. Yoo, "Design loading on deeply buried box culverts," *J. Geotech. Geoenviron. Eng.*, vol. 131, no. 1, pp. 20–27, 2005.

[6] M. Pimentel, P. Costa, C. Félix, and J. Figueiras, "Behavior of reinforced concrete box culverts under high embankments," *J. Struct. Eng.*, vol. 135, pp. 366–375, Apr 2009.

[7] O. S. A. Abuhajar, “Static and seismic soil culvert interaction,” Ph.D. dissertation, Prog. Civ. Environ. Eng., Univ. Western Ontario, Ontario, 2013.

[8] J. D. Marshall, J. B. Anderson, R. L. Meadows, and T. J. Jensen, "Full-scale testing of three-sided precast concrete arch sections," *J. Bridge Eng.*, vol. 19, no. 12, 04014051, 2014.

[9] M. Zoghi and D. N. Farhey, "Performance assessment of a precast-concrete, buried, small arch bridge," *J. Perform. Constr. Facil. Wash.*, vol. 20, pp. 244–252, Aug 2006.

[10] M. K. El Debs, *Projeto Estrutural de Tubos de Seção Retangular de Concreto Armado*, 1a. ed. Ribeirão Preto: Associação Brasileira dos Produtores de Tubos de Concreto, 2008.

[11] R. M. Bennett, S. M. Wood, E. C. Drumm, and N. R. Rainwater, "Vertical loads on concrete box culverts under high embankments," *J. Bridge Eng.*, vol. 10, no. 6, pp. 643–649, 2005.

[12] C. H. Evans, “An examination on arching in granular soils,” M.S. thesis, Dept. Civ. Eng., Massachusetts Inst. Technol., Massachusetts, 1983.

[13] GEOSLOPE International Ltd., *Stress-Deformation Modeling with SIGMA/W*. Calgary, 2013.

[14] Comitté Euro-International Du Béton, *CEB-FIP Model CODE 2010: First Complete Draft, vol. 1* (Bulletin 55). Alemanha, 2010.

[15] M. K. El Debs, *Concreto Pré-Moldado: Fundamentos e Aplicações*, 2a ed. São Paulo: Oficina de Textos, 2017.

[16] J. E. Gumbel, M. P. O’Reilly, L. M. Lake, and D. R. Carder, “The development of a new design method for buried flexible pipes,” in *Europe ’82. Proc. Basel*, 1982.

[17] P. B. Fusco, *Estruturas de Concreto: Solicitações Normais*. Rio de Janeiro: Guanabara Dois, 1981.

[18] Associação Brasileira de Normas Técnicas, *Projeto de Estruturas de Concreto*, NBR 6118, 2014.

[19] A. B. Domingues, “Contribuição ao projeto estrutural de galerias de concreto pré-moldado com seções transversais não usuais,” M.S. thesis, Esc. Eng. São Carlos, Univ. São Paulo, São Carlos, 2017.

[20] F. Leonhardt and E. Mönnig, *Construções em Concreto: Princípios Básicos Sobre a Armação de Estruturas de Concreto Armado, vol. 3.* Rio de Janeiro: Interciência, 1978.

[21] P. B. Fusco, *Técnicas de Armar as Estruturas de Concreto*, 7a ed. São Paulo: PINI, 1995.

[22] Associação Brasileira dos Fabricantes de Tubos de Concreto, *Projeto Estrutural de Galerias e Canais com Aduelas de Concreto Pré-Moldadas*, 2018.

[23] Sistema Nacional de Pesquisa de Custos e Índices da Construção Civil, *Tabela de Preços e Custos de Referência: SINAPI Relatório de Insumos e Composições – Jan/17 – Com Desoneração.* Rio de Janeiro, 2017.

Author contributions: ABD: conceptualization, methodology, numerical analysis, formal analysis, writing; MKD: conceptualization, methodology, supervision.

Editors: Vladimir Guilherme Haach, José Luiz Antunes de Oliveira e Sousa, Guilherme Aris Parsekian.

IBRACON
IBRACON Structures and Materials Journal
Revista IBRACON de Estruturas e Materiais
ISSN 1983-4195 ismj.org
SciELO

ORIGINAL ARTICLE

Advanced computer model for analysis of reinforced concrete and composite structures at elevated temperatures

Modelo computacional avançado para análise de estruturas de concreto armado e mistas em elevadas temperaturas

Natan Sian das Neves[a]
Rodrigo Silveira Camargo[b]
Macksuel Soares de Azevedo[b]

[a]Universidade Federal do Rio de Janeiro – UFRJ, Instituto Alberto Luiz Coimbra de Pós-graduação e Pesquisa de Engenharia – COPPE, Centro de Tecnologia, Programa de Engenharia Civil, Rio de Janeiro, RJ, Brasil

[b]Universidade Federal do Espírito Santo – UFES, Programa de Pós-graduação em Engenharia Civil, Vitória, ES, Brasil

Received 04 September 2020
Accepted 16 November 2020

Abstract: This paper is concerned on the development of a computational model based on finite element procedures for advanced analysis capable of estimating the behavior of reinforced concrete and composite steel-concrete plane structures exposed to fire. The program implemented is called NASEN, the specific thermo-structural module is used to analyze structures under fire conditions. The effects of geometric nonlinearity, material nonlinearity and nonlinear thermal gradients are incorporated into the model, as well as the degradation of material properties with increased temperature. The methodology applied for the solution is based on the unidirectional coupling of the thermal and mechanical solutions. The cross-sections of the structural elements are discretized with two-dimensional meshes for thermal analysis, while the structural analysis uses a one-dimensional beam-column element. Numerical examples are presented to demonstrate the accuracy of the computational code developed in relation to the numerical and experimental solutions found in the literature. In summary, the program adequately predicted the response of the studied structures.

Keywords: finite elements, concrete-steel, fire, thermo-structural, computational model.

Resumo: O presente artigo tem como objetivo o desenvolvimento de um modelo computacional com base nos procedimentos do método dos elementos finitos. A análise avançada é capaz de estimar o comportamento de estruturas planas de concreto armado e, mistas de aço e concreto em situação de incêndio. O programa computacional implementado é denominado de NASEN e, utiliza um módulo termo-estrutural específico para análise de estruturas em condição de incêndio. Incorpora-se ao modelo os efeitos da não linearidade geométrica, não linearidade do material e gradientes térmicos não lineares, bem como a degradação das propriedades dos materiais com aumento da temperatura. A metodologia aplicada para solução tem como base o acoplamento unidirecional das soluções térmicas e mecânicas. As seções transversais dos elementos estruturais são discretizadas com malhas bidimensionais para análise térmica, enquanto a análise estrutural utiliza elemento unidimensional de viga-coluna. Exemplos numéricos são apresentados para demonstrar a precisão do código computacional desenvolvido em relação as soluções numéricas e experimentais encontradas na literatura. O programa computacional prevê adequadamente a resposta das estruturas estudadas.

Palavras-chave: elementos finitos, concreto-aço, incêndio, termo-estrutural, modelo computacional.

How to cite: N. S. Neves, R. S. Camargo, and M. S. Azevedo, “Advanced computer model for analysis of reinforced concrete and composite structures at elevated temperatures,” *IBRACON Struct. Mater. J.*, vol. 14, no. 4, e14410, 2021, https://doi.org/10.1590/S1983-41952021000400010

Corresponding author: Natan Sian das Neves. E-mail: natan.sian@gmail.com
Financial support: FAPES: 34904.539.18954.23022018-8983.
Conflict of interest: Nothing to declare.

1 INTRODUCTION

Reinforced concrete and composite steel-concrete structures are widely used in civil construction as load-bearing mechanism in industrial and resistance buildings, bridges and among other engineering applications. In addition to conventional service loads, these structures may be exposed to fire during their design life. Therefore, the verification of these elements in response to fire is essential for designs and analysis of physical behaviors.

In the design context, the thermal and mechanical response and fire resistance of concrete and composite structural elements are usually characterized by the use of simplified calculation methods and tables based on numerical and experimental research [1]. The simplified calculation methods have a limited scope due to their ability to simulate only simple structural components, for example, Eurocode 2 part 1-2 [2] prescribes a methodology to evaluate the fire resistance of structural members using the isotherm method 500ºC.

In general, the geometric effects, support conditions and advanced physical characteristics of the systems are not considered in simplified methods. In this way, the use of advanced calculation methods based on computational tools allows a investigation on complex and highly nonlinear behavior of structures exposed to fire due to large strains and material degradation.

Currently, several engineering software packages are available in academia and industry, such as the generic solutions ANSYS [3] and ABAQUS [4], and specialist packages in the area of structures under fire conditions, such as SAFIR [5] and VULCAN [6]. In addition to finite element (FE) software packages, the development of computational codes is a methodology used in engineering. This line of research requires a knowledge of the numerical solution procedures, physical-mathematical models and characteristics of the studied physical phenomenon, enabling a wide understanding of the physical behavior of the problem [7]. Computational models able to describe the behavior of structures in fire have been developed considering different physical-mathematical approaches, such as the use of the direct stiffness method based on the stability and bowing functions [8], the approach of the embedded and extended finite element model [9], [10], the use of customized beam finite element with skeletal structures [11] and among other methodology and analysis models [12], [13], [14].

In Brazil, there is few scientific researches in the area of developing computer programs for advanced thermomechanical analysis of reinforced concrete or composite steel-concrete structures subjected to fire. In recent decades, research by Caldas [15], Mouço [16], Ribeiro [17] and Maximiano [18] stands out. Recently, Neves [19] presents the computational model NASEN (Numerical Analysis System for Engineering), a program aimed at solving initial engineering problems in the acoustic, thermal, structural and thermo-structural areas. This study presents the specific module for thermo-structural analysis of concrete or composite plane elements under fire condition, NASEN/TSA-FIRE (Thermal-Structural Analysis-Fire). Among the general characteristics of the code, an updated Lagrangian formulation of a beam-column plane element associated with the fiber model is considered, the effects of thermal gradients on the cross-section, degradation of physical and mechanical properties as a function of temperature, large displacements and the actions of the equivalent thermal forces.

2 BASIC THEORY OF THERMO-STRUCTURAL ANALYSIS

The numerical solution of the thermomechanical problem of structures under high temperatures is based on the knowledge of aspects and parameters related to the modeling of the gases of the environment in fire, the knowledge of the temperature distribution in the cross section of the elements and the behavior of the mechanical response of the structural system.

2.1 Heat transfer analysis

The prediction of the thermal field is computed at the level of the cross-section of the structures under fire condition, using a discretization based on plane elements, as shown in Figure 1. The governing equation of the physical phenomenon is described by the transient differential model of conduction of two-dimensional heat [1], [20], as given by Equation 1.

$$\nabla^{T} D \nabla \theta + f = \rho c \frac{\partial \theta}{\partial t} \tag{1}$$

Where θ is the temperature of the structure, t is the time, f is the internal heat generation, ρ is the density of the material, c is the specific heat and $\mathbf{D} = \lambda \mathbf{I}$ is the thermal conductivity matrix for an isotropic material. In the area of structures in fire, the physical properties of the materials vary with temperature, making Equation 1 nonlinear. The properties of concrete and steel follow the recommendations prescribed in Eurocode 2 part 1-2 [2] and Eurocode 3 part 1-2 [21]. The effects of convection and radiation caused during exposure to fire are considered by the boundary conditions of the problem, according to Equation 2.

$$q_n = h(\theta - \theta_g) = [h_c + h_r](\theta - \theta_g) \tag{2}$$

Since θ_g is the gas temperature in the proximity of the fire exposed member, h_c and h_r are called convection and radiation coefficients respectively. Temperature-time curves are used to simplify the evolution of fire behavior [22], for example, the ISO 834 [23] and ASTM E119 [24] curves, as shown in Equation 3 and Equation 4.

i) ISO 834 fire curve

$$\theta_g = \theta_0 + 345\log(8t+1) \tag{3}$$

ii) ASTM E119 fire curve

$$\theta_g = \theta_0 + 750\left(1 - e^{-3,79533\sqrt{t_h}}\right) + 170,41\sqrt{t_h} \tag{4}$$

Where θ_0 is the initial ambient temperature, t and t_h are the times of exposure to fire in min and hours respectively. In this way, the numerical solution of Equation 1 is based on Galerkin finite element procedures. The approximation of the temperature field is constructed based on the interpolation functions [7], [25], as shown in Equation 5.

$$\theta \approx \sum_{i=1}^{n} N_i \theta_i = N\theta \tag{5}$$

The vector of the interpolation functions is given by $\mathbf{N} = [N_1\, N_2\, \dots N_n]$ and the nodal temperature vector is equal to $\boldsymbol{\theta} = [\theta_1\, \theta_2\, \dots \theta_n]^T$. Thus, applying weighted residual sentences, theorems of differential-integral calculus and the approximation given in Equation 5, the resulting system of equations in matrix form is given by Equation 6.

$$\mathbf{C}_\theta \left\{\frac{\partial \theta}{\partial t}\right\} + \mathbf{K}_\theta \{\theta\} = \mathbf{F}_\theta \tag{6}$$

The total capacitance matrix $\mathbf{K}_\theta$ is composed of the contribution of the thermal conductivity matrix and the matrix due to the combined effects of convection-radiation, as given by Equation 7.

$$K_\theta = \int_\Omega \mathbf{B}^T \mathbf{D} \mathbf{B} d\Omega + \int_\Gamma h N^T N d\Gamma \tag{7}$$

The temperature gradient matrix **B** is written according to the finite element interpolation functions, $\nabla\theta = \nabla\mathbf{N}\boldsymbol{\theta} = \mathbf{B}\boldsymbol{\theta}$. The thermal capacity matrix $\mathbf{C}_\theta$ is given by Equation 8, considering the interpolation functions and the product between density and specific heat.

$$\mathbf{C}_\theta = \int_\Omega \mathbf{N}^T \rho c \mathbf{N} d\Omega \tag{8}$$

The vector of thermal actions $\mathbf{F}_\theta$ is given by Equation 9.

$$\mathbf{F}_\theta = \int_\Omega \mathbf{N}^T f d\Omega + \int_\Gamma h\mathbf{N}^T \theta_g d\Gamma \tag{9}$$

The finite difference technique is applied to approximate the first order temporal differential operator [19]. The effective algebraic system computed at $n+1$ is given by Equation 10.

$$\left(\frac{\mathbf{C}_\theta}{\Delta t} + \beta \mathbf{K}_\theta\right)\{\theta_{n+1}\} = \left(\frac{\mathbf{C}_\theta}{\Delta t} - (1-\beta)\mathbf{K}_\theta\right)\{\theta_n\} + (1-\beta)\mathbf{F}_{\theta,n} + \beta \mathbf{F}_{\theta,n+1} \tag{10}$$

Where Δt is the time step and β is the time integration parameter equal to 2/3, characterizing an unconditionally stable scheme.

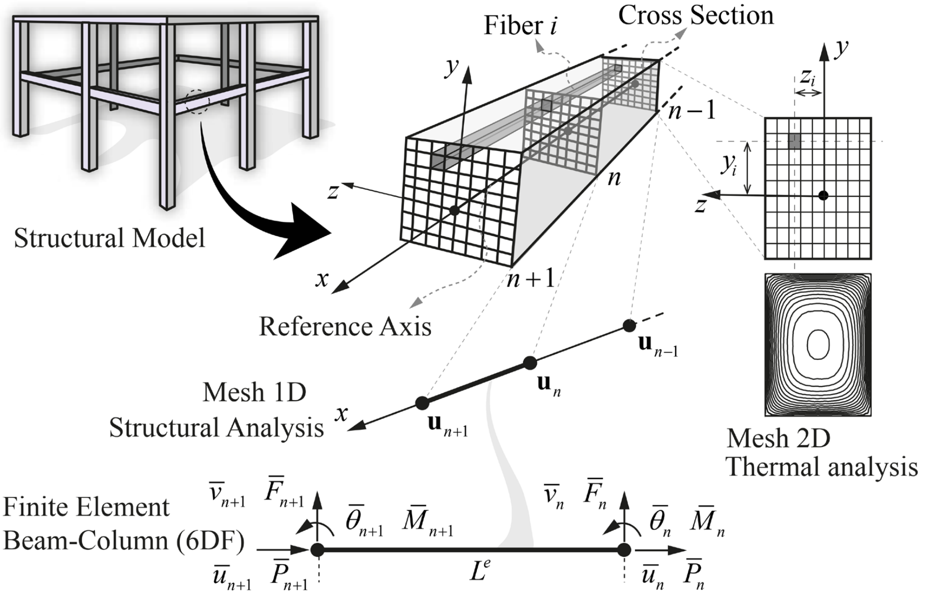

Figure 1. Levels of discretization of the structural element.

2.2 Mechanical analysis

The structural nonlinear analysis is constructed based on the plane beam-column element with six degrees of freedom (6DF), two translations and one rotation at each element node, as shown in Figure 1. Thus, the differential deformation relationships-displacement based on the Green-Lagrange tensor, accounting for axial and shear deformations, as shown below.

$$\varepsilon_{xx} = \frac{du_x}{dx} + \frac{1}{2}\left[\left(\frac{du_x}{dx}\right)^2 + \left(\frac{du_y}{dx}\right)^2\right] \tag{11}$$

$$\varepsilon_{xy} = \frac{1}{2}\left(\frac{du_x}{dy} + \frac{du_y}{dx}\right) + \frac{1}{2}\left(\frac{du_x}{dy}\frac{du_x}{dx} + \frac{du_y}{dy}\frac{du_y}{dx}\right) \tag{12}$$

The first terms represent the linear parts and the other terms correspond to the non-linear parts, according to Equation 11 and Equation 12. The Euler-Bernoulli hypothesis is also adopted, which establishes that the plane cross-sections remain normal to the axis of element in flexion. In this way, the displacements u_x and u_y at a generic point can be associated with the displacements u and v of the beam, as given by Equation 13.

$$u_x = u - y\left(\frac{dv}{dx}\right) \qquad u_y = v \tag{13}$$

Thus, following the principle of virtual displacements and performing some mathematical operations, the integral sentence resulting from the nonlinear structural problem, disregarding the high order terms [26] is given below by Equation 14.

$$\begin{gathered}\int_0^L \left[EA\frac{du}{dx}\frac{d\delta u}{dx} + EI_z\left(\frac{d^2v}{dx^2}\right)\left(\frac{d^2\delta v}{dx^2}\right)\right]dx + \\ \cdots + \frac{1}{2}\int_0^L \left[{}^tF_x\delta\left(\left(\frac{du}{dx}\right)^2 + \left(\frac{dv}{dx}\right)^2\right)\right]dx = \{\delta u\}^T\left\{{}^{t+\Delta t}f - {}^tf\right\}\end{gathered} \tag{14}$$

Based on finite element procedures, the field of axial and vertical displacement is approached with the aid of interpolation functions, as shown in Equation 15 and Equation 16 respectively.

$$u = N_1\bar{u}_1 + N_2\bar{u}_2 = \{\bar{N}_1\}\{\bar{u}\} \tag{15}$$

$$v = N_3\bar{v}_1 + N_4\bar{\theta}_1 + N_5\bar{v}_2 + N_6\bar{\theta}_2 = \{\bar{N}_3\}\{\bar{v}\} \tag{16}$$

The terms $\bar{\mathbf{N}}_1$ and $\bar{\mathbf{N}}_3$ represent the vectors of the interpolation functions, linear for axial displacement and cubic for transversal displacement respectively. The approximations presented in Equation 15 and Equation 16 are applied in the integral formulation of the problem, as shown in Equation 14. As the virtual displacements are arbitrary at the natural boundary, consequently, the resulting algebraic system is given by Equation 17.

$$\left[K_e + K_g\right]\{\Delta d\} = \{\Delta f\} \tag{17}$$

Where $\Delta\mathbf{d}$ and $\Delta\mathbf{f}$ are the displacement and force incremental vectors, respectively. The matrix of elastic stiffness $\mathbf{K}_e$ is obtained by the numerical evaluation of the first terms of Equation 14, as shown below in Equation 18.

$$K_e = \int_0^L \{\bar{N}_1'\}EA\{\bar{N}_1'\}^T dx + \int_0^L \{\bar{N}_3''\}EI\{\bar{N}_3''\}^T dx \tag{18}$$

The nonlinear term is computed in the geometric matrix $\mathbf{K}_g$, given by Equation 19, where a simplified theory is adopted that disregards the combined effects of axial and flexural behavior [27].

$$K_g = \int_0^L {}^tF_x\{\bar{N}_1'\}\{\bar{N}_1'\}^T dx + \int_0^L {}^tF_x\{\bar{N}_3'\}\{\bar{N}_3'\}^T dx \tag{19}$$

Having defined the elementary elastic and geometric matrices for each element of the structural system, the global stiffness matrix is constructed by the composition of the local matrices of each element. In addition, the equivalent axial (*EA*) and flexural (*EI*) stiffnesses are calculated in relation to the fibers of the cross-section, as shown in the following.

$$EA = \int_A E_\theta dA \qquad EI = \int_A E_\theta y^2 dA \tag{20}$$

In the computational model developed, the reduction factor of the elasticity modulus of the concrete as a function of temperature, based on the experimental results obtained by Hertz [28] at the Technical University of Denmark, is approximately equal to the square of the reduction factor of the compressive strength of the concrete. This simplification is a particular characteristic of the zone method described in Eurocode 2 part 1-2 [2].

The equivalent stiffnesses are computed based on the values of the elasticity modulus of the materials. In a fire condition, there are numerous models available in the literature to describe the degradation of the modulus of elasticity of steel [21], [29]-[31] and concrete [2], [32]-[36] as a function of temperature rise, as can be seen in Figure 2.

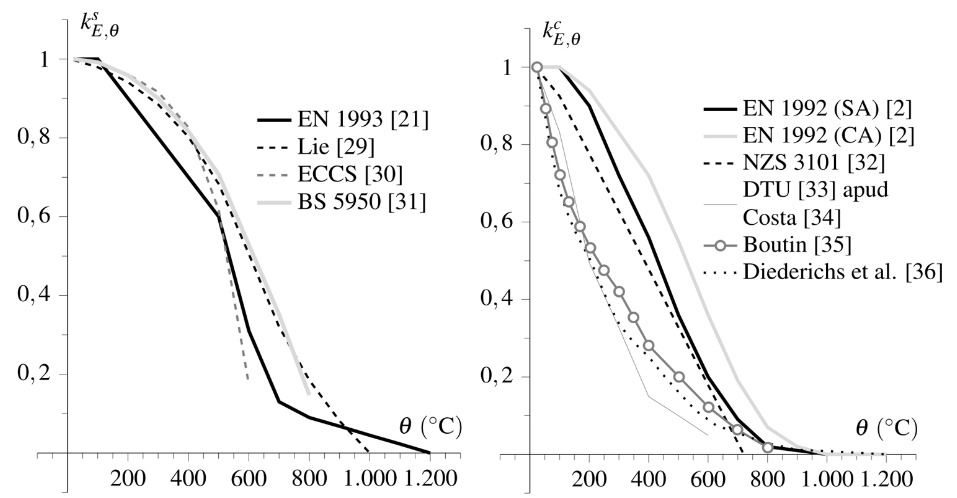

Figure 2. Reduction curves for the elasticity modulus of steel $\left(k^s_{E,\theta}\right)$ and concrete $\left(k^c_{E,\theta}\right)$ as a function of temperature.

The effects of temperature in the cross-section of the structure are computed in the beam-column model based on the vector thermal fixed-end forces $\mathbf{f}_{th}$, consisting of the contributions of the effects of thermal expansion and curvature due to the gradients temperature [16]. The components of the vector are shown in the following.

$$P_\theta = \int_A \varepsilon_{th} E_\theta dA \qquad M_\theta = \int_A \varepsilon_{th} E_\theta y dA \tag{21}$$

Where ε_{th} is coefficient of thermal expansion of the materials due to the increase in temperature in the structural element, following the behavior described in European codes [2], [21]. In addition, the vector thermal fixed-end forces is included in the global force vector of the structural system.

2.3 Unidirectional coupling of thermal and mechanical processes

The two-way unidirectional (or sequential) coupling is based on thermal and mechanical solvers in a similar strategy used in the research by Barros et al. [37], Caldas et al. [38] and Silva and Landesmann [39]. Figure 3 illustrates the general process of the solution steps adopted in the advanced computational model developed. The program starts by performing a structural nonlinear analysis at ambient temperature, considering external loads. In the occurrence of fire, the gas temperature is determined by following the standard temperature-time curves or experimental data from test furnaces. Then, the temperature distribution in the structural cross-section is computed and the material properties and equivalent thermal forces are calculated due to fire exposure for each element.

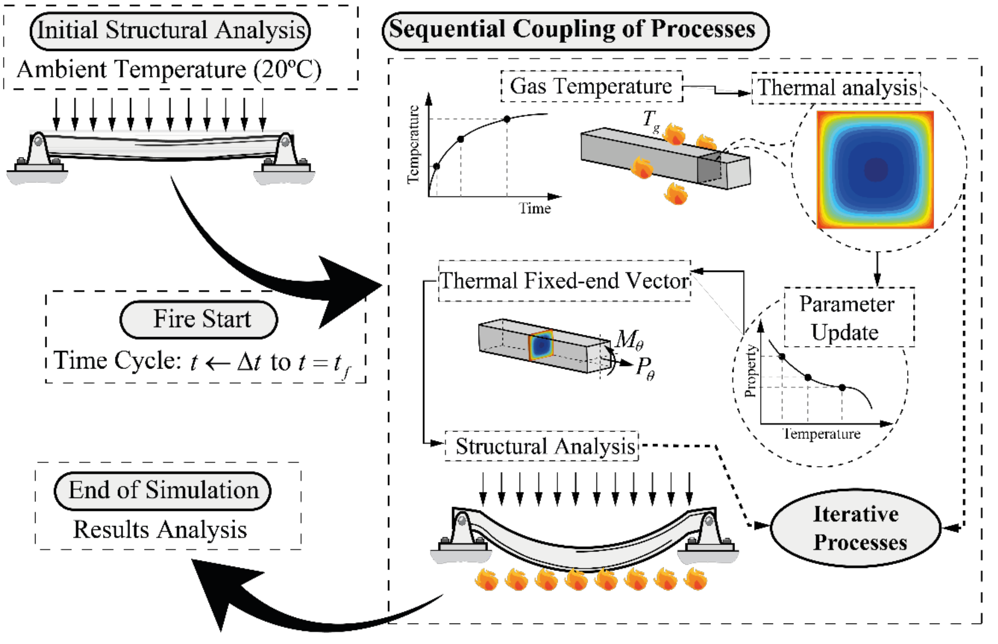

Figure 3. General procedures for solving the thermomechanical problem of structures under fire condition.

In the last solution stage, structural analysis is performed considering the effects of the thermal gradients of the cross-section, obtaining the displacement field. The solution of each system of equations is based on direct methods and iterative processes are implemented due to the nonlinear behavior of the analyzed problems. At the end of the computer simulation an investigation of the results obtained is carried out.

3 NUMERICAL APPLICATION TESTS

The performance evaluation of the developed program is based on the analysis of reinforced concrete and composite steel-concrete structures. The thermophysical properties of the materials and the parameters used in the simulations follow the recommendations of European codes [2], [21], [22]. For concrete, the variation of density with temperature is defined by Equation 22 and the value of 2300 kg/m^3 at 20ºC.

$$\rho_c(\theta) = \begin{cases} \rho_{c,20} & \text{for } 20^\circ\text{C} \le \theta \le 115^\circ\text{C} \\ \rho_{c,20}\left(1 - 0{,}02(\theta - 115)/85\right) & \text{for } 115^\circ\text{C} < \theta \le 200^\circ\text{C} \\ \rho_{c,20}\left(0{,}98 - 0{,}03(\theta - 200)/200\right) & \text{for } 200^\circ\text{C} < \theta \le 400^\circ\text{C} \\ \rho_{c,20}\left(0{,}95 - 0{,}07(\theta - 400)/800\right) & \text{for } 400^\circ\text{C} < \theta \le 1200^\circ\text{C} \end{cases} \quad (22)$$

The specific heat of dry concrete as a function of temperature is determined by Equation 23. In addition, the specific heat of the concrete is influenced by the moisture content of the concrete. According to the recommendations of Eurocode 2 part 1-2 [2], this behavior is modeled by a constant peak value between 100ºC and 115ºC, and followed by a linear decrease between 115ºC and 200ºC. The peak value, for 3% moisture content by weight, is equal to 1470 J/kg K.

$$c_c(\theta)=\begin{cases}900 & \text{for } 20^{\circ}\mathrm{C}\le\theta\le 100^{\circ}\mathrm{C}\\ 900+(\theta-100) & \text{for } 100^{\circ}\mathrm{C}<\theta\le 200^{\circ}\mathrm{C}\\ 1000+(\theta-200)/2 & \text{for } 200^{\circ}\mathrm{C}<\theta\le 400^{\circ}\mathrm{C}\\ 1100 & \text{for } 400^{\circ}\mathrm{C}<\theta\le 1200^{\circ}\mathrm{C}\end{cases} \tag{23}$$

The upper limit of the thermal conductivity of normal weight concrete varying with increasing temperature is described by a quadratic expression, as given by Equation 24.

$$\lambda_c(\theta)=2-0,2451(\theta/100)+0,0107(\theta/100)^2 \qquad \text{for } 20^{\circ}\mathrm{C}\le\theta\le 1200^{\circ}\mathrm{C} \tag{24}$$

For steel elements, the specific mass is constant and equal to 7850 kg/m^3. The specific heat of steel as a function of temperature is determined by Equation 25.

$$c_s(\theta)=\begin{cases}425+7,73\times10^{-1}\theta-1,69\times10^{-3}\theta^2+2,22\times10^{-6}\theta^3 & \text{for } 20^{\circ}\mathrm{C}\le\theta\le 600^{\circ}\mathrm{C}\\ 666-(13002/\theta-738) & \text{for } 600^{\circ}\mathrm{C}\le\theta\le 735^{\circ}\mathrm{C}\\ 545+(17820/\theta-731) & \text{for } 735^{\circ}\mathrm{C}\le\theta\le 900^{\circ}\mathrm{C}\\ 650 & \text{for } 900^{\circ}\mathrm{C}\le\theta\le 1200^{\circ}\mathrm{C}\end{cases} \tag{25}$$

The variation of the thermal conductivity of the steel with the temperature is modeled by a simple mathematical expression, as given by Equation 26.

$$\lambda_s(\theta)=\begin{cases}54-3,33\times10^{-2}\theta & \text{for } 20^{\circ}\mathrm{C}\le\theta\le 800^{\circ}\mathrm{C}\\ 27,3 & \text{for } 800^{\circ}\mathrm{C}\le\theta\le 1200^{\circ}\mathrm{C}\end{cases} \tag{26}$$

In addition, the parameters related to the convection and radiation heat transfer mechanisms, for the face exposed to fire, a convection coefficient equal to 25 W/m$^{2\circ}$C is used, while for the face unexposed to fire the value of the coefficient is taken as 9 W/m$^{2\circ}$C. The emissivity factor, related to the effect of heat transfer by radiation, is equal to 0,7.

3.1 Reinforced concrete beam subjected to fire

A numerical analysis of a simply supported reinforced concrete beam with an overhanging subjected to fire is performed in this section. The structure was subjected to a fire modeled with the ASTM E119 curve [24]. This example is part of the experimental tests carried out at the Construction Technology Laboratories of the Portland Cement Association by Ellingwood and Lin [40]. The beam has an overhang of 1,83 m and length between supports of 6,1 m. The fire acts only on the central span, while the overhang remains at ambient temperature. Figure 4 shows the geometric configuration of the problem.

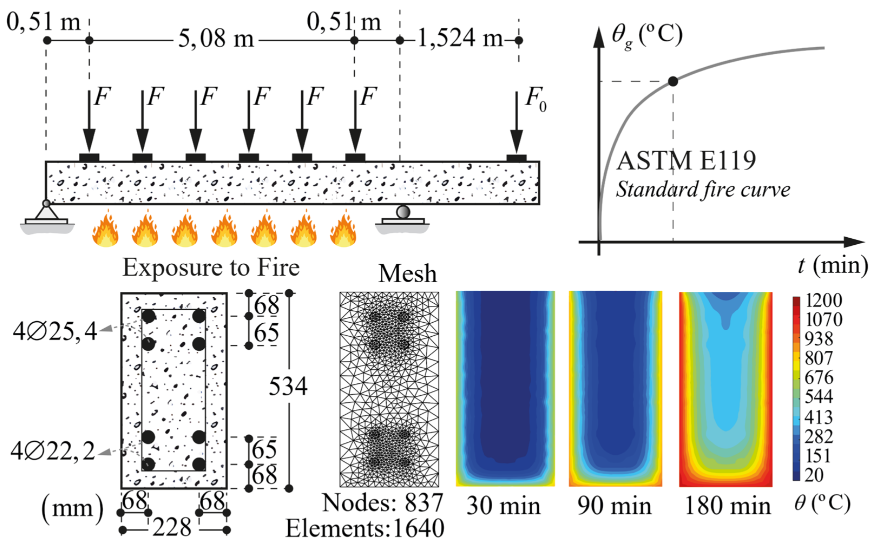

Figure 4. Characteristics of the structural model, details of the reinforced concrete cross-section and temperature distribution for 30, 90 and 180 min exposure to fire.

Equally spaced point loads with magnitude of 44,48 kN are applied throughout the central span, along with a force of 111,2 kN at the end of the overhang. The yield strength of the steel rebars and the compressive strength of concrete are 509,54 MPa and 29,65 MPa, respectively. This example has been numerically analyzed by several authors [10], [15], [18], [41].

The first step of the analysis seeks to validate the temperature increase in the reinforcement steel bars of the section. Results are shown in Figure 5. It is noted that the temperature change in the top and bottom bars of the reinforced concrete section presents acceptable results in relation to reference solutions. Top bars present slightly lower temperature values than bottom ones, due to the upper face of the concrete section not being directly exposed to fire.

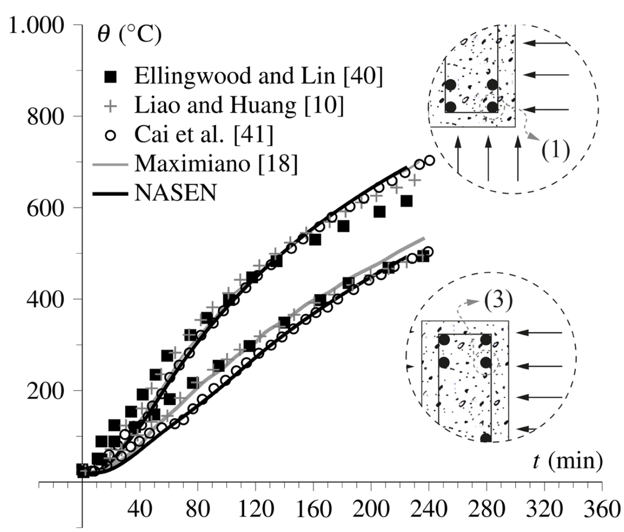

Figure 5. Temperature evolution in the top (3) and bottom (1) steel bars contained in the cross section of the reinforced concrete beam.

Although temperature-time curves are commonly used to evaluate the performance of a numerical model, the thermal response can also be visualized by a two-dimensional temperature field in the cross section of the structure, allowing identification of critical regions and a qualitative estimate of temperature change within the domain. As such, Figure 4 shows the temperature distribution in the reinforced concrete cross-section at 30, 90 and 180 min of fire exposure.

Finally, the evolution of the vertical displacement at mid-span between supports is measured as a function of time of heat exposure. Figure 6 shows a result comparison between NASEN and reference solutions from the literature.

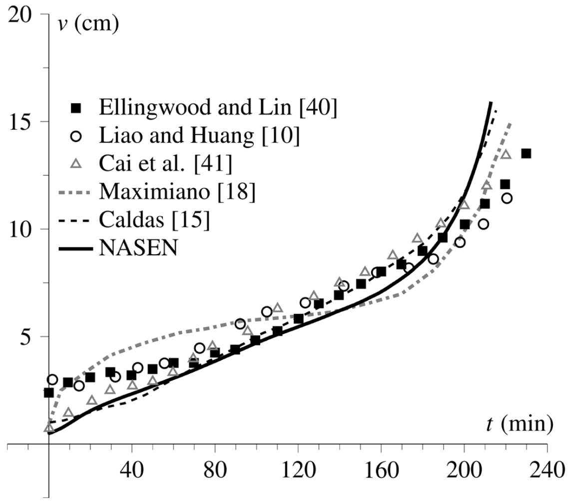

Figure 6. Vertical displacement versus time of heat exposure for reinforced concrete beam.

The results obtained with NASEN present reasonably good values, and the best agreement with the experimental tests occur between 45 and 200 min. Outside of this time range, the values diverge slightly. Furthermore, the solution extracted from NASEN is similar to the results obtained by Caldas [15].

3.2 Reinforced concrete column with eccentric load

At the Technical University of Braunschweig, Hass [42] carried out a series of full-scale experimental tests on reinforced concrete columns exposed to fire. Among the tests performed, three of these cases are studied numerically in Bamonte and Lo Monte [43]. For analysis, the case known as Hass 16 is considered, characterized by a square column of reinforced concrete heated according to the ISO 834 curve [23], length equal to 4,76 m, axial load of 460 kN, eccentricity equal to 9 cm and the dimensions and details of the cross section are shown in Figure 7.

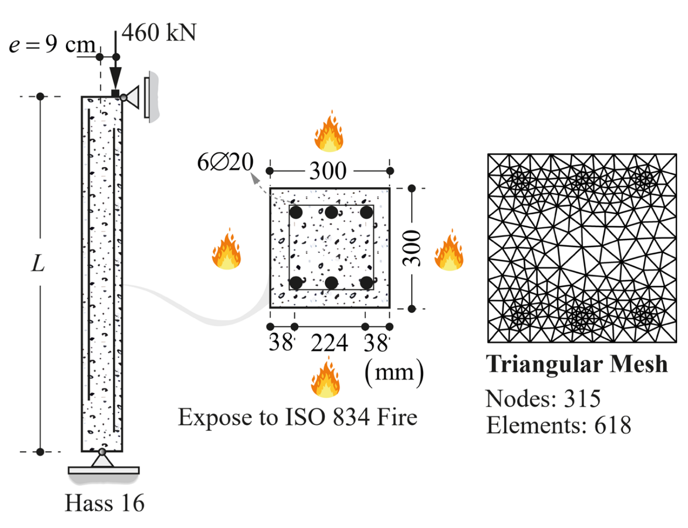

Figure 7. Characteristics of the structural model and details of the cross-section of the square column of reinforced concrete with eccentricity subjected to fire.

Regarding the physical characteristics of the problem, the modulus of elasticity and the yield strength of steel equal to 210 GPa and 462 MPa respectively, while the characteristic value of compressive strength of concrete is equal to 30,7 MPa. The concrete column is discretized into 7 one-dimensional beam-column elements and 618 triangular elements are used to mesh the cross section. The results are based on the analysis of the evolution of the axial displacement measured in the middle of the concrete column, as shown in Figure 8. The numerical solutions obtained in Maximiano [18] and Bamonte and Lo Monte [43] are used to calibrate the performance of the program NASEN. The results are shown to be in good agreement with the previsions in the literature.

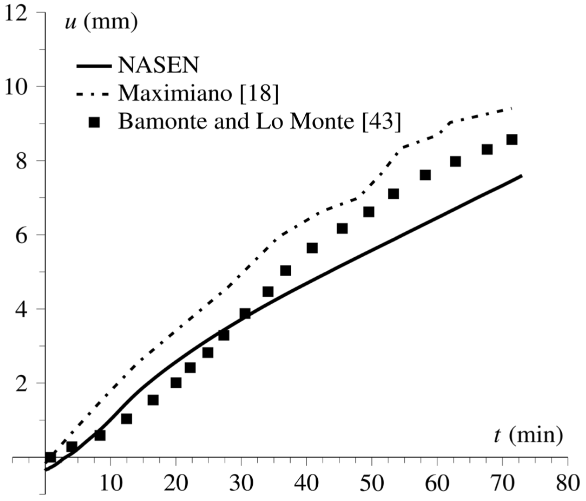

Figure 8. Evolution of axial displacement of the concrete column as a function of time of exposure to fire.

In addition, usually in structural design, simplified calculation methods are applied, for example, the 500ºC isotherm method for concrete structures under fire condition [2]. Using the characteristics of the studied physical problem, the NASEN program can be applied to compute the effective section representative of a concrete region of the inner cross-section the isotherm of 500ºC for 30, 60, 90 and 120 min of exposure to fire, assuming that the concrete with temperature higher than 500ºC is completely neglected, as shown in Figure 9. In a simplified way, the concrete contained in the interior region is not affected by fire, considering the properties of materials at ambient temperature, however, exceptional coefficients are adopted in the elaboration of the structural design [44].

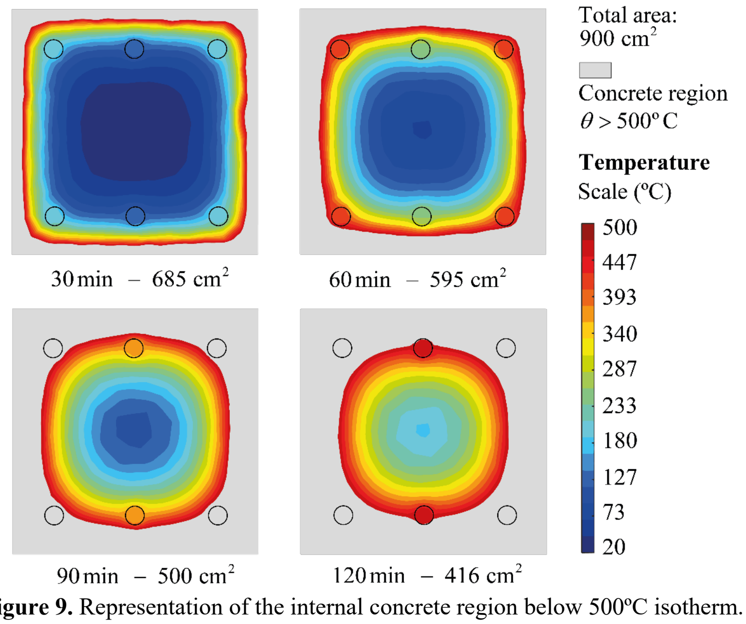

Figure 9. Representation of the internal concrete region below 500ºC isotherm.

Furthermore, another important analysis in the context of fire design of structures is the investigation of the influence of the concrete column cover. Table 1 shows the temperature values measured in the upper steel reinforcing located in the region that is most heated by fire and unfavorable for safety.

Table 1. Temperature in the steel reinforcement (ºC) in relation to the column cover and the time of exposure to fire.

Time (min)	Cover (mm)			
	10	25	38	45
30	545,17	330,71	202,96	152,46
60	737,82	556,04	414,72	348,89
90	867,69	685,41	547,91	479,99
120	942,66	760,40	644,35	577,53

In order to make comparisons and discussions of the results obtained with the computer program, the simplified value of 550ºC is adopted as the reference temperature of the steel reinforcement of the concrete cross section. This value is not prescribed in standards and is used only as a reference value for the present study, since for temperatures above this value, steel shows significant reductions in stiffness and strength. As can be seen in Table 1, the steel reinforcements of the concrete column are exposed to high temperatures when the cover values are lower, which can provide severe risks to the safety of the structure. In contrast, higher values of the concrete column cover, the temperature levels decrease. However, it is important to check the accuracy of the details of the steel reinforcement and the requirements in the preparation of the structural design, in order to guarantee the requirements of resistance and fire safety.

3.3 Steel-concrete composite beam

The thermomechanical behavior of simply supported steel-concrete beams subjected to concentrated loads in a fire situation is studied using an advanced computational model. The system is exposed to the standard temperature-time curve ISO 834 [23]. Two configurations are analyzed, the first case is shown in Figure 10a, where the steel profile is partially encased by the concrete and subject to a symmetrical load equal to 36 kN.

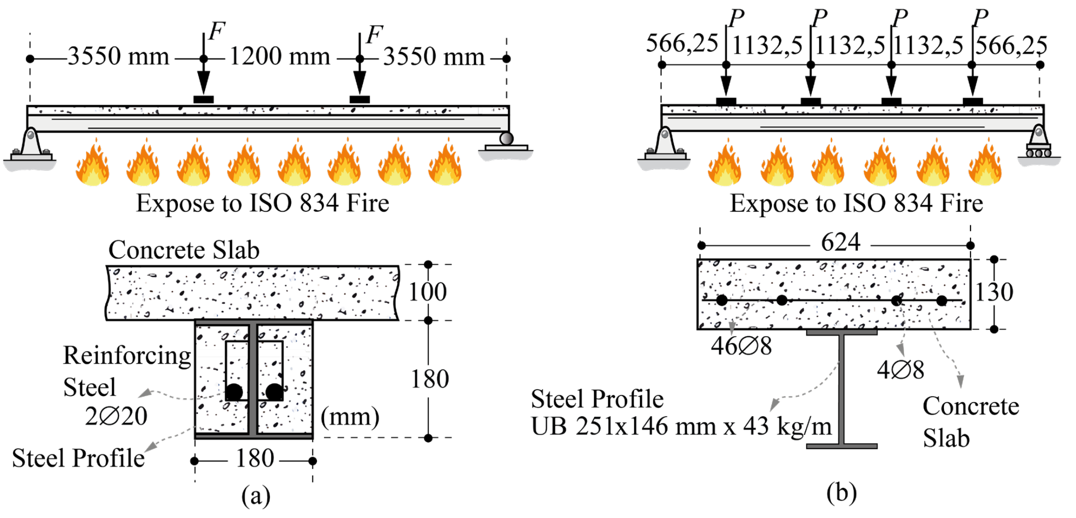

Figure 10. Characteristics and dimensions of the cross-section of the composite steel-concrete beam model with (a) section partially encased with slab and (b) H-section with slab.

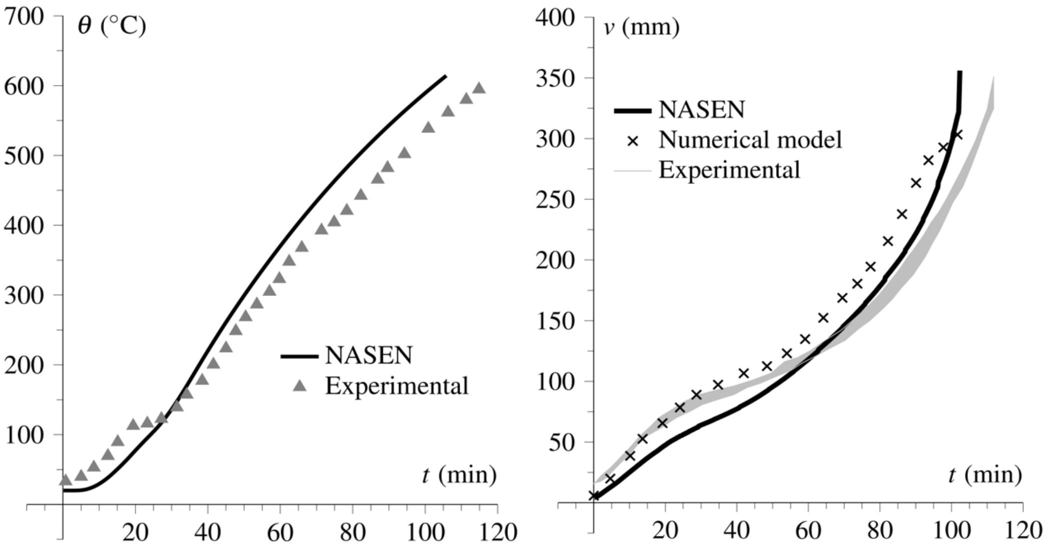

Figure 11. Evolution of temperature and deflection at mid-span of the composite beam as a function of time of exposure to fire.

Dotreppe et al. [45] presented numerical results and experimental tests for first case, carried out at the Technical University of Braunschweig. Results from both approaches are adopted as references to evaluate the numerical results obtained with NASEN. A mesh with 6 one-dimensional elements is adopted to discretize the structural model.

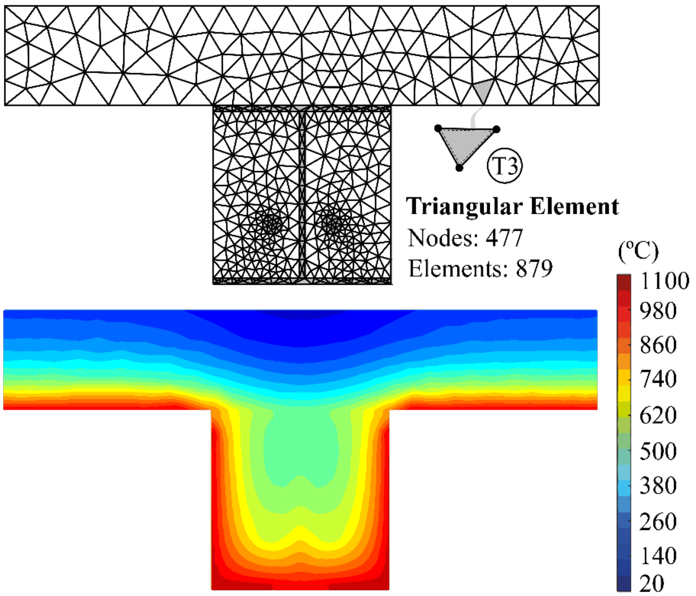

Figure 12. Finite element mesh and thermal field of the cross-section of the steel-concrete composite beam at 105 min of fire exposure.

The validation of results for temperature evolution at the cross section and the deflection of the beam as a function of the time of exposure to fire is shown in Figure 11. It is observed that the results obtained with NASEN once again present satisfactory agreement with the experimental data. Figure 12 shows the two-dimensional mesh with 477 nodes and 879 three-node linear triangular elements used for discretization of the cross-section, as well as the temperature distribution at 105 min of fire exposure.

The second case analyzed is shown in Figure 10b, where the steel profile is only in contact with concrete slab. The beam is subjected to four concentrated loads equal to P with an intensity of 62,36 kN. The support conditions adopted in the structural model allow rotation on the left end and horizontal and rotational displacement are free on the right support. The proposed example is reported, initially, to the tests performed by Wainman and Kirby [46], later, studied numerically by Huang et al. [47].

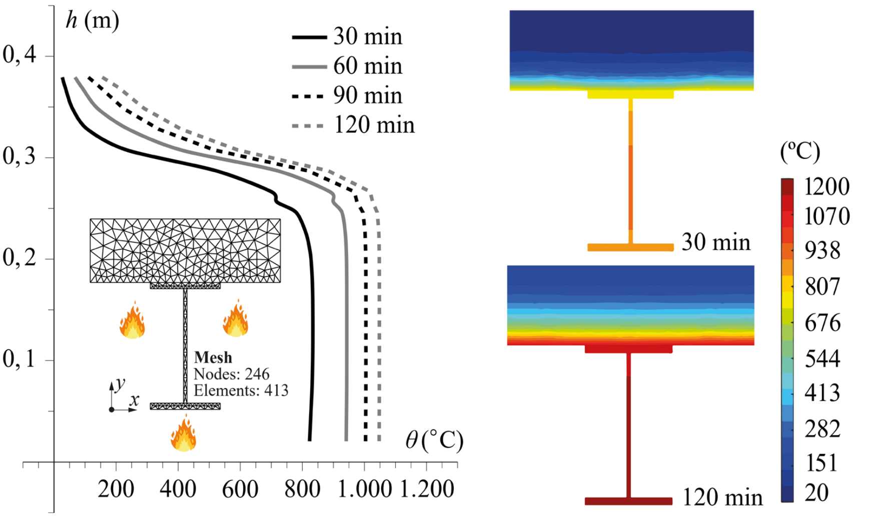

Figure 13. Temperature profile along the symmetry line of the problem and the two-dimensional thermal field for 30 and 120 min of exposure to fire.

The numerical meshes adopted for the discretization of the cross section and the structural model are, respectively, equal to 413 linear triangular elements and 6 one-dimensional finite elements. Figure 13 shows the temperature profile along the center line of symmetry of the cross section. It is observed that the temperature levels in the steel profile remain practically the same, while in the concrete the thermal gradients of temperature are noticed.

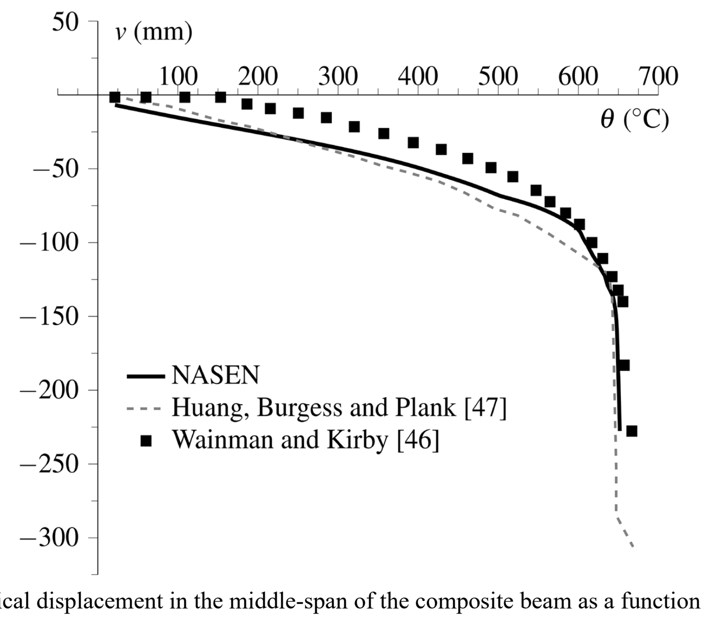

Figure 14. Vertical displacement in the middle-span of the composite beam as a function of temperature.

Figure 14 shows the maximum vertical deflection in the beam in relation to the temperature in the bottom flange of the steel profile. The results obtained with the NASEN program indicate a good agreement between the experimental tests, as well as in relation to the numerical model in the literature. It should be noted that the numerical solution with the developed program shows a more conservative behavior over the temperature increase in the structure compared to the experimental results.

5 CONCLUSIONS

This work presents the nonlinear numerical procedures of finite elements used in the development of the NASEN computational tool for thermomechanical analysis of reinforced concrete and composite steel-concrete plane structures at high temperatures. Different loading configurations, cross-section characteristics and boundary conditions are studied.

The results obtained with the developed program were calibrated with data from computer simulations and experimental tests available in the literature. The predictions of thermal behavior were well evaluated by the developed program, since the solution of scalar problems are already well known in the literature. The presence of non-linearity of the material requires some additional numerical procedures, which does not present difficulties in the implementation of the code. The mechanical responses present results consistent with the predictions in the literature. However, these structural models are more sensitive and complex to simulate in relation to the thermal model. It can be observed in each test performed, the NASEN program and the models in the literature present different behaviors, due to the physical hypotheses adopted in the development of each model.

In general, the results show satisfactory behavior in all cases studied, indicating the good performance of the NASEN program. Hence, this advanced numerical model allows to investigate and simulate adequately the behavior of structures in fire situations. In future projects and research, updates are made to the models and implementation of new computational modules in the program.

ACKNOWLEDGEMENTS

The authors would like to acknowledge FAPES (Foundation for the Support of Research and Innovation of Espírito Santo) for the financial support and PPGEC-UFES (Graduate Program in Civil Engineering of the Federal University of Espírito Santo) for the knowledge, training and infrastructure provided during the development of this research.

REFERENCES

[1] J. A. Purkiss and L. Y. Li, *Fire Safety Engineering Design of Structures*. Boca Raton, Flórida: CRC Press, 2013.

[2] European Committee for Standardization, *Eurocode 2: Design of Concrete Structures – Part 1.2: General Actions - Actions on Structures Exposed to Fire*, EN 1992-1-2. Brussels: CEN, 2004.

[3] Ansys INC, *Ansys Realese 9.0 – Documentation*, Canonsburg, Pensilvânia, EUA: Ansys INC, 2004.

[4] ABAQUS, *14 Documentation* (vol. 6). Providence, Rhode Island, EUA: Dassault Systemes Simulia Corporation, 2014.

[5] J. Franssen, "SAFIR: a thermal/structural program for modeling structures under fire," *Eng. J. Am. Inst. Steel Constr.*, vol. 42, no. 3, pp. 143–158, 2005.

[6] J. Cai, I. Burgess, and R. Plank, "A generalized steel/reinforced concrete beam-column element model for fire conditions," *Eng. Struct.*, vol. 25, no. 6, pp. 817–833, 2003.

[7] J. N. Reddy, *An Introduction to the Finite Element Method*. New York: McGraw-Hill, 1993.

[8] P. R. Prakash and G. Srivastava, "Nonlinear analysis of reinforced concrete plane frames exposed to fire using direct stiffness method," *Adv. Struct. Eng.*, vol. 21, no. 7, pp. 1036–1050, 2018.

[9] X. Yu and Z. Huang, "An embedded FE model for modelling reinforced concrete slabs in fire," *Eng. Struct.*, vol. 30, no. 11, pp. 3228–3238, 2008.

[10] F. Liao and Z. Huang, "An extended finite element model for modelling localized fracture of reinforced concrete beams in fire," *Comput. Struc.*, vol. 152, pp. 11–26, 2015.

[11] R. S. Walls, C. Viljoen, and H. de Clercq, "Analysis of structures in fire as simplified skeletal frames using a customized beam finite element," *Fire Tec.*, vol. 54, no. 6, pp. 1655–1682, 2018.

[12] S. Thelandersson, "Modeling of combined thermal and mechanical action in concrete," *J. Eng. Mech.*, vol. 113, no. 6, pp. 893–906, 1987.

[13] M. B. Dwaikat and V. K. R. Kodur, "A numerical approach for modeling the fire induced restraint effects in reinforced concrete beams," *Fire Saf. J.*, vol. 43, no. 4, pp. 291–307, 2008.

[14] B. A. Izzuddin and A. Y. Elghazouli, "Failure of lightly reinforced concrete members under fire. I: Analytical modeling," *J. Struct. Eng.*, vol. 130, no. 1, pp. 3–17, 2004.

[15] R. B. Caldas, "Análise numérica de estruturas de aço, concreto e mistas em situação de incêndio," Ph.D. dissertation, Univ. Fed. Minas Ger., Belo Horizonte, Brasil, 2008.

[16] D. L. Mouço, Modelo inelástico para análise avançada de estruturas mistas aço-concreto em situação de incêndio. M.S. thesis, Univ. Fed. Rio Jan., Rio de Janeiro, Brasil, 2008.

[17] J. C. L. Ribeiro, "Desenvolvimento e aplicação de um sistema computacional para simulação via Método dos Elementos Finitos do comportamento de estruturas de aço e mistas em situação de incêndio," Ph.D. dissertation, Univ. Fed. Minas Ger., Belo Horizonte, Brasil, 2009.

[18] D. P. Maximiano, "Análise numérica avançada de estruturas de aço e de concreto armado em situação de incêndio," Ph.D. dissertation, Univ. Fed. Ouro Preto, Ouro Preto, Brasil, 2018.

[19] N. S. Neves, “Modelo computacional avançado para análise de estruturas sob ação de gradientes térmicos,” M.S. thesis, Univ. Fed. Esp. Sto., Vitória, Brasil, 2019.

[20] N. S. Neves, M. S. Azevedo, C. B. Barcelos Filho, V. P. Silva, and I. Pierin, "Estudo térmico de pilares mistos de aço e concreto de seção circular em situação de incêndio," *Rev. Estrutura Aco*, vol. 9, pp. 122–140, 2020.

[21] European Committee for Standardization*, Eurocode 3: Design of Steel Structures - Part 1-2: General Rules - Structural Fire Design*, EN 1993-1-2. Brussels: CEN, 2005.

[22] European Committee for Standardization, *Eurocode 1: Actions on Structures - Part 1.2: General Actions - Actions on Structures Exposed to Fire*, EN 1991-1-2. Brussels: CEN, 2002

[23] International Organization for Standardization, *Fire-Resistance Tests: Elements of Building Construction - Part 1.1: General Requirements for Fire Resistance Testing*, ISO 834, 1999.

[24] American Society for Testing and Materials, *Standard Methods of Fire Test of Building Construction and Materials: Test Method*, ASTM E119, 2001.

[25] N. S. Neves, M. S. Azevedo, R. S. Camargo, and V. P. Pinheiro, "Análise térmica bidimensional de perfil de aço sujeita a elevadas temperaturas," in *Anais do X Enc. Cient. Fís. Apl*. São Paulo: Blucher, pp. 71–73, 2019.

[26] Y. B. Yang and S. R. Kuo, *Theory and Analysis of Nonlinear Framed Structures*. New York: Prentice Hall, 1994.

[27] F. L. Porter and G. H. Powell, *Static and Dynamic Analysis of Inelastic Frame Structures*. California: College of Engineering, Earthquake Engineering Research Center, University of California, 1971.

[28] K. D. Hertz, *Betonkonstruktioners Brandtekniske Egenskaber (Fire Properties of Concrete Constructions)*. (Part 1-BYG Rapport, No. R-141). Lyngby, Denmark: Technical University of Denmark (DTU), 1980.

[29] T. T. Lie, *Structural Fire Protection*. Reston, Virgínia, EUA: American Society of Civil Engineers, 1992.

[30] European Convention for Constructional Steelwork – ECCS. *TC 3. Fire Safety of Steel Structures: European Recommendations for the Fire Safety of Steel Structures - Calculation of the Fire Resistance of Load Bearing Elements and Structural Assemblies Exposed to the Standard Fire*. USA: Elsevier, 1983.

[31] British Standard, *Structural Use of Steelwork in Building: Code of Practice for Fire Resistant Design*, BS 5950 part. 8, 1990.

[32] Standard New Zealand, *Concrete Structures Standard Part 1 - the Design of Concrete Structures*, NZS 3101.1, 1995.

[33] Document Technique Unifié – DTU, *Méthode de Prévision par lê Calcul du Comportement au Feu des Structures em Béton*. Paris: CSTB, 1974. 47 p.

[34] C. N. Costa, “Dimensionamento de Elementos de Concreto Armado em Situação de Incêndio,” Tese de Doutorado, Univ. S. Paulo, 2008.

[35] J. P. Boutin, *Pratique du Calcul de la Résistance au Feu des Structures en Béton*. Paris, França: Librairie Eyrolles, 1983.

[36] U. Diederichs, U. M. Jumppanen, and V. Penttala, *Behavior of High Strength Concrete at High Temperatures* (Technical Report, no. 92). Espoo, Finlândia: Department of Structural Engineering, Helsiniki University of Technology, 1989.

[37] R. C. Barros, D. Pires, R. A. Silveira, Í. J. Lemes, and P. A. Rocha, "Advanced inelastic analysis of steel structures at elevated temperatures by SCM/RPHM coupling," *J. Construct. Steel Res.*, vol. 145, pp. 368–385, 2018.

[38] R. B. Caldas, R. H. Fakury, and J. B. M. Sousa Jr., "Finite element implementation for the analysis of 3D steel and composite frames subjected to fire," *Lat. Am. J. Solids Struct.*, vol. 11, no. 1, pp. 1–18, 2014.

[39] J. C. G. Silva, and Landesmann, A., Acoplamento unidirecional para análise fluido-termomecânica de estruturas sob fogo. *Rev. Sul-amer. Eng. Estrut.*, vol. 9, no. 2, pp. 65–82, 2012.

[40] B. Ellingwood and T. D. Lin, "Flexure and shear behavior of concrete beams during fires," *J. Struct. Eng.*, vol. 117, no. 2, pp. 440–458, 1991.

[41] J. Cai, I. Burgess, and R. Plank, "A generalised steel/reinforced concrete beam-column element model for fire conditions," *Eng. Struct.*, vol. 25, no. 6, pp. 817–833, 2003.

[42] R. Hass, *Practical Rules for the Design of Reinforced Concrete and Composite Columns Submitted to Fire*. (Technical Report, No. 69). Braunschweig, Germany: Institut für Baustoffe, Massivbau und Brandschutz der Technischen Universität Braunschweig, 1986.

[43] P. Bamonte and F. Lo Monte, "Reinforced concrete columns exposed to standard fire: Comparison among different constitutive models for concrete at high temperature," *Fire Saf. J.*, vol. 71, pp. 310–323, 2015.

[44] J. S. Suaznabar and V. P. Silva, "Combined axial and flexural loads in short reinforced concrete columns in fire: ultimate limit state curves using 500 C isotherm method," *Rev. IBRACON Estrut. Mater.*, vol. 11, no. 1, pp. 163–182, 2018.

[45] J. C. Dotreppe, J. M. Franssen, and J. B. Schleich, "Computer aided fire resistance for steel and composite structures," *Acier*, vol. 3, pp. 105–112, 1984.

[46] D. Wainman and B. Kirby, *Compendium of UK Standard Fire Test Data, Unprotected Structural Steel–1*. London, UK: British Steel Corporation, 1987.

[47] Z. Huang, I. W. Burgess, and R. J. Plank, "The influence of shear connectors on the behaviour of composite steel-framed buildings in fire," *J. Constructional Steel Res.*, vol. 51, no. 3, pp. 219–237, 1999.

Author contributions: NSN: conceptualization, formal analysis, methodology, writing-original draft, writing-review & editing; RSC, MSA: methodology, conceptualization, supervision, writing-review & editing.

Editors: Osvaldo Manzoli, Guilherme Aris Parsekian.

IBRACON
IBRACON Structures and Materials Journal
Revista IBRACON de Estruturas e Materiais
ISSN 1983-4195 ismj.org
SciELO

ORIGINAL ARTICLE

Numerical investigation on slim floors: comparative analysis of ASB and CoSFB typologies

Investigação numérica sobre slim floors: análise comparativa das tipologias ASB e CoSFB

Tainá Mascarenhas Borghi[a]
Lucas Antônio Morais Oliveira[a]
Ana Lucia Homce de Cresce El Debs[a]

[a]Universidade São Paulo – USP, Escola de Engenharia de São Carlos, Departamento de Engenharia de Estruturas, São Carlos, SP, Brasil

Received 26 June 2020
Accepted 24 November 2020

Abstract: Innovative composite structures have been intensively studied towards meeting the demands of civil construction. An example of such structures is slim floor, comprised of concrete or composite slabs positioned at the height of steel beams, reducing the total height of the floor. In Brazil, studies on this system are still in early stages, and due to the lack of both experience and national normative codes, it is hardly used in civil construction. Given the possible combinations between concrete slabs and steel beams, the system exhibits different typologies. This article reports a numerical investigation on two typologies of slim floor, namely Asymmetric Slimflor Beam (ASB), composed of an asymmetric I beam, and Composite Slim-Floor Beam (CoSFB), comprised of an asymmetric beam with small openings at the top of its web. Nonlinear numerical models of ASB and CoSFB typologies were developed by Finite Element-based software ABAQUS®. The models were calibrated with the use of experimental studies from the literature, and showed high accuracy and good results. After calibration, the materials properties and geometric dimensions of the models, such as height and thickness, were standardized for a comparison of the typologies. The comparative analysis showed the particular characteristics of CoSFB promoted higher stiffness and flexural capacity compared to ASB, and a parametric analysis evaluated the influence of steel and concrete parameters on the flexural behavior of the typologies. The parametric study revealed the steel parameters exerted a more substantial influence on the slim floors behavior than the concrete ones.

Keywords: composite structures, slim floor, Asymmetric Slimflor Beam (ASB), Composite Slim-Floor Beam (CoSFB), numerical analysis.

Resumo: Estruturas mistas inovadoras vêm sendo intensamente estudadas para atender as demandas da construção civil. Um exemplo de tais estruturas é o piso misto de pequena altura, composto por lajes de concreto ou mistas, posicionadas na altura de vigas de aço, reduzindo a altura total do piso. No Brasil, os estudos sobre esse sistema ainda são iniciais e, devido à falta de experiência e de códigos normativos nacionais, ele é pouco utilizado na construção civil brasileira. Devido às inúmeras combinações possíveis entre lajes e vigas de aço, o sistema apresenta diferentes tipologias. Este artigo apresenta uma investigação numérica sobre duas tipologias de piso misto de pequena altura, sendo elas Asymmetric Slimflor Beam (ASB), composta por uma viga I assimétrica, e Composite Slim-Floor Beam (CoSFB), composta por uma viga assimétrica com pequenas aberturas na parte superior da alma. Uma análise numérica não linear em elementos finitos foi realizada com o software ABAQUS, e os modelos numéricos das tipologias ASB e CoSFB foram calibrados a partir de resultados experimentais da literatura. Após a calibração, os modelos foram padronizados de acordo com as propriedades dos materiais e dimensões geométricas, como altura e espessura, para a comparação das tipologias. Uma análise paramétrica avaliou a influência de parâmetros do aço e do concreto no comportamento à flexão dessas tipologias. A calibração numérica apresentou alta precisão e bons resultados e a análise numérica comparativa mostrou que as caracteristicas particulares do CoSFB promoveram maior rigidez e

Corresponding author: Tainá Mascarenhas Borghi. E-mail: tainaborghi@usp.br
Financial support: Conselho Nacional de Desenvolvimento Científico e Tecnológico (CNPq) (Grant number 131455/2018-4) and Coordenação de Aperfeiçoamento de Pessoal de Nível Superior - Brasil (CAPES) – Finance Code 001 and (Grant number 2019/03513-5) - São Paulo Research Foundation (FAPESP).
Conflict of interest: Nothing to declare.

capacidade de flexão em relação ao ASB. O estudo paramétrico revelou que os parâmetros do aço exerceram maior influência que os parâmetros do concreto.

Palavras-chave: estruturas mistas, piso misto de pequena altura, *Asymmetric Slimflor Beam* (ASB); *Composite Slim-Floor Beam* (CoSFB), análise numérica.

How to cite: T. M. Borghi, L. A. M. Oliveira, and A. L. H. C. El Debs, "Numerical investigation on slim floors: comparative analysis of ASB and CoSFB typologies," *Rev. IBRACON Estrut. Mater.*, vol. 14, no. 4, e14411, 2021, https://doi.org/10.1590/S1983-41952021000400011

INTRODUCTION

Studies on composite structures have substantially increased in the global scenario, since such structures benefit from both high tensile strength of the steel and compressive strength of the concrete [1], meeting the current demands for more efficient civil industry and economical and fast construction. Other qualities, e.g., possible reductions in self-weight, ability to overcome large spans with no shoring, buckling attenuation, and more effective fire and corrosion protection, are relevant in comparison to reinforced concrete or steel structures.

Slim floor offers such benefits, since it is composed of a steel beam, concrete or composite slab and shear connections, resembling composite beams. Besides, it reduces the total height of the floor by coupling the concrete slab at the height of the steel beam [2]. Since concrete encases the steel beam, the ultimate capacity and stiffness in normal and fire situations increase, and local instabilities, typical of steel structures, decrease. In addition, slim floor enables a range of different compositions, varying the type of slab and beam employed, or the position and type of shear connections [2].

Among such possibilities from variations in the steel profile, the most studied and used internationally are Asymmetric Slimflor Beam (ASB), Composite Slim Floor Beam (CoSFB), Deltabeam, and Shallow Cellular Composite Floor Beam (SCCFB) (see Figure 1 - schematic models) [3].

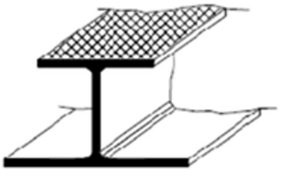

(a) Asymmetric Slimflor Beam (ASB)

(b) Composite Slim Floor Beam (CoSFB)

(c) Deltabeam

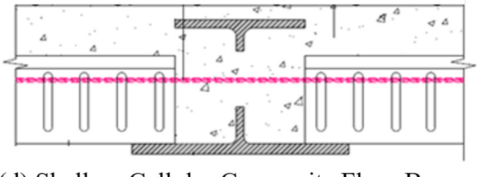

(d) Shallow Cellular Composite Floor Beam (SCCFB)

Figure 1. Slim floor typologies.

Studies on the slim floor system are still incipient in Brazil and, due to the lack of normative codes, it is hardly applied for construction. Furthermore, most research has focused on the behavior of only one typology. This study aims to contribute with the dissemination of knowledge on slim floor through a numerical investigation of the Asymmetric Slimflor Beam (ASB) and Composite Slim Floor Beam (CoSFB). It evaluates the flexural behavior of the two typologies, starting from the models calibration, standardization of the typologies according to the geometric dimensions and properties of the materials for a comparison, and ending with a parametric study.

ASB is composed of a type "I" steel beam with bottom flange width larger than that of top flange. Grooves on the external face of the top flange aim to improve the connection between steel and concrete [4]. CoSFB consists of a symmetric "I" steel beam with small openings at the top of the web and a steel plate wider than the flange welded to the bottom [5]. Figures 2a and 2b, respectively, show the configurations of ASB and its real application in Chasse Church (Germany) [6] and CoSFB and its real application in Dillingen a.d. Donau (Germany) [7].

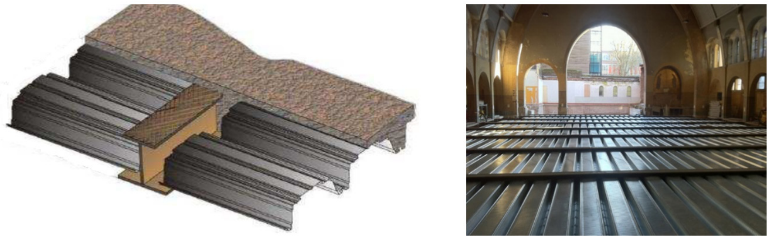

(a) Asymmetric Slimflor Beam (ASB)

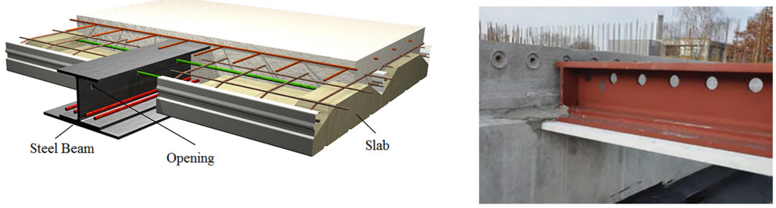

(b) Composite Slim-Floor Beam (CoSFB)

Figure 2. Slim floor.

The ASB was chosen for analysis in the present study because it is the most applied typology in construction worldwide, presenting a proposal for design and study of the behavior already consolidated [8], [9], [4]. Conversely, CoSFB is a new promising typology with some successful applications in Europe [7]. Many studies on the two typologies have been developed since the end of the last century and will be covered in the following section.

STATE OF ART

The main studies on slim floor began with Mullet [8], Mullet and Lawson [9], and Lawson et al. [4], who experimentally investigated Asymmetric Slimflor Beam (ASB) and proposed a design method, according to BS 5950 [10]. Bailey [11] analyzed the behavior of ASB under fire and developed software that predicted its structural behavior in this situation. Through numerical analysis, Mäkeläinen and Ma [12] demonstrated the excellent performance of the typology under those circumstances.

Paes [13] also conducted a numerical analysis and established design recommendations for ASB's ultimate capacity and in-service conditions. The author developed numerical models based on studies of Lawson et al. [4] and Leskelä and Hopia [14] and obtained compatible results. Rackham et al. [15] published guidelines for the design of ASB with concrete hollow core slab, and a calculation procedure based on BS 5950 [10] was established for checking the design in the ultimate and in-service conditions, profile instabilities, shear, torsion and bending resistance. A theoretical study developed by Ahmed and Tsavdaridis [16] provided a summary of the slim floor typologies, characteristics, and design formulations. All above-cited authors contributed to the current design recommendations, presented by Barros [17].

Studies on CoSFB started with Braun et al. [18], and Hechler et al. [5], considered precursors in the theme. They performed push-out and bending tests and evaluated shear, bending, vibration, and deformation, which revealed increases of 100% in load capacity and 150% in stiffness compared to usual composite beams. Sheehan et al. [19] analyzed the degree of shear connection of steel bars and their resistance capacity through shear and bending tests and observed the number of steel bars that passed the beam openings directly influenced the system's flexural strength. Baldassino et al. [20] experimentally evaluated CoSFB's in-service behavior, and observed the final response was affected by concrete´s curing time and creep effects.

Regarding shear connectors on the slim floor, initially only stud bolts welded to the top flange of the profile were used (Figure 3a). De Nardin and El Debs [2] showed such connectors could also be welded to the bottom flange (Figure 3b), to both flanges (Figure 3c), or to the web (Figure 3d), with the former solution providing the best behavior.

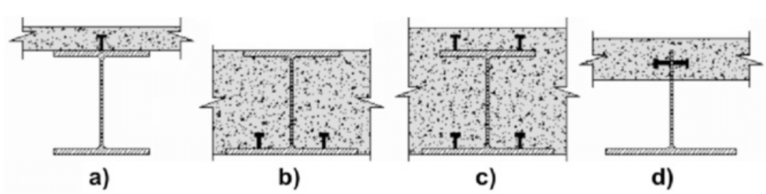

Figure 3. Position of stud bolt.

The shear connections currently used on slim floor have been innovated, and those with steel bars passing through the profile openings are now the most studied (see Ju et al. [21], Leskela et al. [22], Lam et al. [23], Huo and D'Mello [24] and Chen and Limazie [25]). When in contact with concrete, such bars guarantee the shear connection, transferring the longitudinal shear force between the concrete slab and steel beam [26].

Numerical simulations consume fewer financial, human, and time resources, when compared to experimental tests. However, model calibrations require the use of experimental results from previous tests, which enable the identification of the structure´s global response and the parameters that affect it. They imply some tweaks in the numerical model for the matching of numerical and experimental results. Therefore, experimental results of Lawson et al. [4] were employed for ASB, whereas those of Hechler et al. [5] were applied for CoSFB.

The present numerical FE analysis was based on several numerical studies of slim floor, which indicated the most appropriate element type, constitutive relations, mesh and contact interactions (see Rocha [26], Maraveas et al. [27], Leskela et al. [22], Hechler et al. [5], Limazie and Chen [28], Kochem and De Nardin [29], Minhaneli [30] and Soares [31]).

NUMERICAL INVESTIGATION

The numerical investigation was divided into the following three stages: i) calibrations of ASB and CoSFB, ii) standardization of the geometries and materials properties for the comparison of the two models, and iii) a parametric study that evaluated the influence of concrete strength, concrete topping above the steel beam, strength of steel beams and bottom flange thickness on the flexural behavior. ABAQUS® Software was used for the numerical simulation.

In the first stage, the characteristics of the experimental study for the calibration were inserted. The geometrical characteristics of ASB followed a test conducted by Lawson et al. [4] (Figure 4), with 280 ASB 100 profile and composite slab used in the numerical simulation. The reinforcement consisted of 11Ø16 mm transversal bars. For the sake of simplification, the steel deck was not modelled, since its behavior does not affect the flexural response, and its contribution can be disregarded [3]. However, the concrete slab was modeled as if there were a steel deck, due to the influence of the volume of concrete on many parameters, such as system's stiffness, resistance, ductility and collapse mode.

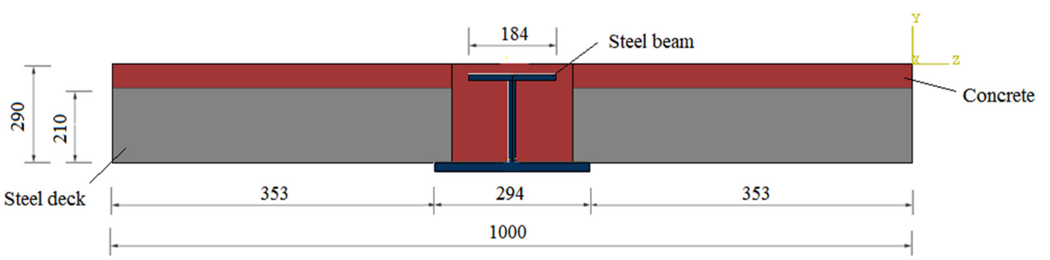

(a) Cross-section

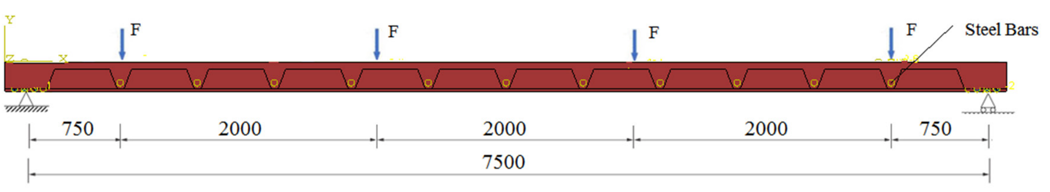

(b) Longitudinal details

Figure 4. Geometrical characteristics of Lawson et al. [4] test (measurements in mm).

Figure 5 shows the geometrical characteristics of CoSFB, according to Hechler et al. [5]. HEM 220 steel profile and composite slab were used and filled with rock wool. The reinforcement consisted of Ø16 mm transversal bars passing through each opening. Since it is a wholly filled slab, its simulation as only concrete was adopted.

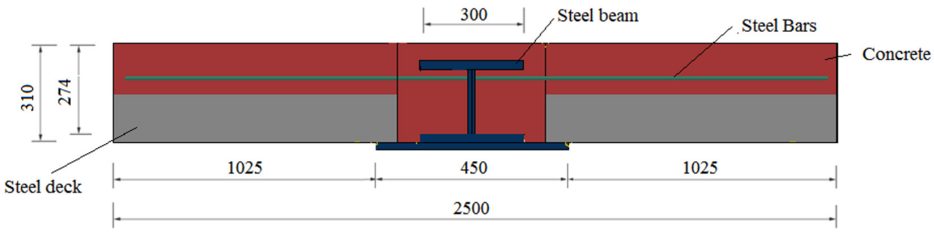

(a) Cross-section

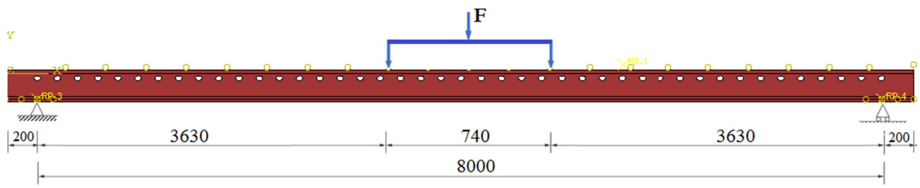

(b) Longitudinal details

Figure 5. Geometrical characteristics of Hechler et al. [5] test (measurements in mm).

The materials properties (Table 1) were taken from the experimental studies [4], [5] used for the calibration.

Table 1. Materials properties.

		ASB		CoSFB	
Beam	Span (m)	7.5		8.0	
	Steel (MPa)	f_y	f_u	f_y	f_u
		405.7	430	500	516
	E (MPa)	200000		190000	
Composite Slab	Width (m)	1.0		2.5	
	Height (m)	0.29		0.31	
	E (MPa)	33873		32000	
	f_cf_{ck} (MPa)	34		30.1	
	f_tf_t (MPa)	3.15		2.9	
Rebars	Lenght (m)	0.43		2.4	
	f_yf_t (MPa)	500		500	
	E (MPa)	210000		210000	

In the calibration phase, the boundary and loading conditions were based on experimental tests. The former was a simply supported beam, and the load was applied in an incremental force. Lawson et al. [4] applied four loads to the beam, as shown in Figure 6a, whereas Hechler et al. [5] applied load centrally to the slab (Figure 6b).

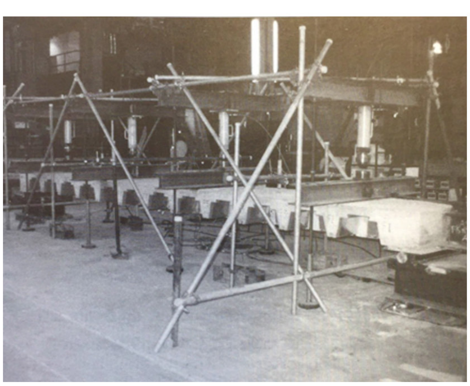

(a) Asymmetric Slimflor Beam (ASB)

(b) Composite Slim-Floor Beam (CoSFB)

Figure 6. Loading condition of experimental tests.

After calibration, the models were standardized for basic geometric dimensions and materials properties, towards a more reliable comparison of the structural behavior of the typologies. The dimensions standardized for the profile were web height, web and top flange thickness and bottom flange area (Figure 7a, 7b), and height, width, and length were uniform for the slab (Figure 7c). The reinforcement consisted of Ø16 mm transversal bars in both models.

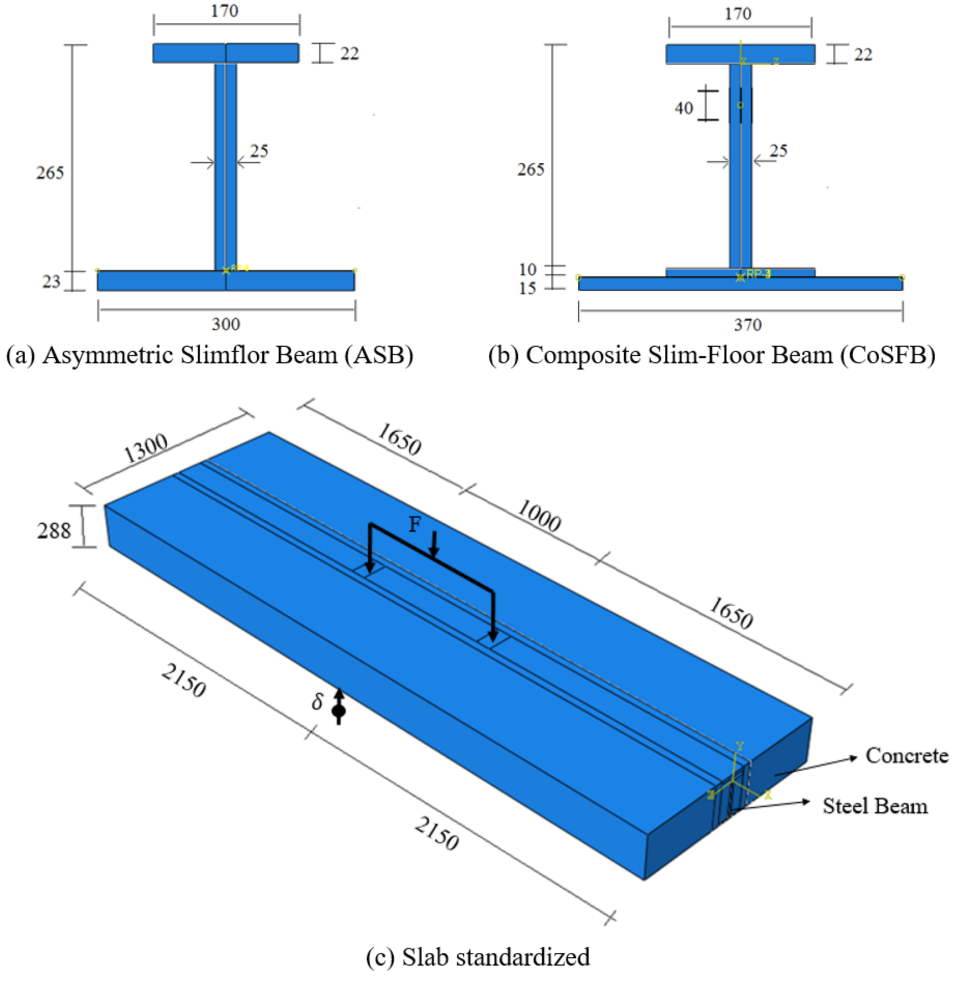

Figure 7. Geometric dimensions standardized (mm).

Composite Slim-Floor Beam is composed of a profile with an additional plate welded to its bottom flange. Therefore, the thickness of the bottom flange is given by the sum of the thicknesses of the two components. Towards standardizing this parameter of ASB and CoSFB, and considering the minimum thickness of the plate is 15 mm, the value of 10 mm was used for the bottom flange of the profile for the obtaining of the same inertias of the steel profile. Standardized profiles are not commercial, and those dimensions were used only for comparison purposes. Table 2 shows the values of the materials properties [3].

Table 2. Materials properties.

Components	f_y (MPa)	f_u (MPa)	E (MPa)	f_{cm} (MPa)	f_t (MPa)
Steel profile	430	550	200000	-	-
Concrete	-	-	32000	30	2.9
Rebars	500	-	210000	-	-

Boundary and loading conditions were also the same for both typologies in the second phase. A simply supported beam was considered, and the loading was an 80 mm displacement incrementally applied at two points, as in the four-point flexural test (Figure 8).

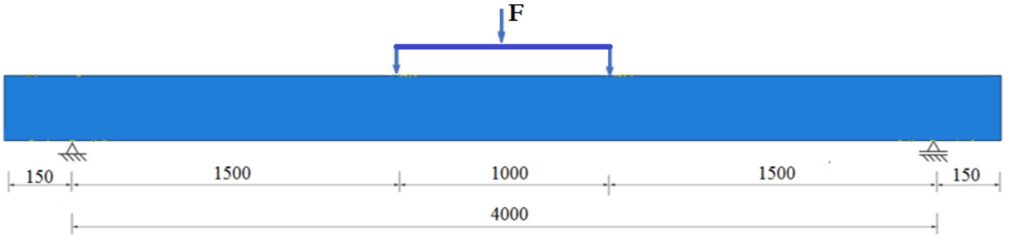

Figure 8. Boundary and loading condition of standardized model (measurements in mm).

Pre-processing parameters, such as element type and constitutive relations, defined for the calibration phase were maintained for the standardization phase.

Element types

A finite element must be chosen in such a way it adequately represents the behavior of each structural component. C3D8R, an eight-node three-dimensional solid element with reduced integration, was used for the concrete slab modelling. However, solid elements require a good mesh refinement for the obtaining of representative solutions, hence, high computational costs. For this reason and according to studies of Rocha [26], Limazie and Chen [28], Kochem and De Nardin [29], Minhaneli [30] and Soares [31], shell element S4R, of four-node of 6-degree freedom and reduced integration, is adequate for the steel profile simulation. The modelling employed two-node three-dimensional beam element B31 for the reinforcement bars. Figure 9 shows the finite elements used in all stages.

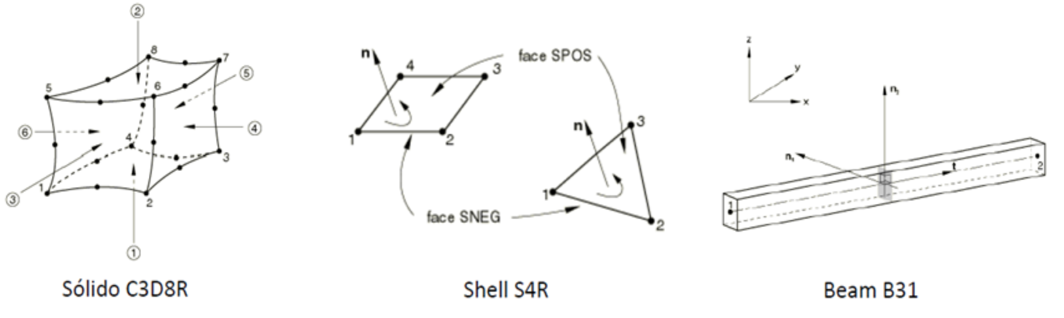

Figure 9. Element types (FE) used.

Materials Constitutive Relations

The numerical simulation considered the nonlinear behavior of the materials. Therefore, the constitutive models that represent this nonlinearity were defined. According to the study of Kochem and De Nardin [29], the model of Sherbourne and Bahaari [32] can represent the nonlinear behavior of the steel profile, and the perfect elastoplastic model is applicable for the representation of the reinforcing bar. Figure 10 shows both models.

Concrete Damaged Plasticity (CDP) was used for the representation of concrete nonlinearities. This model admits two failure mechanisms, namely tensile rupture and compression crushing, and employs a damage variable to represent the loss of concrete stiffness [27]. The use of CDP in ABAQUS® required the definition of some parameters. The first was dilation angle, which measures the slope of the plastic potential for high confinement stresses - low values are related to concretes of fragile behavior, whereas high ones represent a ductile behavior. Another parameter is flow potential eccentricity, defined as a form assumed by the flow surface, usually a hyperbola of 0.1 default value [33].

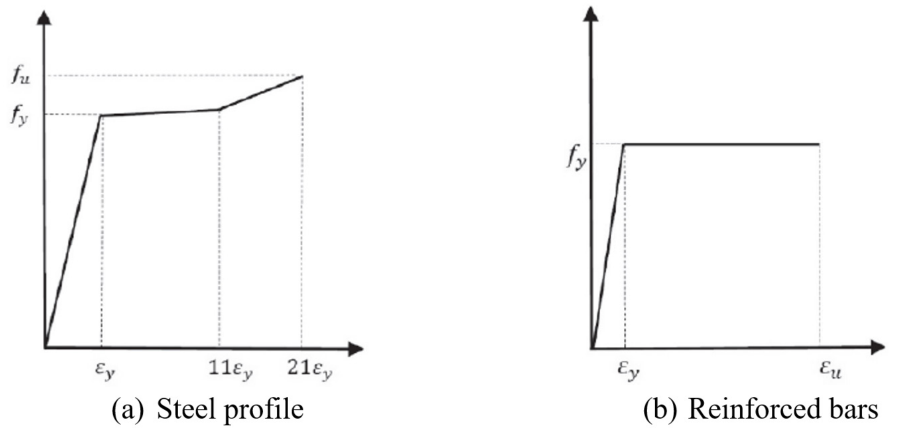

Figure 10. Constitutive models adopted for steel profile and bars.

The biaxial/uniaxial compressive strength ratio was adopted for the description of the point at which concrete fails due to biaxial compression (1.16 default value). The fourth parameter determined was ratio of the distances between the hydrostatic axis and compression meridian and tension meridian (Kc), which defines the shape of the concrete failure surface (the default value in ABAQUS® is 0.6667). Viscosity repairs convergence difficulties when the model shows degradation of stiffness [33]. Table 3 displays the values of the parameters.

Table 3. Parameters of Concrete Damaged Plasticity.

Parameter	Value
Dilation angle	36º
Eccentricity	0.1
f_{b0}/f_{c0}	1.16
Kc	0.6667
Viscosity	0.0001

The stress-strain relationship must be considered for a proper choice of a model that represents the behavior of concrete under tension and compression. In this study, the model developed by Carreira and Chu [34] represents the concrete compression behavior; it considers the softening of the concrete in the compression and is based on the limits of stress and strain. The stress-strain relation is given by Equations 1 and 2 and shown in Figure 11a for $f_{cm} = 30\ \text{MPa}$.

$$\sigma_c = f_{cm} \frac{\beta(\varepsilon / \varepsilon_c^{'})}{\beta - 1 + (\varepsilon / \varepsilon_c^{'})^{\beta}} \tag{1}$$

$$\beta = \frac{1}{1 - \frac{f_{cm}}{\varepsilon_c^{'} E_c}} \tag{2}$$

The model designed by Polak and Genikomsou [35] represents the concrete tension behavior, whose stress-strain relationship under tension is linear-elastic up to the limit of its strength. After the crack opening, the stress-strain curve is characterized by a loss of stiffness, as shown in Figure 11b, for $f_t^{'} = 2.9\ \text{MPa}$ .The mathematical formulation of the tension and compression behavior of the concrete used in CDP is provided in Ribeiro et al. [33].

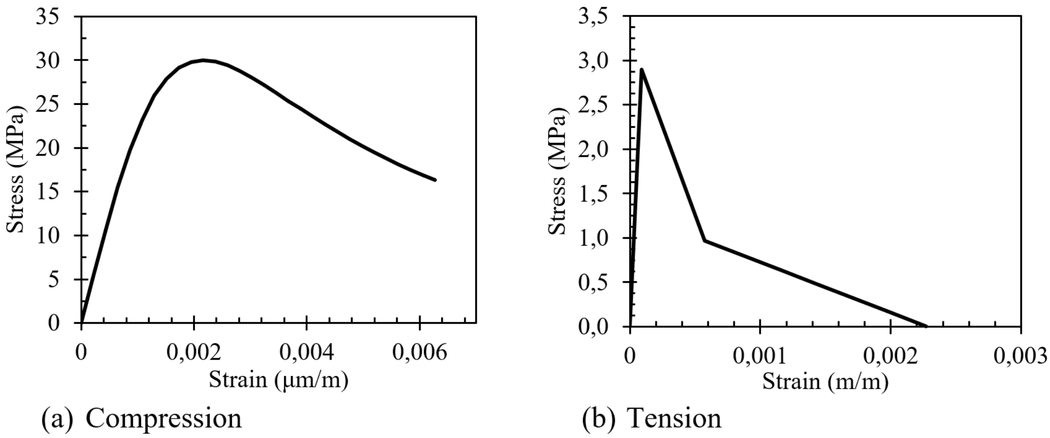

Figure 11. Stress-Strain curve for concrete.

CDP also enables the definition of damage variables, which represent the degradation of the concrete stiffness under concentrated or cyclic loads. The adoption of the compression damage variable was based on Birtel and Mark [36] (Equation 3) and is shown in Figure 12a, and tension damage was given by the model of Pavlović et al. [37] (Equation 4), shown in Figure 12b.

$$d_c = 1 - \frac{\sigma_c E_c^{-1}}{\varepsilon_c^{pl}\left(\frac{1}{b_c} - 1\right) + \sigma_c E_c^{-1}} \tag{3}$$

$$d_t = 1 - \frac{\sigma_t}{ft} \tag{4}$$

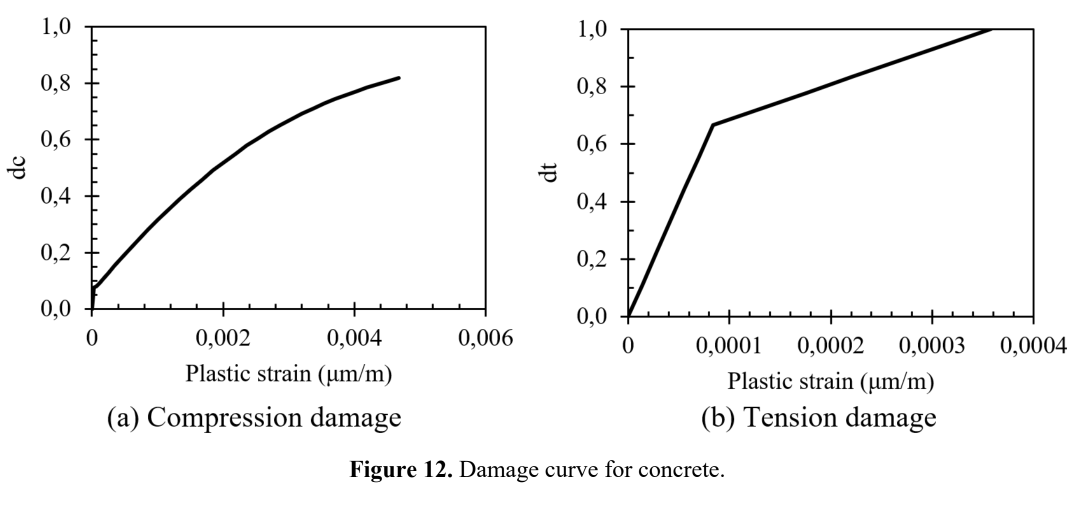

Figure 12. Damage curve for concrete.

Contact modeling

Apart from materials nonlinearities, this numerical model requires the definition of contact nonlinearities for ensuring both concrete slab and steel profile exhibit a composite behavior. Effective tools must be chosen for the interaction between steel profile and concrete slab, and reinforcing bars and concrete slab. Figure 13 shows such contacts [3].

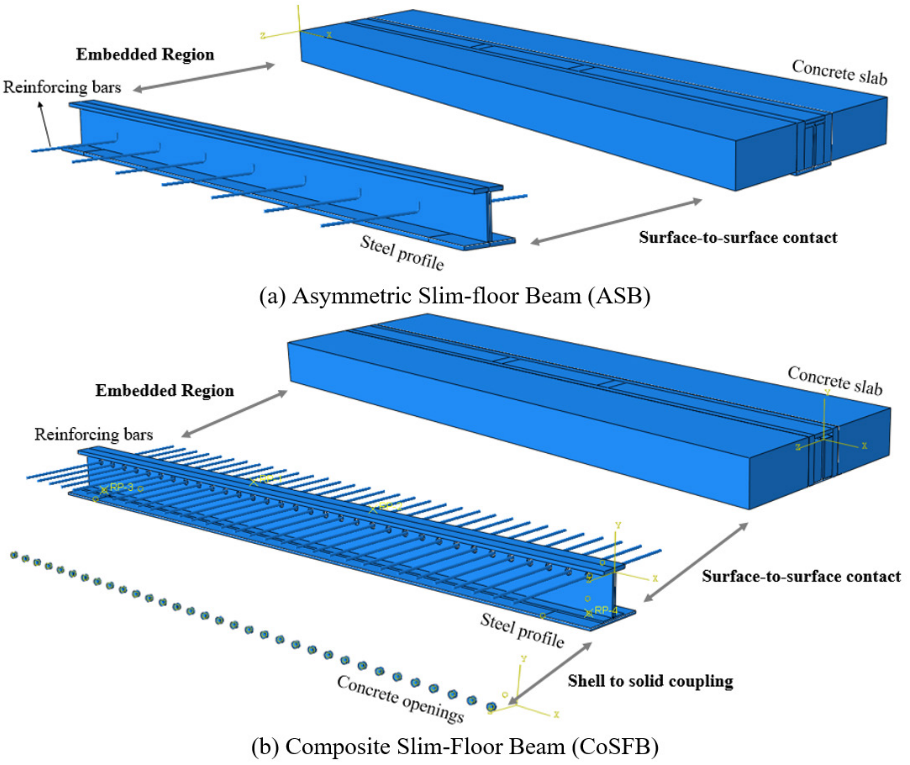

Figure 13. Component contacts.

The connection between reinforcing bars and concrete slab was given by the "*Embedded region*" command, simulating the adhesion of reinforced concrete with restrictions on a body embedded in another one. "*Surface-to-surface contact*" interaction tool was used for the contact between the steel profile and the concrete slab. The normal behavior was defined as "Hard contact", according to which a penetration between surfaces is considered imperceptible, and the tangential behavior, with the "Penalty" formulation, enabled a relative movement of the surfaces with a 0.3 coefficient of friction. Despite the presence of grooves on the top flange of the profile, the use of a different friction coefficient does not influence the results of the flexural behavior; therefore, the friction coefficient used was the same for all contacts between profile and concrete [27].

Regarding CoSFB, the contact between the concrete that passes through the openings and the steel profile was promoted by the "*Shell to solid coupling*" tool. This command connects shell elements to solid ones, coupling the displacement and rotation of the shell nodes to the nearest solid nodes, considered a complete interaction. The connection between rebars and concrete in the web openings was the "*Embedded region*".

Model meshing

Refinement and regularization of elements are two critical factors in the definition of a model's mesh. Towards ensuring the dimensions of each part were equal, a 50 mm x 50 mm x 50 mm mesh was created in the concrete slabs and discretized into 35 mm × 35 mm elements for the steel profiles. The reinforcements mesh was 10 mm. No improvement was observed in the results for more refined mesh values; therefore, they were considered ideal meshes. Figures 14a and 14b show the meshes of the structures for the calibration and standardization phases, respectively.

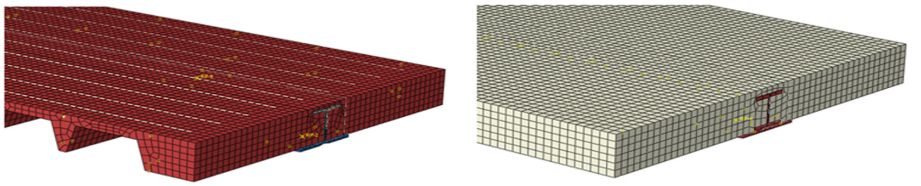

(a) Calibration

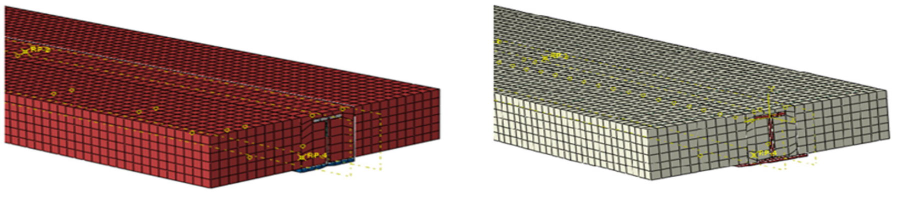

(b) Standardization

Figure 14. Model meshing.

RESULTS AND DISCUSSIONS

The analysis of the results was also divided into three parts. The first provides the calibration results, showing both models were validated according to experimental studies of Lawson et al. [4] and Hechler et al. [5]. Subsequently, a comparative analysis of the flexural behavior of the two typologies based on the results of standardization is presented.

The third part addresses the results of the parametric study and the influence of concrete strength, concrete topping above the steel beam, strength of the steel beams, and bottom flange thickness on the flexural behavior of the typologies.

Models calibration

In the calibration phase, simulations were performed until the numerical models could satisfactorily represent the experimental behavior. The properties of each experimental study were added to ABAQUS, and the parameters involved in the modelling that helped the definition of the structural behavior (e.g., CDP plasticity, aspects of contact interaction, and mesh of the components) were adjusted. The calibration process was conducted through a quantitative comparison between the mid-span load x mid-span deflection curves of the experimental studies and the numerical ones developed in the present study. Figure 15 displays the calibration graph of ASB.

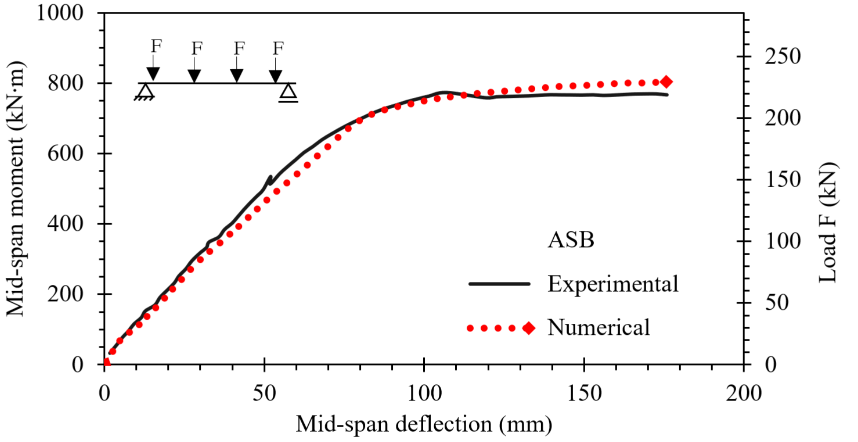

Figure 15. Asymmetric Slimflor Beam calibration.

The error related to the maximum load applied, defined by [(Fexp – Fnum)/Fexp], was used in the quantitative comparison between numerical and experimental curves. The ASB's calibration showed the results of the numerical model are compatible with the experimental ones, with an error of only 5.4% in the maximum load. In the linear phase, the numerical and experimental curves were almost superimposed. Failure modes were compared – a failure occurred with the crushing of the concrete, also identified in the numerical analysis, with longitudinal cracks at the top of the slab. Figure 16 shows the calibration results of Composite Slim-Floor Beam.

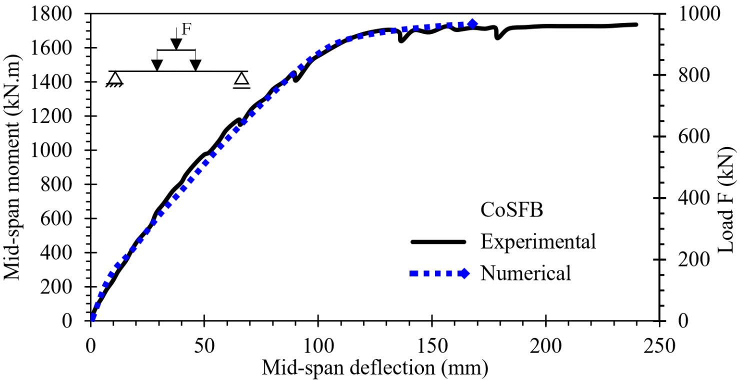

Figure 16. Composite Slim-Floor Beam calibration.

This typology showed an error of only 0.2% in the maximum applied load, and a behavior very similar to that of the experimental study. Both linear and nonlinear phases showed an excellent correlation between experimental and numerical results. The failure mode indicated in the experimental test was the crushing of concrete, also identified in the numerical analysis.

This model required a high computational cost and was unable to converge up to the prescribed displacement due to its geometric complexity, with many nonlinearities involved. Besides, convergence issues are also related to the limitation in the concrete damage plasticity model when type C3D8R finite elements are used [38]. Both calibrated numerical results showed good agreement with those from the experimental studies, therefore, the numerical models were reproducible and sufficiently precise to predict the flexural behavior of the studied typologies.

Comparative analysis

After calibration, the typologies were standardized according to the basic geometric dimensions and materials properties towards a reliable comparison between ASB and CoSFB. The aim of this phase was to understand the way the innovative characteristics of CoSFB, such as web openings, influence the flexural behavior of the system.

A limit deflection value was set for comparison and, due to the lack of a standard for slim floor tests, Eurocode 4 (2004) prescription for composite slabs was used. It establishes the load employed in analyses must be the highest value between the maximum applied load and the load corresponding to a L/50 deflection. The mid-span load x mid-span deflection curve was limited to 86 mm maximum deflection. Figure 17 shows the comparative results of the load-deflection curves for ASB and CoSFB.

According to Figure 16, both typologies exhibited the same behavior in the linear elastic regime, up to the applied load of approximately 200 kN. After this point, the cracking of concrete caused a change in stiffness; CoSFB became more rigid than ASB and showed a higher computational cost due to the presence of openings in the profile, which imposes more nonlinearities.

The material properties, boundary and loading conditions were standardized in this phase. The main difference between ASB and CoSFB was the presence of small openings at the top of the profile web, which enables the passage of steel bars and concrete, thus ensuring the composite behavior and increasing both resistance capacity and stiffness of CoSFB. In comparison to ASB, which has no openings, CoSFB has higher strength and stiffness (Figure 17). Despite a lower strength value, ASB is more frequently used in slim floors and its construction has been consolidated. Its execution is simpler, and the asymmetric profile is more available on the international market.

The main stresses in concrete slabs and the stress based on the von Mises criterion for steel profiles were also analyzed (Figure 18). The grey zones in the slab are the tensioned ones, and the dark grey areas are those that reached compression stress higher than f_c, when the concrete enters plasticity, due to the high load in the composite slab. The crack pattern (red) due to tensile stresses (*Damaget*) is shown at the bottom of Figure 18a, and 18b.

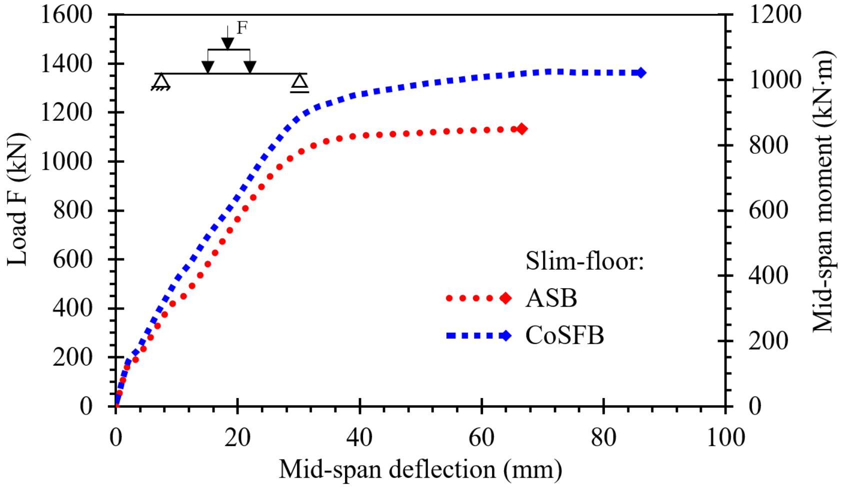

Figure 17. Comparative graph of flexural behavior.

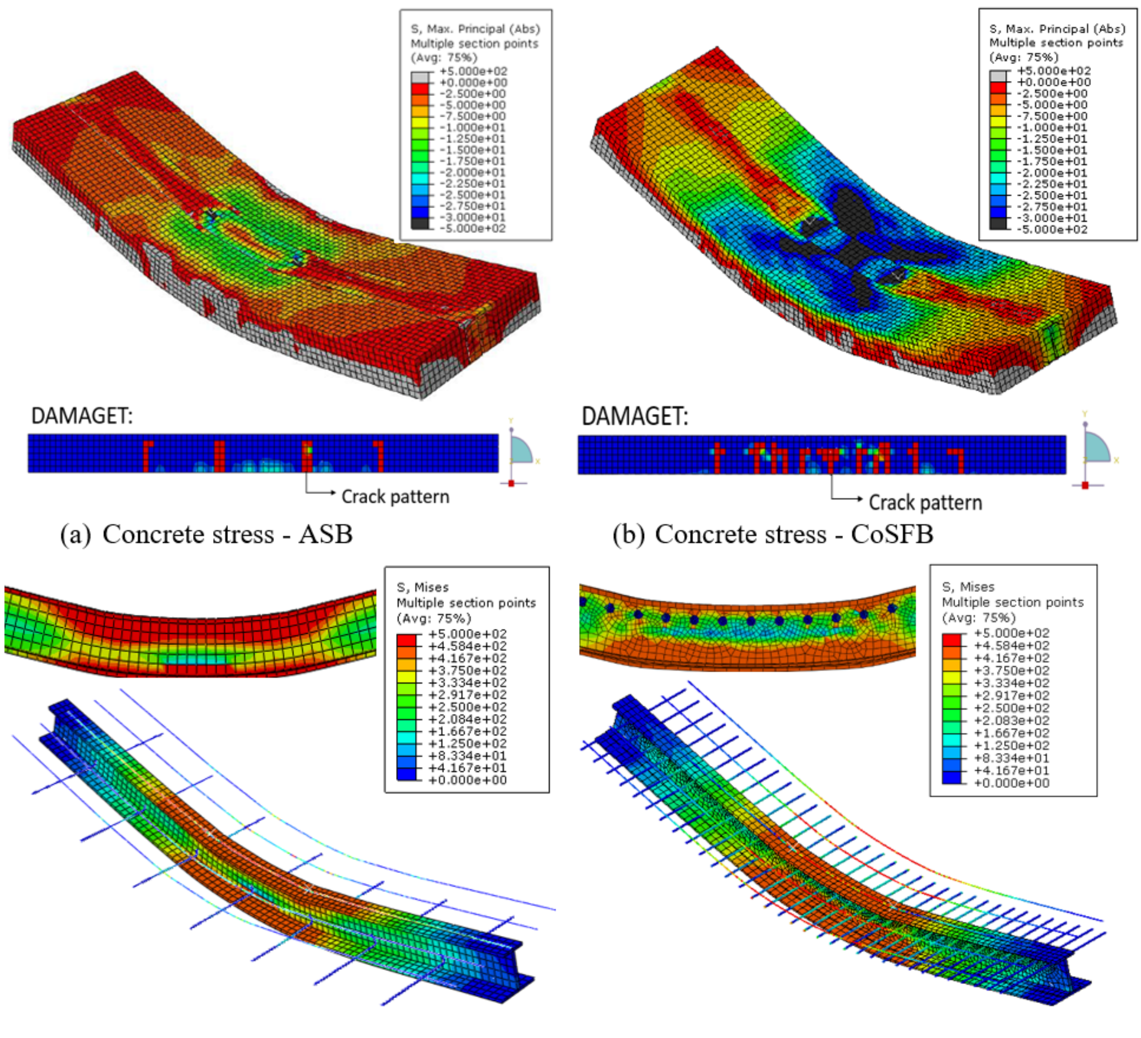

(a) Concrete stress - ASB
(b) Concrete stress - CoSFB
(c) Von Mises stress of steel beam - ASB
(d) Von Mises stress of steel beam - CoSFB

Figure 18. Stress of concrete and steel beam at the ultimate loads (measurements in MPa).

In the final increment (66.6 mm), ASB was subjected to 1134 kN and displayed characteristics of concrete crushing on top of the slab, mainly near the load application. It also showed vertical cracks related to tensile stresses at the bottom of the slab, near the load application points, highlighted in Figure 18a.

CoSFB was subjected to 1356 kN for the same displacement of ASB (66.6 mm). The approximately 20% increase in the CoSFB load led to higher compression stresses in the upper central region of the slab, but with a smaller area of the tensioned concrete. However, this typology exhibited more vertical cracks than ASB, highlighted in Figure 18b. The failure mode was by concrete crushing, as in ASB.

The analysis of von Mises stresses in the profiles revealed the highest stresses are concentrated in the central part of the flanges. However, in ASB, the top flange was more requested, whereas CoSFB regularly distributed the tension between the two flanges and the plate. ASB web showed low-stress values. No stresses concentration was observed in the surroundings of CoSFB openings, since the concrete guarantees the necessary stiffness, highlighted in Figure 18d.

Parametric study

The influence of four parameters, namely concrete strength, concrete topping above the steel beam, strength of steel beams, and bottom flange thickness were chosen from a bibliographic review to be analyzed for both typologies. Two parameters, namely diameter of the openings and percentage of openings with bars crossing them were also analyzed for CoSFB. The parametric study focused on the mid-span load x mid-span deflection curve, and the standardized model was used as a reference.

Concrete strength

Three f_c values, namely 20 MPa, 30 MPa (reference) and 40 MPa, were analyzed. Figure 19 shows the graphs for each typology.

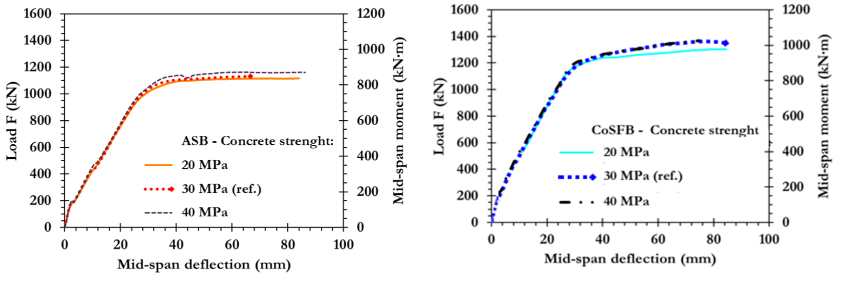

a) ASB b) CoSFB

Figure 19. Load-deflection curve – Concrete strength.

An increase in concrete strength increased the maximum strength without affecting the stiffness of the structure. This parameter does not exert a significant influence on the flexural behavior of the typologies; however, CoSFB was more affected than ASB.

Concrete topping above the steel beam

Three analyses – with no concrete topping, with 23 mm concrete topping (reference), and with 46 mm concrete topping – assessed the influence of the concrete topping above the steel beam on the slim floor. Mid-span load x mid-span deflection curves were obtained for each typology, as shown in Figure 20.

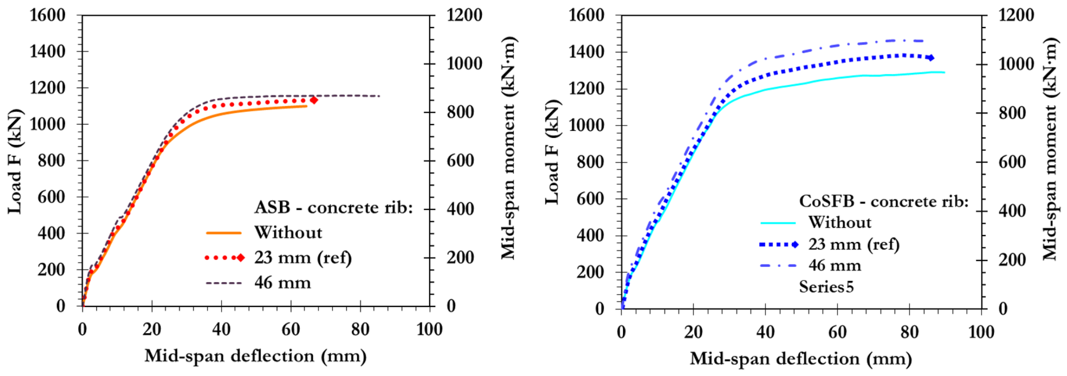

a) ASB b) CoSFB

Figure 20. Load-deflection curve – Concrete topping above the steel beam.

Likewise, this parameter was not significant, especially in ASB, since it did not influence stiffness, and the resistance capacity was slightly increased. However, it was more influential than the previous one.

Strength of steel beams

Three values of yield strength, namely 380 MPa, 430 MPa (reference) and 480 MPa, were chosen for the evaluation of the influence of strength of steel beams, and the ultimate strength was set at 550 MPa. Figure 21 shows the behavior of the typologies.

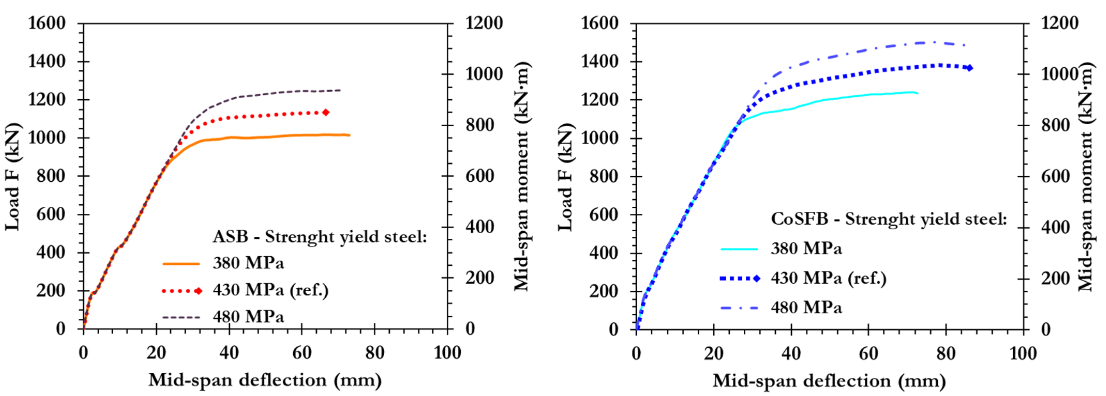

a) ASB b) CoSFB

Figure 21. Load-deflection curve – Strength of steel beams.

The two typologies exhibited very similar behaviors. The strength of the profile considerably influenced the resistance capacity, increasing with the increase in the yield strength. However, stiffness was not affected.

Bottom flange thickness

Three cases for the bottom flange thickness, namely 11.5 mm, 23 mm (reference) and 34.5 mm, were verified. Figure 22 shows the behavior of the two typologies.

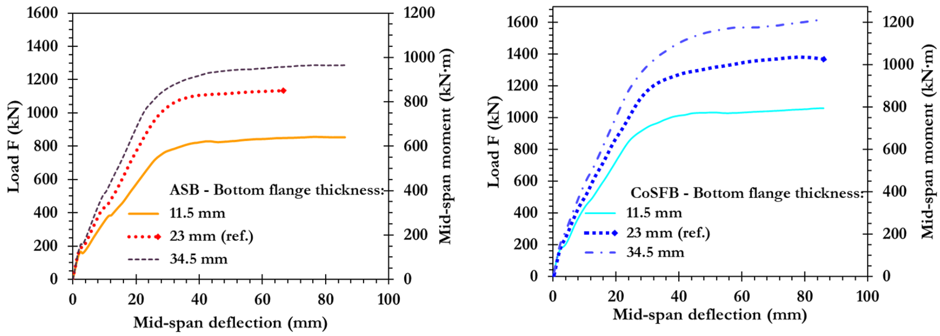

a) ASB b) CoSFB

Figure 22. Load-deflection curve – Bottom flange thickness.

For CoSFB, the two thicknesses whose sum composes it proportionally decreased or increased for the analysis.

A variation in this parameter, which was the most influential in the flexural behavior of the typologies, showed an increase in the bottom flange thickness considerably increases both resistance capacity and stiffness.

Analyses of CoSFB openings

CoSFB differs from ASB mainly due to the presence of web openings, which enable the passage of rebars. Two parametric studies conducted analyzed the behavior of such openings. In the first, the diameter of the openings was varied, analyzing the original size (40 mm), a larger diameter (80 mm) and a smaller diameter (20 mm), and the second focused on the percentage of openings with bars crossing them. The following three cases were analyzed: "100%", which represents the system with the rebars passing through all openings, "50%", with half the openings crossed by rebars, and "0%", with no bar passing through the openings. Figure 23 shows the behavior for each analysis.

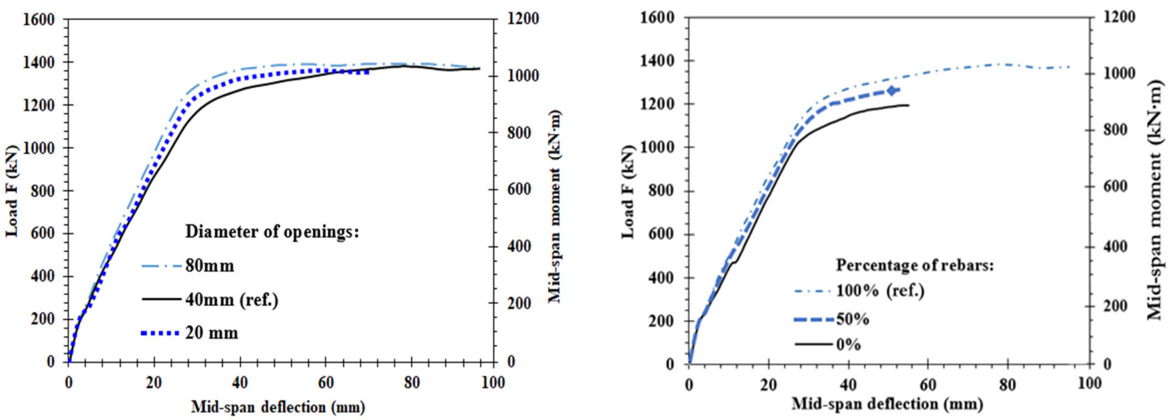

a) Diameter of openings b) Rebars

Figure 23. Load-deflection curve – Analyses of CoSFB openings.

In the first analysis, the diameter of the openings influenced both initial resistance and stiffness of the structure. The 40 mm opening system showed lower initial resistance; however, it increased and reached high values at the end of the analysis. When 20 and 80 mm diameters were used, higher initial resistance was observed; however, convergence for greater displacements of the 20 mm system was hampered by the concrete high compression stresses in the openings, indicating crushing of concrete. Therefore, further analyses are necessary for the establishment of a proper diameter of the system.

The second analysis revealed a reduction in the percentage of rebars passing through the openings decreases the stiffness and capacity of the system. The convergence of the simulation was also affected by the reduction in the number of rebars, indicating a faster degradation of the structure with fewer bars.

CONCLUSIONS

This article has addressed numerical studies on the flexural performance of two different typologies, namely ASB and CoSFB composite beams used in slim-floor, and the results have led to the following conclusions:

- Calibration phase: the numerical simulation reproduced the behavior of the experimental models, and, therefore, can predict their flexural performance. Small divergences between experimental and numerical results are due to limitations in the simulation related to differences between the real properties and those estimated in the numerical model, and simplifications adopted.
- Comparative study: the comparison phase revealed ABS is less stiff and resistant than CoSFB and showed high plastic deformations and a large region of slab tensioned at the end of the simulation. CoSFB showed higher compression stresses, indicating crushing of the concrete at the end of the simulation, with a smaller region of concrete under tension.
- Parametric analysis: two parameters related to concrete (concrete strength and concrete topping above the steel beam) and two others related to the steel profile (strength steel and bottom flange profile thickness) were varied for both typologies. Those in the profile significantly increased resistance and rigidity. The variation in the lower flange thickness was the most influential, whereas concrete strength exerted the lowest influence on the typologies. For CoSFB, analyses of the diameter of the openings and the percentage of openings with bars crossing them revealed the passage of steel bars through the openings improves the structural behavior. Further analyses of the diameter of the openings are necessary for the establishment of a proper diameter of the system and consequent improvement in the behavior of the structure with no concrete crushing.

This study achieved its objective of comparing two typologies of slim floor, i.e., ASB and CoSFB, and performing parametric analyses, with satisfactory and applicable results. It has, therefore, contributed to the dissemination of knowledge on slim floor, presenting some typologies, with important information about ASB and CoSFB and their flexural behaviors.

In practical terms, the choice of a typology must still take into account aspects of technical and economic feasibility. Topics such as labor, ease of acquisition and assembly, logistics, speed of construction and architectural impositions must be considered. Moreover, the capacity of each typology can be improved with the use of specific slabs (e.g., steel deck and hollow-core slabs). Such analyses are suggested for future studies.

ACKNOWLEDGEMENTS

The authors acknowledge the Conselho Nacional de Desenvolvimento Científico e Tecnológico (CNPq) for the financial support given to this research. The study was also financed by the Coordenação de Aperfeiçoamento de Pessoal de Nível Superior - Brasil (CAPES) - Finance Code 001 and grant #2019/03513-5, São Paulo Research Foundation (FAPESP).

REFERENCES

[1] M. Malite, “Sobre o cálculo de vigas mistas aço-concreto: ênfase em edifícios,” M.S. thesis, Dept. Struct. Eng., Univ. São Paulo, São Carlos, 1990.

[2] S. De Nardin and A. L. H. C. El Debs, "Avaliação da influência da posição dos conectores de cisalhamento no comportamento de vigas mistas parcialmente revestidas," *Rev. Esc. Minas*, vol. 61, no. 2, pp. 239–247, 2008., http://dx.doi.org/10.1590/S0370-44672008000200019.

[3] T. M. Borghi, “Contribuição ao estudo do piso misto de pequena altura: análise numérica das tipologias,” M.S. thesis, Dept. Struct. Eng., Univ. São Paulo, São Carlos, 2020.

[4] R. M. Lawson, D. L. Mullet, and J. W. Rackham, *Design of Asymmetric Slimflor Beams Using Deep Composite Decking* (SCI Publication P175). Ascot, UK: The Steel Constr. Inst., 1997.

[5] O. Hechler, M. Braun, R. Obiala, U. Kuhlmann, F. Eggert, and G. Hauf, “CoSFB: composite slim-floor beam: experimental test campaign and evaluation,” in *Proc. VII Int. Conf. Composite Constr. Steel Concr.*, 2016, pp. 158–172. [Online]. Available: https://ascelibrary.org/doi/10.1061/9780784479735.013

[6] Tata Steel. https://www.tatasteelconstruction.com/en_GB/tata-steel-case-studies/other/Chasse-Church (accessed June 26, 2020).

[7] ArcelorMittal, *Slim Floor – an Innovative Concept for Floors*. Luxemburgo, 2017.

[8] D. L. Mullet, *Slim Floor Design and Construction* (SCI Publication P110). Ascot, UK: The Steel Constr. Inst., 1992.

[9] D. L. Mullet and R. M. Lawson, *Slim floor Construction using Deep Decking* (SCI Publication P127). Ascot, UK: The Steel Constr. Inst., 1993.

[10] British Standard, *Structural Use of Steelwork in Buildings – Part 3: Code of Practice for Design of Simple and Continuous Composite Beams*, BS5950-3, 1982.

[11] C. G. Bailey, "The behaviour of asymmetric slim floor steel beams in fire," *J. Construct. Steel Res.*, vol. 50, no. 3, pp. 235–257, 1999, http://dx.doi.org/10.1016/S0143-974X(98)00247-8.

[12] P. Mäkeläinen and Z. Ma, "Fire resistance of composite slim floor beams," *J. Construct. Steel Res.*, vol. 54, no. 3, pp. 345–363, 2000, http://dx.doi.org/10.1016/S0143-974X(99)00059-0.

[13] J. L. R. Paes, "Aportaciones al análisis del comportamiento estructural de sistemas de forjados mixtos tipo "Slim floor," Ph.D. dissertation, Dept. Constr. Eng., Univ. Politéc. Catalunha, Barcelona, Spain, 2003.

[14] M. V. Leskelä and J. Hopia, *Steel Sections for Composite Shallow Floors. Report RLT 0053E.* Oulu, Finland: Univ. Oulu, Struct. Eng. Lab., 2000.

[15] J. W. Rackham, S. J. Hicks, and G. M. Newman, Design of asymmetric slimflor beams with precast concrete slabs. The Steel Construction Institute, 2006.

[16] I. M. Ahmed and K. D. Tsavdaridis, "The evolution of composite flooring systems: applications, testing, modelling and Eurocode design approaches," *J. Construct. Steel Res.*, vol. 155, pp. 286–300, Apr 2019, http://dx.doi.org/10.1016/j.jcsr.2019.01.007.

[17] M. O. Barros, "Análise e dimensionamento de pavimentos mistos slim floor," M.S. thesis, Univ. Nova Lisboa, Lisbon, 2011.

[18] M. Braun et al., "Experimentelle Untersuchungen von Slim-Floor-Trägern in Verbundbauweise," *Stahlbau*, vol. 83, no. 10, pp. 741–749, Oct 2014, http://dx.doi.org/10.1002/stab.201410204.

[19] T. Sheehan, X. Dai, J. Yang, K. Zhou, and D. Lam, "Flexural behaviour of composite slim floor beams," *Structures*, vol. 21, pp. 22–32, Oct 2019, http://dx.doi.org/10.1016/j.istruc.2019.06.021.

[20] N. Baldassino, G. Roverso, G. Ranzi, and R. Zandonini, "Service and ultimate behaviour of slim floor beams: an experimental study," *Structures*, vol. 17, pp. 74–86, 2019, http://dx.doi.org/10.1016/j.istruc.2018.10.001.

[21] Y. K. Ju, D. Kim, and S. Kim, "Experimental assessment of the shear strength of an asymmetric steel composite beam with web openings," *Can. J. Civ. Eng.*, vol. 32, no. 2, pp. 314–328, 2005, http://dx.doi.org/10.1139/l04-094.

[22] M. V. Leskela, S. Peltonen, A. Iliopoulos, and P. Kiriakopoulos, "Numerical and experimental investigations on the vertical shear resistance of boxed steel cross-sections with concrete infill (Deltabeams)," in *EUROSTEEL 2014*, Naples, Italy, 2014.

[23] D. Lam, X. Dai, U. Kuhlmann, J. Raichle, and M. Braun, "Slim-floor construction - design for ultimate limit state," *Steel Constr.*, vol. 8, no. 2, pp. 79–84, 2015, http://dx.doi.org/10.1002/stco.201510019.

[24] B. Y. Huo and C. A. D'Mello, "Shear transferring mechanisms in a composite shallow cellular floor beam with web openings," *Structures*, vol. 9, pp. 134–146, 2017, http://dx.doi.org/10.1016/j.istruc.2016.11.003.

[25] S. Chen and T. Limazie, "Composite slim floor beams with innovative shear connections," *Proc. Inst. Civ. Eng., Struct. Build.*, vol. 171, no. 1, pp. 29–37, 2017., http://dx.doi.org/10.1680/jstbu.16.00171.

[26] F. M. Rocha, "Modelos numéricos de vigas mistas de aço e concreto pertencentes a sistemas de pisos mistos de pequena altura em situação de incêndio," M.S. thesis, Dept. Struct. Eng., Univ. São Paulo, São Carlos, 2012.

[27] C. Maraveas, T. Swailes, and Y. Wang, "A detailed methodology for the finite element analysis of asymmetric slim floor beams in fire," *Steel Constr.*, vol. 5, no. 3, pp. 191–198, Aug 2012, http://dx.doi.org/10.1002/stco.201210024.

[28] T. Limazie and S. Chen, "FE modeling and numerical investigation of shallow cellular composite floor beams," *J. Construct. Steel Res.*, vol. 119, pp. 190–201, 2016., http://dx.doi.org/10.1016/j.jcsr.2015.12.022.

[29] R. F. F. Kochem and S. De Nardin, "Numerical model of beam-to-column composite connection between slim floor system and composite column," *Rev. IBRACON Estrut. Mater.*, vol. 13, no. 2, pp. 348–379, Apr 2020, http://dx.doi.org/10.1590/s1983-41952020000200009.

[30] V. C. Minhaneli, "Avaliação do comportamento estrutural de vigas mistas para sistemas de piso slim floor formadas por perfis de aço com grandes aberturas na alma," M.S. thesis, Fed. Univ. Viçosa, Viçosa, 2018.

[31] L. C. Soares, "Análise via método dos elementos finitos de pisos mistos de pequena altura – Slim Floor," M.S. thesis, Fed. Univ. Ouro Preto, Ouro Preto, 2012.

[32] A. N. Sherbourne and M. R. Bahaari, "M. R. Bahaari, 3D simulation of bolted connections to unstiffened columns – I. T-stub connections," *J. Construct. Steel Res.*, vol. 40, no. 3, pp. 169–187, 1996, http://dx.doi.org/10.1016/S0143-974X(96)00048-X.

[33] P. O. Ribeiro, G. M. S. Gidrão, L. V. Vareda, R. Carrazedo, and M. Malite, "Numerical and experimental study of concrete I-beam subjected to bending test with cyclic load," *Lat. Am. J. Solids Struct.*, vol. 17, no. 3, e266, 2020.

[34] D. J. Carreira and K. Chu, "Stress-strain relationship for plain concrete in compression," *ACI J.*, vol. 82, pp. 797–804, 1985.

[35] M. A. Polak and A. S. Genikomsou, "Finite element analysis of punching shear of concrete slabs using damaged plasticity model in ABAQUS," *Eng. Struct.*, vol. 98, pp. 38–48, 2015., http://dx.doi.org/10.1016/j.engstruct.2015.04.016.

[36] V. Birtel and P. Mark, "Parameterised finite element modelling of RC beam shear failure," in *Proc. 19th Annu. Int. ABAQUS Users' Conf.*, Boston, 2006, pp. 95–108.

[37] M. Pavlović, Z. Marković, M. Veljković, and D. Buđevac, "Bolted shear connectors vs. headed studs behaviour in push-out tests," *J. Construct. Steel Res.*, vol. 88, pp. 134–149, 2013, http://dx.doi.org/10.1016/j.jcsr.2013.05.003.

[38] L. D. Kirchhof, "Uma contribuição ao estudo de vigas mistas aço-concreto simplesmente apoiadas em temperatura ambiente e em situação de incêndio," M.S. thesis, Dept. Struct. Eng., Univ. São Paulo, São Carlos, 2004.

Author contributions: TMB: conceptualization, methodology, numerical analysis, writing, review; LAMO: conceptualization, writing, review; ALHCED: supervision, text review.

Editors: Bruno Briseghella, Guilherme Aris Parsekian.

Rev. IBRACON Estrut. Mater., vol. 14, no. 4, e14412, 2021

IBRACON Structures and Materials Journal
Revista IBRACON de Estruturas e Materiais
ISSN 1983-4195 ismj.org

ORIGINAL ARTICLE

Resistant bending moment to lateral-torsional buckling of continuous steel and concrete composite beams with transverse stiffeners

Momento fletor resistente à flambagem lateral com distorção de vigas mistas contínuas de aço e concreto com enrijecedores transversais

Janaina Pena Soares de Oliveira[a]
João Victor Fragoso Dias[b]
Ricardo Hallal Fakury[b]
Adenilcia Fernanda Grobério Calenzani[c]

[a]Instituto Federal do Espírito Santo – IFES, Departamento de Engenharia Civil, Vitória, ES, Brasil
[b]Universidade Federal de Minas Gerais, Departamento de Engenharia de Estruturas, Belo Horizonte, MG, Brasil
[c]Universidade Federal do Espírito Santo, Departamento de Engenharia Civil, Vitória, ES, Brasil

Received 23 April 2020
Accepted 25 November 2020

Abstract: In this paper, a numerical analysis using the finite element method, employing the commercial code Ansys, is performed to evaluate the influence of transverse stiffeners welded to the web of the steel profile on the lateral stiffness and resistant bending moment of continuous steel and concrete composite beams subjected to lateral-torsional buckling (LTB). The developed numerical model was validated by comparison with the results of tests performed by another researcher. Subsequently, a parametric analysis was carried out for beams with two and three spans, varying the spacing between the stiffeners. Finally, based on the analysis performed, it was concluded that the transverse stiffeners can significantly increase the lateral stiffness and the resistant moment of continuous composite beams. A calculation procedure to obtain this moment is proposed, having as reference the prescriptions of the Brazilian standard ABNT NBR 8800:2008.

Keywords: continuous steel and concrete composite beams, lateral-torsional buckling, transverse stiffeners, resistant bending moment, lateral stiffness.

Resumo: Neste artigo, uma análise numérica usando método dos elementos finitos, com apoio do *software* Ansys, é realizada para avaliar a influência de enrijecedores transversais soldados à alma do perfil de aço na rigidez lateral e no momento fletor resistente de vigas mistas contínuas de aço e concreto à flambagem lateral com distorção (FLD). O modelo numérico desenvolvido foi validado por meio de comparação com os resultados de ensaios realizados por outro pesquisador. Na sequência, foi feita uma análise paramétrica, para vigas com dois e três vãos, variando-se o espaçamento entre os enrijecedores. Finalmente, com base nas análises realizadas, conclui-se que os enrijecedores transversais podem aumentar significativamente a rigidez lateral e o momento resistente de vigas mistas contínuas e um procedimento de cálculo para se obter esse momento, tendo como referência as prescrições da norma brasileira ABNT NBR 8800:2008, é proposto.

Palavras-chave: vigas mistas contínuas de aço e concreto, flambagem lateral com distorção, enrijecedor transversal, momento fletor resistente, rigidez lateral.

How to cite: J. P. S. Oliveira, J. V. F. Dias, R. H. Fakury, and A. F. G. Calenzani, "Resistant bending moment to lateral-torsional buckling of continuous steel and concrete composite beams with transverse stiffeners," *Rev. IBRACON Estrut. Mater.*, vol. 14, no. 4, e14412, 2021, https://doi.org/10.1590/S1983-41952021000400012

Corresponding author: Janaina Pena Soares de Oliveira. E-mail: janaina.pena@ifes.edu.br
Financial support: Conselho Nacional de Desenvolvimento Científico e Tecnológico (CNPq), Coordenação de Aperfeiçoamento de Pessoal de Nível Superior (CAPES) e Fundação de Amparo à Pesquisa do Estado de Minas Gerais (FAPEMIG).
Conflict of interest: Nothing to declare.

1 INTRODUCTION

1.1 Lateral-torsional buckling of continuous steel and concrete composite beams

The most used continuous steel and concrete composite beams are those in which the steel profile, almost always with I section, keeps its continuity on the internal supports, normally consisting of columns of the building's structure.

In these beams, the bottom flange is subjected to compression in the hogging moment region (near the internal supports) and, consequently, may suffer lateral instability, moving in the direction of the minor axis inertia of the steel profile. This flange is subjected to a lateral translation, δ, which is necessarily accompanied by a rotation, θ, since the web needs to bend laterally (distort) for the displacement to occur, according to Figure 1a, resulting in an ultimate limit state known as lateral-torsional buckling (LTB). The occurrence of this phenomenon is facilitated by the concrete slab's bending and the deformation of the connection of this slab with the top flange of the steel profile (shear connection). According to Johnson [1], the displacements δ and θ create a half-wave on each side of the internal supports, with maximum values located in the cross sections between two and three times the height of the steel profile (d) apart from these supports, as shown in Figure 1b. It is important to emphasize that at the internal supports, the bottom flange of steel profile must be laterally constrained.

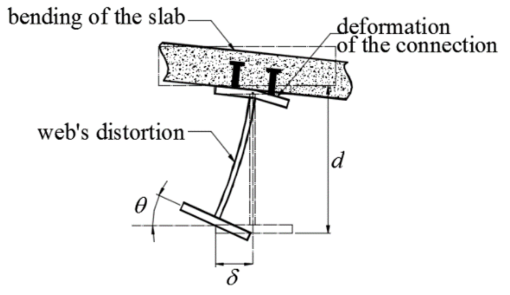

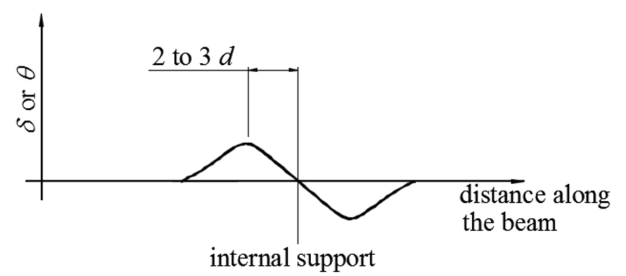

Figure 1. Lateral-torsional buckling

1.2 Inverted "U"- frame mechanism

The Brazilian standard [2] provides an approximate procedure to verify LTB, similar to the European standard [3], which consists of determining the elastic critical moment (M_{cr}) as an initial step to obtain the resistant bending moment. This critical moment is obtained by considering the inverted "U"- frame mechanism, formed by the concrete slab supported by two or more parallel steel beams. This mechanism is different from the usual "T", which consists of a single steel beam under the concrete slab. The use of the inverted "U"- frame mechanism better represents the boundary conditions that are imposed by the floor system to the steel beam.

In the scientific literature and highlight by Calenzani [4], two types of inverted "U"- frame mechanisms are described, the continuous and discrete mechanisms. In the continuous "U"- frame mechanism, the steel and concrete composite beam has transverse stiffeners only at the internal supports. In this type of mechanism, the restriction to lateral translation of the compressed flange is provided only by the concrete slab and by the unstiffened web of the steel profile. In the discrete "U"- frame mechanism, there are transverse stiffeners welded to the web of the steel profile regularly spaced throughout the hogging moment region, which contribute to the distortional rigidity.

1.3 Calculation of the resistant moment to LTB according to standards

The calculation methods of the Brazilian [2] and European [3] standards for determining the LTB resistant moment of continuous composite beams are approximate, considering only the situation of the continuous inverted "U"- frame mechanism, therefore with transverse stiffeners only at the internal supports, and it consists of the following steps:

a) Determination of elastic critical moment at the internal support of the relevant span where the hogging bending moment is greatest. The European standard [3] does not provide an equation for this determination, while the Brazilian standard [2] adopts the formulation proposed by Roik et al. [5], given by:

$$M_{cr} = \frac{C_{dist}\,\alpha_g}{L}\sqrt{\left(G_a J + k_r \frac{L^2}{\pi^2}\right) E_a I_{af,y}} \tag{1}$$

in which E_a and G_a are elasticity and shear modulus of the steel profile, respectively, J is the torsion constant of the profile, $I_{af,y}$ is the second moment of area of the bottom flange of I profile about the axis passing through the web's medium plane (y axis). The α_g factor is associated with the geometry of the cross section of the composite beam and C_{dist} is a coefficient that considers the bending moment distribution along the member's length L. Also, k_r is the rotational stiffness per unit length of the beam expressed by the following equation:

$$k_r = \frac{k_1 + k_2}{k_1 k_2} \tag{2}$$

in which k_1 is the flexural stiffness of the cracked concrete slab in the direction transverse to the I profile and k_2 is the flexural stiffness of the steel web.

The flexural stiffness of the concrete slab is obtained as:

$$k_1 = \alpha \frac{(EI)_2}{a} \tag{3}$$

with α being a coefficient that depends on the beam's position in the floor system ($\alpha = 2$ for an edge beam and $\alpha = 3$ for an inner beam – for an inner beam in a floor with four or more similar beams, $\alpha = 4$ may be used). $(EI)_2$ is the cracked flexural stiffness per unit width of the concrete slab and a is the spacing between the parallel beams of the "U"- frame mechanism.

The steel web's flexural stiffness can be taken as:

$$k_2 = \frac{E_a t_w^3}{4h_0\left(1-\nu^2\right)} \tag{4}$$

in which t_w is the thickness of the web of the steel profile, h_0 is the distance between the geometric centers of the two flanges of the steel profile and υ is the Poisson's ratio for the structural steel.

b) Determination of a slenderness parameter, given by:

$$\lambda_{dist} = \sqrt{\frac{M_{Rk}^{-}}{M_{cr}}} \tag{5}$$

where M_{Rk}^{-} is the nominal resistant bending moment of the beam's cross section at hogging bending moment region, constituted by the steel profile and the longitudinal reinforcements.

c) Determination of the reduction factor χ_{dist} from the value of λ_{dist} with the use of a resistant curve.

d) Determination of the nominal resistant moment of the composite beam, from the value of χ_{dist}, through the expression:

$$M_{dist,Rk}^{-} = \chi_{dist} M_{Rk}^{-} \tag{6}$$

In fact, in step d), both standards already directly prescribe the determination of the design resistant moment, by the equation:

$$M_{dist,Rd}^{-} = \chi_{dist} M_{Rd}^{-} \quad (7)$$

where M_{Rd}^{-} is the design resistant moment of the cross section in the hogging bending moment region, determined in a similar way to M_{Rk}^{-} with the application of partial coefficients to the yield strengths of the steel profile and the longitudinal reinforcement of the slab. However, in this paper, to facilitate comparative analyses and evaluation, the values of the nominal resistant moments were always considered.

Although the procedures of the two standards are similar, besides already mentioned the fact that the European standard [3] does not provide an equation to determine the elastic critical moment, there are also two differences between them that can lead to very different results of the value of the resistant moment to LTB:

1) the resistant curve used to obtain χ_{dist} from the value of λ_{dist} is not the same;
2) the Brazilian standard [2] is only applicable to compact steel sections, with the nominal resistant moment to LTB reaching the plastic moment of the composite cross section, while the European standard [3] is applicable to sections up to Class 3, which are those that can present local instability in an inelastic regime, situation in which the maximum nominal resistant moment is the one corresponding to the beginning of yield of the composite cross section.

The second inequality brings up an inconsistency, that deserves further studies, because steel cross sections are classified differently in the two standards. Thus, it is very common, that, depending on the web's slenderness, the cross section may be classified as compact by the Brazilian standard [2], with the resistant moment reaching the plastic moment, and as Class 3 by the European standard [3], situation in which the resistant moment is limited to that of the beginning of yield.

1.4 Previous studies

The phenomenon of lateral-torsional buckling in continuous composite beams has been studied by several researchers since the 1980s, when Bradford and Trahair [6], Svensson [7] and Goltermann and Svensson [8] addressed the issue of determination of the elastic critical moment. In 1990, Roik et al. [5] proposed an equation to obtain this moment which is still adopted by the current Brazilian standard [2], as stated in the previous subsection. Some further investigation has been made to improve the equation proposed by Roik et al. [5], for example, Hanswille [9], Amaral et al. [10], Dias et al. [11] and Oliveira [12].

In all proposed methods for the determination of M_{cr}, it is necessary obtain the rotational stiffness of the inverted "U"- frame mechanism of the composite beam, represented by k_r. To determine these values of stiffness, experimental or numerical analysis may be performed. However, there is in a literature a practical alternative, with very reliable results, which is to consider it as resulting from the serial association between the flexural stiffness of the slab (k_1), the transverse flexural stiffness of the steel profile's web (k_2) and the stiffness of the shear connection (k_3). This option is adopted by the Brazilian [2] and European [3] standards, neglecting the influence of k_3, since this stiffness is usually very high when compared to the other two. Some studies have been carried out in order to propose equations for the determination of these stiffnesses and analyze their relative influence in the final value of the rotational stiffness k_r, such as Chen [13], Calenzani et al. [14], Chen and Wang [15] and Dietrich et al. [16].

In addition to Brazilian [2] and European [3] standards, which adopt the continuous inverted "U"- frame mechanism as the basis for obtaining the resistant moment to LTB, the Australian [17], [18] and American [19], [20] standard calculation procedures are presented in the literature. These last two standards, however, deal with the phenomenon in a simpler way, based on the conventional theory of lateral-torsional buckling of steel profiles. Rossi et al. [21] compared their numerical results with those of the four mentioned standards and highlighted that the Australian [17], [18] and American [19], [20] standards lead to more conservative results. According Rossi et al. [21], the use of conventional theory of lateral-torsional with only the influence of the steel profile provides inaccurate results since the model is based on inappropriate hypotheses. A procedure for calculating the resistant moment to LTB highlighted by Rossi et al. [21] is proposed by Zhou and Yan [22], that doesn't need the initial determination of the elastic critical moment (M_{cr}). This procedure provides good results, however, is valid only for composite beams subjected to uniform hogging moment.

In continuous composite beams, it can be necessary to use transverse stiffeners to elevate the value of shear strength of the web due to the possibility of instability. These stiffeners, as they also restrict the web distortion, provide additional lateral restraint to bottom flange of the steel profile, which causes an elevation of the elastic critical and LTB resistant moments. In order to evaluate the transverse stiffeners influence in LTB, Chen [13] tested two full-scale prototypes, one with composite beams composing a continuous “U”- frame mechanism (prototype U4) and another with distributed stiffeners along the hogging moment regions, forming in this case the discrete “U”- frame mechanism (prototype U5).

Prototype U4 was composed of two welded beams (U4A and U4B), with double stiffeners welded to the web only at the supports. To prevent lateral and vertical movements between the beams, without restricting rotation in relation to the vertical axis, an internal bracing formed by angles was added in the support section (Figure 2).

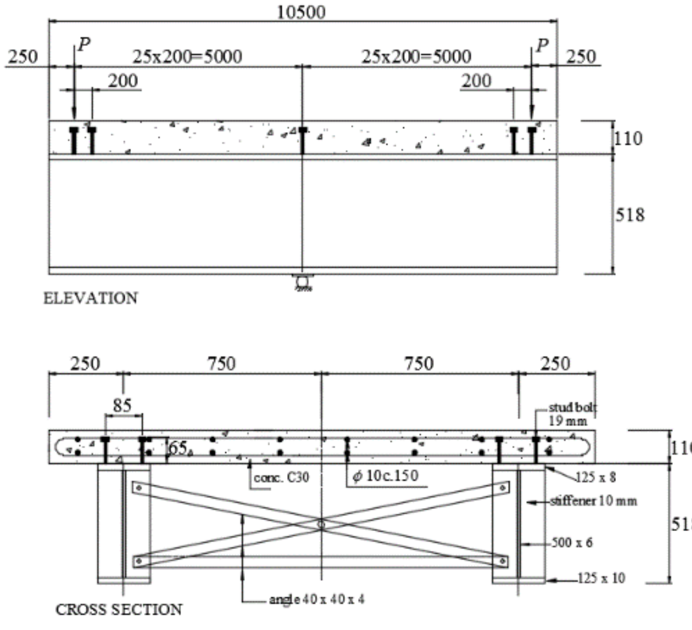

Figure 2. Elevation and cross section of prototype U4 at the support (dimensions in millimeter) [13].

Prototype U5 also was made of two welded beams (U5A and U5B), with cross sections identical to those of U4A and U4B. Chen [13] considered two types of stiffeners in prototype U5: in half of the length of the beam, double stiffeners were adopted (on both sides of the steel profile), spaced every 1,200 mm; in the other half, the stiffeners were welded only to one side of the steel profile, spaced every 600 mm.

Two lateral instability modes were found in the tests by Chen [13]. In prototype U4, without stiffeners, a mode that extended for most of the hogging bending moment region was observed, characterized by an approximate sinusoidal shape, symmetrical in relation to the central section. In prototype U5, however, the lateral instability modes were concentrated close to the support region.

A numerical study to analyze the structural behavior in hogging bending moment of continuous steel and concrete composite beams with transverse stiffeners welded to web of the steel profile was performed by Chen and Wang [15]. In this study, finite element models were implemented using the Ansys software.

Elastic buckling analyses and nonlinear buckling analyses were performed. In the buckling analyses, numerical models were adopted consisting of a simply supported steel beam without transverse stiffeners or by a steel beam with stiffeners, both with the influence of the slab simulated by spring elements with rotational stiffness k_1 and rigid supports to prevent lateral displacement of the top flange. The models were submitted to uniform hogging moment through the application of a moment at the ends of the beams. It was found that the use of stiffeners in the steel profile’s web significantly reduced the wavelength of the buckling mode of the beam and, consequently, raised the elastic critical moment to LTB. Through the parametric studies carried out by the authors Chen and Wang [15], it was possible to verify that this elevation was proportional to the reduction of the spacing between stiffeners and with the increase in the thickness of their plates.

Chen and Wang [15] proposed a calculation procedure for determining the resistant moment to LTB of steel and concrete composite beams with transverse stiffeners at the profile’s web. In this procedure, the authors [15] recommend the adoption of the equation of M_{cr} proposed by Roik et al. [5], that is, Equation 1 presented in this paper, and the calculation steps prescribed by the European standard [3] (see subsection 1.3), using the following equation to obtain the rotational stiffness of the stiffened web:

$$k_{2,e} = \frac{1}{4}\frac{E_a}{1-\upsilon_a^2}\frac{t_w^3}{h_0} + \frac{E_a}{4}\frac{\left(2b_s + t_w\right)^3 t_s}{h_0\, L_u} \tag{8}$$

in which b_s and t_s are the width and thickness of the stiffeners, respectively, and L_u is the spacing between the stiffeners.

1.5 About this paper

In this paper, the objective is to evaluate the influence of transverse stiffeners welded to web of the steel profile in the lateral stiffness and in the value of resistant bending moment of steel and concrete composite beams to lateral-torsional buckling (LTB). It is also an objective of the study to verify the possibility of using the calculation procedure proposed by Chen and Wang [15] together with the Brazilian standard [2] instead of the European standard [3] to determine the resistant bending moment. Strictly speaking, this means using the prescriptions of the Brazilian standard [2], only replacing Equation 4 by Equation 8, since this standard already uses the equation proposed by Roik et al. [5], Equation 1, to determine the elastic critical moment.

To accomplish this objective, a finite element model of composite beams with transverse stiffeners welded to steel profile's web at hogging bending moment region was developed using the Ansys 17.0 software [23], in order to obtain the nominal resistant bending moment to lateral-torsional buckling. Then, this model was validated by comparison with tests results by Chen [13]. In sequence, a parametric analysis was performed for continuous composite beams with two or three spans, varying the spacing between the transverse stiffeners. Finally, the results obtained with the procedure of Chen and Wang [15] combined with the prescriptions of the Brazilian standard [2] were assessed by comparison with the results of the numerical analyses. In addition, as another assessment device, the results obtained with the procedure of Chen and Wang [15] combined with the prescriptions of the European standard [3] were also compared with those of the numerical analyses.

2 FINITE ELEMENT MODELS

2.1 Model definition

In the numerical study conducted in this paper, inner beams of inverted "U"- frame mechanisms, shown in Figure 3a, were analyzed. There is symmetry on concrete slab in relation to the plane parallel to the web that passes through the semidistance between two adjacent beams. Thus, only one steel beam and half of the concrete slab on each side were simulated, with the adoption of appropriate boundary conditions in the cutting planes (free ends) of the slab (horizontal displacements, rotation about the horizontal axis and rotation about the vertical axis, represented by Uz, RotX and RotY, respectively, prevented), as illustrated in Figure 3b.

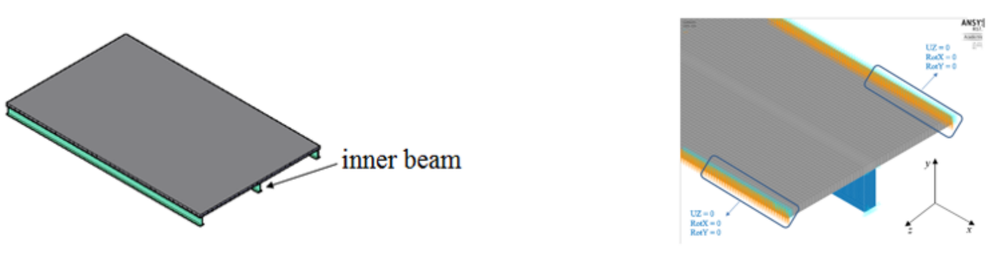

a) Inverted "U"- frame mechanism and inner beam b) Boundary conditions at the free ends of the slab

Figure 3. Inverted "U"- frame mechanism analyzed in this paper.

To assess the resistant bending moment to LTB of extreme spans, the numerical model was composed by two spans and three supports. For inner spans, however the composite beams were represented by a numerical model with three spans and four supports.

All nodes in the bottom flange of steel profile in the support sections of numerical models had translation in the global *y* direction (vertical) restrained and the central node of that flange had the translation in the global *x* direction (longitudinal) restrained, according to Figure 4. Moreover, to simulate the fork supports and prevent the rotation of cross section at the supports, the displacements in the *z* direction (horizontal) were restrained at the extreme nodes of the top and bottom flanges of the steel profile. Transverse stiffeners were modeled on the cross sections at the supports, to eliminate any influence of local deformations.

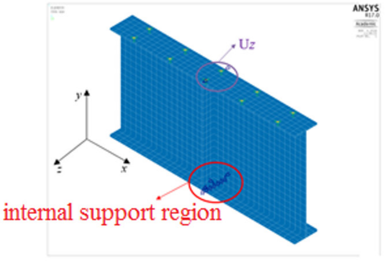

a) Internal support region

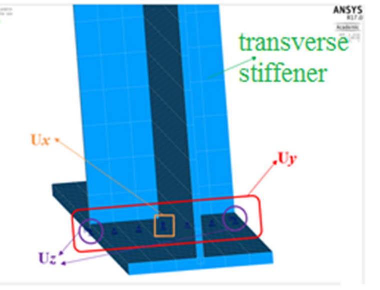

b) Composite beam support

Figure 4. Boundary conditions of numerical models.

The loading of extreme and inner spans of composite beams was applied through a uniformly distributed load per unit area in the upper slab face. For the extreme span of continuous composite beams, the same load was applied to each span of the beam. To analyze the inner span, the situation of constant bending moment diagram was adopted in the analyzed span (inner span), with equal distributed loads applied only to the end spans.

2.2 Used elements

As illustrated in Figure 5, the numerical models consisted of the steel profile and stiffeners, modeled with the shell element *Shell*181, a reinforced concrete slab, modeled with the solid element *Solid*65, and stud bolt shear connectors, modeled with the beam element *Beam*188. To simulate the interaction between the concrete slab and top flange of the steel profile, contact elements *Conta*173 and *Targe*170 were used.

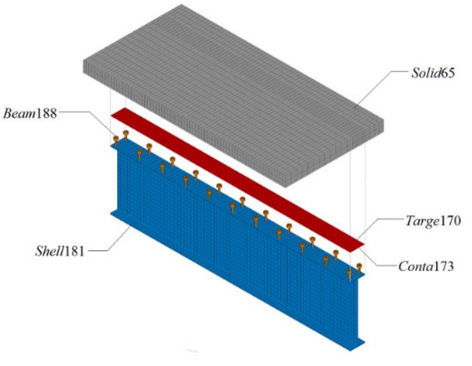

Figure 5. Types of elements adopted in numerical models.

The positive and negative reinforcements of the concrete slab were simulated in a dispersed way in the elements *Solid*65, defining the values of their area ratios in each coordinate axis direction. The positive reinforcement was positioned near bottom face of the slab, from one support to the other in all spans. The negative reinforcement was positioned near the upper slab face, centered on the internal supports with length equal to a quarter the sum of adjacent spans, in order to reach the inflection points of bending moment diagrams as described by the Brazilian standard [2]. This reinforcement also has, for each side, beyond the inflection points, an extension of 10% of the distance between these points, as a safety measure, and an additional extension, l_b, for anchoring purposes, as prescribed by the Brazilian standard [24].

2.3 Constitutive relationships of materials

The uniaxial behavior of the profile's steel, the transverse stiffeners and reinforcements was considered as bilinear elastoplastic, with a first straight until reaching the yield strength, f_y, with tangent modulus equal to steel modulus of elasticity, E_a, and a second straight line with a tangent modulus equal to 1/10,000 of the modulus of elasticity, to avoid numerical convergence problems. Steel is assumed to follow the von Mises yield criterion, with isotropic hardening rule, applicable for ductile material analysis. The values adopted for the modulus of elasticity and Poisson's ratio are equal to 200,000 MPa and 0.3, respectively.

The behavior of concrete under uniaxial compression was modeled based on the stress-strain relationship of the European standard [25]. The Poisson's ratio adopted for concrete was 0.2. It is assumed that the concrete follows the failure criterion of Willam-Warnke, *Solid*65 element's standard criterion. According to European [25] and Brazilian [24] standards, the average tensile strength of the concrete can be obtained using the following equation:

$$f_{ctm} = 0,3 f_{ck}^{2/3} \tag{9}$$

where f_{ck} is the characteristic compressive strength of the concrete.

Initial convergence problems were observed due to concentrations of compression stresses in the concrete slab near the shear connectors. Considering that the behavior of the connection between the slab and the steel profile is not critical in the assessed problem (since there is full shear interaction) and that in hogging bending moment region, the tension behavior of the slab is of greater importance than the compression behavior, it was decided to disable crushing of the concrete in the numerical models of this study. Tests carried out showed that there are no relevant differences in the force-displacement curves of models with and without crushing, which were coincident in the analysis up to the failure point of solution convergence.

In this paper, the values suggested by Contamine et al. [26] were adopted for the shear transfer coefficients for open and closed cracks, equal to 0.6 and 0.9, respectively.

2.4 Mesh study and solution techniques

To define the ideal element size, a mesh study was carried out with 64 numerical models with the same characteristics of the prototype tested by Chen [13], shown in Figure 2. For each model, the total number of elements, the critical LTB force, the percentage variation of this force between the results obtained in the current analysis (more refined mesh) and the previous (less refined mesh) were evaluated. It was concluded that the elements of the steel profile must have a maximum size equal to 30 mm and, those of the concrete slab, 60 mm. These mesh sizes presented results with a relative difference of around 0.05% between two consecutive analysis.

In the numerical model developed in this study, nonlinear analysis with large displacements, considering the geometric imperfections from the manufacturing process and material imperfections resulting from residual stresses in the steel profile was performed. Material nonlinearity is considered by adopting different tensile and compressive strengths for the reinforced concrete and non-linear behavior of steel. Due to the contact between the slab and the top flange of the steel profile, there is also the status nonlinearity.

After determining all the nonlinearities of the numerical models, nonlinear analysis was performed considering the standard incremental-iterative procedure of Newton Raphson. The stiffness matrix adjustment technique was used to accelerate the solution convergence of the numerical model.

2.5 Geometric imperfections and residual stresses

In the validation step of the numerical model, the initial geometric imperfections measured by Chen [13] in prototypes U4 and U5 were adopted. For the consideration of geometric imperfections in the steel profile of parameterization models, a lateral displacement was applied to the nodes of bottom flange with maximum value equal to 80% of the manufacturing tolerance of the profile, as prescribed by European standard [27], located at a distance from the internal support corresponding to three times the height of the steel profile, with its value decreasing according to LTB mode. Figure 6a highlights the region where the geometric imperfection was applied in extreme span models and, Figure 6b, the region in which the imperfection was applied in the internal span models, with the acronym IMPMAX corresponding to the maximum imperfection applied in the numerical model.

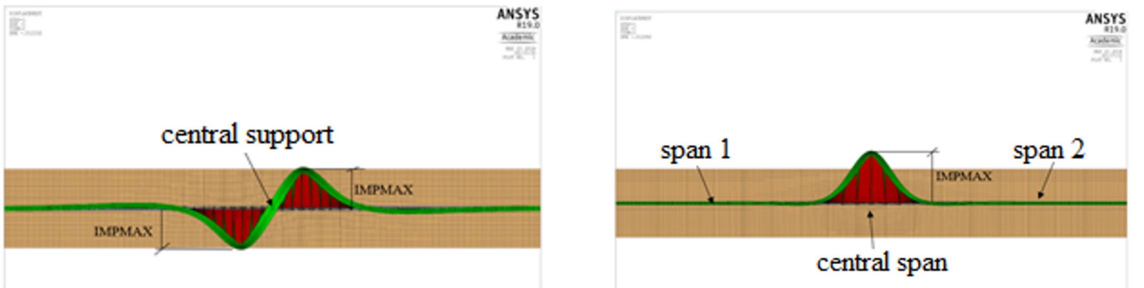

a) Extreme span models b) Inner span models

Figure 6. Geometric imperfection applied in parameterization models.

The residual stresses in steel profiles used in Chen's tests [13], which are welded with laminated edge plates, were not measured. Thus, in the numerical model for the validation of this paper, residual stresses were introduced in the nodes of the finite elements of the flanges and web of the steel profile, with the distribution presented in Figure 7a, considering linear variation in the web and flanges. The maximum tension adopted, equal to 30% of the yield strength of the steel, both in tension and compression, is prescribed by the Brazilian standard [2] for the design of steel beams.

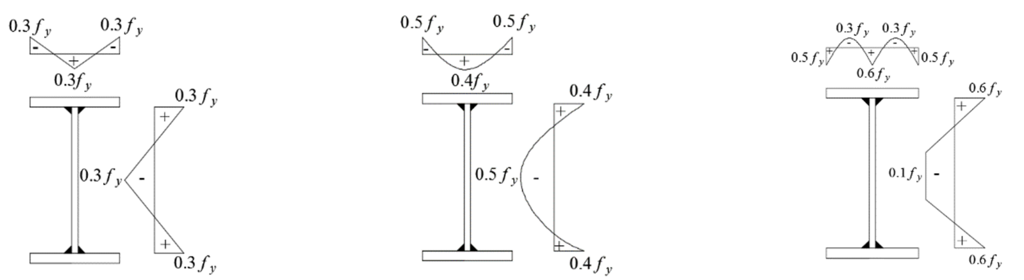

a) Linear distribution of rolled or welded steel profiles with laminated edge plates b) Non-linear distribution of rolled or welded steel profiles with laminated edge plates c) Distribution of welded steel profiles with blowtorch cut edges plates

Figure 7. Types of residual stress distributions analyzed.

Regarding the residual stress distribution of the parametric study models, an evaluation was carried out comparing the results of resistant bending moment to LTB obtained numerically, considering three types of residual stress distribution. One of them corresponds to the distribution adopted in the validation model presented in Figure 7a. The second also corresponds to the distribution of a laminated or welded profile with laminated edge plates, considering nonlinear distribution on the flanges and the web, similar to the distribution studied by Silva [28], presented in Figure 7b. Lastly, the distribution of a welded profile with blowtorch cut edges was considered (Figure 7c) with nonlinear distribution on flanges and linear with a uniform stretch in the web, also studied by Silva [28].

In the numerical models analyzed, a composite beam with two extremes spans of lengths equal to 15 m subjected to a uniformly distributed load of equal value was considered. A spacing between parallel beams, a, of 3 m was adopted. The slab was 120 mm high and negative reinforcements in both directions equal to 20 cm^2/m were adopted. The positive reinforcement adopted in both directions corresponds to 9.5 cm^2/m. The rates adopted for these reinforcements are of the order of 2.5%, and they are in the upper range of the limit recommended by the Brazilian standard [24] in order to facilitate the occurrence of LTB before reaching the plastic moment in the hogging bending moment region. The yield strength of steel profile, f_y, was assumed to be equal to 300 MPa. Table 1 describes the characteristics of the steel profile, in addition to the type of residual stress distribution adopted. The acronym DL corresponds to the distribution represented in Figure 7a, DNL to the distribution of Figure 7b and DPS to the distribution of Figure 7c.

Table 1. Numerical models for residual stress analysis.

model	*d* (mm)	b_f (mm)	t_f (mm)	t_w (mm)	Type of residual stress distribution
TR1	800	200	16	12.5	DL
TR2	700	200	16	12.5	DL
TR3	600	200	16	12.5	DL
TR4	500	200	16	12.5	DL
TR5	400	200	16	12.5	DL
TR6	800	200	16	12.5	DNL
TR7	700	200	16	12.5	DNL
TR8	600	200	16	12.5	DNL
TR9	500	200	16	12.5	DNL
TR10	400	200	16	12.5	DNL
TR11	800	200	16	12.5	DPS
TR12	700	200	16	12.5	DPS
TR13	600	200	16	12.5	DPS
TR14	500	200	16	12.5	DPS
TR15	400	200	16	12.5	DPS

The LTB resistant moment obtained numerically corresponds to the peak of the graph that relates the lateral displacement of the geometric center of bottom flange with the bending moment. Table 2 shows the obtained results, with $M_{R,DL}$ being the bending moment obtained numerically for models TR1 to TR5, $M_{R,DNL}$ the resistant moment of the models TR6 to TR10 and $M_{R,DPS}$ the resistant moment of the models TR11 to TR15. This table also presents the ratio between the resistant moment of models with residual stress distribution represented by the acronym DL as a function of the other residual stress distributions considered in this paper.

Table 2. Numerical results obtained for residual stress analysis.

Model DL	Model DNL	Model DPS	$M_{R,DL}$ (kN·m)	$M_{R,DNL}$ (kN·m)	$M_{R,DPS}$ (kN·m)	$M_{R,DL}$/ $M_{R,DNL}$	$M_{R,DL}$/ $M_{R,DPS}$
TR1	**TR6**	**TR11**	1,553	1,526	1,577	1.02	0.99
TR2	**TR7**	**TR12**	1,414	1,398	1,428	1.01	0.99
TR3	**TR8**	**TR13**	1,220	1,209	1,250	1.01	0.98
TR4	**TR9**	**TR14**	1,009	1,003	1,030	1.01	0.98
TR5	**TR10**	**TR15**	828	816	842	1.01	0.98
average						**1.01**	**0.98**

Table 2 shows that the difference in resistant bending moment for each type of residual stress distribution corresponds to a maximum of 2%. This demonstrates that the type of residual stress adopted in the parametric study has negligible influence on the value of the LTB resistant bending moment. Because of this, in the parametric study developed in this paper, the same residual stress distribution of the validation models was adopted, represented by Figure 7a.

2.6 Results of the numerical validation models

To validate the numerical model developed in this paper, the prototypes U4 and U5 of Chen's study [13], already described, were simulated, with the same materials characteristics, geometric properties and support and loading conditions reported by the author [13].

The values obtained with the numerical modeling of the two prototypes were compared with the values obtained in the tests performed by Chen [13]. Figure 8 shows a curve of the vertical displacement of the beam ends (ends of the cantilever) versus the moment in the supports of each model. It indicates that the resistant bending moment of the numerical simulation of the prototype U4 was equal to 320 kN·m, only 0.66% higher than Chen's result [13], of approximately 318 kN·m. For prototype U5, the maximum bending moment of the numerical simulation was equal to 438.57 kN·m, 7% higher than Chen [13], of about 407 kN·m.

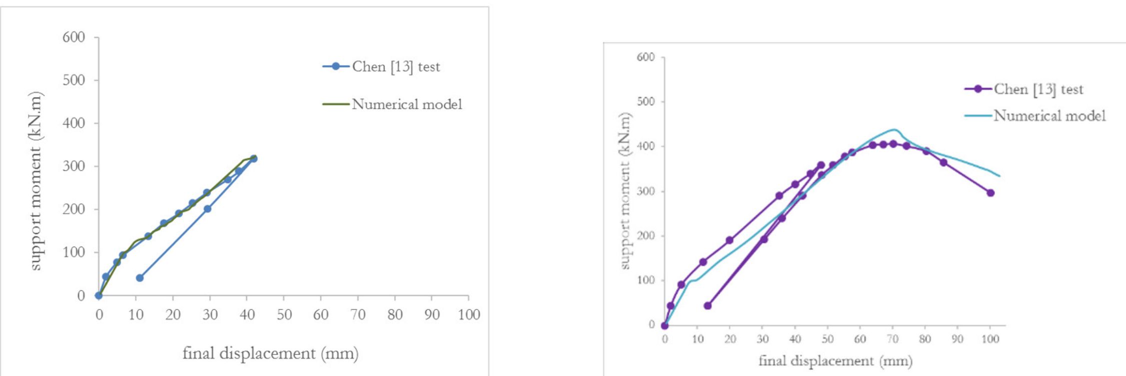

a) Prototype U4 b) Prototype U5

Figure 8. Vertical displacement at the free end of the composite beam.

Another relevant comparison is that of lateral displacement of bottom flange of steel profile at the end of the test. As seen in Figure 9, the numerical results were close to Chen's experimental measurements [13].

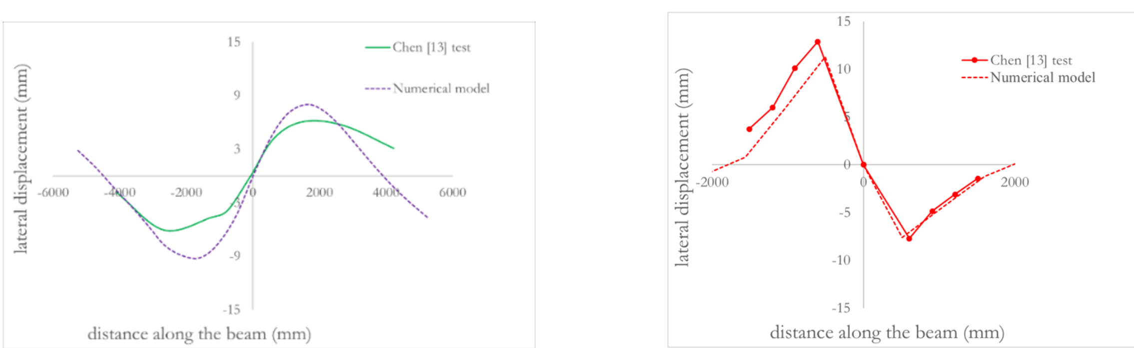

a) Prototype U4 b) Prototype U5

Figure 9. Lateral displacement of the bottom flange of the steel profile.

Therefore, there is an acceptable agreement between the results of the numerical models developed in this paper and Chen's tests [13], both in terms of resistant moment and structural behavior. Thus, the numerical model developed is considered appropriate for the study of LTB in steel and concrete composite beams.

3 PARAMETRIC ANALYSIS

3.1 General considerations

A parametric numerical analysis was performed to evaluate the LTB resistant bending moment of continuous steel and concrete composite beams with transverse stiffeners welded to the web of the steel profile. Figure 10 illustrates the cross section at the internal support of the numerical model adopted as standard in parameterization models. Regarding the spans, the value of 15 m was adopted as default, which corresponds to 25 times the height of the steel profile, a usual proportion in professional practice.

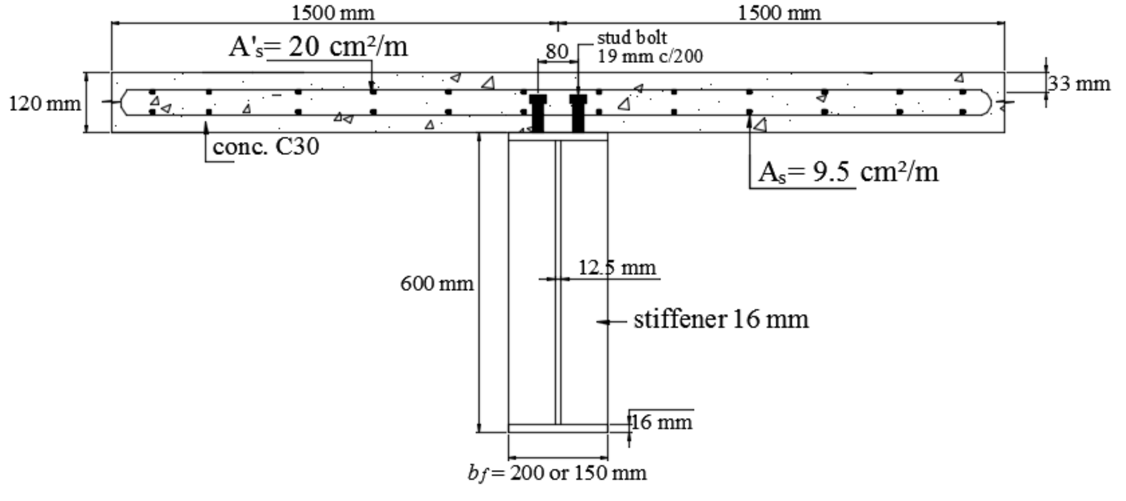

Figure 10. Cross section of the reference numerical model in the internal supports' region.

The mechanical properties of the materials were taken as the same in all analyzed numerical models. The elasticity modulus adopted for steel and concrete were equal to 200,000 MPa and 30,672 MPa, respectively. The Poisson's ratio was equal to 0.30 for steel and 0.2 for concrete. The yield strengths of the steel profile, shear connectors and reinforcement were equal to 300 MPa, 345 MPa and 500 MPa, respectively. Lastly, the compressive strength of concrete was adopted as 30 MPa.

3.2 Parametric models

An analysis of the influence on the lateral-torsional buckling of the transverse stiffeners positioned along the hogging moment region was performed. For this purpose, the numerical models MR1 and MR2 were initially used, which represent continuous composite beams with two spans (extreme span) subjected to uniformly distributed load without transverse stiffeners, with MR1 flange width equal to 150 mm and, MR2, 200 mm. Then, stiffeners were added in the hogging moment region to these models, with the ratio between the spacing between them, *a*, and the height of the steel profile, *d*, equal to 0.625, 1.041, 1.25, 1.5625, 2.08 and 3.125, as shown in Table 3, thus creating models ME1 to ME12. The height and thickness of the web of the steel profile adopted were chosen in order to have a profile that was classified as compact by the Brazilian standard [2] and as Class 3 by European standard [3], situation where the difference between both standards is greater. Then, models MR3 and MR4 were used as reference, without transverse stiffeners, to represent the case of a composite beam with three equal spans (inner span) subjected to uniform hogging bending moment at the central span (the two extreme spans were subjected to a uniformly distributed load), with flange widths of 150 mm in model MR3 and of 200 mm in MR4. In these models, the *a*/*d* ratio was also varied, as previously described, creating models ME13 to ME24.

Table 3. Numerical models for analyzing the stiffeners influence.

Model	Number of spans	d (mm)	b_f (mm)	t_f (mm)	t_w (mm)	a/d
ME1	2	600	150	16	12.5	0.625
ME2	2	600	150	16	12.5	1.041
ME3	2	600	150	16	12.5	1.25
ME4	2	600	150	16	12.5	1.5625
ME5	2	600	150	16	12.5	2.08
ME6	2	600	150	16	12.5	3.125
MR1	2	600	150	16	12.5	-
ME7	2	600	200	16	12.5	0.625
ME8	2	600	200	16	12.5	1.041
ME9	2	600	200	16	12.5	1.25
ME10	2	600	200	16	12.5	1.5625
ME11	2	600	200	16	12.5	2.08
ME12	2	600	200	16	12.5	3.125
MR2	2	600	200	16	12.5	-
ME13	3	600	150	16	12.5	0.625
ME14	3	600	150	16	12.5	1.041
ME15	3	600	150	16	12.5	1.25
ME16	3	600	150	16	12.5	1.5625
ME17	3	600	150	16	12.5	2.08
ME18	3	600	150	16	12.5	3.125
MR3	3	600	150	16	12.5	-
M19	3	600	200	16	12.5	0.625
M20	3	600	200	16	12.5	1.041
M21	3	600	200	16	12.5	1.25
M22	3	600	200	16	12.5	1.5625
M23	3	600	200	16	12.5	2.08
M24	3	600	200	16	12.5	3.125
MR4	3	600	200	16	12.5	-

The adoption of values of 150 mm and 200 mm for the flange width aimed to consider the influence of this dimension. Additionally, it is noteworthy that these two values are within a proportion usually adopted in composite beams, that is, between 1/4 and 1/3 of height of the steel profile and within the limit for the section to be classified as compact by Brazilian standard [2] and as Class 1 by European standard [3].

4 ANALYSIS OF RESULTS

Table 4 shows the plastic moment for each section for the analyzed numerical model, M_{Pl}^{-}, obtained considering the steel profile and longitudinal reinforcement in the support section. There are also the results obtained numerically for the nominal resistant bending moment to LTB, $M_{dist,Rk,num}^{-}$, and the results obtained analytically from the nominal bending moment to LTB, considering the procedure of the European standard [3], $M_{dist,Rk,Eurocode}^{-}$, and the procedure of the Brazilian standard [2], $M_{dist,Rk,ABNT}^{-}$, both adopting Equation 8, proposed by Chen and Wang [15] for the calculation of the web's rotational stiffness. For the $M_{dist,Rk,Eurocode}^{-}$ calculation procedure, the steps mentioned in subsection 1.3 were adopted, considering the elastic critical moment, M_{cr}, proposed by Roik et al. [5]. The ratio between the LTB resistant moment of the analyzed model and the model taken as reference is also shown in this table. In the case of models ME1 to ME6, model MR1 is used as reference model (without stiffeners along the hogging moment region) and, for models ME7 to ME12, model MR2 was the reference. For the models ME13 to ME18, the reference model is MR3 and, lastly, for models ME19 to ME24, the reference model is MR4. Furthermore, the ratios between the numerical nominal resistant bending moment to LTB, $M_{dist,Rk,num}^{-}$, and the analytical bending moment obtained according to the European standard [3], $M_{dist,Rk,Eurocode}^{-}$, and Brazilian standard [2], $M_{dist,Rk,ABNT}^{-}$ are presented.

Table 4. Results obtained for the analysis of the transverse stiffeners influence.

Model	M_{pl}^{-} (kN·m)	$M_{dist,Rk,num}^{-}$ (kN·m)	$M_{dist,Rk,num,current}^{-}$ / $M_{dist,Rk,num,reference}^{-}$	$M_{dist,Rk,Eurocode}^{-}$ (kN·m)	$M_{dist,Rk,ABNT}^{-}$ (kN·m)	$M_{dist,Rk,Eurocode}^{-}$ / $M_{dist,Rk,num}^{-}$	$M_{dist,Rk,ABNT}^{-}$ / $M_{dist,Rk,num}^{-}$
ME1	1,205	1,147	1.15	787	1,151	0.69	1.00
ME2		1,129	1.13	787	1,149	0.70	1.02
ME3		1,118	1.12	787	1,148	0.70	1.03
ME4		1,107	1.11	787	1,147	0.71	1.04
ME5		1,104	1.10	787	1,145	0.71	1.04
ME6		1,085	1.09	787	1,142	0.73	1.05
MR1		1,000	1.00	769	1,072	0.77	1.07
		average				**0.72**	**1.04**
ME7	1,345	1,324	1.09	921	1,302	0.70	0.98
ME8		1,308	1.07	921	1,301	0.70	0.99
ME9		1,288	1.06	921	1,300	0.72	1.01
ME10		1,306	1.07	921	1,299	0.71	0.99
ME11		1,290	1.06	921	1,298	0.71	1.01
ME12		1,267	1.04	921	1,297	0.73	1.02
MR2		1,220	1.00	921	1,238	0.75	1.01
		average				**0.72**	**1.00**
ME13	1,325	1,155	1.47	671	1,057	0.58	0.92
ME14		1,136	1.44	665	1,049	0.59	0.92
ME15		1,093	1.39	663	1,045	0.61	0.96
ME16		1,079	1.37	658	1,040	0.61	0.96
ME17		1,026	1.30	652	1,031	0.64	1.00
ME18		1,023	1.30	641	1,015	0.63	0.99
MR3		787	1.00	477	744	0.61	0.95
		average				**0.61**	**0.96**
ME19	1,465	1,318	1.31	841	1,246	0.64	0.95
ME20		1,308	1.30	838	1,243	0.64	0.95
ME21		1,294	1.29	836	1,241	0.65	0.96
ME22		1,285	1.28	834	1,239	0.65	0.96
ME23		1,251	1.25	831	1,235	0.66	0.99
ME24		1,242	1.24	824	1,228	0.66	0.99
MR4		1,004	1.00	622	955	0.62	0.95
		average				**0.65**	**0.96**
		global average				**0.67**	**0.99**

The results of the numerical analysis indicate that the use of stiffeners in the hogging moment region, as expected, can provide a significant increase in the value of the resistant moment to LTB. Also, as expected, this increase is grater with the shortest spacing between the stiffeners and with the greatest difference between the value of the resistant moment of composite beam without stiffeners and the plastic moment of the cross section of the composite beam in the hogging moment. In the cases treated in this paper, the smallest increase was of 4%, in model ME12, in which the spacing between the stiffeners was the maximum adopted (a/d = 3.125) and the ratio $M_{pl}^{-} / M_{dist,Rk,num}^{-}$ was the smallest in the beam without stiffeners (1,345/1,220 = 1.10). In turn, the biggest increase was of 47%, in model ME13, in which the spacing between the stiffeners was the minimum adopted (a/d = 0.625) and the ratio $M_{pl}^{-} / M_{dist,Rk,num}^{-}$ was the largest in the beam without stiffeners (1,325/787 = 1.68).

Regarding the results of the resistant bending moment obtained with the prescriptions of the standards, it is observed that, by the European standard [3], the ratio between the obtained moment and the numerical one was between 0.58 and

0.77, with overall average of 0.67. By the Brazilian standard [2], that ratio was between 0.92 and 1.05, with overall average of 0.99. It is worth mentioning that, in both standards, M_{cr} was calculated with Equation 1, proposed by Roik *et al* [5], and the web's rotational stiffness with Equation 8 for composite beams with transverse stiffeners, as recommended by Chen and Wang [15]. Thus, it is observed that the results obtained by the European standard [3] were very conservative and, as can be noted in Table 4, for models ME1 to ME5 and ME7 to ME12, there was no variation in the LTB resistant bending moment, since the factor χ_{dist} was always at the curve's plateau, with a maximum value equal to 1.0.

The main reason why the resistant moment obtained by the European standard [3] is smaller than that obtained by the Brazilian standard [2] is due to the fact that the steel profiles are classified as Class 3 by the European standard [3], which limits the resistant moment to the moment corresponding to the beginning of yield, while, by Brazilian standard [2], the profiles are classified as compact and can reach the plastic moment. For the European standard [3], the web of the steel profile would be classified as Class 1 or Class 2 if the ratio between the height and thickness of the web were less or equal to 35.6. As the ratio obtained is 45.4, lower than 72.7 (upper limit for Class 3), the profile was classified as Class 3. The Brazilian standard [2] takes as parameter twice the height of the compressed part of the web divided by its thickness for profile classification (this ratio is equal to 84 for the profiles analyzed), with the upper limit for the section to be compact equal to 97.

Based on the above, it appears that the use of Brazilian standard [2] calculation procedure to obtain the LTB resistant moment of continuous steel and concrete composite beams with transverse stiffeners, determining the rotational stiffness of the web of the steel profiles through the equation proposed by Chen and Wang [15], Equation 8 presented in this paper, leads to good results. It can also be concluded that the use of this equation in conjunction with the Brazilian standard [2] led to better results than with the European standard [3], in beams where the steel profile is classified as compact by the first and as Class 3 by the second. Possibly, in cases where the steel profiles of the composite beams are Class 1 or 2 according to the European standard [3], the results obtained according to it will approximate those of the Brazilian standard [2].

Figure 11a shows the von Mises stress values when the resistant moment is reached in the steel profile of the model with a greater number of transverse stiffeners in the hogging moment region, ME7, as well as in Figure 11b for the model ME12 which has a smaller number of stiffeners in this region. It is possible to clearly observe that for these models, the yielded region was similar, regardless of the number of stiffeners in the hogging moment region. This confirms that the resistant gain is very low in relation to the composite beam without transverse stiffeners after adding transverse stiffeners in the hogging moment region in composite beams that present the resistant moment close to the plastic moment.

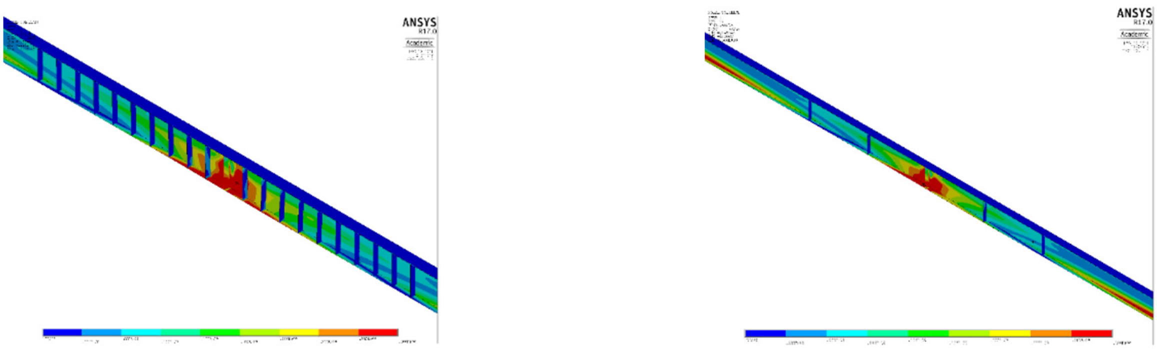

a) ME7 model b) ME12 model

Figure 11. Von Mises stress in the steel profile of models ME7 and ME12.

As can be seen in Figure 12a, where von Mises stress values are also shown in the steel profile, the model with highest number of transverse stiffeners in the hogging moment region, ME13, presents a yielded region larger than that of the ME18 model, Figure 12b, which has a smaller number of stiffeners in this region, when the resistant moment is reached. It is worth mentioning that for these models, the gain in resistant capacity was much greater because the resistant moment for the case without stiffener is quite distant from the plastic moment of the composite beam. This demonstrates, once again, that by adding stiffeners in the hogging moment region, LTB becomes more difficult to occur, with plastification growing and the tendency for collapse to occur due to full plastification of the cross section, in a limit condition.

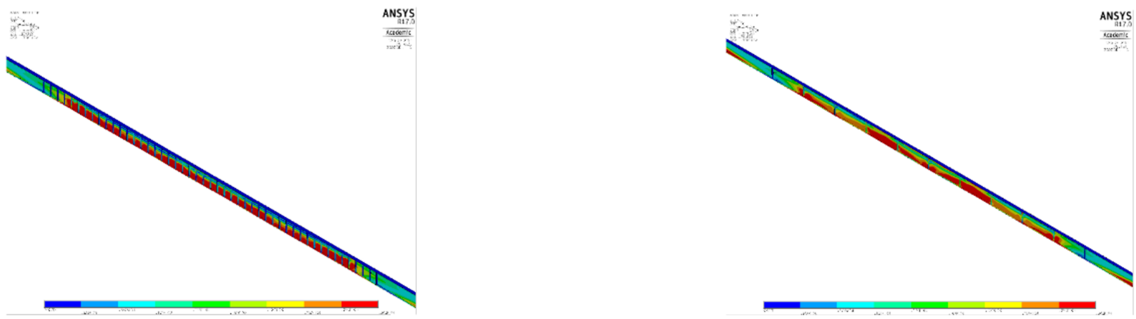

a) ME13 model b) ME18 model

Figure 12. Von Mises stress in the steel profile of models ME13 and ME18.

The lateral displacements of the bottom flanges of numerical models MR2 (model without stiffener in the hogging moment region) and ME7 (model with stiffener) are shown in Figure 13a when the maximum moment is reached in the respective beams. The same is shown in Figure 13b for numerical models MR3 (model without stiffener) and ME13 (model with stiffener). It can be seen that for composite beams with identical cross sections, the beam with transverse stiffeners welded in the hogging moment region has a higher LTB resistant moment and has significantly reduced lateral displacement of the compressed flange in relation to the beam without stiffeners. It is thus observed that although the gain in value of the resistant bending moment in the ME7 model was small, of only 9%, there was a considerable increase in the stiffness of the beam regarding the lateral displacement of the bottom flange, as shown in Figure 13a.

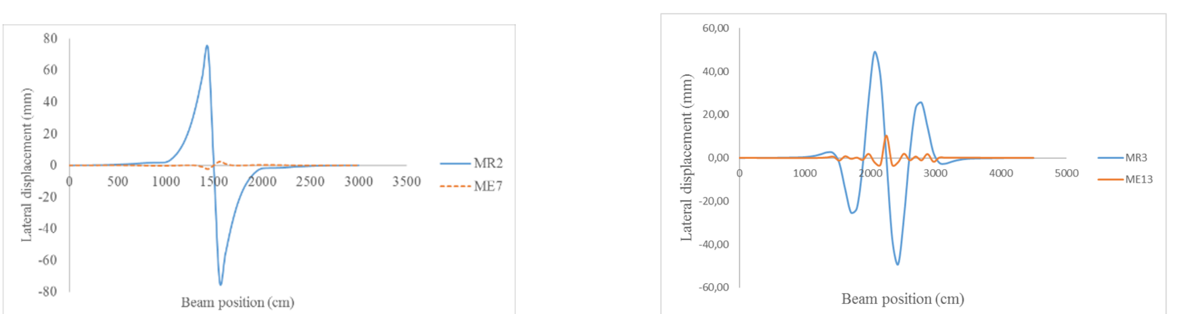

a) MR2 and ME7 models b) MR3 and ME13 models

Figure 13. Lateral displacement of the bottom flange of the steel profile.

5 CONCLUSIONS

In this paper, it was observed that the placement of transverse stiffeners regularly spaced in the hogging moment region of continuous composite beams increases the resistant moment, which was already expected. Is was also observed that this increase is greater, the smaller the spacing between stiffeners and the more distant the value of the resistant moment of composite beams without stiffeners to the plastic moment of the cross section of the composite beams in the hogging moment region, also as expected.

Composite beams with stiffeners in the hogging moment regions in which the steel profile is classified as compact by the Brazilian standard [2] and as a Class 3 by the European standard [3] were studied. In these beams, based on the results, it can be concluded that the method of calculation of the European standard [3] to obtain the moment resistant to LTB, using the elastic critical moment equation (M_{cr}) of Roik et al. [5], Equation 1, and the expression of the rotational stiffness of the stiffened web presented by Chen and Wang [15], Equation 8, presents very conservative results, with overall average of 0.67 in relation to the moments obtained numerically. By the method of calculation of the Brazilian standard [2], with the rotational stiffness of the stiffened web obtained by Chen and Wang [15], the results obtained were closer to the numerical ones, with overall average of 0.99 in relation to the moments obtained numerically.

Therefore, from the presented study, it can be concluded that the resistant moment to LTB of continuous steel and concrete composite beams with compact steel profile and transverse stiffeners in the hogging moment region can be obtained with a good level of accuracy through the procedures described in the Brazilian standard [2], with the web's rotational stiffeness determined with Equation 8, presented by Chen and Wang [15].

ACKNOWLEDGEMENTS

The authors would like to acknowledge the support provided by the Brazilian public agencies Conselho Nacional de Desenvolvimento Científico e Tecnológico (CNPq), Coordenação de Aperfeiçoamento de Pessoal de Nível Superior (CAPES) and Fundação de Amparo à Pesquisa do Estado de Minas Gerais (FAPEMIG).

REFERENCES

[1] R. P. Johnson, *Composite Structures of Steel and Concrete: Beams, Slabs, Columns and Frames for Buildings*, 3rd ed. Warwick, U.K.: Blackwell, 2004.

[2] Associação Brasileira de Normas Técnicas, *Projeto de Estruturas de Aço e de Estruturas Mistas de Aço e Concreto de Edifícios*, NBR 8800, 2008.

[3] European Committee for Standardization, *Eurocode 4: Design of Composite Steel and Concrete Structures. Part 1-1: General Rules and Rules for Buildings*, EN 1994-1-1, 2004.

[4] A. F. G. Calenzani, "Proposição de procedimento para a determinação da rigidez rotacional de vigas mistas contínuas e semicontínuas com perfis de alma senoidal," Ph.D. dissertation, Progr. Pós-grad. Eng. Estrut., Univ. Fed. Minas Gerais, Belo Horizonte, 2008.

[5] K. Roik, G. Hanswille, and J. Kina, "Solution for the lateral torsional buckling problem of composite beams," *Stahlbau*, no. 59, pp. 327–332, 1990. [em alemão].

[6] M. A. Bradford and N. S. Trahair, "Distortional buckling of I-beams," *J. Struct.*, vol. 107, pp. 355–370, 1981.

[7] S. E. Svensson, "Lateral buckling of beams analysed as elastically supported columns subject to a varying axial force," *J. Construct. Steel Res.*, no. 5, pp. 179–193, 1985.

[8] P. Goltermann and S. E. Svensson, "Lateral distortional buckling: predicting elastic critical stress," *J. Struct. Eng.*, vol. 114, no. 7, pp. 1606–1625, 1988.

[9] G. Hanswille, "Lateral torsional buckling of composite beams: comparison of more accurate method with Eurocode 4," *Compos. Constr. Steel Concr.*, vol. IV, pp. 105–116, 2002.

[10] T. V. Amaral, J. P. S. Oliveira, A. F. G. Calenzani, and F. B. Teixeira, "Lateral-distorional buckling of continuous steel-concrete composite beam," *Ibracon Struct. Mater. J.*, vol. 11, no. 4, pp. 719–756, 2018.

[11] J. V. F. Dias, J. P. S. Oliveira, A. F. G. Calenzani, and R. H. Fakury, "Elastic critical moment of lateral-distortional buckling of steel-concrete composite beams under uniform hogging moment," *Int. J. Struct. Stab. Dyn.*, vol. 19, no. 7, pp. 1950079, 2019.

[12] J.P.S. Oliveira, "Nova proposição para verificação do estado-limite de flambagem lateral com distorção de vigas mistas de aço e concreto," Ph.D. dissertation, Progr. Pós-grad. Eng. Estrut., Univ. Fed. Minas Gerais, Belo Horizonte, 2018.

[13] S. Chen, "Instability of composite beams in hogging bending," Ph.D. dissertation, Dep. Eng., Univ. Warwick, 1992.

[14] A. F. G. Calenzani, R. H. Fakury, F. A. Paula, F. C. Rodrigues, G. Queiroz, and R. J. Pimenta, "Rotational stiffness of continuous composite beams with sinusoidal-web profiles for torsional buckling," *J. Construct. Steel Res.*, vol. 79, pp. 22–33, 2012.

[15] S. Chen and X. Wang, "Finite element analysis of distortional lateral buckling of composite beams with transverse web stiffeners," *Adv. Struct. Eng.*, vol. 15, no. 9, pp. 1607–1616, 2012.

[16] M. Z. Dietrich, A. F. G. Calenzani, and R. H. Fakury, "Analysis of rotational stiffness of steel-concrete composite beams for lateral-torsional buckling," *Eng. Struct.*, vol. 198, 109554, 2019.

[17] Standard Association of Australia. Standard Association of New Zealand, *Composite Structures - Composite Steel Concrete Construction in Buildings*, AS/NZS 2327, 2017.

[18] Standards Association of Australia, *Steel Structures*, AS 4100, 1998.

[19] American Institute of Steel Construction, *AISC Specifications for Structural Steel Buildings*, ANSI/AISC 360-16, 2016.

[20] American Association of State and Highway Transportation Officials, *AASHTO LRFD Bridge Design Specifications, 8th ed. with 2017 Interim Provisions.* Washington: AASHTO, 2017.

[21] A. Rossi, R. S. Nicoletti, A. S. C. Souza, and C. H. Martins, "Numerical assessment of lateral distortional buckling in steel-concrete composite beams," *J. Construct. Steel Res.*, vol. 172, 106192, 2020.

[22] W. B. Zhou and W. J. Yan, "Refined nonlinear finite elemento modelling towards ultimate bending moment calculation for concrete composite beams under negative moment," *Thin-walled Struct.*, vol. 116, pp. 201–211, 2017.

[23] Ansys, Inc., *Release 17.0 Documentation for Ansys.* Canonsburg, 2016.

[24] Associação Brasileira de Normas Técnicas, *Projeto de Estruturas de Concreto – Procedimentos*, NBR 6118, 2014.

[25] European Committee for Standardization, *Eurocode 2: Design of Concrete Structures. Part 1-1: General Rules and Rules for Buildings*, EN 1992-1-1, 2004.

[26] are R. Contamine, A. Si-Larbi, N. Q. Than, and P. Hamelin, "Numerical modeling of reinforced concrete beams under shear stress with and without external textile-reinforced concrete reinforcement," *J. Reinf. Plast. Compos.*, vol. 30, no. 15, pp. 1293–1303, 2011.

[27] European Committee for Standardization, *Eurocode 3: Design of Steel Structure. Part 1-5: Plated Structural Elements*, EN 1993-1-5, Brussels, 2006.

[28] A. L. R. C. Silva, “Análise numérica não-linear da flambagem local de perfis de aço estrutural submetidos à compressão uniaxial,” Ph.D. dissertation, Progr. Pós-grad. Eng. Estrut., Univ. Fed. Minas Gerais, Belo Horizonte, 2006.

Authors contributions: JPSO: conceptualization, methodology, data processing and writing the paper; JVFD: conceptualization, formal analysis and general review; RHF: funding acquisition, supervision and general review; AFGC: formal analysis and general review.

Editors: Leandro Trautwein, Guilherme Aris Parsekian.

IBRACON

IBRACON Structures and Materials Journal

Revista IBRACON de Estruturas e Materiais

ISSN 1983-4195 *ismj.org*

ORIGINAL ARTICLE

Effect of water/cement ratio on micro-nanomechanical properties of the interface between cementitious matrix and steel microfibers in ultra-high performance cementitious composites

Efeito da relação água/cimento nas propriedades micro-nanomecânicas da interface entre matriz cimentícia e microfibras metálicas em materiais cimentícios de ultra-alto desempenho

Vanessa Fernandes Cesari[a]
Fernando Pelisser[a]
Philippe Jean Paul Gleize[a]
Milton Domingos Michel[b]

[a]Universidade Federal de Santa Catarina – UFSC, Departamento de Engenheira Civil, Florianópolis, SC, Brasil
[b]Universidade Estadual de Ponta Grossa – UEPG, Departamento de Engenharia de Materiais, Ponta Grossa, PR, Brasil

Received 19 July 2020
Accepted 15 November 2020

Abstract: Ultra-high performance concretes with steel microfibers have been studied in depth with the aim of producing more efficient and durable structures. The performance of these materials depends on the characteristics of the interface between microfibers and cementitious matrix. This research investigates the micro-nanomechanical properties of the interfacial transition zone between the steel microfibers and the matrix of ultra-high performance cementitious composite. The effect of the water/cement ratio and distance from the microfiber were analyzed. The results confirm the formation of high-density calcium-silicate-hydrate (HD C-S-H) matrix at higher concentrations than low-density calcium-silicate-hydrate (LD C-S-H) for w/c ratios of 0.2 and 0.3. The properties in cementitious matrix interface with steel microfibers were very similar to that measured for the cement paste, and no significant difference was observed regarding the distance to the microfibers in relation to the elastic modulus, hardness and chemical composition. Thus, the authors can conclude that the formation of a less resistant region does not occur at the interfacial transition zone cement paste/microfibers.

Keywords: calcium-silicate-hydrate, ultra-high performance concrete, interfacial transition zone, steel microfibers, nanoindentation.

Resumo: Concretos de ultra-alto desempenho com microfibras metálicas têm sido bastante estudados com objetivo de produzir estruturas mais eficientes e duráveis. O desempenho deste material é dependente das características da interface entre as microfibras e a matriz cimentícia. Este trabalho tem como objetivo investigar as propriedades micro-nanomecânicas da zona de transição interfacial entre as microfibras metálicas e a matriz cimentícia de materiais cimentícios de ultra-alto desempenho através das variáveis relação água/cimento e distância da fibra. Os resultados obtidos mostram a formação silicatos de cálcio hidratados de alta densidade (HD C-S-H) em maior quantidade do que silicatos de cálcio hidratados de baixa densidade (LD C-S-H) para relações água/cimento de 0,2 e 0,3. As propriedades medidas na interface entre as microfibras metálicas e a matriz cimentícia foram muito semelhantes àquelas medidas na pasta de cimento. Também não foram observadas diferenças significativas no módulo de elasticidade, dureza e composição química conforme a distância da fibra foi variada. Sendo assim, os autores concluem que não há ocorrência de uma região mais fraca na zona de transição entre a pasta e as microfibras.

Palavras-chave: silicato de cálcio hidratado, concreto de ultra-alto desempenho, zona de transição interfacial, microfibras metálicas, nanoindentação.

Corresponding author: Vanessa Fernandes Cesari. E-mail: vanessacesari@yahoo.com.br
Financial support: This work was financed by Coordination for the Improvement of Higher Education Personnel (CAPES), the Foundation for Research and Innovation of the State of Santa Catarina (FAPESC), the National Council of Technological and Scientific Development (CNPq, fellowship under grant number 304589/2019-5).
Conflict of interest: Nothing to declare.

How to cite: V. F. Cesari, F. Pelisser, P. J. P. Gleize, and M. D. Michel, "Effect of water/cement ratio on micro-nanomechanical properties of the interface between cementitious matrix and steel microfibers in ultra-high performance cementitious composites" *IBRACON Struct. Mater. J Rev. IBRACON Estrut. Mater.*, vol. 14, no. 4, e14413, 2021, https://doi.org/10.1590/S1983-41952021000400013

1. INTRODUCTION

Ultra-high performance concrete (UHPC) is frequently studied in order to develop more efficient materials for use in engineering projects. UHPC is produced with high binder consumption, a very low water/binder ratio, the absence of large aggregates and the use of steel microfibers [1]. This concrete presents high resistance to both compressive and flexural strength [2]. It is composed of Portland cement, additional cementitious materials and steel microfibers, superplasticizer admixture and proposes the elimination of steel reinforcement in the production of prefabricated slabs of reduced thicknesses. Steel microfibers contribute to reinforcing the concrete due to their size, surface area and the adherence to the cementitious matrix, increasing resistance to microcracking and tensile strength. However, the presence of steel fibers in the matrix, as well as aggregates, act as a solid element, causing the wall effect [3] [4]. According to Scrivener et al. [3], the presence of a solid element prevents the packaging of the particles next to it to be equal to the packaging and distribution of the same particles in the rest of the matrix. This leads to the occurrence of a more fragile zone (interfacial transition zone, ITZ) with different properties from the rest of the matrix.

UHPC are treated as homogeneous continuum materials in macroscale. At mesoscale, cement matrix, aggregates and fiber phases become discernible. Scaling down to nanoscale, material is divided into several phases, e.g. C-S-H, CH and porosity [4]. Macromechanical properties like strength and ductility of UHPC depends fundamentally on the micro-nanoproperties, especially at the fiber-matrix ITZ [5]. And the bonding between fiber and matrix depends fundamentally on the crystalline nanostructure in ITZ [4]. Increasing the portion of UHD/HD C-S-H and consequently lowing LD C-S-H and porous phase helps densification cementitious matrix and so enhancing fiber-matrix bond. Therefore, studying the properties of the ITZ in micro-nanoscale is fundamental for the development of ultra-high performance cementitious composites.

Water/cement (w/c) ratios and aggregate size are known to affect the ITZ microstructure and porosity [6]. However, recent studies show that the ITZ in high performance concretes has a packing density of hydration products equivalent to the cementitious matrix. This effect is attributed to the use of silica fume and the very low w/c ratio used [7]. Sorelli et al. [8] were the first to characterize the nanomechanical properties at the interface of the cementitious matrix with steel microfibers, using instrumented nanoindentation. The authors verified that no region showed mechanical properties inferior to the matrix; however only one concrete composition was evaluated at different scale levels from the hydrated cement nanostructure to the aggregates and microfibers used [8].

In contrast, studies have evaluated the effect of nanoparticles of calcium carbonate and nanosilica at the interface between steel microfibers and cementitious matrix in order to improve the characteristics of this region and consequently the mechanical properties of ultra-high performance concretes [5], [9]. Using nanoindentation, Xu et al. [4] conducted comprehensive research to evaluate the effect of two types of microfiber (steel and polypropylene) and w/c ratios of 0.35, 0.40 and 0.45 on the fiber-matrix ITZ. The authors verified that the fiber type lead to ITZs with different thicknesses, 30 μm for steel and 15 μm for polypropylene fibers. The effect of the w/c ratio was also significant mainly regarding the packing of the C-S-H particles [4]. More high-density C-S-H regions (HD C-S-H, with elastic modulus $E \approx 30$ GPa) and less low-density C-S-H regions (LD C-S-H, with elastic modulus $E \approx 20$ GPa) were observed, in different proportions, when the w/c ratio was reduced [4]. However, the research did not include a w/c ratio close to 0.2, which is characteristic of UHPC.

Given the above, in this research, the micro-nanomechanical properties of the ITZ between steel microfibers and the cementitious matrix were evaluated for low w/c ratios (0.20 and 0.30) mixtures aiming to study C-S-H particle packing in order to contribute to the development of UHPC. Instrumented nanoindentation and scanning electron microscopy combined with chemical analysis by energy-dispersive spectrometry (SEM-EDS) techniques were used as tools to evaluate the mechanical properties of the material.

2. MATERIALS AND EXPERIMENTAL PROGRAM

2.1. Materials

Concrete pastes were produced using the following materials: i) Portland cement CPII-F-40 (similar to CEM II-EN 197-1), with 6 to 10% limestone addition and compressive strength of 40 MPa at the age of 28 days according to

Brazilian standard NBR 16697 [10]; ii) polycarboxylate-based superplasticizer ADVA^{TM} CAST 585 (Grace Construction Products); and iii) steel microfibers, commercially known as Dramix® OL 13/.20 (Bekaert), 0.20 mm in diameter and 13 mm in length, with a form factor (l/d) of 65.

Water/cement ratio and fiber content ranged from 0.2 to 0.3 and from 0 to 2% by weight of cement, respectively. Fiber content of 2% corresponds to approximately 0.4% of total paste volume (vf=0.4). Superplasticizer content was kept constant at 1% by weight of cement.

2.2. Mixing procedure

A planetary type, vertical axis, speed adjustable mixer with two speed grades and 5 liters capacity was used for the following mixing steps: a) add superplasticizer to water content and mix; b) mix at low speed while adding the cement over 30 s; c) mix at low speed for a further 30 s, total 1 min; d) mix at high speed for 1 min; e) return to low speed and mix for 30 s while adding the steel fibers; f) mix at low speed for a further 30 s, total 3 min; g) stop mixing and scrape the material adhered to the walls of the bowl using a spatula; h) restart mixing at high speed for 2 min, total 5 min.

Cylindrical samples measuring 20×35 mm (diameter×height) were casted. The specimens were demolded 24 hours after casting and were then placed in water immersion cure (temperature 23 ± 2° C) until the test date (28 days).

2.3. Sample preparation

Samples were cut approximately 5 mm thick using a low speed metallographic cutter (Buehler Isomet) and diamond blades.

During the first step, the sample surface was polished using silicon carbide papers (800, 1200 and 2000 grades), approximately 10 min each, while constantly monitoring preparation efficiency under an optical microscope. During the second step, polishing was performed using diamond spray particles (four stages of increasing fineness, 6 µm, 3 µm, 1 µm and 0.25 µm) to obtain a very flat, smooth surface finish [11]. The samples were polished for approximately 30 min at each stage, using a 450 rpm rotation. After each grinding/polishing stage, the samples were placed in an ultrasonic bath (15 min) to remove dust and diamond particles left on the surface or in the porous structure. After preparation, the samples were stored in a vacuum desiccator until tested.

2.4. Nanoindentation investigation

Elastic modulus and hardness were determined using a Berkovich indenter following the method described by Oliver and Pharr [12].

Hardness is obtained by penetrating the indenter the surface of the sample until a given load. Shortly after removing the load, the sample is analyzed under an optical microscope to determine the area of the residual plastic impression. Hardness is defined as the ratio between the maximum penetration load and the area measured.

Elastic modulus is obtained from load-unload curves constructed with the nanoindentation test results and is determined by the slope of the unloading curve according to Equation 1:

$$E_r = \frac{\sqrt{\pi} \cdot S_{max}}{2 \cdot \beta \cdot \sqrt{A}} \qquad \text{Equation 1}$$

where "β" is a constant dependent on the indenter geometry, "S_{max}" is the rigidity obtained experimentally from the upper part of the unloading curve, "A" is the projected contact area, "P" is the load and "h" is the displacement of the indenter, such that (Equation 2):

$$S_{max} = \frac{dP}{dh} \qquad \text{Equation 2}$$

where "E_r" is the reduced elastic modulus, which includes the effects of non-rigid indenters, i.e. it is related to the elastic modulus of the sample and the indenter through Equation 3:

$$\frac{1}{E_r} = \frac{1-\nu_i^2}{E_i} + \frac{1-\nu^2}{E} \qquad \text{Equation 3}$$

where "E_i" and "ν_i" are the elastic modulus and the Poisson ratio of the indenter material and "E" and "ν" are the elastic modulus the Poisson ratio of the penetrated material.

Nanomechanical properties were determined in cement pastes with and without microfibers using two loads, 100 mN and 50 mN, corresponding to matrix A and matrix B, respectively. Each matrix was composed of four rows with seven indentation points approximately 30 µm from each other, i.e. 28 indentations in each matrix (4×7 points). The technique was also performed in two (3×8) complementary matrices (matrix 1 and matrix 2) placed near the interface between the cementitious matrix and steel microfiber, i.e. 24 indentations, and one (4×7) matrix over the fiber surface, i.e. 28 indentations approximately 30 µm from each other. SEM micrographs show the regions at the microfiber-paste interface. Chemical analysis by Energy Dispersive x-ray Spectrometry (EDS) was also performed at the interface with the microfiber to investigate chemical changes and determine any association between these changes and microstructural and mechanical changes. Loads of 50 mN and 100 mN were used to investigate a slightly larger contact area.

3 RESULTS

3.1. Cement Paste

Micro-nanoscale instrumented nanoindentation was used to measure the hardness and elastic modulus of the pastes and the microfiber-paste interface. Figure 1 shows the results of hardness and elastic modulus for w/c ratios of 0.2 and 0.3 using loads of 100 mN (matrix A) and 50 mN (matrix B). Figure 2 shows that the most significant effect of microfiber addition was on hardness and the least significant was on the elastic modulus. The load variation between 100 and 50 mN applied in the matrices A and B, respectively (Figure 1 and Figure 2), showed no significant effect. This could be associated with the homogeneity of the material analyzed.

Although the loads used (50 and 100 mN) are higher than that recommended to characterize the nanomechanical properties of cement (2 mN), the objective was to characterize a slightly wider area in relation to the surface, especially at the interface with microfibers. However, to achieve this, previous studies were also considered. In their study on the nanomechanical properties of two types of synthesized cement (Ca/Si ratios of 0.7 and 2.1), Pelisser et al. [13] observed no significant differences in the nanomechanical properties of C-S-H among loads of 2 mN, 4 mN, 8 mN, 16 mN and 32 mN loads. Matrices were also evaluated using 1 mN, 2 mN, 4 mN, 8 mN, 16 mN, 32 mN, 64 mN, 128 mN, 256 mN and 512 mN, in which minor differences were observed between the smallest and largest loads adopted [13]. Other authors have also verified that there are no significant differences in the micro-nanomechanical properties of cement, measured between 10 and 300 mN [14] and between 6 and 50 mN [15].

The w/c ratio had a significant effect on the results of the nanomechanical tests, achieving values of 34 GPa and 28 GPa for elastic modulus and 0.87 GPa and 0.80 GPa for hardness, when using w/c ratios of 0.2 and 0.3, respectively (matrix A). The difference was approximately 20% for elastic modulus and 10% for hardness, and this is the result of an increase in packing density of C-S-H particles for a w/c ratio of 0.2. The histograms in Figure 3 show major formation of C-S-H particles with higher hardness (Figure 3a) and elastic modulus (Figure 3b) for a w/c ratio of 0.2 compared with that of 0.3. Considering that LD C-S-H particles have a characteristic elastic modulus below 25 GPa and HD C-S-H above 25 GPa, the results show the formation of 96% of HD C-S-H and 4% of LD C-S-H when the w/c ratio was 0.2, and 63% of HD C-S-H and 37% of LD C-S-H when the w/c ratio was 0.3.

Several authors [16], [17] have stated that C-S-H can be divided into two types, low-density (LD C-S-H) and high-density (HD C-S-H), which show elastic modulus results of around 18 GPa (LD C-S-H or E<25GPa) and 29 GPa (HD C-S-H or E>25GPa), and approximate hardness of 0.4 GPa (LD C-S-H) and 0.8 GPa (HD C-S-H). A phase denominated ultra-high density (UHD) C-S-H is formed when very low w/c ratios are used, and it exceeds the values of nanomechanical properties of HD C-S-H, with approximate E and H values of 40-50 GPa and 1.5-2 GPa, respectively, slightly below the results obtained for calcium hydroxide [16]. Considering that, results show the formation of 96% of HD C-S-H and 4% of LD C-S-H when the w/c ratio was 0.2, and 63% of HD C-S-H and 37% of LD C-S-H when the w/c ratio was 0.3.

When evaluating the effect of the w/c ratios (0.2 and 0.3) by instrumented nanoindentation, Vandamme, et al. [17] observed the predominant formation of HD C-S-H and UHD C-S-H for a w/c of 0.20 (97% HD C-S-H and UHD C-S-H and 3% LD C-S-H) and a significant reduction in HD C-S-H and UHD C-S-H for a w/c of 0.30 (70% HD C-S-H and UHD C-S-H and 30% LD C-S-H). These results were obtained for a cementitious matrix without microfibers.

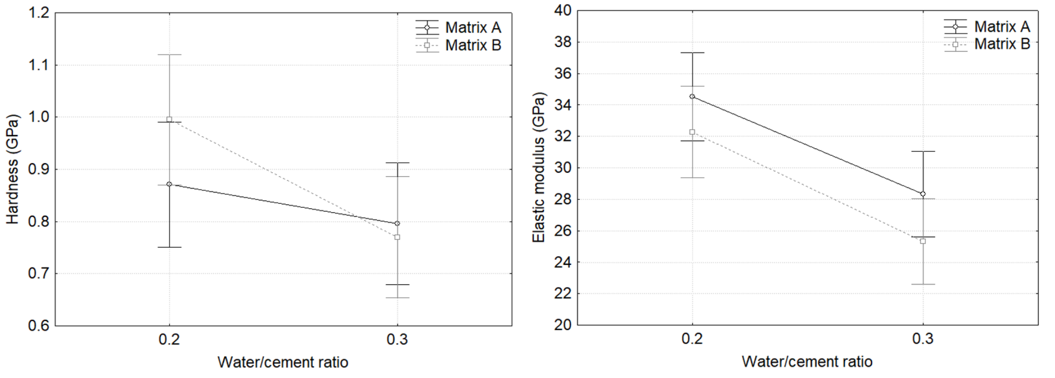

a) b)

Figure 1. Results of hardness (a) and elastic modulus (b) obtained by the nanoindentation technique applied to cement pastes with w/c ratios of 0.2 and 0.3 without steel microfibers, varying the load from 100 mN (matrix A) to 50 mN (matrix B).

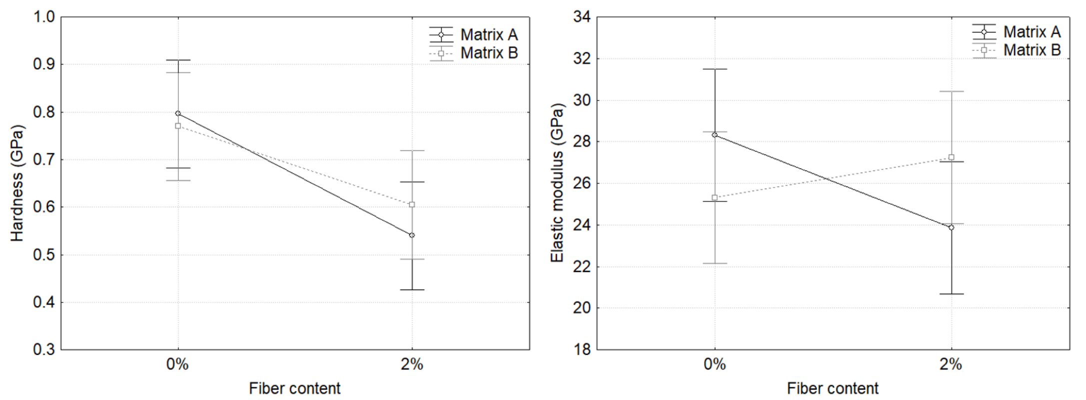

a) b)

Figure 2. Results of hardness (a) and elastic modulus (b) obtained by the nanoindentation technique applied to cement pastes with w/c ratio of 0.3 with and without steel microfibers, varying the load from 100 mN (matrix A) to 50 mN (matrix B).

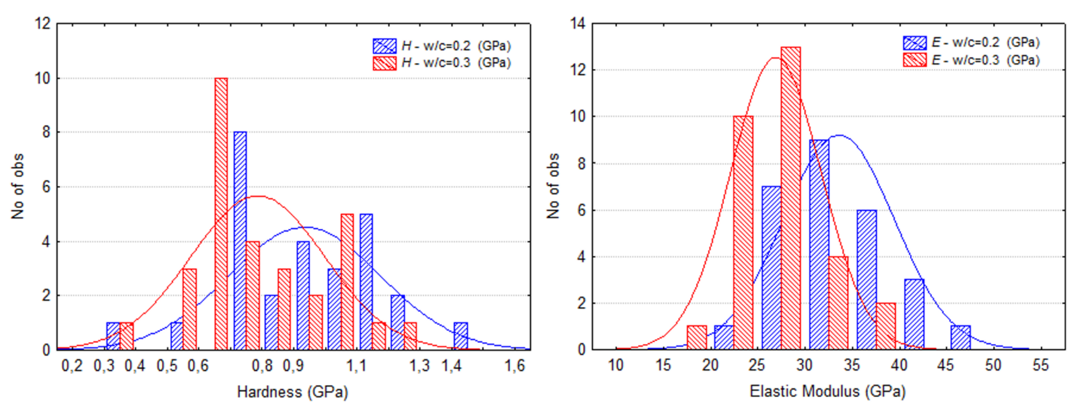

a) b)

Figure 3. Histogram showing the effect of the w/c ratio on the hardness (a) and elastic modulus (b).

3.2. Interfacial transition zone cement paste/microfiber

Considering the micro-nanomechanical characterization performed here, at the matrix-steel microfiber interface, Figure 4 and Figure 5 show micrographs of the two matrices (matrix 1 and 2, with w/c=0.30) near the paste-fiber interface on each side of the same microfiber. Matrix 1 was placed slightly further away from the microfiber, a distance of ~60 µm, due to the microporosity observed at the interface with the fiber (Figure 4), while matrix 2 was placed closer, a distance of ~30 µm.

Figure 6 presents the hardness and elastic modulus results, considering the effect of the distance of each row of indentation points in relation to the microfiber. For matrix 1 (farther from the microfiber), a tendency towards increased hardness and a greater increase in the elastic modulus was observed when the distance from the microfiber was greater. This resulted in a mean elastic modulus of approximately 30 MPa, 40 MPa and 45 MPa (Figure 6b) for distances of approximately 60 µm (row 3), 90 µm (row 2) and 120 µm (row 1), respectively. Although matrix 1 shows some variation regarding microfiber distance, this variation was not significant (p=0.087), as observed in the statistical analysis (ANOVA) (Table 1). A significant difference was observed between the two matrices (p=0.044), performed on both sides of the fiber, such that the approximate mean value of the elastic modulus for matrix 1 was 38±4 GPa and for matrix 2 was 32±4 GPa.

Table 1. ANOVA for elastic modulus (GPa).

Factor (GPa)	SS	dF	MS	F-value	p-value
Matrix	469.68	1	469.68	4.3793	0.044939
Row	567.71	2	283.86	2.6467	0.087382
Matrix × Row	167.09	2	83.54	0.7790	0.467941
Error	3217.49	30	107.25		

SS: sum of squares; dF: degrees of freedom; MS: mean squares.

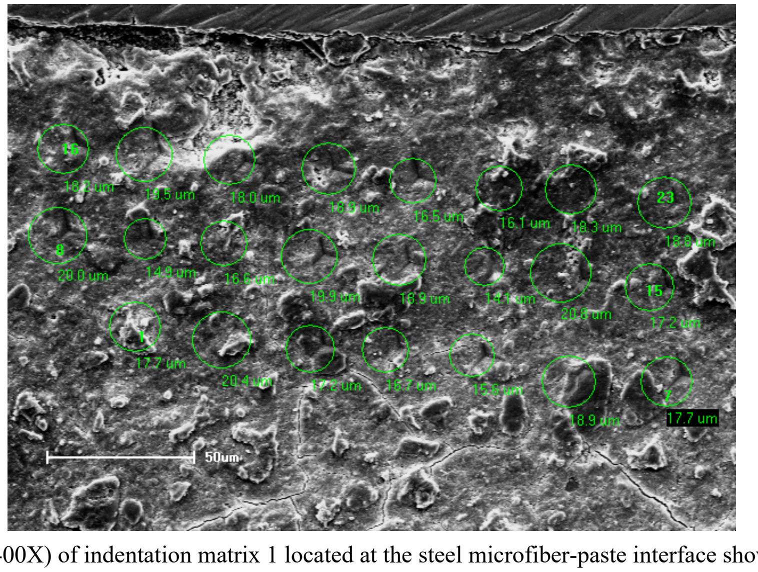

Figure 4. Micrograph (400X) of indentation matrix 1 located at the steel microfiber-paste interface showing all 24 indentation points ~30 µm from each other, distributed in 8 columns and 3 rows (24 points highlighted).

Regarding the formation of the LD C-S-H and HD C-S-H phases, matrix 1 showed 14% LD C-S-H and 84% HD C-S-H, while matrix 2 showed 27% LD C-S-H and 73% HD C-S-H. Considering all the results at the interface with the microfiber, since no significant difference was observed between the indentation distances, the formation of 20% LD C-S-H and 80% HD C-S-H was verified. These results are very similar to those obtained for the cementitious matrix without fibers, particularly those obtained for matrix 2; moreover, they reinforce the fact that the micro-nanomechanical properties at the interface with the steel microfibers are equivalent to the cementitious matrix. Results also showed a significant increase in HD C-S-H (80%) compared with those obtained by Xu et al. [4] for a w/c ratio of 0.35 (31% HD

C-S-H). Authors verified the formation of low modulus C-S-H (~13 GPa), characterized by a region of porosity, probably due to the higher w/c ratio. The results obtained in the present work were also very similar to those reported by Vandamme et al. [17], who obtained 70% HD C-S-H and 30% LD C-S-H formation for a w/c ratio of 0.3, while determining the nanomechanical properties of cementitious pastes with low w/c ratios (between 0.15 and 0.40).

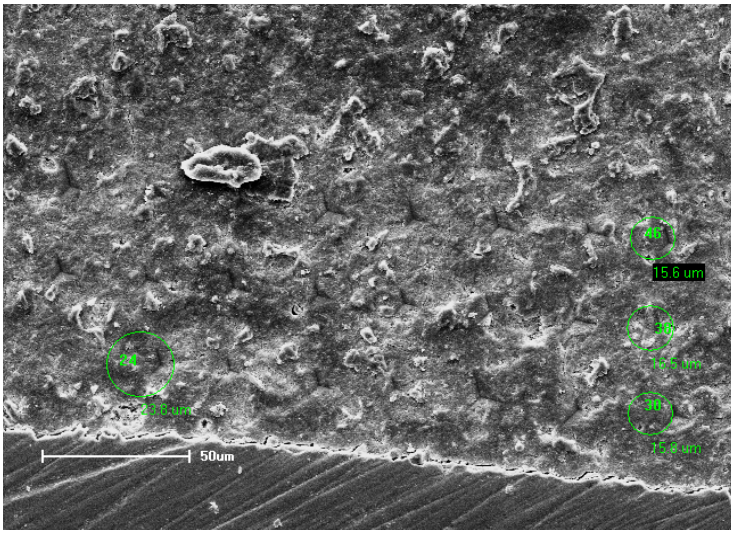

Figure 5. Micrograph (400X) of indentation matrix 2 located at the steel microfiber-paste interface showing all 24 indentation points ~30 µm from each other, distributed in 8 columns and 3 rows (4 points highlighted).

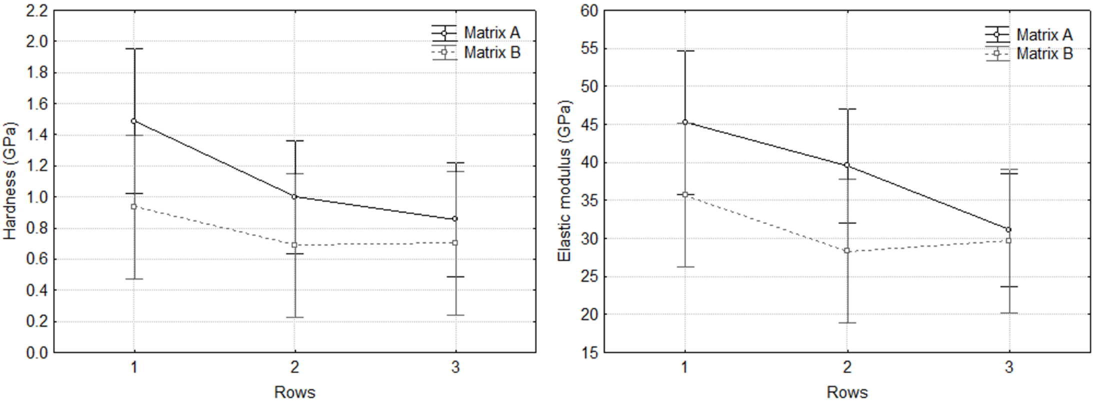

a) b)

Figure 6. Mean results of hardness (a) and elastic modulus (b) obtained by the nanoindentation technique for two different 24 indentation points matrices located at the microfiber-paste interface, where row 1 is the farthest and row 3 is the closest to the fiber.

Figure 7 shows the load versus displacement curves, indicating the mean values for each row of matrix 2. Figure 8 presents an indentation curve, characterized as a non-hydrated cement particle, due to the high elastic modulus [17]; this was the only value excluded from the mean results (Figure 6). Figure 9 shows the relation between the results of elastic modulus and hardness, together with histograms, for the two matrices. The elastic modulus results were predominantly between 20 GPa and 40 GPa and HD C-S-H (E>25 GPa) formation was much higher than that of LD C-S-H.

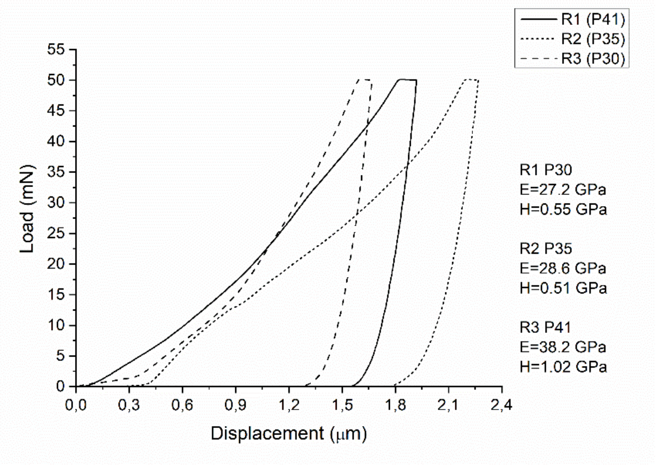

Figure 7. Matrix 2: force versus displacement curves showing representative indentation for each row (R1, R2, R3).

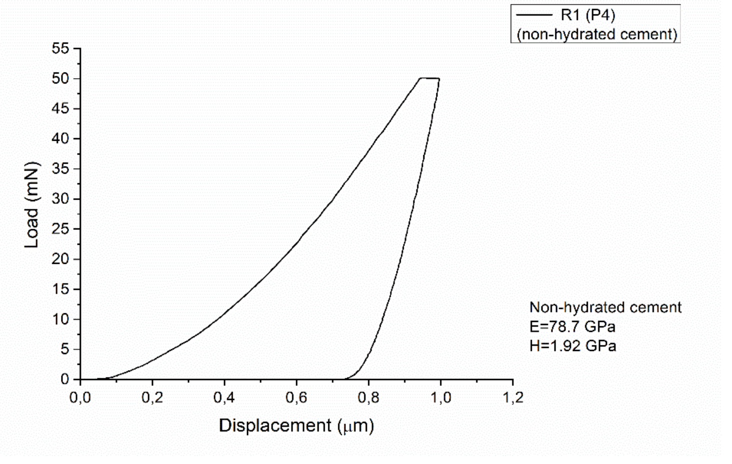

Figure 8. Force versus displacement curve showing particle indentation of non-hydrated cement.

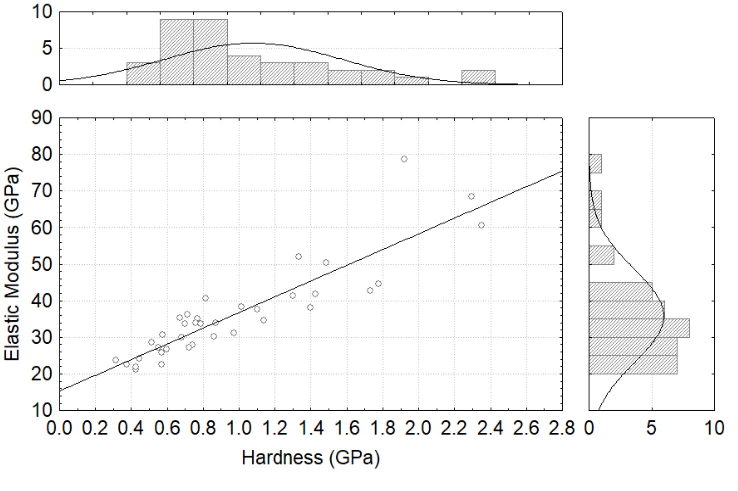

Figure 9. Relation between results of elastic modulus and hardness obtained by the nanoindentation technique for matrices 1 and 2 and histograms.

Table 2 shows that similar behavior was observed at the steel microfiber-cementitious matrix interface, where the mean values of elastic modulus varied between 28 GPa and 45 GPa and those of hardness varied between 0.7 GPa and 1.5 GPa. Regarding the distance between the microfiber and the micro-nanomechanical properties of the cementitious matrix, no significant differences were verified in the results.

Table 2. Average results obtained at the steel microfiber-cementitious matrix interface.

Matrix 1			Matrix 2		
Row	**Hardness (GPa)**	**Elastic Modulus (GPa)**	**Row**	**Hardness (GPa)**	**Elastic Modulus (GPa)**
1 - 120μm	1.49 ± 0.61	45.3 ± 10.4	1 - 90μm	0.94 ± 0.50	35.7 ± 15.0
2 - 90μm	1.00 ± 0.57	39.6 ± 12.2	2 - 60μm	0.69 ± 0.40	28.3 ± 6.0
3 - 60μm	0.86 ± 0.52	31.1 ± 8.7	3 - 30μm	0.70 ± 0.30	29.7 ± 5.9
Mean	1.06 ± 0.59	37.7 ± 11.6	Mean	0.78 ± 0.40	31.2 ± 9.8

In addition, an indentation matrix (4×7) was also performed on the microfiber inserted in the paste (Figure 10) and the mean hardness value was 6.66 ± 0.11 GPa, while the mean elastic modulus was 178.2 ± 2.55 GPa. The indentation results presented low variability and were similar to those obtained by Sorelli et al. [8] who reported approximately 202 ± 20 GPa.

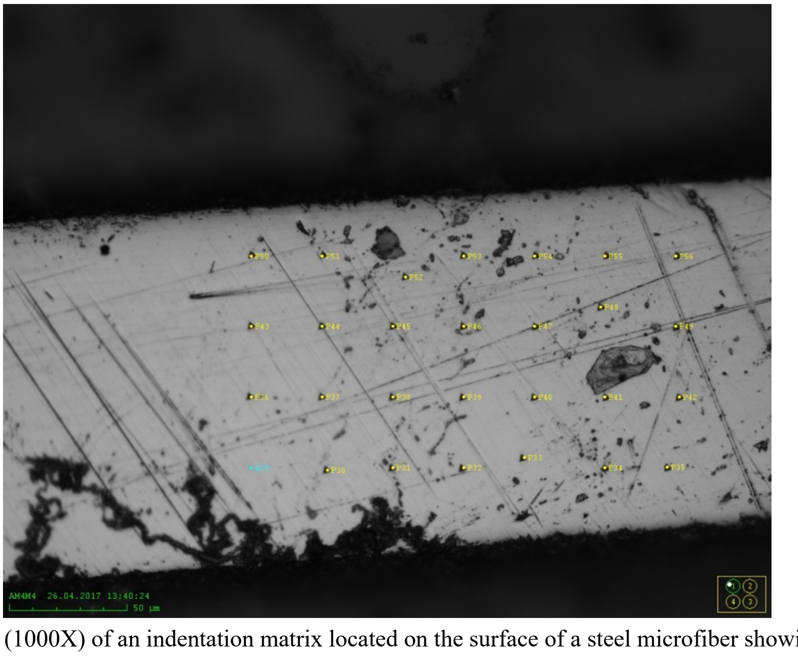

Figure 10. Micrograph (1000X) of an indentation matrix located on the surface of a steel microfiber showing all 28 indentation points ~30 μm from each other, distributed in 7 columns and 4 rows.

3.3. Interfacial transition zone: chemical characterization

In addition, four chemical analyses (EDS) were performed at the microfiber-paste interface, within an area of approximately 100 μm^2, from the closest point (D1 – Table 3) to the farthest from the fiber (D4 – Table 3). These analyses were performed at two different sites around the fiber to detect any local changes in calcium (Ca) and calcium hydroxide (CH) concentrations. Table 3 presents the EDS results for two sites around the fiber. The authors analyzed other zones at the microfiber-paste interface and showed similar behavior to those presented here (results not shown).

A higher concentration of Ca (influencing the Ca/Si ratio) was verified at D1 compared with D2, D3 and D4 in zone 1. However, analysis in zone 2 did not confirm these results; rather higher Ca concentrations were verified at D1 and

D4, while D2 and D3 presented lower concentrations. Thus, it can be concluded that calcium concentration varies locally and this appears to be independent of the proximity to the microfiber.

Table 3. Chemical composition at the steel microfiber-cementitious matrix interface.

Element	Region 1				Region 2			
	D1	**D2**	**D3**	**D4**	**D1**	**D2**	**D3**	**D4**
Ca	39.70	30.38	29.86	31.63	37.66	36.16	34.79	37.36
O	32.27	31.55	33.19	31.91	27.44	30.39	30.89	28.92
C	15.30	14. 12	14.79	12.32	13.00	12.95	14.33	13.14
Si	4.45	10.91	10.75	11.91	7.10	9.55	9.10	7.48
K	2.75	5.14	5.13	5.82	4.11	4.74	4.05	3.49
Fe	4.40	4.33	3.05	3.02	7.94	3.44	3.15	5.33
Al	0.00	2.45	2.07	2.51	1.77	2.04	2.13	2.69
Mg	1.12	1.12	1.16	0.88	0.98	0.72	1.14	1.36
Ca/Si	8.92	2.78	2.78	2.66	5.30	3.79	3.82	4.99

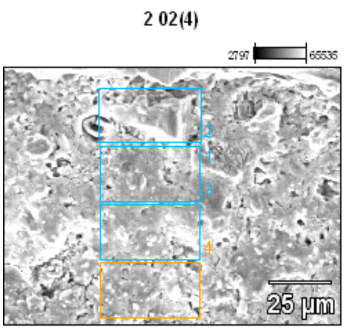

SEM image (300X)

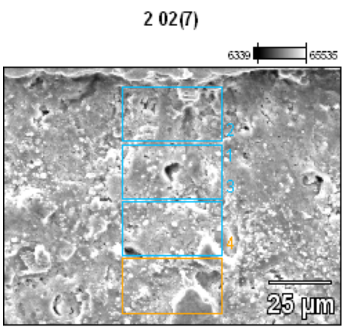

SEM image (300X)

In addition, Figure 11 shows a micrograph of the surface of the microfiber where chemical analysis (EDS), performed at two spots, showed the presence of Zn, Cu and Fe in approximate quantities of 75%, 20% and 5%, respectively.

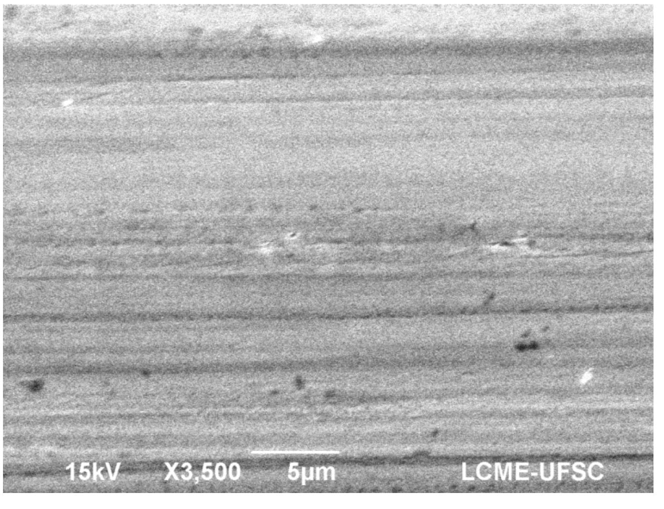

Figure 11. Micrograph (3500X) of the surface of a steel microfiber.

4. DISCUSSION

Xu et al. [4] studied the ITZ between steel microfibers and cementitious matrix of cement pastes with w/c ratios from 0.35 to 0.45 and showed that the w/c ratio had a significant effect on the nanomechanical properties. Results showed the formation of LD C-S-H of 26%, 37%, 32% and HD C-S-H of 31%, 23%, 15%, for w/c ratios of 0.35, 0.40 and 0.45, respectively. Other phases were also identified, such as CH (E>50 GPa) and clinker (E>80 GPa). Authors also observed an increase in HD C-S-H from 15% to 31% when the w/c ratio decreased from 0.45 to 0.35.

However, Xu et al. [4] concluded that the distance was not significant in determining nanomechanical properties in their evaluation of the combined effect of the w/c ratio and the distance (from 5 μm to 50 μm) between the indentation and the steel microfiber interface (500 μm in diameter and 13 mm in length). The authors observed a trend towards reduction, explained by the fact that steel fibers show hydrophilic behavior, i.e. water can spread along their surface. After 28 days, a layer of iron oxide forms on the surface, making the surface more hydrophilic and causing an increase in the w/c ratio at the interface, because the fiber is not absorbent [18].

Sorelli et al. [8] characterized UHPC (w/c between 0.19 and 0.21) at several levels (level 1: C-S-H matrix; level 2: cement paste; level 3: concrete; level 4: UHPC). Based on a combination of nanoindentation tests, SEM and XRD, the authors concluded there is strong evidence that there is no interface zone between the matrix and fibers in UHPC. This is due to the predominant presence of HD C-S-H in UHPC, which guarantees the uniform composite behavior of the cementitious matrix.

In this study, a reduction in the w/c ratio to values below 0.35, of 0.30 and 0.20, caused a significant increase in the mechanical properties of the C-S-H, leading to the formation of 63% (0.30) and 96% (0.20) of HD C-S-H. The formation of HD C-S-H doubles for a w/c ratio of 0.30 (63%), in relation to 0.35 [4], and triples for a w/c ratio of 0.20 (96%), in relation to 0.35 [4]. These results are close to those obtained by Sorelli et al. [8], when quantifying the percentage of HD C-S-H formation in UHPC (86%) by nanoindentation, and the results obtained by Vandamme et al. [17], who verified the formation of 97% of HD C-S-H, for a w/c ratio of 0.20, when evaluating only pastes without fibers.

The mentioned authors [4], [8] confirmed that the micro-nanomechanical properties of the cementitious matrix are the same at the interface with steel microfibers, considering w/c ratios between 0.20 and 0.45. They also reported a predominant formation of HD C-S-H for a w/c ratio of 0.20, while for a w/c ratio of 0.30, there was a significant reduction in the formation of HD C-S-H.

5. CONCLUSIONS

This research evaluated the effect of the w/c ratio and the micro-nanomechanical behavior at the steel microfiber-cementitious matrix interface on the development of ultra-high performance cementitious composite.

The effect of w/c ratios of 0.2 and 0.3 on the micro-nanomechanical properties of the cementitious matrix were significant, with 34 GPa and 28 GPa for elastic modulus and 0.87 GPa and 0.80 GPa for hardness, respectively. This difference was due to a higher density of packing of C-S-H particles, forming more HD C-S-H. The results show the formation of 96% HD C-S-H and 4% LD C-S-H when the w/c ratio was 0.2, and 63% HD C-S-H and 37% LD C-S-H when the w/c ratio was 0.3.

The results obtained at the interface with the steel microfibers were practically the same as those obtained for the cementitious matrix. Thus, the authors can conclude that the formation of a less porous or less resistant region does not occur at the interface with the steel microfibers. The predominant formation of HD C-S-H (80%) in relation to LD C-S-H (20%) was verified.

The good adhesion of the cementitious matrix with the steel microfibers explains the satisfactory performance of ultra-high strength concretes, particularly regarding their tensile strength. Improvements in the mechanical performance, economic aspects and durability studies are fundamental to disseminate the knowledge and application of this type of concrete.

6. ACKNOWLEDGEMENTS

The authors gratefully acknowledge the financial support of the Coordination for the Improvement of Higher Education Personnel (CAPES), the Foundation for Research and Innovation of the State of Santa Catarina (FAPESC), the National Council of Technological and Scientific Development (CNPq, fellowship under grant number 304589/2019-5), the Central Laboratory of Electronic Microscopy of the Federal University of Santa Catarina (LCME-UFSC) for the SEM micrographs and Belgo Bekaert for donating the fibers used herein.

7. REFERENCES

[1] C. Shi, Z. Wu, J. Xiao, D. Wang, Z. Huang, and Z. Fang, “A review on ultra high performance concrete: Part I. Raw materials and mixture design,” *Constr. Build. Mater.*, vol. 101, pp. 741–751, 2015, doi: https://doi.org/10.1016/j.conbuildmat.2015.10.088.

[2] E. Shaheen and N. G. Shrive, “Cyclic loading and fracture mechanics of Ductal® concrete,” *Int. J. Fract.*, vol. 148, no. 3, pp. 251–260, 2007. https://doi.org/10.1007/s10704-008-9199-1.

[3] K. L. Scrivener, A. K. Crumbie, and P. Laugesen, “The interfacial transition zone (ITZ) between cement paste and aggregate in concrete,” *Interface Sci.*, vol. 12, no. 4, pp. 411–421, 2004. https://doi.org/10.1023/B:INTS.0000042339.92990.4c.

[4] L. Xu, F. Deng, and Y. Chi, "Nano-mechanical behavior of the interfacial transition zone between steel-polypropylene fiber and cement paste," *Constr. Build. Mater.*, vol. 145, pp. 619–638, 2017. http://dx.doi.org/10.1016/j.conbuildmat.2017.04.035.

[5] Z. Wu, C. Shi, and K. H. Khayat, “Multi-scale investigation of microstructure, fiber pullout behavior, and mechanical properties of ultra-high performance concrete with nano-CaCO3 particles,” *Cem. Concr. Compos.*, vol. 86, pp. 255–265, 2018. https://doi.org/10.1016/j.cemconcomp.2017.11.014.

[6] A. Elsharief, M. D. Cohen, and J. Olek, “Influence of aggregate size, water cement ratio and age on the microstructure of the interfacial transition zone,” *Cem. Concr. Res.*, vol. 33, no. 11, pp. 1837–1849, 2003, doi: https://doi.org/10.1016/S0008-8846(03)00205-9.

[7] S. Zhao and W. Sun, "Nano-mechanical behavior of a green ultra-high performance concrete," *Constr. Build. Mater.*, vol. 63, pp. 150–160, 2014. http://dx.doi.org/10.1016/j.conbuildmat.2014.04.029.

[8] L. Sorelli, G. Constantinides, F.-J. Ulm, and F. Toutlemonde, “The nano-mechanical signature of ultra high performance concrete by statistical nanoindentation techniques,” *Cem. Concr. Res.*, vol. 38, no. 12, pp. 1447–1456, 2008. https://doi.org/10.1016/j.cemconres.2008.09.002.

[9] Z. Wu, C. Shi, K. H. Khayat, and S. Wan, “Effects of different nanomaterials on hardening and performance of ultra-high strength concrete (UHSC),” *Cem. Concr. Compos.*, vol. 70, pp. 24–34, 2016, doi: https://doi.org/10.1016/j.cemconcomp.2016.03.003.

[10] Associação Brasileira de Normas Técnicas. *Cimento Portland – Resquisitos*, NBR 16697, 2018.

[11] F. Pelisser, P. J. P. Gleize, and A. Mikowski, “Structure and micro-nanomechanical characterization of synthetic calcium–silicate–hydrate with Poly(Vinyl Alcohol),” *Cem. Concr. Compos.*, vol. 48, pp. 1–8, 2014. https://doi.org/10.1016/j.cemconcomp.2014.01.004.

[12] W. C. Oliver and G. M. Pharr, “An improved technique for determining hardness and elastic modulus using load and displacement sensing indentation experiments,” *J. Mater. Res.*, vol. 7, no. 6, pp. 1564–1583, 1992. https://doi.org/10.1557/JMR.1992.1564.

[13] F. Pelisser, P. Gleize, and A. Mikowski, “Effect of the Ca/Si molar ratio on the micro/nanomechanical properties of synthetic C–S–H measured by nanoindentation,” *J. Phys. Chem. C.*, vol. 116, pp. 17219–17227, 2012, https://doi.org/10.1021/jp302240c.

[14] D. K. Chanda et al. “Synthesis of calcium based nano powders for application in conservation and restoration of heritage mortar,” *SN Applied Sciences*, vol. 2, no. 3, pp. 340, 2020. https://doi.org/10.1007/s42452-020-2138-0.

[15] A. Leemann and P. Lura, “E-modulus of the alkali–silica-reaction product determined by micro-indentation,” *Constr. Build. Mater.*, vol. 44, pp. 221–227, 2013. https://doi.org/10.1016/j.conbuildmat.2013.03.018.

[16] G. Constantinides and F.-J. Ulm, “The nanogranular nature of C–S–H,” *J Mech Phys Solids*, vol. 55, no. 1, pp. 64–90, 2007. https://doi.org/10.1016/j.jmps.2006.06.003.

[17] M. Vandamme, F.-J. Ulm, and P. Fonollosa, “Nanogranular packing of C–S–H at substochiometric conditions,” *Cem. Concr. Res.*, vol. 40, no. 1, pp. 14–26, 2010. https://doi.org/10.1016/j.cemconres.2009.09.017.

[18] J. Wambach, A. Wokaun, and A. Hiltpold, “Oxidation of stainless steel under dry and aqueous conditions: oxidation behaviour and composition,” *Surf Interface Anal.*, vol. 34, no. 1, pp. 164–170, 2002. https://doi.org/10.1002/sia.1275.

Author contributions: VFC: Conceptualization, Investigation, Writing-Original draft preparation, Methodology. FP: Supervision, Conceptualization, Methodology, Data curation, Writing-Original draft preparation, Writing- Reviewing and Editing. PJPG: Visualization, Investigation. MDM: Conceptualization, Methodology, Data curation.

Editors: Rebecca Gravina, Guilherme Aris Parsekian.

IBRACON Structures and Materials Journal
Revista IBRACON de Estruturas e Materiais
ISSN 1983-4195 ismj.org

ORIGINAL ARTICLE

Effects of dowel bars misalignment in jointed plain concrete pavements – A numerical analysis considering thermal differentials and bonded slab-base interface

Efeitos do desalinhamento vertical e horizontal de barras de transferência de carga em pavimentos de concreto simples – uma análise numérica considerando diferenciais térmicos e aderência entre placa e base

Eric Ribeiro da Silva[a,b]
José Tadeu Balbo[a]
Andréia Posser Cargnin[a]

[a]Universidade de São Paulo – USP, Departamento de Engenharia de Transportes, São Paulo, SP, Brasil
[b]Universidade Presbiteriana Mackenzie, Departamento de Engenharia Civil, São Paulo, SP, Brasil

Received 17 May 2020
Accepted 16 November 2020

Abstract: Joints in concrete pavements are built to allow slab volumetric variations avoiding random cracks. Moreover, as they are discontinuities, the use of dowel bars prevents loss of load transfer across joints. During bars installation or even concrete casting, misalignments and misallocations of those devices may occur, affecting the concrete pavement structural performance. This study explores the effects of such non-conformities in the positioning of dowel bars through numerical modeling, using the 3D finite element program EverFE2.25. For, numerical simulations, bending stresses in concrete slabs of a typical bus corridor were ascertained, varying misalignments types and magnitudes (vertical tilt and horizontal skew), base type (cemented and asphalt), slab/base interface bond conditions and concrete thermal differential. Results disclosed the contribution of using bonded base in reducing stresses, even when the dowels were severely misaligned while slabs were subjected to high thermal differentials.

Keywords: plain concrete pavements, dowel bars misalignment, numerical analysis, structural evaluation.

Resumo: As juntas em pavimentos de concreto são construídas com o objetivo de permitir a expansão e contração do concreto quando de alterações nas condições climáticas, impedindo a ocorrência de fissuras de retração de secagem aleatórias. Contudo, como as juntas serradas causam descontinuidades nos pavimentos, gerando o formato típico das placas, as barras de transferência de carga são introduzidas para evitar que a capacidade de transferência de carga do pavimento de concreto seja reduzida. Quando do posicionamento dessas barras em pista e mesmo durante a concretagem do pavimento podem ocorrer desalinhamentos, que por sua vez podem afetar o desempenho estrutural e funcional do sistema mesmo de maneira precoce. Assim, a investigação dos efeitos de desconformidades no posicionamento dessas barras nas tensões de serviço em pavimentos de concreto simples, por meio de modelagem numérica, torna-se ponto de partida para a melhoria das especificações e restrições normativas sobre o assunto. Nesse estudo foram realizadas simulações numéricas por meio do Método dos Elementos Finitos, com o programa EverFE 2.25 (em 3D) de estrutura típica de pavimento de concreto simples em corredor de ônibus quando foram então avaliados os tipos e magnitudes de desalinhamentos (rotações verticais e horizontais), tipos de base (cimentada e asfáltica) de apoio das placas, condições de aderência entre placas e base, bem como ocorrência ou não de gradientes de temperatura entre topo e fundo da placa. Os resultados evidenciaram a significativa contribuição da aderência entre a placa de concreto e a base para a redução das tensões de tração na flexão no concreto, mesmo quando as barras se encontrassem severamente desalinhadas e as placas sujeitas a diferenciais térmicos elevados.

Palavras-chave: pavimentos de concreto simples, desalinhamento de barras de transferência de carga, análise numérica, avaliação estrutural.

Corresponding author: José Tadeu Balbo. E-mail: jotbalbo@usp.br
Financial support: CAPES – Foundation for the Coordination and Improvement of Higher Education Personal, Ministry of Education – by the Ph.D. scholarships provided to the first and third authors.
Conflict of interest: Nothing to declare.

How to cite: E. R. Silva, J. T. Balbo, and A. P. Cargnin, “Effects of dowel bars misalignment in jointed plain concrete pavements – A numerical analysis considering thermal differentials and bonded slab-base interface,” *Rev. IBRACON Estrut. Mater.*, vol. 14, no. 4, e14414, 2021, https://doi.org/10.1590/S1983-41952021000400014

1 INTRODUCTION

One of the most specific characteristics in concrete pavements is the presence of contraction joints, normally built to enable the concrete expansion and contraction during its cure and under severe weather conditions, avoiding the occurrence of random shrinkage cracks [1], [2].

However, as joints create discontinuities in concrete pavements, their presence reduces the load transfer capacity, requiring, therefore, the introduction of a load transfer mechanism across these joints [3]. This is accomplished by using dowel bars, which enable partial transfer of stresses to the nearby slab, forcing successive slabs to work simultaneously in the joint limits (this effect is known as “load transfer”) [4], [5]. Such bars have smooth surfaces and are greased prior to concrete pouring to allow the concrete slabs horizontal contraction and expansion movements since the they work detached from the dry concrete. The main mechanism of load transfer supplied at joints by dowel bars is shearing.

The load transfer mechanism between neighboring slabs decreases deflections and stresses at the slab’s edges and corners, beyond helping to ensure a satisfactory pavement performance, preventing future distresses development such as corner breaks and pumping followed by faulting [6], [7].

Aiming to provide maximum load transfer capacity, the dowel bars are positioned parallel to the concrete slab bottom surface and pavement longitudinal axis, at the slab half-height [2], [4], [7]. Moreover they shall be longitudinally centered in the transverse joints and parallel to the direction of movement of the slabs in relation to joint; they may be also used at longitudinal joints in areas with random or non-directional traffic, as well as in diagonal directions load movements on concrete slabs [1]. Dowel bars are also greased to fully avoid adherence to concrete, allowing free horizontal movements.

The placement of such kind of load transfer mechanism in concrete pavements may be conducted in two different ways: using metal dowel baskets positioned and fixed on the pavement base before concrete casting; or using an automated mechanical dowel bar inserter attached to the concrete pavement machine, which places the dowel bars soon after concrete casting [4], [5], [7]. One should note that for both methods correct placement of the dowel bars is essential to guarantee good structural and functional pavement performance over its service life.

However, during the dowel bars placement, misalignment and misallocation may occur (Figure 1) due to lack of controlling their position and alignment, dowel baskets inappropriate stiffness, as well as failure when fixing the dowel baskets on the base, or even during the concrete casting. In the case of dowel bars inserter, concrete mixture design is considered the most critical factor influencing both dowel bars placement and its stability into the plastic concrete [8].

One of the main problems associated with the control of dowel bars alignment and positioning is the potential for locking the joint [9]. In the case of joints with dowel bars, alignment and positioning disagreements may affect the concrete slabs movements during its expansion and contraction (due to thermal and moisture changes) causing, consequently, the system malfunction, even leading to concrete transversal cracks parallel to the joints.

The locking of an isolated joint does not impair the pavement performance. Nevertheless, the risk of breaking the slab is increased when successive joints are locked due to joint restriction movements leading to spalling in the severe cases. Furthermore, the dowel bars vertical tilt should be limited in order to avoid shear cracks or spalling above or below the bars and a concrete minimum cover warranted to avoid the steel corrosion [7], [10].

For these reasons, dowel bars alignment and positioning have been of concern since the 1930s [10]. Most of the road agencies in developed countries with tradition on constructing concrete pavements set out tolerances for controlling dowel bars positioning and alignment during its placement.

Such limits are commonly expressed in terms of deviations at the dowel bar ends related to the designed position and its length (for instance, 6 mm for a dowel bar with length of 460 mm) or in terms of percentage length. Some authors, nonetheless, present only rotating tolerances (horizontal skew and vertical tilt) in relation to the correct position through the dowel inclination (usually expressed in radians).

In Brazil, the misalignment tolerance for individual dowels related to its correct position accepted by road agencies [11], [12] corresponds to ±1% of the bar length and at least two-thirds of the dowels in a single joint shall present a maximum deviation of ±0,7%. However, as shown in Table 1, such tolerances do not match the typical standards applied in countries with a vast history on concrete pavement construction, like Germany and USA.

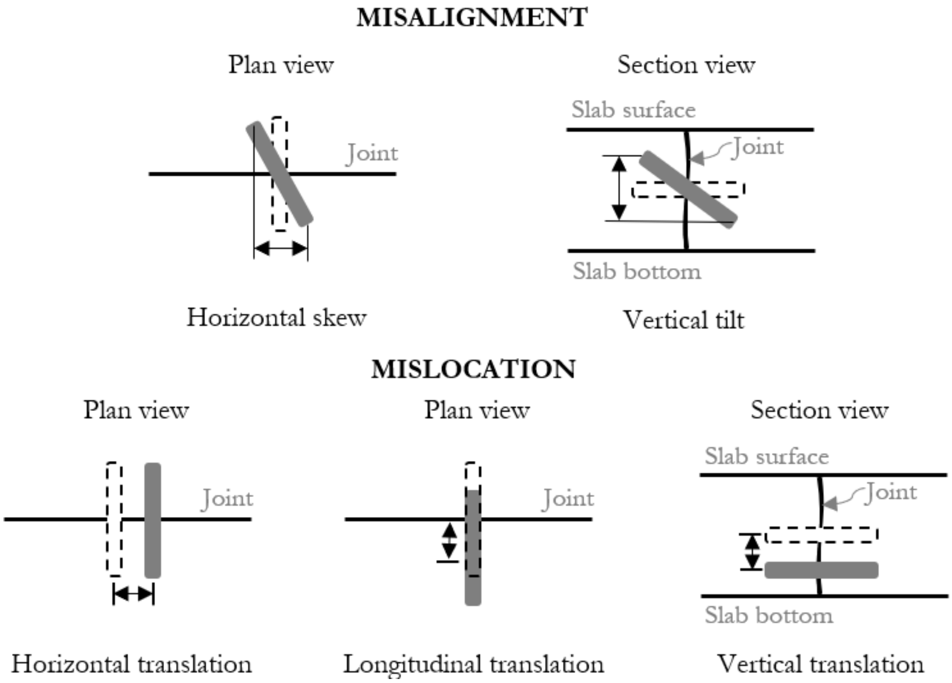

Figure 1. Main misalignment and misallocation types in dowel bars (Source: Adapted from Tayabji [3]).

Table 1. Misalignment and misallocation tolerances.

Country	Vertical tilt	Horizontal skew	Longitudinal translation	Vertical translation	Source
Brazil	1.0%	1.0%	1.0%	1.0%	DER-SP [11], DNIT [12]
Germany	4.2%	4.2%	11.1%		Rao et al. [4]
USA	3.3%	3.3%	11.1%	5.6%	FHWA [10], ACPA [9]

Over the last decades, investigations on concrete pavements mechanical behavior employing the finite element method (FEM) have increasingly spread. Most of these studies are concentrated on the load transfer efficiency analysis in concrete pavement joints with aligned dowel bars [13]. Only a limited number of investigations sought to understand the interaction mechanism between misaligned dowel bars and the concrete. Examples of such studies can be found elsewhere [13], [14], [15], [16].

However, these studies pursued to understand mainly the interaction mechanism between dowel bars and concrete slabs focused on the joint vicinity, investigating the stresses and the damage caused by the misalignment. Curling of slabs due to concrete curing and concrete top-bottom thermal differential, as well as the effects of bonding or not bonding the concrete to the underneath pavement stiff bases, are well understood as supporting factors to be taken into account on joint behavior analysis since they will interfere in the system response as a whole.

Thereby, the current study addresses the effects of dowel bars misalignment combined (horizontal skew and vertical tilt) with positive thermal gradient (mostly found in roads in tropical environments), comprising the bond effect given at the slab/base interface, on the structural response of a jointed-plain concrete pavement (JPCP), through numerical simulations using the FEM, accomplished by simulations applying EverFE 2.25 software [14].

1.1 Justification

Transversal joints are the most critical elements for plain concrete pavements performance. Depending on pavement bases capabilities to partially transfer loads from both sides of joints, flexural stresses on concrete slabs can increase when dowel bars are misplaced, and such alteration is not commonly considered in the structural design of concrete pavement structures by design guides. Furthermore, studying the dowel bars misallocations are of paramount importance for future standardization for building such structural devices in concrete pavements, either plain or reinforced ones.

2 NUMERICAL MODEL DESCRIPTION

The FEM software EverFE 2.25 was used in this study since it was developed specifically for JPCP analysis purposes, with an intuitive graphic interface (Figure 2), beyond it enables the parametric study of up to nine concrete slabs (in a 3 x 3 arrangement), settled on even three elastic layers and subgrade.

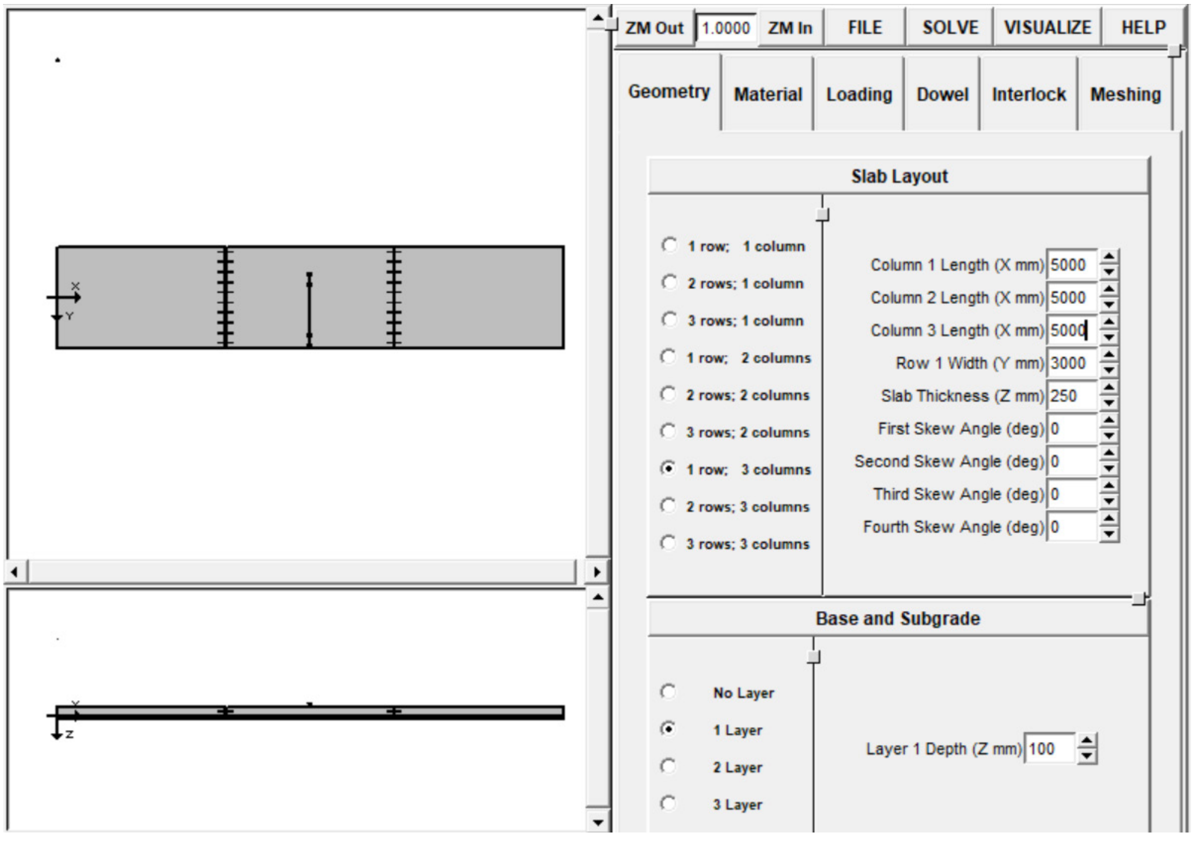

Figure 2. Example of the **graphic int**erface in the software EverFE 2.25.

Additionally, EverFE 2.25 allows the analysis of linear and non-linear thermal gradient effects on concrete slabs, assessment of different concrete slab/base bond conditions, and the analysis of pavement structures with or without dowel bars in the transverse joints, as well as specification of dowel bars misalignments or misallocations. For models with lateral slabs, tie bars may be introduced in the longitudinal joints.

Concrete slabs and base layer are discretized by 20-noded quadratic brick elements; the subgrade is discretized by 8-noded planar quadratic elements that incorporate the dense liquid foundation model and the load transfer by the aggregate interlocking at the joint; shear transfer at the slab/base interface is discretized by 16-noded quadratic interface elements [17], as illustrated in Figure 3.

Dowels and tie bars are molded by embedded flexural finite elements, which allow the precise location of dowels and tie bars, regardless the mesh lines, permitting relevant savings in the computing time, making easier the load transfer efficiency simulation without requiring a highly refined mesh at the joint limits [14].

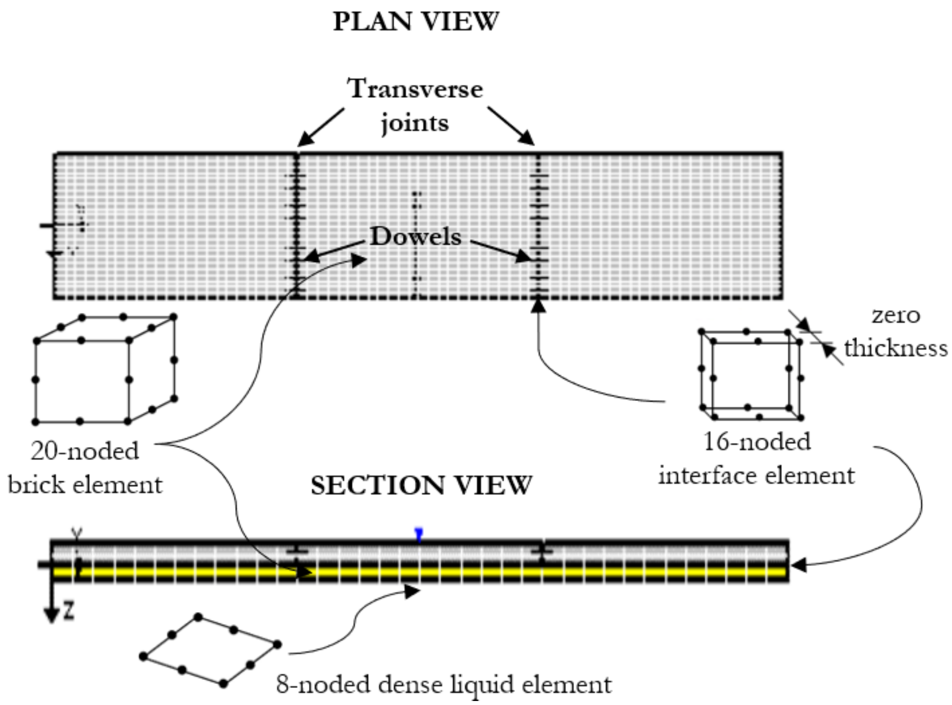

Figure 3. Finite elements used in the EverFE 2.25 discretization (Source: adapted from Davids et al. [14]).

The software algorithm pinpoints precisely the individual flexural elements inside the solid elements mesh, solving first the dowel bars intersection with the solid element faces and, afterwards, partitioning each dowel bar in at least 20 quadratic flexural elements individually incorporated [14].

EverFE 2.25 also allows to consider either the slab/base perfect bond or the full separation between them. In both cases, the concrete slab and base do not share nodes, and the nodal restraints are used to meet the contact conditions required [17]. The interaction degree at the concrete slab and base interface is defined through the shear stress (τ_0) and the relative slip (δ_0) ratio between the concrete slab and the base, characterized by an initial stiffness k_{SB} (MPa/mm), distributed in the horizontal direction [14], as depicted in Figure 4.

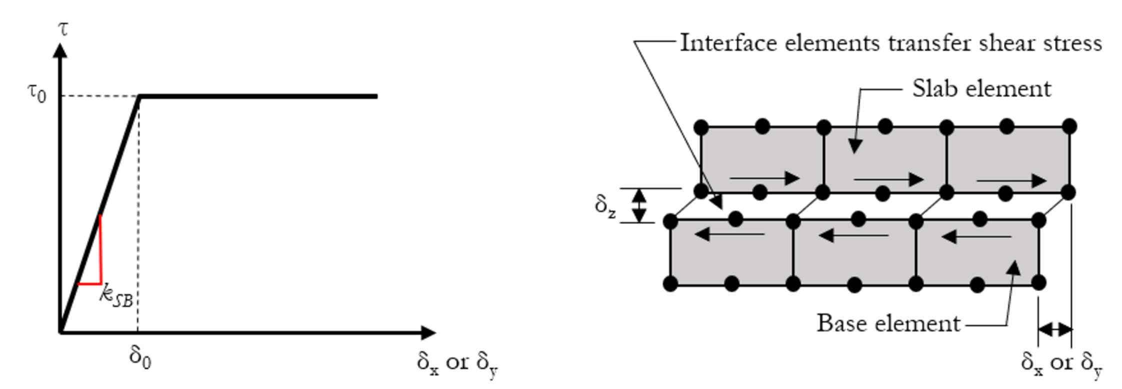

a) Interaction between the concrete slab and base layer

b) Shear transfer in the interface between the concrete slab and base layer

Figure 4. Shear transfer between the concrete slab and base layer modeling in the EverFE 2.25 (Source: adapted from Davids et al. [14]).

2.1 Concrete pavement structure modeling

To simulate a typical bus corridor's structure, a system with three concrete slabs (in single lane) upon base layer and subgrade was employed. Concrete slabs simulated were 5.0 m long, 3.0 m wide and 250 mm thick.

The simulations were carried out in two steps. Firstly, concrete slabs over a 100 mm thick unbonded cement-treated base layer were simulated regarding the misalignment limits put in place by road authorities in order to verify how such limits affect the flexural stresses due to positive thermal differential. Joint openings of 0.5 mm and 1.25 mm were simulated as well to assess their impact on the stresses. It is worth to highlight that the joint opening is significantly limited in concrete slabs under tropical climate because the top-bottom average temperature in the coldest and hottest conditions are around 19.5 and 33°C [18], respectively, whereas the average temperature at the time of concrete set is around 27.5°C [19].

The second step comprised the simulations considering the dowel misalignments higher than the limits stablished by road authorities to check their impact on the concrete flexural stresses. Regarding the concrete pavement structures analyzed herein, simulations included bonded and unbonded cement-treated base as well as bonded and unbonded asphalt base; therefore, the pavement structures are three-layered systems comprising slab, base and subgrade.

For all the analyzed cases the modulus of subgrade reaction employed was k = 30 MPa/m for a fair elastic soil. Table 2 summarizes the parameters adopted in the 752 cases analyzed in the numerical simulations.

Table 2. Parameters and values adopted for numerical simulations.

Parameter	Unit	Value adopted
Concrete slab thickness	mm	250
Cement treated base thickness	mm	100
Asphalt base thickness	mm	60
Modulus of elasticity (concrete)	MPa	30,000
Modulus of elasticity (cement-treated base)	MPa	11,000
Modulus of elasticity (asphalt base)	MPa	7,000
Poisson ratio (concrete)	-	0.15
Poisson ratio (cement-treated material)	-	0.20
Poisson ratio (asphalt mix)	-	0.30
Modulus of subgrade reaction	MPa/m	30
Concrete slabs length	mm	5,000
Concrete slabs width	mm	3,000
Thermal differential	°C	0; 5; 10; 15 and 20
Single Axle Load	kN	80
Dowel bars length	mm	460
Dowel bars diameter	mm	32
Distance between dowel bars	mm	300
Dowel bars' modulus of elasticity	MPa	210,000
Dowel bars' Poisson ratio		0.3

The non-adherence condition between the concrete slab and the cement-treated base was defined in the EverFE 2.25 assuming a low interaction degree in the slab/base interface through the shear stress and relative slip ratio between the concrete slab and the base layer. So, it was admitted an initial shear stiffness distributed along the horizontal direction kSB = 0,0001 MPa/mm (expected value when a polyethylene plastic canvas is used on the base before concrete casting to avoid the adhesion between the concrete slab and base) [14].

Loading was simulated considering the effect of an 80 kN single dual wheel axle, positioned on the central slab longitudinal edge, with one of the wheels very close to the slab edge, and centered on the middle. Moreover, linear positive thermal differential between the slab top and bottom ranging from 0°C to 20°C were simulated.

Each transverse joint has 10 dowel bars with 32 mm of diameter and length of 460 mm, positioned each 300 mm along the joint. It was also assumed the dowel bars were not bonded to the concrete and there was no looseness between them and the surrounding concrete.

For all the analyzed cases the finite elements mesh was identical for both directions x and y, employing 24 elements in the plane and element along the slab cross-section.

2.2 Dowel bars positioning at transverse joints

In order to investigate the effects of dowel bars misalignment on JPCP maximum flexural stresses, the following conditions were simulated:

- Dowel bars properly positioned (aligned).
- Uniform horizontal skew (UHS) with all dowel bars presenting the same rotation in the plane (x,y).
- Non-uniform horizontal skew (NUHS) with all dowel bars presenting the same rotation in the plane (x,y), alternating the rotation direction (clockwise and anticlockwise) of successive bars.
- Uniform vertical tilt (UVT) with all dowel bars presenting the same rotation in the plane (x,z).
- Non-uniform vertical tilt (NUVT) with all dowel bars presenting the same rotation in the plane (x,z), alternating the direction rotation (clockwise and anticlockwise) of successive bars.

The amplitude of the dowel bars misalignments assumed in the second step of the numerical simulations are described in Table 3, wherein the misalignment corresponding values in rad, degrees, and percentages are presented.

Table 3. Amplitude of the dowel bars misalignment considered for simulations.

Misalignment amplitude		
rad	degrees	%
0	0	0
1/36	1.59	2.78
1/18	3.18	5.56
1/12	4.77	8.33
1/9	6.37	11.11
1/6	9.55	16.67
1/4	14.32	25.00
1/3	19.10	33.33
1/2	28.65	50.00

Dowel bars definitions in the EverFE 2.25 software are implemented in the “Dowel” flap (Figure 5); clicking on any one dowel bar opens a window (Figure 6) which allows the user to define the translations in the directions x and z, as well as the rotations in the plane (x, y) attributing values to “alpha” angle and in the plane (y, z) giving values to “beta” angle, both in degrees. This parametrization may be performed individually, or the same configuration can be applied for all dowel bars in a certain transverse joint (in case of uniform misalignments).

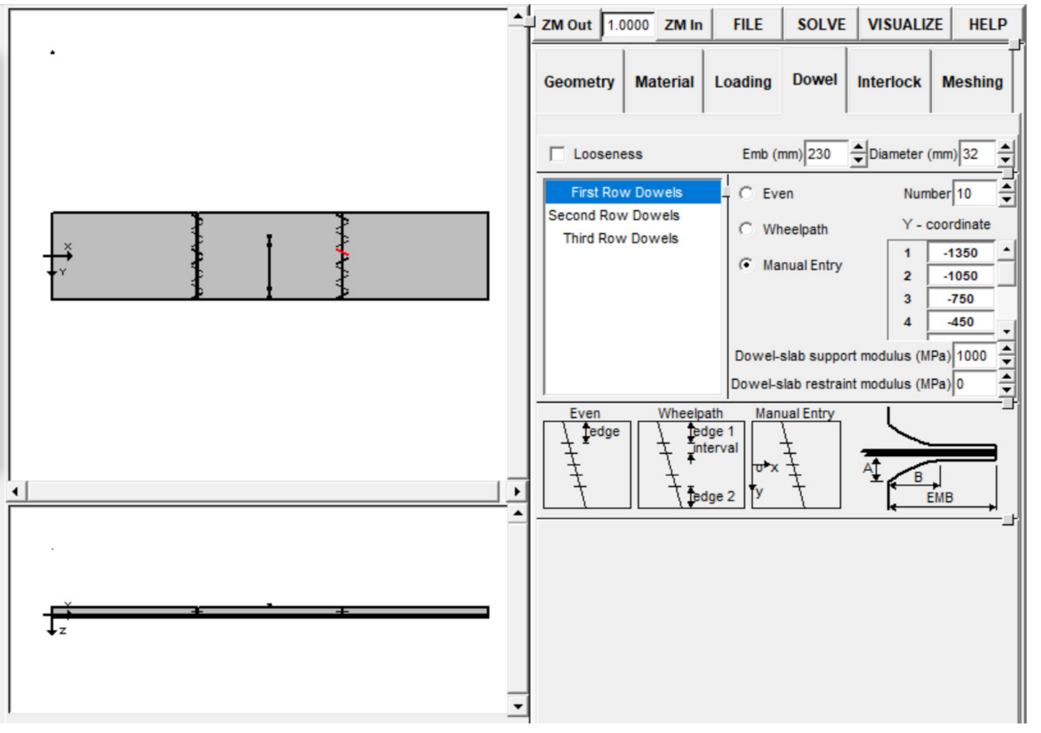

Figure 5. EverFE 2.25 flap for parametrizing dowel bars characteristics in transverse joints.

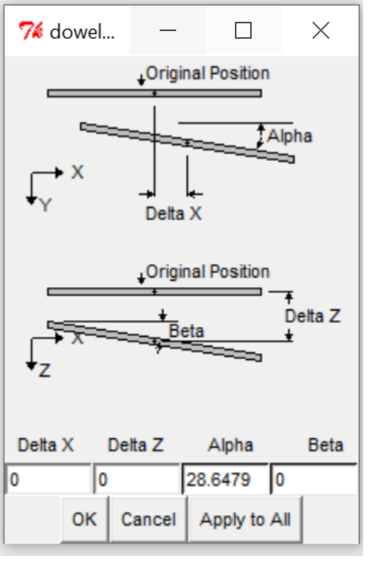

Figure 6. EverFE 2.25 window for determining dowel bars positions in the transverse joints.

3 RESULTS AND DISCUSSIONS

3.1 Analysis of dowel bars properly positioned

Firstly, it was assessed the thermal gradient effects on the maximum flexural stresses, i.e., when the simulations involved the dowel bars positioning compliance along the transverse joints (Figure 7). One should note that the slab/base adherence causes an expressive reduction on the maximum stresses for high thermal differential because of the neutral axis displacement towards the slab bottom [1].

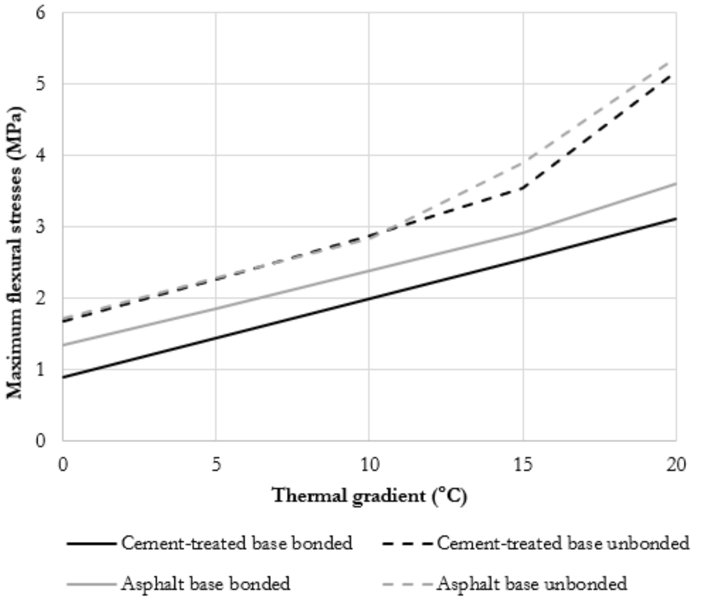

Figure 7. Thermal gradient effect on the maximum flexural stresses when dowel bars are properly positioned.

In addition, when the concrete slab and base were bonded, the maximum flexural stresses were always recorded at the bottom of the concrete slab. However, when the concrete slab was unbounded to cement-treated base, for a thermal gradient of 20°C, the maximum stress was recorded at the top of the concrete slab; otherwise, for asphalt base unbounded to the concrete slab and thermal differential of 15°C and 20°C, the maximum flexural stresses were recorded at the middle of the concrete slab.

Comparing the thermal gradient effects considering bond between slab and base, it was observed that maximum flexural stresses were about 14% to 50% higher when the asphalt base was considered rather than the cement-treated base.

On the other hand, considering slab unbounded to base it was observed that, for thermal gradient up to 10°C, the maximum flexural stresses were almost the same. Only for cases with thermal differential of 15°C and 20°C the maximum flexural stresses recorded in asphalt base were 10% and 4% higher, respectively, than values got for cement-treated base.

3.2 Analysis of the joint opening and thermal differentials on the dowel bars misalignments limits admitted by road authorities

Results obtained from simulations combining the joint opening and dowel bars misalignment limits put in place by road authorities in Brazil, the United Stated and Germany are presented in Table 4.

Table 4. Maximum principal stresses caused by joint opening.

Misalignment amplitude		Joint opening	Maximum principal stresses (MPa)			
degrees	%		UVT	UHS	NUVT	NUHS
0.00	0.0	0.50	1.686	1.686	1.686	1.686
0.57	1.0	0.50	1.686	1.686	1.686	1.686
1.89	3.3	0.50	1.687	1.686	1.686	1.686
2.41	4.2	0.50	1.687	1.686	1.686	1.686
0.00	0.0	1.25	1.686	1.686	1.686	1.686
0.57	1.0	1.25	1.686	1.686	1.686	1.686
1.89	3.3	1.25	1.687	1.686	1.686	1.686
2.41	4.2	1.25	1.687	1.686	1.686	1.686

The joint opening was simulated taking into account that, in tropical climate, the fluctuation in the concrete slab average temperature between the coldest and hottest condition is around 13.5°C, so that the joint width due to the slab contraction is significantly limited, roughly 0.75 mm.

The results for the different misalignment types (UHS, NUHS, UVT and NUVT) in Table 4 show the stress variation due to joint opening is markedly low, limited to 0.06% regarding the tropical climate characteristics.

The stress results combining the dowel bars misalignment and the concrete slab thermal differential are presented in Table 5. It is noted the increase in the flexural stresses due to dowels misalignment is too low when the tolerances fixed by the road authorities are considered.

Table 5. Maximum principal stresses caused by misalignment and thermal differential.

Misalignment amplitude		ΔT (°C)	Maximum principal stresses (MPa)			
degrees	%		UVT	UHS	NUVT	NUHS
0.00	0.0	0	1.686	1.686	1.686	1.686
0.57	1.0	0	1.686	1.686	1.686	1.686
1.89	3.3	0	1.687	1.686	1.686	1.686
2.41	4.2	0	1.687	1.686	1.686	1.686
0.00	0.0	5	2.271	2.271	2.271	2.271
0.57	1.0	5	2.271	2.271	2.271	2.271
1.89	3.3	5	2.271	2.271	2.271	2.271
2.41	4.2	5	2.271	2.271	2.271	2.271
0.00	0.0	10	2.873	2.873	2.873	2.873
0.57	1.0	10	2.873	2.873	2.873	2.873
1.89	3.3	10	2.873	2.873	2.873	2.873
2.41	4.2	10	2.873	2.873	2.873	2.873
0.00	0.0	15	3.530	3.530	3.530	3.530
0.57	1.0	15	3.532	2.873	3.756	3.530
1.89	3.3	15	3.532	3.531	3.532	3.532
2.41	4.2	15	3.532	3.531	3.532	3.532
0.00	0.0	20	5.169	5.169	5.169	5.169
0.57	1.0	20	5.172	5.170	5.171	5.170
1.89	3.3	20	5.178	5.171	5.174	5.171
2.41	4.2	20	5.181	5.170	5.177	5.171

One should note the result from simulation comprising the non-uniform vertical tilt (NUVT) of 1% and thermal differential of 15°C; it is observed the maximum stress obtained in this specific combination is higher than maximum stress obtained for NUVT values of 3.3% and 4.2% considering the same thermal differential. This is a counterintuitive result which might be related to limitations in the numerical model employed.

3.3 Combined effect analysis of thermal gradients and dowel bars placement non-conformities

Analyzing the combined effects of thermal differential and dowel bars placement non-conformities on the flexural stresses, it was noted that, in general, the flexural stress rise was lower than 0.5% in cases with thermal differential beneath 10°C.

In cases with concrete slab bonded to the base layer, dowel bars placement disagreements lead to small growth in the flexural stresses with maximum values around 0.3% higher than maximum stresses obtained when dowel bars were properly placed.

On the other hand, for the slab to base unbounded condition the flexural stresses with dowel bars misaligned were 6.4% and 13.2% higher for asphalt and cement-treated base, respectively, compared to structures exposed to the same thermal differential, but without dowel bars misalignments.

Thereby, the obtained results spotlight the positive effect of bonding concrete slab and base layer on reducing concrete slab flexural stresses even when the dowel bars sharply misaligned and the slabs are submitted to high thermal differential.

The maximum flexural stresses obtained for the bonded condition under thermal differential of 20°C and different misalignments are depicted in Figure 8, whereas the maximum flexural stresses obtained for asphalt base layer situation and similar conditions are illustrated in Figure 9.

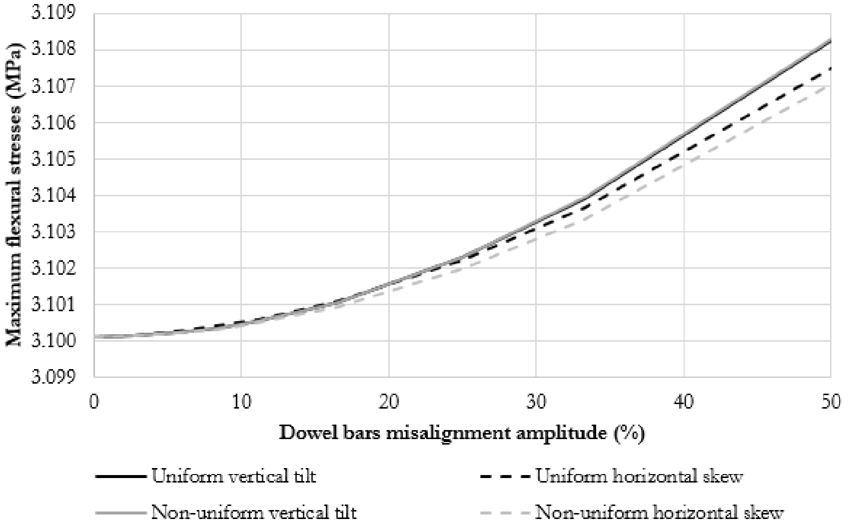

Figure 8. Flexural stresses in concrete slab bonded to cement-treated base for top-bottom thermal differential of 20°C.

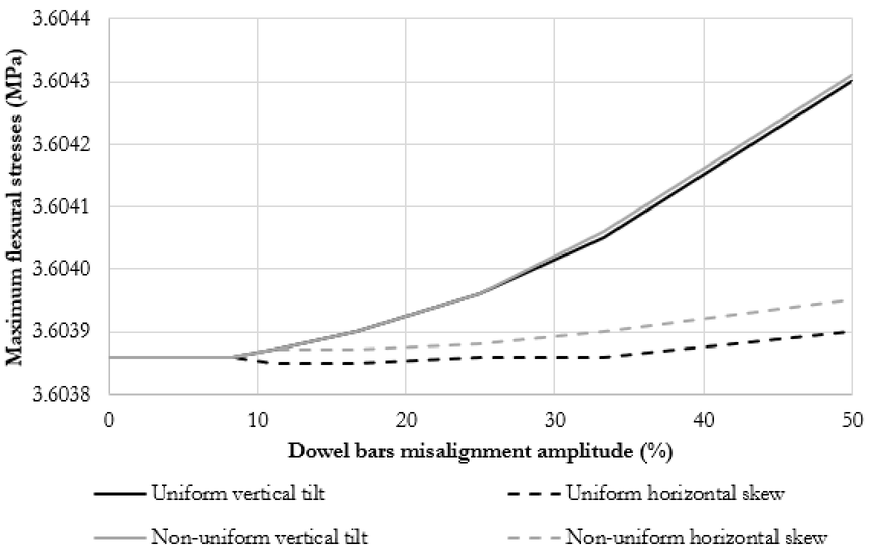

Figure 9. Flexural stresses in concrete slab bonded to asphalt base for top-bottom thermal differential of 20°C.

These results show that even in extreme misalignment conditions, combined with high thermal differential, the flexural stresses growth has a small extent when the concrete slab and base are fully bonded.

Figures 10 and 11 show the results obtained considering the same type of misalignment. In Figure 10 are presented the structural response curves regarding the magnitude of the dowel bars uniform horizontal skew expressed in terms of percentage (horizontal axle) on the maximum flexural stresses for the several cases investigated using cement-treated base, whereas in Figure 11 are presented the respective results considering the asphalt base option.

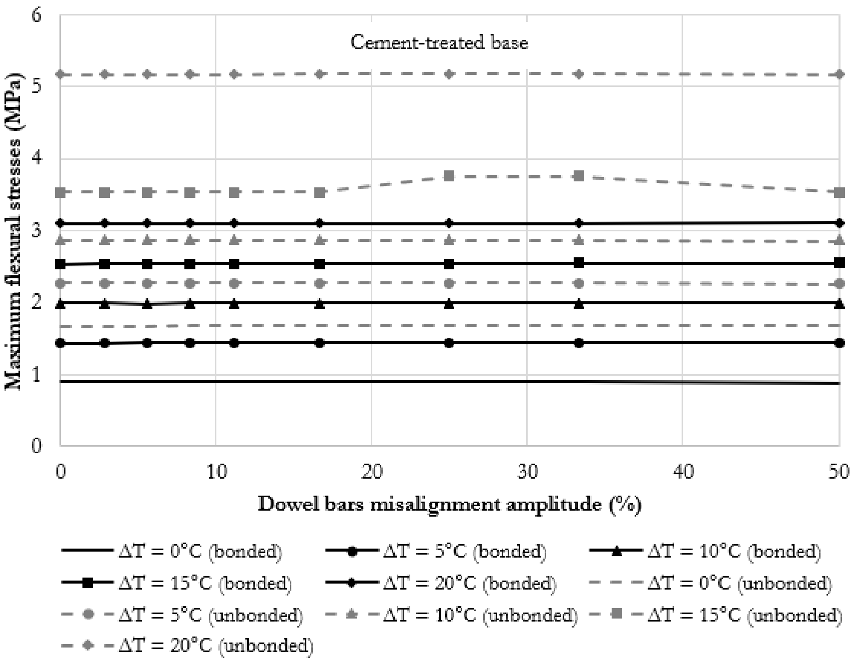

Figure 10. Flexural stresses in concrete slabs placed over cement-treated base according to dowel bars uniform horizontal skew and thermal differential.

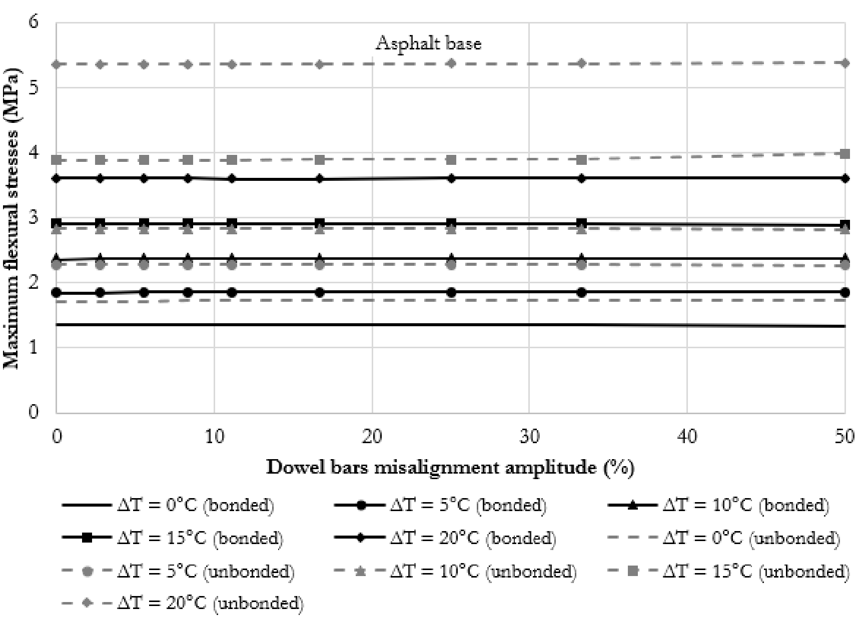

Figure 11. Flexural stresses in concrete slabs placed over asphalt base according to dowel bars uniform horizontal skew and thermal differential.

In Figure 12 are depicted a colormap with the principal stresses in the concrete slabs and their deformed shape regarding unbonded cement-treated base, uniform horizontal skew of 16.67% and thermal differential of 20°C.

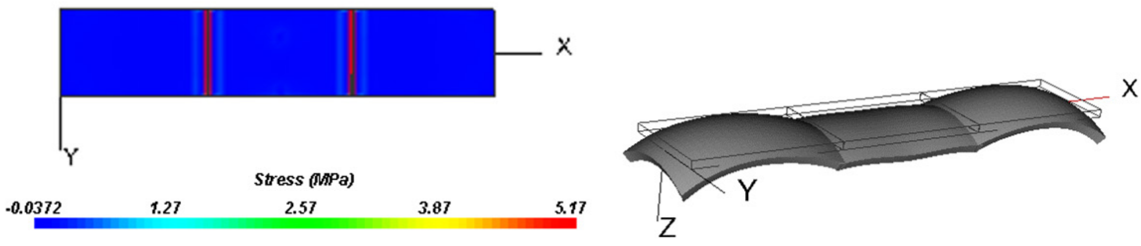

Figure 12. Example of the principal stresses colormap and the deformed shape of the system.

4 CONCLUSIONS

This study sought to investigate the effects of dowel bars misalignments on the maximum flexural stresses for a JPCP through numerical modeling using the FEM software EverFE 2.25. So, it was simulated a typical bus corridor's structure with bars submitted to different misalignment magnitudes and types combined with positive thermal differential. The joint opening effect on the stresses due to dowel bars misalignment regarding the limits put in place by the road authorities for structures under tropical climate characteristics was analyzed as well. Additionally, the investigations included the effect of base type (cement-treated and asphalt mixture) as well as the bonding conditions between concrete slab and base. The result analyses allow summarizing the main findings as follows:

- When the dowel bars are properly positioned and the concrete slab is unbounded to base, with thermal differential up to 10°C, it was observed the maximum flexural stresses were roughly the same. Only for thermal differential of 15°C and 20°C, the maximum flexural stresses were higher for asphalt mix base than cement-treated base, considering they unbounded beneath the concrete slab.
- As the difference between the concrete slab average temperature for the coldest and the hottest condition in rather unexpressive in tropical climate, the stress increments du to joint opening obtained from numerical simulations were minor and can be spared.
- For thermal differential lower than 10°C, even regarding dowel bars sharply misaligned, the increase in the maximum flexural stress was very small and they may be spared.
- Dowel bars misalignments did not induce significant increase in flexural stresses during simulations, considering the concrete slab bonded to the base layer.
- Dowel bars misalignments caused relevant increases on the flexural stresses of 6.4% and 13.2%, respectively, for asphalt mix and cement-treated base unbounded to the upper slab, compared to structures under the same conditions but with dowel bars positioned properly.

Thereby, slab/base bonding contributes expressively to reduce slab flexural stresses, even when the dowel bars are sharply misaligned, and the concrete slab is submitted to high thermal differential. Such a contribution affects positively the pavement durability in front of damages caused by the concrete fatigue process. Further research on this field will permit to issue consistent standard for of dowel bars installation, uses and toleration of its misalignment, pursuing for the best pavement performance.

In view of actual under certification of manpower for concrete pavement construction in developing countries where such a pavement choice is not a tradition, what brings worst scenarios about dowel bars installation control, as well as the bond effect between slabs and bases beneficial for reducing environmental loads effects, the main conclusion of the current study is to promote the best efficient construction method even under labor inability: to specify construction procedures to fully grease the dowel bars and simultaneously to bind the fresh concrete to the bases; such directive shall improve the concrete pavement transversal joints performance as a whole. This decision must be accomplished in the design phases and not left for site construction period possible considerations.

At last, to ensure full bond condition at the interface slab/asphalt mix it is required the use of a special binder coat over the asphalt base surface prior to concrete laying, what is well accomplished through the use of epoxy primers; however, costs shall be a concern before specifying such binders due to large surface areas to be treated in pavement construction.

ACKNOWLEDGEMENTS

The authors are grateful to CAPES – Foundation for the Coordination and Improvement of Higher Education Personal Ministry of Education – by the Ph.D. scholarships provided to the first and third authors.

REFERENCES

[1] J. T. Balbo, *Pavimentos de Concreto*, São Paulo: Editora Signer, 2009.

[2] K. Hoegh and L. Khazanovich, "Laboratory investigation of misaligned dowel behavior," *J. Test. Eval.*, vol. 38, no. 1, pp. 127–135, 2010.

[3] S. D. Tayabji, "Dowel placement tolerances for concrete pavements," *Transp. Res. Rec.*, vol. 1, pp. 47–54, 1986.

[4] S. Rao et al., "Evaluation of dowel constructability in Portland cement concrete pavements," *Transp. Res. Rec.*, no. 2098, pp. 86–93, 2009. http://dx.doi.org/10.3141/2098-09.

[5] T. Sturges, A. Frankhouser, and A. R. Abbas, "Evaluation of dowel bar alignment from a two-step dowel bar insert," *Int. J. Pavement Eng.*, vol. 15, no. 5, pp. 438–448, 2014. http://dx.doi.org/10.1080/10298436.2013.815354.

[6] American Concrete Pavement Association, *Design and Construction of Joints for Concrete Streets*, Skokie: Concrete Information, 1992.

[7] Federal Highway Administration, *Concrete Pavement Joints* (Technical Advisory, T 5040.30). Washington: Federal Highway Administration, 2019.

[8] American Concrete Pavement Association, *Evaluating and Optimizing Dowel Bar Alignment (Concrete Pavement Research and Technology* (Special Report). Skokie, Illinois: ACPA, 2006.

[9] American Concrete Pavement Association, *Dowel Bar Alignment and Location for Placement by Mechanical Dowel Bar Insertion. Guide Specification*. Skokie, Illinois: ACPA, 2013.

[10] Federal Highway Administration, *Best Practices for Dowel Placement Tolerances. Tech Brief – Concrete Pavement Technology Program*, HIF-07-021, 2007.

[11] Departamento de Estradas de Rodagem do Estado de São Paulo, *Pavimento de Concreto de Cimento Portland sobre Plataforma de Terraplenagem – Manual*. DER-SP ET-DE-P00/039, 2007.

[12] Departamento Nacional de Infraestrutura de Transportes, *Pavimento Rígido – Execução de Pavimento Rígido com Equipamento de Fôrmas Deslizantes – Especificação de Serviço*, DNIT 049/2013-ES, 2013.

[13] M. Prabhu, A. H. Varma, and N. Buch, "Experimental and analytical investigation of mechanistic effects of dowel misalignment in jointed concrete pavements," *Transp. Res. Rec.*, no. 2037, pp. 12–29, 2007. http://dx.doi.org/10.3141/2037-02.

[14] W. Davids et al., "Three-dimensional finite element analysis of jointed plain concrete pavement with EverFE2.2," *Transp. Res. Rec.*, no. 1853, pp. 92–99, 2003. http://dx.doi.org/10.3141/1853-11.

[15] P. Leong et al., "Finite difference modeling of misaligned dowel bars and their effects on joint performance," *Transp. Res. Rec.*, no. 1946, pp. 101–110, 2006. http://dx.doi.org/10.1177/0361198106194600112.

[16] P. Saxena et al., "Laboratory and analytical modelling of dowel," *Int. J. Pavement Eng.*, vol. 13, no. 3, pp. 209–215, 2012. http://dx.doi.org/10.1080/10298436.2011.596936.

[17] W. Davids, *EverFE Theory Manual*. Orono: Department of Civil and Environmental Engineering, University of Maine, 2003.

[18] J. T. Balbo, and A. A. Severi, "Thermal gradients in concrete pavements in tropical environment: Experimental appraisal," *Transp. Res. Rec.*, vol. 1809, no. 1, pp. 12–22, 2002. http://dx.doi.org/10.3141/1809-02.

[19] A. P. Cargnin, and J. T. Balbo, "Field calibration of shrinkage crack width model for CRCP in tropical climate," *J. Transp. Eng. Part B Pavements*, vol. 146, no. 3, 2020. http://dx.doi.org/10.1061/JPEODX.0000209.

Author contributions: ERS: data curation, formal analysis, methodology, writing, conceptualization; JTB: methodology, writing, funding acquisition, supervision, revision and APC: writing, translation, revision.

Editors: Osvaldo Manzoni, Guilherme Aris Parsekian.

IBRACON Structures and Materials Journal
Revista IBRACON de Estruturas e Materiais
ISSN 1983-4195 ismj.org

ORIGINAL ARTICLE

Fatigue safety level provided by Brazilian design standards for a prestressed girder highway bridge

Nível de segurança à fadiga proporcionado pelas normas brasileiras de projeto em relação à uma ponte rodoviária com longarinas protendidas

Anselmo Leal Carneiro[a]
Enson de Lima Portela[b]
Túlio Nogueira Bittencourt[c]
André Teófilo Beck[d]

[a]Universidade Federal do Rio de Janeiro – UFRJ, Campus Macaé, Macaé, RJ, Brasil
[b]Instituto Federal do Ceará – IFCE, Departamento de Construção Civil, Fortaleza, CE, Brasil
[c]Universidade de São Paulo – USP, Escola Politécnica, São Paulo, SP, Brasil
[d]Universidade de São Paulo – USP, Escola de Engenharia de São Carlos, São Carlos, SP, Brasil

Received 15 April 2020
Accepted 02 December 2020

Abstract: It is well known that highway bridges are subjected to fatigue as they work under live loads with different frequencies and amplitude. The safety level for fatigue required by Brazilian codes is still unknown, especially for prestressed concrete girders. Also, current studies on fatigue reliability of bridges only evaluate bending. This work assesses the fatigue safety level provided by Brazilian design standards for a concrete highway bridge, using weigh-in-motion (WIM) data of an important federal Brazilian highway, BR-381 (Fernão Dias Highway). The Palmgren-Miner rule is considered to evaluate the service life and reliability indexes, from the fatigue point of view, of prestressed girders designed according to Brazilian codes. Using limited and complete prestressing levels, different traffic volumes are considered. It is found that the fatigue safety levels of longitudinal and transverse reinforcements are larger than the ones recommended by the international literature.

Keywords: fatigue, highway bridges, concrete girders, weigh-in-motion, safety assessment.

Resumo: As pontes rodoviárias, por receberem um carregamento variável proveniente do tráfego de veículos, são suscetíveis ao fenômeno de fadiga. O nível de segurança à fadiga proporcionado pelas normas brasileiras, porém, ainda é desconhecido, especialmente em relação às pontes com longarinas protendidas. Além disso, as publicações sobre confiabilidade à fadiga em pontes de concreto consideram apenas análise à flexão. Este trabalho avalia o nível de segurança à fadiga que as normas brasileiras de projeto proporcionam para uma ponte rodoviária de concreto, utilizando dados de pesagem em movimento (*weigh-in-motion* – WIM) de uma importante rodovia federal brasileira, a BR-381 (Rodovia Fernão Dias). Mediante a regra de Palmgren-Miner, avalia-se a vida útil e os índices de confiabilidade, sob o aspecto da fadiga, das longarinas protendidas dimensionadas conforme as normas brasileiras. Utiliza-se a protensão limitada e completa e consideram-se diferentes volumes de tráfego. Verifica-se que os níveis de segurança à fadiga das armaduras longitudinais e transversais são maiores que aqueles recomendados pela literatura internacional.

Palavras-chave: fadiga, pontes rodoviárias, longarinas de concreto, pesagem em movimento, avaliação da segurança.

How to cite: A. L. Carneiro, E. L. Portela, T. N. Bittencourt, and A. T. Beck, "Fatigue safety level provided by Brazilian design standards for a prestressed girder highway bridge," *Rev. IBRACON Estrut. Mater.*, vol. 14, no. 4, e14415, 2021, https://doi.org/.10.1590/S1983-41952021000400015

Corresponding author: Anselmo Leal Carneiro. E-mail: anselmo.lc@hotmail.com
Financial support: CAPES and CNPq.
Conflict of interest: Nothing to declare.

1 INTRODUCTION

Fatigue occurs due to stress fluctuations from in-service variable loads that, after a certain number of cycles, may lead to fracture of the material. From the point of view of the loads, fatigue is a Service Limit State - SLS and, from the resistance point of view, it has a character of Ultimate Limit State – ULS. In highway bridges, the number of stress cycles from the traffic determines the fatigue life of the structure. From the design point of view, fatigue is verified considering live load models.

The current Brazilian live load model as in NBR 7188 [1] is shown in Figure 1. This model was originally adopted from the Germany code, as stated by Pfeil [2]. By that time, the Germany live load model was an analogy of a war tank and a platoon crossing the bridge. As the current Brazilian code still uses this model, the procedure developed by Rüsch to estimate the load effect on bridge slabs are still valid and can be applied for the Brazilian live load model. It can be seen from Figure 1 that the contact area of the wheel with the pavement is 0.1 m^2. According to Brazilian code, the live load model must be weighted by a coefficient related to impact, number of lanes and additional safety coefficients as in NBR 8681 [3]. For fatigue verification in girders, it requires use of a coefficient $\psi_{1,fad} = 0.5$ for spans lengths up to 100 meters.

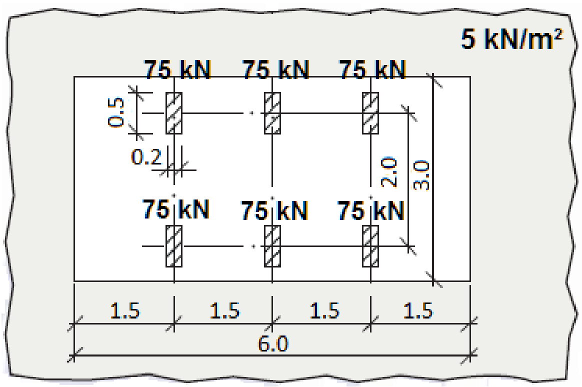

Figure 1. Brazilian live load model, dimension in meters (adapted from NBR 7188 [1]).

Carneiro et al. [4] evaluated the live load model as in NBR 7188 [1], from the unlimited fatigue life point of view, using traffic data from two HS-WIM stations in Brazil (BR-381 and BR-290) and proposed a new fatigue live load model for unlimited fatigue life. The authors indicated that the bias factor of the Brazilian model can vary a lot and may not correspond to the infinite fatigue life approach. Other studies on the assessment of current Brazilian live load model for bridges using real traffic data, are related only to ULS, as seen in Portela [5]. Thus, the reliability indexes of concrete bridges designed with the current Brazilian live load model, especially for prestressed girders, are still unknown in terms of fatigue.

With that in mind, this work assesses the fatigue safety level provided by Brazilian design standards in relation to a concrete highway bridge, using weigh-in-motion (WIM) data of an important federal Brazilian highway, BR-381 (the same data used in Carneiro et al. [4]). The fatigue service life and fatigue reliability indexes for a design life of 50 years are evaluated for prestressed concrete girders designed according to Brazilian codes, in terms of bending moment, shear force and torsion. The cumulative linear damage method, also known as the Palmgren-Miner rule, is considered. For the probabilistic analysis, the Latin Hypercube Sampling - LHS simulation method and the First-Order Reliability Method – FORM, are used. It is important to mention that this paper does not assess the safety of an existing bridge, which real monitoring is more appropriate, but it presents a methodology to evaluate the fatigue safety level provided by design standards.

2 FATIGUE SAFETY ASSESSMENT

2.1 Literature review of fatigue reliability in concrete bridges

Crespo-Minguillón and Casas [6] present a probabilistic model for fatigue analysis in prestressed bridges. The model uses the S-N curves and the Palmgren-Miner rule to define fatigue strength of reinforcing and prestressing steel. Using traffic data, they assessed the reliability of a slab bridge in terms of bending. They concluded that from the fatigue life point of view the bridge failure was unlikely to occur.

Rodrigues et al. [7] evaluated the fatigue reliability indexes of two-girder concrete bridges in Brazil. Only short-span (7 m, 10 m and 13 m) bridges were considered in terms of ULS and fatigue. It is important to note, however, that this structural solution, widely used in Brazil over the past years, is no longer the common application in current bridge design. They used traffic data from a static weighing station in São Paulo, from 2005, measured for 204 days. The work concluded that the safety levels, especially in relation to fatigue, are lower than desired. The study only performed bending analysis and the methodology was based on the work of Crespo-Minguillón and Casas [6].

Wassef et al. [8] calibrated the partial safety factors for SLS and fatigue in relation to concrete bridges in the United States. They used data from fifteen different WIM stations around the country, measured for one year. The authors used the infinite fatigue life approach and considered only girder bending.

Yan et al. [9] presented a methodology for assessing the fatigue reliability of short span bridges subjected to real traffic. The authors applied the methodology on a girder and determined the fatigue reliability indexes of longitudinal reinforcements.

Other works like Junges [10], Wang et al. [11], Mankar et al. [12] and [13] presented methodologies and case-studies to assess the fatigue reliability of monitored bridges. Junges [10] measured stress in two Brazilian reinforced concrete bridges and concluded that flexural reinforcement failure is unlikely to occur. Wang et al. [11] also evaluated flexural reinforcement of concrete girders. Mankar et al. [12] and [13] evaluated concrete bridge slabs in terms of fatigue in concrete and reinforcement, respectively. In Mankar et al. [12] the authors used test data to present stochastic models of S-N curves for concrete in compression. In an extensive literature review, no work was found on fatigue reliability assessment of stirrups.

2.2 Fatigue resistance

In order to determine the fatigue strength, the S-N curve is used. This curve is a plot of the magnitude of an alternating stress (S) and the number of cycles to failure (N) for a given material, as shown in Equation 1. Figure 2 depicts the curve of Equation 1 in logarithmic scale. The parameters of reinforcement S-N curves from *fib* [14] model code are shown in Table 1.

$$N.\Delta\sigma^{m} = K \tag{1}$$

where m and K : material-related constants; N : number of cycles to failure; $\Delta\sigma$: stress range.

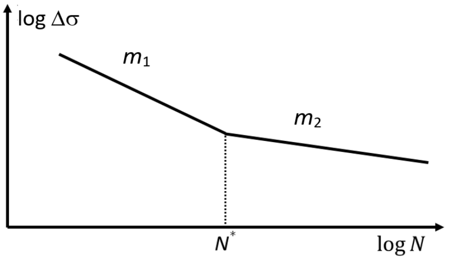

Figure 2. S-N curves for reinforcement (adapted from *fib* [14] and NBR 6118 [15]]).

Table 1. Parameters of characteristic S-N curves from *fib* [14].

Case	m_1	m_2	$\Delta\sigma_{Rsk}$ (MPa) at N^* = 10^6 cycles	$\Delta\sigma_{Rsk}$ (MPa) at 10^8 cycles	$K_1 = N \times \Delta\sigma^{m1}$	$K_2 = N \times \Delta\sigma^{m2}$
Reinforcing steel (straight bars $\phi_s \leq 16$ mm)	5	9	210	125	4.08×10^{17}	7.45×10^{26}
Prestressing steel (postensioning curved tendons)	3	7	120	65	1.73×10^{12}	4.90×10^{20}

Note: m_1, m_2 and N^* are indicated in Figure 2 and $\Delta\sigma_{Rsk}$ is the characteristic stress range.

To determine the fatigue strength of bent bars with mandrel diameter "D" lower than 25ϕ_s, where ϕ_s is the bar diameter, the model code indicates multiplication of straight bar values by a reduction factor $\xi = 0.35 + 0.026D/\phi_s$, also proposed by EN 1992-1-1 [16]. The standards, however, do not make clear if the values obtained with the reduction factor should be used for stirrups.

According to Plos et al. [17], the fatigue strength of bent bars is reduced because the steel undergoes plastic deformation through bending, leading to microcracks. The smaller the bending radius of curvature, the smaller is the fatigue strength. The report adds that bending of stirrups is an exception since tests revealed that, in most cases, stirrups fail in the straight part, due to shear; thus, outside the bent zone. This can also be verified in Higgins et al. [18], [19] and Bachman et al. [20]. Thus, Souza et al. [21] indicate that straight bar S-N curves can be used for stirrups. Hillebrand and Hegger [22] and Hillebrand et al. [23] conducted experimental tests on prestressed concrete beams and also verified that stirrups fail in the straight part.

NBR 6118 [15] considers a reduction factor to determine the fatigue strength of stirrups. Because of this, the design of stirrups for bridge girders, following the Brazilian standard, is usually governed by fatigue. This is not the case for the design of longitudinal reinforcements. The standard considers the stress related to $2\text{x}10^6$ cycles for fatigue design verification. For straight bars (reinforcing steel) and stirrups, with diameters up to 16 mm, these values are $\Delta_{fsd,fad} = 190$ MPa and $\Delta_{fsd,fad} = 85$ MPa, respectively. The value for straight bars is in accordance with the S-N curve from *fib* [14] (194 MPa for $2\text{x}10^6$ cycles). The value of 85 MPa corresponds to the application of the reduction factor ξ with $D = 3\phi_s$ to the straight bar value (194 x 0.428 ≈ 85). For the fatigue design verification, the partial safety factor for steel is 1.0 (characteristic stress).

2.3 Fatigue Damage

For variable stress amplitudes, the cumulative fatigue damage calculation may be performed according to the Palmgren-Miner rule, as in Equation 2. In this linear damage rule the failure occurs when the damage reaches a value known as Miner damage at failure (*DM*).

$$Damage = \sum_i \frac{q_i}{N_i} \leq DM \tag{2}$$

where q_i : number of cycles obtained from the load spectra for each stress range amplitude; N_i : number of cycles relative to the failure for each stress range amplitude (obtained from the S-N curve).

Theoretically, Miner damage at failure (*DM*) should be equal to one. However, as it is an empirical rule, critical damage observed in practice is a random variable. For deterministic analysis, *DM* = 1 is generally considered.

2.4 Fatigue service-life estimation

Considering the fatigue damage related to a one-year load spectra and *DM* = 1 in Equation 2 (deterministic analysis), the fatigue service life, in years, may be estimated based on Equation 3.

$$T_F = \frac{1}{Damage_{(1\,year)}} \tag{3}$$

where T_F : Fatigue service life; $Damage_{(1\,year)} = \Sigma(q_i / N_i)$ for one year, where q_i and N_i are presented in Section 2.3.

2.5 Probabilistic analysis for fatigue

Crespo-Minguillón and Casas [6] consider the Weibull distribution to represent fatigue strength (number of cycles to failure) randomness. The expressions for the probability density function, $f_N(n)$ and cumulative distribution function, $F_N(n)$ are given as:

$$f_N(n)=\frac{\alpha}{u-n_0}\cdot\left(\frac{n-n_0}{u-n_0}\right)^{\alpha-1}.exp\left[-\left(\frac{n-n_0}{u-n_0}\right)^{\alpha}\right],n\geq n_0 \tag{4}$$

$$F_N(n)=1-exp\left[-\left(\frac{n-n_0}{u-n_0}\right)^{\alpha}\right],n\geq n_0 \tag{5}$$

where α : shape parameter; u : scale parameter; n_0 : lower limit (this value is always 0.0 for strictly positive variables, such as the fatigue strength).

Considering n_0 = 0, the relationship between moments (mean and variance) and parameters is given by Equations 6 and 7, where Γ() represents the Gamma function.

$$\mu_N=u\Gamma\left(1+\frac{1}{\alpha}\right) \tag{6}$$

$$\sigma_N{}^2=u^2\left[\Gamma\left(1+\frac{2}{\alpha}\right)-\Gamma^2\left(1+\frac{1}{\alpha}\right)\right] \tag{7}$$

For μ_N e $\sigma_N{}^2$ determined experimentally, the shape parameter α can be determined iteratively by Equation 8, as reported by Melchers and Beck [24]. With the value of α, the scale parameter u may be determined from Equation 6.

$$1+\left(\frac{\sigma_N}{\mu_N}\right)^2=\frac{\Gamma\left(1+\frac{2}{\alpha}\right)}{\Gamma^2\left(1+\frac{1}{\alpha}\right)} \tag{8}$$

For the fatigue safety assessment, based on Palmgren-Miner rule, the limit state function, as mentioned by Crespo-Minguillón and Casas [6], is given by:

$$G(\mathbf{X})=DM-\sum_i\frac{1}{N_i} \tag{9}$$

where X : vector of random variables involved (the random variables are indicated in Table 6, as described in Sections 4 and 5); DM : Miner damage at failure, which is the resistance variable; $1/N_i$: elementary damage due to each stress range cycle from the load spectra; $\sum(1/N_i)$: damage due to the load spectra for the reference period considered (50 years or 100 years, normally, for the design service life of bridges), which is the load effect variable.

According to Weibull distribution, Crespo-Minguillón and Casas [6] present S-N curves for reinforcing steel (straight bars) and prestressing steel (posttensioning curved tendons) for a 50% confidence level, as indicated in Table 2. In this paper, several simulations of the random variables are performed and different values of $\sum(1/N_i)$ are calculated using the S-N curves from Table 2. Then, the probability distribution, moments and parameters of the dependent variable $\sum(1/N_i)$ are obtained.

As reported by Crespo-Minguillón and Casas [6], the randomness of *DM* comes from the randomness of S-N curves. The authors present parameters for Miner damage variable in tests characterized by constant-amplitude stress cycles for reinforcing steel (straight bars) and prestressing steel (posttensioning curved tendons) for different S-N intervals (DM_i in Table 3).

Table 2. Parameters of S-N curves for a 50% confidence level (adapted from Crespo-Minguillón and Casas [6]).

Case	Δσ (MPa)	*N*	*m*	$K = N \times \Delta\sigma^m$
Reinforcing steel (straight bars)	≥ 245	≤ 2 x 10^6	6	4.33 x 10^{20}
	< 245	> 2 x 10^6	9	6.39 x 10^{27}
	> 205	< 10^7		
	≤ 205	> 10^7	11	2.69 x 10^{32}
Prestressing steel (postensioning curved tendons)	≥ 165	≤ 10^6	3	165^3 x 10^6
	< 165	> 10^6	7	165^7 x 10^6

Table 3. Parameters of variable DM_i (adapted from Crespo-Minguillón and Casas [6]).

Case	Δσ (MPa)	Mean	Standard deviation	α	u
Reinforcing steel (straight bars)	≥ 245	1.104	0.463	2.57	1.24
	< 245	1.154	0.556	2.19	1.30
	> 205				
	≤ 205	1.169	0.618	1.97	1.32
Prestressing steel (postensioning curved tendons)	≥ 165	1.041	0.274	4.28	1.14
	< 165	1.072	0.367	3.21	1.20

For a spectrum of variable amplitude stress cycles, the parameters of *DM* for the limit state function (9) can be obtained with the weighting of DM_i related to the damage for each interval of stress range, as reported by Crespo-Minguillón and Casas [6] and Rodrigues et al. [7]. Therefore, in order to acquire the parameters of *DM* for (9), related to all stress ranges, the following procedure can be applied:

- For each simulation of the random variables (Table 6), the percentages of $\sum(1/N_i)$ corresponding to each interval of stress range (limits in Tables 2 and 3) are obtained;
- At the end of all simulations, the average percentages of $\sum(1/N_i)$ corresponding to each interval for all simulations are obtained;
- By simulation, for each interval, several DM_i values are generated, compatible with the respective weighting (average percentage);
- With the DM_i values for all the intervals, the probabilistic distribution and the parameters of the *DM* variable are evaluated.

In this paper, the simulations are performed using the Latin Hypercube Sampling – LHS simulation technique, which permit to obtain reasonable results with a reduced number of simulations. With the parameters of the variables of the limit state function, the FORM method is used, within StRAnD (Beck [31]), to calculate the reliability indexes. The LHS and FORM can be verified in Melchers and Beck [24] and Nowak and Collins [32].

3 WEIGH-IN-MOTION – WIM

3.1 Description of the system and WIM station

Regarding the relevance of actual traffic, this work uses vehicle records obtained from a high-speed weigh-in-motion (HS-WIM) station, as shown in Figure 3. The system is installed on road lanes, and vehicles are registered with no need to stop or to lower their speeds. In general, the system consists of lines of piezoelectric sensors, inductive loops, temperature sensors and a device to collect and analyze the records. Inductive loops detect vehicles, measure the distance between axles and speed, while piezoelectric sensors are responsible for weighting.

In this work, the data from the BR-381 (Fernão Dias Highway, which connects the states of São Paulo and Minas Gerais) station is used (same data used in Carneiro et al. [4]). The system is installed in two road lanes in the same direction (Minas Gerais to São Paulo), as indicated in Figure 3c. For each vehicle that passes over the sensors, the system provides information such as day, hour, lane, speed, total length, total weight, axle spacing and axle weight. The system was installed in July 2015 and the station remained in operation until 2019. The HS-WIM system avoids evasion, as drivers do not notice it. In addition, due to the continuous process of obtaining data (24 hours a day, on consecutive days), the system also yields the real frequency of vehicle occurrences, which is essential for fatigue analysis. These particularities give the technology a great advantage over static weighing stations. In the static weighing process, overloaded vehicles can trace alternative routes, the multiple presence occurrences are unknown, and the data is not collected 24 hours a day, in days and months in a row.

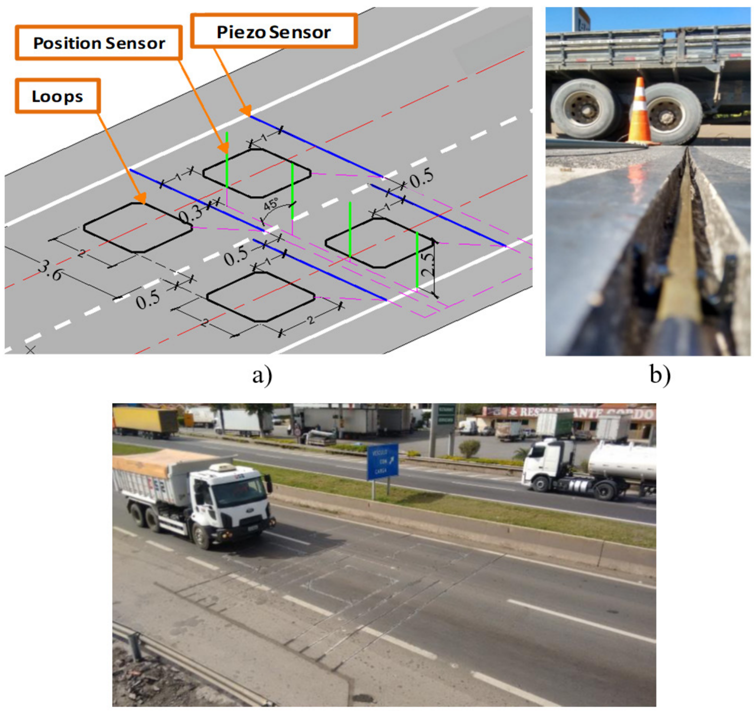

a) b)

c)

Figure 3. HS-WIM system: a) layout and sensors position [4], [5]; b) weighting sensor before grout in BR-381 [4], [5], [33]; c) final appearance of the pavement in BR-381 [5], [33] (position sensors, which detect when vehicles change lanes, was not installed).

As WIM sensors are strongly influenced by temperature variation, the system must undergo periodic calibrations. In these measurements, a truck of known weight passes through the sensors at varying speeds, at different times of the day. From July 2015 to August 2017, five calibrations were conducted on the WIM system in BR-381 (July 2015, October 2015, February 2016, February 2017 and May 2017). The error, in relation to the total weight of the trucks, is around 10%. In Brazil, considering the reduced number of WIM stations, the use of this system is not common.

3.2 Filtering process and traffic characteristics

Even with calibrations, the system might present incorrect measurements: weights greater than the maximum traction capacity, or smaller than the self-weight, are some examples. Furthermore, several data are unnecessary for the study of live load for bridges. Passenger vehicles and light trucks, for instance, can be neglected, in most analyses, due to irrelevant load effect on the bridge. Thus, WIM data needs to be filtered before it can be used.

The filtering criteria need to be defined considering the characteristics of the Brazilian fleet and may vary according to the analysis need, in other words ULS, SLS or fatigue. Among the 14 criteria used in Wassef et al. [8], one filter eliminates trucks with total weight less than 90 kN. As reported by Laranjeiras [34], trucks weighing less than 70 kN accumulate fatigue damage that is irrelevant to the safety of the structure, even if they occur many times.

The following list presents, in order, the filters that were applied to the station considered. The filters were set after a research of National Department of Transportation resolutions (DNIT [35]–[37]) and truck manufacturers catalogs. Vehicles that fit any of the filters have been excluded.

1- **GVW ≤ 62 kN** (GVW is the total gross vehicle weight). This limit is set based on the maximum physical limit of GVW of lightweight two axle truck (*veículo semi-leve* in Portuguese). This criterion has the objective of removing irrelevant light trucks.
2- **Pi ≤ 22 kN**, where "Pi" is the axle weight. This value represents the steering axle load of maximum GVW of lightweight two axle trucks.
3- **Pd > 320 kN**, where "Pd" is the weight referring to the double tandem. This limit is set based on the heaviest axle weight of a double tandem found in the catalogs of truck manufactures in Brazil. This filter also contributes to eliminate records with GVW greater than the maximum traction capacity of the vehicle. For the sake of comparison, the legal limit for double tandem according to Brazilian regulations is 170 kN.
4- **di ≤ 0.92 m**, where "di" is the distance between axles. In Brazil, the minimum wheel diameter for a tandem was found to be 0.87 meters. Adding the wheel spacing of 0.05 meters, the final minimum distance between axles is 0.92 meters.
5- **C > 36 m**, where "C" is the total length of the vehicle. In Brazil, the maximum length allowed is 30 meters. On top of this value, an error margin was considered.
6- **C > 15.4 m and GVW ≤ 104.3 kN**. This filter screens out the unrealistic long and light trucks, and possible considerations of two trucks in following position as a single unit. The length is defined based on the 14-meter trucks (common in Brazil), with a margin of error of 10%. The GVW is defined based on the sum between 42.3 kN (axle with lower carrying capacity of a 14-meter truck) and 62 kN (minimum GVW for the other truck according to Filter 1).
7- **Pi > 180 kN**. Among all catalogs that were investigated, the maximum carrying capacity (physical limit) of a single axle was found to be 180 kN. This filter also contributes to eliminate records with GVW greater than the maximum traction capacity of the vehicle. For the sake of comparison, Brazilian legislation established the weight limit of single axles in 100 kN.
8- **GVW ≥ 1.1∑Pi or GVW ≤ 0.9∑Pi**, where "∑Pi" represents the sum of the weights of the axles. This criterion considers a margin of error of 10% on total weights.
9- **∑di > C**, where "∑di" represents the sum of axle spacings. This filter eliminates incorrect data of the wheelbase or the truck length.
10- **C < 5 m**. This filter eliminates incorrect truck length data.
11- **V > 170 Km/h**, where "V" is the vehicle speed. As in Brazil there are records of trucks traveling at 160 Km/h, the value of 170 Km/h was set as a limit. It should be mentioned that the occurrence of such events is rare.
12- **P1 > 100 kN**, where "P1" is the weight of the first axle (front). According to truck manufacturers catalogs this value is the maximum carrying capacity of the first axle.
13- **GVW > 1500 kN**. This limit is set based on the maximum carrying capacity found in catalogs, which corresponds to a nine-axle truck.

To determine the traffic load effect, WIM station data from September 2016 to May 2017 (273 days), is taken into account. It was found that use of a longer period of data does not significantly change the results.

Before filtering, the average daily traffic is 13292. After filtering, only 27% of the entire sample is considered as valid trucks. The first and second filters are responsible for filtering out 68% and 3.5% of the records, respectively. The other filters together eliminate only 1.5% of the records. It is worth mentioning that Filter 8 did not exclude any records. This indicates that the measurements of weights (total and individual per axle) are consistent. Filter eleven removes only one truck per month on average. Filters 3 and 7 eliminate less than one truck per day on average (0,3 for Filter 3 and 0,8 for Filter 7).

In this paper, the records are analyzed using *Microsoft Excel* spreadsheets. After filtering, the Average Daily Truck Traffic (ADTT) is 3655, where 83% of trucks are on the right lane (slow lane). The ADTT varies from 1079 to 5103. Table 4 shows some statistics for twelve most frequent classes, which represents 95% of the data after filtering, and the respective legal weights (5% of tolerance). It is worth pointing out, nevertheless, that a possible reduction in the values of Filters 1 and 2 would change the statistics of two-axle truck 2C (DNIT class). The maximum GVW obtained are higher than the limits imposed by Brazilian law.

The maximum GVW obtained was 1193 kN, corresponding to nine-axle truck 3M6 (DNIT class). Figure 4 shows the histogram for GVW for class 3M6 and Figures 5 to 7 show the histogram for weights for first axle, double tandem and triple tandem, respectively, for class 3M6. Figure 8 shows the histogram for weights for a single axle for class 3I3

(DNIT class), which is the heaviest class with single axles in Table 4. Based on the histograms presented, it is noted that the maximum weights obtained do not reach the values of filters 3, 7, 12 or 13.

To assess the sensitivity of Filter 1 in relation to the safety analysis, the value of 62 kN was changed to 90 kN, as used in Wassef et al. [8]. It was found that the results presented in Section 5 did not change, that is, the value of 62 kN is shown to be sufficient and may even be increased to eliminate a larger number of trucks, unnecessary for the analysis.

Table 4. Statistics for twelve most frequent classes of BR-381 from September 2016 to May 2017.

Silhouette	Class (DNIT)	Frequency (%)	GVW (kN)	Legal GVW (kN)
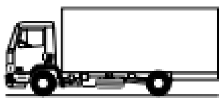	2C	14.96	62.0 (min.) 272.5 (max.) 100.8 (aver.)	168.0
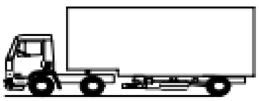	2S1	1.89	69.9 (min.) 359.8 (max.) 154.2 (aver.)	273.0
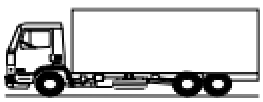	3C	23.33	66.7 (min.) 417.1 (max.) 166.7 (aver.)	242.0
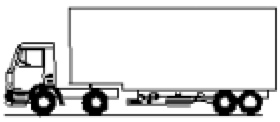	2S2	13.03	99.3 (min.) 497.4 (max.) 190.9 (aver.)	347.0
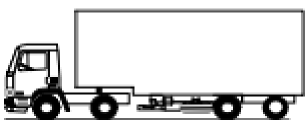	2I2	2.05	100.1 (min.) 529.6 (max.) 196.8 (aver.)	378.0
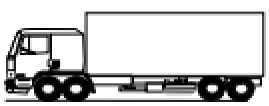	4CD	2.68	96.0 (min.) 504.1 (max.) 242.8 (aver.)	305.0
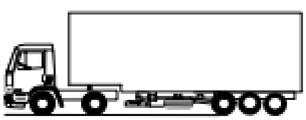	2S3	9.45	124.2 (min.) 704.5 (max.) 325.1 (aver.)	436.0
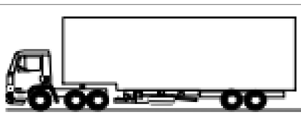	3S2	1.98	128.2 (min.) 630.1 (max.) 260.0 (aver.)	420.0
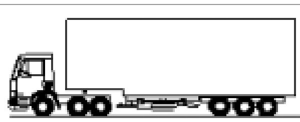	3S3	14.77	139.8 (min.) 869.2 (max.) 414.6 (aver.)	509.3
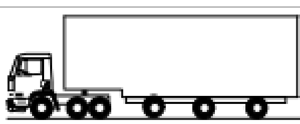	3I3	3.13	143.1 (min.) 760.2 (max.) 448.0 (aver.)	556.5
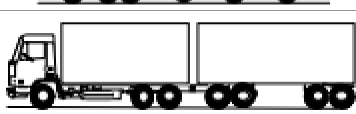	3D4	4.5	183.3 (min.) 1026.1 (max.) 502.1 (aver.)	599.0
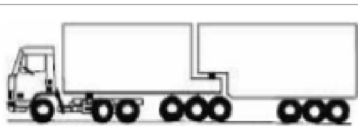	3M6	2.68	240.8 (min.) 1192.7 (max.) 660.2 (aver.)	777.0

Notes: GVW is the Gross Vehicle Weight; Legal GVW considers 5% of tolerance; min.: minimum; max.: maximum; aver.: average

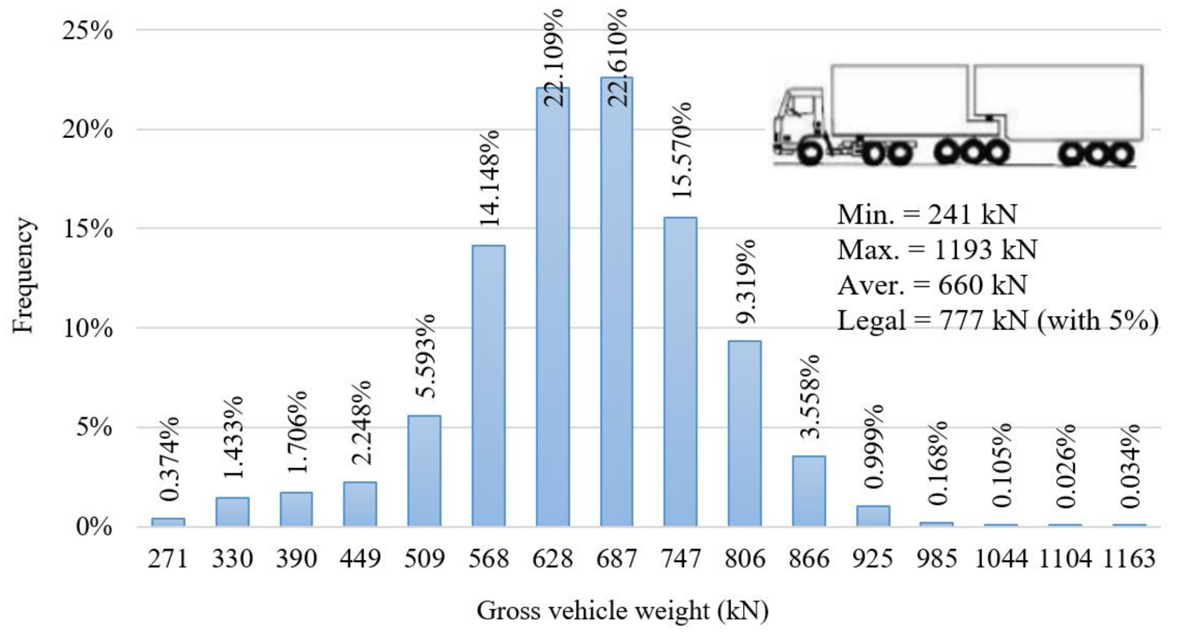

Figure 4. Histogram for GVW for class 3M6 (the horizontal axis shows the average values for each interval).

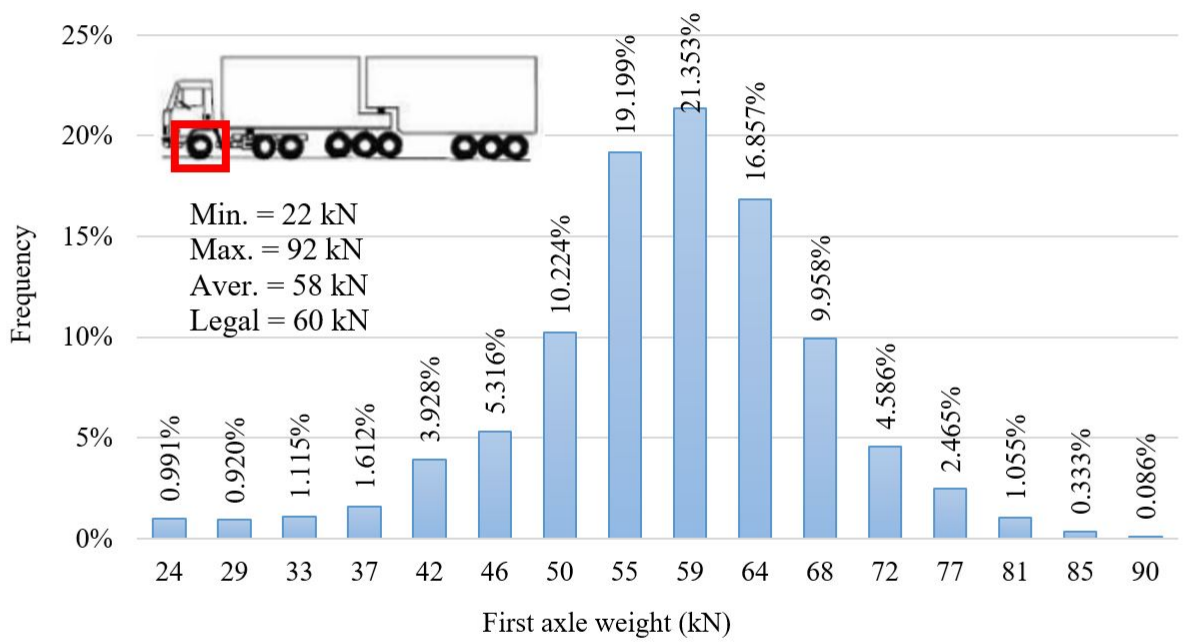

Figure 5. Histogram for weight for first axle for class 3M6 (the horizontal axis shows the average values for each interval).

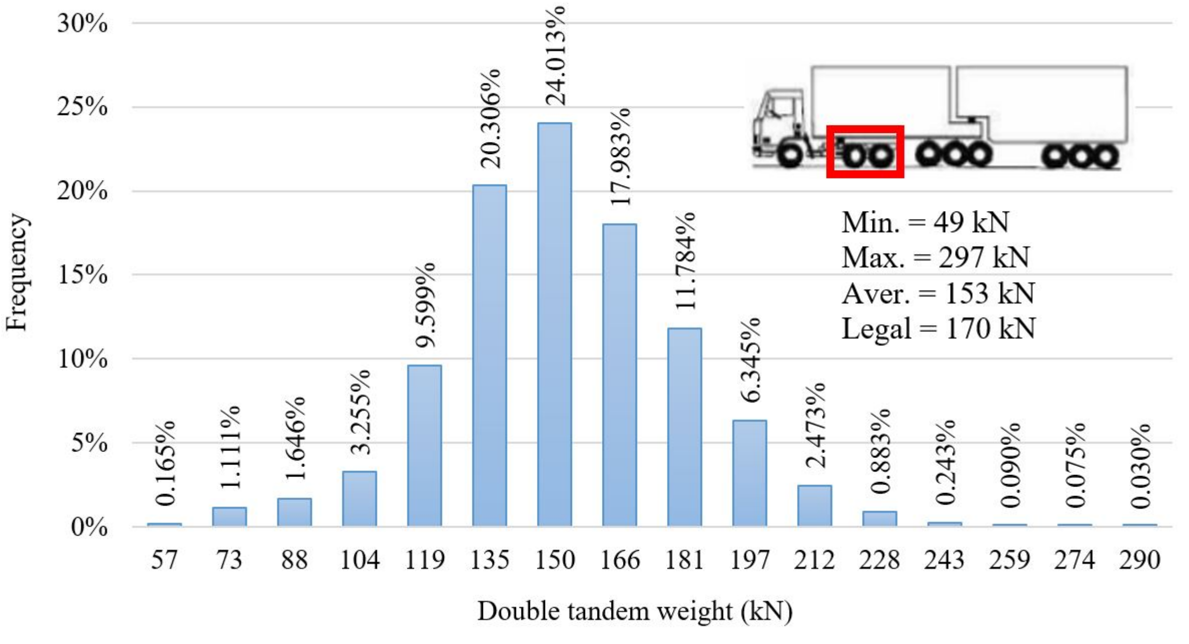

Figure 6. Histogram for weight for double tandem for class 3M6 (the horizontal axis shows the average values for each interval).

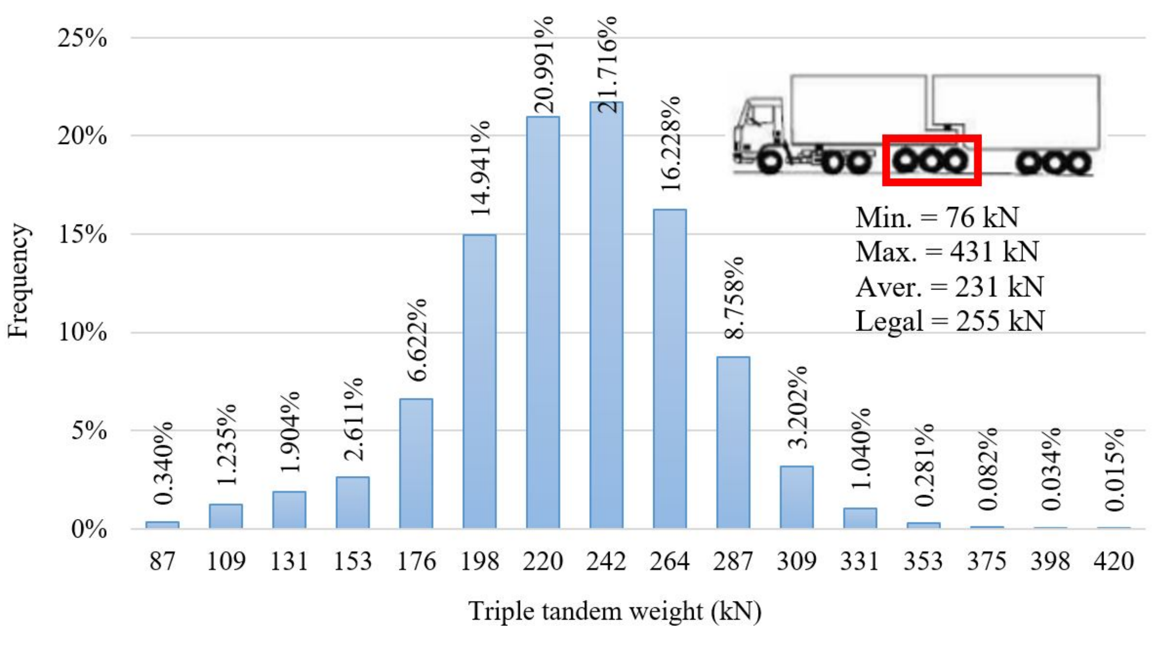

Figure 7. Histogram for weight for triple tandem for class 3M6, which the horizontal axis shows the average values for each interval (the histogram for both triple tandem are similar).

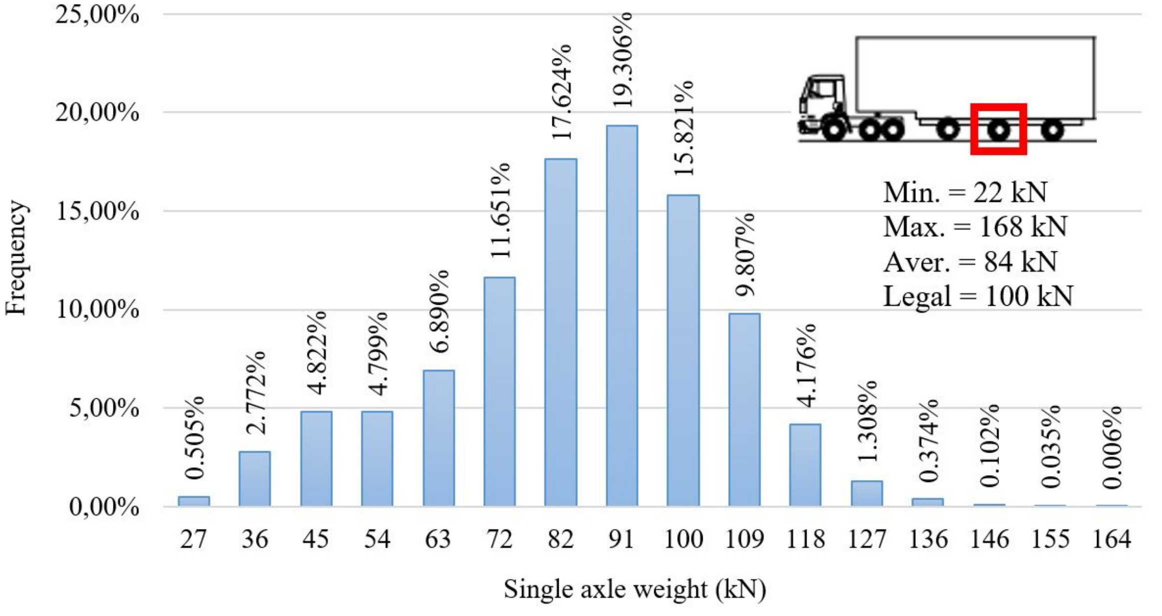

Figure 8. Histogram for weight for single axle for class 3I3, which the horizontal axis shows the average values for each interval (the histogram for single axles for 3I3 are similar).

4 EVALUATED BRIDGE AND TRAFFIC STRESS RANGE IN THE REINFORCEMENT

4.1 Evaluated bridge

This work evaluates the fatigue safety of the bridge girders illustrated in Figure 9. The dimensions were obtained from a real bridge that has a simply supported span of 28 meters and crossbeams only on supports. The girders are designed based on the Brazilian Design Standards, considering the ULS, SLS and Fatigue Limit States. The same reinforcement detailing for all girders is considered, i.e., the greatest rebar areas are considered.

The transverse load distribution is performed according to the Fauchart's method, using the Ftool program (Martha [38]). The method, which can be verified in Stucchi and Skaf [39], is also used for the traffic load effect. For the pavement, a total load of 3.2 kN/m^2 is considered (5 cm of pavement with weight of 24 kN/m^3 and an additional load of 2 kN/m^2 for paving improvements). Two possibilities are considered for the design, one with limited prestressing and another with complete prestressing level. Prestressing losses are considered as 25%. The Additional Impact Coefficient (CIA, in Portuguese) of NBR 7188 [1] is not computed in the design, since the coefficient should be only applied to slabs and crossbeams in the vicinity of the joints.

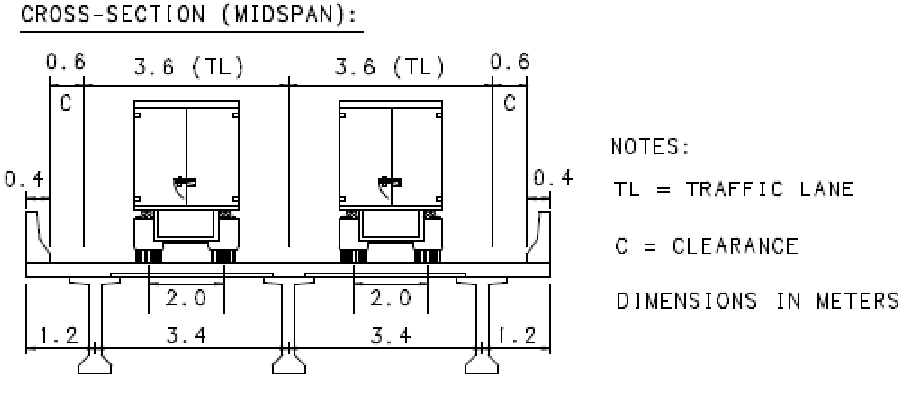

Figure 9. Bridge section.

The stirrups design, about the ULS and fatigue, consider the combination of shear force with torsional moment. It is important to observe, however, that the maximum shear and torsion for design are not simultaneous. The section close to the support without web enlargement, indicated in Figure 10, even with shear smaller than the section adjacent to the support, show the greatest stress range for stirrups in fatigue verification and the largest calculated area of transverse reinforcement. The calculated reinforcement area for stirrups for ULS (section indicated in Figure 10) needed to be increased to meet fatigue assessment, that is, the stirrups design was controlled by fatigue. Flexural fatigue analysis did not affect the areas of longitudinal reinforcement.

The NBR 6118 [15] provides two models for transverse reinforcement design based on the truss model. In Model I, the strut angle assumes a fixed value of 45 degrees; whereas in Model II, this angle may vary from 30 to 45 degrees. Furthermore, the portion of the shear force resisted by complementary mechanisms of the truss model differs from one model to another. Based on the standards equations, it is noticeable that Model II is more refined, while Model I is simpler. For the studied bridge, Model II with an angle of 30 degrees led to smaller areas for transverse reinforcement (reduction of around 15%, comparing to Model I). Thus, Model II is adopted in design, to obtain the smallest possible reliability indexes, according to design prescriptions by NBR 6118 [15].

The girder dimensions are indicated in Figure 10, and the calculated reinforcement areas are shown in Table 5. The compressive strength of concrete at 28 days (f_{ck}) is 40 MPa for precast beams and 30 MPa for slabs. The yield stress of reinforcing steel (f_{yk}) is 500 MPa. The strength (f_{ptk}) and yield stress (f_{pyk}) of prestressing steel are 1900 and 1710 MPa, respectively. The modules of elasticity for reinforcing and prestressing steel are 210 and 200 GPa, respectively, as indicated by NBR 6118 [15]. The secant modulus of elasticity of concrete is given as a function of f_{ck}, as indicated by NBR 6118 [15], and granite is considered as coarse aggregate.

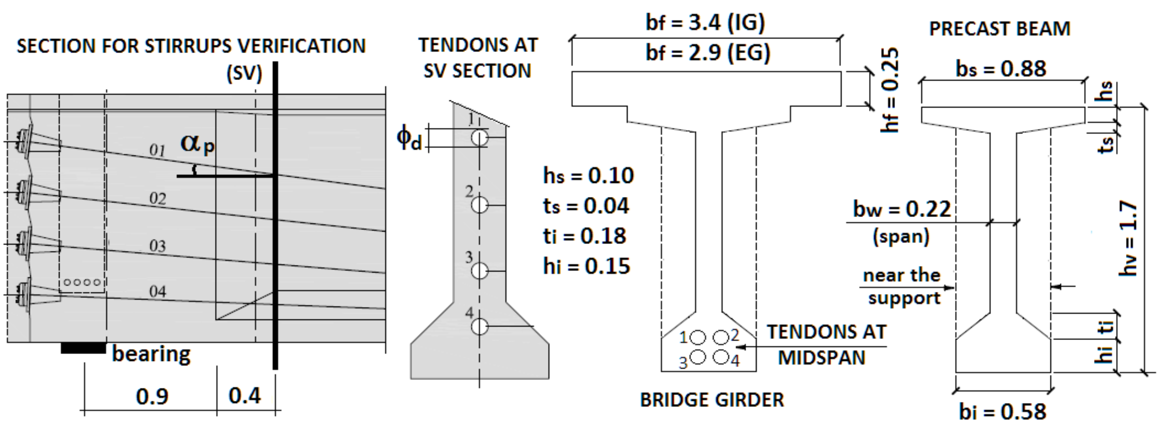

Figure 10. Bridge girder details, dimensions in meters (EG: exterior girder; IG: interior girder).

For complete prestressing, it was found that the longitudinal reinforcing would not be necessary. In this case, the ratio of 0.09% is used for reinforcing, which corresponds to $0.5\rho_{mín}$, where $\rho_{mín}$ is the minimum ratio of longitudinal reinforcement (reinforcing and prestressing) for beams recommended by NBR 6118 [15]. The value of $0.5\rho_{mín}$ was obtained based on the minimum ratio for positive reinforcing in one-way prestressed slabs of NBR 6118 [15], as recommended by IBRACON [40].

Table 5. Reinforcement areas according to prestress levels.

Prestress level	Prestressing steel (A_p)	Longitudinal reinforcing steel (A_s)	Two-legged stirrup (A_{sw}/s)
Limited	40 cm^2 (40 strands; ϕ_p = 12.7mm)	24.13 cm^2 (12 bars; ϕ_s = 16mm)	14.02 cm^2/m (ϕ_s = 12.5mm; s = 17.5cm)
Complete	48 cm^2 (48 strands; ϕ_p = 12.7mm)	12.06 cm^2 (6 bars; ϕ_s = 16mm)	8.98 cm^2/m (ϕ_s = 10mm; s = 17.5cm)

Notes: A_{sw}: cross-section area of the stirrups; s: longitudinal spacing between the stirrups.

4.2 Traffic load effect

For the transverse load distribution on the girders, the trucks are assumed to be in the center of the traffic lanes and the value of 2 meters is adopted for the transverse wheel spacing, as illustrated in Figure 9. For the longitudinal analysis, the bending moment is calculated at midspan, the shear force and the torsional moment are calculated adjacent to the support, and the influence lines were implemented in *Microsoft Excel*. To determine the shear force and the torsional moment at the critical section (Figure 10), the load effects obtained by the influence line are linearly reduced.

To consider dynamic amplification, the factor presented in Almeida et al. [41] is used. Using trucks with five and six axles, with a total weight of 450 kN, the authors performed dynamic monitoring on Brazilian bridges with spans ranging from 7.5 to 45 meters. Equation 10 presents the obtained dynamic application factor (*DAF*). For the considered span length, this coefficient varies between 1.11 and 1.37, according to the WIM vehicle speed.

$$DAF = 1.099 + 1.439 S_v \quad (10)$$

where S_v : speed parameter (dimensionless); $S_v = \pi v / (L\omega)$; v : vehicle speed, in m/s; L : span length, in meters; ω : bridge natural angular frequency, in rad/s; $\omega = 2\pi\, 95.4 / L^{0.933}$.

The traffic passage along the bridge generates irregular load cycles, with variable frequency and amplitudes, which does not enable straight use of the Palmgren-Miner rule. Then, the *Rainflow* counting method is used, which makes it possible to obtain individual cycles. Before performing the *Rainflow* count, however, a computational routine was implemented to obtain the load effects, at the considered sections, due to the traffic passage along the span of the structure. The load effects are obtained both for the single-vehicle passage and multiple presences.

To identify the situation of single and multiple presences, a routine was implemented to the WIM data, in *Microsoft Excel* spreadsheets, that uses the following information:

- truck travel lane;
- truck speed;
- the time vehicle goes over the sensor (resolution of 0.01 sec);
- the overall length of the vehicle's axle group;
- bridge span length (simply supported structures).

The single passages of the vehicle on the bridge, i.e., when there are no axles of other trucks at the same time on the bridge, present the occurrence of 85% for the considered span (15% of vehicles are in multiple presence). The "side-by-side" case, i.e., when the front axle spacing between two vehicles, in different lanes, is less than half the length of the axle group of the first vehicle, present the occurrence of 2.35% in relation to the total valid trucks. Hence, for every 100 trucks on average, one is next to the other.

Using the *Rainflow* counting procedure and calculating the safety levels, it was found that, except for the side-by-side case, the other situations of multiple presences can be replaced, without loss to the analysis, by the individual passage of the vehicles. The results presented in Section 5 are the same when considering the different situations of multiple presences (15%) and when considering only the "side-by-side" case (2.35%) as multiple presence. This occurs because, except for the side-by-side case, the position of the second vehicle in the other cases of multiple presences, for the considered span, coincides with the lower ordinates of the influence lines. It also applies to the case of three or more vehicles on the bridge. It is essential to observe, however, that for longer span lengths or continuous bridges, other situations of multiple presences might be relevant.

Applying *Rainflow* and calculating the safety levels, it was also found that the method can be substituted, without loss to the analysis, by the maximum vehicles load effects at the studied sections. The results, presented in Section 5, are the same when using the *Rainflow* method and when considering only the maximum vehicle load effects in the considered sections. This occurs because, except for the cycles related to the maximum load effects, the other cycles obtained with *Rainflow,* accumulate irrelevant damages, since they present, in their majority, small load effects in magnitude. It is important to note, however, that for other bridge scenarios, such as continuous structures, for instance, the cycles obtained by *Rainflow* can be relevant.

With the traffic load effects, the stress range in the reinforcement and the damage for each girder of the bridge are calculated. Overall, the stress range in the reinforcement is determined according to Equation 11, where σ_{max} and σ_{min} are maximum and minimum stresses, respectively.

$$\Delta\sigma = \sigma_{max} - \sigma_{min} \quad (11)$$

The equations for calculating the stress range in the reinforcement are presented in the following sections. Although the present paper considers only prestressed girders, the equations also apply to reinforced elements. In this case, it is enough to eliminate the parcels related to prestressing.

4.3 Stress range in prestressing steel

For the stress calculation in longitudinal reinforcement, *fib* [14] recommends the cracked section to be considered, if for any combination of loads at SLS, cracking occurs. For the girders of the studied bridge, there is cracking due to traffic. Applying Equation 11, the stress range in the prestressed reinforcement, $\Delta\sigma_{(A_p)}$, at stage 2, for the midspan section, is given by Equation 12, where the dimensions of the girders are presented in Figure 10.

$$\Delta\sigma_{(A_p)} = \frac{M_q . x_2}{I_e} . \frac{(d_p - x_2)}{x_2} . \frac{E_p}{E_{cs}} \tag{12}$$

where

M_q : bending moment at midspan due to each traffic cycle;

x_2 : neutral axis depth of the section at stage 2, measured from the compressed face of the section (it is calculated using girder dimensions and reinforcement area);

d_p : effective depth related to prestressed reinforcement (distance from the center of gravity of the prestressing steel to the compressed section face);

E_p : modulus of elasticity of prestressing steel;

E_{cs} : secant elasticity modulus of concrete;

I_e : effective moment of inertia of cracked section (Branson's inertia) at midspan, according to the equation:

$$I_e = \left(\frac{M_r}{M_{s,máx}}\right)^3 I + \left[1 - \left(\frac{M_r}{M_{s,máx}}\right)^3\right] I_2 \le I \tag{13}$$

I : Moment of inertia of gross concrete section (it is calculated according to girder dimensions);

I_2 : moment of inertia of the section at stage 2 (calculated using girder dimensions and reinforcement area);

$M_{s,máx}$: maximum bending moment at midspan, given by M_g+$M_{q,WIM,max,}$ where M_g is the bending moment due to dead loads (M_{g1}+ M_{g2}+ M_{g3}) and $M_{qWIM,máx}$ is the maximum bending moment due to traffic (with impact) for the considered period for the WIM data;

M_{g1}: bending moment at midspan due to the self-weight of the precast beam;

M_{g2}: bending moment at midspan due to the self-weight of the slab and barriers;

M_{g3}: bending moment at midspan due to pavement;

M_r : Cracking moment of the section at midspan, calculated based on Equation 14, with absolute values;

$$M_r = \left(f_{ct,f} + \frac{(\sigma_{0p} - \Delta\sigma_p).A_p}{A} + \frac{(\sigma_{0p} - \Delta\sigma_p).A_p.e_p.y_{inf}}{I}\right).\frac{I}{y_{inf}} \tag{14}$$

e_p : eccentricity of the tendons at midspan section (distance from the center of gravity of the prestressed reinforcement to the center of gravity of gross concrete section; $e_p = d_p - (h_v + h_f - y_{inf})$;

y_{inf} : distance from the bottom face of the section to the center of gravity of gross concrete section (calculated using girder dimensions);

$f_{ct,f}$: tensile strength of concrete in bending; $f_{ct,f}$ = $0.252 f_c^{2/3}$, for T sections with $f_c \le 50$ MPa (f_c is the concrete compressive strength at 28 days, in megapascals);

A : gross area of concrete section (calculated using girder dimensions);
A_p : total area of prestressing reinforcement (all the strands);
σ_{0p} : initial stress in prestressing;
$\Delta\sigma_p$: prestress losses.

4.4 Stress range in longitudinal reinforcing steel

According to *fib* [14], the effect of differences in bond behavior of prestressing and reinforcing steel must be considered by multiplying the stress in the reinforcing steel by the factor η_s. Thus, the stress range calculation in the longitudinal reinforcing steel, $\Delta\sigma_{(A_s)}$, at stage 2, for the midspan section, is given by:

$$\Delta\sigma_{(A_s)} = \frac{M_q . x_2}{I_e} . \frac{(d_s - x_2)}{x_2} . \frac{E_s}{E_{cs}} . \eta_s \tag{15}$$

where

$$\eta_s = \frac{1 + \dfrac{A_p}{A_s}}{1 + \dfrac{A_p}{A_s} . \sqrt{\xi_p \dfrac{\phi_s}{\phi_p}}} \geq 1 \tag{16}$$

d_s : effective depth related to reinforcing steel (distance from the center of gravity of the reinforcing steel to the compressed section face);
A_s : area of reinforcing steel;
ϕ_s : diameter of reinforcing steel in the relevant section (the smallest diameter);
ϕ_p : diameter of prestressing steel (for bundles, an equivalent diameter $\phi_{eq} = 1.6\sqrt{A_{p,b}}$ is chosen, where $A_{p,b}$ is the cross-section area of the bundle);
E_s : modulus of elasticity of reinforcing steel;
ξ_p : ratio of bond strength of prestressing steel and high-bond reinforcing steel. For strands in post-tensioned members, the value of ξ_p is 0.4.

In NBR 6118 [15], the same factor η_s is recommended both for reinforcing steel and bonded prestressed steel. In this work, however, it is considered only for the reinforcing steel, according to *fib* [14].

4.5 Stress range in stirrups

Applying Equation 11, the stress range in the stirrups, $\Delta\sigma_{(A_{sw}/s)}$, for the critical section (Figure 10), is given by Equation 17. As the bridge only have crossbeams on the supports, in addition to the shear force, the torsional moment must also be considered.

$$\Delta\sigma_{(A_{sw}/s)} = \left(\frac{|V_1 - V_2|}{0.9 d_s \left(\dfrac{A_{sw}}{s} \right)} + \frac{\Delta T}{2 A_e \left(\dfrac{A_{90}}{s} \right)} \right) \sqrt{\tan\theta} \tag{17}$$

where
A_{sw} : Cross-sectional area of the stirrups at the section under consideration;
s : longitudinal spacing between the stirrups in the evaluated section;

θ: inclination angle of the compression diagonals (struts) regarding the longitudinal axis of the girder (without correction, since the parcel $\sqrt{tan\theta}$ makes de adjustment in the inclination for fatigue). This angle is 45 degrees for Truss Model I and might vary between 30 to 45 degrees for Truss Model II. In this paper, Model II with a 30-degree angle is considered.

$$V_1 = V_g + V_q - V_p - 0.5V_c \geq 0,\ if\ \left(V_g + V_q - V_p\right) \geq 0$$

$$V_1 = V_g + V_q - V_p + 0.5V_c \leq 0,\ if\ \left(V_g + V_q - V_p\right) < 0$$

$$V_2 = V_g - V_p - 0.5V_c \geq 0,\ if\ \left(V_g - V_p\right) \geq 0$$

$$V_2 = V_g - V_p + 0.5V_c \leq 0,\ if\ \left(V_g - V_p\right) < 0$$

V_g: absolute value of the shear force at the section under consideration due to dead loads ($V_g = V_{g1} + V_{g2} + V_{g3}$);
V_{g1}: absolute value of the shear force at the section under consideration due to the self-weight of the precast beam;
V_{g2}: absolute value of the shear force at the section under consideration due to the self-weight of the slab and barriers;
V_{g3}: absolute value of the shear force at the section under consideration due to the pavement;
V_q: absolute value of the shear force at the section under consideration due to each traffic cycle;
V_p: absolute value of the shear force at the section under consideration due the prestressing;

$$V_p = A_{p,b}\left(\sigma_{0p} - \Delta\sigma_p\right)\Sigma sin\alpha_p$$

α_p : angle of inclination of the tendon in relation to the longitudinal axis of the girders at the section under consideration (Figure 10);
V_c: parcel of the shear force resisted by the complementary mechanisms of the truss (it is important to note that, as indicated by NBR 6118 [15], a 50% reduction is considered in V_c to calculate V_1 and V_2. In NBR 6118 [42], the reduction was not indicated for Truss Model II).
$V_c = V_{c0}$, for Model I in reinforced elements (not used in this paper);
$V_c = V_{c1}$, for Model II in reinforced elements (not used in this paper);
$V_c = V_{c0}(1+M_0/M_{s,máx}) \leq 2V_{c0}$, for Model I in prestressed elements (not used in this paper);
$V_c = V_{c1}(1+M_0/M_{s,máx}) \leq 2V_{c1}$, for Model II in prestressed elements;
$V_{c1} = V_{c0}$, when $V_{s,máx} \leq V_{c0}$

$$V_{c1} = \left[\left(V_{R2} - V_{s,máx}\right) / \left(V_{R2} - V_{c0}\right)\right].V_{c0},\ when\ V_{s,máx} > V_{c0}$$

$$V_{c0} = 0.6\, f_{ct} b_{w,ef} d_s$$

V_{R2}: shear force strength regarding the diagonal compression failure of concrete;
$V_{R2} = 0.27\left[1 - \left(f_c / 250\right)\right] f_c b_{w,ef} d_s sin\left(2\theta\right)$, with f_c in MPa;
$V_{s,máx}$: maximum shear force at the analyzed section, given by $V_g + V_{qWIM,máx} - V_p$, where $V_{qWIM,máx}$ is the maximum shear force due to traffic (with impact) for the considered period for the WIM data;
f_{ct}: tensile strength of concrete; $f_{ct} = 0.21 f_c^{2/3}$, to $f_c \leq 50$ MPa, with f_c in MPa;
$b_{w,ef} = b_w - 0.5\phi_d,\ where\ \phi_d > b_w / 8$;
ϕ_d: diameter of the prestressing duct (Figure 10).

Fusco [43] explains that the ratio between the decompression moment (M_0) and the maximum moment in the region under analysis is a relative measure of the possible cracking degree of the member. Strictly speaking, the author elucidates that the decompression moment could be substituted by the cracking moment M_r (Equation 14). Thereby, this work computes M_r instead of M_0 and $M_{s,máx} = M_g + M_{qWIM,máx}$, where M_g is the nominal moment due to the dead loads ($M_{g1}+ M_{g2}+ M_{g3}$) and $M_{qWIM,máx}$, is the maximum moment due to traffic (with impact), all referring to midspan.

Regarding torsion, the variation of torsional moment ΔT assumes an absolute value of T_q, as long as there is no inversion in the direction between ($T_g + T_q$) and T_g. In the case of an inversion, ΔT is given by the highest absolute value between ($T_g + T_q$) e T_g.

T_q: torsional moment at the section under consideration from the traffic, associated with V_q;

T_g: torsional moment at the section under consideration due to the dead loads ($T_g = T_{g1} + T_{g2} + T_{g3}$);

T_{g1}: torsional moment at the section under consideration due to the self-weight of the precast beams;

T_{g2}: torsional moment at the section under consideration due to the self-weight of the slab and barriers;

T_{g3}: torsional moment at the section under consideration due to the pavement;

A_e : area enclosed by the centerlines of the wall of the equivalent hollow section, including inner hollow areas (section composed by rectangles as indicated in Stucchi and Skaf [39]). It is calculated according to girder dimensions, considering h_e = 10.5 cm;

h_e: wall thickness of the equivalent hollow section ($2c_1 \leq h_e \leq A/u_p$);

c_1: distance between the axis of the longitudinal corner rebar and the lateral face of the section;

A: total area of the cross-section (gross area of concrete);

u_p: perimeter of cross-section;

A_{90} : reinforcement area, perpendicular to the axis of the beam, contained in the equivalent wall. For the section under consideration, $A_{90} = A_{sw} / 2$ (two-legged stirrup).

5 FATIGUE-SAFETY ASSESSMENT

In this paper, fatigue safety is assessed for different traffic volumes. For the studied WIM station, the Average Daily Truck Traffic (ADTT) for two lanes is 3655. It is worth noting that the ADTT computes only heavy vehicles, according to the filter criteria presented. For fatigue-safety assessment, Rodrigues et al. [7] used ADTT = 5000 and Crespo-Minguillón and Casas [6] used ADTT = 6000 (both for two traffic lanes). Wassef et al. [8] used ADTT = 5000. The present paper assesses fatigue safety for three ADTT: 2500, 5000 and 7500. The correction in the traffic volume, therefore, is made by multiplying the damage calculated for the WIM traffic by the ratio ADTT/3655.

All results presented in this Section correspond to bridge girders designed following NBR 6118 [15]. The reliability indexes and fatigue life estimates for stirrups are evaluated using S-N curves for straight bars, as justified by several studies (Section 2.2).

5.1 Fatigue service life estimation

For the damage calculation (Equation 2), related to fatigue service life estimation, the S-N curves from *fib* [14] are utilized, as indicated in Table 1 (characteristic values), where all the variables are computed with deterministic values. The concrete strength under shear force is considered with $f_{ct} = f_{ctd}$, where $f_{ctd} = 0.15 f_{ck}^{2/3}$. The calculated damage is extrapolated for a year-period, considering the correction in ADTT and with Equation (3) the values for fatigue life of the girders are estimated.

Based on the Palmgren-Miner model, Jacob and Labry [44] explain that the estimates below 50 years are not adequate for a bridge project, estimates between 50 and a few hundred years can be considered as acceptable or good and estimates greater than 1000 years indicate unlimited fatigue life. These indicators, however, are only preliminary, since the conclusion about fatigue safety should be based, mainly, on the reliability indexes (probabilistic analysis performed in the next Section). This because even if the analysis considers the real spectrum of vehicles traveling over a bridge, the fatigue life calculation is based on deterministic values (characteristic S-N curves; characteristic concrete strength; DM = 1; nominal values for dead loads, reinforcement areas and elements dimensions), which, in reality, present variability.

The fatigue life estimation was performed for all girders. The estimates of longitudinal reinforcements (midspan section) and stirrups (section indicated in Figure 10) of all girders, for all ADTT considered, were found to be higher than 1000 years for both limited and complete prestressing, which indicates infinite fatigue life.

5.2 Reliability indexes

In literature, different values are observed for the target reliability index (β_t) for fatigue. Aspects such as consequences of failures, inspection, repair possibility or reference period may influence the choice of β_t. For a reference period of 50 years, *fib* [45] proposes β_t = 3.1 for the calibration of the partial safety factors for fatigue. For the same reference period, ISO 13822 [46] indicates β_t = 2.3 in the case of the possibility of inspecting the member subjected to fatigue and β_t = 3.1, in the case of no inspection possibility. Thus, the reinforcement in the concrete structures fits in β_t = 3.1, as stated by *fib* [45]. It is worth to mention that *fib* [45] recommends β_t = 3.8 for ULS, corresponding to medium consequences of failure, and β_t = 1.5 for SLS, corresponding to irreversible service failure. According to the model code, the value of β_t = 3.1 for fatigue corresponds to the ULS assessment in the case of low consequence of failure. For the unlimited fatigue life approach, which is not the case of the present paper, Wassef et al. [8] indicates β_t = 1.0.

The reliability indexes of the girders are calculated by evaluation of the limit state function, according to Equation 9, for the longitudinal reinforcement (midspan section) and stirrups (section indicated in Figure 10), for the design service life of 50 years (compatible with the reference period of β_t from *fib* [45]). The reliability indexes are calculated for the girders that presented the highest values of $\sum(1/N_i)$, related to the longitudinal and transverse reinforcement.

The random variables are presented in Table 6, where some of them are Brazilian statistics, as reported by Santiago [25], [26] and Santiago et al. [47], [48]. Other variables consider the statistics utilized in Nowak [27] and Wassef et al. [8]. The statistics for the dead load, obtained from Nowak [27], are computed in this work directly in the loads, i.e., the span length is considered as deterministic. Variables from Section 4 which are not indicated in Table 6 are considered as deterministic. For each random variable, related to longitudinal or transverse reinforcement, 50 values are generated by using the Latin Hypercube Sampling - LHS simulation technique. Crespo-Minguillón and Casas [6] also considers this number of simulations using LHS.

Table 6. Random variables (indicated in Figure 10 and Section 4).

Category	Variable	Distribution	Mean / Nominal	CV[1]	Remarks
Material characteristics	f_c (f_{ck} = 40 MPa)	Normal	1.16	0.11	Santiago [25]
	E_{cs}	Normal	1.04	0.04	Santiago [26]
	E_p	Normal	1.03	0.02	Santiago [26]
	E_s	Normal	1.03	0.02	E_p
	A_p, $A_{p,b}$	Lognormal	1.03	0.01	Santiago [25]
	A_s, A_{sw}	Lognormal	1.03	0.01	A_p
	σ_{0p}	Normal	0.97	0.08	Used in Wassef et al. [8][2]
	$\Delta\sigma_p$	Normal	1.05	0.10	Used in Wassef et al. [8][3]
Girder geometric data	b_s, b_w, b_i, b_f	Normal	1.00	0.04	Used in Wassef et al. [8][4]
	h_v, h_f, h_s, h_i	Normal	1.00	0.025	Used in Wassef et al. [8][4]
	t_s, t_i	Normal	1.00	0.025	h_s, h_i
	d_p, d_s	Normal	1.00	0.04	Used in Wassef et al. [8][4]
Load effect for dead loads	M_{g1}, V_{g1}, T_{g1}	Normal	1.03	0.08	Nowak [27]
	M_{g2}, V_{g2}, T_{g2}	Normal	1.05	0.10	Nowak [27]
	M_{g3}, V_{g3}, T_{g3}	Normal	1.10	0.25	Nowak [27]

Note 1: CV is the coefficient of variation (standard deviation/mean) Note 2: From Gross and Burns [28] Note 3: From Gross and Burns [28] and Tadros et al. [29] Note 4: From Naaman and Siriaksorn [30]

The damage relative to the WIM data is calculated for each simulation, according to the S-N curves indicated in Table 2, and extrapolated for the intended reference period (50 years) considering the correction of ADTT. With the calculated values, the probability distribution, moments, and parameters of the dependent variable $\sum(1/N_i)$ are obtained, which represents the load effect variable in the limit state function (9). The interior girder showed the highest values of $\sum(1/N_i)$ for the stirrups, and the exterior girder (near to rightmost lane) presented the highest values of $\sum(1/N_i)$ for the longitudinal reinforcement.

The damage calculation is performed using *Microsoft Excel*, while the simulations and parameters obtaining are performed in *Matlab*. It is found that the $\sum(1/N_i)$ variable fit the Lognormal distribution. Using ADTT = 5000 and limited prestressing, for example, Figure 11 shows the 50 values of $\sum(1/N_i)$ for stirrups of interior girder in Lognormal probability paper (moments and parameters are indicated in Table 9).

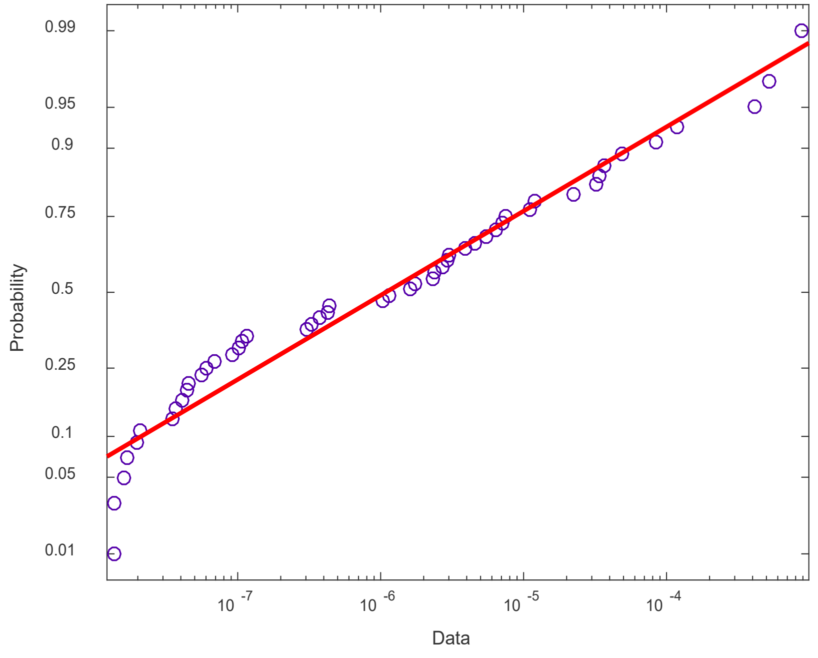

Figure 11. Values of dependent variable $\sum(1/N_i)$ for stirrups in Lognormal probability paper considering limited prestressing and ADTT = 5000.

After all simulations for limited and complete prestressing, for all ADTT values considered, it is verified that almost all calculated stress ranges are lower than 205 MPa for reinforcing steel (longitudinal and stirrups) and all stress ranges are lower than 165 MPa for prestressing steel. Therefore, the parameters of *DM*, which is the variable of resistance in the limit state function, can be obtained directly from Table 3 (Weibull distribution) and the procedure presented in Section 2.5, for weighting of DM_i, does not need to be applied.

Tables 7, 8 and 9 present moments for $\sum(1/N_i)$ and *DM* according to reinforcement, ADTT and prestress level. Using FORM, and the StRAnD [31] software, the fatigue reliability indexes are obtained, as indicated in Tables 7, 8 and 9. The longitudinal reinforcement (prestressing and reinforcing) and stirrups have shown fatigue reliability indexes higher than the intended value for design (β_t = 3.1). As expected, the reliability indexes decrease with the increase in traffic volume. The increase in ADTT from 5000 to 7500, however, did not significantly change the results. Complete prestressing presents higher safety levels than limited prestressing for both longitudinal reinforcements and stirrups. Although the Brazilian live load model is not in accordance with the unlimited fatigue life approach, as stated by Carneiro et al. [4], the design criteria, which involve partial safety factors and stress limits for fatigue design, guaranteed satisfactory fatigue safety levels for the evaluated bridge.

Table 7. Moments for dependent variables and reliability indexes (β) for prestressing steel (exterior girder) for design service life of 50 years.

ADTT (average daily truck traffic)	Prestress level	∑(1/Ni) - Lognormal		*DM* - Weibull		β
		Mean	Standard deviation	Mean	Standard deviation	
2500	Limited	6.302×10^{-3}	1.516×10^{-2}	1.072	0.367	4.1
	Complete	1.233×10^{-3}	1.319×10^{-3}	1.072	0.367	5.8
5000	Limited	1.260×10^{-2}	3.031×10^{-2}	1.072	0.367	3.7
	Complete	2.464×10^{-3}	2.636×10^{-3}	1.072	0.367	5.4
7500	Limited	1.891×10^{-2}	4.550×10^{-2}	1.072	0.367	3.4
	Complete	3.697×10^{-3}	3.954×10^{-3}	1.072	0.367	5.2

It is important to mention that according to EN 1992-2 [49], a fatigue design verification is generally not necessary for prestressing and longitudinal reinforcing steel, in regions where, under the frequent combination of actions (including prestressing) only compressive stresses occur at the extreme concrete fibres (like complete prestressing of NBR 6118 [15]). The high reliability indexes for complete prestressing from Tables 7 and 8 for longitudinal reinforcements confirm the EN 1992-2 [49] consideration.

Table 8. Moments for dependent variables and reliability indexes (β) for reinforcing steel (exterior girder) for design service life of 50 years.

ADTT (average daily truck traffic)	Prestress level	∑(1/Ni) - Lognormal		*DM* - Weibull		β
		Mean	Standard deviation	Mean	Standard deviation	
2500	Limited	1.247×10^{-3}	1.271×10^{-2}	1.169	0.618	4.0
	Complete	7.825×10^{-4}	1.803×10^{-3}	1.169	0.618	4.6
5000	Limited	2.494×10^{-3}	2.544×10^{-2}	1.169	0.618	3.7
	Complete	1.565×10^{-3}	3.608×10^{-3}	1.169	0.618	4.3
7500	Limited	3.740×10^{-3}	3.812×10^{-2}	1.169	0.618	3.5
	Complete	2.348×10^{-3}	5.412×10^{-3}	1.169	0.618	4.1

Table 9. Moments for dependent variables and reliability indexes (β) for stirrups (interior girder) for design service life of 50 years.

ADTT (average daily truck traffic)	Prestress level	∑(1/Ni) - Lognormal		*DM* - Weibull		β
		Mean	Standard deviation	Mean	Standard deviation	
2500	Limited	6.108×10^{-5}	6.874×10^{-3}	1.169	0.618	4.6
	Complete	5.512×10^{-5}	3.472×10^{-4}	1.169	0.618	5.3
5000	Limited	1.224×10^{-4}	1.379×10^{-2}	1.169	0.618	4.4
	Complete	1.102×10^{-4}	6.945×10^{-4}	1.169	0.618	5.0
7500	Limited	1.832×10^{-4}	2.062×10^{-2}	1.169	0.618	4.3
	Complete	1.654×10^{-4}	1.042×10^{-3}	1.169	0.618	4.9

6 CONCLUSIONS

This work assessed the fatigue safety level provided by Brazilian design standards for a concrete highway bridge, using weigh-in-motion (WIM) data of an important federal Brazilian highway. The fatigue service life and fatigue reliability indexes for design life (50 years) were evaluated for prestressed girders. Using limited and complete prestressing levels, different traffic volumes were considered.

It was found that multiple presence trucks can be safely replaced by the analysis of individual trucks, except for side-by-side truck case. In addition, the *Rainflow* cycle method can be replaced by the maximum vehicles load effects. The design of longitudinal reinforcements (reinforcing and prestressing) and stirrups according to Brazilian codes ensured fatigue reliability indexes higher than values recommended by *fib* [45], that is, given the design conditions, it is unlikely that these reinforcements will fail due to fatigue. All fatigue life estimates exceeded 1000 years, which indicates unlimited fatigue life. Although the Brazilian live load model does not comply with the unlimited fatigue life approach, as stated by Carneiro et al. [4], the partial safety factors and stress limits for fatigue design guaranteed satisfactory fatigue safety levels for the evaluated bridge. It is important that the methodology presented in this paper be applied to a greater number of concrete bridges, to provide more general assessment of fatigue safety levels provided by Brazilian design standards.

ACKNOWLEDGEMENTS

This study has been co-sponsored by CNPq, CAPES, Arteris S.A. and ANTT. The authors gratefully acknowledge the support of this research.

REFERENCES

[1] Associação Brasileira de Normas Técnicas, *Carga Móvel Rodoviária e de Pedestres em Pontes, Viadutos, Passarelas e Outras Estruturas*, NBR 7188, 2013.

[2] W. Pfeil, *Pontes em Concreto Armado.* Rio de Janeiro, R.J.: Livros Técnicos e Científicos, 1979.

[3] Associação Brasileira de Normas Técnicas, *Ações e Segurança nas Estruturas – Procedimento*, NBR 8681, 2003.

[4] A. L. Carneiro, E. L. Portela, and T. N. Bittencourt, "Development of Brazilian highway live load model for unlimited fatigue life," *Rev. IBRACON Estrut. Mater.*, vol. 13, no. 4, pp. e13407, 2020, http://dx.doi.org/10.1590/S1983-41952020000400007.

[5] E. L. Portela, "Analysis and development of a live load model for Brazilian concrete bridges based on WIM data," Ph.D. dissertation, Polytech. Sch., Univ. São Paulo, São Paulo, Brasil, 2018. Accessed: Apr. 15, 2020. [Online]. Available: https://www.teses.usp.br/teses/disponiveis/3/3144/tde-11122018-151658/pt-br.php

[6] C. Crespo-Minguillón and J. R. Casas, "Fatigue reliability analysis of prestressed concrete bridges," *J. Struct. Eng.*, vol. 124, no. 12, pp. 1458–1466, 1998.

[7] J. F. S. Rodrigues, J. R. Casas, and P. A. O. Almeida, "Fatigue-safety assessment of reinforced concrete (RC) bridges: application to the Brazilian highway network," *Struct. Infrastruct. Eng.*, vol. 9, no. 6, pp. 601–616, 2013, http://dx.doi.org/10.1080/15732479.2011.598939.

[8] W. G. Wassef et al., *Calibration of AASHTO LRFD Concrete Bridge Design Specifications for Serviceability, NCHRP Project 12-83.* Washington, DC: National Academy of Sciences, 2014. Accessed: Apr. 15, 2020. [Online]. Available: : https://www.nap.edu/catalog/22407/calibration-of-aashto-lrfd-concrete-bridge-design-specifications-for-serviceability

[9] D. Yan et al., "Lifetime fatigue reliability evaluation of short to medium span bridges under site-specific stochastic truck loading," *Adv. Mech. Eng.*, vol. 9, no. 3, pp. 1–12, 2017, http://dx.doi.org/10.1177/1687814017695047.

[10] P. Junges, "Análise de fadiga em pontes curtas de concreto armado a partir de dados de sistemas B-WIM," Ph.D. dissertation, Univ. Fed. Sta. Catarina, Florianópolis, SC, Brasil, 2017.

[11] C. S. Wang et al., "Fatigue reliability assessment method for concrete girder bridges," in *Proc. Int. Conf. on Maintenance, Monitoring, Safety, Risk and Resilience of Bridges and Bridge Networks*, IABMAS, 2016.

[12] A. Mankar et al., "Probabilistic reliability framework for assessment of concrete fatigue of existing RC bridge deck slabs using data from monitoring," *Eng. Struct.*, vol. 201, no. 109788, pp. 1–11, 2019, http://dx.doi.org/10.1016/j.engstruct.2019.109788.

[13] A. Mankar, S. Rastayesh, and J. D. Sorensen, "Fatigue Reliability analysis of Cret De l'Anneau Viaduct: a case study," *Struct. Infrastruct. Eng.*, vol. 16, no. 4, pp. 762–771, 2020, http://dx.doi.org/10.1080/15732479.2019.1633361.

[14] Fédération Internationale du Béton, *vol. 2, Model Code 2010.* Lausanne, Suiça: FIB, 2010.

[15] Associação Brasileira de Normas Técnicas, *Projeto de Estruturas de Concreto – Procedimento*, NBR 6118, 2014.

[16] European Committee for Standardization, *Eurocode 2: Design of concrete structures – Part 1-1: General rules and rules for buildings*, EN 1992-1-1, 2004.

[17] M. Plos et al., *Non-Linear Analysis and Remaining Fatigue Life of Reinforced Concrete Bridges. Background Document D4.5* (Sustainable Bridges, Assessment for Future Traffic Demands and Longer Lives). Bruxelas, Bélgica: European Commission, 2007.

[18] C. Higgins et al., "High-cycle fatigue of diagonally cracked RC bridge girders: laboratory tests," *J. Bridge Eng.*, vol. 12, no. 2, pp. 226–236, 2007, http://dx.doi.org/10.1061/(ASCE)1084-0702(2007)12:2(226).

[19] C. Higgins et al., *Assessment Methodology for Diagonally Cracked Reinforced Concrete Deck Girders* (Final Report, SPR 350-SR 500-91). Washington, D.C.: Oregon Department of Transportation, Federal Highway Administration, 2004.

[20] P. M. Bachman, M. E. Kreger, and J. E. Breen, *An Exploratory Investigation of Shear Fatigue Behavior of Prestressed Concrete Girders* (Research Report, 465-1). Austin, Texas: Center for Transportation Research, The University of Texas at Austin, 1987.

[21] C. Souza et al., "Fatigue analysis of box-girder webs subjected to in-plane shear and transverse bending induced by railway traffic," *Eng. Struct.*, vol. 54, pp. 248–261, 2013, http://dx.doi.org/10.1016/j.engstruct.2013.04.008.

[22] M. Hillebrand and J. Hegger, "Fatigue testing of shear reinforcement in prestressed concrete t-beams of bridges," *Appl. Sci. (Basel)*, vol. 10, no. 16, pp. 5560, 2020, http://dx.doi.org/10.3390/app10165560.

[23] M. Hillebrand, F. Teworte, and J. Hegger, "Shear fatigue of prestressed I-beams with shear reinforcement," *Struct. Concr.*, pp. 1–15, 2020, http://dx.doi.org/10.1002/suco.202000187.

[24] R. E. Melchers and A. T. Beck, *Structural Reliability Analysis and Prediction*, 3rd ed. London: Wiley, 2018.

[25] W. C. Santiago, "Calibração baseada em confiabilidade dos coeficientes parciais de segurança das principais normas brasileiras de projeto estrutural", Doctoral dissertation, Univ. S. Paulo, São Carlos, SP, Brasil, 2019.

[26] W. C. Santiago, *Calibração baseada em confiabilidade dos coeficientes parciais de segurança de normas brasileiras de projeto estrutural* (Texto do exame de qualificação). São Carlos, SP: Universidade de São Paulo, 2017.

[27] A. S. Nowak, *Calibration of the LRFD Bridge Design Code* (NCHRP Report, 368). Washington, D.C.: Transportation Research Board, National Research Council, 1999.

[28] S. Gross and N. Burns, *Field Performance of Prestressed High Performance Concrete Highway Bridges in Texas* (Research Report, 9-580/589-2). Austin, Texas: Texas Department of Transportation, Center for Transportation Research, University of Texas at Austin, 2000.

[29] M. Tadros et al., *Prestress Losses in Pretensioned High-Strength Concrete Bridge Girders* (NCHRP Report, 496). Washington, DC: Transportation Research Board of the National Academies, 2003.

[30] A. E. Naaman and A. Siriaksorn, "Reliability of partially prestressed beams at serviceability limit states," *PCI J.*, vol. 27, no. 6, pp. 66–85, 1982.

[31] A. T. Beck, "StRAnD – Structural Reliability Analysis and Design: manual do usuário", São Carlos, SP, Brasil: USP, 2008.

[32] A. Nowak and K. Collins, *Reliability of Structures.* New York, NY, USA: McGraw-Hill, 2013.

[33] Agência Nacional de Transportes Terrestres. *Desenvolvimento do Modelo de Deterioração de Pavimentos Asfálticos com Uso de Instrumentação e Sistema Weigh in Motion* (Relatório final). Brasília, D.F.: ANTT, 2016.

[34] A. C. R. Laranjeiras "Fadiga das estruturas de concreto," in *An. II Simp. EPUSP Estrut. Concr.*, São Paulo, SP, Brasil, 1990.

[35] Departamento Nacional de Infraestrutura de Transportes. *Quadro de Fabricantes de Veículos*. Brasília, DF: Ministério dos Transportes, 2005.

[36] Departamento Nacional de Infraestrutura de Transportes. *Quadro de Fabricantes de Veículos. Versão 4.1*. Brasília, DF: Ministério dos Transportes, 2007.

[37] Departamento Nacional de Infraestrutura de Transportes. *Quadro de Fabricantes de Veículos*. Brasília, D.F.: Ministério dos Transportes, 2009.

[38] L. F. Martha, *Ftool: Interactive-Graphics Program for Structural Analysis. Version 4.00*. 2018. Accessed: Apr. 15, 2020. [Online]. Available: https://webserver2.tecgraf.puc-rio.br/ftool

[39] F. R. Stucchi and K. J. Skaf, *Pontes e Grandes Estruturas: Projeto de Superestrutura em Concreto Protendido*. São Paulo, SP: Escola Politécnica, Universidade de São Paulo, 2006.

[40] Instituto Brasileiro do Concreto, *Comentários e Exemplos de aplicação,* ABNT NBR 6118:2014, 2015.

[41] P. A. O. Almeida, J. F. S. Rodrigues, and A. B. Lima, *Critérios de Otimização de Projetos de Pontes a Partir de Espectros de Aceleração Induzidas por Veículos nos Tabuleiros*. São Paulo, SP: LSE, 2010.

[42] Associação Brasileira de Normas Técnicas, *Projeto de Estruturas de Concreto – Procedimento*, NBR 6118, 2003.

[43] P. B. Fusco, *Estruturas de Concreto: Solicitações Tangenciais.* Pini Ltda, São Paulo, 2008.

[44] B. Jacob and D. Labry, "Evaluation of the effects of heavy vehicles on bridges: fatigue,", in *7th International symposium on heavy vehicle weights & dimensions*, Delft, 2002.

[45] Fédération Internationale du Béton, *vol. 1, Model Code 2010*. Lausanne, Suiça: FIB, 2012.

[46] International Organization for Standardization. *Bases for Design of Structures – Assessment of Existing Structures*, ISO 13822, 2010.

[47] W. C. Santiago, H. M. Kroetz, and A. T. Beck, "Reliability-based calibration of Brazilian structural design codes used in the design of concrete structures," *Rev. IBRACON Estrut. Mater.*, vol. 12, no. 6, 2019. http://dx.doi.org/10.1590/s1983-41952019000600004.

[48] W. C. Santiago et al., "Reliability-based calibration of main Brazilian structural design codes," *Lat. Am. J. Solids Struct.*, vol. 17, no. 1, pp. e245, 2020, http://dx.doi.org/10.1590/1679-78255754.

[49] European Committee for Standardization, *Eurocode 2: Design of Concrete Structures - Part 2: Concrete Bridges – Design and detailing rules*, EN 1992-2, 2005.

Author contributions: ALC: conceptualization, methodology, formal analysis, writing, proofreading; ELP: data curation, writing review, proofreading; TNB: data curation, funding acquisition, supervision, proofreading; ATB: formal analysis, writing review, proofreading.

Editors: Mauro Real, Guilherme Aris Parsekian.